



THE UNIVERSITY
of ADELAIDE

Hemodynamics of Diseased Coronary Arteries

NAVID FREIDONIMEHR

School of Mechanical Engineering
The University of Adelaide
South Australia, 5005
Australia

A thesis submitted in fulfilment of the requirements
for the degree of Ph.D. in Mechanical Engineering

June 16, 2021

Ph.D. Thesis

June 16, 2021

School of Mechanical Engineering
The University of Adelaide
Adelaide, Australia

Typeset by the author using L^AT_EX.
Printed in Australia

Copyright © 2021 Navid Freidoonimehr, and The University of Adelaide,
Australia

All right reserved. No part of this report may be used or reproduced in any form or by any means, or stored in a database or retrieval system without prior written permission of the university except in the case of brief quotations embodied in critical articles and reviews.

Abstract

Cardiovascular diseases are one of the main causes of death worldwide. A common cardiovascular disease is atherosclerosis, caused by plaque deposition on the arterial wall which leads to the obstruction of the blood flow, known as stenosis. Atherosclerosis can form in any part of the arterial system but it may have serious consequences when located in one of the coronary arteries which supply blood to the heart. Plaque formation inside a coronary artery influences the flow behaviour and leads to the development of turbulence structures with physiological consequences, such as pressure drop. Percutaneous coronary intervention (PCI) is one of the most common treatments for coronary artery diseases (CADs). There are several benefits of PCI over other alternative methods for treatment of CADs including lower risks of complications and much shorter recovery period. However, it can result in thrombosis and in-stent restenosis, which are the major drawbacks of coronary stent placement in patients with CADs. It was shown that the likelihood of occurrence of restenosis and thrombosis is a function of the wall shear stress (WSS) distribution. The motivation for the research presented in this thesis is to develop an understanding of the hemodynamics of stenosed and stented coronary arteries with an ultimate goal of improving patient outcomes. This can only be achieved if the effect of stenoses and stents on the flow behaviour in arteries is well-characterised. Hence, in this thesis the relationship between the shape of stenosis, stent pattern, the downstream transitional flow behaviour, and the hemodynamic parameters is investigated.

The research presented in this thesis is focused on the development of an in-depth understanding of the hemodynamics of diseased coronary arteries. Extensive pressure drop measurements, visualisation of the flow using particle image velocimetry (PIV), and computational modelling of the flow were conducted. Attention was mainly given to the stenosed and stented coronary arteries by investigating their influence on the flow behaviour, including velocity profile, pressure drop, time-averaged and -dependent WSS, and turbulent kinetic energy.

The need for modelling the temporal geometric variations of the coronary arteries during a cardiac cycle for the investigation of the hemodynamics is discussed. Temporal geometric variations of the coronary arteries during a cardiac cycle are classified as a superposition of the changes in the position, curvature and torsion of the coronary artery and the variations in lumen cross-sectional shape due to distensible wall motion induced by the pulse pressure and/or contraction of the myocardium in a cardiac cycle. A sensitivity analysis was conducted to evaluate the effects of temporal geometric variations of the coronary arteries on the pressure drop and WSS. The results show that neglecting the effects of temporal geometric variations results in less than 5% deviation of the time-averaged pressure drop and WSS values. However, they lead to an approximately 20% deviation in the temporal geometric variations of hemodynamic parameters, such as

time-dependent WSS. Based on the presented discussion, the temporal geometric variations of coronary arteries were not modelled in this thesis and the focus was on modelling the flow dynamics to develop an in-depth understanding of the flow features inside the stenosed and stented coronary arteries.

In the next stage of the research, a model incorporating the plaque geometry, the pulsatile inlet flow and the induced turbulence in a stenosed coronary artery was developed and validated against numerical and experimental data. The transitional flow behaviour was quantified by investigation of the changes in the turbulent kinetic energy. The results suggest that there is a high risk of the formation of a secondary stenosis at a downstream distance of equal to 10 times the artery diameter in the regions to the side and downstream of the initial stenosis due to existence of the recirculation zones and low shear stresses. The applicability of the obtained results was tested with a patient-specific stenosed coronary artery model.

Furthermore, for the non-invasive determination of the pressure drop in a stenosed artery model a mathematical model incorporating different physical parameters such as blood viscosity, artery length and diameter, flow rate and flow profile, and shape and degrees of stenosis, was developed. Extensive experimental pressure measurements were conducted for a wide range of degrees and shapes of stenosis to form a database in the process of the development of this equation. The validity of the developed relationship was also tested for the stenosed coronary artery models with the physiological flow profile of the left and right coronary arteries by comparing the pressure drop obtained from the developed equation and those from the experimental measurements. Moreover, the effect of artery curvature on the pressure drop and fractional flow reserve (FFR) was investigated. The results show that neglecting the effect of artery curvature results in under-estimation of pressure drop by about 25–35%. The developed equation can determine the pressure drop inside a stenosed coronary artery using the measurement of the flow profile inside the artery as well as the images of the stenosed coronary artery.

In order to develop an understanding of the hemodynamic performance of coronary stents, the effect of stent design on the hemodynamics of stented arteries was investigated experimentally and numerically. An innovative PIV technique was implemented for the visualisation of the entire flow and the investigation of WSS within the stent struts without covering the region of interest inside a stented coronary artery model. This novel technique was based on the construction of a transparent stented artery using silicone cast in one piece, instead of inserting a metal or non-metallic stent inside a cast artery model, which are translucent and distort the field of view. The results show that WSS is strongly dependent on the design of the stent. It was also shown that the likelihood of occurrence of restenosis is strongly dependent on strut depth and thickness, the distance between two consecutive struts, and the shape of the connector between the struts.

This thesis provides an improved understanding of the hemodynamics of diseased coronary arteries with an ultimate goal of improving patient outcomes. The findings will provide a basis for improvement of the most common CAD diagnostic and treatment methods. Based on the results of this research, the susceptible regions for the formation of a new stenosis downstream of the initial stenosis can be determined. Identification of these locations, which are a function of different physical and geometrical parameters, such as shape, degree and eccentricity of the initial stenosis, can provide the necessary information for prevention of the distal propagation of stenoses. Furthermore, the equation developed

to evaluate FFR non-invasively in this research can be used as a gatekeeper to prevent unnecessary FFR procedures for all patients. This will result in better patient outcomes and reduce costs related to unnecessary invasive FFR which will benefit the health system. In addition, the results of this study provide a better understanding of the effect of stents on the flow which can be used to improve stent designs.

Declaration

I certify that this work contains no material which has been accepted for the award of any other degree or diploma in my name, in any university or other tertiary institution and, to the best of my knowledge and belief, contains no material previously published or written by another person, except where due reference has been made in the text. In addition, I certify that no part of this work will, in the future, be used in a submission in my name, for any other degree or diploma in any university or other tertiary institution without the prior approval of the University of Adelaide and where applicable, any partner institution responsible for the joint-award of this degree.

I acknowledge that copyright of published works contained within this thesis resides with the copyright holder(s) of those works.

I also give permission for the digital version of my thesis to be made available on the web, via the University's digital research repository, the Library Search and also through web search engines, unless permission has been granted by the University to restrict access for a period of time.

I acknowledge the support I have received for my research through the provision of an Australian Government Research Training Program Scholarship.

Navid Freidoonimehr

Acknowledgements

I would like to thank my principal supervisor, Prof Maziar Arjomandi, for his unwavering support, relentless encouragement, and invaluable guidance throughout the past three years. I truly appreciate the support of my co-supervisors, Dr Rey Chin and Prof Anthony Zander. I have learnt a lot from you all, and I am very grateful for your insightful supervision without which this thesis would not have been completed. I really appreciate the time and effort that you all put into my work.

I would also like to thank the support provided by the technical staff of the Mechanical and Electronic workshops, particularly Phil Schmidt, Thomas Stanef, Scott Letton, Hayden Westell, Robert Dempster, Pascal Symons, Jozef Kumberger, Jason Peak, and Ian Linke for helping me with the design and manufacturing of my experimental rigs. I would like to thank Dr. Fabien Voisin for his kind support and help at the Phoenix High Performance Computing (HPC) service at the University of Adelaide.

To my supportive family, thank you for your love and never-ending support. To my father, my mother, my beautiful sisters, Marjan and Elham, who have always been around to support me. I can only hope one day I am as half as thoughtful and considerate as you have been to me. To my gorgeous wife, Azadeh. Thank you for your unlimited love and support. This journey has been as much hard work for you as it has been for me. Being colleagues, sharing ideas, guiding through the challenges, and more importantly your endless love make this journey possible for me.

I would like to thank my friends and officemates for their encouragement and all the good times that we spent together, which were always refreshing throughout the journey of the Ph.D., specifically to Amir, Nima, and Mahyar, with whom I have shared the ups-and-downs of my Ph.D., and finally to my long-standing friends, Milad, Sajad, and Behnam.

Finally, I would like to acknowledge the financial support I have received for my research through the provision of an Australian Government Research Training Program Scholarship.

Acronyms

BMS	bare-metal stent
CABG	coronary artery bypass grafting
CAD	coronary artery disease
CFD	computational fluid dynamics
CVD	cardiovascular disease
DES	drug-eluting stent
DNS	direct numerical simulation
FFR	fractional flow reserve
FOV	field of view
IHD	ischemic heart disease
ISR	in-stent restenosis
LAD	left anterior descending coronary artery
LCA	left coronary artery
LCx	left circumflex coronary artery
LDL	low-density lipoprotein
LES	large eddy simulation
LMCA	left main coronary artery
OSI	oscillatory shear index
PCI	percutaneous coronary intervention
PIV	particle image velocimetry
POD	proper orthogonal decomposition
RCA	right coronary artery
RMS	root-mean-square
TAWSS	time-averaged wall shear stress
TKE	turbulent kinetic energy
WSS	wall shear stress

Contents

Abstract	ii
Declaration	v
Acknowledgements	vi
Acronyms	vii
List of Figures	xii
List of Tables	xxviii
1 Introduction	1
1.1 Background	1
1.2 Aims and objectives	4
1.3 Thesis outline	5
1.4 Publications arising from this thesis	7
1.5 Thesis format	8
References	8
2 Literature review	11
2.1 Hemodynamic fundamentals	11
2.1.1 Blood vessels	11
2.1.2 Blood rheology	13
2.2 Coronary artery disease	14
2.2.1 Coronary artery structure	15
2.2.2 Coronary arterial stenosis morphology	16
2.3 Mechanical representatives of coronary artery disease	22

2.3.1	Transitional flow behaviour	22
2.3.2	Shear stress	29
2.3.3	Pressure drop and FFR	32
2.4	Treatment of coronary artery disease by stent implantation	39
2.4.1	Computational fluid dynamics modelling of stented arteries	41
2.4.2	Experimental investigation of the hemodynamics of stented arteries	46
2.5	Concluding remarks and perspectives	49
	References	50
3	Effects of temporal geometric variations of the coronary arteries	60
3.1	Chapter overview	60
3.2	Effects of temporal geometric variations of the coronary arteries	62
3.2.1	Introduction	65
3.2.2	Effect of dynamic vessel motion of coronary arteries on the flow behaviour	70
3.2.3	Effect of wall compliance of the coronary arteries on the flow behaviour	74
3.2.4	Discussion	81
	References	84
4	Transitional flow behaviour in a stenosed coronary artery	90
4.1	Chapter overview	90
4.2	Transitional flow in a stenosed coronary artery	92
4.2.1	Introduction	95
4.2.2	Model geometry and its development	98
4.2.3	Results and discussion	104
4.2.4	Conclusion	122
	References	123
5	Effect of shape of the stenosis on the hemodynamics of blood flow	126
5.1	Chapter overview	126
5.2	Effect of shape of the stenosis	128
5.2.1	Introduction	131
5.2.2	Model geometry and computational methodology	133

5.2.3	Results and discussion	142
5.2.4	Conclusions	153
5.2.5	Acknowledgement	154
5.2.6	Conflict of interest	154
5.2.7	Data availability statement	154
	References	155
6	Pressure drop in stenosed coronary arteries	159
6.1	Chapter overview	159
6.2	Pressure drop in straight stenosed coronary arteries	161
6.2.1	Introduction	164
6.2.2	Methodology	167
6.2.3	Results	175
6.2.4	A pulsatile model with the physiological flow profile of the coronary artery: case studies	183
6.2.5	Conclusions	186
	References	187
6.3	Pressure drop in curved stenosed coronary arteries	191
6.3.1	Introduction	194
6.3.2	Experimental setup	197
6.3.3	Results	200
6.3.4	Discussion	202
6.3.5	Conclusions	208
	References	209
7	Hemodynamics of stented arteries	214
7.1	Chapter overview	214
7.2	Flow visualisation of the stented arteries	216
7.2.1	Introduction	219
7.2.2	Materials and methods	221
7.2.3	Results	230
7.2.4	Discussion	233
7.2.5	Conclusions	235
	References	236

7.3	Computational modelling of the stented arteries	240
7.3.1	Introduction	243
7.3.2	Methodology	244
7.3.3	Results	247
7.3.4	Conclusion	250
	References	250
8	Conclusions and future work	252
8.1	Investigation of the post-stenotic transition to turbulence inside stenosed coronary arteries	252
8.2	Establishment of a link between variations in the shape of stenosis and the downstream blood flow behaviour	253
8.3	Development of a non-invasive approach to evaluate pressure drop inside coronary arteries	255
8.4	Investigation of the hemodynamics of stented arteries	256
8.5	Recommendations for future work	256
	References	259
	Appendices	260
	Effect of degree of stenosis on the pulsatile flow pressure drop	A-1
	Hemodynamic of a coronary artery: a PIV measurement	B-1

List of Figures

1.1	Australia’s leading causes of death in 2019 based on Australian Bureau of Statistics (2020) data.	1
1.2	The blockage of the LAD and the diagonal branch at different locations for a 48-year-old man (Basavarajaiah and Qadir 2015).	2
1.3	Stenotic flow behaviour inside an artery demonstrating the susceptible locations for flow separation (Libby 2015).	3
1.4	Representative digital images of coronary artery cross-sections, depicting the range of atherosclerotic stenosis based on their shapes (Beach et al. 2011).	4
2.1	Structural layers of a normal artery vessel (Patel 2019).	12
2.2	(a) The blood viscosity as a function of vessel diameter (Costa 2016) and (b) blood viscosity obtained from Newtonian, Casson, and Carreau-Yasuda models as a function of shear rate. The range of shear rate for different blood vessels is also shown in part (b) (Baratchi et al. 2017; Boyd et al. 2007; Cho and Kensey 1991; Loscalzo and Schafer 2003). The vertical dashed line in part (a) refers to the threshold vessel diameter of 0.3 mm, above which the viscosity is constant.	15
2.3	Schematics of a coronary arterial tree illustrating the main arteries, reproduced from Baylor College of Medicine (2020).	16
2.4	Schematics of the plaque geometrical morphology parameters including (a) the plaque length, degree of stenosis which is defined as $S = A_1/A_0 \times 100$, eccentricity, and stenosis sharpness ((b) shows a curved stenosis without sharpness and (c) shows a stenosis with a sharp edge). l is the plaque length, defined as the stream-wise length of a stenosis. A_0 and A_1 are the cross-sectional area of the unobstructed artery and the minimum constricted cross sectional area, respectively.	17
2.5	(a) Intravascular ultrasound (IVUS) image of a vulnerable atherosclerotic plaque of the RCA showing multiple luminal irregularities. (b) shows a mild concentric lesion at the distal portion at the location of A, (c) shows a significant eccentric lesion with 67% plaque area at the proximal portion at the location of B, and (d) shows an eccentric lesion at the very proximal portion at the location of C (Yamagishi et al. 2000).	18

2.6	Variation of instantaneous stream-wise velocity normalised by the mean inlet velocity along the stream-wise centreline of the vessel normalised with the artery diameter for steady flow through the 75% axisymmetric and eccentric stenosis models at $Re = 1000$ (Varghese et al. 2007a). . . .	19
2.7	Instantaneous vorticity magnitude contours for steady flow through the eccentric stenosis model, shown on top, at $Re = 1000$ for mid-cross-sectional (a) $x - z, y = 0$ and (b) $x - y, z = 0$ planes (Varghese et al. 2008). . . .	19
2.8	Variations of pressure drop gradient for (a) RCA and (b) LAD arteries with eccentric and concentric shapes of stenosis (Guleren 2013). The solid blue and dashed orange lines refer to concentric and eccentric shapes of a stenosis, respectively.	20
2.9	Coherent structures coloured by instantaneous normalised vorticity magnitude (Ozden et al. 2020). Vorticity is normalised by u_{max}/D	21
2.10	Normalised (a) mean pressure changes and (b) TKE along the centrelines of stenosed models (Ozden et al. 2020). Pressure is normalised by ρu_{max}^2 , where u_{max} is the maximum velocity in a cardiac cycle in the artery model and TKE is normalised by the maximum velocity squared (u_{max}^2). $x/D = 0$ is the stream-wise position located at the end of the stenosis.	22
2.11	A schematic of the flow inside a stenosed artery model showing jet flow and reverse flow regions, recirculation zones, and velocity profiles in different stream-wise locations, adapted from Caro et al. (2011).	23
2.12	Contour plot of TKE for different Reynolds number including (a) $Re = 750$, (b) $Re = 1400$ and (c) $Re = 2000$ in an asymmetric constricted rectangular channel (Mittal et al. 2003). h is the height of the channel.	25
2.13	(a) Computational domain and coordinate system of the stenotic channel and (b) time history of the stream-wise velocity fluctuation normalised by its maximum value (u''/u''_{max}) based on phase-averaging over the last three pulsation cycles, along the central streamline ($y/h = 0.5$ and $z/h = 1.5$) and for $Re = 2000$ (Molla et al. 2012).	26
2.14	(a) Schematic of a symmetric stenotic rectangular channel and the coordinate system, and TKE profiles for (b) different Reynolds numbers with $S = 75\%$, and (c) different degrees of stenosis with $Re = 2000$ along the central streamline of the domain (Khair et al. 2015). h is the height of the channel.	27
2.15	Distribution of mean value of TKE normalised by the area-averaged velocity as a function of Reynolds number for three runs of a porcine blood sample (Biswas et al. 2016).	27
2.16	Coherent vortical structures of the Q-criterion coloured by the normalised instantaneous axial vorticity in the unsteady flow field for different phases in a pulsatile cycle for the common carotid artery model (Jabir and Lal 2016).	28

2.17	Contour maps of the TKE production rate per unit volume (Π) for two stenosis models: left column with $S = 45\%$ and a stenosis length of 20 mm and right column with $S = 48\%$ and a stenosis length of 16 mm at (a) $t/T = 0.125$, (b) $t/T = 0.175$, and (c) $t/T = 0.225$, respectively (Choi et al. 2018).	28
2.18	Arterial wall showing blood flow profile, shear stress and pressure acting on the endothelial cell (Ohashi and Sato 2005).	29
2.19	Non-dimensionalised time- and spanwise-averaged profile of the WSS ($\tau_w/\frac{1}{2}\rho U^2$) in a constricted channel for (a) different Reynolds numbers at $S = 75\%$ and (b) different degrees of stenosis at $Re = 2000$ (Khair et al. 2015). S refers to the degree of stenosis.	31
2.20	(a) WSS contour of the simulated coronary system showing an artificial plaque, highlighted in a circular red line, with $S = 70\%$ at the proximal of LCx (Melchionna et al. 2013). The plaque was modified from a vessel geometry of a typical clinical angiography. (b) zoomed-view of the the plaque showing the flow streamlines.	31
2.21	(a) Blood pressure and flow rate during a cardiac cycle as well as a schematic of the geometry of the coronary arterial tree, and (b) 2D unwrapped maps of WSS in the proximal LAD for different phases in a cardiac cycle (Eslami et al. 2019).	32
2.22	Schematic of FFR measurement, reproduced from Abbott (2020). $P_{proximal}$ is the proximal (aortic) pressure and P_{distal} is the distal coronary pressure.	33
2.23	Schematics of a simplified coronary artery model and the corresponding geometrical parameters. D is the internal diameter of the artery, t is the arterial thickness, L is the length of the artery, l is the length of the stenosis, r is the curvature radius, θ is the curvature angle, P_1 and P_2 are the pressure of the blood flow at the inlet and outlet, respectively, and V_1 and V_2 are the velocity of the blood flow at the inlet and outlet, respectively.	34
2.24	Free body diagram of the fluid disk element in a healthy simplified artery model. x and y are the stream-wise and vertical components in a Cartesian coordinate system, R is the arterial radius, $\pi R^2 P$ and $\pi R^2(P + dP)$ are the pressure forces acting on the fluid element disk, the control volume highlighted in red, and $2\pi R dx \tau_w$ is the shear force acting on the control volume with the stream-wise length of dx	34
2.25	Static pressure profile along the axis of the artery for different curvature angle (Yao et al. 2000). The stream-wise position in horizontal axis is normalised by the artery diameter.	38
2.26	Non-dimensionalised time- and spanwise-averaged profile of the wall pressure for (a) different Reynolds numbers with $S = 75\%$ and (b) different degrees of stenosis at $Re = 2000$ (Khair et al. 2015).	38
2.27	Pressure drop measured across multiple sequential stenoses with different flow rates (Li et al. 2017).	39

2.28	Stent deployment procedure (a) in a coronary artery where blood flow is obstructed by the growth of atherosclerotic plaque, the lesion is reached by a cardiac catheter encased in an inflatable balloon and wire-mesh stent, (b) the balloon is inflated to expand the stent, to dilate the artery and to compress the plaque, and (c) the balloon is subsequently deflated and withdrawn with the catheter, leaving the stent expanded against the arterial wall, adapted from The Editors of Encyclopaedia Britannica (2020). . . .	40
2.29	A schematic of potential complications of coronary stenting including (a) ISR and (b) stent thrombosis, adapted from Jeudy et al. (2011). Reprinted with permission from Curfman GD, Morrissey S, Jarcho JA, et al. Drug-eluting coronary stents—promise and uncertainty. N Engl J Med 2007, 8;356 (10):1059-1060, Copyright Massachusetts Medical Society.	40
2.30	Shear rate contours for (a) $L_s/D_s = 3.53$ with a 4 mm vessel, (b) $L_s/D_s = 5.88$ with a 2 mm vessel, and (c) $L_s/D_s = 10.55$ with the 4 mm vessel at peak diastolic flow (Berry et al. 2000). The lowest shear rates were observed in between the struts and the highest shear rates were located at the tops of the struts in all cases.	42
2.31	WSS distribution corresponding to (a) rectangular and (b) circular arc stent struts with different aspect ratios (Jiménez and Davies 2009). . . .	44
2.32	Flow stagnation areas at the mean flow rate for different stents during the accelerating phase of the flow cycle (Duraiswamy et al. 2009). In this graph, yellow indicates no flow separation and green indicates flow stagnation.	44
2.33	Spatial TAWSS distribution and plots of data from extracted lines on each side for (a) apposed and (b) severe malapposed cases (Jiang et al. 2019).	45
2.34	(a) Model of a stent made of Plexiglas, and normalised transversal velocity contour in the gap between two struts at (b) flow rate = 60 ml/min and (c) flow rate = 144 ml/min (Benard et al. 2003). The velocity is normalised by the mean flow velocity of 0.15 m/s.	47
2.35	Spatial profile of TAWSS in a XIENCE V stented artery, shown on top, for three regions of interest: (a) upstream, (b) mid-stent and (c) downstream at $Re = 160$ (Charonko et al. 2009). Standard deviation of the time history at each point is shown to give an indication of the relative temporal variability at each location. Wall regions marked as blocked were obscured by other struts in the FOV.	48
2.36	Raw PIV images of the vessel (a) without and (b) with an implanted stent, and (c) time-averaged velocity contour of the stented vessel (Tomaszewski et al. 2020).	49
3.1	Coronary angiogram showing the position of left coronary arteries during (a) diastole and (b) systole (reproduced from Mohlenkamp et al. (2002)).	66

3.2	Magnitude of changes in the displacement vector of the middle segment of the three main coronary arteries along the orthogonal axis and b) displacement of the proximal, middle, and distal segments of the RCA over a cardiac cycle (Johnson et al. 2004).	67
3.3	Intravascular ultrasound images of LAD in diastole (on the left) and systole (on the right). The inner tracing marks the lumen-intima boundary, and the outer tracing the outer margin of the intima-media layer (Shaw et al. 2002).	68
3.4	In vivo pulsatile flow velocity waveforms measured at the inlet of RCA arterial tree in porcine heart and dynamic changes of elastic vessel diameter represented by instantaneous diameter - mean diameter) / mean diameter $\times 100$ (Huo et al. 2009).	68
3.5	The normalised WSS versus the normalised time for the inner and outer walls of RCA for the cases with and without dynamic vessel motions at the location of tiny red line shown in schematics of the artery with (a) the steady inlet flow and (b) the pulsatile inlet flow. Time is normalized by the cardiac period and WSS is normalised with the steady inlet Poiseuille WSS value (Zeng et al. 2003). The blue solid line refers to the dynamic motion model and the orange dashed line refers to the model without dynamic motion. Inner wall refers to the wall closer to the centre of curvature and the outer wall is the furthest away wall from the centre of curvature. . . .	71
3.6	Correlations of (a) and (b) TAWSS between the dynamic and static wall models and correlations of (c) and (d) oscillatory shear index between the dynamic and static wall models of the patient-specific right coronary artery. (a) and (c) refer to the beginning to systole and (b) and (d) refer to the peak of the diastole in a cardiac cycle (Torii et al. 2009a).	72
3.7	WSS values in a cardiac cycle at the myocardial location of the artery, show in green dot, for the location proximal to the bifurcation (Prosi et al. 2004).	72
3.8	Temporal axial inner and outer WSS distribution at a) 5 diameters and b) 9 diameters from the LAD inlet and c) axial TAWSS distribution along the inner and outer walls of the LAD (Kolandavel et al. 2006). The blue solid line refers to the dynamic model and orange dashed line refers to the static model.	73
3.9	Normalised WSS versus normalised time for the inner and outer walls of RCA considering dynamic vessel motion for the cases with and without artery compliance for the locations near the a) proximal and b) distal of the artery (Zeng et al. 2003). Inlet flow rate which is normalised by the time-averaged flow rate is also plotted in part b. Time is normalized by the cardiac period and WSS is normalised with the steady inlet Poiseuille WSS value. The blue solid line refers to the case with compliance and orange dashed line refers to the case without compliance. The flow rate profile is also shown in black dot-dashed line.	78

3.10	Temporal WSS in a cardiac cycle for a) three locations in a main trunk of RCA, as shown top right and b) the locations in the bifurcated branch of RCA with diameter ratio = 0.5 ($DR = 0.5$), shown on the top left and $DR = 0.8$, shown on the top right (Huo et al. 2009). The blue solid line refers to the elastic wall and the orange dashed line refers to the rigid wall.	78
3.11	Comparison of a) TAWSS and b) OSI contours between the FSI model (top) considering both temporal variations of the RCA arteries and rigid-wall model (bottom) (Torii et al. 2009b).	79
3.12	TAWSS contour of the left coronary artery bifurcation model with (a) rigid wall model and (b) FSI model results (Malvè et al. 2012).	79
3.13	a) WSS distribution in a cardiac cycle at the end of the LM branch, beginning of the LCx branch and beginning of the LAD branch (Bahrami and Norouzi 2018). The blue solid line refers to the hyperplastic model and the orange dashed line refers to the rigid model. b) OSI contour for rigid and hyperelastic wall models.	79
3.14	a) Correlation of TAWSS between the rigid and FSI models at each 3 mm subsegment of the coronary arterial tree, shown in top right, with a total of 704 subsegments and b) Correlation of TAWSS between the rigid and FSI models for four quadrant at each cross section (Eslami et al. 2019). TAWSS had an excellent correlation with a $r - squared = 0.99$ in both subsegment and sub-arc analysis.	81
3.15	Comparison of the 2D unwrapped map of WSS of a) proximal LAD and b) proximal RCA obtained from rigid wall model (left column) and FSI (right column) for the peak flow and pressure phases in a cardiac cycle and the TAWSS (Eslami et al. 2019).	81
4.1	Transition to turbulence in combined steady and oscillatory flow showing the laminar and turbulent regions based on the different values of Reynolds numbers and Stokes'-layer-thickness ratio (Lodahl et al. 1998).	97
4.2	Schematic diagram of 3D asymmetric stenosed coronary artery with different degrees of stenosis shown with the percentage of area reduction.	99
4.3	Structured mesh for the stenosis model with 67% degree of stenosis using ICEM 18.2 with 640000 elements.	100
4.4	The physiological velocity waveform of the coronary artery adopted from (Davies et al. 2008).	101
4.5	(a) Schematic diagram of the artery model ($D=12.6$ mm) with stenosis (Peterson and Plesniak 2008)), (b) Pump input waveform, (c) Fully developed pulsatile pipe flow velocity at various phases, and (d) Centreline velocity waveforms at 2D upstream and downstream of the mid-stenosis section (For part (c) and (d): lines are the obtained numerical result of this project and the triangular symbols are experimental data obtained from (Peterson and Plesniak 2008)).	102

4.6	Schematic of the defined cross-sectional planes in stream-wise direction with more concentration near the stenosis and after it.	104
4.7	Area-weighted average of TKE for 48 different cross-sectional planes at max acceleration phase for different cycles of the case 3.	104
4.8	Area-weighted average of TKE for 48 different cross-sectional planes in stream-wise direction at four phases of the case 3.	107
4.9	Instantaneous coherent structures identified by the lambda-2 criterion ($\lambda_2 = -0.01$) coloured by the stream-wise velocity showing the downstream vortical structures at four phases in the fourth pulsation cycle of the case3 representing the max (a) deceleration and (c) acceleration and (b) min and (d) max velocities.	108
4.10	Instantaneous velocity profile along different lateral lines in different stream-wise locations at four phases in the fourth pulsation cycle of the case3.	109
4.11	Static pressure distribution along the stream-wise line located at $y = -1$ mm at four phases in the fourth pulsation cycle of the case3.	110
4.12	(a) Wall shear stress contour and different lines along the steam-wise direction at maximum velocity phase in the fourth pulsation cycle of the case3 and stream-wise distribution of the wall shear stress along the (b) top line, (c) side line and (d) bottom line at four phases in the fourth pulsation cycle of the case3.	111
4.13	Wall shear stress contour of max velocity phase of the fourth pulsation cycle of the case3 from (a) top view and (b) bottom view.	112
4.14	Wall shear stress stream-wise distribution for different lateral and vertical positions of max velocity phase of the fourth pulsation cycle of the case3.	113
4.15	Velocity contours and vectors at different planes and lines including (a) vertical direction, (b) lateral direction and (c) different circular cross-sectional planes of max velocity phase of the fourth pulsation cycle of the case3.	114
4.16	Area-weighted average of TKE for 48 different cross-sectional planes in stream-wise direction at max velocity phase of the fourth pulsation cycle for (a) different heart working condition ranging from resting to hyperemic heart working condition and (b) different degrees of stenosis including 16%, 39.1% and 67%.	115
4.17	Static pressure distribution along the stream-wise line located at $y = -1$ mm at max velocity phase of the fourth pulsation cycle for (a) different heart working condition ranging from resting to hyperemic heart working condition and (b) different degrees of stenosis including 16%, 39.1% and 67%.	116
4.18	Stream-wise distribution of the wall shear stress along the (a) top line, (b) side line and (c) bottom line at max velocity phase of the fourth pulsation cycle for different heart working condition ranging from resting to hyperemic flow condition (left side) and different degrees of stenosis including 16%, 39.1% and 67% (right side).	118

4.19	Schematic of the patient specific coronary artery model and the defined cross-sectional planes in stream-wise direction.	119
4.20	Velocity contours at different cross-sectional planes in stream-wise direction for different phases: (a) maximum deceleration, (b) minimum velocity, (c) maximum acceleration, and (d) maximum velocity of the third pulsation cycle for the hyperemic flow conditions.	120
4.21	Two different views of wall shear stress contours for different phases of the third pulsation cycle for the hyperemic flow conditions.	121
4.22	Area-weighted average of TKE for 35 different cross-sectional planes in stream-wise direction versus distance of the centre of planes from the inlet and plane numbers for different phases of the fourth pulsation cycle for the hyperemic flow conditions.	122
5.1	(a) A schematic of a stenosed coronary artery model with a crescent shape of the stenosis, (b) the other cross-sectional shapes of the stenosis investigated in the study and (c) the inlet time-dependent physiological left coronary artery flow velocity used for the simulation with the mean flow rate of 3.9 ml/s. All cross-sectional cases had a similar degree of stenosis of 73% representing a severe stenosis. The dashed vertical line in part (c) shows the maximum velocity phase in a cardiac cycle.	134
5.2	Structured mesh elements for stenosed coronary artery models with concentric and eccentric elongated shape of the stenosis in stream-wise and cross-sectional planes created using ICEM.	136
5.3	A schematic of the coronary arterial test rig showing the PIV setup and the cast stenosed coronary artery model.	137
5.4	Comparison of the velocity contour and vectors obtained from a) developed CFD model and b) PIV experiment for a case with an asymmetric stenosis and 67% degree of stenosis at the mean flow rate of 115 ml/min and the physiological left coronary artery flow profile (Freidoonimehr et al. 2021). The zone 1 is the jet flow regime, zone 2 is the recirculation zone and zone 3 is downstream flow. Comparison of the velocity profiles of mean stream-wise velocity normalised by maximum stream-wise velocity obtained from CFD and PIV at four stream-wise distances is shown in part (c). The black solid lines show the CFD data and the red circular symbols show the PIV results.	138
5.5	(a) Time history of the last 3 cycles of the instantaneous stream-wise velocity components as a function of stream-wise distance for pulsatile flow of the case with the bean-shape concentric stenosis, (b) phase-averaged stream-wise velocity component as a function of stream-wise distance, and (c) the fluctuating stream-wise velocity component as a function of stream-wise distance.	140

5.6	Mean stream-wise velocity contours in $y - z$ plane with $x = 0$ for different shapes of stenosis including a) round concentric, b) round eccentric, c) oval concentric, d) oval eccentric, e) elongated concentric, f) elongated eccentric, g) half-moon concentric, h) half-moon eccentric, i) bean-shape concentric, j) bean-shape eccentric, and k) crescent.	143
5.7	Instantaneous stream-wise velocity contours at the maximum velocity phase in the fourth pulsation cycle in $y - z$ plane with $x = 0$ for different shapes of stenosis including a) round concentric, b) round eccentric, c) oval concentric, d) oval eccentric, e) elongated concentric, f) elongated eccentric, g) half-moon concentric, h) half-moon eccentric, i) bean-shape concentric, j) bean-shape eccentric, and k) crescent.	144
5.8	Instantaneous cross-sectional velocity contours in $x - y$ plane at different stream-wise distances, $z/D = 1$ (first row), $z/D = 3$ (second row), and $z/D = 5$ (last row), at the maximum velocity phase in the fourth pulsation cycle for different shapes of stenosis including a) round concentric, b) round eccentric, c) oval concentric, d) oval eccentric, e) elongated concentric, f) elongated eccentric, g) half-moon concentric, h) half-moon eccentric, i) bean-shape concentric, j) bean-shape eccentric, and k) crescent.	144
5.9	Instantaneous stream-wise vorticity magnitude contours normalised by W_i/D at the maximum velocity phase in the fourth pulsation cycle for a) concentric and b) eccentric half-moon shape of stenosis. W_i is the mean inlet velocity.	145
5.10	Pressure drop along the length of the artery model at the maximum velocity phase in the fourth pulsation cycle for different shapes of stenosis.	145
5.11	TKE contours in $y - z$ plane with $x = 0$ for different shapes of stenosis including a) round concentric, b) round eccentric, c) oval concentric, d) oval eccentric, e) elongated concentric, f) elongated eccentric, g) half-moon concentric, h) half-moon eccentric, i) bean-shape concentric, j) bean-shape eccentric, and k) crescent. The red dashed boxes show the regions of maximum TKE.	146
5.12	Area-averaged TKE for different cross-sectional planes in stream-wise direction with a consecutive distance of D for a) mean value and b) maximum TKE values in a cardiac cycle for different shapes of stenosis. $z/D = 0$ is the location of stenosis centre.	147
5.13	First two POD modes of stream-wise velocity fluctuating component in $y - z$ plane with $x = 0$ starting at $z/D = 1$ for different shapes of stenosis including a) round eccentric, b) oval concentric, c) oval eccentric, d) elongated concentric, e) elongated eccentric, f) half-moon concentric, g) half-moon eccentric, h) bean-shape concentric, i) bean-shape eccentric, and j) crescent. The vertical axis is the artery diameter in $y - z$ plane. First mode is shown on the left and the second mode is shown on the right. The percentage in the parenthesis on top of each contour shows the contribution to the TKE of each mode. In the contour plots of modes 1 and 2, regions with orange (positive) and blue (negative) colours are with opposite sign.	148

5.14	The contribution to TKE of the first ten modes of POD for different shapes of the stenosis.	149
5.15	Spectral entropy of stream-wise instantaneous velocity component for different cross-sectional planes in stream-wise direction with a consecutive distance of D for different shapes of stenosis. $z/D = 0$ is the location of stenosis centre. The grey shaded zone represents the transitional region starting from $S_d = 0.7$ to $S_d = 1.1$	150
5.16	Energy spectral of centre-point stream-wise velocity fluctuations for different a) concentric and b) eccentric shapes of the stenosis. The stream-wise distances where the PSDs are plotted vary based on the shape of the stenosis, which are shown with a ‘plus’ sign in Fig. 5.7.	150
5.17	Energy spectral of centre-points stream-wise velocity fluctuations at different stream-wise distances for a) half-moon eccentric and b) crescent cases.	152
5.18	Unwrapped WSS distributions downstream of the stenosis starting at $z/D = 1$ at the maximum velocity phase in the fourth pulsation cycle for different shapes of stenosis including a) round concentric, b) round eccentric, c) oval concentric, d) oval eccentric, e) elongated concentric, f) elongated eccentric, g) half-moon concentric, h) half-moon eccentric, i) bean-shape concentric, j) bean-shape eccentric, and k) crescent.	153
6.1	Cross sections of different shapes of the stenosed coronary arteries categorised in three main sections including circular stenosis shapes (a–e), elliptic stenosis shapes (f–j) and sharp-edge shapes (k–o). All can be categorised in different degrees of stenosis and levels of eccentricity (different concentric and eccentric cases are displayed.) [Thomas G Beach, Chera L Maarouf, Reed G Brooks, Scophil Shirohi, Ian D Daug, Lucia I Sue, Marwan N Sabbagh, Douglas G Walker, LihFen Lue, and Alex E Roher, BMC Geriatrics, Vol.11, 3, 2011; licensed under a Creative Commons Attribution (CC BY) license.].	170
6.2	Vertical (top row) and longitudinal (bottom row) cross sections of different stenoses considered in this study including a) axisymmetric, b) eccentric, c) sharp-edge concentric, and d) asymmetric (In all cases, $S = 0.84$). The outer light shaded area is the artery wall and the inner dark shaded area introduces the stenosis.	170
6.3	Schematic of the cross section of an artery with eccentric stenosis (top). Bottom shows different levels of eccentricity considered in this study including a) $e = 0$, b) $e = 0.29$, c) $e = 0.5$, d) $e = 0.8$, and e) $e = 1$ (In all cases, $S = 0.84$). The shaded area introduces the stenosis.	171
6.4	Cross section of a semi-blocked artery with $10D$ upstream and $20D$ downstream of the blockage and different plaque lengths considered in this study.	171
6.5	Different flow profiles employed in this study a) sinusoidal flow profile (Eq. 6.5) and b) Fourier series flow profile (Eq. 6.6) to train the pulsatile part of the developed pressure drop equation with $q_{mean} = 295$ ml/min. The constant flow rate in the shaded area is used to calculate blockage parameter.	172

6.6	a) Schematic of the test setup and b) Experimental test setup: (1) centrifugal pump; (2) flow sensor; (3) settling chamber; (4) pressure sensor; (5) 3D-printed test section; (6) valve; (7) water reservoir; (8) computer, power supply and DAQ card.	174
6.7	Relative surface height of the 3D-printed model with ABS material using Surface Roughness Measuring Tester Mitutoyo SJ-410.	175
6.8	Pressure drop for different degrees of stenosis inside a coronary artery model with an axisymmetric stenosis for a wide range of flow rate.	176
6.9	Pressure drop versus a wide range of flow rate for different shapes of stenosis including axisymmetric, eccentric, sharp-edge concentric, and asymmetric inside a coronary artery model with $S = 0.84$ for a wide range of flow rate.	177
6.10	Blockage factor versus different degrees of stenosis for different shapes of stenosis including axisymmetric, eccentric, sharp-edge concentric and asymmetric for the case with the plaque length of $2D$	178
6.11	Blockage pressure drop and factor versus different degrees of stenosis for the cases with the estimated (square symbol) and actual (triangular symbol) wetted areas and the stenosis shape of the sharp-edge concentric. Blockage pressure drops (solid lines) are displayed at the flow rate of 325 ml/min.	179
6.12	Blockage factor versus different degrees of eccentricity starting from zero degree of eccentricity corresponding the axisymmetric case to maximum degree of eccentricity (equals to one) corresponding to the eccentric case for two different degrees of stenosis ($S = 0.51$ and 0.84) with the plaque length of $2D$	180
6.13	Experimental pressure drop as well as its viscous friction and blockage pressure drops for different plaque lengths and the axisymmetric shape of the stenosis for the case with $S = 0.64$ and the flow rate of 325 ml/min.	180
6.14	Pulsatility factor versus different degrees of stenosis for different shapes of stenosis including axisymmetric, eccentric, sharp-edge concentric, and asymmetric as well as the corresponding second-order power fit profile for the case with the plaque length of $2D$	181
6.15	Evaluated pressure drop (dashed line) based on the developed equation (Eq. 6.7) and the experimental pressure drop (solid line) for the second order Fourier series with $A = 0.5$ and $T = 3$ and different shapes and degrees of stenosis including a) asymmetric with $S = 0.58$, b) eccentric with $S = 0.64$, c) axisymmetric with $S = 0.75$, and d) sharp edge concentric with $S = 0.895$. The maximum mean and peak deviations are about 0.7% and 1%, respectively.	182
6.16	Flowchart of using the developed pressure drop equation for different conditions.	183
6.17	Physiological pulsatile left and right coronary artery blood flow profiles.	184

6.18	a) Evaluated pressure drop based on the developed equation and the experimental pressure drop and b) different components of it including viscous friction, blockage and pulsation parts for the left coronary artery flow profile with the stenosis shape of the sharp edge concentric and $S = 0.52$. . .	184
6.19	a) Evaluated pressure drop based on the developed equation and the experimental pressure drop and b) different components of it including viscous friction, blockage and pulsation parts for the left coronary artery flow profile with the stenosis shape of the axisymmetric and $S = 0.64$	185
6.20	a) Evaluated pressure drop based on the developed equation and the experimental pressure drop and b) different components of it including viscous friction, blockage and pulsation parts for the right coronary artery flow profile with the stenosis shape of the asymmetric and $S = 0.71$	185
6.21	a) Evaluated pressure drop based on the developed equation and the experimental pressure drop and b) different components of it including viscous friction, blockage and pulsation parts for the right coronary artery flow profile with the stenosis shape of the eccentric and $S = 0.88$	186
6.22	a) Schematic of the test setup to measure FFR in curved coronary artery models, b) a view of the experimental test rig displaying a curved model of artery with $\theta = 90^\circ$, and c) Schematic of curved coronary artery model showing different related parameters including curvature angle and radius, degree of stenosis and downstream length.	198
6.23	Schematics of a) centre of curvature cross section with different degrees of stenosis, b) curved artery models with different curvature angles and c) cross sectional view of three-dimensional-printed artery models. The degree of stenosis and curvature radius in parts b and c are $S = 78\%$ and $r/D = 5$, respectively.	199
6.24	(a) Schematics of a 90° curved coronary artery model with the degree of stenosis of 78% and different downstream length including $3D$, $5D$, $10D$, and $20D$ and (b) FFR and pressure drop values versus different downstream lengths for different flow rates.	200
6.25	FFR and pressure drop values versus flow rate for different degree of stenosis and different curvature angles including (a) $\theta = 30^\circ$, (b) $\theta = 60^\circ$ and (c) $\theta = 90^\circ$. For all the cases, curvature radius is equal to $5D$. Horizontal black dashed line refers to the critical value of FFR (FFR = 0.8).	202
6.26	FFR and pressure drop values versus flow rate for different curvature angles with $S = 78\%$ and a curvature radius of $5D$	203
6.27	(a) Schematics of curved arteries with different curvature radius and $S = 78\%$ and $\theta = 90^\circ$ and (b) FFR and pressure drop values versus different curvature radii for different flow rates and $S = 78\%$ and curvature angle of 90°	203

6.28	The physiological pulsatile left coronary artery blood flow profile (Davies et al. 2008) and the developed experimental blood flow profile. The black solid line is the physiological left coronary artery blood flow profile, as the input of the pump, and the dashed red line is the developed experimental blood profile measured by the flowmeter.	205
6.29	Mean values of pressure drop over a cardiac cycle versus different degree of stenosis for different curved artery models including straight (without curvature), 30°, 60°, and 90° with $r/D = 5$. Pressure drop for straight artery is calculated based on the corresponding artery length with the bend angle of 30°.	206
6.30	Phase-averaged experimental pressure drop and the calculated values based on the first three terms of Eq.6.9 for straight artery versus dimensionless cycle period for $S=78\%$ and two curvature angles including (a) $\theta = 30^\circ$ and (b) $\theta = 90^\circ$ with $r/D = 5$. Solid line refers to the calculated pressure drop based on Eq.6.9 for straight artery and dashed line refers to the experimental pressure drop.	207
6.31	Phase-averaged experimental pressure drop and the calculated values based on the Eq.6.9 for curved artery model and that of obtained based on the bend head loss equation by White (1929) for a healthy artery with $\theta = 90^\circ$ without stenosis and two curvature radii including a) $r/D = 5$ and b) $r/D = 7$. Solid line refers to the experimental pressure drop, dashed line refers to the calculated pressure drop based on Eq.6.9, and dashed-dotted line refers to the calculated pressure drop based on the bend head loss equation by White (1929).	208
7.1	Steps for generating a transparent silicone model of stented coronary artery showing a) casting rods of different stents, b) schematics of the stented artery mould, c) the final stent D casted model, d) detail view of the stent region of the casted artery, and e) geometrical specifications of a single pattern of each stent.	222
7.2	Casting rod of stent B, b) 2D view of the raw intensity image of the selected area shown in part a, c) 3D surface contour of the selected area showing the curvature of the stent model and the depth of the struts, d) surface roughness contour of the area shown by orange dashed line box in part b after removing the effect of model curvature, e) height histogram of the area highlighted in part b, and f) roughness profile across the line shown in part b. The locations of struts as well as their depths and thicknesses are shown in the grey shaded area.	224

7.3	Comparison of the surface quality of the stent rod and the cast stent silicone model. a) and b) shows the 2D raw intensity image and 3D surface contour of the stent rod, and c) and d) shows the 2D raw intensity image and 3D surface contour of the cast stent silicone model, e) roughness profile across the line shown in Fig 7.3a, and f) roughness profile across the line shown in Fig 7.3c of the cast stent silicone model. The locations of struts as well as their depths and thicknesses are shown in the grey shaded area. In parts b and d, the curvature of the stent rod and cast stent silicone model is removed to better visualise the depth of the struts. The angles of the edges are also displayed in Figs. 7.3e and 7.3f.	226
7.4	a) Schematics of the coronary artery test rig, b) schematics of PIV setup, c) photograph of the PIV setup, d) timing diagram for the synchronisation of the laser and camera with the external trigger from the centrifugal pump. e) The physiological pulsatile left coronary artery blood flow profile (Davies et al. 2008) and the developed experimental blood flow profile. This waveform, as an inlet velocity, was modelled using the first 32 Fourier modes of Fast Fourier Transform (FFT) that accurately represents the original waveform (with less than one percent difference between the maximum flow velocities during a cardiac cycle).	227
7.5	a) 3D view of the region of interest to calculate the WSS with the considered coordinate system and b) PIV light intensity image of the stent A with yellow solid line representing the wall boundary.	231
7.6	a) Area illuminated by the laser, b) contour of mean stream-wise velocity during a cardiac cycle for the stent A and c) time dependent value of spatially-averaged WSS for the stent A. The solid blue line shows the spatially-averaged WSS and the yellow area represents the variation of the spatially-averaged WSS with green and red dash lines referring to locally minimum and maximum values.	232
7.7	Spatial profile of the phase-averaged WSS values for different stents for the ROI shown by the laser sheet. The grey shaded areas are the location of stent struts. The green and red dash lines refer to minimum and maximum velocity phases during a cardiac cycle, respectively. The solid blue line shows the mean value of the time-averaged WSS and the yellow area covers the variation of the time-averaged WSS during a cardiac cycle.	233
7.8	a) Effect of different types of stent on phase and spatially averaged WSS in two phases in a cardiac cycle. The WSS results for artery wall and stent struts are presented per length of the arterial wall and stent struts located in the region of interest. b) Effect of different types of stent on OSI for spatially mean and maximum values near the struts.	234

7.9	a) Variation of non-dimensional time-averaged WSS of different stent models studied in this study and the ones reported in the literature for the locations both on the struts and between the struts. The time-averaged WSS is non-dimensionalised using $(\frac{1}{2})\rho U^2$. Each bar represents the minimum and maximum ranges of the variations in non-dimensional time-averaged WSS on the strut and in the distance between them. Light blue shaded area shows the stents in this study. b) Comparison of non-dimensional time-averaged WSS in the zone adjacent to one stent strut of two stents including Absorb (Chiastra et al. 2014) and stent B from the current study. The grey shaded area is the location of stent struts. The horizontal axis shows the stream-wise distance normalised by the corresponding stent thickness to allow a comparison between the stents of different thickness.	236
7.10	Schematics of the coronary artery test rig.	245
7.11	The physiological pulsatile left coronary artery blood flow profile (Davies et al. 2008) and the developed experimental blood flow profile.	245
7.12	Four models of the stents employed in this study.	246
7.13	Schematic of the stented artery covered with stent C showing the dimensions and the coordinate system.	246
7.14	A close-up view of the mesh structures for the stent D with a zoom view of the mesh near the stent struts.	247
7.15	A comparison between the CFD and PIV results of the spatial profile of the phase-averaged WSS for the stent B for the phase with maximum velocity in a cardiac cycle. The grey shaded area shows the location of stent struts.	248
7.16	a) The stream-wise velocity contour and streamline of mid-cross-sectional plane for the stent C and near the stent struts micro-recirculation structures of b) stent A, c) stent B, d) stent C, and e) stent D for the phase with maximum velocity during a cardiac cycle.	249
7.17	Unwrapped contour plots of WSS for a) two phases of minimum (top) and maximum (bottom) velocities during a cardiac cycle for stent B, and b-d) a phase with maximum velocity in a cardiac cycle for the other stents. The horizontal axis shows the stream-wise direction, normalised by the artery diameter. The vertical axis shows the angular direction.	249
7.18	A comparison of the spatially-averaged WSS for different stent models in the phase with maximum flow rate in a cardiac cycle. The comparison includes the values of spatially-averaged WSS on the location of stent struts, adjacent to them as well as the total values.	250
A-1	Schematic diagram of 3D asymmetric diseased coronary artery with different degrees of stenosis shown with the percentage of degrees of stenosis.	A-6
A-2	a) Schematic of the test setup and b) Experimental test setup: (1) centrifugal pump; (2) flow sensor; (3) settling chamber; (4) pressure sensor; (5) 3D-printed test section; (6) valve; (7) water reservoir; (8) computer, power supply and DAQ card.	A-7

A-3	The physiological pulsatile inlet velocity boundary condition (Huo and Kassab 2006).	A-7
A-4	The pressure drop calculated from Darcy-Weisbach equation and measured across different degrees of stenosis in the pipe with flow rate change for different viscosities of a) 1.8 mPa.s ($200 < Re < 600$), b) 3.2 mPa.s ($115 < Re < 350$) and c) 6.4 mPa.s ($60 < Re < 180$).	A-9
A-5	Pressure drop for different degrees of stenosis and viscosities for a) flow rate = 120 ml/min and b) 250 ml/min.	A-10
A-6	The pressure drop measured across the stenotic pipe with flow rate change for a 74.2% degree of stenosis.	A-11
B-1	A transparent artery model with blockage made out of Sylgard 184 silicone.	B-6
B-2	Two different views of the test rig displaying different components. . . .	B-6
B-3	The physiological pulsatile inlet velocity boundary condition (Davies et al. 2008).	B-7
B-4	Three phases of interest in a cardiac cycle for PIV measurement. Three shaded areas represent three different dt considered for PIV measurement corresponding to different flow rates.	B-8
B-5	Three regions of interest including recirculation zone, jet flow regime and downstream zone.	B-9
B-6	Velocity profile versus time during a cardiac cycle for different stream-wise nodes in the jet flow regime (radially located on the centre of the jet regime).	B-9
B-7	Stream-wise velocity contours, streamlines and velocity vectors for three different cases including minimum and maximum velocity during a cardiac cycle and the steady velocity corresponding to the mean velocity of a cardiac cycle.	B-10
B-8	TKE for four different radially located lines distributed in stream-wise direction from close to the centre of the blockage (line a) to downstream of it (line d).	B-11

List of Tables

2.1	Average segment length and luminal diameter of three coronary arteries (Douglas et al. 1988). Prox refers to the proximal segment, mid to the middle segment, and distal to the distal segment.	16
3.1	Average ratios of motion in middle and distal segments of LAD, LCx and RCA with respect to the proximal segment movement obtained from 15 patients (Johnson et al. 2004).	67
3.2	Diameter and distance from ostium of different coronary artery segments from 4 patients (Park et al. 2016).	68
3.3	Studies in the literature focusing on the effect of temporal variations of the coronary arteries on the hemodynamic parameters.	84
4.1	Different cases considered to study the laminar-turbulent blood flow transition of a pulsatile flow.	105
4.2	The maximum values of area-weighted average of TKE for different cases considered in this study.	117
6.1	Curve fit parameters of the blockage factor (kt) versus degree of stenosis (S) for two extremum cases of the stenosis shape with and without sharp edge and eccentricity as $kt = a \times \exp(b \times S) + c \times \exp(d \times S)$	178
6.2	Mean and peak errors of the evaluated pressure drop for different cases with different shapes and degrees of stenosis.	182
6.3	Comparison between the mean values of the experimental pressure drop over a cardiac cycle and the calculated values based on the straight artery model (Eq.6.9), for different curvature angles and degree of stenoses. 0% degree of stenosis denotes the model without stenosis.	205
7.1	Roughness parameters for the evaluation of surface unevenness of the selected area in Figure 7.2d.	223
7.2	Different cases used for validation of the results. These cases are chosen from literature that have the closest matching parameters to the current experiment.	235

Chapter 1

Introduction

1.1 Background

Cardiovascular diseases (CVDs) are a group of disorders related to the heart and blood vessels. CVDs are the leading causes of death by contributing to more than half (about 54%) of deaths in 2015 worldwide (World Health Organization 2015). In 2015, Ischemic heart disease (IHD) and stroke were the world's biggest killers (World Health Organization 2015). IHD, also known as coronary artery disease (CAD), is a disease of the vessels supplying blood to the heart muscles. In Australia, CVD, including IHD, heart failure, and cardiac arrhythmias, is a major cause of death with 24,300 deaths in 2019 with a total of about 21% of all causes of death (Australian Bureau of Statistics 2020). The statistics of the leading causes of death in 2019 are illustrated in Fig. 1.1 which shows IHD is the leading cause of death in Australia with 16% of the total.

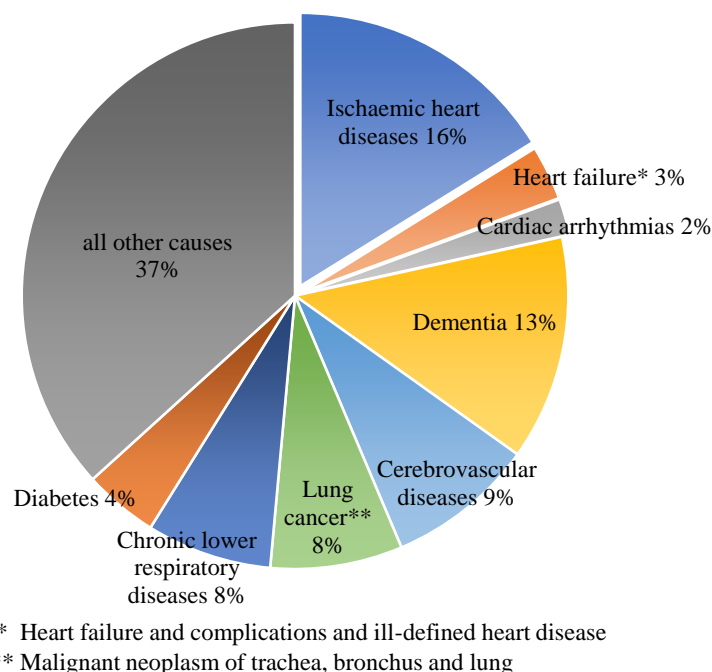


Figure 1.1: Australia's leading causes of death in 2019 based on Australian Bureau of Statistics (2020) data.

CADs mainly occur because of a reduction in the cross section of blood vessels due to plaque formation which may result in difficulties in blood delivery to the various human organs. Lipid, calcium, low-density Lipoprotein (LDL), and also a specific type of white blood cells, macrophage cell, are different materials that can cause the formation of plaques. A coronary angiogram of the left anterior descending artery (LAD), one of the main coronary arteries, and the diagonal branch is displayed in Fig. 1.2. The artery blockage, which is called stenosis, can be seen at different locations after the bifurcations and in the diagonal branch.

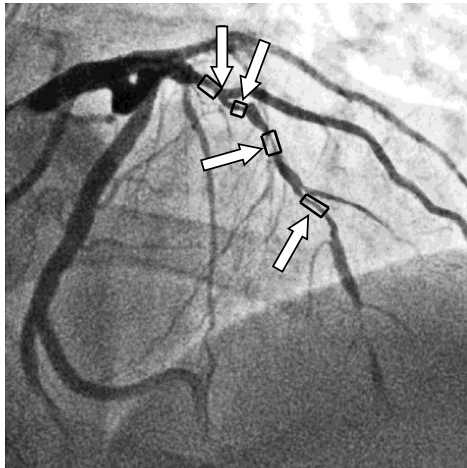


Figure 1.2: The blockage of the LAD and the diagonal branch at different locations for a 48-year-old man (Basavarajaiah and Qadir 2015).

The blockages in a coronary artery create considerable pressure drop in the arteries at the location of the constrictions. Pressure drop is an important physical parameter as it relates to the power required by the heart to supply the organs with sufficient oxygenated blood. Higher pressure drop means a higher heart muscle effort for providing the same blood flow rate to different organs for proper operation of the organs. The pressure drop is mainly due to the turbulence occurring downstream of the stenoses because of the changes in the flow patterns. The effect of the formation of the stenosis on the flow behaviour is schematically shown in Fig. 1.3. The blood flow before the stenotic region of a coronary artery is mainly laminar due to the low flow rate, and it changes to transitional flow after the stenosis because of the formation of a jet flow due to the reduction in the artery cross section. This results in the formation of separation zones immediately after the stenosis with a lower wall shear stress (WSS). WSS is an indicative parameter for diseased coronary arteries used widely in clinical assessments. As reported in the literature the extremes of WSS are recognised as a potential marker for determination of rapidly progressing CAD (Eshtehardi et al. 2012; Stone et al. 2003). Hence, laminar flow separation, due to the increase in the velocity and the change in the fluid structure, is most likely to occur after the constricted sections of coronary arteries. The available studies over-simplified the laminar flow separation investigations through considering some unrealistic assumptions such as constricted channel instead of stenosed artery model and steady inflow condition instead of pulsatile profile. Hence, examination of laminar flow separation of patient-specific geometries is almost absent in the literature. Therefore, it is of great importance to investigate the effect of stenosis on the pressure drop, flow patterns, potential separation zones, and transitional flow behaviour.

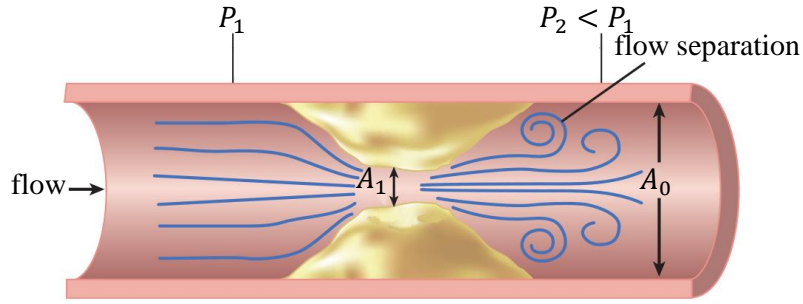


Figure 1.3: Stenotic flow behaviour inside an artery demonstrating the susceptible locations for flow separation (Libby 2015).

One of the most common clinical methods for evaluation of pressure drop across a stenotic coronary artery is fractional flow reserve (FFR). For measuring FFR, a microcatheter connected to a miniaturised pressure sensor is inserted into the coronary artery to measure the pressure before and after the stenotic section (Achenbach et al. 2017). The use of an intra-coronary pressure wire has been validated *ex vivo* and *in vivo* and has been shown in clinical studies to lead to improved outcomes for patients, largely through the avoidance of unnecessary stenting of non-significant lesions. However, this method is complex, invasive and has a high procedural risk. It is reported in the literature that invasive FFR carries more than 1/1000 risk of heart attack, stroke, and death, as it requires instrumentation of the coronary artery and is also expensive (Morris et al. 2015; Patel et al. 2010). It is reported in the literature that about half of the patients who undergo invasive tests such as FFR, to measure the severity of the blockage, have no significant blockage (Douglas et al. 2016) and hence, are unnecessarily subjected to its risks and costs. It is also reported that 61% of patients would prefer to avoid an invasive angiogram if there was an available non-invasive option for them (Douglas et al. 2015). Thus, there is a need for the development of a non-invasive method able to produce an estimation of FFR that is capable of closely representing pressure drop measured by the invasive FFR. Furthermore, one of the most common treatments for CAD is coronary stent implantation, an invasive alternative with minimal consequences for coronary artery bypass grafting (CABG) surgery. Although there are several benefits of stenting over the CABG such as lower risks of complications and much shorter recovery period, it can result in thrombosis and in-stent restenosis (ISR) which are the major drawbacks of the coronary stent placement (Kastrati et al. 2001). It is shown that there is a direct link between low WSS locations and ISR and thrombosis and consequently patient outcomes (Chatzizisis et al. 2007; Gijssen et al. 2019). The locations with a lower WSS, especially adjacent to the stent struts, are the potential locations for the formation of ISR and thrombosis (Koskinas et al. 2012; Morlacchi et al. 2011). Although the stent geometry is usually limited by the manufacturing processes, it can play an important role in the improvement of hemodynamic performance (Mejia et al. 2009). It is also shown that different commercial stents result in different levels of WSS especially adjacent to the struts (Charonko et al. 2009). Therefore, the potential for the formation of ISR and thrombosis should be better understood by investigating the WSS distributions for different typical commercial stent designs with different geometrical features (Beier et al. 2016).

Furthermore, a stenosis inside the coronary arteries can be formed in different shapes, as shown in Fig. 1.4. The plaques may occupy almost the entire cross section of the artery

or just a small part of it. The percentage of the artery blocked due to the formation of the plaques, known as the degree of stenosis, is another important parameter which affects the pressure drop across the coronary arteries. Furthermore, eccentricity, which represents the bias from the centre of the hosting artery to the centre of the stenosis, is another important parameter in classification of stenoses based on their shapes. It is reported in the literature that the shape of a stenosis can considerably change the hemodynamics of the stenosed arteries. For example, as discussed by Ohara et al. (2008), for patients suffering from a high degree of stenosis in their carotid artery, independent of other risk factors and features of plaque morphology, an eccentric plaque can cause more severe cerebrovascular diseases compared to patients with concentric stenoses.

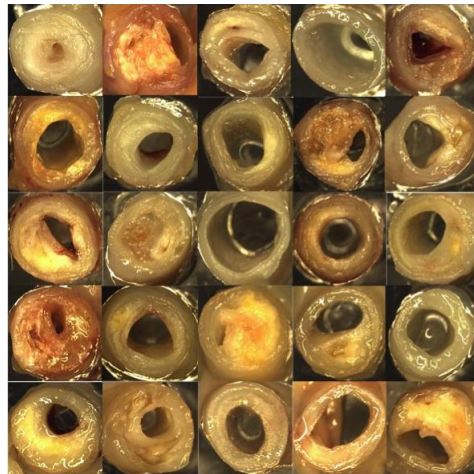


Figure 1.4: Representative digital images of coronary artery cross-sections, depicting the range of atherosclerotic stenosis based on their shapes (Beach et al. 2011).

The motivation for the research presented in this thesis is to improve patient outcomes by providing a better understanding of the hemodynamics of stenosed and stented coronary arteries. This goal can only be achieved if the effect of stenoses and stents on the flow is well characterised. Hence, the correlation between the effect of stenosis and its shape and the transitional flow behaviour on the hemodynamic parameters is investigated in this study. This knowledge can be employed to better evaluate the severity of diseased coronary arteries. Furthermore, the results of this study will help to better understand the effect of stents on the flow and hence to improve the stent. The findings will provide a basis for improvement of the most common CAD diagnostic and treatment methods.

1.2 Aims and objectives

The overall aim of the present research is to develop an in-depth knowledge of the flow inside stenosed and stented coronary arteries. First, the effect of stenosis on the downstream hemodynamics is characterised with the development of a computational model, as one of the research methods of this study. This knowledge is essential as the changes in the downstream flow behaviour has important potential pathological consequences, whereby the pressure drop forces the heart muscles to work harder. While the first objective focuses on the effect of stenosis on the downstream flow behaviour, the second objective, more specifically, investigates the effect of the shape of the stenosis by clas-

sifying CADs based on the shape of the stenosed sections. A systematic study on the effect of different possible shapes of the stenosis on the hemodynamic parameters and downstream blood flow behaviour is conducted in detail.

After developing an in-depth knowledge on the effect of stenosis on the downstream flow behaviour in the first two objectives, the third objective seeks the development of a non-invasive model to evaluate pressure drop and FFR inside the stenosed arteries. This was undertaken experimentally based on the extensive pressure measurements, as the other research method of this study. The development of a tool that can measure pressure drop inside a stenosed coronary artery using only blood parameters, the flow profile inside the artery, and the images of the stenosed coronary artery, and thus based on non-invasive imaging methods, can help in early detection of atherosclerosis.

Finally, the last objective is to investigate the hemodynamics of the stented arteries experimentally and numerically. Flow visualisation of the stented arteries is of great importance in order to provide a better understating of the flow features near the stented regions of the arteries. This knowledge is almost missing in the literature because all the flow visualisation measurements, to date, are limited due to the use of metallic or non-metallic stents, which partially obscure the field of view (FOV). To achieve this objective, a novel technique to visualise the entire flow and to investigate the WSS within the stent struts without covering the FOV inside a stented coronary artery model is introduced. With the employment of the novel developed technique and the computational model, the effect of different stent patterns on the WSS is investigated to identify the locations with a high potential for formation of restenosis.

The research objectives are summarised as the following:

- Investigation of the post-stenotic transition to turbulence inside the stenosed coronary arteries,
- Establishment of a link between the shape of stenosis and the downstream blood flow behaviour,
- Development of a non-invasive model to evaluate pressure drop inside the coronary arteries,
- Investigation of the effect of the stent pattern on the hemodynamics of the stented arteries.

1.3 Thesis outline

The current thesis comprises eight distinct chapters. The current chapter introduces the subject matter, provides an overview of the thesis and the research objectives. Chapter 2 is an extensive review of the literature in the field of research, highlighting the gaps in knowledge and the significance of the current research. Chapter 3 reviews one of the challenging subjects in the field of research. Chapter 4 to Chapter 7, which comprise the main body of the thesis, present six manuscripts and three conference papers that have been published or are under review in peer-reviewed journals. The research methods and the experimental findings are detailed in these manuscripts. In the final chapter (Chapter 8),

a summary of the findings and the obtained conclusions, along with recommendations for future work, are presented. The following gives a brief description of the content, and scope of each chapter.

Chapter 2 starts with an outline of the coronary artery morphology, its blood vessel types and rheologies followed by a literature review of the main causes of atherosclerosis and different coronary arterial stenosis morphologies. An extensive literature review is provided discussing the mechanical metrics for predicting CADs including turbulence, shear stress, pressure drop and FFR. This section continues with a discussion of one of the treatments of CAD, named coronary stent implantation, and provides a review of the numerical and experimental studies related to the hemodynamics of the stented arteries. The literature review is aimed at identifying the key gaps in knowledge addressed in the current research.

Chapter 3 discusses the importance of modelling the temporal geometric variations of the coronary arteries in a cardiac cycle for the investigation of the hemodynamics. Temporal geometric variations of the coronary arteries during a cardiac cycle are classified as a superposition of the changes in the position, curvature and torsion of the coronary artery axis markers and the variations in lumen cross-sectional shape due to distensible wall motion induced by the pulse pressure and/or contraction of the myocardium in a cardiac cycle. The studies from the literature which model or disregard the temporal geometric variations of the coronary arteries on the hemodynamic parameters are discussed. The results show that neglecting the effects of temporal geometric variations is expected to result in less than 5% deviation of the time-averaged pressure drop and WSS values and also less than 20% deviation of the temporal geometric variations of hemodynamic parameters, such as time-dependent WSS or oscillatory shear index (OSI). This chapter provides guidelines for the analysis conducted in the rest of this thesis. Based on the discussion presented in this chapter and since the aim of this research is to develop an in-depth understandings of the flow features inside the stenosed and stented coronary arteries, the effect of temporal geometric variations of the coronary arteries are disregarded in this thesis.

In Chapter 4, in order to identify the effect of stenosis on the downstream hemodynamics, the correlation between the plaque geometry, the pulsatile inlet flow and the induced turbulence in a stenosed coronary artery model is investigated computationally. The transitional flow behaviour is quantified by investigation of the changes in the turbulent kinetic energy (TKE). The results suggest that there is a high risk of the formation of a secondary stenosis at a downstream distance equal to 10 times the artery diameter in the regions to the side and downstream of the initial stenosis due to the existence of the recirculation zones and low shear stresses. The applicability of the obtained results is also tested with a patient-specific stenosed coronary artery model.

Chapter 5 presents the effect of the shape of stenosis on the hemodynamics of the stenosed coronary arteries. Different possible shapes of the stenosis including round, oval, bean-shape, half moon, and crescent with and without eccentricities on the hemodynamics are investigated experimentally and numerically. A computational model, validated against the particle image velocimetry (PIV) experimental results, is developed to solve the Navier-Stokes equations. The mean and instantaneous velocity contours, pressure drop, WSS distribution, and TKE contour and profile are calculated. The transitional flow behaviour is also investigated by power spectra density (PSD) analysis. Further-

more, the Snapshot proper orthogonal decomposition (POD) is employed to identify the coherent structures downstream of the stenotic sections. The results show that for some shapes of the stenosis such as round concentric, having even a severe degree of stenosis results in less serious hemodynamic complications such as a less pressure drop compared to the other shapes of the stenosis at the same degree of stenosis.

In Chapter 6, a relationship for the non-invasive estimation of the pressure drop in a stenosed coronary artery model as a function of different physical parameters such as blood viscosity, artery length and diameter, flow rate and flow profile, and shape and degrees of stenosis is developed. Extensive experimental pressure measurements are conducted for a wide range of degrees and shapes of stenosis. The validity of the developed equation is also tested for the stenosed coronary artery models with the physiological flow profile of the left and right coronary arteries by comparing pressure drop obtained from the developed equation and those from the experimental measurements. In the second part of this chapter, the effect of artery curvature on the pressure drop and FFR is investigated. The results show that neglecting the effect of the artery curvature results in an under-estimation of pressure drop by about 25–35%. The developed equation is able to determine the pressure drop inside a stenosed coronary artery non-invasively using the measurement of the flow profile inside the artery as well as the images of the stenosed coronary artery.

Chapter 7 investigates the effect of stent design on the hemodynamics of the stented arteries experimentally and numerically. A novel technique is presented for the visualisation of the entire flow and the investigation of WSS within the stent struts without covering the FOV inside a stented coronary artery model using PIV. This novel technique is based on the construction of a transparent stented artery using silicone cast in one piece, instead of inserting a metal or non-metallic stent inside a cast artery model, which are translucent and distort the FOV. The developed technique helps to improve the stent designs to achieve better patient outcomes. The results show that WSS is strongly dependent on the design of the stent.

In Chapter 8, the key conclusions made from the present research are discussed. Furthermore, recommendations for subsequent future work for deeper understanding of the hemodynamics of stenosed and stented coronary arteries are presented.

The appendices section presents two conference publications at *21st Australasian Fluid Mechanics Conference* and *IX Australian Conference on Laser Diagnostics*.

1.4 Publications arising from this thesis

The research presented in this thesis has directly led to generation of six journal manuscripts and three peer-reviewed conference articles:

- **Journal papers**

- Navid Freidoonimehr, Maziar Arjomandi, Nima Sedaghatizadeh, Rey Chin, Anthony Zander (2020). “Transitional turbulent flow in a stenosed coronary artery with a physiological pulsatile flow”. *International Journal for Numerical Methods in Biomedical Engineering* 36 pp. e3347.

- Navid Freidoonimehr, Rey Chin, Anthony Zander, Maziar Arjomandi (2020). “An experimental model for pressure drop evaluation in a stenosed coronary artery”. *Physics of Fluids* 32 pp. 021901.
- Navid Freidoonimehr, Maziar Arjomandi, Anthony Zander, Rey Chin (2021). “Effect of artery curvature on the coronary fractional flow reserve”. *Physics of Fluids* 33 pp. 031906.
- Navid Freidoonimehr, Maziar Arjomandi, Anthony Zander, Rey Chin (2021). “A novel technique towards investigating wall shear stress within the stent struts using particle image velocimetry”. *Experiments in Fluids* 62 pp. 133.
- Navid Freidoonimehr, Rey Chin, Anthony Zander, Maziar Arjomandi (2021). “A review on the effect of temporal geometric variations of the coronary arteries on the hemodynamic parameters”. *Journal of Biomechanical Engineering*, under review.
- Navid Freidoonimehr, Rey Chin, Anthony Zander, Maziar Arjomandi (2021). “Effect of shape of the stenosis on the hemodynamics of a stenosed coronary artery”. *Physics of Fluids*, under review.

- **Refereed conference papers**

- Navid Freidoonimehr, Rey Chin, Maziar Arjomandi, Anthony Zander (2018). “Effect of degree of stenosis on the pulsatile flow pressure drop in a coronary artery”. *21st Australasian Fluid Mechanics Conference*, Adelaide, Australia.
- Navid Freidoonimehr, Rey Chin, Maziar Arjomandi, Anthony Zander (2019). “Hemodynamic of a coronary artery: a PIV measurement”. *IX Australian Conference on Laser Diagnostics*, Adelaide, Australia.
- Navid Freidoonimehr, Maziar Arjomandi, Anthony Zander, Rey Chin (2020). “Hemodynamics of stented coronary arteries: Experimental and numerical investigations”. *22nd Australasian Fluid Mechanics Conference*, Brisbane, Australia.

1.5 Thesis format

The current thesis has been submitted as a portfolio of publications in accordance with the University of Adelaide’s formatting criteria. The printed and online versions of this thesis are identical, and the electronic version is available in PDF format.

References

Achenbach S, Rudolph T, Rieber J, Eggebrecht H, Richardt G, Schmitz T, Werner N, Boenner F, and Mollmann H (2017). “Performing and interpreting fractional flow reserve measurements in clinical practice: An expert consensus document”. *Interventional Cardiology* 12.2, pp. 97–109.

- Australian Bureau of Statistics (2020). *Australia's leading causes of death, 2019*. URL: <https://www.abs.gov.au/statistics/health/causes-death/causes-death-australia/2019>.
- Basavarajaiah S and Qadir M (2015). "Hybrid strategy for long diffuse coronary lesion". *JACC: Cardiovascular Interventions* 8.11, pp. 1518–1521.
- Beach TG, Maarouf CL, Brooks RG, Shirohi S, Daugis ID, Sue LI, Sabbagh MN, Walker DG, Lue L, and Roher AE (2011). "Reduced clinical and postmortem measures of cardiac pathology in subjects with advanced Alzheimer's Disease". *BMC Geriatrics* 11, p. 3.
- Beier S, Ormiston J, Webster M, Cater J, Norris S, Medrano-Gracia P, Young A, and Cowan B (2016). "Hemodynamics in idealized stented coronary arteries: important stent design considerations". *Annals of Biomedical Engineering* 44.2, pp. 315–329.
- Charonko J, Karri S, Schmieg J, Prabhu S, and Vlachos P (2009). "In vitro, time-resolved PIV comparison of the effect of stent design on wall shear stress". *Annals of Biomedical Engineering* 37.7, pp. 1310–1321.
- Chatzizisis YS, Coskun AU, Jonas M, Edelman ER, Feldman CL, and Stone PH (2007). "Role of endothelial shear stress in the natural history of coronary atherosclerosis and vascular remodeling: molecular, cellular, and vascular behavior". *Journal of the American College of Cardiology* 49.25, pp. 2379–2393.
- Douglas PS, De Bruyne B, Pontone G, Patel MR, Norgaard BL, Byrne RA, Curzen N, Purcell I, Gutberlet M, Rioufol G, Hink U, Schuchlenz HW, Feuchtner G, Gilard M, Andreini D, Jensen JM, Hadamitzky M, Chiswell K, Cyr D, Wilk A, Wang F, Rogers C, and Hlatky MA (2016). "1-year outcomes of FFRCT-guided care in patients with suspected coronary disease: The platform study". *Journal of the American College of Cardiology* 68.5, pp. 435–445.
- Douglas PS, Pontone G, Hlatky MA, Patel MR, Norgaard BL, Byrne RA, Curzen N, Purcell I, Gutberlet M, Rioufol G, Hink U, Schuchlenz HW, Feuchtner G, Gilard M, Andreini D, Jensen JM, Hadamitzky M, Chiswell K, Cyr D, Wilk A, Wang F, Rogers C, and De Bruyne B (2015). "Clinical outcomes of fractional flow reserve by computed tomographic angiography-guided diagnostic strategies vs. usual care in patients with suspected coronary artery disease: the prospective longitudinal trial of FFR(CT): outcome and resource impacts st". *European Heart Journal* 36.47, pp. 3359–3367.
- Eshtehardi P, McDaniel MC, Suo J, Dhawan SS, Timmins LH, Binongo JN, Golub LJ, Corban MT, Finn AV, Oshinski JN, Quyyumi AA, Giddens DP, and Samady H (2012). "Association of coronary wall shear stress with atherosclerotic plaque burden, composition, and distribution in patients with coronary artery disease". *Journal of the American Heart Association* 1.4, e002543.
- Gijsen F, Katagiri Y, Barlis P, Bourantas C, Collet C, Coskun U, Daemen J, Dijkstra J, Edelman E, Evans P, Heiden K van der, Hose R, Koo BK, Krams R, Marsden A, Migliavacca F, Onuma Y, Ooi A, Poon E, Samady H, Stone P, Takahashi K, Tang D, Thondapu V, Tenekecioglu E, Timmins L, Torii R, Wentzel J, and Serruys P (2019). "Expert recommendations on the assessment of wall shear stress in human coronary arteries: existing methodologies, technical considerations, and clinical applications". *European Heart Journal* 40.41, pp. 3421–3433.
- Kastrati A, Mehilli J, Dirschinger J, Pache J, Ulm K, Schühlen H, Seyfarth M, Schmitt C, Blasini R, Neumann FJ, and Schömig A (2001). "Restenosis after coronary placement of various stent types". *The American Journal of Cardiology* 87.1, pp. 34–39.

- Koskinas KC, Chatzizisis YS, Antoniadis AP, and Giannoglou GD (2012). “Role of endothelial shear stress in stent restenosis and thrombosis”. *Pathophysiologic Mechanisms and Implications for Clinical Translation* 59.15, pp. 1337–1349.
- Libby P (2015). “The vascular biology of atherosclerosis”. *Braunwald’s heart disease: A textbook of cardiovascular medicine*. Ed. by DPZ Douglas L. Mann Peter Libby, Robert O. Bonow, Eugene Braunwald. Tenth Edit. Elsevier Saunders. Chap. 41, pp. 873–890.
- Mejia J, Ruzzeh B, Mongrain R, Leask R, and Bertrand OF (2009). “Evaluation of the effect of stent strut profile on shear stress distribution using statistical moments”. *BioMedical Engineering OnLine* 8.1, p. 8.
- Morlacchi S, Keller B, Arcangeli P, Balzan M, Migliavacca F, Dubini G, Gunn J, Arnold N, Narracott A, Evans D, and Lawford P (2011). “Hemodynamics and in-stent restenosis: micro-CT images, histology, and computer simulations”. *Annals of Biomedical Engineering* 39.10, p. 2615.
- Morris PD, Vosse FN van de, Lawford PV, Hose DR, and Gunn JP (2015). ““Virtual” (computed) fractional flow reserve: current challenges and limitations”. *JACC: Cardiovascular Interventions* 8.8, pp. 1009–1017.
- Ohara T, Toyoda K, Otsubo R, Nagatsuka K, Kubota Y, Yasaka M, Naritomi H, and Minematsu K (2008). “Eccentric stenosis of the carotid artery associated with ipsilateral cerebrovascular events”. *American Journal of Neuroradiology* 29.6, pp. 1200–1203.
- Patel MR, Peterson ED, Dai D, Brennan JM, Redberg RF, Anderson HV, Brindis RG, and Douglas PS (2010). “Low diagnostic yield of elective coronary angiography”. *The New England Journal of Medicine* 362.10, pp. 886–895.
- Stone PH, Coskun AU, Kinlay S, Clark ME, Sonka M, Wahle A, Ilegbusi OJ, Yeghiazarians Y, Popma JJ, Orav J, Kuntz RE, and Feldman CL (2003). “Effect of endothelial shear stress on the progression of coronary artery disease, vascular remodeling, and in-stent restenosis in humans”. *Circulation* 108.4, pp. 438–444.
- World Health Organization (2015). *The top 10 causes of death*. URL: <http://www.who.int/en/>.

Chapter 2

Literature review

In this chapter, an overview of the literature on the hemodynamics of coronary arteries is provided. The chapter starts with a fundamental description of the blood flow inside the arteries in Section 2.1. Section 2.2 begins with an introduction of the structure of the coronary arteries and continues with a review of the literature on the effect of the shape of the stenosis on the hemodynamic parameters. Mechanical metrics for coronary artery disease (CAD) prediction including the levels of flow turbulence, shear stress, pressure drop, and fractional flow reserve (FFR) are discussed in Section 2.3. In Section 2.4, a review of the literature on the effect of stent design, as one of the treatments of CAD, is provided. The chapter concludes with a summary of the research gaps and the objectives of the thesis in Section 2.5.

2.1 Hemodynamic fundamentals

The arterial wall properties and blood rheology influence the hemodynamics of coronary arteries. Hence, this section briefly discusses the wall properties of arteries including their different layers and the rheology of blood by mainly focusing on the non-Newtonian feature of the blood.

2.1.1 Blood vessels

Blood vessels are defined as the organs of a circulatory system responsible for transportation of blood through the body. There are two types of blood vessels in a circulatory system. The first type of blood vessels are the arteries through which the pumped blood from the heart flows. The other type of blood vessels are the veins through which the blood flows back towards the heart. The Young's modulus, E , of a typical soft tissue, composing the artery wall, is very low ($E \approx 1$ MPa) compared to typical engineering materials (usually E is in the order of GPa) (Akhtar et al. 2011). Therefore, the vessel walls are compliant and hence, they store volume during systole and return that volume during diastole. This results in maintaining a nearly steady flow during a cardiac cycle.

Normal arteries have a tri-layer structure, as shown in Fig. 2.1, comprised of:

- **Tunica intima:** This layer is the innermost layer, composed of a thin layer of endothelial cell. The tunica intima makes less contribution to the elasticity of the arterial wall, since it is very thin in a healthy young individual. However, the intima thickens and also stiffens with age so its contribution to the elasticity of the wall changes with ageing. Furthermore, the formed plaque, as the result of atherosclerosis - the most common disease of the arterial walls - can result in pathological changes of the intimal components. These pathological changes are associated with significant alterations in the mechanical properties of the arterial wall.
- **Tunica media:** This layer is the most dominant part of the wall structure and hence plays an important role in the mechanical properties of the vessel. The tunica media consists of a complex 3D network of smooth muscle cells. It is normally the layer with the largest thickness among arterial wall layers. Furthermore, the role of the media layer is to give elasticity and contractility to the vessel.
- **Tunica adventitia:** This layer is the outermost layer covered by a loose connective tissue with thick collagen bundles (Akhtar et al. 2011). The tunica adventitia is less stiff compared to the media at low pressures and in the load-free configuration. However, at the higher levels of pressure, the adventitia changes to a stiff “cover-like” tube preventing the artery from rupture or overstretch (Holzapfel et al. 2000). Furthermore, the thickness of the adventitia depends on the type of the artery, whether it is elastic or muscular, the physiological function of the blood vessel, and its topographical site.

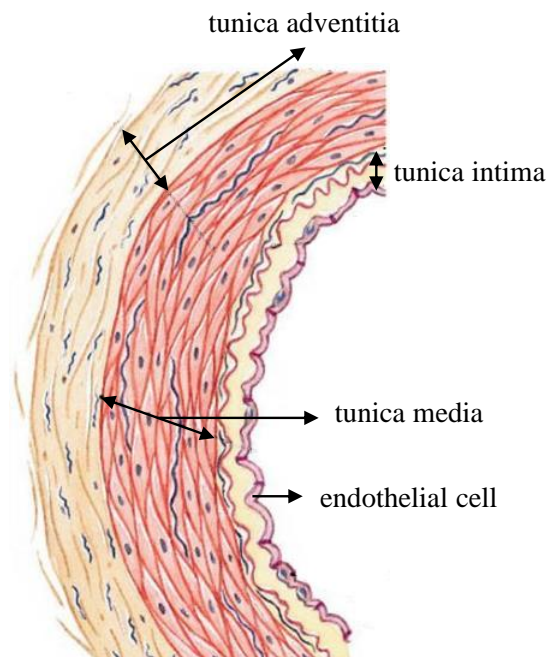


Figure 2.1: Structural layers of a normal artery vessel (Patel 2019).

All vessels are characterised by these layers with some differences in their thicknesses. The difference in the thicknesses of the layers is related to the type of the vessel, and whether they are an artery or a vein. Another difference is related to their role, whether they are responsible to provide fresh blood to the heart muscles, such as coronary arteries, or to the brain and head, such as carotid arteries. The mechanical properties of the

blood vessel comprising these layers are non-linear. This means that the more an artery is stretched, the more difficult it becomes to dilate it further (Roy 1881). Vessel wall elasticity, as a measure of the arterial ability to expand and contract with cardiac pulsation and relaxation (Godia et al. 2007), could be considered as a factor that affects hemodynamic parameters. However, if the target of a study is to investigate the pressure drop, FFR and time-averaged wall shear stress (TAWSS), as the most widely used clinical metrics, neglecting the effect of wall flexibility on these hemodynamic parameters is expected to result in a negligible deviation on the computed values. For example, it was reported in the literature that assuming healthy arteries to be rigid and hence disregarding its elasticity changes the pressure drop and the computed FFR values insignificantly with less than 2% and about 0.26% obtained from the results of Mirramezani et al. (2018) and Siogkas et al. (2015), respectively. Furthermore, it was shown that the rigid wall model of the coronary arterial tree was able to capture almost all the variations in the wall shear stress (WSS) distributions as the elastic model, with slight differences in the magnitude of WSS values with an excellent Pearson correlation ($r = 0.99$) (Eslami et al. 2019). Detailed discussion on the effect of arterial elasticity of the coronary arteries on the hemodynamic parameters is presented in Chapter 3 and also the conditions in which the elasticity of the coronary arteries can be neglected are discussed.

In addition, as the artery walls become harder and stiffer with ageing and lose their flexibility, considering arteries to be rigid results in a more reliable estimation of hemodynamic parameters. This mitigates further the deviations reported in the literature between the results of flexible and rigid wall simulations for these cases. It is widely covered in the literature that arterial stiffness is a key arterial alteration during the ageing process (Benetos 2017; Mitchell et al. 2004; Sun 2015), which is recognised as a primary risk factor of all CVDs (Kohn et al. 2015). The age-related arterial stiffness results from an attempt of the arterial system to limit the reduction in storage capacity of the arterial system with increasing age (Samijo et al. 1998). Furthermore, arterial stiffness has a relation with atherosclerotic lesions. It was reported that the patients with CVDs often develop central artery stiffness (Benetos et al. 2002). Therefore, as the focus of this thesis is to investigate the hemodynamics of the coronary arteries, the artery wall is considered to be rigid, as further explained in Chapter 3.

2.1.2 Blood rheology

Blood, rheologically, is a suspension of different elements, such as red and white blood cells, and platelets, in a relatively homogeneous liquid, the blood plasma (Koeppen and Stanton 2018). The rheological properties of blood are characterised by the properties of its components and their interaction with each other. The viscosity of blood is a function of several factors, such as plasma viscosity, hematocrit level as a volume percentage of red blood cells in blood, blood cell distribution, and the mechanical properties of blood cells (Baskurt and Meiselman 2003). Blood, as a whole, behaves as a non-Newtonian fluid showing the features of non-Newtonian fluids such as deformation rate dependency and viscoelasticity. Blood is mainly non-Newtonian due to the high concentration of red blood cells and their unique mechanical properties, such as elasticity and the ability to aggregate forming 3D structures at a low deformation rate (Bodnár et al. 2011). Red blood cells have a tendency to move along the high-velocity regions formed in the middle of the vessel, leaving a thin film of plasma moving along the surface of vessels at a lower

velocity. This leads to variation in viscosity along the cross-section of the vessel, with an increased viscosity in the middle of the vessel at a lower shear rate and decreased viscosity near the walls at a higher shear rate. This effect of red blood cells is most important in very small blood vessels where the effect of non-Newtonian parameters are significant (Baratchi et al. 2017).

There are different techniques in the literature employed to simulate the non-Newtonian nature of the blood. One of the techniques is to simulate blood as a two-phase mixture of red blood cells inside the plasma (Alonso et al. 1993). The other technique is to use continuous viscosity functions. This technique is widely used in the literature due to its low computational costs and smooth velocity profiles obtained from it. There are different functions in the literature that are used to represent the shear thinning behaviour of the blood. The Casson model (Blair 1959), as a yield stress blood model, is one of these functions. A Casson fluid is a shear thinning fluid with an infinite viscosity at zero shear rates, a yield stress below which no flow occurs and viscosity becomes constant at infinite rates of shear (Kelessidis and Maglione 2006). The other model is Carreau-Yasuda which is developed based on a different shear-rate-dependent function (Bernabeu et al. 2013). The main advantage of the Carreau-Yasuda model over the Casson model is that it is continuous for all shear rates larger than zero (Boyd et al. 2007).

Despite the non-Newtonian behaviour of blood, it can be considered as a Newtonian fluid in certain circumstances (Haynes 1960; Koeppen and Stanton 2018; Nichols et al. 2011; Jahangiri et al. 2017). As reported by Haynes (1960), blood behaves as a Newtonian liquid in tubes in which the internal diameter is large compared with the size of the red blood cells. Figure 2.2a shows that the viscosity of blood diminishes progressively as tube diameter decreases to less than approximately 0.3 mm (Costa 2016). Hence, blood can be considered as a homogenous liquid with a viscosity that is independent of the velocity gradient in large arteries (Koeppen and Stanton 2018; Nichols et al. 2011). Furthermore, Cho and Kensey (1991) reported that the effect of non-Newtonian behaviour of the blood on the pressure drop across the artery is significant for flows with a Reynolds number of less than 100. The Reynolds number is defined as $Re = \rho U D / \mu$, where ρ is the blood density, U is the mean velocity inside the coronary arteries, D is the artery diameter, and μ is the blood kinematic viscosity. Since the Reynolds number inside the coronary arteries is larger than 100, blood can be assumed as Newtonian. Moreover, as suggested by Costa (2016), Johnston et al. (2006), and Jahangiri et al. (2017), blood behaves as a Newtonian fluid at shear rates greater than 100 s^{-1} and considering that the shear rates applied to the coronary arteries are larger than 100 s^{-1} (Sakariassen et al. 2015), as shown in Fig. 2.2b, blood in the coronary arteries can be considered as a Newtonian fluid. Therefore, in this thesis, blood is considered to be Newtonian.

2.2 Coronary artery disease

As discussed in the Chapter 1, the geometry of a stenosis is an important parameter affecting the hemodynamics of the coronary arteries. This section starts with a short introduction of the coronary artery structure focusing on the main branches of the coronary arterial tree and their geometric specifications in Section 2.2.1. In Section 2.2.2, the literature focusing on the effect of shape of the stenosis on the flow behaviour inside the

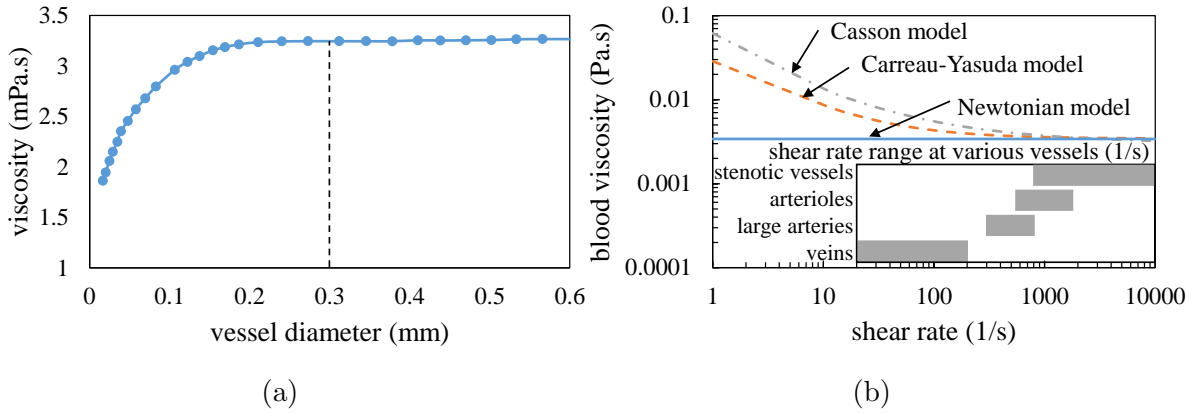


Figure 2.2: (a) The blood viscosity as a function of vessel diameter (Costa 2016) and (b) blood viscosity obtained from Newtonian, Casson, and Carreau-Yasuda models as a function of shear rate. The range of shear rate for different blood vessels is also shown in part (b) (Baratchi et al. 2017; Boyd et al. 2007; Cho and Kensey 1991; Loscalzo and Schafer 2003). The vertical dashed line in part (a) refers to the threshold vessel diameter of 0.3 mm, above which the viscosity is constant.

stenosed coronary artery models is reviewed.

2.2.1 Coronary artery structure

The main coronary arteries in a coronary arterial tree include right (RCA), left main (LMCA), circumflex (LCx), and left anterior descending (LAD) coronary arteries, as shown in Fig. 2.3. A coronary arterial tree consists of different types of arteries including semi-straight arteries, coronary bifurcations and curved arteries. From the fluid mechanics point of view, any angulations or bifurcations in vascular structures leads to a change in the hemodynamics of coronary arteries (Kantarci et al. 2011).

Coronary arteries are located on the heart muscles, wrapped around the entire heart, and are responsible for supplying fresh oxygenated blood to the heart muscles. They originate from the aortic valve and divide into two major arteries including left and right coronary arteries. Left coronary arteries (LCAs) supply the blood to the left side of the heart muscle including the left ventricle and the left atrium. LMCA bifurcates into LCx, supplying blood to the posterolateral left ventricle, and LAD, supplying blood to the anterolateral myocardium and apex. Furthermore, RCAs supply blood to the right ventricle and the right atrium (Johns Hopkins Medicine 2020). Table 2.1 shows the average segment length and diameter of three main coronary arteries. This table illustrates that the arteries closer to the main branches are larger in diameter compared to those located at distal locations.

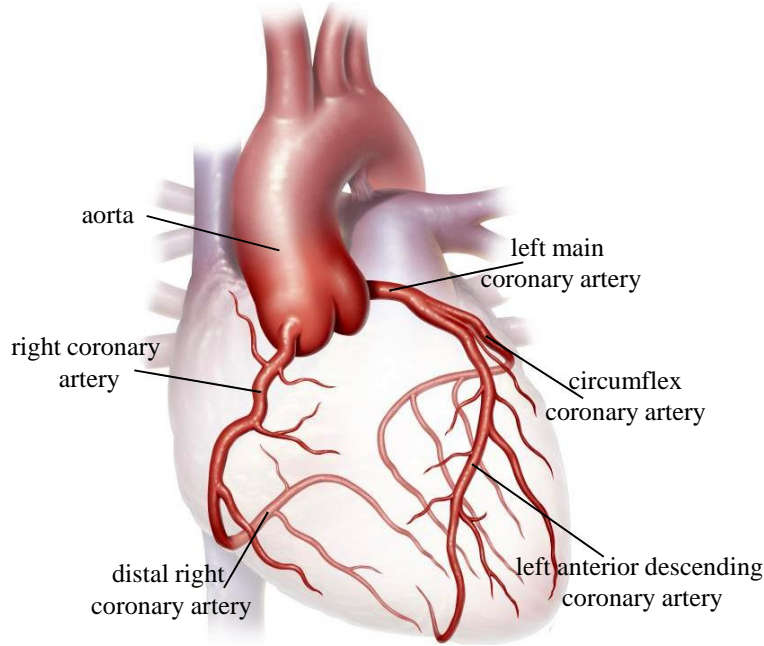


Figure 2.3: Schematics of a coronary arterial tree illustrating the main arteries, reproduced from Baylor College of Medicine (2020).

Table 2.1: Average segment length and luminal diameter of three coronary arteries (Douglas et al. 1988). Prox refers to the proximal segment, mid to the middle segment, and distal to the distal segment.

	LAD		LCx	RCA		
	prox	mid		prox	mid	distal
Length (cm)	4.2	1.9	1.1	2.7	3.6	2.9
Lumen (mm)	4.9	4.6	3.8	3.1	3.1	2.7

2.2.2 Coronary arterial stenosis morphology

The plaque inside the arteries may occupy almost the entire cross section of the artery (severe constriction case) or just a small part of it (mild constriction case). Plaque geometrical morphology parameters, such as cross sectional shape of the stenosis, stenosis length, degree of stenosis, and the eccentricity of the stenosis, are important parameters influencing flow behaviour and consequently the pressure drop inside the coronary arteries. These parameters can be used to classify the geometry of the stenosis. Figure 2.4 shows the plaque geometrical parameters including the definitions of degree of stenosis, eccentricity, and plaque length. It was reported in the literature that not only the severity of a stenosis, but also the eccentricity and to a lesser degree the length of the lesion have a significant impact on the severity of CAD (Meier et al. 1983).

Eccentricity represents the bias from the centre of a hosting artery to the centre of the stenosis, as shown in Fig. 2.4 which is defined as

$$e = \frac{E_1 - E_2}{E_1} \times 100, \quad (2.1)$$

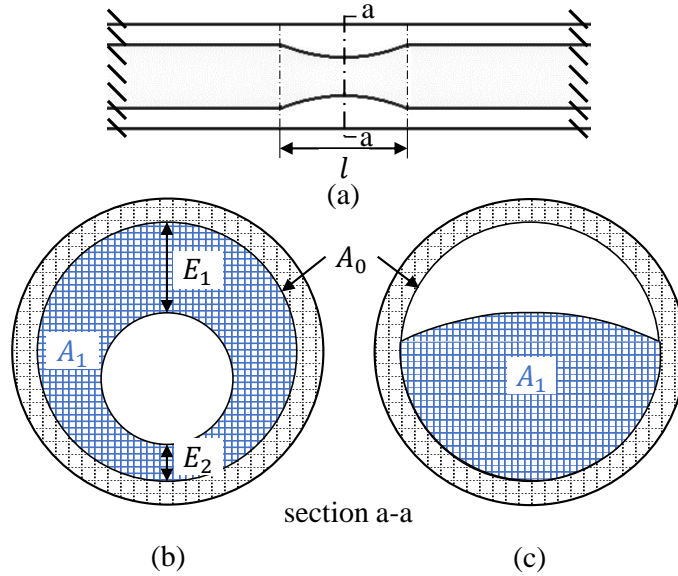


Figure 2.4: Schematics of the plaque geometrical morphology parameters including (a) the plaque length, degree of stenosis which is defined as $S = A_1/A_0 \times 100$, eccentricity, and stenosis sharpness ((b) shows a curved stenosis without sharpness and (c) shows a stenosis with a sharp edge). l is the plaque length, defined as the stream-wise length of a stenosis. A_0 and A_1 are the cross-sectional area of the unobstructed artery and the minimum constricted cross sectional area, respectively.

where E_1 and E_2 are the maximum and minimum thickness of the plaque, respectively. This parameter varies from the case with no eccentricity, i.e., equal to zero, to the highest eccentricity, i.e., equal to unity. Figure 2.5 shows multiple sequential stenoses with different levels of eccentricity in a patient-specific RCA. According to Ohara et al. (2008), lesions in real arteries are mostly eccentric. Furthermore, as discussed by Ohara et al. (2008), for patients suffering from a high degree of stenosis in their carotid artery (70% and more), independent of other risk factors and features of plaque morphology, an eccentric plaque can cause more severe cerebrovascular diseases compared to the patients with concentric stenoses. Moreover, eccentricity can cause considerable changes in the flow behaviour such as velocity distribution, WSS and level of flow turbulence after the blockage.

Apart from eccentricity, the other important parameter in classification of the shape of a stenosis is the edge sharpness, which affects the flow characteristics, such as pressure loss (Usmani and Muralidhar 2016). The stenosis inside the arteries can be formed either with or without any sharp edges, as displayed in Fig. 2.4. A longer recirculation zone and a higher pressure drop are reported by Young and Tsai (1973b) for an asymmetric stenosis with a sharp edge compared to an axisymmetric one without a sharp edge.

Another important parameter that affects the stenosis physical morphology is the plaque length, i.e. the stream-wise length of a stenosis. The changes in the plaque length affect the stenosis morphology and consequently influence the flow behaviour and hemodynamic parameters downstream of the stenosis. It was found that the length of a recirculation zone is a direct function of the plaque length (Stroud et al. 2000). Furthermore, the upstream and downstream facing angles of the stenosis are other important parameters. Based on the results of Belzacq et al. (2014), it was found that the

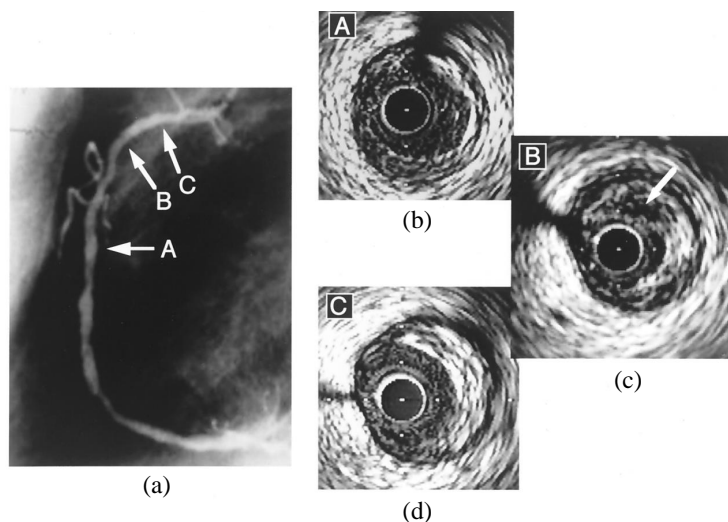


Figure 2.5: (a) Intravascular ultrasound (IVUS) image of a vulnerable atherosclerotic plaque of the RCA showing multiple luminal irregularities. (b) shows a mild concentric lesion at the distal portion at the location of A, (c) shows a significant eccentric lesion with 67% plaque area at the proximal portion at the location of B, and (d) shows an eccentric lesion at the very proximal portion at the location of C (Yamagishi et al. 2000).

cross-sectional stenosis steepness or the presence of a bump in the stenosis increased the mechanical stresses in a plaque by more than 50% compared to the case with the same degree of stenosis and plaque length and without a cross-sectional stenosis steepness or a bump. This implies that the degree of stenosis is not the only criterion in determining the mechanical behaviour of the diseased arteries.

In this section, so far, the geometrical parameters of a plaque were introduced and their influence on the downstream flow behaviour were discussed. The studies in the literature focusing on the effects of stenosis geometrical parameters on the flow behaviour are discussed in the rest of this section. In a study by Varghese et al. (2007a) with a the steady flow through a 75% degree of stenosis for concentric and eccentric models, a significant divergence between the stream-wise velocity distributions was observed at $3D$ downstream of the stenosis, where D is the internal diameter of the artery model, as shown in Fig. 2.6. It was also found that the laminar flow underwent transition at about $6D$ after the stenosis and stayed turbulent up to $12D$ downstream in the eccentric case. After $12D$, the level of the fluctuations reduced and reached an asymptotic value, which was lower than the corresponding value of the axisymmetric case. Their results showed that the transition to turbulence was quantified by the large temporal and spatial gradients of shear stress, with significant axial and circumferential variations in the instantaneous WSS. Moreover, in another study, it was shown that a small eccentricity ($e = 5\%$) can trigger post-stenotic transition to turbulence and promote turbulent flow compared to the case without an eccentricity (Varghese et al. 2008). Figure 2.7 shows the contours of instantaneous vorticity magnitude for the steady flow through the eccentric stenosis model for two perpendicular planes. The results showed that the jet flow, created after the stenosis, was more uneven in the plane with eccentricity compared to the other perpendicular plane. Moreover, the jet flow was skewed toward the wall in the direction of stenosis eccentricity, such that on the other side of the downstream wall velocity and consequently WSS were lower.

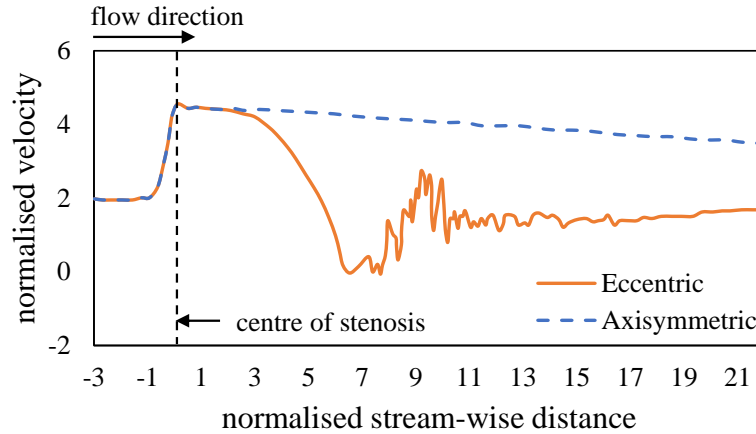


Figure 2.6: Variation of instantaneous stream-wise velocity normalised by the mean inlet velocity along the stream-wise centreline of the vessel normalised with the artery diameter for steady flow through the 75% axisymmetric and eccentric stenosis models at $Re = 1000$ (Varghese et al. 2007a).

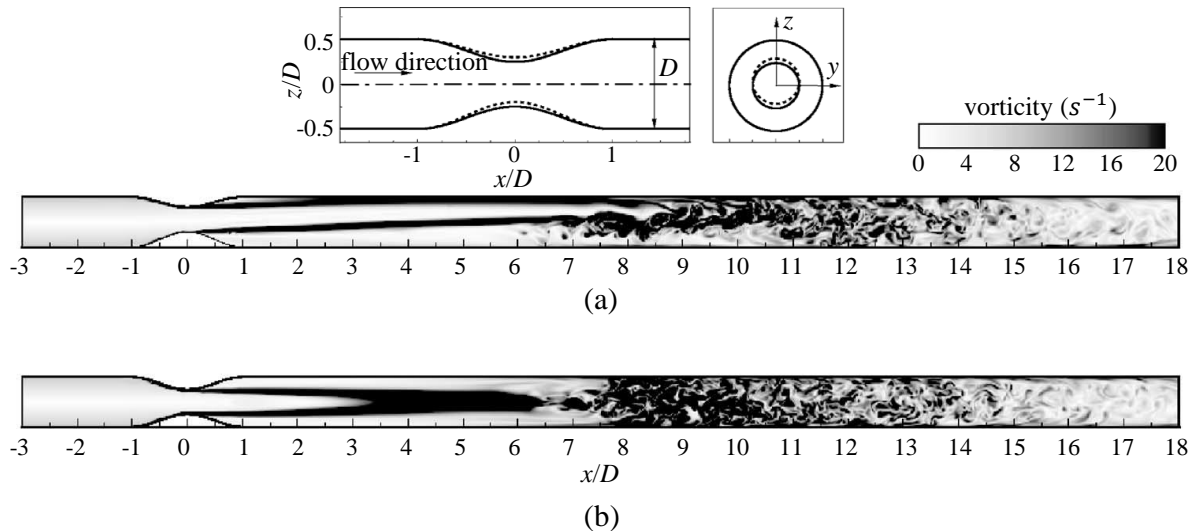


Figure 2.7: Instantaneous vorticity magnitude contours for steady flow through the eccentric stenosis model, shown on top, at $Re = 1000$ for mid-cross-sectional (a) $x - z$, $y = 0$ and (b) $x - y$, $z = 0$ planes (Varghese et al. 2008).

In another study on the pulsatile blood flow in an atherosclerotic human artery with eccentric plaques by Lorenzini and Casalena (2008), it was shown that the length of the consequent flow disturbance downstream of the stenosis was a function of the stenotic shape and height. In their study, they considered three shapes of eccentric stenosis including trapezium, semi-ellipse and triangle. The peak velocities were dependent on the shape and height of the stenosis. The relationships between the length of the flow recirculation zone and shear rate, stenosis severity, and lesion eccentricity under resting and hyperemic flow conditions were investigated by Javadzadegan et al. (2013). The results showed that increasing stenosis severity and lesion eccentricity can both increase length of flow recirculation and strength of shear rate in human coronary arteries. Furthermore, it was shown that the flow recirculation was more sensitive to mild changes in the severity of intermediate stenoses compared to the peak shear. Moreover, the flow characteristics

through the specific concentric and eccentric plaque shapes for two coronary arteries, namely LAD and RCA, was studied by Guleren (2013). Figure 2.8 shows the pressure gradient variation in a cardiac cycle for these cases. The results showed that the eccentric stenosis model with a triangular-like cross-section produced a larger pressure drop compared to the concentric model.

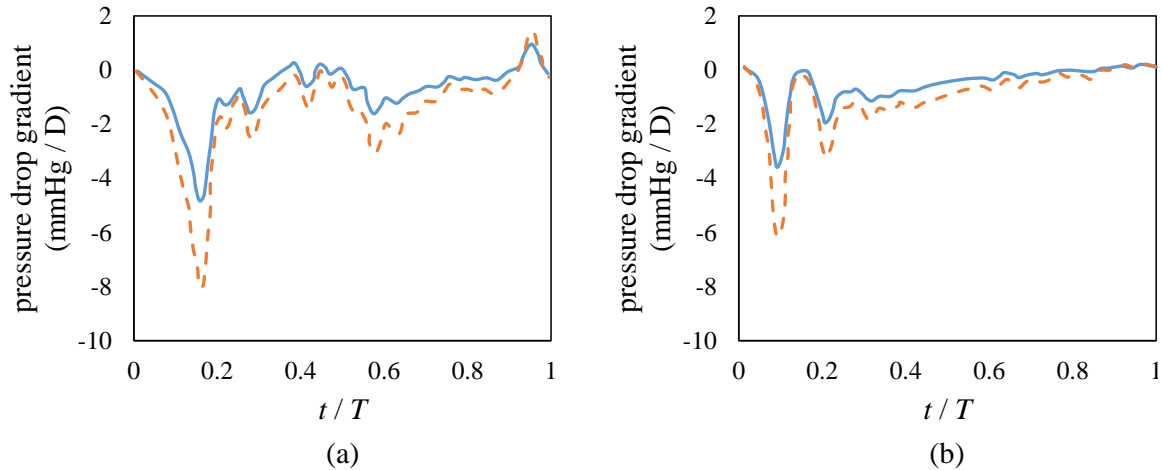


Figure 2.8: Variations of pressure drop gradient for (a) RCA and (b) LAD arteries with eccentric and concentric shapes of stenosis (Guleren 2013). The solid blue and dashed orange lines refer to concentric and eccentric shapes of a stenosis, respectively.

The effect of stenosis geometry on hemodynamics was investigated by Caruso et al. (2015). They compared three different shapes of stenosis including parabolic, trapezoid and elliptical with the same degree of stenosis inside a RCA. Their results showed that the elliptical shape stenosis was characterised by areas with multi-directional velocity and high WSS, and was the worst shape hemodynamically. On the other hand, they found that the least hemodynamically dangerous shape of a stenosis was the parabolic. In a study of the flow through an asymmetric stenosis, Jabir and Lal (2016) found that the velocity profiles were skewed towards the opposite side of the blocked part immediately after the asymmetric stenosis. The distribution of WSS over the artery wall was uneven due to the turbulent breakdown of the jet generated due to a reduction in the cross-sectional area of the stenosis and hence an increase in the flow velocity. The jet flow effect changed the turbulent structures and shifted the eddies far downstream, along with the presence of geometric eccentricity of stenosis. Furthermore, Jeon et al. (2018) investigated the effect of a trapezium shape stenosis on the flow field around the stenosis for pulsatile flow. In their study, different trapezium shapes of stenoses were generated by varying the contraction, plateau, and expansion sections of the stenosis. It was shown that the TAWSS of a mild contraction was greater than that of a sudden contraction around the stenotic region. Furthermore, the effect of contraction shape of the stenosis on the average pressure profile along the centreline of the stenotic flow was higher compared to the expansion shape. In addition, the pressure drop through sudden contractions was higher than those through mild contractions. In another study, the relationship between the morphological parameters in the eccentric coronary stenosis and the post-stenotic flow characteristics was investigated by Xie et al. (2018). Their results showed that the detailed geometry patterns including level of eccentricity, stenosis length, and shape of the stenosis had a great impact on the post-stenotic flow behaviour in an eccentric

coronary stenosis. For example, the increase of the stenosis length led to an increase in the length of the recirculation zone. Further, a higher maximum shear rate and a larger recirculation zone were observed in models with a sharper stenosis shape.

In a recent study by Ozden et al. (2020), the effect of stenosis shape on the post-stenotic flow behaviour including pressure fluctuations and the sound emitted from a constricted blood vessel was studied. Figure 2.9 shows the coherent structures at the phase with maximum velocity in a cardiac cycle. It was shown that the jet flow created from the high slope and overlapping models had shorter length compared to the other models. Therefore, for the high slope and overlapping models, the formation of vortical structures was promoted and started at the exit of the stenotic section. For the other models, the transformation occurred after a certain distance from the stenosis exit. Moreover, the highest values of magnitude of vorticity along the centreline of the flow jet core were seen for the overlapping and high slope models and the lowest value was seen in the asymmetric model. Furthermore, Fig. 2.10 shows the changes in the mean pressure and turbulent kinetic energy (TKE) along the centreline of the core of the jet for different stenosis shapes. It was found that an overlapping model gave a peak TKE value 1.3 times higher than the other models and the second peak TKE value was related to the stenosis model with a high slope. This showed that the effect of the presence of overlap and high entrance slope on the level of flow turbulence. Their results showed that the presence of a high slope at the stenosis entrance and/or an overlap of more than one stenosis shortened the length of the jet flow, triggered the flow turbulence, and increased the TKE and magnitude of pressure fluctuations at the post-stenotic regions.

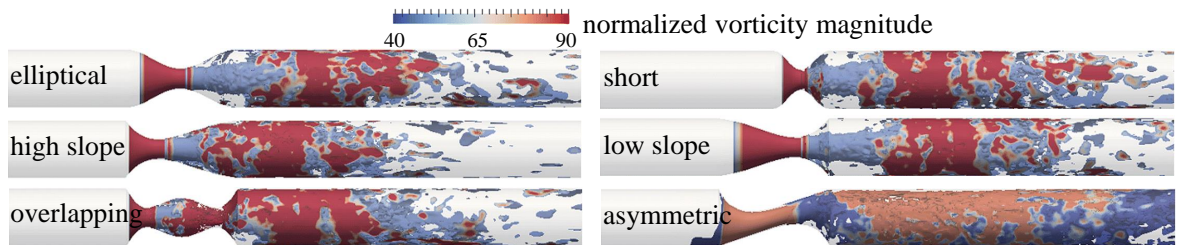


Figure 2.9: Coherent structures coloured by instantaneous normalised vorticity magnitude (Ozden et al. 2020). Vorticity is normalised by u_{max}/D .

To conclude, this section summarised the studies in the literature focusing on the effect of the shape of the stenosis on the flow behaviour. It was discussed that apart from the degree of stenosis, there are other geometrical parameters of a stenosis which affect the hemodynamics of the flow inside stenosed arteries. However, the studies in the literature, to date, focusing on the effect of stenosis on the flow behaviour were mainly limited to the effect of the variation of shape of the stenosis in the stream-wise plane and considered the cross-sectional shape of the stenosis to be circular. Only a few studies in the literature studied the effect of the cross-sectional shape of the stenosis. It is known that the cross-sectional shape of a stenosis varies significantly including crescent, half-moon, elongated, oval, slit-like, and round (Waller 1989), as shown in Fig. 1.4. Thus, in this thesis, the discussed shortcoming is addressed by investigating the effect of cross-sectional shape of a stenosis on the blood flow behaviour and hemodynamic parameters.

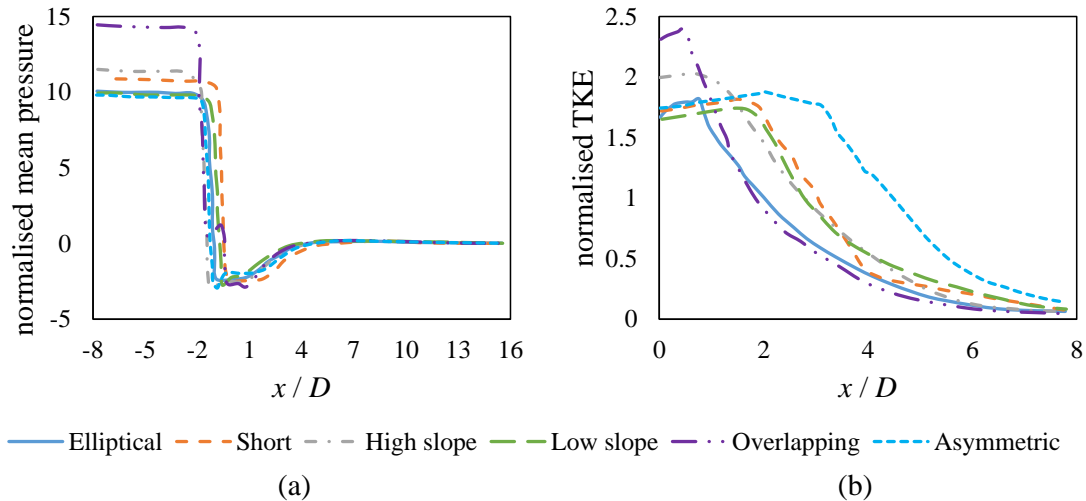


Figure 2.10: Normalised (a) mean pressure changes and (b) TKE along the centrelines of stenosed models (Ozden et al. 2020). Pressure is normalised by ρu_{max}^2 , where u_{max} is the maximum velocity in a cardiac cycle in the artery model and TKE is normalised by the maximum velocity squared (u_{max}^2). $x/D = 0$ is the stream-wise position located at the end of the stenosis.

2.3 Mechanical representatives of coronary artery disease

The presence of a stenosis inside the coronary arteries changes the pattern of the flow after the blockage. This may result in transitional flow behaviour downstream of the stenotic section and changes in the WSS distribution and pressure drop. These mechanical metrics of CADs are of great importance from the fluid mechanics point of view, as they help to better understand the hemodynamics of the diseased coronary arteries in the regions downstream of the stenosis. Section 2.3.1 starts with a short explanation of TKE, as one of the parameters used to investigate the transitional flow behaviour, followed by a review of the literature focusing on the effects of different geometrical and physiological parameters on the transitional flow behaviour in the models of the stenosed coronary artery. Section 2.3.2 first defines WSS and its time-averaged and -dependent parameters, such as TAWSS and oscillatory shear index (OSI). This section continues with a review of the studies investigating different parameters influencing the WSS distribution in stenotic coronary arteries. Section 2.3.3 starts by introducing the major parameters influencing the pressure drop inside the stenotic coronary artery models and their mathematical formulations. Thereafter, studies in the literature focusing on the effect of different governing parameters on the pressure drop and FFR inside the stenosed coronary arteries using mathematical, computational or in-vitro experimental models are reviewed.

2.3.1 Transitional flow behaviour

The blood flow in a coronary arterial system is almost laminar with an average Reynolds number of about 200 for a healthy coronary artery in the resting heart working condi-

tion (Moreno and Bhaganagar 2013). However, transition to turbulence can be observed because of the high velocity fluctuations at different locations. The velocity fluctuations occur due to the arterial stenoses and at curved or bifurcated sections. When an atherosclerosis is formed, the flow downstream of the stenosis becomes transitional due to the instabilities created by the obstruction. The constriction inside the artery results in a jet flow, pushing the blood through the artery at a higher velocity which creates recirculation zones around the jet section, as shown in Fig. 2.11. Therefore, laminar flow separation and transition to turbulence, due to an increase in the velocity and the change in the fluid structure, is most likely to happen after the constricted sections. Flow transition to turbulence in an artery leads to a higher WSS and consequently a higher pressure drop inside the artery. Transition to turbulence inside the arteries is characterised by a sudden increase in the TKE. TKE is calculated from the root-mean-square (RMS) of the velocity fluctuations given by $TKE = \frac{1}{2}(\overline{(u')^2} + \overline{(v')^2} + \overline{(w')^2})$ where u' , v' and w' are the velocity fluctuations in different directions in a Cartesian coordinate system. TKE is a fundamental parameter indicative of the energy of turbulence which is associated with eddies in a turbulent flow. In the context of the flow inside the stenosed coronary artery models, the flow is initially laminar upstream of the stenosis with the TKE equal to zero. As the flow passes through the stenotic section, the flow becomes unstable and the eddies start to form leading to an increase in the TKE. In other words, the transitional flow behaviour appears as a jump in the TKE. Further downstream of the stenotic section, where the eddies break up, the flow is relaminarised, and consequently, the TKE decays. The production and dissipation of TKE or conversion between these two determine the mechanical energy loss or pressure drop. The resultant pressure drop which is affected by turbulence across the stenosis is used in hospitals to diagnose the stenosis (Choi et al. 2018).

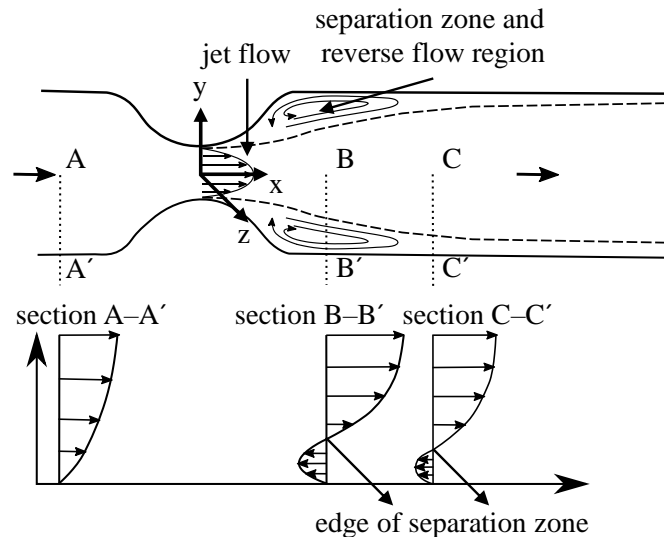


Figure 2.11: A schematic of the flow inside a stenosed artery model showing jet flow and reverse flow regions, recirculation zones, and velocity profiles in different stream-wise locations, adapted from Caro et al. (2011).

There are a few parameters that can trigger turbulent structures inside a coronary artery model. The literature shows that turbulence in the flow was triggered by the presence of arterial stenoses despite the fact that there are almost no turbulent structures in the healthy semi-straight coronary arteries. One of the parameters triggering turbulence

is the geometry of the plaque. Both the shape of the plaque and the degree of stenosis considerably affect the downstream transitional flow behaviour. The effect of geometry of the plaques on the blood flow behaviour is extensively discussed in Section 2.2.2. Another parameter that can trigger turbulence is the heart pulsation. Many of the studies in the literature investigating the turbulence in a stenosed artery model assumed a steady inlet velocity profile (Biswas et al. 2016). However, turbulence inside a constricted coronary artery with a pulsatile flow is different from a model with a steady flow, since the effect of the flow acceleration and deceleration on the flow unsteadiness is not considered. Furthermore, the physiological flow is pulsatile with a complex time varying profile (Zhu et al. 2018). In general, the flow just downstream of a constriction is dominated by an accelerating/decelerating jet that forms during each pulsatile cycle (Beratlis et al. 2007). However, there are different hypotheses applied in the literature that the pulsatile flow inside the coronary arteries can promote or delay the transition to turbulence. For example, it was found that for a sinusoidal oscillatory flow along a simple pipe, transition to turbulence was delayed by superimposing an oscillatory flow on the steady one (Lodahl et al. 1998). Therefore, the effect of flow pulsation on the transitional flow behaviour inside a stenosed coronary artery is not well-understood.

The correlation between the critical Reynolds number and different pulsatile conditions, including the Womersley number and the oscillatory Reynolds number, in a pipe flow was investigated by Trip et al. (2012). The Womersley number is defined as $Wo = (D/2)\sqrt{(2\pi/T)(\rho/\mu)}$, where T is the time period of the heart pulsation cycle. Their results showed that the pulsatility of the flow does not play a role in the transition of the flow, since in their experiments different Womersley numbers yielded similar transition behaviour. Furthermore, variations of the oscillatory Reynolds number also appeared to have little effect, so that the transition seemed to be determined only by the mean Reynolds number. In another study, the transition to turbulence in a pulsating pipe flow was studied by Xu et al. (2017). They found that at small Womersley numbers, the dynamics was dominated by the decay of turbulence during the slower part of the cycle and hence transition was delayed significantly. On the other hand, at the high frequency limit, i.e. large Womersley numbers, the transition threshold appeared to be unaffected by the flow pulsation. In another study, Xu and Avila (2018) showed that increasing the pulsation amplitude and lowering the frequency improved the stability of the flow. However, these results cannot be generalised due to their limitations, including the lack of considering the effect of blockage of the pipe and also the use of a simplified sinusoidal pulsatile flow profile, which has identical flow acceleration and deceleration profiles, compared to that of the physiological pulsatile flow. In addition, the Reynolds number range considered in these studies was higher than those of coronary arteries. Finally, the geometry considered in the previous studies was mainly a simplified model of the artery, a pipe, without focusing on the patient-specific geometries. Therefore, more studies need to be conducted to further investigate whether heart pulsations trigger or mitigate the transition to turbulence inside stenosed coronary arteries.

This section continues with the review of the studies focusing on the effect of different parameters on the transitional flow behaviour inside stenosed coronary artery models. A pulsatile flow in an asymmetric constricted channel as a simple model for blood flow in a constricted artery was studied by Mittal et al. (2003). Their results showed that for the range of Reynolds numbers from 750 to 2000, the flow downstream of the constriction was dominated by two shear-layers, one of which separated from the constriction and

the other from the opposite wall, as shown in Fig. 2.12. Furthermore, the intensity of the turbulent fluctuations increased with the Reynolds number. On the other hand, the stream-wise extent of the region of intense turbulent fluctuations was found to be reduced with increasing the Reynolds number. This is because as the Reynolds number increases, both separated shear layers become more unstable and roll up into vortices at a shorter stream-wise distance after the stenotic section. Their results also showed that the flow transitioned to turbulence downstream of the region where the separated shear layers reattached to the channel walls for Reynolds numbers higher than about 1000.

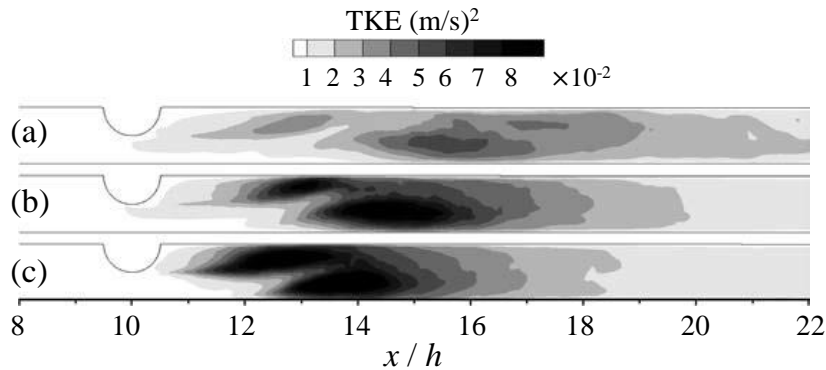


Figure 2.12: Contour plot of TKE for different Reynolds number including (a) $Re = 750$, (b) $Re = 1400$ and (c) $Re = 2000$ in an asymmetric constricted rectangular channel (Mittal et al. 2003). h is the height of the channel.

Moreover, the physics of pulsatile flows within a 3D channel with an eccentric stenosis was studied by Molla et al. (2012) using the large-eddy simulation (LES) method. Figure 2.13 presents the time history of the stream-wise normalised velocity fluctuations. The flow was predominantly laminar upstream of the stenosis, as the magnitude of the velocity fluctuation was negligible in this region. When the flow passed through the stenosis, turbulence was triggered and turbulent fluctuations became the strongest within $1 \leq x/h \leq 6$. Further downstream of the stenosis, the magnitude of the velocity fluctuations decreased, as the flow gradually relaminarised. The results showed that the flow field driven by the pulsatile inlet condition underwent laminar-turbulent-laminar patterns in the stream-wise direction, triggered by the stenosis. In another study by Khair et al. (2015), direct numerical simulation (DNS) was employed to investigate the laminar-turbulent transitional behaviour of the pulsatile flow in a constricted channel. As shown in Fig. 2.14 for the higher values of Reynolds number and higher degrees of stenosis, the peak value of TKE and hence the transition moved closer to the constricted location. A higher level of TKE in the immediate post-stenotic region was closely related to the interaction between the two shear layers formed at the top and bottom walls. These shear layers separated from the stenosis and produced intense pairwise vortices in the post-stenotic region. After reaching the transitional point, the TKE value decayed gradually, representing the beginning of the flow re-laminarisation.

The TKE profile in a straight pipe with a steady flow was investigated by Biswas et al. (2016), as shown in Fig. 2.15. It was shown that by increasing the Reynolds number, the flow changed from laminar to transitional accompanied by an increase in the value of TKE. In their study, the transition to turbulence occurred at a Reynolds number of around 2900, as illustrated with a jump in the TKE profile. Their results showed that

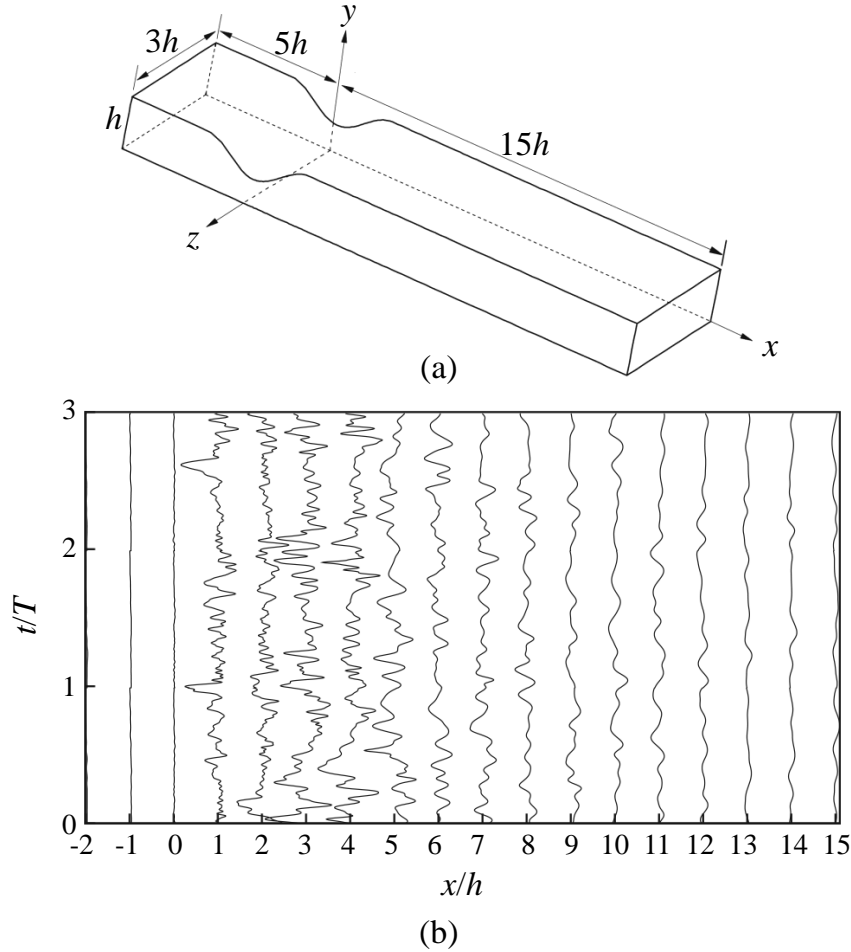


Figure 2.13: (a) Computational domain and coordinate system of the stenotic channel and (b) time history of the stream-wise velocity fluctuation normalised by its maximum value (u''/u''_{max}) based on phase-averaging over the last three pulsation cycles, along the central streamline ($y/h = 0.5$ and $z/h = 1.5$) and for $Re = 2000$ (Molla et al. 2012).

in the absence of constriction in the flow or flow pulsation, the transition occurred at a higher Reynolds number compared to cases with a blockage inside an artery model and flow pulsation. Moreover, the flow through an asymmetric stenosis with an elliptical cross section was studied by Jabir and Lal (2016) using LES. Although the pulsatile flow inside the carotid arteries is different from that of coronary arteries, the results presented in their study provide useful information on the coherent structures in the post-stenotic regions. Their results, in Fig. 2.16, show that at the onset of the inlet pulse, the flow field contained traces of the weak vortical rings generated in the previous cycle and underwent substantial deformation further downstream. Accelerated jetting of the fluid through the stenosis, at the phase of $T/8$, created a series of fast moving planar vortical rings, while at the end of the cycle most of the vortical structures were advected from the domain.

Characterisation of the flow around two different stenosis models with a pulsatile flow condition was performed by Choi et al. (2018). Figure 2.17 shows the contour maps of the TKE production rate per unit volume for these stenosis models and at three phases in a pulsatile cycle using particle image velocimetry (PIV). The results showed that the TKE production rate had high values near two shear layers. The first shear layer separated from the throat of the stenosis, and the other formed at the upper wall, especially at the

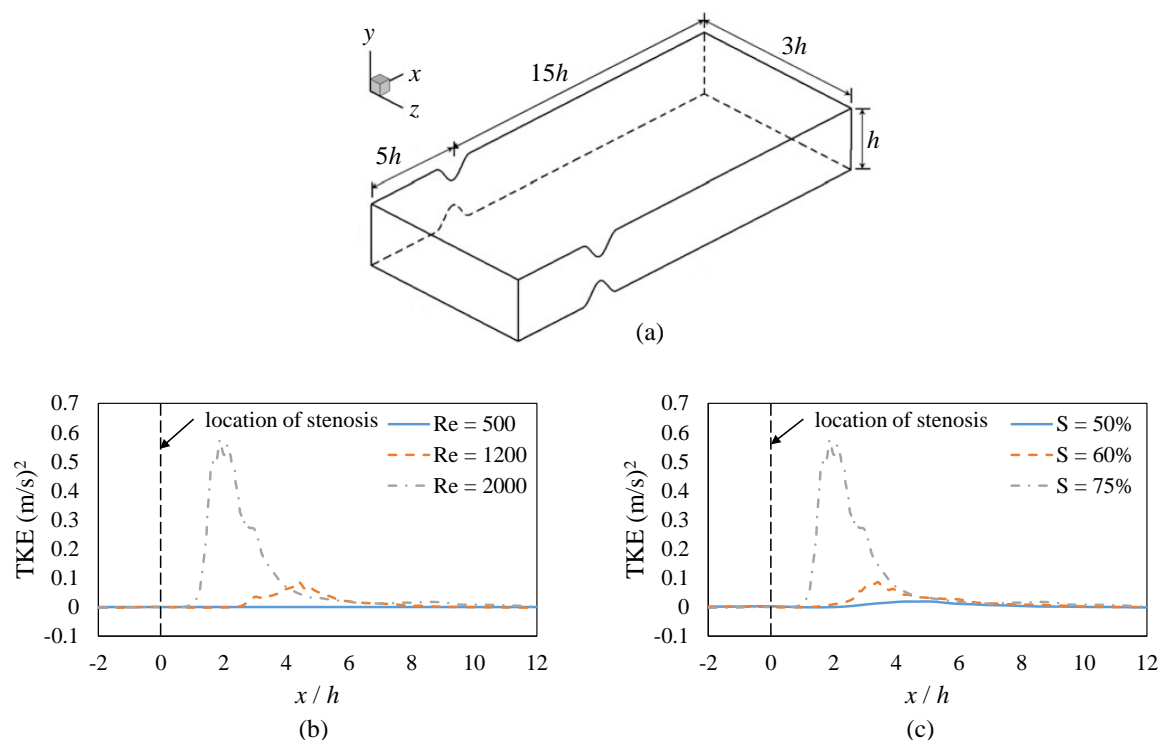


Figure 2.14: (a) Schematic of a symmetric stenotic rectangular channel and the coordinate system, and TKE profiles for (b) different Reynolds numbers with $S = 75\%$, and (c) different degrees of stenosis with $Re = 2000$ along the central streamline of the domain (Khair et al. 2015). h is the height of the channel.

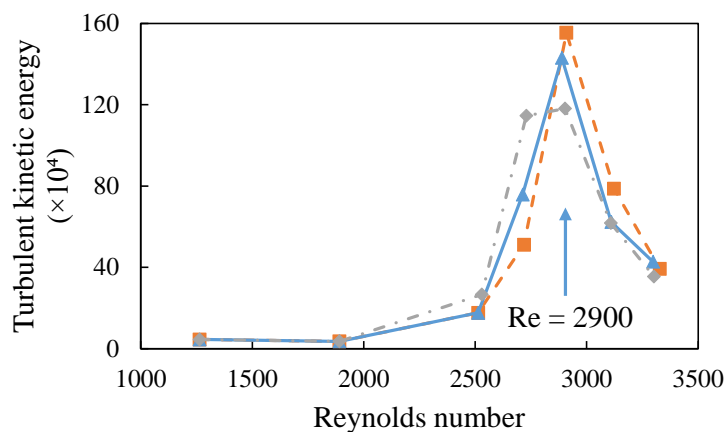


Figure 2.15: Distribution of mean value of TKE normalised by the area-averaged velocity as a function of Reynolds number for three runs of a porcine blood sample (Biswas et al. 2016).

maximum flow rate condition (Fig. 2.17b). A strong shear layer induced vortex shedding (Boghossian and Cassel 2013), and often induced a turbulent stenotic flow (Varghese et al. 2007b). Furthermore, the stenosis model with a higher degree of stenosis and a shorter stenosis length created higher rates of TKE production compared to the other case and hence resulted in a higher pressure drop.

The studies in the literature, as discussed in this section, provide a basis for the tran-

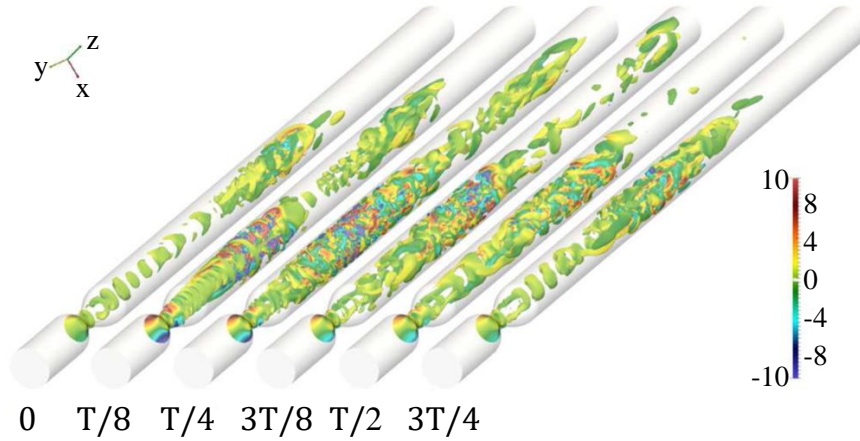


Figure 2.16: Coherent vortical structures of the Q-criterion coloured by the normalised instantaneous axial vorticity in the unsteady flow field for different phases in a pulsatile cycle for the common carotid artery model (Jabir and Lal 2016).

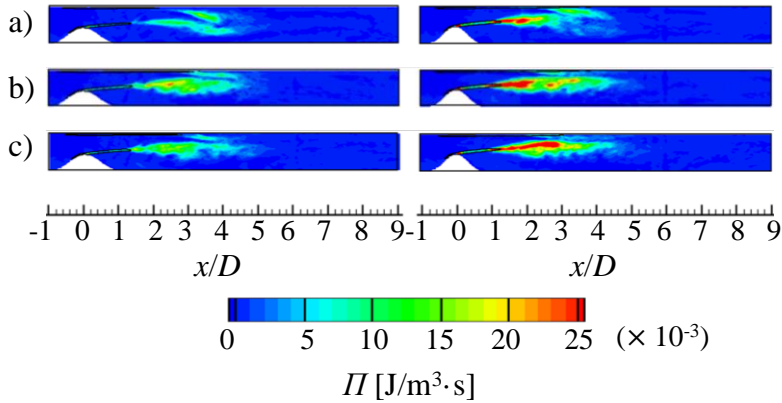


Figure 2.17: Contour maps of the TKE production rate per unit volume (Π) for two stenosis models: left column with $S = 45\%$ and a stenosis length of 20 mm and right column with $S = 48\%$ and a stenosis length of 16 mm at (a) $t/T = 0.125$, (b) $t/T = 0.175$, and (c) $t/T = 0.225$, respectively (Choi et al. 2018).

sitional flow behaviour inside the healthy and diseased models of an artery with steady or pulsatile flow. The literature was limited to simplified models of the coronary arteries, such as a straight pipe or a constricted rectangular channel instead of considering the patient-specific geometric features of the coronary arteries. Furthermore, they are based on simplified assumptions, such as considering steady blood flow through the arteries instead of a pulsatile flow. The presence of the geometric irregularities in the patient-specific coronary artery models can change the transitional flow behaviour, since any geometric irregularities usually result in changes in the local cross sectional area of the artery and consequently changes in the velocity components. Furthermore, as discussed earlier, the presence of a physiological flow profile can change the time-dependent hemodynamic parameters. Therefore, there is a need to better understand the transitional flow behaviour inside the patient-specific stenosed coronary artery models with a physiological blood flow profile.

2.3.2 Shear stress

The fluid flow inside an artery has a parabolic velocity profile with zero velocity at the wall, no slip condition, and maximum velocity at the cross-sectional centre of the artery as shown in Fig. 2.18. The friction between the arterial wall and the blood flow creates a tangential force exerted by the wall on the fluid in a direction on the local tangent plane, which is defined as WSS. For Newtonian fluids, the WSS is proportional to the velocity gradient at the artery wall, as

$$\tau_w = \mu \left(\frac{\partial u}{\partial y} \right)_{y=0}, \quad (2.2)$$

where τ_w is the WSS, μ is the blood dynamic viscosity, u is the flow velocity parallel to the wall and y is the normal distance to the wall.

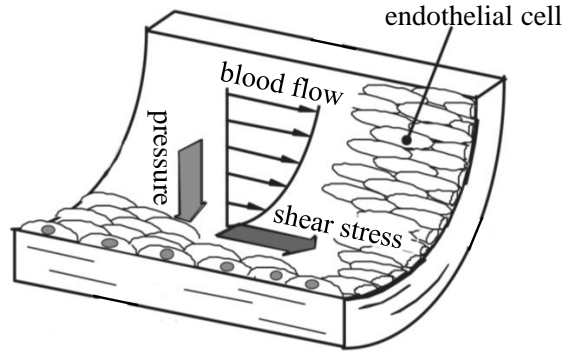


Figure 2.18: Arterial wall showing blood flow profile, shear stress and pressure acting on the endothelial cell (Ohashi and Sato 2005).

Another important hemodynamic parameter is the TAWSS, which is defined as

$$TAWSS = \frac{1}{T} \int_0^T |\tau_w| dt, \quad (2.3)$$

where T represents the period of one cardiac cycle. This parameter is more correlated with intimal thickening, as an abnormal accumulation of cells in the vascular intima due to a physiologic healing response to injury to the blood vessel wall, compared to the time-dependent WSS (Keynton et al. 2001).

It was shown that an oscillatory flow is a more effective predictor of intimal thickening, as the endothelial layer is sensitive to flow reversal. Therefore, a unidirectional high or low WSS may not be an accurate metric in predicting intimal thickening (Himburg et al. 2004). The OSI, as a dimensionless hemodynamic metric, measures the oscillatory nature of the flow and quantifies the deviations in the direction of the WSS vector throughout a cardiac cycle, and is defined as

$$OSI = \frac{1}{2} \left(1 - \frac{\frac{1}{T} \left| \int_0^T \tau_w dt \right|}{\frac{1}{T} \int_0^T |\tau_w| dt} \right), \quad (2.4)$$

OSI is calculated based on the time and position-dependent results of phase-averaged WSS during a cardiac cycle. This metric falls within the range of 0-0.5, where a value of 0.5 indicates a pure oscillatory flow with no net forward motion and a high possibility of endothelial dysfunction. Conversely, a value of zero indicates a purely forward motion with no oscillatory flow (Fulker 2016).

Endothelial cells form a single cell layer that lines all blood vessels. These cells are in direct contact with the blood flow and hence are constantly exposed to the mechanical forces that blood applies on the arterial wall. In in-vivo experimental studies, it was found that arterial regions exposed to low WSS at baseline were associated with increased measures of the plaque bulk, increased lipid accumulation and vascular remodelling. Luminal remodelling changes vascular geometry and in turn alters the local flow fields and WSS (Chatzizisis et al. 2008). Thus, vascular geometry and local WSS are known as important risk-factors in CAD. Furthermore, local hemodynamic factors, in particular low WSS, play a major role in the atherosclerosis location, underlining the importance of studying the WSS magnitude and distribution in coronary arteries (Chatzizisis et al. 2008).

Endothelial shear stresses also influence the artery dimensions and the wall composition in different ways during the progression of atherosclerotic plaque (Wentzel et al. 2012). In a study by Stone et al. (2003), it was shown that regions of low WSS (< 0.91 Pa) develop progressive atherosclerosis and inward remodelling, areas of normal physiological WSS remain quiescent, and areas of increased WSS (> 2.7 Pa) exhibit outward remodelling. Inward and outward remodelling denote a reduction and an increase in vessel size, respectively. Furthermore, the results of Gijssen et al. (2008) showed that the elevated WSS was associated with the elevated strain within the plaque, which implied that the high WSS may destabilise plaques and lead to a plaque rupture. On the other hand, Rikhtegar et al. (2012) showed that although low WSS is necessary for plaque formation, its presence alone is not sufficient to predict future plaque locations. They showed that time-dependent hemodynamic parameters, i.e. OSI, have a larger efficacy for the prediction of future plaque events compared to the WSS.

Figure 2.19 presents the results of the normalised WSS for different Reynolds numbers and degrees of stenosis in a constricted channel (Khair et al. 2015). The results show that the WSS increased with an increase in the Reynolds number, since the stream-wise velocity increased. Furthermore, by reducing the cross sectional area of the channel from $S = 50\%$ to $S = 75\%$, the mean WSS increased. For narrower channels, the mean velocity field increased and hence, the mean WSS increased. Moreover, based on the negative values of WSS, representing the reverse flow in the recirculation region, the separation and reattachment points occurred earlier as the Reynolds number and degree of stenosis increased.

The risk assessment for the presence of an atherosclerotic plaque inside a patient-specific coronary arterial tree was studied by Melchionna et al. (2013) by introducing an artificial stenosis at different locations. Figure 2.20 shows WSS contours in a simulated coronary system with an artificial stenosis in the LCx proximal. It was shown that a severe stenosis led to major alterations of the local fluid flow parameters, most notably the WSS distribution at the location of stenosis and downstream. Figure 2.21 shows the 2D unwrapped maps of WSS in the proximal LAD for different phases in a cardiac cycle (Eslami et al. 2019). At the beginning of the proximal LAD, higher values of WSS were

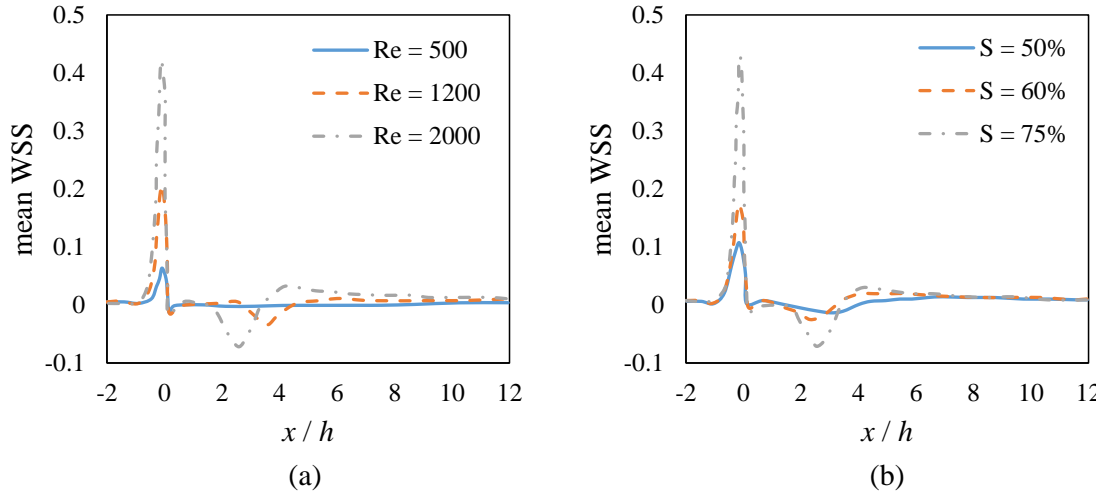


Figure 2.19: Non-dimensionalised time- and spanwise-averaged profile of the WSS ($\tau_w/\frac{1}{2}\rho U^2$) in a constricted channel for (a) different Reynolds numbers at $S = 75\%$ and (b) different degrees of stenosis at $Re = 2000$ (Khair et al. 2015). S refers to the degree of stenosis.

observed on the left side of the contours due to the presence of the luminal narrowing. Further downstream of the stenotic section, WSS values were reduced, as shown on the right side of the contours. This is due to the regions of recirculation immediately after the stenosis creating flow reversal and low WSS. Furthermore, the results show that the WSS values increased with an increase in the blood flow rate in a cardiac cycle with the highest WSS values related to the peak LAD flow phase and the lowest related to the phase of mid systole.

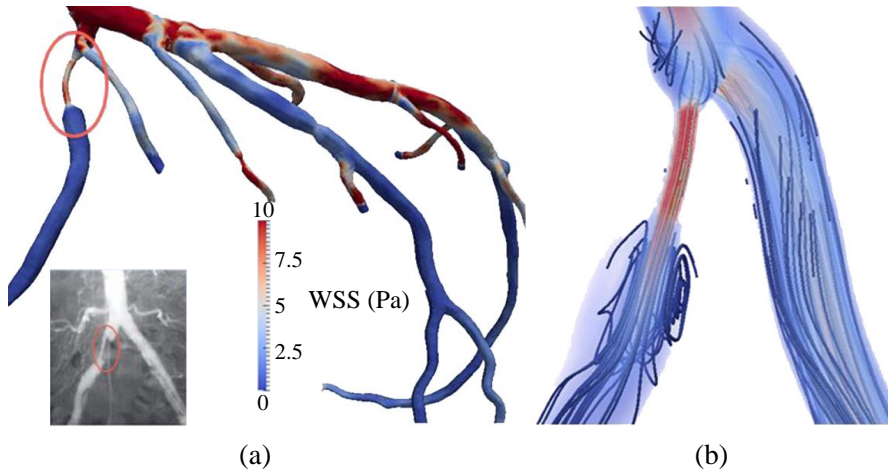


Figure 2.20: (a) WSS contour of the simulated coronary system showing an artificial plaque, highlighted in a circular red line, with $S = 70\%$ at the proximal of LCx (Melchionna et al. 2013). The plaque was modified from a vessel geometry of a typical clinical angiography. (b) zoomed-view of the the plaque showing the flow streamlines.

This section summarised the studies in the literature focusing on the effect of different governing geometrical and physiological parameters on the WSS distribution inside the models of stenosed coronary arteries. It was noted that extreme values of WSS result in vascular remodelling such that regions with low WSS are prone to atherosclerotic plaque

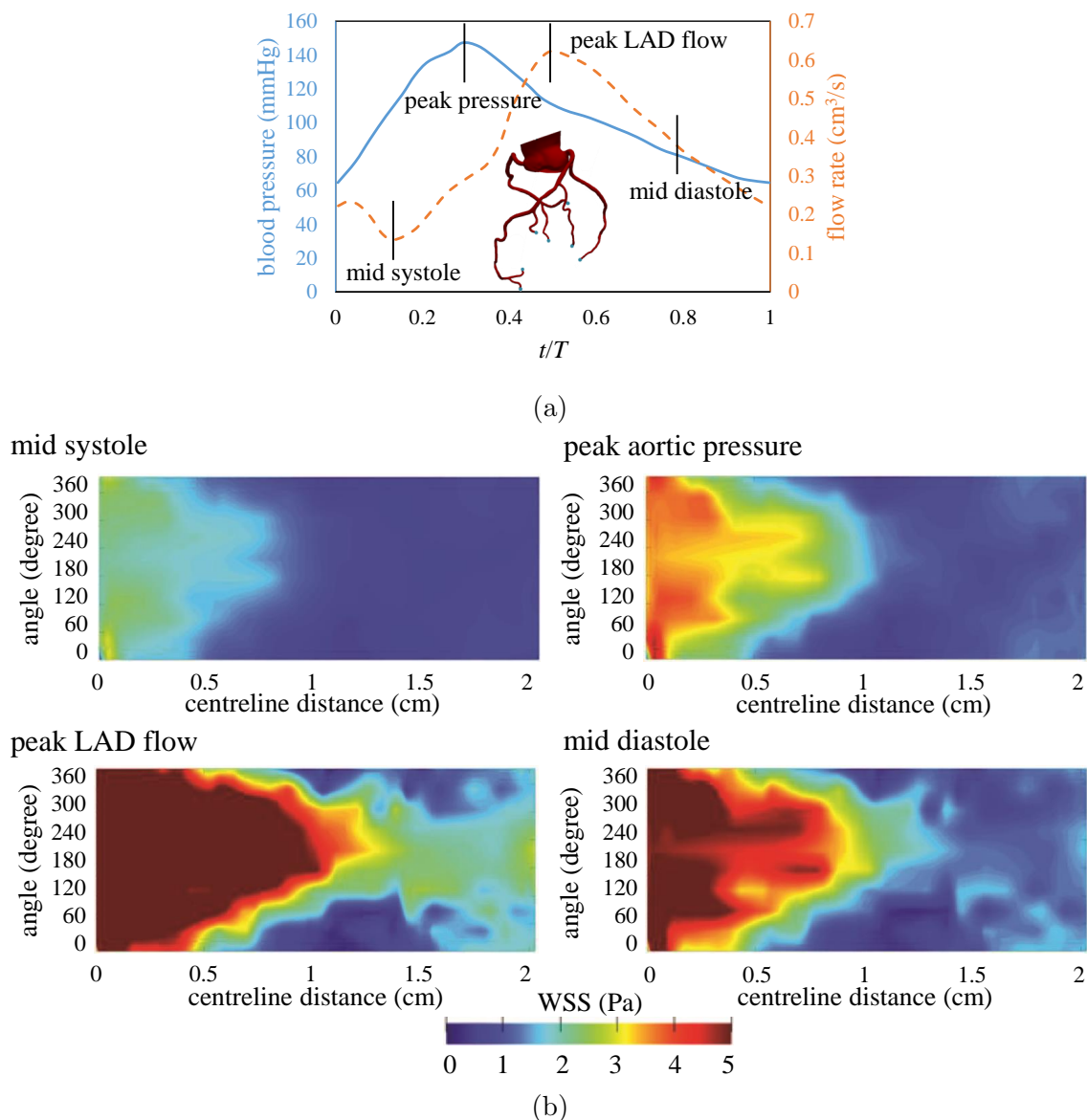


Figure 2.21: (a) Blood pressure and flow rate during a cardiac cycle as well as a schematic of the geometry of the coronary arterial tree, and (b) 2D unwrapped maps of WSS in the proximal LAD for different phases in a cardiac cycle (Eslami et al. 2019).

progression and regions with high WSS values are likely to experience plaque rupture due to plaque destabilisation.

2.3.3 Pressure drop and FFR

The amount of pressure drop represents the severity of CAD, as discussed in Chapter 1. In general, arterial irregularities and stenoses inside coronary arteries create a pressure drop. FFR, as one of the most common clinical methods for evaluation of pressure drop across a stenotic coronary artery, is defined as the ratio of the distal coronary pressure (P_{distal}) to the proximal (aortic) pressure ($P_{proximal}$), as

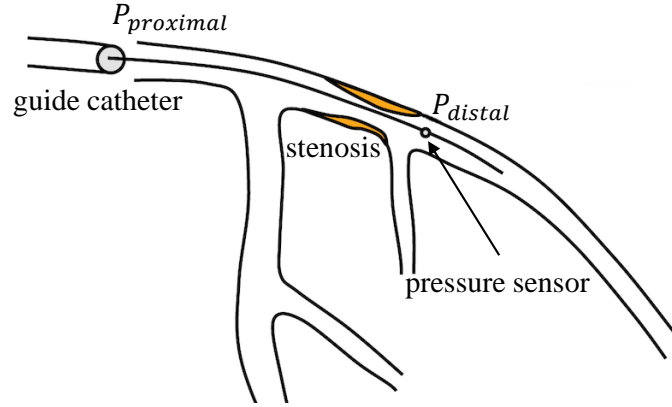


Figure 2.22: Schematic of FFR measurement, reproduced from Abbott (2020). $P_{proximal}$ is the proximal (aortic) pressure and P_{distal} is the distal coronary pressure.

$$FFR = \frac{P_{distal}}{P_{proximal}}, \quad (2.5)$$

As schematically shown in Fig. 2.22, FFR is measured by inserting a guiding catheter with a pressure sensor connected on its tip to the location of stenosis and measuring the distal coronary pressure of the stenosis and the aortic pressure (proximal) during maximal hyperemia. In a normal healthy coronary artery, FFR is expected to be close to unity, regardless of the patient or the specific vessel studied (Pijls et al. 1995). An FFR value of 0.75 or less identifies ischemia-causing coronary stenoses with an accuracy of more than 90% which mostly require revascularisation (Tonino et al. 2009). Furthermore, for the FFR values greater than 0.8, medical therapy is suggested as it represents non-ischemia-producing stenosis. However, FFR values between 0.75 to 0.8 are in the grey zone, where either revascularisation or medical therapy may be suggested as a treatment (Pijls et al. 2007).

From dimensional analysis, the pressure drop across a simplified coronary artery model, (Fig. 2.23), can be expressed in the form

$$\Delta P = P_1 - P_2 = f\left(Re, \frac{L}{D}, \frac{A_1}{A_0}, \frac{l}{D}, e, \theta, r, t, E, \frac{dV}{dt}\right), \quad (2.6)$$

where ΔP is the pressure drop along the artery with the length of L and the internal diameter of D , Re is the Reynolds number ($= \rho U D / \mu$), ρ is the fluid density, U is the time-averaged mean velocity in the unobstructed section of the artery, μ is the fluid viscosity, A_0 and A_1 represent the cross-sectional area of the unobstructed artery and the minimum constricted cross sectional area, respectively, l is the plaque length, e is the plaque eccentricity, V is the instantaneous velocity of the unobstructed artery (averaged over the entire cross section), θ is the artery curvature degree, r is the artery curvature radius, t is the artery wall thickness, and E is Young modulus of the artery wall.

The pressure drop along a simplified stenotic coronary artery model with a pulsatile flow is a function of different major effects. The pressure drop due to the viscous friction effect is the first effect, which is a function of the fluid velocity inside the artery, fluid viscosity, artery length, and its internal diameter. The Darcy-Weisbach equation is an

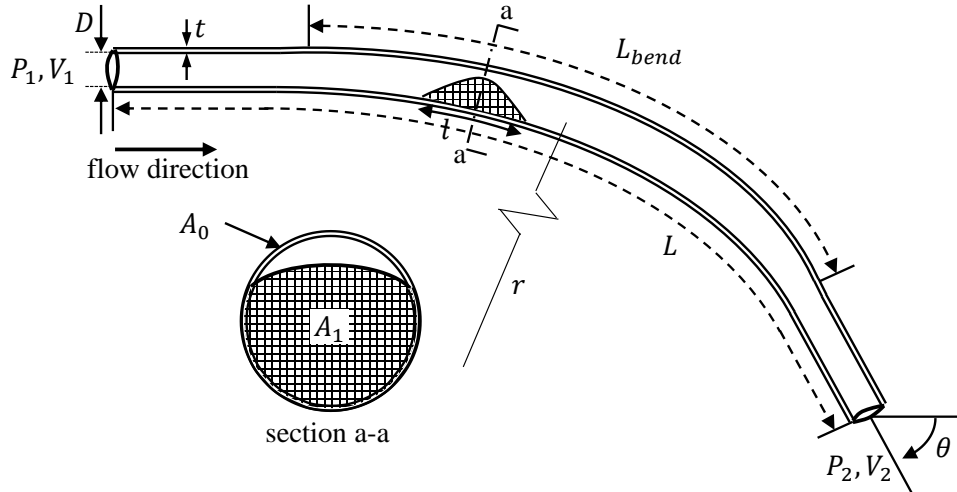


Figure 2.23: Schematics of a simplified coronary artery model and the corresponding geometrical parameters. D is the internal diameter of the artery, t is the arterial thickness, L is the length of the artery, l is the length of the stenosis, r is the curvature radius, θ is the curvature angle, P_1 and P_2 are the pressure of the blood flow at the inlet and outlet, respectively, and V_1 and V_2 are the velocity of the blood flow at the inlet and outlet, respectively.

empirical equation used for the calculation of the pressure drop due to the viscous friction along a given length of the coronary artery modelled as a uniform pipe using the mean velocity of the blood flow. As displayed in Fig. 2.24, this equation is derived based on the force balance between the pressure and shear forces of the fluid disk element. Darcy-Weisbach equation is defined as

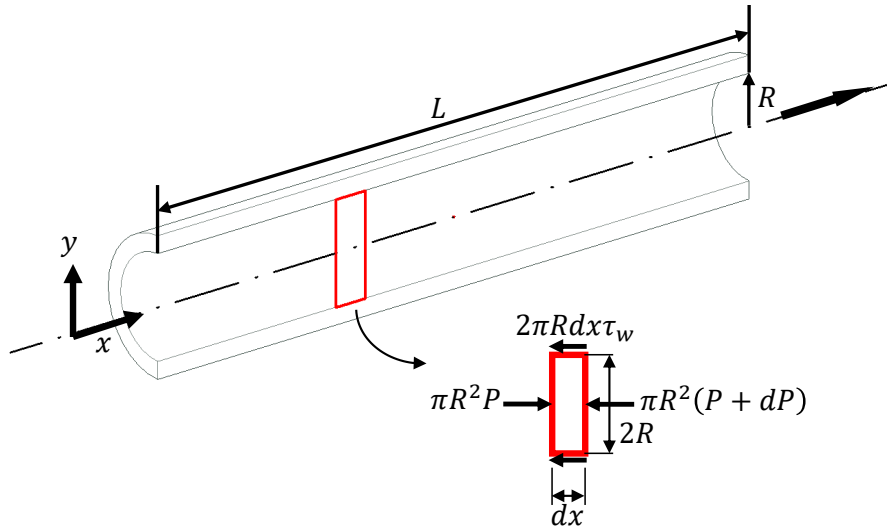


Figure 2.24: Free body diagram of the fluid disk element in a healthy simplified artery model. x and y are the stream-wise and vertical components in a Cartesian coordinate system, R is the arterial radius, $\pi R^2 P$ and $\pi R^2 (P + dP)$ are the pressure forces acting on the fluid element disk, the control volume highlighted in red, and $2\pi R dx \tau_w$ is the shear force acting on the control volume with the stream-wise length of dx .

$$\Delta P_{viscous} = f \frac{L}{D} \frac{\rho U^2}{2}, \quad (2.7)$$

where $f(= 8\tau_w/\rho U^2)$ is the Darcy friction factor. Since the laminar flow assumption is valid and applicable in the majority of healthy coronary arterial systems (Zhu et al. 2018), the Darcy friction factor for the laminar flow in a circular pipe model is determined by $f = 64/Re$. This means that for laminar flow, the friction factor is only a function of the Reynolds number and is independent of the surface roughness of the artery. Substituting the Darcy friction factor into the Darcy-Weisbach equation, the pressure drop equation due to the viscous friction becomes

$$\Delta P_{viscous} = \frac{128}{\pi} \frac{\mu \dot{Q}}{D^4} L, \quad (2.8)$$

where \dot{Q} is the flow rate.

The second major effect is related to the blockage of the artery, which is dependent on the geometry of the stenosis, such as its degree, shape, eccentricity, and the plaque length. The Bernoulli equation in the stream-wise direction of the artery model is employed to calculate the pressure drop due to the blockage effect, as

$$\Delta P_{blockage} = \frac{kt}{2} \left(\left(\frac{A_0}{A_1} \right)^2 - 1 \right) \rho V |V|, \quad (2.9)$$

where kt is a constant which can be determined experimentally.

The third effect is related to the pulsatility of the flow, which is a function of the time derivation of the instantaneous fluid velocity. The pressure drop due to the acceleration and deceleration caused by the pulsatility of the flow can be calculated by applying the stream-wise momentum equation (Young and Tsai 1973a), as

$$\Delta P_{pulsatile} = ku \rho L \frac{dV}{dt}, \quad (2.10)$$

where ku is a constant which is a function of the acceleration and deceleration of the flow.

Equations 2.8–2.10 are for a straight artery model. However, since most of the arteries in the arterial system are of curved shape, neglecting the effect of arterial curvature can lead to inaccuracies, such as substantial quantitative differences in the WSS distribution, pressure drop, and FFR (Siggers and Waters 2005; Verkaik et al. 2009). Moreover, based on the clinical studies, arterial diseases primarily occur in curved areas or bifurcations of blood vessels rather than within the straight sections of the blood vessels (Malek et al. 1999). Therefore, the effect of artery curvature on the flow behaviour is required to be considered for an accurate prediction of WSS and pressure drop.

In order to account for the effect of curvature of the arteries, another term should be added for the evaluation of pressure drop, which is related to the turbulence losses induced due to the curvature of the arteries. It was shown that pressure drop due to

curvature of the artery is a function of curvature radius and angle of the artery (Stultz and Kitto 2005), as

$$\Delta P_{curvature} = \frac{kb}{2} \rho V |V|, \quad (2.11)$$

where kb is the bend head loss coefficient that needs to be determined experimentally and it is a function of curvature angle and radius. It should be noted that the location of a stenosis in the curved arteries, whether it is located in the centre of curvature or proximal or distal to the curvature in the semi-straight parts of the artery, is an important parameter affecting the pressure drop.

Wall elasticity is another parameter affecting the pressure inside the arteries, which is a function of the material properties of the artery wall and the external pressure acting on the artery wall. Elasticity of the arteries contributes to maintaining a relatively constant pressure in the arteries despite the pulsatile nature of blood flow. Assuming the arterial wall is thin, cylindrical, isotropic, homogeneous, incompressible, and linearly elastic, the relationship between the pressure and area of the arteries, according to Formaggia et al. (2006) and Mirramezani et al. (2018), is

$$P(x, t) - P_{ext} = P_d + \frac{4}{3} \frac{\sqrt{\pi} E t}{A_d} (\sqrt{A} - \sqrt{A_d}), \quad (2.12)$$

where P_{ext} is the external pressure acting on the artery wall induced by the surrounding tissues, and P_d and A_d are the reference values of diastolic pressure and area, respectively. However, as mentioned in Section 2.1.1, ageing results in stiffening of the arteries by increasing the Young's modulus. Both the arterial wall thickness (Dinno et al. 2000; Najjar et al. 2005) and Young's modulus (Geest et al. 2004; Sun 2015) are reported to be increased with ageing. Furthermore, the arterial stiffness has a relation with the atherosclerotic lesions. It was reported that patients with cardiovascular diseases often develop central artery stiffness (Benetos et al. 2002). It was also reported by Khanafer et al. (2011) that the elastic modulus of the human coronary arteries increases from 1.5 MPa for the healthy arteries to 3.8 MPa for atherosclerotic vessels. On the other hand, arterial wall thickness is another parameter which is also affected by the presence of atherosclerosis inside the arteries. It was reported by Gradus-Pizlo et al. (2003) that the arterial wall thickness of the left anterior descending coronary artery is greater in patients with coronary atherosclerosis (1.9 ± 0.3 mm) than in those with normal coronary arteries (1.0 ± 0.1 mm). Therefore, in the presence of atherosclerosis inside the coronary arteries and ageing, the pressure inside the arteries, in the absence of the external pressure, remains almost the same as the reference pressure.

There are different parameters influencing the pressure drop inside the arteries. Some of these parameters were employed in the literature to present algebraic models for the evaluation of the pressure drop. Young and Tsai (1973a) and Young and Tsai (1973b) presented an algebraic equation for the estimation of the pressure drop both for steady and unsteady flows. Their model was based on two stenosis models including an axisymmetric model and a non-symmetric shape with a half round-edge and a half sharp-edge. Although their results showed strong influence of the geometry on the pressure drop, the applicability of their model for other shapes of stenosis was not investigated.

In another study, different stenosed valves were used to simulate an aortic stenosis and develop an equation to estimate the pressure drop (Clark 1976). This study was performed using steady flow measurement of the pressure drop. Furthermore, Seeley and Young (1976) studied the effect of the length and the degree of stenosis of a blunt plaque on the pressure drop across an arterial stenosis by using an in-vitro steady flow test. They also investigated the pressure drop across multiple stenoses by considering two blunt plugs in series. Their experimental results showed that the pressure drop induced by multiple stenoses cannot be estimated by a summation of the pressure drops for single stenoses unless the spacing between them exceeded a critical distance which is a function of the Reynolds number. Their model was developed based on steady flow and hence the effect of the unsteadiness of the flow inside the arteries on the pressure was not considered.

Based on the conservation of energy, Huo et al. (2012) developed an analytical model to determine FFR. Their model considered various energy losses along the length of a stenosis, such as convective and diffusive energy losses as well as the energy loss due to the sudden constriction and expansion in the lumen area. However, their model was only based on steady flow and considered the length and the degree of stenosis as the only parameters affecting the pressure drop. More recently, different algebraic models based on computational fluid dynamics (CFD) simulations were presented by Mirramezani et al. (2018) to compute pressure drop in the coronary arterial stenosis. Their models ranged from 1D to 3D time-dependent simulations. Their results showed that viscous dissipation and flow separation had a significant contribution to the pressure drop inside the stenotic arteries.

To conclude, there are a number of algebraic pressure drop equations in the literature. These models were found to exhibit a wide variation in their predictions and are limited due to the lack of consideration of the effect of shape of the stenosis and flow profile. None of the developed models in the literature considered the effect of the shape of the stenosis, its level of eccentricity, and curvature. Furthermore, the models in the literature have been developed for specific flow profiles and their applicability to any general forms of the flow profiles has not been thoroughly investigated. Therefore, development of a mathematical model which is able to evaluate pressure drop by considering the effects of different parameters, such as shape of the stenosis, curvature of the artery, and pulsation of the flow, is of great importance.

Apart from the studies with a focus on the mathematical modelling of pressure drop inside the diseased coronary arteries, there are studies in the literature focusing on the investigation of the effect of different physiological and geometrical parameters of the blood flow on the pressure drop and FFR (Figuerola et al. 2006; Siogkas et al. 2015; Wu et al. 2015). Yao et al. (2000) developed a computational model of 3D blood flow in curved arteries with elliptic stenosis. Figure 2.25 shows the effect of artery curvature on the pressure drop in a model of a curved artery. The results show that the pressure at the throat area was lower and the pressure recovery downstream was slower when the angle of curvature increased, indicating that the presence of curvature augmented the increased flow resistance due to the stenotic lesions. Furthermore, it was found that a mild stenosis in a curved artery resulted in a more intense secondary flow structure and a higher WSS in comparison to a higher degree of stenosis in a straight artery.

Figure 2.26 shows the profiles of the time and spanwise-averaged wall pressure at different Reynolds numbers and degrees of stenosis (Khair et al. 2015). Based on the

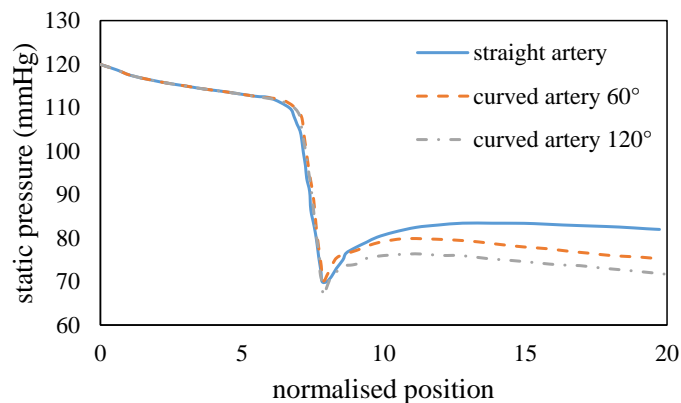


Figure 2.25: Static pressure profile along the axis of the artery for different curvature angle (Yao et al. 2000). The stream-wise position in horizontal axis is normalised by the artery diameter.

results, the wall pressure drops significantly at the centre of the stenosis due to the channel constriction. A higher pressure drop was observed when the Reynolds number and degree of stenosis were increased. The former was also reported by Paul and Molla (2012). The latter is due to the flow speeding up as the degree of stenosis increases, the flow speeds up resulting in a larger pressure drop. In another study, Li et al. (2017) investigated the relationship between the flow and pressure in an idealised multiple sequential stenoses coronary artery model. Figure 2.27 presents pressure drop across the multiple sequential stenoses as a function of the flow rate. Their results showed that pressure drop was linearly correlated with flow rate irrespective of the number of stenosis.

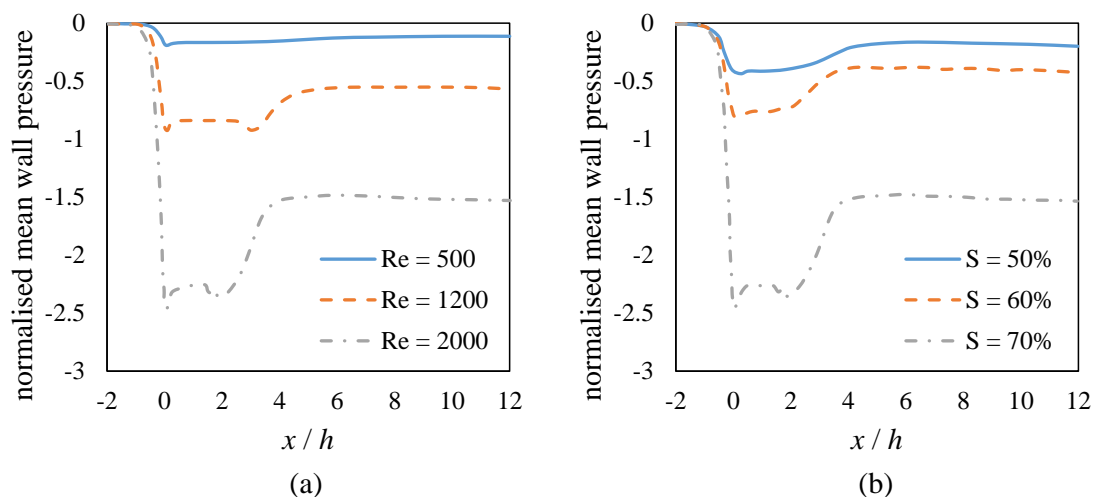


Figure 2.26: Non-dimensionalised time- and spanwise-averaged profile of the wall pressure for (a) different Reynolds numbers with $S = 75\%$ and (b) different degrees of stenosis at $Re = 2000$ (Khair et al. 2015).

In this section, the studies in the literature with a focus on the effect of different parameters on the pressure drop and FFR inside the stenosed coronary arteries were reviewed. Different parameters affecting the pressure inside the stenosed coronary arteries were discussed and the corresponding studies were reviewed. The studies in the literature focusing on the development of a mathematical model for the investigation of pressure

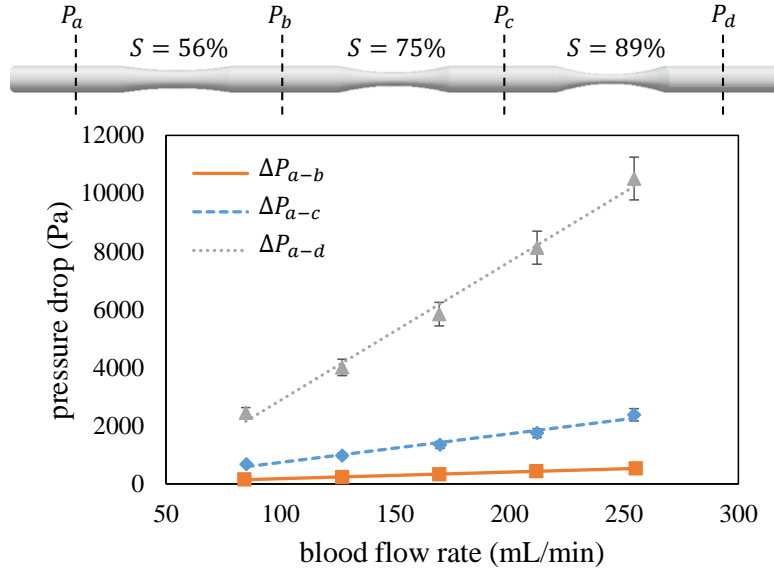


Figure 2.27: Pressure drop measured across multiple sequential stenoses with different flow rates (Li et al. 2017).

drop are however limited. The developed models mainly fail to consider the effect of the shape of the stenosis or blood flow profile for the pressure drop investigation. Furthermore, the effect of arterial curvature on the pressure drop and FFR, which is of great importance, is almost missing in the literature. As most of the arterial diseases occur in curved areas of the arteries rather than within the straight sections of the blood vessels, this effect needs to be considered.

2.4 Treatment of coronary artery disease by stent implantation

Coronary stent implantation, as a minimally invasive alternative for coronary artery bypass graft (CABG) surgery, is one of the most common treatments for CAD. Figure 2.28 shows the stent deployment procedure including the insertion of catheter at the location of lesion, inflation of the balloon, placement of the stent, releasing the balloon and finally removing the catheter with balloon. Although there are several benefits of stenting over the CABG, such as lower risks of complications and much shorter recovery period, it can result in thrombosis and in-stent restenosis (ISR) which are the major drawbacks of coronary stent placement in patients with CAD (Kastrati et al. 2001a). Figure 2.29 shows a schematic of the ISR and thrombosis inside a stented artery model. Stent thrombosis is a thrombotic blockage of a coronary stent that is usually an acute process in contrast to ISR, which is a gradual narrowing of the stent lumen due to proliferation and migration of vascular smooth muscle cells inside the stented artery. In general clinical practice, it was reported that the expected rate of early stent thrombosis is about 1% (Lotfi and Reejhsinghani 2015). Furthermore, the incidence of ISR was reported to be 17–41% for the bare-metal stents (BMSs) and less than 10% for drug-eluting stents (DES) (Buccheri et al. 2016). It was shown that there is a direct link between the low WSS locations and the chances of ISR and thrombosis, and consequently patient outcomes (Chatzizisis

et al. 2008; Chatzizisis et al. 2007; Gijzen et al. 2019). It was reported that the locations with a lower WSS, especially adjacent to the stent struts, were potential locations for the formation of ISR and thrombosis (Koskinas et al. 2012; Morlacchi et al. 2011).

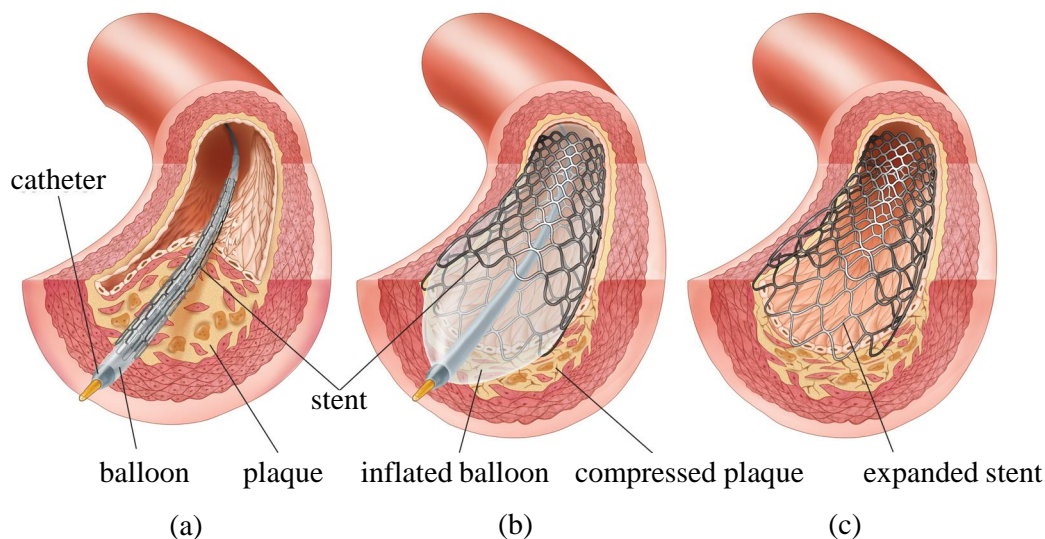


Figure 2.28: Stent deployment procedure (a) in a coronary artery where blood flow is obstructed by the growth of atherosclerotic plaque, the lesion is reached by a cardiac catheter encased in an inflatable balloon and wire-mesh stent, (b) the balloon is inflated to expand the stent, to dilate the artery and to compress the plaque, and (c) the balloon is subsequently deflated and withdrawn with the catheter, leaving the stent expanded against the arterial wall, adapted from The Editors of Encyclopaedia Britannica (2020).

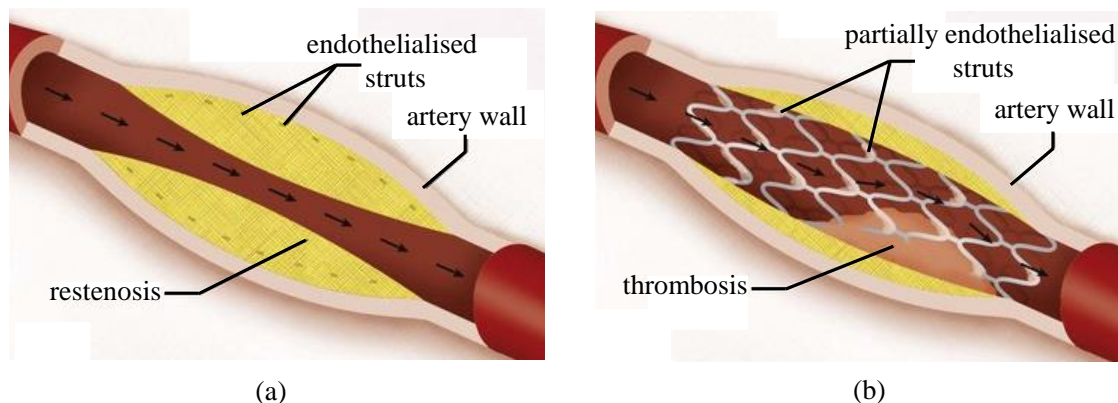


Figure 2.29: A schematic of potential complications of coronary stenting including (a) ISR and (b) stent thrombosis, adapted from Jeudy et al. (2011). Reprinted with permission from Curfman GD, Morrisey S, Jarcho JA, et al. Drug-eluting coronary stents—promise and uncertainty. *N Engl J Med* 2007, 8;356 (10):1059-1060, Copyright Massachusetts Medical Society.

Furthermore, literature suggests that there is a direct link between the shape of the struts, their thicknesses and patterns with WSS distributions and hence the chances of ISR and thrombosis. It was reported that the regions immediately downstream of the strut intersections are highly susceptible to restenosis, whereas a high shear stress at the

strut intersection may cause platelet activation and free emboli formation (Rajamohan et al. 2006). Moreover, the main hemodynamic effect of a stent in the coronary artery is an overall reduction of the WSS in the entire treated region in the immediate post-implantation period (Chiastra et al. 2020). It was reported that the use of stents with thinner struts is associated with a significantly lower chance of ISR after coronary artery stenting (Balossino et al. 2008; Kastrati et al. 2001b). However, there are some drawbacks to thinner struts such as less successful drug delivery for DESs and reduced angiographic visibility (Pache et al. 2003). Furthermore, it was shown that for struts with a tear drop profile, up to 96% of the area between the struts is exposed to WSS levels above the critical values which promotes the onset of restenosis, while for the square profile, the corresponding value is 19.4% (Mejia et al. 2009). It is also shown that different commercial stents generate different levels of WSS especially adjacent to the struts (Balossino et al. 2008; Charonko et al. 2009). To conclude, although the shape of the stent geometry is usually controlled by the manufacturing processes, it can play an important role in the improvement of hemodynamic performance (Mejia et al. 2009).

The design of a stent, as one of the many factors affecting the stent implantation clinical outcomes, is a function of different parameters including strut material strength and biocompatibility, flexibility, surface properties, strut thickness, strut cross section, drug coatings for DES, and improved deployment with prevention of malapposition (Jiménez and Davies 2009). For example, it was shown by Yazdani et al. (2004) that the mechanical properties of the stents directly affect the resident time of blood, promote platelet attachment, and alter the normal physiologic shear stresses on the endothelial cells, which could lead to the failure of stents. As another example, it was shown that implantation of a stent that artificially straightens the normal curvature of a coronary artery introduces profound changes in WSS. These alterations are most pronounced in the proximal and distal areas of the stented region as compared to a flexible stent that conforms to the native anatomy (LaDisa et al. 2006). Hence, it was suggested that improved stent flexibility may be beneficial not only for device delivery, but also from a fluid dynamics perspective as well.

To conclude, the possibilities of ISR and thrombosis may be better understood by investigating WSS distributions for different typical commercial stent designs with different geometrical features (Beier et al. 2016). There are several in-vitro experimental and numerical studies in the literature investigating the hemodynamic performance of stented arteries with the aim to better understand the WSS of the stented arteries to identify the causes of ISR and thrombosis (Foin et al. 2017; Ng et al. 2017). The following Section 2.4.1 and Section 2.4.2 review the numerical and experimental studies in the literature focusing on the hemodynamic investigation of the stented arteries, respectively.

2.4.1 Computational fluid dynamics modelling of stented arteries

Numerical analysis of the flow behaviour near the wall, specifically for identification of micro-recirculation zones near the stent struts and evaluation of WSS distribution to resolve the flow is a useful complement to in-vitro experiments in advancing knowledge. A CFD model which is validated against experiments can help to improve the understanding of the flow features and hemodynamics of stented arteries. The micro-recirculation zones

adjacent to the struts and the WSS distributions of stented arteries are examples of the parameters that can be calculated using a CFD model. However, calculation of these parameters is very challenging in experiments. This section summarises the CFD studies in the literature focusing on stented arteries.

The local flow separation created by a metallic stent in a coronary artery model was studied by Berry et al. (2000) using a 2D CFD model (Fig. 2.30). They used a dye injection method for flow visualisation to provide a qualitative picture of the stent hemodynamics. Their results showed that the sizes of the stagnation zones were larger under exercise conditions, and the largest stagnation zones were observed distal to the stent strut. Furthermore, recirculation zones were continuous from one strut to the next when the strut spacing (L_s) was small. Results from a greater strut spacing (more than six strut diameter (D_s)) showed that the stagnation zones were separated for at least part of the cardiac cycle. Since their experimental results were obtained based on a dye injection method, they are used for qualitative comparison of the results. Another limitation of their study was related to conducting a 2D computational simulation rather than a 3D simulation. Considering that the instantaneous flow behaviour, especially near the wall, is highly 3D, assuming stented arteries to be 2D may result in unreliable estimation of the flow patterns near the wall and hence the WSS distributions.

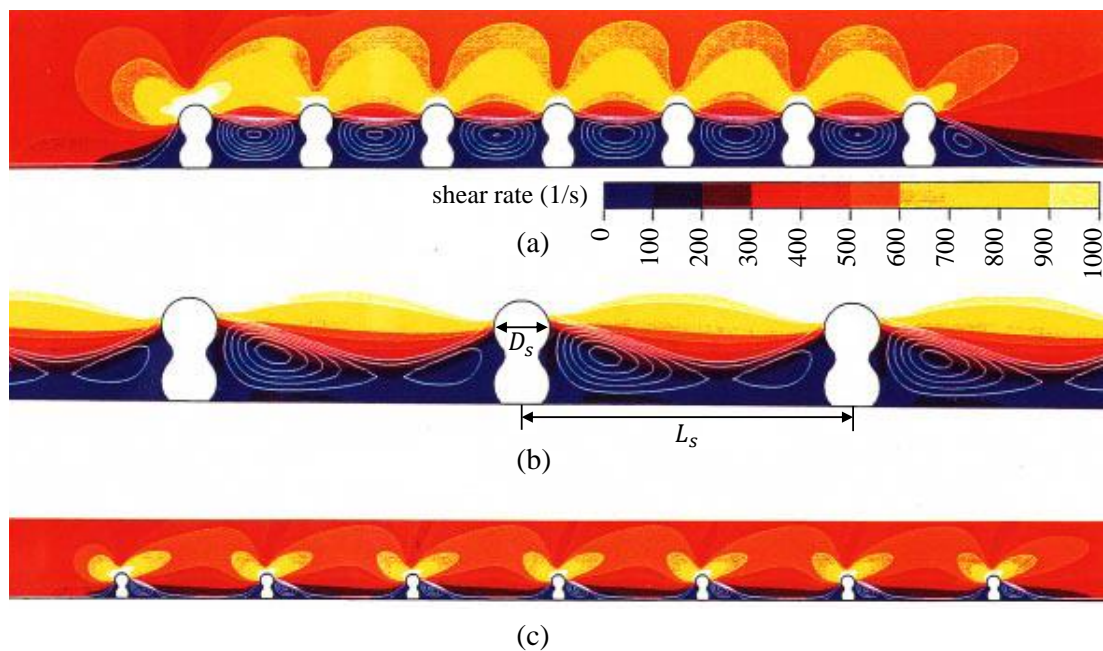


Figure 2.30: Shear rate contours for (a) $L_s/D_s = 3.53$ with a 4 mm vessel, (b) $L_s/D_s = 5.88$ with a 2 mm vessel, and (c) $L_s/D_s = 10.55$ with the 4 mm vessel at peak diastolic flow (Berry et al. 2000). The lowest shear rates were observed in between the struts and the highest shear rates were located at the tops of the struts in all cases.

In another study, the effect of a stent on the blood flow behaviour was investigated by Natarajan and Mokhtarzadeh-Dehghan (2000). Their study was based on numerical simulation using a finite element technique. They only used experimental results to validate the numerical simulation results based on a simplified non-physiological flow profile. Their results showed that the predicted TAWSS around the top of the struts was 2-3 times greater than that in the equivalent normal artery. Furthermore, a protrusion of just 0.2 mm in a 2.8 mm nominal diameter vessel caused a reduction in the

space- and TAWSS by approximately half. Based on their results, they suggested that thin, flat-walled stents are more favourable from a fluid mechanics point of view. Better hemodynamic performance of the stents with thinner struts was also noted in a study by Balossino et al. (2008). However, there are some drawbacks for the development of stent geometries with the features they suggested. As an example, as mentioned earlier, drawbacks for the use of thinner struts are associated with a reduced amount of drug delivery in DESs and reduced angiographic visibility (Pache et al. 2003).

A 3D CFD modelling of changes in WSS produced by stent implantation for a canine LAD was investigated by LaDisa et al. (2003). Their results showed that the minimum value of WSS decreased by 77% in stented vessels compared to unstented vessels. Furthermore, regions of low WSS extended at the stent outlet and were localised to the regions where the adjacent axial strut spacing was minimised and the circumferential distance between the struts was greatest within the stent. In another study by the same authors (LaDisa et al. 2004), it was suggested that stent designs with a reduced number of struts and reduced thickness were less likely to subject the vessel to the levels of WSS which promote the occurrence of restenosis. Furthermore, in another study, it was shown that the change in vascular geometry of the artery after stent implantation is an important determinant of WSS distributions that may be associated with the likelihood of restenosis (LaDisa et al. 2005).

A parametric comparison of strut design patterns in stented arteries was investigated by He et al. (2005). Based on the results, they provided some guidelines to improve the hemodynamic performance of future stent design. For example, it was suggested that inter-strut spacing should be larger in order to restore the disturbed flow, struts should be oriented to the flow direction in order to reduce the area of flow recirculation, longitudinal connectors should be used only as necessary, and should be parallel to the flow direction.

The effect of the cross section of the struts on the local shear forces was studied by Jiménez and Davies (2009) by investigating rectangular and streamline shapes of strut cross section with different aspect ratios, as shown in Fig. 2.31. Based on their results, non-streamlined stent struts, such as rectangular cross-section geometries, can be modified by decreasing the strut height, and consequently lessening the effect of strut height on the flow field. The reduction in thickness not only decreases the recirculation volume, but also decreases the area of the endothelium exposed to disturbed flow and hence increases the probability of endothelialisation of adjacent tissue, which is a favourable outcome. On the other hand, a streamlined design for the struts can minimise flow recirculation zones, which is an optimal condition for clinical success. To conclude, it was reported that a streamlined strut will be less likely to create the conditions necessary for the development of recirculation zones and high shear stress peaks over the surface, even at higher strut thicknesses, than a thinner non-streamlined strut.

The near-wall flow characteristics of stented arteries for four commercially available stent designs were investigated computationally in a study by Duraiswamy et al. (2009). In their study, the stented artery was simulated as a flat rectangular stented vessel. Their results showed that the flow remained fully recirculating during the entire flow cycle, mostly at the proximal and distal ends of the concave and convex portions of the strut. Furthermore, the connectors were the locations with the highest potential for flow stagnation, with the second potential location related to the distal and proximal of the

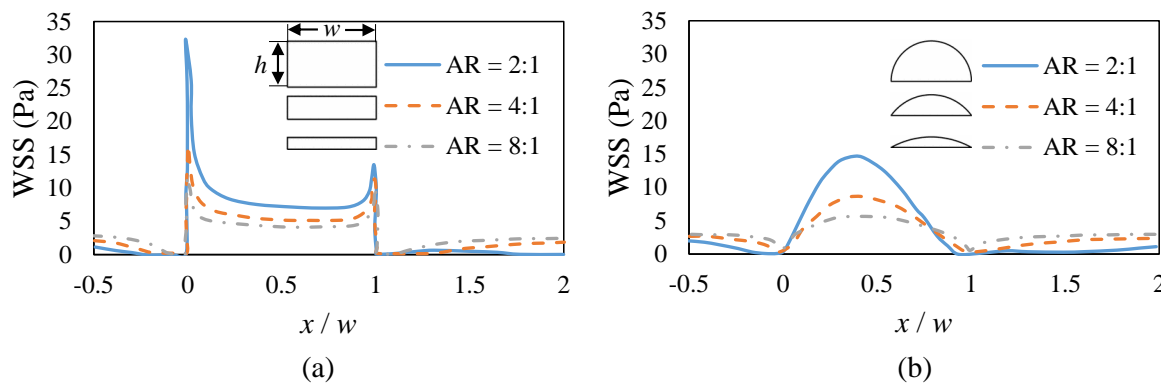


Figure 2.31: WSS distribution corresponding to (a) rectangular and (b) circular arc stent struts with different aspect ratios (Jiménez and Davies 2009).

struts, as shown in Fig. 2.32. The most hemodynamically favourable stent based on their simulations was in agreement with those reported by the clinical data with lower restenosis rate.

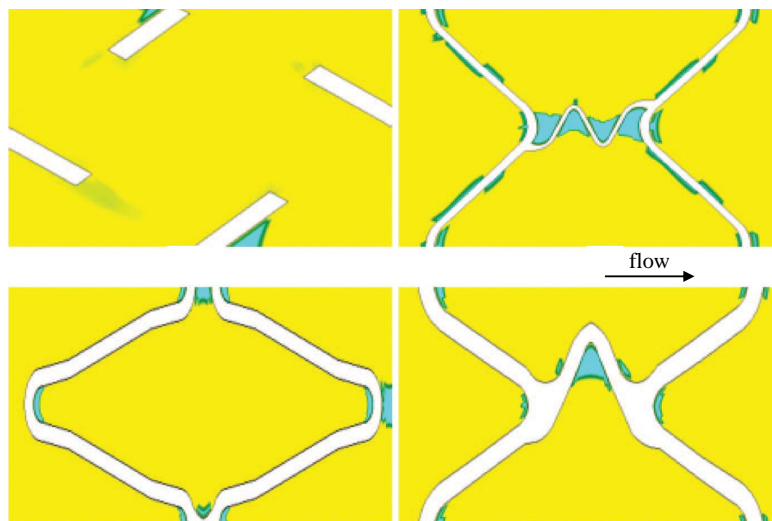


Figure 2.32: Flow stagnation areas at the mean flow rate for different stents during the accelerating phase of the flow cycle (Duraiswamy et al. 2009). In this graph, yellow indicates no flow separation and green indicates flow stagnation.

The hemodynamic differences between five different stent patterns used in clinical practice were investigated by Pant et al. (2010). The differences in the stents were in their pattern design and the other geometrical parameters, such as artery diameter and length, while strut thickness and height were kept the same. In their study, they introduced an index called hemodynamic low and reverse flow index (HLRFI) to account for the weighted average of areas of both low WSS and reversed flow, as an indicative parameter of a stent resistance to restenosis. Their results showed that for similar strut spacings, the design of the connector, especially its length in the cross-flow direction, significantly influenced the blood flow. Connectors were reported to be an essential component of a stent design as their presence makes the stent flexible, which in turn improves the stent deployment procedure. In another study, the effects of the stent design parameters, such as strut spacing, thickness, luminal protrusion, and malapposition, were evaluated

by Beier et al. (2016) on the time-averaged and instantaneous WSS and WSS gradient. Among the studied parameters, their results showed that an increased luminal protrusion has higher negative effect on the WSS distribution making it prone to restenosis compared to the other parameters.

Furthermore, a 3D CFD simulation of stent models with either square or circular cross-section struts inside an idealised coronary artery was conducted by Poon et al. (2014) to analyse the effect of different levels of incomplete stent apposition on the changes in arterial hemodynamics. As discussed at the beginning of section 2.4, deployment of a coronary stent can sometimes lead to an incomplete stent apposition, which is an undesirable side effect of coronary stent implantation. Malapposition distance, as a measure of incomplete stent apposition, is defined as the distance between the strut and the host artery wall. If the struts are attached to the wall, which is favourable, the malapposition distance is zero. Their results showed that the struts with a circular cross section delayed the flow chaotic process compared to square cross-sectional struts at the same malapposition distance and also reduced the level of fluctuations found in the flow field. In another study, the effects of an incomplete stent apposition in arteries with an elliptical cross section were studied computationally by Jiang et al. (2019). In their study, the stents were partially embedded on the minor axis sides of the ellipse and malapposed on the major axis side. Figure 2.33 shows the spatial TAWSS distribution for a perfectly apposed case (with a 50% embedment) and a case that is severely malapposed. Their results showed that an incomplete stent apposition leads to high TAWSS at the proximal end of the stent and low values at the incomplete stent apposition transition region and the distal end.

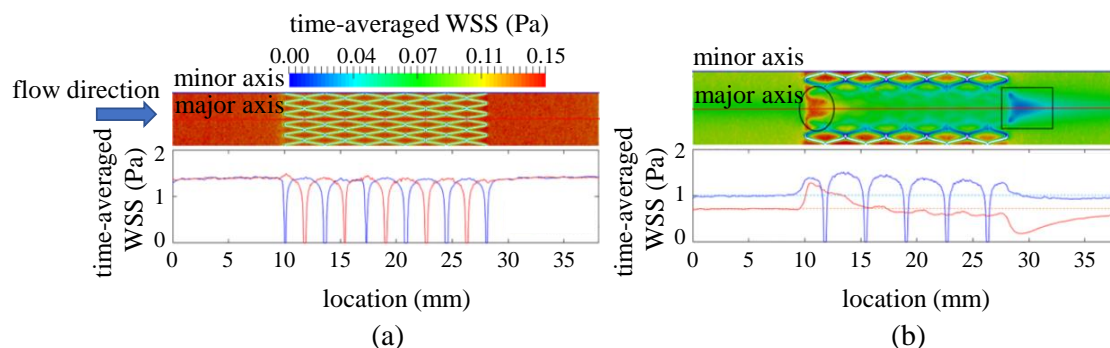


Figure 2.33: Spatial TAWSS distribution and plots of data from extracted lines on each side for (a) apposed and (b) severe malapposed cases (Jiang et al. 2019).

This section summarised the studies in the literature focusing on the computational modelling of the stented arteries with the aim to identify the effects of different stent parameters, such as strut thickness, stent pattern, inter-strut distance, and connector shape, on the hemodynamic parameters. The findings in the literature provide an important insight to the effect of different stent geometrical parameters on the potential of ISR and stent thrombosis. For example, it was shown that micro-recirculations can cover the area between two consecutive struts depending on the stream-wise distance between them. Furthermore, the use of stream-wise struts resulted in a more hemodynamically compatible stent compared to the non-stream-wise stents. It was also shown that the connectors between the stent patterns are the locations with the most potential for restenosis, since they are the location with low values of WSS. However, computational studies in

the literature were limited due to the lack of experimental validation of the simulated models. The flow visualisation experimental studies to investigate hemodynamics of the stented arteries were limited to date, as discussed in Section 2.4.2.

2.4.2 Experimental investigation of the hemodynamics of stented arteries

This section reviews the experimental studies with a focus on the hemodynamics of stented coronary arteries in the literature. The focus of this thesis is to investigate flow behaviour inside stented coronary arteries. Therefore, only in-vitro experimental studies are discussed, since the information which can be achieved from in-vivo studies is limited. The in-vitro experimental studies of the stented arteries were mainly based on flow visualisation techniques such as PIV or dye injection methods. The latter results in a qualitative visualisation of the flow, while the application of PIV has been limited due to the presence of metallic stent struts which blocks the field of view (FOV). This section reviews the flow-visualisation-based studies of stented arteries in the literature and discusses the limitations of these methods.

The blood flow through a stented section was investigated by Benard et al. (2003) using PIV. Figure 2.34 displays the normalised velocity contour in the gap between two struts in a plane perpendicular to the branches for two different flow rates. The results show that the recirculation area expanded with an increased flow rate. In order to prevent complexities related to the curvature effects of the cylindrical artery model, such as diffraction effects and the shaded area due to the presence of many edges in the FOV and the laser beam deviation, they used a transparent rectangular Plexiglas channel. The stent patterns were reproduced on one of its flat inner surfaces. Another simplification in their study related to the use of steady flow as the inlet flow instead of a physiological pulsatile flow. This assumption resulted in a lack of information on the effect of velocity gradient in a cardiac cycle on the hemodynamics.

The effect of inter-strut spacing on the flow behaviour was investigated by Duraiswamy et al. (2005). Their experiment was based on using fluorescently labelled platelets to allow for spatial observation of wall attachment in the inter-strut spacings. They used nucleic acid stain mepacrine to fluorescently label the platelets obtained from blood of human volunteers. In their experiment, the movement and adhesion of the platelets were detected with a microscope equipped with a mercury arc lamp. Their results showed that platelet deposition was highest within the intermediate strut spacing, with the optimal ratio of two consecutive struts over the strut depth of 4, compared to the cases with smaller and larger distances between two struts.

As the first in-vitro study measuring flow parameters inside stented arteries at full scale, Charonko et al. (2009) investigated the flow behaviour within the stented region near the wall using time-resolved digital PIV for four DESs and a BMS. They deployed commercial DESs inside arteries cast from silicone, as shown in Fig. 2.35. They reported that the stent struts along the artery wall disturbed the nearby flow, making it more receptive to changes in direction, and decreased the peak WSS. Their results showed that for stents with thicker struts, there was a greater velocity deficit near the wall behind the struts, depressing the near-wall gradients and therefore the measured WSS values.

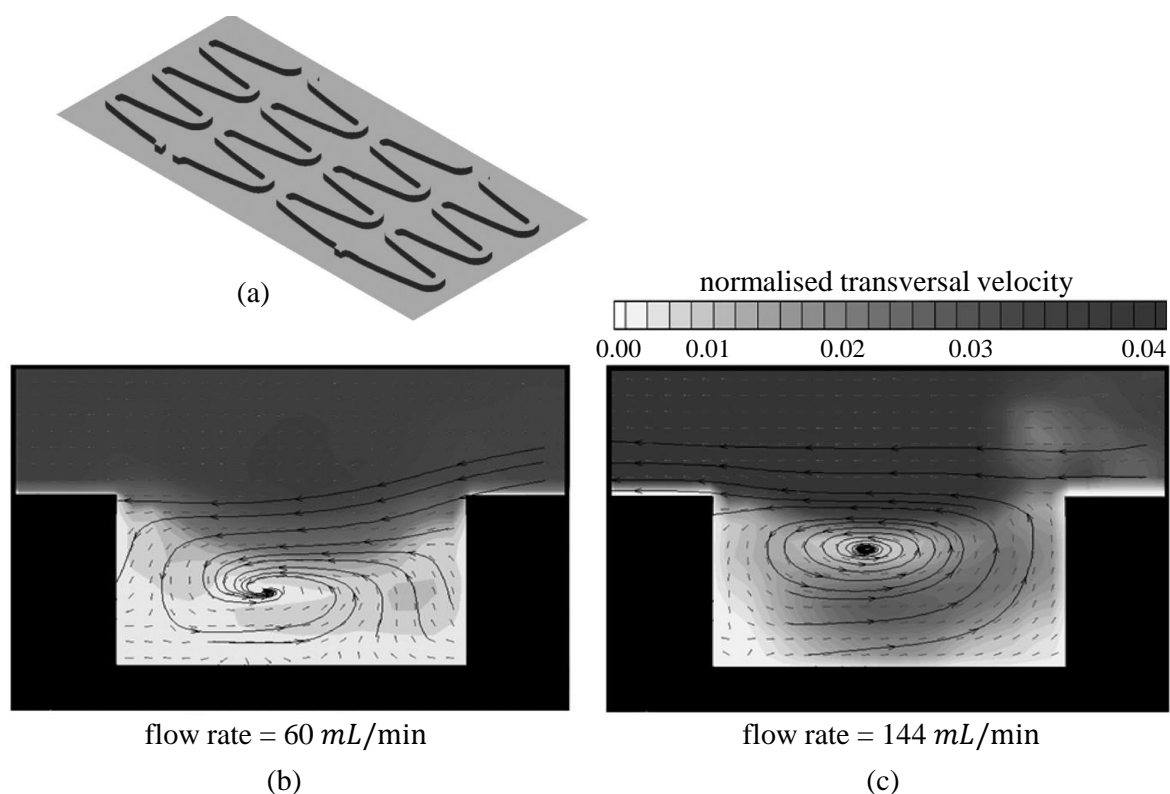


Figure 2.34: (a) Model of a stent made of Plexiglas, and normalised transversal velocity contour in the gap between two struts at (b) flow rate = 60 ml/min and (c) flow rate = 144 ml/min (Benard et al. 2003). The velocity is normalised by the mean flow velocity of 0.15 m/s.

They also noted that apart from the thickness of the struts, the strut pattern is another parameter affecting WSS. A lower spatial averaged WSS was observed for the stent with more closely spaced struts. In other words, a denser network of struts allows less distance for the flow to recover before the next strut and hence can result in lower WSS values overall. In another study by the same authors (Charonko et al. 2010), they studied the distributions of WSS and OSI for different configurations including baseline (the normal stenting procedure), over-expanded (inflated to 125%), increased artery diameter, two overlapped stents, and increased stent length experimentally using time-resolved digital PIV. Stent overlapping was defined as the presence of more than two stents within a single treated lesion. In addition, stent over-expansion occurs by over-expanding the stent with a second balloon that is used for the adjacent stent. Stent over-expansion affects the alignment of the stent geometry. They reported an overall correlation between decreased WSS values and elevated OSI for all configurations. Moreover, the overlapped stents resulted in a disturbed flow and a WSS deficit region downstream of the overlapped region. They also found that over-expansion of the stent with a second balloon led to higher WSS at the inlet and lower values at the mid-stent location. Their results in both studies, however, were limited because of the obscuration of the FOV by the stent struts, which limited their measurement at the locations obstructed by the struts and those locations shadowed by the other struts.

In a recently published study, Tomaszewski et al. (2020) investigated the flow inside stented arteries experimentally using PIV. Figure 2.36 shows the raw PIV images of the

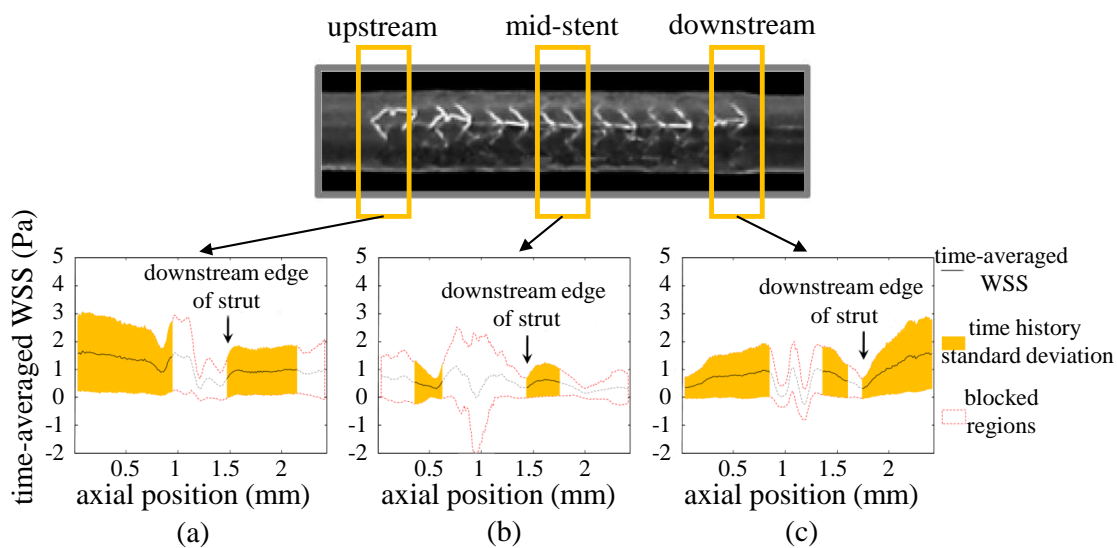


Figure 2.35: Spatial profile of TAWSS in a XIENCE V stented artery, shown on top, for three regions of interest: (a) upstream, (b) mid-stent and (c) downstream at $Re = 160$ (Charonko et al. 2009). Standard deviation of the time history at each point is shown to give an indication of the relative temporal variability at each location. Wall regions marked as blocked were obscured by other struts in the FOV.

vessel with and without the stent as well as the time-averaged flow velocity contours in the stented vessel. It was shown that the PIV technique was able to present the flow behaviour of the bulk flow far away from the artery walls and at the locations which are not obscured by the struts. The limitation of the PIV studies of the stented arteries is illustrated in this figure as the black-covered areas.

There are also other studies in the literature investigating the effect of stents on coronary bifurcated arteries experimentally and numerically, such as Brindise et al. (2017), García Carrascal et al. (2018), García García et al. (2017), and Raben et al. (2015). In all mentioned bifurcation studies, PIV is used to validate the developed CFD models and provide useful information on the hemodynamic parameters of the stented arteries. For example, a lower spatial-averaged WSS was observed for stents with more closely spaced struts and hence, these types of stent patterns are more susceptible to the formation of restenosis. Furthermore, the stent deployment procedure is of great importance for minimising the chances of restenosis. It was shown that the procedure should aim to prevent over or under expansion of the stent inside the artery and also to minimise the overlapping length between two stents. However, all the studies in the literature with a focus on in-vitro flow visualisation investigation of the flow behaviour inside stented arteries were limited due to obscuration of the view of the region of interest by the stent struts. This obscuration effect caused by the stent struts has resulted in dark regions in the PIV images, hence velocity measurements were not available at these locations (Raben et al. 2015).

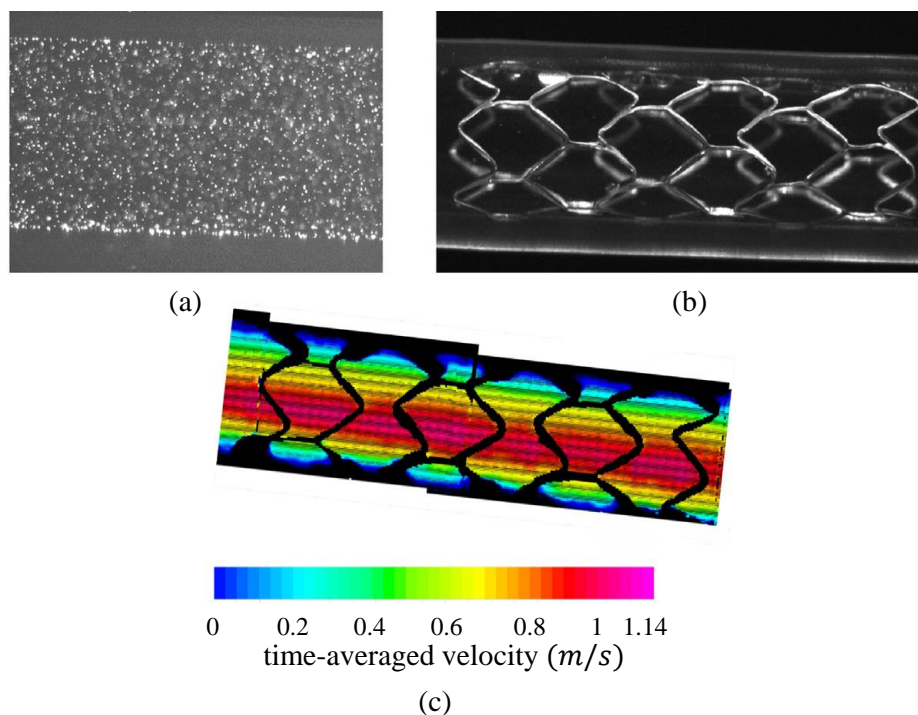


Figure 2.36: Raw PIV images of the vessel (a) without and (b) with an implanted stent, and (c) time-averaged velocity contour of the stented vessel (Tomaszewski et al. 2020).

2.5 Concluding remarks and perspectives

As discussed in Section 2.1.1, the mechanical properties of coronary blood vessels are characterised by the mechanical properties of their constitutive layers. Since coronary arteries are located on the heart muscles, the blood flow in coronary arteries is affected by the physiological movement of the vessels which depend on the specific geometry of the arteries, the cardiac motion, the arterial pressure waveform, and finally, the material properties of the arterial wall. Therefore, Chapter 3 discusses the effects of coronary arterial motion and flexibility on the hemodynamic parameters of the coronary arteries, such as pressure drop and WSS. Furthermore, Chapter 3 aims to investigate the conditions in which these temporal geometric variations need not be modelled based on the target of the study.

The literature review presented in this chapter shows that a blockage inside the coronary arteries can significantly change the transitional flow behaviour inside them. It was shown that turbulence in the flow was triggered in the presence of arterial stenosis and heart pulsation. Studies in the literature, as discussed in Section 2.3.1, were limited due to their simplified models of the coronary arteries, such as a pipe or channel, instead of patient-specific coronary arteries. The other limitation is simplified flow assumption, such as steady flow inside the artery models instead of a pulsatile flow. Therefore, a better understanding of the transitional flow behaviour inside stenosed coronary artery models with a physiological blood flow profile is yet to be determined. Hence, Chapter 4 presents the correlation between the plaque geometry, the pulsatile inlet flow and the induced turbulence in simplified stenosed and patient-specific stenosed coronary artery models.

A significant lack of knowledge about the effect of the shape of the stenosis on the flow behaviour is evidenced from the literature reviewed in Section 2.2.2. The literature was mainly limited to investigation of the effect of the stream-wise shape of the stenosis. However, the cross-sectional shapes of the stenosis can be significantly different, and this effect was not thoroughly studied in the literature. The research presented in Chapter 5 investigates the effect of the cross-sectional shape of the stenosis including crescent, half-moon, elongated, oval, and round on the transitional flow behaviour.

As discussed in Section 2.3.3, there are several studies in the literature aiming to develop a mathematical model to evaluate pressure drop inside the arteries. However, the developed models were limited and the effects of the shape of the stenosis and the curvature of the artery on the pressure drop and FFR were not considered. Considering the effect of artery curvature on the calculation of pressure drop is of great importance, as it was reported that the majority of the arterial diseases occur in the curved sections of the arteries rather than within the straight sections. In Chapter 6, a mathematical model is developed to evaluate the pressure drop inside stenosed coronary arteries with different shapes of stenosis for both straight and curved models of coronary arteries.

Extensive research gaps exist in the literature regarding hemodynamic investigation of stented coronary arteries, specifically in in-vitro experimental studies. As highlighted in the literature review in Section 2.4, there are several in-vitro experimental and numerical studies investigating the hemodynamic performance of stented coronary arteries with the aim to better understand the effect of the stent design on the extremes of the WSS distributions near the struts. However, the in-vitro flow visualisation studies in the literature have been limited due to the opacity of the stent struts. This limitation results in obscuration of the FOV and hence limitation of the results obtained from the in-vitro flow visualisation techniques. In Chapter 7, an innovative PIV technique is developed for the visualisation of the entire flow and the investigation of WSS within the stent struts without covering the FOV inside a stented coronary artery model. Furthermore, the hemodynamic results obtained from this technique as well as the developed numerical simulation are presented for four models of DES stents in this chapter.

References

- Abbott (2020). *Measuring physiological indices - FFR, RFR, IMR, CFR*. URL: <https://www.cardiovascular.abbott/int/en/hcp/products/percutaneous-coronary-intervention/physiology-indices/ffr.html>.
- Akhtar R, Sherratt MJ, Cruickshank JK, and Derby B (2011). “Characterizing the elastic properties of tissues”. *Materials Today* 14.3, pp. 96–105.
- Alonso C, Pries AR, and Gaehtgens P (1993). “Time-dependent rheological behavior of blood at low shear in narrow vertical tubes”. *American Journal of Physiology* 265.2 Pt 2, H553–61.
- Balossino R, Gervaso F, Migliavacca F, and Dubini G (2008). “Effects of different stent designs on local hemodynamics in stented arteries”. *Journal of Biomechanics* 41.5, pp. 1053–1061.

- Baratchi S, Khoshmanesh K, Woodman OL, Potocnik S, Peter K, and McIntyre P (2017). “Molecular sensors of blood flow in endothelial cells”. *Trends in Molecular Medicine* 23.9, pp. 850–868.
- Baskurt OK and Meiselman HJ (2003). “Blood rheology and hemodynamics”. *Seminars in Thrombosis and Hemostasis* 29.5, pp. 435–450.
- Baylor College of Medicine (2020). *Coronary artery disease and coronary bypass surgery*. URL: <https://www.bcm.edu/healthcare/specialties/cardiovascular-medicine/cardiothoracic-surgery/coronary-artery-disease-coronary-bypass>.
- Beier S, Ormiston J, Webster M, Cater J, Norris S, Medrano-Gracia P, Young A, and Cowan B (2016). “Hemodynamics in idealized stented coronary arteries: important stent design considerations”. *Annals of Biomedical Engineering* 44.2, pp. 315–329.
- Belzacq T, Avril S, Leriche E, and Delache A (2014). “Mechanical action of the blood onto atheromatous plaques: influence of the stenosis shape and morphology”. *Computer Methods in Biomechanics and Biomedical Engineering* 17.5, pp. 527–538.
- Benard N, Coisne D, Donal E, and Perrault R (2003). “Experimental study of laminar blood flow through an artery treated by a stent implantation: characterisation of intra-stent wall shear stress”. *Journal of Biomechanics* 36.7, pp. 991–998.
- Benetos A (2017). “Assessment of arterial stiffness in an older population: the interest of the cardio-ankle vascular index (CAVI)”. *European Heart Journal Supplements* 19.suppl_B, B11–B16.
- Benetos A, Waeber B, Izzo J, Mitchell G, Resnick L, Asmar R, and Safar M (2002). “Influence of age, risk factors, and cardiovascular and renal disease on arterial stiffness: clinical applications”. *American Journal of Hypertension* 15.12, pp. 1101–1108.
- Beratlis N, Balaras E, and Kiger K (2007). “Direct numerical simulations of transitional pulsatile flow through a constriction”. *Journal of Fluid Mechanics* 587, pp. 425–451.
- Bernabeu MO, Nash RW, Groen D, Carver HB, Hetherington J, Krüger T, and Coveney PV (2013). “Impact of blood rheology on wall shear stress in a model of the middle cerebral artery”. *Interface Focus* 3.2, p. 20120094.
- Berry JL, Santamarina A, Moore JE, Roychowdhury S, and Routh WD (2000). “Experimental and computational flow evaluation of coronary stents”. *Annals of Biomedical Engineering* 28.4, pp. 386–398.
- Biswas D, Casey D, Crowder D, Steinman D, Yun Y, and Loth F (2016). “Characterization of transition to turbulence for blood in a straight pipe under steady flow conditions”. *Journal of Biomechanical Engineering* 138.7, pp. 1–12.
- Blair GWS (1959). “An equation for the flow of blood, plasma and serum through glass capillaries”. *Nature* 183.4661, pp. 613–614.
- Bodnár T, Sequeira A, and Prosi M (2011). “On the shear-thinning and viscoelastic effects of blood flow under various flow rates”. *Applied Mathematics and Computation* 217.11, pp. 5055–5067.
- Boghosian ME and Cassel KW (2013). “A pressure-gradient mechanism for vortex shedding in constricted channels”. *Physics of Fluids* 25.12, p. 123603.
- Boyd J, Buick JM, and Green S (2007). “Analysis of the Casson and Carreau-Yasuda non-Newtonian blood models in steady and oscillatory flows using the lattice Boltzmann method”. *Physics of Fluids* 19.9, p. 093103.
- Brindise MC, Chiastra C, Burzotta F, Migliavacca F, and Vlachos PP (2017). “Hemodynamics of stent implantation procedures in coronary bifurcations: An in vitro study”. *Annals of Biomedical Engineering* 45.3, pp. 542–553.

- Buccheri D, Piraino D, Andolina G, and Cortese B (2016). “Understanding and managing in-stent restenosis: a review of clinical data, from pathogenesis to treatment”. *Journal of Thoracic Disease* 8.10, E1150–E1162.
- Caro C, Pedley TJ, Schroter RC, and Seed WA (2011). *The Mechanics of the Circulation*. Cambridge: Cambridge University Press.
- Caruso MV, Rosa SD, Indolfi C, and Fragomeni G (2015). “Computational analysis of stenosis geometry effects on right coronary hemodynamics”. *37th Annual International Conference of the IEEE Engineering in Medicine and Biology Society (EMBC)*. IEEE.
- Charonko J, Karri S, Schmieg J, Prabhu S, and Vlachos P (2009). “In vitro, time-resolved PIV comparison of the effect of stent design on wall shear stress”. *Annals of Biomedical Engineering* 37.7, pp. 1310–1321.
- Charonko J, Karri S, Schmieg J, Prabhu S, and Vlachos P (2010). “In vitro comparison of the effect of stent configuration on wall shear stress using time-resolved particle image velocimetry”. *Annals of Biomedical Engineering* 38.3, pp. 889–902.
- Chatzizisis YS, Jonas M, Coskun AU, Beigel R, Stone BV, Maynard C, Gerrity RG, Daley W, Rogers C, Edelman ER, Feldman CL, and Stone PH (2008). “Prediction of the localization of high-risk coronary atherosclerotic plaques on the basis of low endothelial shear stress: an intravascular ultrasound and histopathology natural history study”. *Circulation* 117.8, pp. 993–1002.
- Chatzizisis YS, Coskun AU, Jonas M, Edelman ER, Feldman CL, and Stone PH (2007). “Role of endothelial shear stress in the natural history of coronary atherosclerosis and vascular remodeling: molecular, cellular, and vascular behavior”. *Journal of the American College of Cardiology* 49.25, pp. 2379–2393.
- Chiastra C, Dubini G, and Migliavacca F (2020). “Chapter 11 - Hemodynamic perturbations due to the presence of stents”. *Biomechanics of Coronary Atherosclerotic Plaque*. Ed. by J Ohayon, G Finet, and RI Pettigrew. Vol. 4. Academic Press, pp. 257–278.
- Cho YI and Kensey KR (1991). “Effects of the non-Newtonian viscosity of blood on flows in a diseased arterial vessel. Part 1: Steady flows”. *Biorheology* 28.3-4, pp. 241–262.
- Choi W, Park JH, Byeon H, and Lee SJ (2018). “Flow characteristics around a deformable stenosis under pulsatile flow condition”. *Physics of Fluids* 30.1, p. 011902.
- Clark C (1976). “The fluid mechanics of aortic stenosis—I. Theory and steady flow experiments”. *Journal of Biomechanics* 9.8, pp. 521–528.
- Costa ED (2016). “Hemodynamics in the left coronary artery - numerical and in vitro approaches”. PhD thesis. Department of Chemical Engineering, University of Porto.
- Dinunno FA, Jones PP, Seals DR, and Tanaka H (2000). “Age-associated arterial wall thickening is related to elevations in sympathetic activity in healthy humans”. *American Journal of Physiology-Heart and Circulatory Physiology* 278.4, H1205–H1210.
- Douglas PS, Fiolkoski J, Berko B, and Reichek N (1988). “Echocardiographic visualization of coronary artery anatomy in the adult”. *Journal of the American College of Cardiology* 11.3, pp. 565–571.
- Duraiswamy N, Jayachandran B, Byrne J, Moore JE, and Schoepfoerster RT (2005). “Spatial distribution of platelet deposition in stented arterial models under physiologic flow”. *Annals of Biomedical Engineering* 33.12, pp. 1767–1777.
- Duraiswamy N, Schoepfoerster RT, and Moore JE (2009). “Comparison of near-wall hemodynamic parameters in stented artery models”. *Journal of Biomechanical Engineering* 131.6.
- Eslami P, Tran J, Jin Z, Karady J, Sotoodeh R, Lu MT, Hoffmann U, and Marsden A (2019). “Effect of wall elasticity on hemodynamics and wall shear stress in patient-

- specific simulations in the coronary arteries”. *Journal of Biomechanical Engineering* 142.2, pp. 245031–2450310.
- Figuroa CA, Vignon-Clementel IE, Jansen KE, Hughes TJ, and Taylor CA (2006). “A coupled momentum method for modeling blood flow in three-dimensional deformable arteries”. *Computer Methods in Applied Mechanics and Engineering* 195.41–43, pp. 5685–5706.
- Foin N, Lu S, Ng J, Bulluck H, Hausenloy DJ, Wong PE, Virmani R, and Joner M (2017). “Stent malapposition and the risk of stent thrombosis: mechanistic insights from an in vitro model”. *EuroIntervention* 13.9, e1096–e1098.
- Formaggia L, Lamponi D, Tuveri M, and Veneziani A (2006). “Numerical modeling of 1D arterial networks coupled with a lumped parameters description of the heart”. *Computer Methods in Biomechanics and Biomedical Engineering* 9.5, pp. 273–288.
- Fulker D (2016). “Experimental and computational study of haemodialysis vascular access”. PhD thesis. School of Mechanical and Manufacturing Engineering, University of New South Wales.
- García Carrascal P, García García J, Sierra Pallares J, Castro Ruiz F, and Manuel Martín FJ (2018). “Benchmark for numerical models of stented coronary bifurcation flow”. *Journal of Biomechanical Engineering* 140.9.
- García García J, García Carrascal P, Castro Ruiz F, Manuel Martín F, and Fernández JA (2017). “Effects of bifurcation-specific and conventional stents on coronary bifurcation flow. An experimental and numerical study”. *Journal of Biomechanics* 54, pp. 64–72.
- Geest JPv, Sacks MS, and Vorp DA (2004). “Age dependency of the biaxial biomechanical behavior of human abdominal aorta”. *Journal of Biomechanical Engineering* 126.6, pp. 815–822.
- Gijsen FJH, Wentzel JJ, Thury A, Mastik F, Schaar JA, Schuurbiens JCH, Slager CJ, Giessen WJ van der, Feyter PJ de, Steen AFW van der, and Serruys PW (2008). “Strain distribution over plaques in human coronary arteries relates to shear stress”. *American Journal of Physiology-Heart and Circulatory Physiology* 295.4, H1608–H1614.
- Gijsen F, Katagiri Y, Barlis P, Bourantas C, Collet C, Coskun U, Daemen J, Dijkstra J, Edelman E, Evans P, Heiden K van der, Hose R, Koo BK, Krams R, Marsden A, Migliavacca F, Onuma Y, Ooi A, Poon E, Samady H, Stone P, Takahashi K, Tang D, Thondapu V, Tenekecioglu E, Timmins L, Torii R, Wentzel J, and Serruys P (2019). “Expert recommendations on the assessment of wall shear stress in human coronary arteries: existing methodologies, technical considerations, and clinical applications”. *European Heart Journal* 40.41, pp. 3421–3433.
- Godia EC, Madhok R, Pittman J, Trocio S, Ramas R, Cabral D, Sacco RL, and Rundek T (2007). “Carotid artery distensibility: a reliability study”. *Journal of Ultrasound in Medicine* 26.9, pp. 1157–1165.
- Gradus-Pizlo I, Bigelow B, Mahomed Y, Sawada SG, Rieger K, and Feigenbaum H (2003). “Left anterior descending coronary artery wall thickness measured by high-frequency transthoracic and epicardial echocardiography includes adventitia”. *The American Journal of Cardiology* 91.1, pp. 27–32.
- Guleren KM (2013). “Numerical flow analysis of coronary arteries through concentric and eccentric stenosed geometries”. *Journal of Biomechanics* 46.6, pp. 1043–1052.
- Haynes RH (1960). “Physical basis of the dependence of blood viscosity on tube radius”. *American Journal of Physiology* 198, pp. 1193–1200.

- He Y, Duraiswamy N, Frank AO, and Moore JE (2005). “Blood flow in stented arteries: a parametric comparison of strut design patterns in three dimensions”. *Journal of Biomechanical Engineering* 127.4, pp. 637–647.
- Himburg HA, Grzybowski DM, Hazel AL, LaMack JA, Li XM, and Friedman MH (2004). “Spatial comparison between wall shear stress measures and porcine arterial endothelial permeability”. *American Journal of Physiology-Heart and Circulatory Physiology* 286.5, H1916–H1922.
- Holzapfel GA, Gasser TC, and Ogden RW (2000). “A new constitutive framework for arterial wall mechanics and a comparative study of material models”. *Journal of Elasticity and the Physical Science of Solids* 61.1, pp. 1–48.
- Huo Y, Svendsen M, Choy JS, Zhang ZD, and Kassab GS (2012). “A validated predictive model of coronary fractional flow reserve”. *Journal of the Royal Society Interface* 9.71, pp. 1325–1338.
- Jabir E and Lal SA (2016). “Numerical analysis of blood flow through an elliptic stenosis using large eddy simulation”. *Proceedings of the Institution of Mechanical Engineers, Part H: Journal of Engineering in Medicine* 230.8, pp. 709–726.
- Javadzadegan A, Yong ASC, Chang M, Ng ACC, Yiannikas J, Ng MKC, Behnia M, and Kritharides L (2013). “Flow recirculation zone length and shear rate are differentially affected by stenosis severity in human coronary arteries”. *American Journal of Physiology-Heart and Circulatory Physiology* 304.4, H559–H566.
- Jeon BJ, Chang HJ, Yoo YH, and Choi HG (2018). “A numerical study on the effect of trapezium stenosis shape on the axisymmetric flow field around stenosis”. *Journal of Mechanical Science and Technology* 32.6, pp. 2651–2658.
- Jeudy J, Waite S, and Chen JJS (2011). “Imaging of coronary revascularization: coronary stents and bypass grafts”. *Cardiovascular Imaging*. Ed. by V Ho. St. Louis, Mo: Saunders/Elsevier. Chap. 10, pp. 515–532.
- Jiang B, Thondapu V, Poon EKW, Barlis P, and Ooi ASH (2019). “Numerical study of incomplete stent apposition caused by deploying undersized stent in arteries with elliptical cross sections”. *Journal of Biomechanical Engineering* 141.5.
- Jiménez JM and Davies PF (2009). “Hemodynamically driven stent strut design”. *Annals of Biomedical Engineering* 37.8, pp. 1483–1494.
- Johns Hopkins Medicine (2020). *Anatomy and function of the coronary arteries*. URL: <https://www.hopkinsmedicine.org/health/conditions-and-diseases/anatomy-and-function-of-the-coronary-arteries>.
- Johnston BM, Johnston PR, Corney S, and Kilpatrick D (2006). “Non-Newtonian blood flow in human right coronary arteries: Transient simulations”. *Journal of Biomechanics* 39.6, pp. 1116–1128.
- Kantarci M, Gündogdu F, Doganay S, Duran C, Kalkan ME, Sagsoz ME, Kucuk O, Karakaya A, Kucuk A, and Akgün M (2011). “Arterial bending angle and wall morphology correlate with slow coronary flow: Determination with multidetector CT coronary angiography”. *European Journal of Radiology* 77.1, pp. 111–117.
- Kastrati A, Mehilli J, Dirschinger J, Pache J, Ulm K, Schühlen H, Seyfarth M, Schmitt C, Blasini R, Neumann FJ, and Schömig A (2001a). “Restenosis after coronary placement of various stent types”. *The American Journal of Cardiology* 87.1, pp. 34–39.
- Kastrati A, Mehilli J, Dirschinger J, Dotzer F, Schühlen H, Neumann FJ, Fleckenstein M, Pfafferott C, Seyfarth M, and Schömig A (2001b). “Intracoronary stenting and angiographic results”. *Circulation* 103.23, pp. 2816–2821.

- Kelessidis V and Maglione R (2006). “Modeling rheological behavior of bentonite suspensions as Casson and Robertson–Stiff fluids using Newtonian and true shear rates in Couette viscometry”. *Powder Technology* 168.3, pp. 134–147.
- Keynton RS, Evancho MM, Sims RL, Rodway NV, Gobin A, and Rittgers SE (2001). “Intimal hyperplasia and wall shear in arterial bypass graft distal anastomoses: An in vivo model study”. *Journal of Biomechanical Engineering* 123.5, pp. 464–473.
- Khair A, Wang BC, and Kuhn DCS (2015). “Study of laminar–turbulent flow transition under pulsatile conditions in a constricted channel”. *International Journal of Computational Fluid Dynamics* 29.9-10, pp. 447–463.
- Khanafer K, Duprey A, Zainal M, Schlicht M, Williams D, and Berguer R (2011). “Determination of the elastic modulus of ascending thoracic aortic aneurysm at different ranges of pressure using uniaxial tensile testing”. *The Journal of Thoracic and Cardiovascular Surgery* 142.3, pp. 682–686.
- Koeppen B and Stanton B (2018). *Berne & Levy physiology*. Philadelphia, PA: Elsevier - HealthSciences Division.
- Kohn JC, Lampi MC, and Reinhart-King CA (2015). “Age-related vascular stiffening: causes and consequences”. *Frontiers in Genetics* 6, p. 112.
- Koskinas KC, Chatzizisis YS, Antoniadis AP, and Giannoglou GD (2012). “Role of endothelial shear stress in stent restenosis and thrombosis”. *Pathophysiological Mechanisms and Implications for Clinical Translation* 59.15, pp. 1337–1349.
- LaDisa JF, Guler I, Olson LE, Hettrick DA, Kersten JR, Warltier DC, and Pagel PS (2003). “Three-dimensional computational fluid dynamics modeling of alterations in coronary wall shear stress produced by stent implantation”. *Annals of Biomedical Engineering* 31.8, pp. 972–980.
- LaDisa JF, Olson LE, Douglas HA, Warltier DC, Kersten JR, and Pagel PS (2006). “Alterations in regional vascular geometry produced by theoretical stent implantation influence distributions of wall shear stress: analysis of a curved coronary artery using 3D computational fluid dynamics modeling”. *BioMedical Engineering OnLine* 5.1.
- LaDisa JF, Olson LE, Guler I, Hettrick DA, Audi SH, Kersten JR, Warltier DC, and Pagel PS (2004). “Stent design properties and deployment ratio influence indexes of wall shear stress: a three-dimensional computational fluid dynamics investigation within a normal artery”. *Journal of Applied Physiology* 97.1, pp. 424–430.
- LaDisa JF, Olson LE, Guler I, Hettrick DA, Kersten JR, Warltier DC, and Pagel PS (2005). “Circumferential vascular deformation after stent implantation alters wall shear stress evaluated with time-dependent 3D computational fluid dynamics models”. *Journal of Applied Physiology* 98.3, pp. 947–957.
- Li S, Chin C, Thondapu V, Poon EKW, Monty JP, Li Y, Ooi ASH, Tu S, and Barlis P (2017). “Numerical and experimental investigations of the flow–pressure relation in multiple sequential stenoses coronary artery”. *The International Journal of Cardiovascular Imaging* 33.7, pp. 1083–1088.
- Lodahl CR, Sumer BM, and Fredsøe J (1998). “Turbulent combined oscillatory flow and current in a pipe”. *Journal of Fluid Mechanics* 373, pp. 313–348.
- Lorenzini G and Casalena E (2008). “CFD analysis of pulsatile blood flow in an atherosclerotic human artery with eccentric plaques”. *Journal of Biomechanics* 41.9, pp. 1862–1870.
- Loscalzo J and Schafer AI (2003). *Thrombosis and hemorrhage*. Philadelphia: Lippincott Williams & Wilkins.

- Lotfi A and Reejhsinghani R (2015). “Prevention of stent thrombosis: challenges and solutions”. *Vascular Health and Risk Management*, p. 93.
- Malek AM, Alper SL, and Izumo S (1999). “Hemodynamic shear stress and its role in atherosclerosis”. *JAMA* 282.21, pp. 2035–2042.
- Meier B, Gruentzig AR, Hollman J, Ischinger T, and Bradford JM (1983). “Does length or eccentricity of coronary stenoses influence the outcome of transluminal dilatation?” *Circulation* 67.3, pp. 497–499.
- Mejia J, Ruzzeh B, Mongrain R, Leask R, and Bertrand OF (2009). “Evaluation of the effect of stent strut profile on shear stress distribution using statistical moments”. *BioMedical Engineering OnLine* 8.1, p. 8.
- Melchionna S, Amati G, Bernaschi M, Bisson M, Succi S, Mitsouras D, and Rybicki FJ (2013). “Risk assessment of atherosclerotic plaques based on global biomechanics”. *Medical Engineering & Physics* 35.9, pp. 1290–1297.
- Mirramezani M, Diamond S, Litt H, and Shadden SC (2018). “Reduced order models for transstenotic pressure drop in the coronary arteries”. *Journal of Biomechanical Engineering*, p. 31005.
- Mitchell GF, Parise H, Benjamin EJ, Larson MG, Keyes MJ, Vita JA, Vasani RS, and Levy D (2004). “Changes in arterial stiffness and wave reflection with advancing age in healthy men and women”. *Hypertension* 43.6, pp. 1239–1245.
- Mittal R, Simmons SP, and Najjar F (2003). “Numerical study of pulsatile flow in a constricted channel”. *Journal of Fluid Mechanics* 485, pp. 337–378.
- Molla MM, Wang BC, and Kuhn DCS (2012). “Numerical study of pulsatile channel flows undergoing transition triggered by a modelled stenosis”. *Physics of Fluids* 24.12, p. 121901.
- Moreno C and Bhaganagar K (2013). “Modeling of stenotic coronary artery and implications of plaque morphology on blood flow”. *Modelling and Simulation in Engineering* 2013, p. 14.
- Morlacchi S, Keller B, Arcangeli P, Balzan M, Migliavacca F, Dubini G, Gunn J, Arnold N, Narracott A, Evans D, and Lawford P (2011). “Hemodynamics and in-stent restenosis: micro-CT images, histology, and computer simulations”. *Annals of Biomedical Engineering* 39.10, p. 2615.
- Najjar SS, Scuteri A, and Lakatta EG (2005). “Arterial aging”. *Hypertension* 46.3, pp. 454–462.
- Natarajan S and Mokhtarzadeh-Dehghan MR (2000). “A numerical and experimental study of periodic flow in a model of a corrugated vessel with application to stented arteries”. *Medical Engineering & Physics* 22.8, pp. 555–566.
- Ng J, Bourantas CV, Torii R, Ang HY, Tenekecioglu E, Serruys PW, and Foin N (2017). “Local hemodynamic forces after stenting: implications on restenosis and thrombosis”. *Arteriosclerosis, Thrombosis, and Vascular Biology* 37.12, pp. 2231–2242.
- Nichols W, O’Rourke M, and Vlachopoulos C (2011). *McDonald’s blood flow in arteries, Sixth edition: Theoretical, experimental and clinical principles*. CRC Press.
- Ohara T, Toyoda K, Otsubo R, Nagatsuka K, Kubota Y, Yasaka M, Naritomi H, and Minematsu K (2008). “Eccentric stenosis of the carotid artery associated with ipsilateral cerebrovascular events”. *American Journal of Neuroradiology* 29.6, pp. 1200–1203.
- Ohashi T and Sato M (2005). “Remodeling of vascular endothelial cells exposed to fluid shear stress: experimental and numerical approach”. *Fluid Dynamics Research* 37.1-2, pp. 40–59.

- Ozden K, Sert C, and Yazicioglu Y (2020). “Effect of stenosis shape on the sound emitted from a constricted blood vessel”. *Medical & Biological Engineering & Computing* 58.3, pp. 643–658.
- Pache J, Kastrati A, Mehilli J, Schühlen H, Dotzer F, Hausleiter J, Fleckenstein M, Neumann FJ, Sattelberger U, Schmitt C, Müller M, Dirschinger J, and Schömig A (2003). “Intracoronary stenting and angiographic results: strut thickness effect on restenosis outcome (ISAR-STEREO-2) trial”. *Journal of the American College of Cardiology* 41.8, pp. 1283–1288.
- Pant S, Bressloff NW, Forrester AIJ, and Curzen N (2010). “The influence of strut-connectors in stented vessels: a comparison of pulsatile flow through five coronary stents”. *Annals of Biomedical Engineering* 38.5, pp. 1893–1907.
- Patel MS (2019). “Investigating telomere length dynamics In human endothelial cells”. PhD thesis. Department of Cardiovascular Sciences, University of Leicester.
- Paul MC and Molla MM (2012). “Investigation of physiological pulsatile flow in a model arterial stenosis using large-eddy and direct numerical simulations”. *Applied Mathematical Modelling* 36.9, pp. 4393–4413.
- Pijls NH, Gelder BV, Voort PV der, Peels K, Bracke FA, Bonnier HJ, and Gamal MIE (1995). “Fractional flow reserve”. *Circulation* 92.11, pp. 3183–3193.
- Pijls NH, Schaardenburgh P van, Manoharan G, Boersma E, Bech JW, Veer M van’t, Bär F, Hoorntje J, Koolen J, Wijns W, and Bruyne B de (2007). “Percutaneous coronary intervention of functionally nonsignificant stenosis”. *Journal of the American College of Cardiology* 49.21, pp. 2105–2111.
- Poon EK, Barlis P, Moore S, Pan WH, Liu Y, Ye Y, Xue Y, Zhu SJ, and Ooi AS (2014). “Numerical investigations of the haemodynamic changes associated with stent malapposition in an idealised coronary artery”. *Journal of Biomechanics* 47.12, pp. 2843–2851.
- Raben JS, Morlacchi S, Burzotta F, Migliavacca F, and Vlachos PP (2015). “Local blood flow patterns in stented coronary bifurcations: an experimental and numerical study”. *Journal of Applied Biomaterials & Functional Materials* 13.2, pp. 116–126.
- Rajamohan D, Banerjee RK, Back LH, Ibrahim AA, and Jog MA (2006). “Developing pulsatile flow in a deployed coronary stent”. *Journal of Biomechanical Engineering* 128.3, pp. 347–359.
- Rikhtegar F, Knight JA, Olgac U, Saur SC, Poulikakos D, Marshall W, Cattin PC, Alkadhi H, and Kurtcuoglu V (2012). “Choosing the optimal wall shear parameter for the prediction of plaque location—A patient-specific computational study in human left coronary arteries”. *Atherosclerosis* 221.2, pp. 432–437.
- Roy CS (1881). “The elastic properties of the arterial wall”. *The Journal of Physiology* 3.2, pp. 125–159.
- Sakariassen KS, Orning L, and Turitto VT (2015). “The impact of blood shear rate on arterial thrombus formation”. *Future Science OA* 1.4, pp. 30–39.
- Samijo SK, Willigers JM, Barkhuysen R, Kitslaar P, Reneman RS, Brands PJ, and Hoeks APG (1998). “Wall shear stress in the human common carotid artery as function of age and gender”. *Cardiovascular Research* 39.2, pp. 515–522.
- Seeley BD and Young DF (1976). “Effect of geometry on pressure losses across models of arterial stenoses”. *Journal of Biomechanics* 9.7, pp. 439–448.
- Siggers JH and Waters SL (2005). “Steady flows in pipes with finite curvature”. *Physics of Fluids* 17.7, p. 77102.

- Siogkas PK, Papafaklis MI, Sakellarios AI, Stefanou KA, Bourantas CV, Athanasiou LS, Exarchos TP, Naka KK, Michalis LK, Parodi O, and Fotiadis DI (2015). “Patient-specific simulation of coronary artery pressure measurements: an in vivo three-dimensional validation study in humans”. *BioMed Research International* 2015. Ed. by K Bendjelid, p. 628416.
- Stone PH, Coskun AU, Kinlay S, Clark ME, Sonka M, Wahle A, Ilegbusi OJ, Yeghiazarians Y, Popma JJ, Orav J, Kuntz RE, and Feldman CL (2003). “Effect of endothelial shear stress on the progression of coronary artery disease, vascular remodeling, and in-stent restenosis in humans”. *Circulation* 108.4, pp. 438–444.
- Stroud JS, Berger SA, and Saloner D (2000). “Influence of stenosis morphology on flow through severely stenotic vessels: implications for plaque rupture”. *Journal of Biomechanics* 33.4, pp. 443–455.
- Stultz SC and Kitto JB (2005). *Steam: Its generation and use*. 41st ed. The Babcock & Wilcox Company. Chap. 3-14.
- Sun Z (2015). “Aging, arterial stiffness, and hypertension”. *Hypertension* 65.2, pp. 252–256.
- Jahangiri M, Saghafian M, and Sadeghi MR (2017). “Numerical simulation of non-Newtonian models effect on hemodynamic factors of pulsatile blood flow in elastic stenosed artery”. *Journal of Mechanical Science and Technology* 31.2, pp. 1003–1013.
- The Editors of Encyclopaedia Britannica (2020). *Atherosclerosis*. URL: <https://www.britannica.com/science/atherosclerosis>.
- Tomaszewski M, Sybilski K, Baranowski P, and Małachowski J (2020). “Experimental and numerical flow analysis through arteries with stent using particle image velocimetry and computational fluid dynamics method”. *Biocybernetics and Biomedical Engineering* 40.2, pp. 740–751.
- Tonino PA, Bruyne BD, Pijls NH, Siebert U, Ikeno F, `t Veer M van, Klauss V, Manoharan G, Engstrøm T, Oldroyd KG, Lee PNV, MacCarthy PA, and Fearon WF (2009). “Fractional flow reserve versus angiography for guiding percutaneous coronary intervention”. *New England Journal of Medicine* 360.3, pp. 213–224.
- Trip R, Kuik DJ, Westerweel J, and Poelma C (2012). “An experimental study of transitional pulsatile pipe flow”. *Physics of Fluids* 24.1, p. 014103.
- Usmani AY and Muralidhar K (2016). “Pulsatile flow in a compliant stenosed asymmetric model”. *Experiments in Fluids* 57.12, pp. 186–210.
- Varghese SS, Frankel SH, and Fischer PF (2008). “Modeling transition to turbulence in eccentric stenotic flows”. *Journal of Biomechanical Engineering* 130.1, p. 014503.
- Varghese SS, Frankel SH, and Fischer PF (2007a). “Direct numerical simulation of stenotic flows. Part 1. Steady flow”. *Journal of Fluid Mechanics* 582, pp. 253–280.
- Varghese SS, Frankel SH, and Fischer PF (2007b). “Direct numerical simulation of stenotic flows. Part 2. Pulsatile flow”. *Journal of Fluid Mechanics* 582, pp. 281–318.
- Verkaik AC, Beulen BWAMM, Bogaerds ACB, Rutten MCM, and Vosse FNVD (2009). “Estimation of volume flow in curved tubes based on analytical and computational analysis of axial velocity profiles”. *Physics of Fluids* 21.2, p. 23602.
- Waller BF (1989). “The eccentric coronary atherosclerotic plaque: morphologic observations and clinical relevance”. *Clinical Cardiology* 12.1, pp. 14–20.
- Wentzel JJ, Chatzizisis YS, Gijsen FJH, Giannoglou GD, Feldman CL, and Stone PH (2012). “Endothelial shear stress in the evolution of coronary atherosclerotic plaque and vascular remodelling: current understanding and remaining questions”. *Cardiovascular Research* 96.2, pp. 234–243.

- Wu J, Liu G, Huang W, Ghista DN, and Wong KKL (2015). “Transient blood flow in elastic coronary arteries with varying degrees of stenosis and dilatations: CFD modelling and parametric study”. *Computer Methods in Biomechanics and Biomedical Engineering* 18.16, pp. 1835–1845.
- Xie X, Li Y, and Xie S (2018). “Computation of hemodynamics in eccentric coronary stenosis: A morphological parametric study”. *Technology and Health Care* 26, pp. 229–238.
- Xu D and Avila M (2018). “The effect of pulsation frequency on transition in pulsatile pipe flow”. *Journal of Fluid Mechanics* 857, pp. 937–951.
- Xu D, Warnecke S, Song B, Ma X, and Hof B (2017). “Transition to turbulence in pulsating pipe flow”. *Journal of Fluid Mechanics* 831, pp. 418–432.
- Yamagishi M, Terashima M, Awano K, Kijima M, Nakatani S, Daikoku S, Ito K, Yasumura Y, and Miyatake K (2000). “Morphology of vulnerable coronary plaque: insights from follow-up of patients examined by intravascular ultrasound before an acute coronary syndrome”. *Journal of the American College of Cardiology* 35.1, pp. 106–111.
- Yao H, Ang KC, Yeo JH, and Sim EK (2000). “Computational modelling of blood flow through curved stenosed arteries”. *Journal of Medical Engineering & Technology* 24.4, pp. 163–168.
- Yazdani SK, Moore JE, Berry JL, and Vlachos PP (2004). “DPIV measurements of flow disturbances in stented artery models: adverse affects of compliance mismatch”. *Journal of Biomechanical Engineering* 126.5, pp. 559–566.
- Young DF and Tsai FY (1973a). “Flow characteristics in models of arterial stenoses. II. Unsteady flow”. *Journal of Biomechanics* 6.5, pp. 547–559.
- Young DF and Tsai FY (1973b). “Flow characteristics in models of arterial stenoses — I. Steady flow”. *Journal of Biomechanics* 6.4, pp. 395–410.
- Zhu C, Seo JH, and Mittal R (2018). “Computational modelling and analysis of haemodynamics in a simple model of aortic stenosis”. *Journal of Fluid Mechanics* 851, pp. 23–49.

Chapter 3

Effects of temporal geometric variations of the coronary arteries

3.1 Chapter overview

This chapter investigates the effects of temporal geometric variations of the coronary arteries on the hemodynamic parameters. The temporal geometric variations of coronary arteries during a cardiac cycle are classified as a superposition of the changes in the position, curvature and torsion of the coronary artery axis markers and the variations in lumen cross-sectional shape due to the distensible wall motion induced by a pressure pulse and/or contraction of the myocardium in a cardiac cycle. As discussed in Section 2.1.1, blood vessels are flexible and move during a cardiac cycle, such that their movement can affect the behaviour of the flow contained within them. Literature suggests that depending on the parameters of interest and the type of artery, the changes in artery geometry can be ignored. If this assumption is valid, the modelling of the flow behaviour inside the coronary arteries will be much easier, as will in-vitro experiments.

This chapter reviews the studies in the literature comparing the effect of modelling or disregarding the temporal geometric variations of coronary arteries for hemodynamic investigations. The review of the literature is focused on two sections including the effects of wall compliance and dynamic vessel motion on the hemodynamic parameters.

It is shown that depending on the target of a study, considering arteries to be rigid and neglecting the effects of their temporal geometric variations can result in an accurate estimation of the hemodynamic parameters. If the target is to investigate the pressure drop, fractional flow reserve and time-averaged wall shear stress, as the most widely used clinical metrics, neglecting the effect of temporal geometric variations in the numerical modelling is expected to result in less than 5% deviations of their values. Furthermore, the literature suggests that introducing the effects of ageing and atherosclerosis on the stiffness of the coronary arteries reduces the effect of temporal geometric variations of coronary artery for the investigation of structural stresses of the arteries as well as the time-dependent variations of hemodynamic parameters. As the artery wall becomes harder and stiffer with ageing and loses its flexibility, considering arteries to be rigid results in a more reliable estimation of hemodynamic parameters. This mitigates further the deviations reported in the literature between the results of compliant and rigid wall

simulations for these cases. On the other hand, if the target of the study is to investigate the effect of temporal geometric variations of the coronary arteries on the structural stresses of the arteries, failure to consider the effect of temporal geometric variations may result in considerable changes in the calculated structural stresses. Furthermore, if the target is to study the temporal geometric variations of hemodynamic parameters such as temporal wall shear stress or oscillatory shear index particularly at the location of bifurcations, it was shown that on-average about 20% deviation exists between the results of those considering the effect of temporal geometric variations of coronary arteries and those simplifying the arteries to be rigid.

Therefore, the results in the literature show that neglecting the effects of temporal geometric variations is expected to result in less than 5% deviation of the time-averaged pressure drop and wall shear stress values and also less than 20% deviation of the temporal geometric variations of hemodynamic parameters, such as time-dependent wall shear stress and oscillatory shear index. Hence, since the aim of this thesis is to develop an in-depth understanding of the flow features inside stenosed and stented coronary arteries, the effect of temporal geometric variations of the coronary arteries are disregarded in the rest of this thesis and the coronary arteries are modelled using a rigid artery model with no dynamic vessel motion during a cardiac cycle.

3.2 Effects of temporal geometric variations of the coronary arteries

This section consists of the following submitted journal article:

Navid Freidoonimehr, Rey Chin, Anthony Zander, Maziar Arjomandi (2021). “A review on the effect of temporal geometric variations of the coronary arteries on the hemodynamic parameters”. *Journal of Biomechanical Engineering*, under review.

The article is identical to its submitted format with the following exceptions:

- The numbering of figures, tables and equations have been altered to include the chapter number.
- The position of some figures and tables have been changed to improve legibility.

Statement of Authorship

Title of paper	Effect of temporal variations of the coronary arteries on the hemodynamic parameters
Publication Status	<input type="checkbox"/> Published <input type="checkbox"/> Accepted for Publication <input checked="" type="checkbox"/> Submitted for Publication <input type="checkbox"/> Unpublished and Unsubmitted work written in manuscript style
Publication Details	Freidoonimehr, N., Chin, R., Zander, A., and Arjomandi, M., "Effect of temporal variations of the coronary arteries on the hemodynamic parameters", Journal of Biomechanical Engineering, under review

Principal Author

Name of Principal Author (Candidate)	Navid Freidoonimehr		
Contribution to the Paper	Developed ideas, performed data analysis and interpreted results, wrote manuscript, and acted as corresponding author		
Overall percentage (%)	75%		
Certification:	This paper reports on original research I conducted during the period of my Higher Degree by Research candidature and is not subject to any obligations or contractual agreements with a third party that would constrain its inclusion in this thesis. I am the primary author of this paper.		
Signature		Date	15/02/2021

Co-Author Contributions

By signing the Statement of Authorship, each author certifies that:

- i the candidate's stated contribution to the publications is accurate (as detailed above);
- ii permission is granted for the candidate to include the publication in the thesis; and
- iii the sum of all co-author contributions is equal to 100% less the candidate's stated contribution

Name of Co-Author	Rey Chin		
Contribution to the Paper	Supervised the development of the research, participated in developing ideas and concepts, helped in interpretation of results, provided critical revision of manuscript.		
Signature		Date	15/02/2021

Name of Co-Author	Anthony Zander		
Contribution to the Paper	Supervised the development of the research, participated in developing ideas and concepts, helped in interpretation of results, provided critical revision of manuscript.		
Signature		Date	15/02/2021

Name of Co-Author	Maziar Arjomandi	
Contribution to the Paper	Supervised the development of the research, participated in developing ideas and concepts, helped in interpretation of results, provided critical revision of manuscript.	
Signature	Date	15/02/2021

A review on the effect of temporal geometric variations of the coronary arteries on the hemodynamic parameters

Navid Freidoonimehr, Rey Chin, Anthony Zander, and Maziar Arjomandi

Abstract

Temporal variations of the coronary arteries during a cardiac cycle are defined as the superposition of the changes in the position, curvature, and torsion of the coronary artery axis markers and the variations in the lumen cross-sectional shape due to the distensible wall motion induced by the pulse pressure and contraction of the myocardium in a cardiac cycle. This review discusses whether the modelling the temporal variations of the coronary arteries is needed for the investigation of the hemodynamics specifically in time critical applications such as a clinical environment. The numerical modellings in the literature which model or disregard the temporal variations of the coronary arteries on the hemodynamic parameters are discussed. The results in the literature show that neglecting the effects of temporal variations is expected to result in less than 5% deviation of the time-averaged pressure drop and wall shear stress values and also less than 20% deviation of the temporal variations of hemodynamic parameters, such as time-dependent wall shear stress and oscillatory shear index. This review study can be considered as a guide for the future studies to outline the conditions in which temporal variations of the coronary arteries can be neglected, while providing a reliable estimation of hemodynamic parameters.

3.2.1 Introduction

Development of an atherosclerotic plaque inside the coronary arteries, as one of the major coronary artery diseases, is shown to be associated with the extreme of the hemodynamic parameters such as pressure drop and wall shear stress (WSS) and geometric features of the coronary arteries (Wahle et al. 2006). As one of their unique features, in a cardiac cycle, coronary arteries move along their centreline and their cross section expands and contracts. These temporal variations may affect the hemodynamics of the coronary arteries by changing the flow velocities and their gradients. The common methods for investigation of the hemodynamic parameters in the diseased coronary arteries are the application of numerical simulation using computational fluid dynamics (CFD) and fluid structure interaction (FSI). The simulation of coronary arteries including their temporal variations with the aim of investigation of the hemodynamic parameters needs sophisticated numerical models and high computational resources. Therefore, in most studies idealised numerical models in which the artery motions and compliances are neglected are commonly used. While it is an acceptable practice, the effect of the dynamic motions of the arteries on the hemodynamic parameters still requires further scrutiny. This study aims to identify the conditions in which the effect of temporal variations can be disregarded in a numerical simulation and quantify their impact on hemodynamic parameters

in a cardiovascular system.

The temporal variations of coronary arteries can be categorised into two types. The first type is related to the displacement of coronary arteries along their centreline in a cardiac cycle. Since coronary arteries are located on heart muscles, blood flow in coronary arteries is affected by the physiological movement of the vessels which depends on the specific geometry of the arteries, the cardiac motion, the arterial pressure waveform, and finally, the material properties of the arterial wall. In coronary arteries, the vascular geometry varies dynamically owing to the cardiac motion and vessel compliance (Torii et al. 2009a). Due to their attachment to the moving myocardium, they undergo movements and deformations, during a cardiac cycle (Ding and Friedman 2000), which are spatially inhomogeneous. The movements can be recognised based on the changes in the curvature and torsion of the centrelines of the coronary arterial lumen (Puentes et al. 1998; Ding and Friedman 2000) as well as the dislocation of the coronary artery without change of the length or shape of the arterial segment (O’Loughlin et al. 2011). Figure 3.1 displays the coronary angiogram showing the position of left coronary arteries during diastole and systole. The figure shows two extreme positions of the coronary arteries in a cardiac cycle. Due to the sensitivity of hemodynamics to curvature and since through this displacement the curvature of the arteries changes, the motions of coronary artery may influence its hemodynamics.

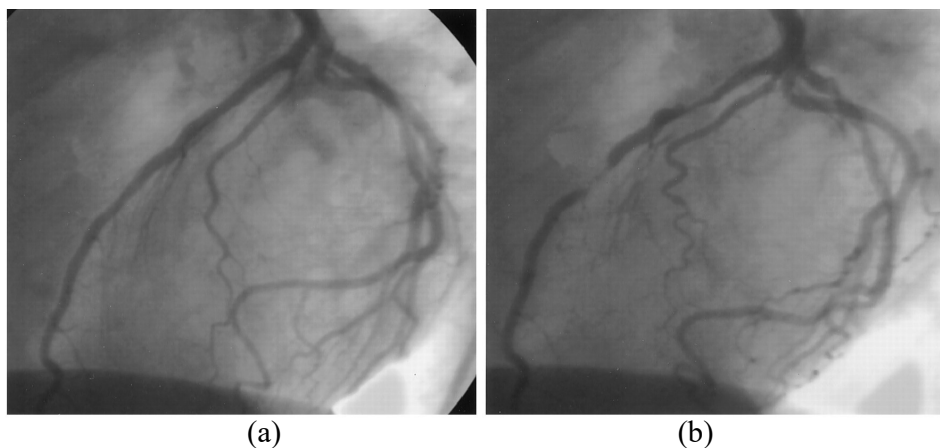


Figure 3.1: Coronary angiogram showing the position of left coronary arteries during (a) diastole and (b) systole (reproduced from Mohlenkamp et al. (2002)).

Different coronary arteries do not undergo similar displacements during a cycle. Figure 2a shows the changes in the location of the coronary arteries in a cardiac cycle due to the movement of the centreline of the middle segment of three main coronary arteries including left anterior descending coronary artery (LAD), left circumflex coronary artery (LCx) and right coronary artery (RCA) along the orthogonal axis in a cardiac cycle (Johnson et al. 2004). The magnitude of changes in displacement vector is calculated based on the square root of sum of displacement squared values in different directions, as shown in Fig. 3.1. It is shown that the RCA motion is greater than the other two arteries. The overall displacement of the RCA is 2.1 ± 0.7 times more than that of the LAD and 2.1 ± 1.5 more than that of the LCx. Furthermore, in order to compare the displacement of different segments of RCA, Fig. 3.2b shows the displacement of the proximal, middle, and distal segments of the RCA over a cardiac cycle obtained from biplane x-ray angiography films (Johnson et al. 2004). Each segment of RCA experiences a similar motion trajectory,

although the mid and distal segments of the RCA have a slightly larger displacement. Moreover, Table 3.1 presents the average ratios of the motion in the middle and distal segments of LAD, LCx and RCA compared to the proximal segment (Johnson et al. 2004). The LCx shows almost the same ratio of movements as RCA in the middle and distal segments. However, the LAD does not show any significant differences in magnitude of displacement among its three segments.

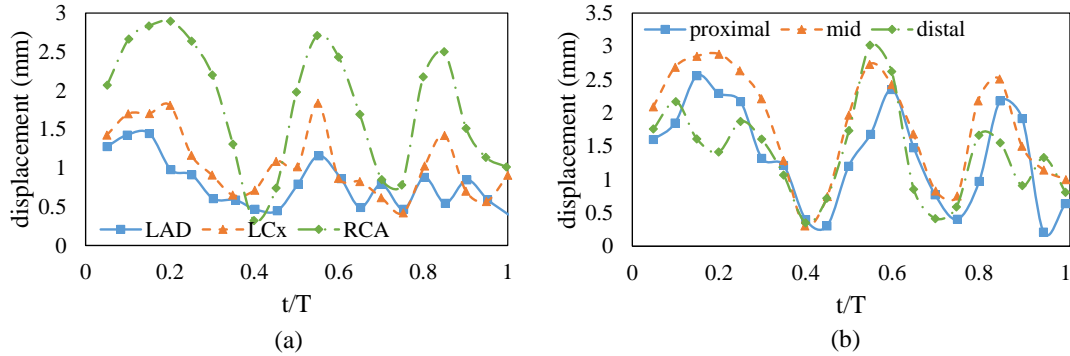


Figure 3.2: Magnitude of changes in the displacement vector of the middle segment of the three main coronary arteries along the orthogonal axis and b) displacement of the proximal, middle, and distal segments of the RCA over a cardiac cycle (Johnson et al. 2004).

Table 3.1: Average ratios of motion in middle and distal segments of LAD, LCx and RCA with respect to the proximal segment movement obtained from 15 patients (Johnson et al. 2004).

	LAD	LCx	RCA
middle	1.1	1.5	1.6
distal	1.0	1.6	1.4

The second type of temporal variations of coronary arteries is related to the variation of the lumen cross-sectional geometry of arteries in a cardiac cycle. This motion, which also can occur in other major arteries, is due to the distensible wall motion induced by the pulse pressure and/or contraction of the myocardium (Zeng et al. 2003). Vessel wall distensibility, as a measure of the arterial ability to expand and contract with cardiac pulsation and relaxation (Godia et al. 2007), is considered as a factor that affects pressure drop and most hemodynamic parameters. The increased distensibility of the arterial walls will likely lead to decreased resistance to flow and a lower pressure gradient across the stenosis (Yong et al. 2017). It is worth mentioning that the diameter of the coronary arteries varies based on the type of the arteries and their stream-wise locations, as shown in Fig. 3.1 and tabulated in Table 3.2. Figure 3.3 shows the intravascular ultrasound (IVUS) images of LAD in diastole and systole (Shaw et al. 2002) which demonstrates that the minimum and maximum lumen areas occur near the end of diastole and peak systole, respectively (Shaw et al. 2002). Figure 3.4 presents the in vivo pulsatile flow velocity waveforms measured at the inlet of RCA arterial tree in porcine heart and the dynamic changes of elastic vessel diameter (Huo et al. 2009). As shown in Fig. 3.4, the dynamic changes of RCA diameter in a cardiac cycle are in the range of -7% to $+12\%$.

An accurate numerical model should be able to provide an accurate evaluation of the hemodynamic parameters and at the same time, it should not be developed based on

Table 3.2: Diameter and distance from ostium of different coronary artery segments from 4 patients (Park et al. 2016).

	LCx		LAD		
	proximal	distal	proximal	mid	distal
distance from ostium (mm)	15	70	10	30	55
diameter (median) (mm)	3.8	2.4	2.8	2.1	1.5

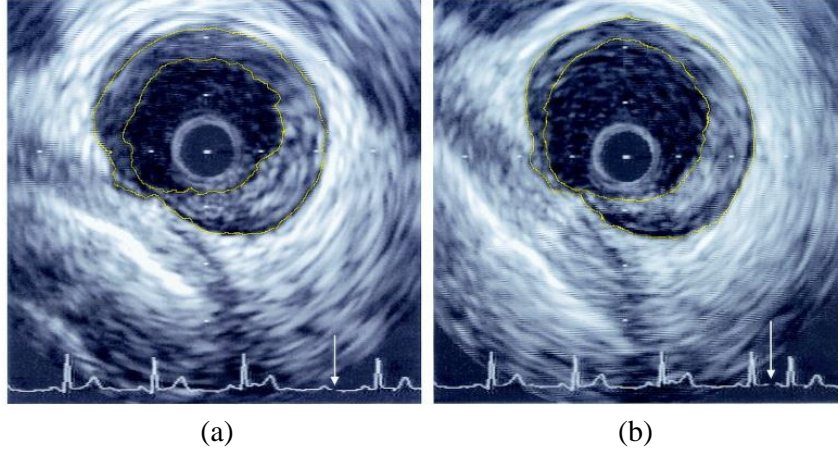
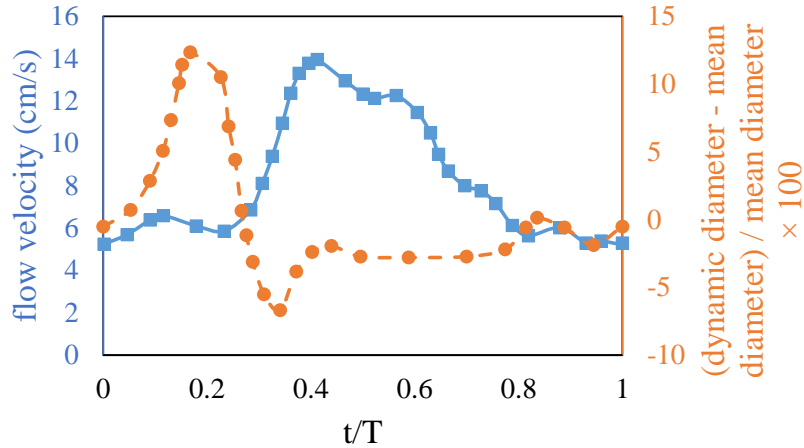


Figure 3.3: Intravascular ultrasound images of LAD in diastole (on the left) and systole (on the right). The inner tracing marks the lumen-intima boundary, and the outer tracing the outer margin of the intima-media layer (Shaw et al. 2002).

Figure 3.4: In vivo pulsatile flow velocity waveforms measured at the inlet of RCA arterial tree in porcine heart and dynamic changes of elastic vessel diameter represented by instantaneous diameter - mean diameter) / mean diameter $\times 100$ (Huo et al. 2009).

too simplified or too complex assumptions (Brown et al. 2012). An accurate simulation of coronary arteries should consider the combined effects of a) the motion of the fluid inside the arteries, b) the motion of the vessels due to their elasticity and c) the dynamic displacement of the vessels due to the cardiac motion in a cardiac cycle (Hirschhorn et al. 2020). Where it is required to consider the effect of cardiac motion in the numerical simulation, the widely-used method in the literature is to specify the wall displacement of the arteries using dynamic mesh model. The displacement boundary condition for one

end of the artery is assumed to be fixed while no fixed boundary condition is used for the other end in order to let the artery move freely to simulate the effect of dynamic motion of the coronary arteries. This assumption is valid mainly for the simulations of RCA or LCx due to the larger displacement of the middle and distal of the artery compared to the proximal section, as discussed earlier. However, for the simulation of LAD, considering one-end fixed displacement boundary condition is not a feasible approach due to almost the same relative displacement of the proximal, middle and distal of the LAD.

On the other side, the common practice in the literature for the numerical modelling of the effect of wall elasticity is to conduct Fluid Structure Interaction (FSI) simulation by considering the interaction between the fluid flow and the arterial wall. This allows the pulsatile fluid flow to exert pressure on the arterial wall and at the same time, wall expansion or shrinkage due to its elasticity are transferred back to the fluid domain to calculate the flow parameters again. Such numerical simulation of coronary arteries requires the information about the thickness and material properties of the vessel wall as well as how the coronary arteries are mechanically constrained in the chest with the information of the material properties of the surrounding tissues and muscles. However, none of this information is often available for one specific patient. Even an FSI simulation with simplified assumptions with a constant thickness isotropic material without considering the effect of cardiac motion is computationally expensive and time-consuming (Zhong et al. 2018), and may not be readily implemented in clinical practice (Eslami et al. 2019). It is reported by Brown et al. (2012) that an FSI simulation of a patient-specific aorta with a mild coarctation took 145.5 hours, while the corresponding CFD simulation took 6.8 hours which is about 20 times faster than the FSI simulation. All their simulations were conducted on a standard desktop computer of Dell PowerEdge T710 using 4, 2.93 GHz Intel Xeon X5570 processors in local parallel. Due to the challenges related to the complexities of performing FSI and several unknown parameters, as discussed by Morris et al. (2016), identification of the condition in which a non FSI simulation can provide reliably accurate results is critical. However, the importance of considering the effects of temporal variations of coronary arteries for the investigation of hemodynamic parameters is still not well known. As the hemodynamic parameters such as pressure drop, WSS, and oscillatory shear index (OSI), to characterise the degree of shear reversal in a pulsatile flow throughout the cardiac cycle (Amaya et al. 2016), are indicative parameters for diseased coronary arteries which are widely used in clinical applications, an accurate estimation of these parameters through numerical simulations is crucial. For instance, it has been widely reported in the literature the extremes of WSS are recognised as a potential marker for determination of rapidly progressing coronary artery diseases (Chatzizisis et al. 2007, 2008; Eshtehardi et al. 2012; Gijssen et al. 2013; Samady et al. 2011; Stone et al. 2003; Timmins et al. 2015). Hence, the target of this review is to provide an improved understanding of the effects of temporal variations of coronary arteries on the variations of WSS and OSI.

This study comprises a literature review of the studies focusing on the comparison of the hemodynamic parameters obtained from the numerical simulations developed with and without considering the effects of dynamic vessel motion and wall compliance of the coronary arteries on the hemodynamic parameters. Furthermore, the importance of considering the effect of temporal variations of the coronary arteries in numerical or experimental modellings of hemodynamics of coronary arteries is discussed based on the results of the previous studies in the literature.

3.2.2 Effect of dynamic vessel motion of coronary arteries on the flow behaviour

As discussed in the previous section, since different coronary arteries undergo different displacements, the effect of dynamic vessel motion on the hemodynamic parameters varies for different coronary arteries. The studies in the literature show that the effect of dynamic vessel motion on the RCA is more considerable compared to the LAD due to their larger displacement ratios of its different segment locations. The studies in the literature focusing on the effect of dynamic vessel motion of the coronary arteries on the flow behaviour are investigated in this section. In a study by Zeng et al. (2003), the effects of cardiac-induced motion on hemodynamics in a patient-specific RCA were investigated based on the Finite Element Method (FEM) using the arbitrary Lagrangian–Eulerian (ALE) formulation with the time derivative in referential form and the spatial derivatives transformed into the spatial domain. A detailed explanation of ALE formulation can be found in (Hughes et al. 1981; Takashi and Hughes 1992). By changing the computation domain due to the dynamic vessel motion effect, the FEM mesh was updated based on a semi-torsional spring analogy model (Zeng and Ethier 2003). In order to evaluate the relative importance of RCA motion, flow pulsation, and the interaction between motion and flow pulsation, steady and pulsatile inflow conditions were studied. Figure 3.5 shows the effect of flow pulsatility and dynamic vessel motion on the temporal variation of WSS at a mid-stream-wise location of RCA shown by the red line in Fig. 3.5a for both inner and outer walls. Figure 3.5a presents the results of the steady inlet flow and Fig. 3.5b shows the results of the pulsatile inlet flow. WSS value for the ‘average geometry’, calculated by time-averaging the position of each marker on the RCA axis over a cardiac cycle, with the steady inflow condition had the same mean value and its fluctuating parts were overestimated or underestimated with the maximum of 35% compared to the case when the dynamics motion was modelled. However, the presence of flow pulsation results in reducing the differences between the results to about 11%, as shown in Fig. 3.5b. Their results showed that the RCA motion has a small effect on time-averaged WSS (TAWSS) patterns. However, it has a larger effect on the temporal variation of WSS, but even this effect is overshadowed by the variations in WSS due to the flow pulsation.

In another study on the effect of dynamic vessel motion on the RCA, Torii et al. (2009a) investigated the hemodynamic parameters including TAWSS and OSI in a patient-specific RCA. To analyse the effect of vessel motion, haemodynamic simulations with a fixed geometry at different time instances during a cardiac cycle were performed, and the results were compared with the dynamic model. To quantify the similarity in the haemodynamic parameters from the results of the dynamic and static wall models, Figure 3.6 shows the correlations between TAWSS and OSI for the models at the beginning of the systole and peak of the diastole. Each point in these plots corresponds to a location on the lumen surface with the value of its haemodynamic parameter obtained from the moving wall model on the horizontal axis and the one from the static model on the vertical axis. The results showed that the TAWSS is similar for the dynamic and static wall models, both qualitatively and quantitatively with a regression line gradient of 0.82–0.92 and a correlation coefficient of 0.89–0.95. Conversely, the OSI showed much poorer correlations with a regression line gradient of 0.22–0.32 and a correlation coefficient of 0.38–0.60. The reason of the poorer correlation of OSI compare to TAWSS is the fact that OSI is a parameter representing not only the oscillatory nature of the hemodynamics, but also

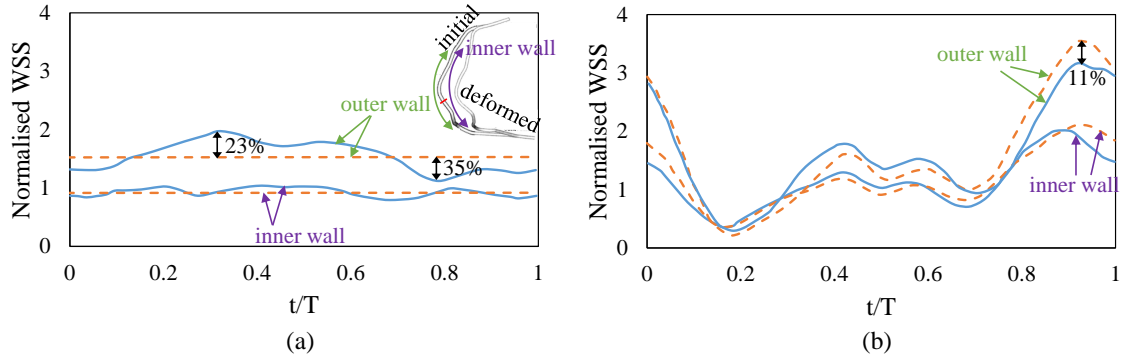


Figure 3.5: The normalised WSS versus the normalised time for the inner and outer walls of RCA for the cases with and without dynamic vessel motions at the location of tiny red line shown in schematics of the artery with (a) the steady inlet flow and (b) the pulsatile inlet flow. Time is normalized by the cardiac period and WSS is normalised with the steady inlet Poiseuille WSS value (Zeng et al. 2003). The blue solid line refers to the dynamic motion model and the orange dashed line refers to the model without dynamic motion. Inner wall refers to the wall closer to the centre of curvature and the outer wall is the furthest away wall from the centre of curvature.

the directional variation relative to the axis. However, in TAWSS, as the time-averaged variation of WSS, the oscillatory nature of the flow is not clearly visible. Their findings suggest that neglecting dynamic motion of the RCA is acceptable if TAWSS is the primary focus of the numerical modelling. However, this assumption may result in underestimation of hemodynamic parameters related to the oscillatory nature of the blood flow such as OSI.

As mentioned earlier, LAD responds differently to the effect of dynamic vessel motion compared to the RCAs due to the different relative displacements at different arterial segments. The effect of dynamic vessel motion on hemodynamics of a realistic model of the bifurcation of the LAD and its first diagonal branch was investigated by Prosi et al. (2004). They modelled artery as attached to the surface of a sphere with time varying radius according to the experimental dynamic curvature data to simulate the motion of the coronary arteries. FEM code with an ALE formulation with the Dirichlet boundary condition at the artery wall for the wall velocity which is obtained from the vessel wall movement was developed. It is to note that the blood flow patterns are significantly different in the vicinity of bifurcations, and therefore the resulting WSS distributions cannot be adequately estimated by CFD simulations performed on isolated single arterial segments. They studied dynamic vessel motion effect by modelling three static vessel geometries including the vessel with the minimum or maximum curvature in a cardiac cycle and the average curvature model. The temporal variation of WSS in a cardiac cycle for the myocardial location proximal to the bifurcation (position A) considering different static curvature models is shown in Fig. 3.7. Modelling the dynamic vessel motion as the constant average curvature of the artery in a cardiac cycle resulted in a maximum 12% variation in the calculated temporal WSS at the myocardial location. Furthermore, the results showed that the average of maximum deviations of the temporal WSS due to considering the constant average curvature in four locations including myocardial, pericardial, inner and, outer, reduced from 21% at the proximal to the bifurcation (position A) to 12% at the distal to the bifurcation (position B). This means that the dynamic

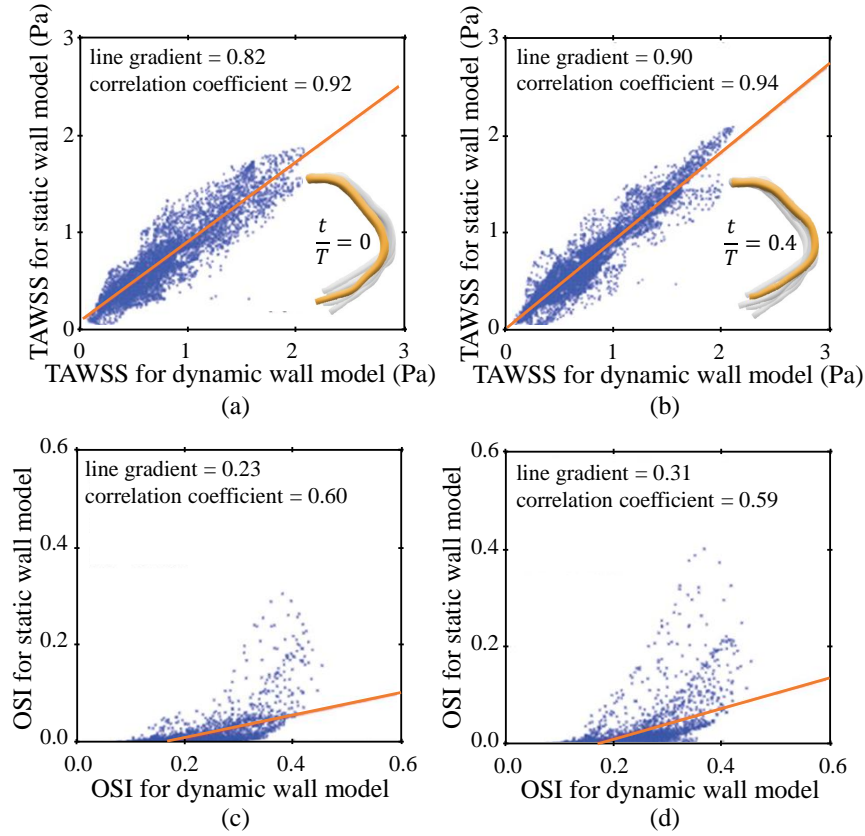


Figure 3.6: Correlations of (a) and (b) TAWSS between the dynamic and static wall models and correlations of (c) and (d) oscillatory shear index between the dynamic and static wall models of the patient-specific right coronary artery. (a) and (c) refer to the beginning to systole and (b) and (d) refer to the peak of the diastole in a cardiac cycle (Torii et al. 2009a).

vessel motion of the artery has a larger effect on WSS at the locations near the bifurcation.

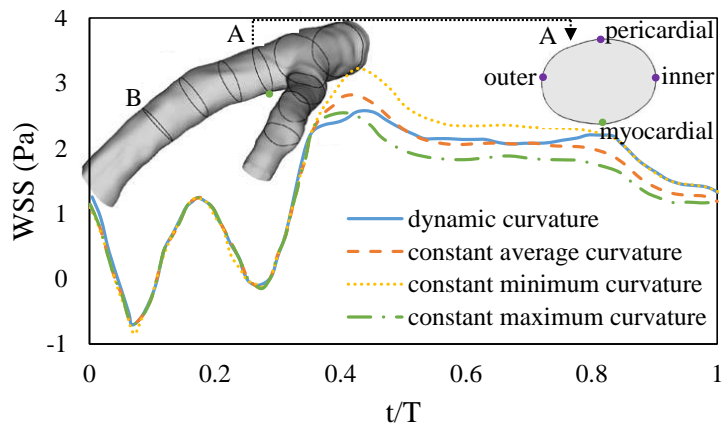


Figure 3.7: WSS values in a cardiac cycle at the myocardial location of the artery, show in green dot, for the location proximal to the bifurcation (Prosi et al. 2004).

In another study focusing on the effect of dynamic vessel motion on the LAD, Kolan-davel et al. (2006) studied the effect of time varying curvature on the WSS of a simplified

model of the LAD. The commercial CFD solver Fluent with the dynamic mesh model based on ALE approach was employed to simulate the effect of dynamic vessel motion. Figure 3.8 shows the temporal WSS and TAWSS distributions for different axial locations for dynamic and static models. The results showed that both wall motion and flow pulsatility produced instantaneous variations in the outer and inner WSS which were similar to the WSS distribution in the pulsatile flow with static wall model. Furthermore, the instantaneous and mean WSS distribution in the pulsatile flow dynamic model closely followed that of the pulsatile flow static model except in the central section where the curvature was high. These results suggest that the effects of wall motion on temporal WSS patterns are only secondary to the pulsatile flow effects and agree well with the findings of other dynamic model studies.

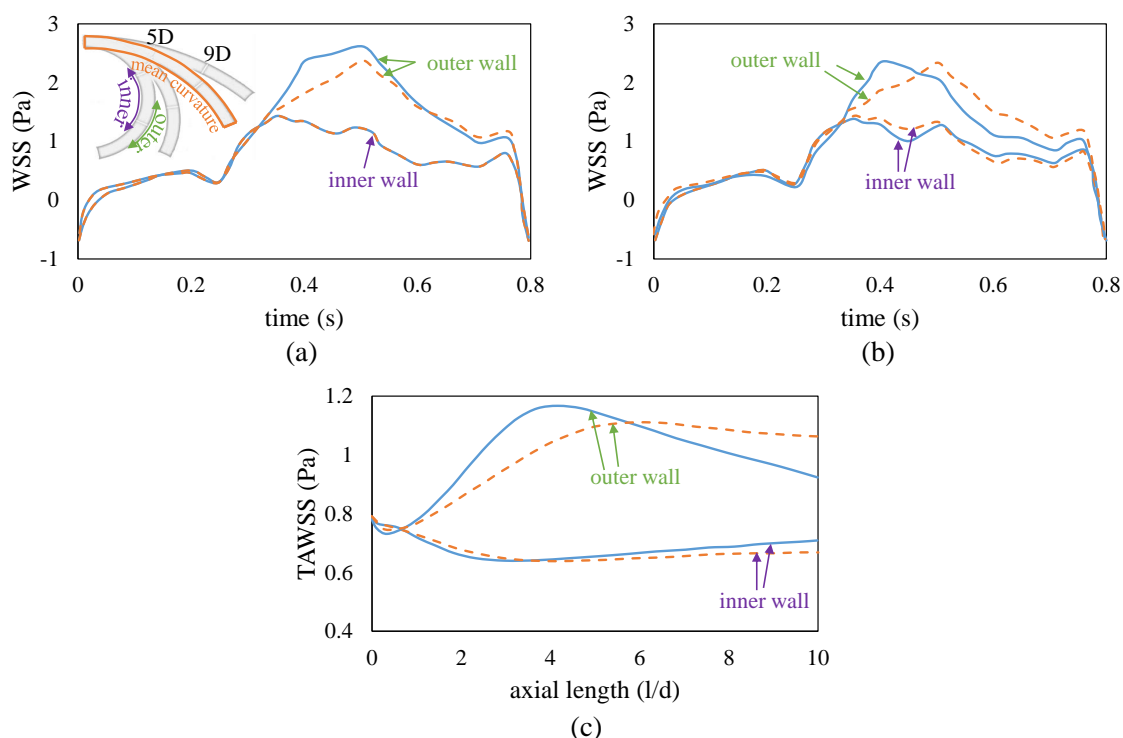


Figure 3.8: Temporal axial inner and outer WSS distribution at a) 5 diameters and b) 9 diameters from the LAD inlet and c) axial TAWSS distribution along the inner and outer walls of the LAD (Kolandavel et al. 2006). The blue solid line refers to the dynamic model and orange dashed line refers to the static model.

Furthermore, Hasan et al. (2013) studied the effect of cardiac motion including bending and stretching on the coronary blood flow inside a segment of stenosed patient-specific LAD model. A finite volume method using ANSYS CFX accompanied with ALE method to model the moving blood vessel walls was employed to simulate the effect of dynamic vessel motion. Their results showed that even though the bending motion of the coronary artery may significantly affect the blood cell trajectory, it has a little effect on flow parameters including blood flow velocity, blood shear stress, and WSS. However, they found that wall normal stresses (axial, circumferential, and radial stress) are greatly affected by the blood vessel wall motion.

To conclude, the review of literature on the effect of dynamic vessel motion shows that various coronary arteries behave differently when the effect of dynamic vessel motions

considered in modelling of the hemodynamic parameters. This effect on the RCAs due to their larger relative displacement of different segments results in larger changes in the hemodynamic parameters compared to the LADs. The results in literature showed that the effect of dynamic vessel motion on the hemodynamic parameters are only secondary to the pulsatile flow effect in the coronary arteries. Furthermore, the effect of dynamic vessel motion on the TAWSS compared to the oscillatory hemodynamic parameters such as time-dependent WSS and OSI is negligible. This means that if the focus of the study is to simulate the effect of dynamic vessel motion on the time-averaged hemodynamic parameters, ignoring this effect results in the acceptable estimation of the time-averaged hemodynamic parameters. There are also some studies in the literature, as mentioned earlier such as Prosi et al. (2004) and Torii et al. (2009a), that instead of dynamic simulation of the effect of cardiac motion on the hemodynamic parameters, a static modelling of coronary arteries at multiple time instances in a cardiac cycle has been investigated. Employment of this approach results in simplification of complexities of the realistic dynamic modeling of the coronary arteries. It was shown that it results in a more accurate estimation of hemodynamic parameters compared to case of neglecting effect of dynamic motion of the coronary arteries and considering arteries without any movements in a cardiac cycle. It is expected that differences between the static (for different time-snapshots in a cardiac cycle) and dynamic wall models are different for the simulation of the entire coronary artery tree compared to a single artery. The reason is due to an interaction of different branches of coronary arteries with each other such that the differences can be intensified at the location of bifurcations, as discussed earlier.

3.2.3 Effect of wall compliance of the coronary arteries on the flow behaviour

It is reported in the literature that in larger vessels, comparisons of WSS in elastic versus rigid walls have shown up to 25% (Lantz et al. 2011), 17% (Liu et al. 2001), and 4–15% (Liu et al. 2001; Zhao et al. 2000) difference in the aorta, femoral, and carotid arteries, respectively. This section is mainly focused on the coronary artery studies in the literature in which they provided a comparison on the effect of wall compliance. Pressure drop and fractional flow reserve (FFR) are also reviewed in this section to find out the effect of wall compliance of coronary arteries on them. It is reported that assuming healthy coronary arteries to be rigid and hence disregarding its elasticity changes the pressure drop and the computed FFR values insignificantly with less than 2% and about 0.26% obtained from the results of (Mirramezani et al. 2018) and (Siogkas et al. 2015), respectively.

To measure arterial stiffness, the Pulse Wave Velocity (PWV) is used. It is defined based on the propagation of the pressure wave in a pipe (Nabeel et al. 2020). The elastic property of the wall of an artery plays an important part in determining the velocity of propagation of a pulse wave (Nichols et al. 2011). Blood pressure pulse initiating from the heart at each cardiac cycle propagates through the circulatory system with a specific velocity of PWV. To find the relation between the pressure wave speed and the arterial wall stiffness parameters of the arteries, Moens–Korteweg equation was developed based on the Newton’s second law of motion applied to a small fluid element inside the arteries, as:

$$PWV = \sqrt{\frac{Et}{\rho D}} \quad (3.1)$$

where E is the Young modulus of the arterial wall, t is the artery thickness, ρ is the fluid density, and D is the arterial diameter. This equation is derived by assuming properties of artery walls to be isotropic and experiencing isovolumetric change with pulse pressure (Gosling and Budge 2003). As PWV is a function of the wall thickness, arterial diameter and Young modulus, it varies for different arteries.

PWV differs in some conditions due to the changes in its dependent parameters. Atherosclerotic arteries have a higher values of Young's modulus. Arterial stiffness has a relation with the atherosclerotic lesions. It is reported that the patients with cardiovascular diseases often develop the central artery stiffness (Benetos et al. 2002). It is reported by Khanafer et al. (2011) that the elastic modulus of the human coronary arteries increases from 1.5 MPa for the healthy arteries to 3.8 MPa for the atherosclerotic vessels. On the other side, arterial wall thickness is another parameter which is also affected by the presence of atherosclerosis inside the arteries. It is reported by Gradus-Pizlo et al. (2003) that arterial wall thickness of left anterior descending coronary artery is greater in patients with coronary atherosclerosis (1.9 ± 0.3 mm) than in those with normal coronary arteries (1.0 ± 0.1 mm).

Apart from the presence of atherosclerosis, ageing is another important phenomenon affecting the mechanical and geometrical parameters of the arteries. Ageing is defined as the age-related decline in physiological function of the arteries essential for survival and fertility (Sun 2015). It is widely covered in the literature that arterial stiffness is a key arterial alteration during the ageing process (Benetos 2017; Mitchell et al. 2004; Sun 2015), which is recognised as a primary risk factor of all cardiovascular diseases (Kohn et al. 2015). The age-related arterial stiffness results from an attempt of the arterial system to limit the reduction in blood volumetric storage capacity of the arterial system with increasing age (Samijo et al. 1998). Both the arterial wall thickness (Dinenno et al. 2000; Najjar et al. 2005) and Young's modulus (Geest et al. 2004; Sun 2015) are reported to be increased by ageing. Therefore, it is shown that formation of atherosclerosis inside the coronary arteries and ageing are two phenomena resulting in higher values of PWV due to the stiffening of the arteries.

Feng and Khir (2010) determined PWV as a function of the changes in vessel diameter and flow velocity inside the arteries, as $PWV = (1/2)D\frac{dV}{dD}$. This equation shows that in order to maintain the blood flow velocity inside the arteries, the changes in diameter of the arteries in a cardiac cycle decrease for elderly patients with atherosclerotic arteries due to increasing PWV. This means that for elderly patients suffering from atherosclerosis, the changes in the diameter of the arteries in a cardiac cycle due to the arterial compliance become less. For example, considering the wall thickness and Young's modulus of the healthy and atherosclerotic arteries, as explained previously, the changes in the diameter of the atherosclerotic arteries in a cardiac cycle is about 45.6% of healthy arteries.

Propagation of the pressure wave inside a pipe can also be explained based on the water hammer phenomenon in pipeline systems. Water hammer is a pressure wave created when a moving fluid is forced to stop or suddenly change the direction (Rennels 2012). This phenomenon commonly happens when a valve closes suddenly at an end of a pipeline

system, and hence a pressure wave propagates in the pipe. The pulsatility of the blood flow due to the pumping of the blood from the aortic valve inside the coronary arteries creates an effect similar to the water hammer phenomenon. The characteristic time (t_{rt}), specified by the water hammer, is defined as the time required for the pressure wave to make a round trip of the pipe with the length of L , as $t_{rt} = 2L/a$, where a is velocity of the pressure wave, speed of sound, of the fluid in the pipe, and is defined as:

$$a = \sqrt{\frac{\frac{B}{\rho}}{1 + \frac{B}{E} \frac{D}{t} \psi}} \quad (3.2)$$

where B is the bulk modulus of the fluid and ψ is the pipe support factor. Considering coronary artery as a thick-walled pipe, $D/t < 10$, which are free to expand throughout, ψ is defined as, $\psi = \frac{2t}{D}(1 + \nu) + \frac{D}{D+t}$, where ν is the Poisson's ratio of the pipe material. For the case of the blood inside an artery, and $D = 3$ mm, $t = 1$ mm, $B = 2.65$ GPa, $\rho = 1096$ kg/m³, $E = 1.5$ MPa, and $\nu = 0.49$, the speed of sound is obtained as $a = 16.63$ m/s. Using the calculated speed of sound and for an artery with the length of 30 mm, the time required for the pressure wave to make a round trip of the artery is $t_{rt} = 3.6$ ms. It is reported in the literature that when the valve is closed slowly compared to the transit time, t_{rt} , the elasticity of the pipe can be neglected (Yao et al. 2015). As discussed in Rennels (2012), there is a direct relation between the pressure drop induced due to elasticity and the valve closure time, as $\frac{\Delta P}{\Delta P_{max}} = \frac{t_{rt}}{t_{cl}}$, where ΔP_{max} is the water hammer pressure drop and ΔP is the pressure drop induced with the valve closure time of t_{cl} . Therefore, the slower the valve closure results in less pressure drop due to the wall elasticity. The valve closure time, defined for the water hammer effect, inside the coronary arteries is considered as the duration of the systole in a cardiac cycle. During the systole, the heart muscle contracts and consequently, constricts the blood inside the coronary arteries. Therefore, even for the hyperemic flow condition which has the lowest time period for a cardiac cycle, valve closure time inside the coronary arteries is about two orders of magnitude larger than the transit time. Hence, the results of water hammer analysis support the conclusion that the effect of the elasticity of the wall of the coronary arteries is negligible.

Furthermore, formation of atherosclerosis inside the coronary arteries and ageing have similar effects on the speed of sound as the PWV. For example, for the atherosclerotic arteries with the corresponding Young's modulus and wall thickness, as explained previously, the speed of sound increases to $a = 30.14$ m/s and consequently, transit time drops down to $t_{rt} = 2$ ms. Therefore, atherosclerosis and ageing, as two phenomena which increased the speed of sound, provide further support for rigid artery modelling due to the significant reduction of arterial elasticity.

This section continues with a discussion on the studies in the literature focusing on the effect of wall compliance on the hemodynamic parameters. There are two main approaches in the literature to consider the effect of wall compliance of the coronary arteries in the numerical simulations. One of them is to employ FEM with an ALE formulation to account for the effect of wall compliance as the moving mesh which is based on a mesh-updating algorithm, similar to the method explained in the previous section to account for the effect of dynamic vessel motion. The other approach is to employ a fully-coupled FSI to investigate the effect of wall compliance. This method is based on the active interaction of the fluid domain and the structural domain, arterial

wall, which is solved iteratively within each time step by applying appropriate boundary conditions at the fluid–structure interface. The latter approach provides more reliable results of the effect of wall compliance due to the fact that FSI model is coupled and determined iteratively at each time-step by applying the proper boundary conditions at the interface between the blood flow and arterial wall, which is missing in the first approach. At each time step, the force and displacement data are exchanged between the fluid and structural solvers.

Using FEM with an ALE formulation, Zeng et al. (2008) built upon their previous study (Zeng et al. 2003) by investigating the effect of artery compliance on the WSS for a branchless patient-specific RCA model. Figure 3.9 presents the WSS results of inner and outer walls in a cardiac cycle at two regions of proximal and distal of the artery for the cases with and without considering the effect of artery compliance. The results show that the artery compliance affects the WSS heterogeneously. Artery compliance mainly changes the WSS at the distal region of RCA. As shown in Fig. 3.9b, coronary compliance results in the phase changes in the WSS time history under physiological pulsatile inflow conditions without changing the temporal gradient of the local WSS and the bounds of the WSS magnitude. In other word, artery compliance does not cause considerable changes to the WSS vector patterns nor to the localization of WSS minima along the RCA. Hence, they concluded that the effect of compliance in the proximal region of the RCA can be neglected and also the effect of artery compliance in the distal region of the RCA needs to be further evaluated using more completed model of RCA considering major RCA branches distal to it. In another study using the similar method, the effects of vessel compliance on flow pattern in porcine epicardial right coronary arterial tree were discussed by Huo et al. (2009) in Fig. 3.10. It was shown that the elastic vessel wall has a relatively small effect on the temporal WSS in the main trunk in the arterial system. In this case, rigid-wall assumption resulted in a maximum of 3% error in the values of peak WSS. However, rigid-wall assumption resulted in more deviation of the results for the WSS values in the branch of the bifurcated arteries with a maximum of 6% error in the values of peak WSS for the arterial bifurcations.

Using a fully-coupled FSI simulation, the effect of wall compliance on coronary hemodynamic of the patient-specific RCA was investigated by Torii et al. (2009b). In their simulations, the arterial wall was modelled as a nine parameter Mooney–Rivlin hyper-elastic material. As acknowledged by Torii et al. (2009b), the arterial walls, due to having multiple compositions including collagen fibres, are known to have heterogeneous and anisotropic structure (Holzapfel and Ogden 2006). However, in their simulations (Torii et al. 2009b), the arterial wall was assumed to have a homogeneous and isotropic material. Comparison of the computational results between the FSI and rigid-wall models, as shown in Fig. 3.11 shows the insignificant differences in TAWSS and OSI (4.5% and 2.7% difference in maximum TAWSS and OSI, respectively), although the predicted wall displacement was comparable with the vessel diameter. Furthermore, their results showed that the diameter variation of RCA during a cardiac cycle is one order of magnitude smaller than the vessel diameter, implying that the effect of diameter variation on RCA hemodynamics is likely to be small. However, differences in instantaneous WSS profiles were noticeable in their study, especially in the distal region of the artery. As mentioned by Torii et al. (2009b), one possible reason is the lack of surrounding tissue such as myocardium and pericardium in their model, which restricts the radial motion, reduces the wall displacement, and finally results in the less noticeable differences between

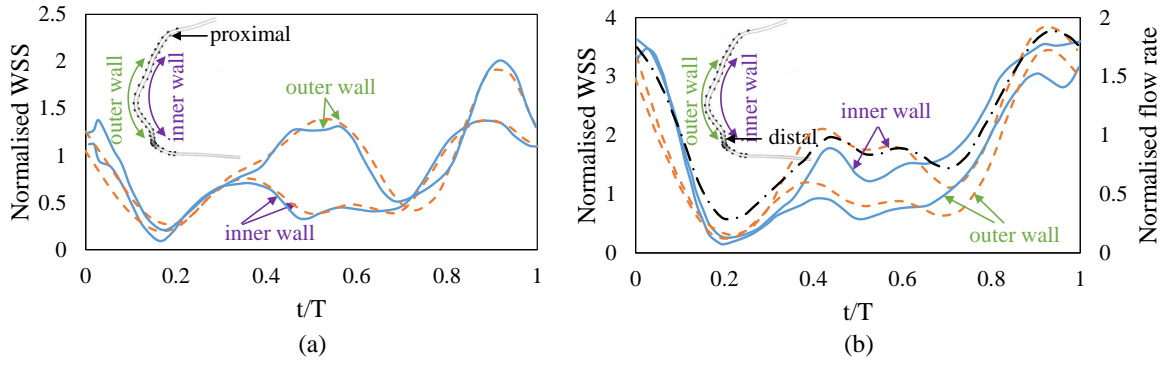


Figure 3.9: Normalised WSS versus normalised time for the inner and outer walls of RCA considering dynamic vessel motion for the cases with and without artery compliance for the locations near the a) proximal and b) distal of the artery (Zeng et al. 2003). Inlet flow rate which is normalised by the time-averaged flow rate is also plotted in part b. Time is normalized by the cardiac period and WSS is normalised with the steady inlet Poiseuille WSS value. The blue solid line refers to the case with compliance and orange dashed line refers to the case without compliance. The flow rate profile is also shown in black dot-dashed line.

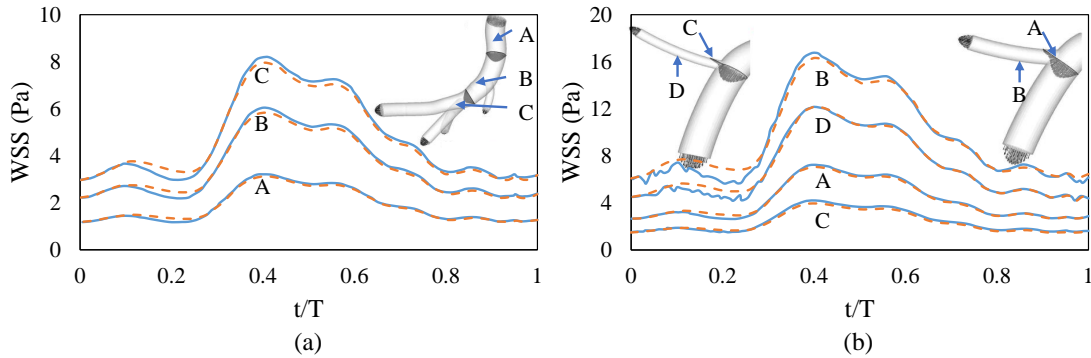


Figure 3.10: Temporal WSS in a cardiac cycle for a) three locations in a main trunk of RCA, as shown top right and b) the locations in the bifurcated branch of RCA with diameter ratio = 0.5 ($DR = 0.5$), shown on the top left and $DR = 0.8$, shown on the top right (Huo et al. 2009). The blue solid line refers to the elastic wall and the orange dashed line refers to the rigid wall.

the results of FSI and CFD simulations.

In another study, Fig. 3.12 shows the TAWSS contour of coronary bifurcation model obtained from FSI and rigid wall models. The results of TAWSS shows a good agreement between the FSI and rigid wall models both qualitatively and quantitatively with the maximum 5% associated error on the TAWSS due to considering rigid wall assumption.

Furthermore, the results of WSS distribution at the main bifurcation of the left coronary arteries was shown in Fig. 3.13, obtained by Bahrami and Norouzi (2018). A fully-coupled FSI method with an ALE formulation was employed to simulate the effects of dynamic vessel motion and the wall compliance simultaneously. In their study, the coronary wall was modelled using a hyperelastic material model called nine parameters Mooney–Rivlin. The results showed that the WSS errors associated with the rigid wall

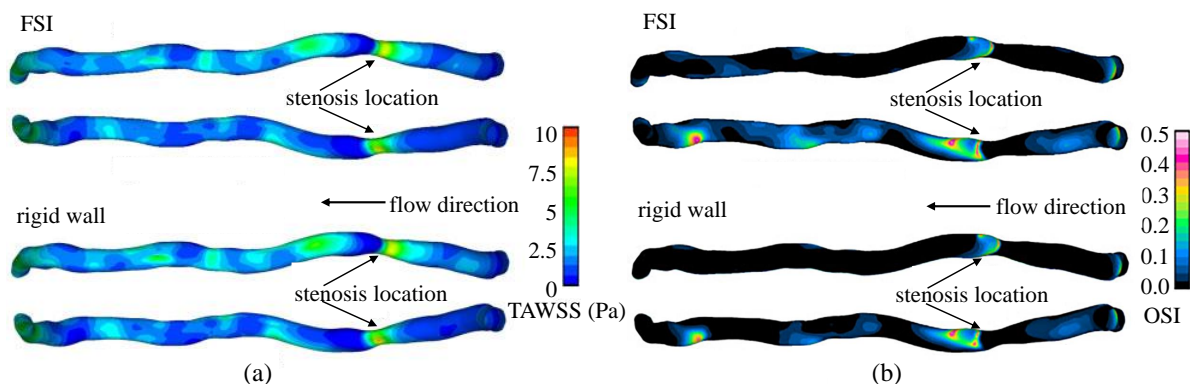


Figure 3.11: Comparison of a) TAWSS and b) OSI contours between the FSI model (top) considering both temporal variations of the RCA arteries and rigid-wall model (bottom) (Torii et al. 2009b).

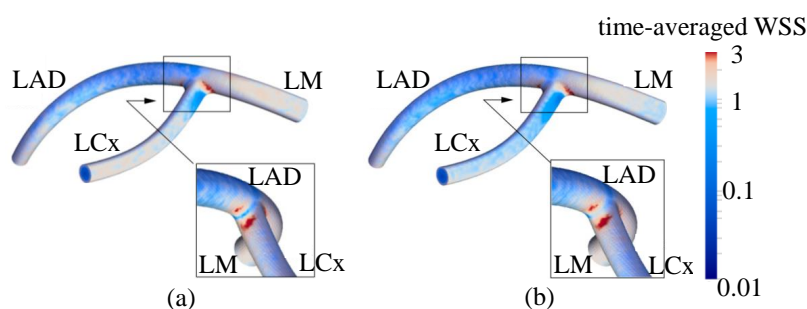


Figure 3.12: TAWSS contour of the left coronary artery bifurcation model with (a) rigid wall model and (b) FSI model results (Malvè et al. 2012).

assumption instead of hyperplastic wall in the left main (LM) coronary artery model is less than 6%. However, this number increased for about 16% and 37% for the beginning of the LCx and the LAD artery, respectively. Furthermore, OSI contours of the study showed that the rigid wall assumption resulted in qualitatively similar OSI values compared to the hyperelastic wall model.

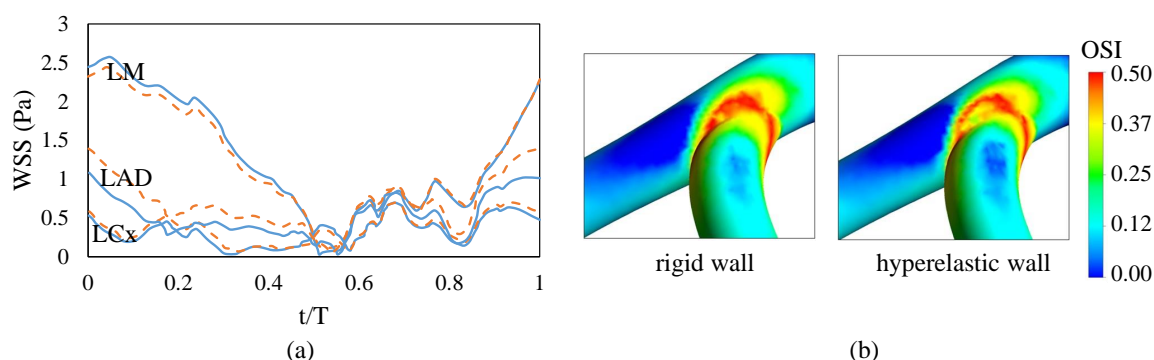


Figure 3.13: a) WSS distribution in a cardiac cycle at the end of the LM branch, beginning of the LCx branch and beginning of the LAD branch (Bahrami and Norouzi 2018). The blue solid line refers to the hyperplastic model and the orange dashed line refers to the rigid model. b) OSI contour for rigid and hyperelastic wall models.

More recently, Eslami et al. (2019) investigated the role of wall elasticity on WSS for the patient-specific coronary arterial trees (CATs). An FSI wall modelling with the

coupled momentum method (CMM) was employed to model the elastic walls. A detailed explanation of CMM can be found in (Figueroa et al. 2006). Their study provided an improved evaluation of the effect of wall elasticity of the coronary arteries on the hemodynamic parameters by considering the whole CAT instead of focusing on a single coronary artery. Figure 3.14 shows the correlation of TAWSS between the rigid and FSI models. The correlation was conducted based on the, first, a set of 3 mm subsegment of the coronary arterial tree with a total of 704 subsegments (Fig. 3.14a) and a set of 704 subsegments with a division of 90-degree arcs (Fig. 3.14b) to test if the FSI simulation has an effect in highly curved arteries. The results of both comparisons showed that the TAWSS values obtained from FSI and CFD were highly correlated with an excellent Pearson correlation ($r = 0.99$). The mean values of TAWSS were reported to be 1.56 ± 1.06 Pa and 1.6 ± 1.05 Pa in the rigid and FSI models, respectively. Furthermore, the comparison results of each 90-degree arc division showed that the wall elasticity has a negligible effect in TAWSS in highly curved arteries, which agrees with the sensitivity analysis of the effect of curvature in section 2. Figure 3.15 shows the comparison results of instantaneous 2D unwrapped map of WSS for the proximal LAD and RCA at two phases in a cardiac cycle as well as the TAWSS contour. The results showed that the instantaneous values of WSS were slightly different when comparing the FSI and rigid wall models especially at the location of stenosis and its immediate downstream, as shown in the Fig. 3.15a. However, the rigid wall model was able to capture almost all the variations in the WSS distributions as of FSI model with slight differences in the magnitude of WSS values. To conclude, their results showed no significant differences in TAWSS justifying the use of rigid wall models for future larger population studies. One of the limitations of their study, as acknowledged by the authors, was the use of homogeneous isotropic material for the coronary arteries. It was shown by Williamson S. D. et al. (2003) that the choice of more realistic material for the coronary arteries such as anisotropic material make the artery less deformable and hence would even further reduce the necessity of considering the effect of wall compliance for coronary artery hemodynamic investigation. Another limitation of their work, as also acknowledged by the authors, was the use of CMM model instead of using the ALE formulation which is the gold standard model for the deformable wall simulations. The reason is because of the required significantly more computationally expenses for the ALE formulation compared to the CMM.

The review of the literature on the effect of wall compliance shows that disregarding this effect on the TAWSS results in less than 5% error. Wall compliance has a larger effect on the temporal WSS compared to the TAWSS especially at the location of bifurcations including bifurcation apex and the near locations. Further downstream of the bifurcations along the branches, this effect diminishes and the results of considering and disregarding the effect of wall compliance become closer to each other. Moreover, in all studies in the literature focusing on the effect of wall compliance, the arterial wall was modelled as an isotropic and homogeneous material. However, it is widely studied in the literature that the choice of more realistic material for the coronary arteries such as anisotropic material makes the artery less deformable and hence would even further reduce the necessity of considering the effect of wall compliance for coronary artery hemodynamic investigation.

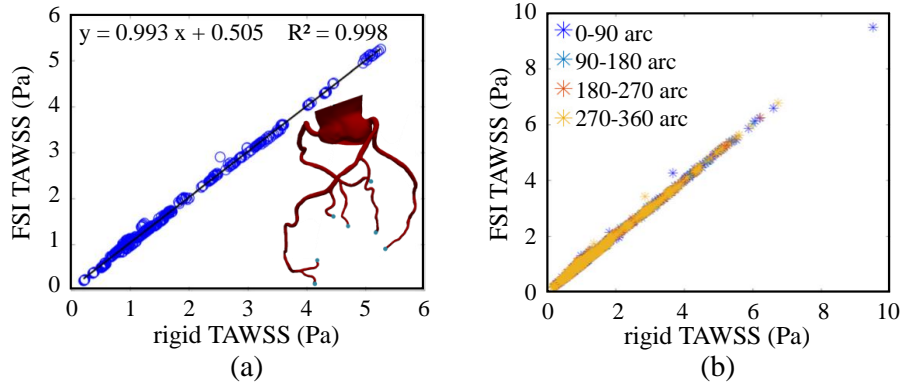


Figure 3.14: a) Correlation of TAWSS between the rigid and FSI models at each 3 mm subsegment of the coronary arterial tree, shown in top right, with a total of 704 subsegments and b) Correlation of TAWSS between the rigid and FSI models for four quadrant at each cross section (Eslami et al. 2019). TAWSS had an excellent correlation with a $r - squared = 0.99$ in both subsegment and sub-arc analysis.

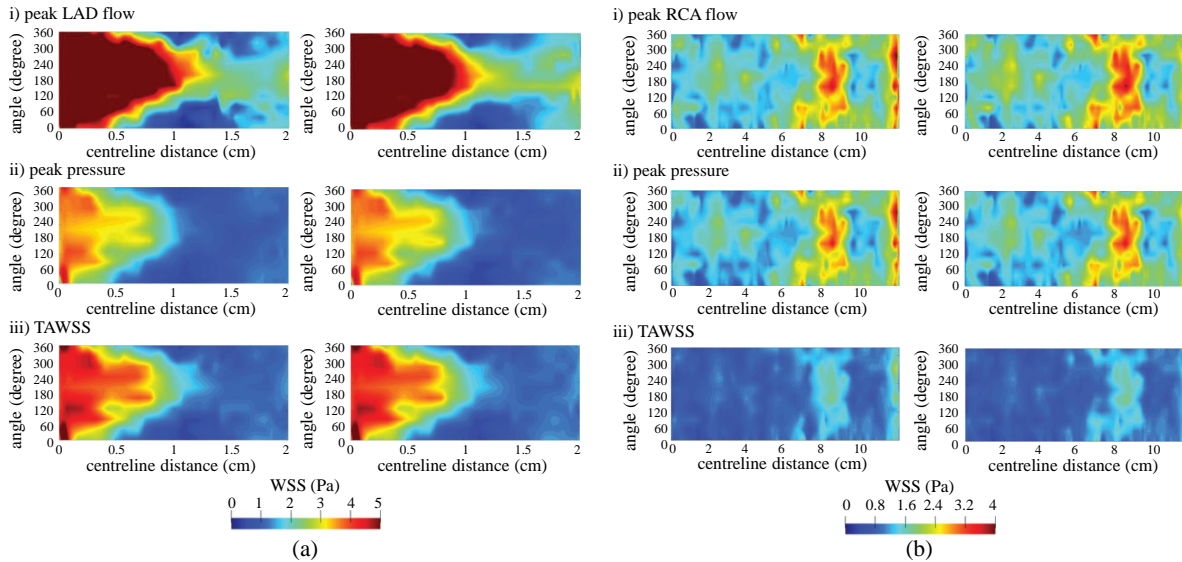


Figure 3.15: Comparison of the 2D unwrapped map of WSS of a) proximal LAD and b) proximal RCA obtained from rigid wall model (left column) and FSI (right column) for the peak flow and pressure phases in a cardiac cycle and the TAWSS (Eslami et al. 2019).

3.2.4 Discussion

A summarise of the studies in the literature investigating the effect of considering and disregarding the temporal variations of the coronary arteries on the hemodynamic parameters in numerical modelling is tabulated in Table 3.3. The results of the effect of cardiac-induced motion on the temporal WSS and TAWSS show a deviation of up to 21% and 8%, respectively for different arteries. The results of the effect of wall compliance on the temporal WSS, TAWSS, and OSI show a deviation of up to 37%, 5%, and 2.7%, respectively. It is found that the instantaneous values of WSS were slightly different when comparing the effect of wall compliance. The reason is due to the presence of wall deformation, which produces flow and pressure waves which propagate at a finite speed

through the arteries, in contrast to the rigid case which produces instantaneous wave propagation. However, when the focus of a study is on the investigation of TAWSS, the wave propagation speed effect dissipates and results in similar TAWSS values along the vessel in the rigid and compliant models (Eslami et al. 2019). It is also important to mention that the maximum deviations for all the hemodynamic parameters are related to the bifurcated arteries specially at the location of bifurcation and proximal to it on the branches which means that for the studies of hemodynamic parameters near the bifurcations, it is important to consider the effects of temporal variations on the hemodynamic parameters.

To conclude, the necessity of considering the effect of temporal variations of coronary arteries depends on the focus of the study. The review of literature suggests that for the following cases, the effect of temporal variations can be considered negligible in the numerical modelling:

- If the focus is to investigate the time-averaged pressure drop and FFR, as the most widely used clinical metrics, or TAWSS, neglecting the effect of temporal variations on these hemodynamic parameters in a numerical modelling is expected to result in less than 5% deviations of the results. It also result in a quicker and less computationally expensive calculation of hemodynamic parameters. Development of a fast model which is able to accurately estimate the hemodynamic parameters is of great importance in time-critical applications such as the clinical environment.
- Introducing the effects of ageing and atherosclerosis on the stiffness of the coronary arteries reduces the effect of temporal variations of coronary artery for the investigation of structural stresses of the arteries as well as the time-dependent variations of hemodynamic parameters. As the artery wall becomes harder and stiffer with ageing and loses its flexibility, considering arteries to be rigid results in more reliable estimation of hemodynamic parameters. This mitigates further the deviations reported in the literature between the results of compliant and rigid wall simulations for these cases.

On the other side, for the following cases, it is suggested that the effect of temporal variations needs to be included in the simulations:

- If the target is to study the temporal variations of hemodynamic parameters such as temporal WSS or OSI particularly at the location of bifurcations, it was shown that on-average about 20% deviations between the results of those considering the effect of temporal variations of coronary arteries and those simplifying the arteries to be rigid.
- If the target of the study is either RCA or LCx, the effect of cardiac-induced motion on the temporal variations of the hemodynamic parameters is more significant. It was shown that the LM or LAD experience less motion in a cardiac cycle due to the effect of cardiac-induced motion.

Finally, it is recommended as a future work that a comprehensive simulation is required to accurately investigate the effects of temporal variations on the hemodynamic

parameters. This simulation should cover the entire coronary arterial system in order to account for the interaction of different branches on coronary arteries with each other. The methodology suggested for this simulation is a combination of fully-coupled FSI with the ALE formulation and a realistic choice of wall arterial material with a heterogeneous and anisotropic structure. This simulation will help to provide a better understanding of the effect of temporal variations of the coronary arteries for the investigation of their hemodynamics. However, such simulation is highly computationally expensive and difficult to conduct. Furthermore, for the detailed analysis of the flow features inside the diseased or stented arteries, conducting an accurate CFD simulation which is able to resolve the smallest spatial and temporal scales of the flow is the only option considering the current available computational resources. The reason is due to the higher computational resources required to conduct an FSI simulation, as mentioned earlier, which always result in compromising the spatial and temporal resolutions of the simulations that is limited by the computational costs (Pons et al. 2020). Finally, it is suggested that, as a future study, the effect of temporal geometric variations of the coronary arteries on the structural stresses of the arteries needs to be further investigated, since failure to consider these effects may result in considerable changes in the calculated structural stresses such as von Mises stress.

Table 3.3: Studies in the literature focusing on the effect of temporal variations of the coronary arteries on the hemodynamic parameters.

	artery	reference	solver	targeted location	mean absolute percentage deviation			
					temporal WSS	TAWSS	OSI	
cardiac-induced	RCA	Zeng et al. (2003)	FEM	near distal	12%	7%	–	
		Torii et al. (2009a)	CFD*	–	–	5%	–	
	LAD**	Prosi et al. (2004)	FEM	proximal the first diagonal branch distal the first diagonal branch	21%	–	–	
		Kolandavel et al. (2006)	CFD*	5D from inlet 9D from inlet	3.5% 13.5%	3% 8%	– –	
wall compliance	RCA	Torii et al. (2009b)	FSI	stenosis throat stenosis distal stenosis distal	32% 28% 25%	– 4.5% –	– 2.7% –	
		Zeng et al. (2008)	FEM	proximal distal proximal the main trunk middle of the main trunk distal the main trunk	10% 27% 3% 3% 3%	– – – – –	– – – – –	
		Huo et al. (2009)	FEM	bifurcation apex with $DR = 0.8$ distal the bifurcated branch with $DR = 0.8$ bifurcation apex with $DR = 0.5$ distal the bifurcated branch with $DR = 0.5$	2.5% 4.5% 5% 3%	– – – –	– – – –	
		LCAB	Bahrami and Norouzi (2018)	FSI	end of LM beginning of LAD beginning of LCx	6% 37% 16%	– – –	– – –
			Malvè et al. (2012)	FSI	–	–	5%	–
		CAT	Eslami et al. (2019)	FSI	704 subsegments of CAT with a 3 mm by 3 mm area of each subsegment	–	2%	–

* In these studies, the dynamic wall motion was incorporated by specifying the wall displacement using dynamic mesh model.

** In these studies, the LAD model inlet was considered to be fixed and the outlet was considered to be moveable due to the cardiac-induced motion. However, as shown earlier, the in-vivo data of LAD does not show any significant differences in magnitude of motion among its three segments including proximal, middle and distal.

References

Amaya R, Cancel LM, and Tarbell JM (2016). “Interaction between the stress phase angle (SPA) and the oscillatory shear index (OSI) affects endothelial cell gene expression”. *PLoS One* 11.11, e0166569.

- Bahrami S and Norouzi M (2018). “A numerical study on hemodynamics in the left coronary bifurcation with normal and hypertension conditions”. *Biomechanics and Modeling in Mechanobiology* 17.6, pp. 1785–1796.
- Benetos A (2017). “Assessment of arterial stiffness in an older population: the interest of the cardio-ankle vascular index (CAVI)”. *European Heart Journal Supplements* 19.suppl.B, B11–B16.
- Benetos A, Waeber B, Izzo J, Mitchell G, Resnick L, Asmar R, and Safar M (2002). “Influence of age, risk factors, and cardiovascular and renal disease on arterial stiffness: clinical applications”. *American Journal of Hypertension* 15.12, pp. 1101–1108.
- Brown AG, Shi Y, Marzo A, Staicu C, Valverde I, Beerbaum P, Lawford PV, and Hose DR (2012). “Accuracy vs. computational time: Translating aortic simulations to the clinic”. *Journal of Biomechanics* 45.3, pp. 516–523.
- Chatzizisis YS, Coskun AU, Jonas M, Edelman ER, Feldman CL, and Stone PH (2007). “Role of endothelial shear stress in the natural history of coronary atherosclerosis and vascular remodeling: molecular, cellular, and vascular behavior”. *Journal of the American College of Cardiology* 49.25, pp. 2379–2393.
- Chatzizisis YS, Jonas M, Coskun AU, Beigel R, Stone BV, Maynard C, Gerrity RG, Daley W, Rogers C, Edelman ER, Feldman CL, and Stone PH (2008). “Prediction of the localization of high-risk coronary atherosclerotic plaques on the basis of low endothelial shear stress”. *Circulation* 117.8, pp. 993–1002.
- Dinenno FA, Jones PP, Seals DR, and Tanaka H (2000). “Age-associated arterial wall thickening is related to elevations in sympathetic activity in healthy humans”. *American Journal of Physiology-Heart and Circulatory Physiology* 278.4, H1205–H1210.
- Ding Z and Friedman MH (2000). “Dynamics of human coronary arterial motion and its potential role in coronary atherogenesis”. *Journal of Biomechanical Engineering* 122.5, pp. 488–492.
- Eshtehardi P, McDaniel MC, Suo J, Dhawan SS, Timmins LH, Binongo JN, Golub LJ, Corban MT, Finn AV, Oshinski JN, Quyyumi AA, Giddens DP, and Samady H (2012). “Association of coronary wall shear stress with atherosclerotic plaque burden, composition, and distribution in patients with coronary artery disease”. *Journal of the American Heart Association* 1.4, e002543.
- Eslami P, Tran J, Jin Z, Karady J, Sotoodeh R, Lu MT, Hoffmann U, and Marsden A (2019). “Effect of wall elasticity on hemodynamics and wall shear stress in patient-specific simulations in the coronary arteries”. *Journal of Biomechanical Engineering* 142.2, pp. 245031–2450310.
- Feng J and Khir A (2010). “Determination of wave speed and wave separation in the arteries using diameter and velocity”. *Journal of Biomechanics* 43.3, pp. 455–462.
- Figuroa CA, Vignon-Clementel IE, Jansen KE, Hughes TJ, and Taylor CA (2006). “A coupled momentum method for modeling blood flow in three-dimensional deformable arteries”. *Computer Methods in Applied Mechanics and Engineering* 195.41–43, pp. 5685–5706.
- Geest JPV, Sacks MS, and Vorp DA (2004). “Age dependency of the biaxial biomechanical behavior of human abdominal aorta”. *Journal of Biomechanical Engineering* 126.6, pp. 815–822.
- Gijssen F, Giessen A van der, Steen A van der, and Wentzel J (2013). “Shear stress and advanced atherosclerosis in human coronary arteries”. *Journal of Biomechanics* 46.2, pp. 240–247.

- Godia EC, Madhok R, Pittman J, Trocio S, Ramas R, Cabral D, Sacco RL, and Rundek T (2007). “Carotid artery distensibility: a reliability study”. *Journal of Ultrasound in Medicine* 26.9, pp. 1157–1165.
- Gosling RG and Budge MM (2003). “Terminology for Describing the Elastic Behavior of Arteries”. *Hypertension* 41.6, pp. 1180–1182.
- Gradus-Pizlo I, Bigelow B, Mahomed Y, Sawada SG, Rieger K, and Feigenbaum H (2003). “Left anterior descending coronary artery wall thickness measured by high-frequency transthoracic and epicardial echocardiography includes adventitia”. *The American Journal of Cardiology* 91.1, pp. 27–32.
- Hasan M, Rubenstein DA, and Yin W (2013). “Effects of Cyclic Motion on Coronary Blood Flow”. *Journal of Biomechanical Engineering* 135.12. URL: <https://doi.org/10.1115/1.4025335>.
- Hirschhorn M, Tchantchaleishvili V, Stevens R, Rossano J, and Throckmorton A (2020). “Fluid–structure interaction modeling in cardiovascular medicine – A systematic review 2017–2019”. *Medical Engineering & Physics* 78, pp. 1–13.
- Holzappel GA and Ogden RW (June 3, 2006). *Mechanics of Biological Tissue*. Springer-Verlag GmbH.
- Hughes TJ, Liu WK, and Zimmermann TK (1981). “Lagrangian-Eulerian finite element formulation for incompressible viscous flows”. *Computer Methods in Applied Mechanics and Engineering* 29.3, pp. 329–349.
- Huo Y, Choy JS, Svendsen M, Sinha AK, and Kassab GS (2009). “Effects of vessel compliance on flow pattern in porcine epicardial right coronary arterial tree”. *Journal of Biomechanics* 42.5, pp. 594–602.
- Johnson KR, Patel SJ, Whigham A, Hakim A, Pettigrew RI, and Oshinski JN (2004). “Three-dimensional, time-resolved motion of the coronary arteries”. *Journal of Cardiovascular Magnetic Resonance* 6.3, pp. 663–673.
- Khanafer K, Duprey A, Zainal M, Schlicht M, Williams D, and Berguer R (2011). “Determination of the elastic modulus of ascending thoracic aortic aneurysm at different ranges of pressure using uniaxial tensile testing”. *The Journal of Thoracic and Cardiovascular Surgery* 142.3, pp. 682–686.
- Kohn JC, Lampi MC, and Reinhart-King CA (2015). “Age-related vascular stiffening: causes and consequences”. *Frontiers in Genetics* 6, p. 112.
- Kolandavel MK, Freund ET, Ringgaard S, and Walker PG (2006). “The effects of time varying curvature on species transport in coronary arteries”. *Annals of Biomedical Engineering* 34.12, pp. 1820–1832.
- Lantz J, Renner J, and Karlsson M (2011). “Wall shear stress in a subject specific human aorta — influence of fluid-structure interaction”. *International Journal of Applied Mechanics* 03.04, pp. 759–778.
- Liu Y, Lai Y, Nagaraj A, Kane B, Hamilton A, Greene R, McPherson DD, and Chandran KB (2001). “Pulsatile flow simulation in arterial vascular segments with intravascular ultrasound images”. *Medical Engineering & Physics* 23.8, pp. 583–595.
- Malvè M, García A, Ohayon J, and Martínez MA (2012). “Unsteady blood flow and mass transfer of a human left coronary artery bifurcation: FSI vs. CFD”. *International Communications in Heat and Mass Transfer* 39.6, pp. 745–751.
- Mirramezani M, Diamond S, Litt H, and Shadden SC (2018). “Reduced order models for transstenotic pressure drop in the coronary arteries”. *Journal of Biomechanical Engineering*, p. 31005.

- Mitchell GF, Parise H, Benjamin EJ, Larson MG, Keyes MJ, Vita JA, Vasani RS, and Levy D (2004). “Changes in arterial stiffness and wave reflection with advancing age in healthy men and women”. *Hypertension* 43.6, pp. 1239–1245.
- Mohlenkamp S, Hort W, Ge J, and Erbel R (2002). “Update on myocardial bridging”. *Circulation* 106.20, pp. 2616–2622.
- Morris PD, Narracott A, Tengg-Kobligk H von, Silva Soto DA, Hsiao S, Lungu A, Evans P, Bressloff NW, Lawford PV, Hose DR, and Gunn JP (2016). “Computational fluid dynamics modelling in cardiovascular medicine”. *Heart* 102.1, pp. 18–28.
- Nabeel PM, Kiran VR, Joseph J, Abhidev VV, and Sivaprakasam M (2020). “Local Pulse Wave Velocity: Theory, Methods, Advancements, and Clinical Applications”. *IEEE Reviews in Biomedical Engineering* 13, pp. 74–112.
- Najjar SS, Scuteri A, and Lakatta EG (2005). “Arterial aging”. *Hypertension* 46.3, pp. 454–462.
- Nichols W, O’Rourke M, and Vlachopoulos C (2011). *McDonald’s blood flow in arteries, Sixth edition: Theoretical, experimental and clinical principles*. CRC Press.
- O’Loughlin AJ, Byth K, French JK, Richards DA, Hennessy A, Denniss AR, and Kovoov P (2011). “The compression type of coronary artery motion in patients with ST-segment elevation acute myocardial infarction and normal controls: a case-control study”. *BMC research notes* 4, p. 51.
- Park EA, Lee W, Park SJ, Kim YK, and Hwang HY (2016). “Influence of coronary artery diameter on intracoronary transluminal attenuation gradient during CT angiography”. *JACC: Cardiovascular Imaging* 9.9, pp. 1074–1083.
- Pons R, Guala A, Rodríguez-Palomares JF, Cajas JC, Dux-Santoy L, Teixidó-Tura G, Molins JJ, Vázquez M, Evangelista A, and Martorell J (2020). “Fluid-structure interaction simulations outperform computational fluid dynamics in the description of thoracic aorta haemodynamics and in the differentiation of progressive dilation in Marfan syndrome patients”. *Royal Society Open Science* 7.2, p. 191752.
- Prosi M, Perktold K, Ding Z, and Friedman MH (2004). “Influence of curvature dynamics on pulsatile coronary artery flow in a realistic bifurcation model”. *Journal of Biomechanics* 37.11, pp. 1767–1775.
- Puentes J, Roux C, Garreau M, and Coatrieux JL (1998). “Dynamic feature extraction of coronary artery motion using DSA image sequences”. *IEEE Transactions on Medical Imaging* 17.6, pp. 857–871.
- Rennels H (May 3, 2012). *Pipe Flow*. John Wiley & Sons. 310 pp.
- Samady H, Eshtehardi P, McDaniel MC, Suo J, Dhawan SS, Maynard C, Timmins LH, Quyyumi AA, and Giddens DP (2011). “Coronary artery wall shear stress is associated with progression and transformation of atherosclerotic plaque and arterial remodeling in patients with coronary artery disease”. *Circulation* 124.7, pp. 779–788.
- Samijo SK, Willigers JM, Barkhuysen R, Kitslaar P, Reneman RS, Brands PJ, and Hoeks APG (1998). “Wall shear stress in the human common carotid artery as function of age and gender”. *Cardiovascular Research* 39.2, pp. 515–522.
- Shaw JA, Kingwell BA, Walton AS, Cameron JD, Pillay P, Gatzka CD, and Dart AM (2002). “Determinants of coronary artery compliance in subjects with and without angiographic coronary artery disease”. *Journal of the American College of Cardiology* 39.10, pp. 1637–1643.
- Siogkas PK, Papafaklis MI, Sakellarios AI, Stefanou KA, Bourantas CV, Athanasiou LS, Exarchos TP, Naka KK, Michalis LK, Parodi O, and Fotiadis DI (2015). “Patient-specific simulation of coronary artery pressure measurements: an in vivo three-dimensional

- validation study in humans”. *BioMed Research International* 2015. Ed. by K Bendjelid, p. 628416.
- Stone PH, Coskun AU, Kinlay S, Clark ME, Sonka M, Wahle A, Ilegbusi OJ, Yeghiazarians Y, Popma JJ, Orav J, Kuntz RE, and Feldman CL (2003). “Effect of endothelial shear stress on the progression of coronary artery disease, vascular remodeling, and in-stent restenosis in humans”. *Circulation* 108.4, pp. 438–444.
- Sun Z (2015). “Aging, arterial stiffness, and hypertension”. *Hypertension* 65.2, pp. 252–256.
- Ding Z and Friedman MH (2000). “Quantification of 3-D coronary arterial motion using clinical biplane cineangiograms”. *International Journal of Cardiovascular Imaging* 16.5, pp. 331–346.
- Takashi N and Hughes TJ (1992). “An arbitrary Lagrangian-Eulerian finite element method for interaction of fluid and a rigid body”. *Computer Methods in Applied Mechanics and Engineering* 95.1, pp. 115–138.
- Timmins LH, Molony DS, Eshtehardi P, McDaniel MC, Oshinski JN, Samady H, and Giddens DP (2015). “Focal association between wall shear stress and clinical coronary artery disease progression”. *Annals of Biomedical Engineering* 43.1, pp. 94–106.
- Torii R, Keegan J, Wood NB, Dowsey AW, Hughes AD, Yang GZ, Firmin DN, McG Thom SA, and Xu XY (2009a). “The effect of dynamic vessel motion on haemodynamic parameters in the right coronary artery: a combined MR and CFD study”. *British Journal of Radiology* 82 Spec No, S24–32.
- Torii R, Wood NB, Hadjiloizou N, Dowsey AW, Wright AR, Hughes AD, Davies J, Francis DP, Mayet J, Yang GZ, Thom SAM, and Xu XY (2009b). “Fluid–structure interaction analysis of a patient-specific right coronary artery with physiological velocity and pressure waveforms”. *Communications in Numerical Methods in Engineering* 25.5, pp. 565–580.
- Wahle A, Lopez JJ, Olszewski ME, Vigmostad SC, Chandran KB, Rossen JD, and Sonka M (2006). “Plaque development, vessel curvature, and wall shear stress in coronary arteries assessed by X-ray angiography and intravascular ultrasound”. *Medical Image Analysis* 10.4, pp. 615–631.
- Williamson S. D., Lam Y., Younis H. F., Huang H., Patel S., Kaazempur-Mofrad, and Kamm RD (2003). “On the sensitivity of wall stresses in diseased arteries to variable material properties”. *Journal of Biomechanical Engineering* 125.1, pp. 147–155.
- Yao E, Kember G, and Hansen D (2015). “Analysis of water hammer attenuation in applications with varying valve closure times”. *Journal of Engineering Mechanics* 141.1, p. 04014107.
- Yong ASC, Javadzadegan A, Fearon WF, Moshfegh A, Lau JK, Nicholls S, Ng MKC, and Kritharides L (2017). “The relationship between coronary artery distensibility and fractional flow reserve”. *PLoS One* 12.7, e0181824–e0181824.
- Zeng D, Boutsianis E, Ammann M, Boomsma K, Wildermuth S, and Poulikakos D (2008). “A study on the compliance of a right coronary artery and its impact on wall shear stress”. *Journal of Biomechanical Engineering* 130.4, p. 41014.
- Zeng D, Ding Z, Friedman MH, and Ethier CR (2003). “Effects of cardiac motion on right coronary artery hemodynamics”. *Annals of Biomedical Engineering* 31.4, pp. 420–429.
- Zeng D and Ethier C (2003). “A mesh-updating scheme for hemodynamic simulations in vessels undergoing large deformations”. *Journal of Engineering Mathematics* 47.3/4, pp. 405–418.

- Zhao SZ, Xu XY, Hughes AD, Thom SA, Stanton AV, Ariff B, and Long Q (2000). “Blood flow and vessel mechanics in a physiologically realistic model of a human carotid arterial bifurcation”. *Journal of Biomechanics* 33.8, pp. 975–984.
- Zhong L, Zhang JM, Su B, Tan RS, Allen JC, and Kassab GS (2018). “Application of patient-specific computational fluid dynamics in coronary and intra-cardiac flow simulations: challenges and opportunities”. *Frontiers in Physiology* 9.742.

Chapter 4

Transitional flow behaviour in a stenosed coronary artery

4.1 Chapter overview

This chapter explores the transitional flow behaviour downstream of stenosed coronary arteries via numerical modelling. As discussed in the literature review chapter, the presence of a blockage inside coronary arteries can significantly alter the behaviour of the flow, resulting in laminar flow separation, and transition to turbulence. As reviewed in Section 2.3.1, the literature suggests that, apart from the presence of an arterial stenosis, heart pulsation can also affect the transition to turbulence by promoting or delaying it. Hence, an in-depth understanding of the transitional flow behaviour inside stenosed coronary arteries with a physiological pulsatile flow profile can help to identify the impacted regions downstream of the stenotic sections.

In this chapter, the correlation between the plaque geometry, the pulsatile inlet flow and the induced turbulence in a stenosed coronary artery model is investigated computationally. A computational fluid dynamics (CFD) model is developed to simulate the pulsatile blood flow inside a stenosed coronary artery model. The CFD model is validated against experimental data from the literature which show that the developed CFD model is able to accurately model the flow inside coronary arteries. Pressure drop, flow velocity and wall shear stress are determined for the stenosed coronary artery models with three different degrees of asymmetric stenosis including mild, moderate and severe stenoses and for different heart working conditions. The heart working condition refers to different cardiac cycle duration and blood flow rate inside the coronaries ranging from rest to hyperemic heart conditions. Furthermore, the transitional flow behaviour is quantified by investigation of the changes in the turbulent kinetic energy. A simplified model of a coronary artery is first developed and then, in order to illustrate the applicability of the obtained results to realistic geometries, a patient-specific stenosed coronary artery model is studied as well.

The findings of this study based on the results of both the simplified and the patient-specific coronary artery models show that there is a high risk of the formation of a secondary stenosis at a downstream distance equal to 10 times the artery diameter in the regions to the side and downstream of the first asymmetric stenosis due to the exis-

tence of strong recirculation zones and low shear stresses. Furthermore, flow separation initiates on the side of the asymmetric stenosis and expands to its opposite side further downstream. The transition to turbulence is identified by a jump in the TKE profile that starts from $5D$ downstream of the stenotic section and continues to about $10D$, where the blood flow relaminarises.

The results provide a good prediction of the pressure drop and blood flow rate in stenosed coronary arteries, which can be applied in the investigation of the heart muscle workout and the required heart power. The results also suggest that one way to achieve a medically stable condition for a patient suffering from an advanced atherosclerosis is to prevent them from hyperemia. Furthermore, it is shown that there is a stream-wise distance beyond the stenotic section in which the flow is disturbed. It is suggested that it is important to monitor this region in addition to the stenotic section, as the near downstream is a susceptible location for the formation of another stenosis.

4.2 Transitional flow in a stenosed coronary artery

This section consists of the following published journal article:

Navid Freidoonimehr, Maziar Arjomandi, Nima Sedaghatizadeh, Rey Chin, Anthony Zander (2020). “Transitional turbulent flow in a stenosed coronary artery with a physiological pulsatile flow”. *International Journal for Numerical Methods in Biomedical Engineering*, 36 pp. e3347.

The article is identical to its published format with the following exceptions:

- The numbering of figures, tables and equations have been altered to include the chapter number.
- The position of some figures and tables have been changed to improve legibility.

The article in its published format is available at:

<https://doi.org/10.1002/cnm.3347>

Statement of Authorship

Title of paper	Transitional turbulent flow in a stenosed coronary artery with a physiological pulsatile flow
Publication Status	<input checked="" type="checkbox"/> Published <input type="checkbox"/> Accepted for Publication <input type="checkbox"/> Submitted for Publication <input type="checkbox"/> Unpublished and Unsubmitted work written in manuscript style
Publication Details	Freidoonimehr, N., Arjomandi, M., Sedaghatizadeh, N., Chin, R., and Zander, A., "Transitional turbulent flow in a stenosed coronary artery with a physiological pulsatile flow", International Journal for Numerical Methods in Biomedical Engineering 36: e3347, 2020

Principal Author

Name of Principal Author (Candidate)	Navid Freidoonimehr	
Contribution to the Paper	Developed ideas, conducted experiments, performed data analysis and interpreted results, wrote manuscript, and acted as corresponding author	
Overall percentage (%)	75%	
Certification:	This paper reports on original research I conducted during the period of my Higher Degree by Research candidature and is not subject to any obligations or contractual agreements with a third party that would constrain its inclusion in this thesis. I am the primary author of this paper.	
Signature	Date	15/02/2021


Co-Author Contributions


By signing the Statement of Authorship, each author certifies that:

- i the candidate's stated contribution to the publications is accurate (as detailed above);
- ii permission is granted for the candidate to include the publication in the thesis; and
- iii the sum of all co-author contributions is equal to 100% less the candidate's stated contribution

Name of Co-Author	Maziar Arjomandi	
Contribution to the Paper	Supervised the development of the research, participated in developing ideas and concepts, helped in interpretation of results, provided critical revision of manuscript.	
Signature	Date	15/02/2021

Name of Co-Author	Nima Sedaghatizadeh	
Contribution to the Paper	Helped in the development of the research, contributed in academic discussion and manuscript review.	
Signature	Date	25/02/2021

Name of Co-Author	Rey Chin		
Contribution to the Paper	Supervised the development of the research, participated in developing ideas and concepts, helped in interpretation of results, provided critical revision of manuscript.		
Signature		Date	15/02/2021

Name of Co-Author	Anthony Zander		
Contribution to the Paper	Supervised the development of the research, participated in developing ideas and concepts, helped in interpretation of results, provided critical revision of manuscript.		
Signature		Date	15/02/2021

Transitional turbulent flow in a stenosed coronary artery with a physiological pulsatile flow

Navid Freidoonimehr, Maziar Arjomandi, Nima Sedaghatizadeh, Rey Chin, and Anthony Zander

Abstract

The turbulence in the blood flow, caused by plaque deposition on the arterial wall, increases by the combined effect of the complex plaque geometries and the pulsatile blood flow. The correlation between the plaque geometry, the pulsatile inlet flow and the induced turbulence in a constricted artery is investigated in this study. Pressure drop, flow velocity and wall shear stress are determined for stenosed coronary artery models with three different degrees of asymmetric stenosis and for different heart working conditions. A Computational Fluid Dynamics model, validated against experimental data published in the literature, was developed to simulate the blood pulsatile flow inside a stenosed coronary artery model. The transitional flow behaviour was quantified by investigation of the changes in the turbulence kinetic energy. It was shown that the separation starts from the side of the asymmetric stenosis and spreads to its opposite side further downstream. The results suggest that there is a high risk of the formation of a secondary stenosis at a downstream distance equal to 10- times of the artery diameter at the side and bottom regions of the first stenosis due to the existence of the recirculation zones and low shear stresses. Finally, a stenosed patient specific coronary artery model was employed to illustrate the applicability of the obtained results for real geometry models. The results of this study provide a good prediction of pressure drop and blood flow rate, which can be applied in the investigation of the heart muscle workout and the required heart power.

Keywords: pulsatile flow; artery plaque; transition; coronary artery; stenosis; turbulence

4.2.1 Introduction

Cardiovascular diseases (CVDs), a group of disorders related to the heart and blood vessels, are one of the main causes of death, contributing to more than half of the population deaths in 2015. One of blood vessel disorders is atherosclerosis which is caused by plaque deposition on the arterial wall and may lead to the obstruction of the blood flow known as stenosis. Lipid, calcium, low-density lipoprotein (LDL), and a specific type of white blood cells (macrophage cell) are different components that can cause the formation of the plaques. Arterial stenosis happens as a consequence of thrombosis which is caused due to a number of chemical, biological, biomechanical and physiological factors (Cheng et al. 2019). Thrombosis is a blood clot abnormally formed inside a blood vessel, which is blocking the normal blood flow. Atherosclerosis can be formed in any parts of the arterial

system but if it is formed in one of the coronary arteries, it may cause a heart attack or other associated serious health problems.

The flow in most part of coronary arteries is laminar due to the low Reynolds number (Re) if there is no disturbance (For a healthy coronary artery in the resting heart working condition, Re is about 200 (Moreno and Bhaganagar 2013)). When an atherosclerosis is formed, the flow downstream of the stenosis becomes transitional due to the instabilities created by the obstruction. The constriction inside the artery results in a jet flow, pushing the blood through the artery at higher velocity which creates recirculation zones around the jet section. Therefore, laminar flow separation and transition to turbulence, due to an increase in the velocity and the change in the fluid structure, is most likely to happen after the constricted sections. Blood flow was reported to be uniform in both internal and external carotid artery (both left and right sides of bifurcation) for the healthy artery, while changes in flow patterns were seen in the presence of a plaque inside the artery which formed reversed flow patterns along the inner wall of the diseased internal carotid artery models (Kefayati and Poepping 2013). Flow transition to turbulence in an artery leads to a higher wall shear stress (WSS) resulting in a higher pressure drop inside the artery. Turbulence can also affect the important haemodynamic indexes such as wall shear stress as well as the location and persistence in time of recirculation regions. Therefore, it is important to predict the location of the transition to turbulence after the constrictions.

One of the parameters which triggers turbulence is the heart pulsation. Transition to turbulence in combined steady and sinusoidal oscillatory flow ($U = U_m \sin(\omega t)$) for different values of Stokes'-layer-thickness ratio is displayed in Fig. 4.1 (Lodahl et al. 1998) where U_m is the maximum value of the sinusoidal oscillatory flow velocity at the centreline of the pipe, Re_c is the steady Reynolds number, Re_ω is the oscillatory boundary-layer flow Reynolds number, δ is the Stokes layer thickness. As shown in Fig. 4.1, for the highest value of Stokes'-layer-thickness ratio ($R/\delta = 3.1$), laminar flow regime can be a valid assumption for a steady flow Re of more than 2000 and oscillatory boundary-layer flow Re above 10^6 . Many of the studies in the literature which investigated turbulence in a stenosed artery model assumed a steady inlet velocity profile (Biswas et al. 2016). However, turbulence inside the constricted coronary artery with the pulsatile flow is different from a model with the steady flow since the effect of the flow acceleration and deceleration on the dynamics of the flow is not considered by the steady flow assumption. Furthermore, the physiological flow is pulsatile with a complex time varying profile (Zhu et al. 2018). Therefore, turbulent structures inside the coronary artery models need to be investigated under the pulsatile flow regime.

Another parameter which triggers the turbulent structures is the geometry of the plaques. Both shape of the plaque and the degree of stenosis, which represents the area reduction percentage, considerably affect the downstream flow behaviour. The flow characteristics such as the length of the recirculation zone and pressure losses are strongly dependent on the general shape of the stenosis (Usmani and Muralidhar 2016). A longer recirculation zone and a higher pressure drop were reported by Young and Tsai (1973) for an asymmetric stenosis compared to the axisymmetric one with a similar degree of stenosis. Axisymmetric stenosis leads to the formation of an axisymmetric jet flow after the constricted section which is slightly deflected to the same side of the stenosis. Hence, the other side of the stenosis is a susceptible location for the plaque growth (Tambasco and Steinman 2003). While most of the studies in the literature are focused on the axisymmetric-shaped stenosis (Ojha et al. 2006; Peterson and Plesniak 2008; Varghese

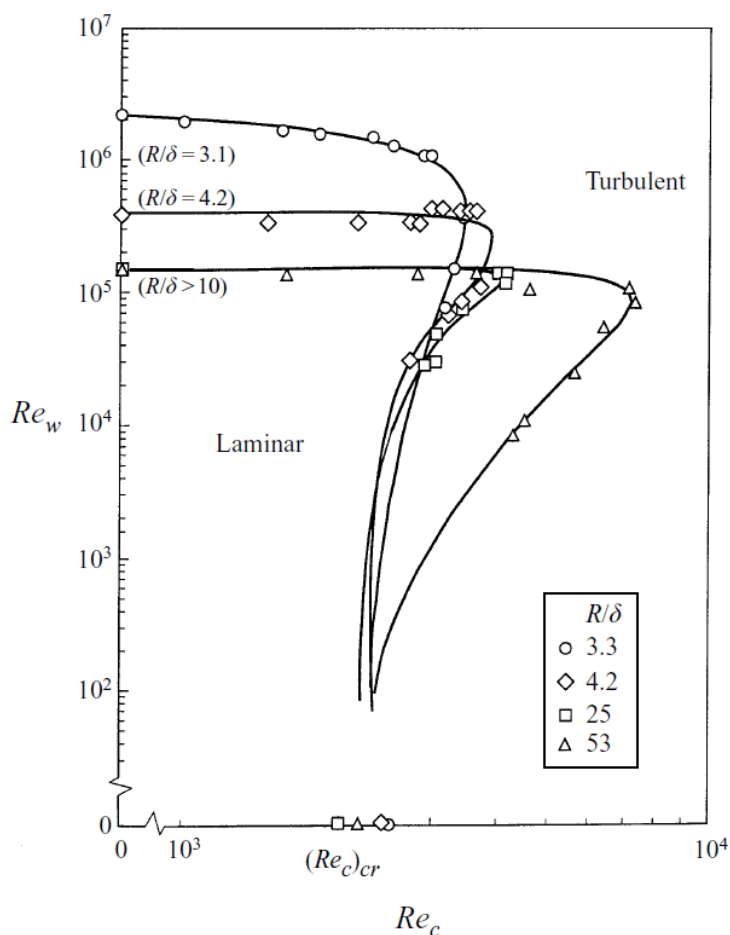


Figure 4.1: Transition to turbulence in combined steady and oscillatory flow showing the laminar and turbulent regions based on the different values of Reynolds numbers and Stokes'-layer-thickness ratio (Lodahl et al. 1998).

et al. 2008), an asymmetric stenosis inside an artery model has only been investigated in a few studies. Based on the considerable differences in downstream flow behaviour between the axisymmetric and asymmetric constrictions (as mentioned above) and due to the high possibility of the formation of asymmetric stenosis inside the coronary arteries (Waller 1989), in this study the effect of the asymmetric stenosis on the flow behaviour inside the coronary artery models is investigated.

A review of the existing literature shows that the pulsatile arterial flow and the geometry of the plaque are important parameters which control the blood flow structure and its transition to turbulence. The effect of these parameters on the induced turbulence in the arterial flow is however not well understood. Hence, this study aims to investigate the transitional flow behaviour downstream of a plaque in a stenosed coronary artery with a physiological pulsatile inlet velocity. Different cases including different degrees of stenosis and a range of resting to hyperemic heart working conditions are studied. Blood flow pattern in each case is observed to develop an understanding of the flow behaviour upstream and downstream of the constriction. Turbulence kinetic energy (TKE) as an indicator of transition to turbulence and the wall shear stress is evaluated for the different cases. Furthermore, pressure drop along the stenosed artery, which represents the power required by the heart to supply the heart muscles with a uniform and constant blood

flow rate, is determined. A patient specific coronary artery geometry with a blockage is investigated to discuss the applicability of the results obtained from the idealised model of the coronary artery. The results of this study will contribute to a better understanding of the changes in TKE and WSS after the asymmetric stenosis in the coronary artery models, which can be applied for determination of the susceptible locations after the stenotic region for the plaque growth by the cardiologists.

4.2.2 Model geometry and its development

Stenosed coronary artery model

A schematic diagram of a stenosed coronary artery and the computational domain are presented in Fig. 4.2. In general, based on their shape the coronary arteries can be categorised into straight, curved and bifurcated. In order to develop a general understanding of the transition to turbulence in a stenosed coronary artery, instead of a patient-specific geometry of the artery which varies from a patient to another an idealised artery model with a circular cross section and straight length was considered in this study. To investigate the validity of the developed results for real arteries, a patient specific coronary artery model is studied. The results are discussed in the results and discussion section. The stenosed coronary artery was modelled as an asymmetric hemispherical constriction inside a rigid pipe. The assumption of rigidity of the pipe is valid since the diseases related to the blockage of the coronary artery mostly occur with ageing (as a primary risk factor of all cardiovascular diseases (Kohn et al. 2015)), and the artery wall becomes harder and stiffer with ageing (as a common disorder), and thereby loses its flexibility. Furthermore, the changes in the diameter of the coronary artery during a cardiac cycle do not change the Reynolds number in such a way that the flow behaviour changes. Consequently, the blood flow inside the coronary artery remains laminar in the presence of the changes in the artery diameter. Moreover, in a study by Torii et al. (2009), it was shown that the effects of wall compliance on time-averaged WSS and oscillatory shear index (OSI) were insignificant. Many studies in the literature have also modelled the artery wall as solid such as Foucault et al. (2017), Liu et al. (2015), Plesniak and Bulusu (2016), and Zhu et al. (2018).

As shown in Fig. 4.2, the three different degrees of stenosis were studied, including a mild stenosis, 16% area reduction, a moderate stenosis, 39.1%, and a severe stenosis, 67%. These three degrees of stenosis were selected to cover a wide range of coronary artery diseases from the early stage to near the final stage. Since the stenosis was modelled as an asymmetric hemispherical constriction, each degree of stenosis corresponds to a specific diameter of the hemispherical constriction shape. In other word, 16%, 39.1% and 67% degrees of stenosis were modelled with the hemispherical diameter of $3/10 D$, $1/2 D$ and $7/10 D$ (D is the diameter of a healthy coronary artery), respectively. Since the flow inside the artery was pulsating, the pipe length was extended from both sides (a $10-D$ length before and a $20-D$ after the stenosis section) as considered by Peterson and Plesniak (2008) to eliminate the artificial effects of the inlet and the outlet on the region of interest as well as to observe the flow behaviour, including jet flow effect, separation and recirculation zones, after the constricted section.

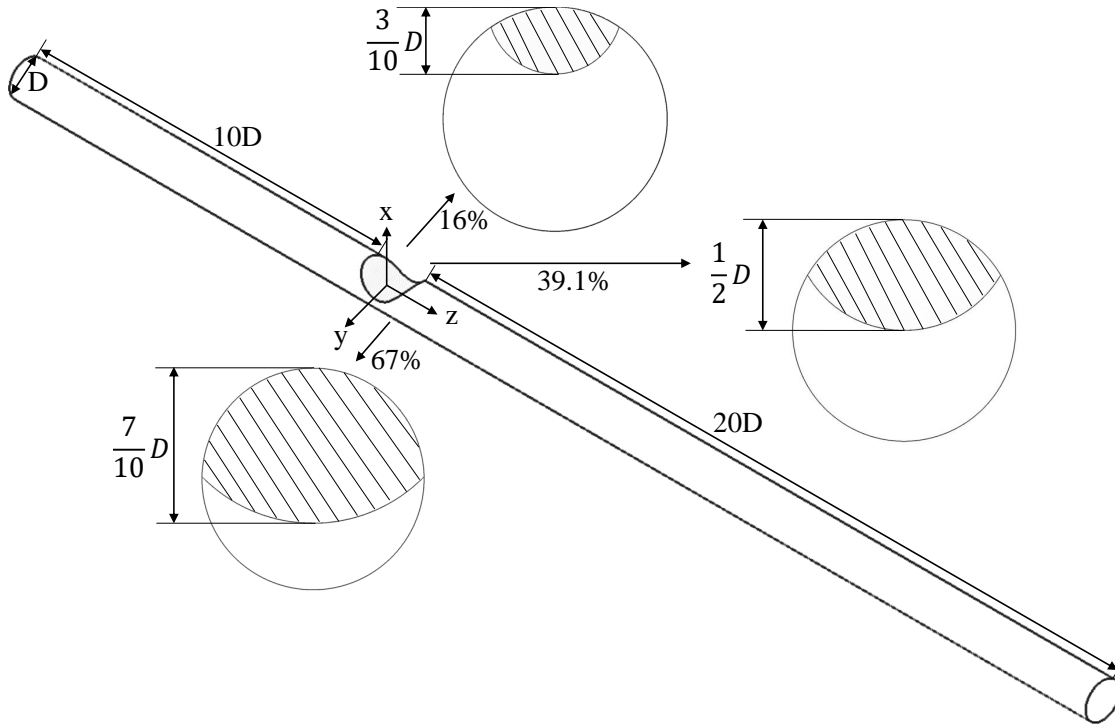


Figure 4.2: Schematic diagram of 3D asymmetric stenosed coronary artery with different degrees of stenosis shown with the percentage of area reduction.

Numerical algorithm

ANSYS FLUENT 18.2 (ANSYS, Inc.) was employed to simulate the pulsatile blood flow inside the stenosed coronary artery model by solving the governing incompressible Navier-Stokes equations. The SIMPLE pressure-velocity coupling method was employed. A Womersley velocity profile (Womersley 1955) was employed at the inlet to represent fully developed pulsatile flow (Li et al. 2017). This selection also reduces the computational cost because there is no need to use a long extended length before the inlet for development of the flow. Furthermore, as shown by Moyle et al. (2006) the choice of fully developed Womersley velocity profile at the inlet of an artery gives a good estimation of in-vivo three time-dependent components of measured velocity of an artery which is usually practically unavailable. For the momentum equations, second order upwind scheme and for the pressure discretisation, second order scheme were employed (Li et al. 2017). The residual error convergence threshold was set as 10^{-5} . A time step size of 5×10^{-5} s was selected such that the Courant number is much less than unity which means that fluid particles move from cell to cell within one time step (at most). The chosen time scale results in 6,600 to 20,000 time steps per cardiac cycle (for resting and hyperemic flow conditions, respectively) which is in the same range as used by Valen-Sendstad and Steinman (2014). In their study, they showed that the range of high resolution time step and mesh elements provides a correct prediction of wall shear stress especially near the vulnerable regions compared to the normal resolution solutions.

In the present study, the blood was modelled as a Newtonian fluid as the diameter of the coronary artery model is about 3 mm. According to Nichols et al. (2011), blood can be assumed as a Newtonian fluid in arteries with a diameter above 0.5 mm due to the high Reynolds number. Furthermore, blood is found to behave as a Newtonian

fluid at shear rates greater than 100 s^{-1} (Jahangiri et al. 2017). As the shear rates applied to the coronary arteries are larger than 100 s^{-1} (Sakariassen et al. 2015), the employed Newtonian assumption is valid. Moreover, in the arteries with diameters larger than 1 mm, blood behaves as a single-phase homogeneous viscous fluid (Haynes 1960). Therefore, in this study, blood was modelled as a single-phase Newtonian fluid model. The blood density, ρ , was set as 1060 kg/m^3 (Cutnell et al. 2015) and its kinematic viscosity, μ , was set to $0.0034 \text{ Pa}\cdot\text{s}$ (Li et al. 2017).

The maximum mean and peak Reynolds numbers in coronary arteries even in hyperemic working condition are about 500 and 900, respectively (Lodahl et al. 1998). Therefore, the flow regime throughout the domain remains laminar (as recommended by Zhu et al. (2018)) and a laminar solver is able to resolve all flow details. Hence, the laminar solver was employed in this study. Four different structured grids with 205000, 421000, 640000, and 1035000 elements were employed to perform a mesh independency study and finally a fine structured grid with 640000 elements was adopted using ICEM 18.2, as shown in Fig. 4.3. The fine mesh structure was chosen to make sure that the first layer height near the wall leads to y^+ less than one to make sure that the solver is capable of solving the smallest length scales of the flow. Furthermore, the choice of structured mesh elements results in faster convergence and higher resolution comparing to the unstructured mesh elements with the same number of elements.

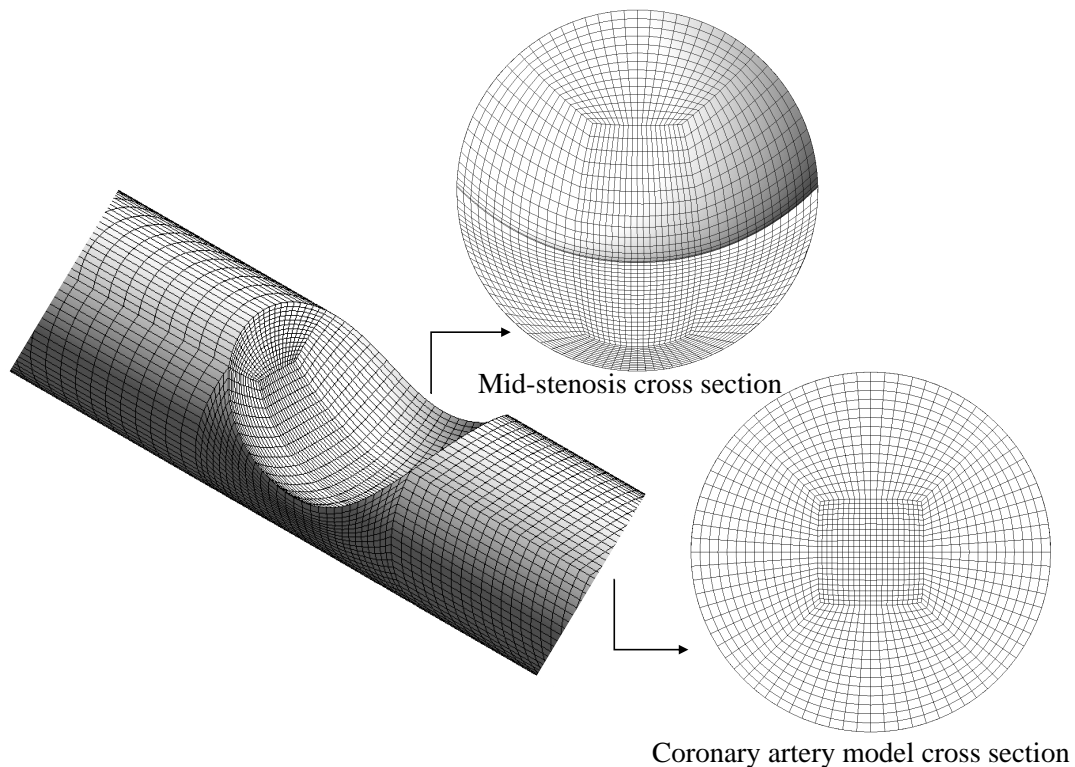


Figure 4.3: Structured mesh for the stenosis model with 67% degree of stenosis using ICEM 18.2 with 640000 elements.

Boundary conditions

A physiological flow waveform corresponding to the coronary artery was employed as the velocity inlet (Davies et al. 2008), as shown in Fig. 4.4. This waveform was modelled using the first 32 Fourier modes of Fast Fourier Transform (FFT) which accurately represented the original waveform with a maximum error of 1.4%. A user defined function (UDF) C-file based on the waveform FFT terms was written to address the inlet condition. As shown in Fig. 4.3, the blood flow cycle in the coronary artery is divided into two phases, systolic and diastolic. The flow rate is higher in the diastolic phase since during the systolic phase the heart muscle contracts and consequently, constricts the coronary heart vessels. During the diastolic phase, the heart muscles relax and hence, enable the blood to flow through the coronary arteries. Because of the contraction of the heart muscles during the systole, coronary blood flow rate reaches its minimum during the cardiac cycle. By relaxing the heart muscles after the contraction, the blood flow is pumped to the coronary arteries similar to a jet flow. The highest acceleration happens during this phase and the blood pushing continues towards its maximum velocity happening during the diastolic phase of the cardiac cycle. After that, the blood flow rate reduces to complete the cardiac cycle. The maximum deceleration happens during this part of the cardiac cycle. Four velocity and acceleration optimal time steps in the flow waveform, shown in Fig. 4.4, were of interest in this study including the time corresponding to the maximum and minimum velocity as well as the maximum acceleration and deceleration.

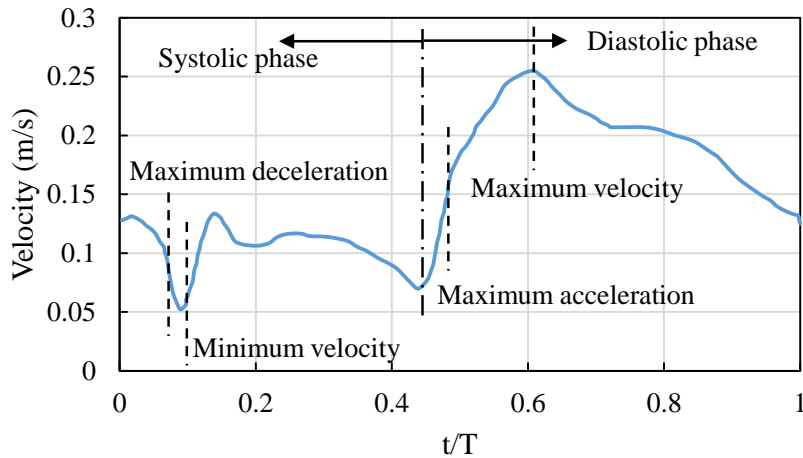


Figure 4.4: The physiological velocity waveform of the coronary artery adopted from (Davies et al. 2008).

The selection of outlet boundary condition has an insignificant effect on the haemodynamic behaviour. Therefore, pressure outlet with a zero-pressure boundary condition was considered in this study according to Liu et al. (2015). Furthermore, no-slip boundary condition at the walls was considered.

Validation of the model

In order to validate the numerical model of the pulsatile flow inside a constricted pipe, a comparison was made using the experimental results of Peterson and Plesniak (2008). Their work was focused on a pulsatile flow in a constricted artery model with the waveform

shown in Fig. 4.5b. Their stenosis model was axisymmetric generated by revolving an offset cosine curve about the artery axis of symmetry as follows:

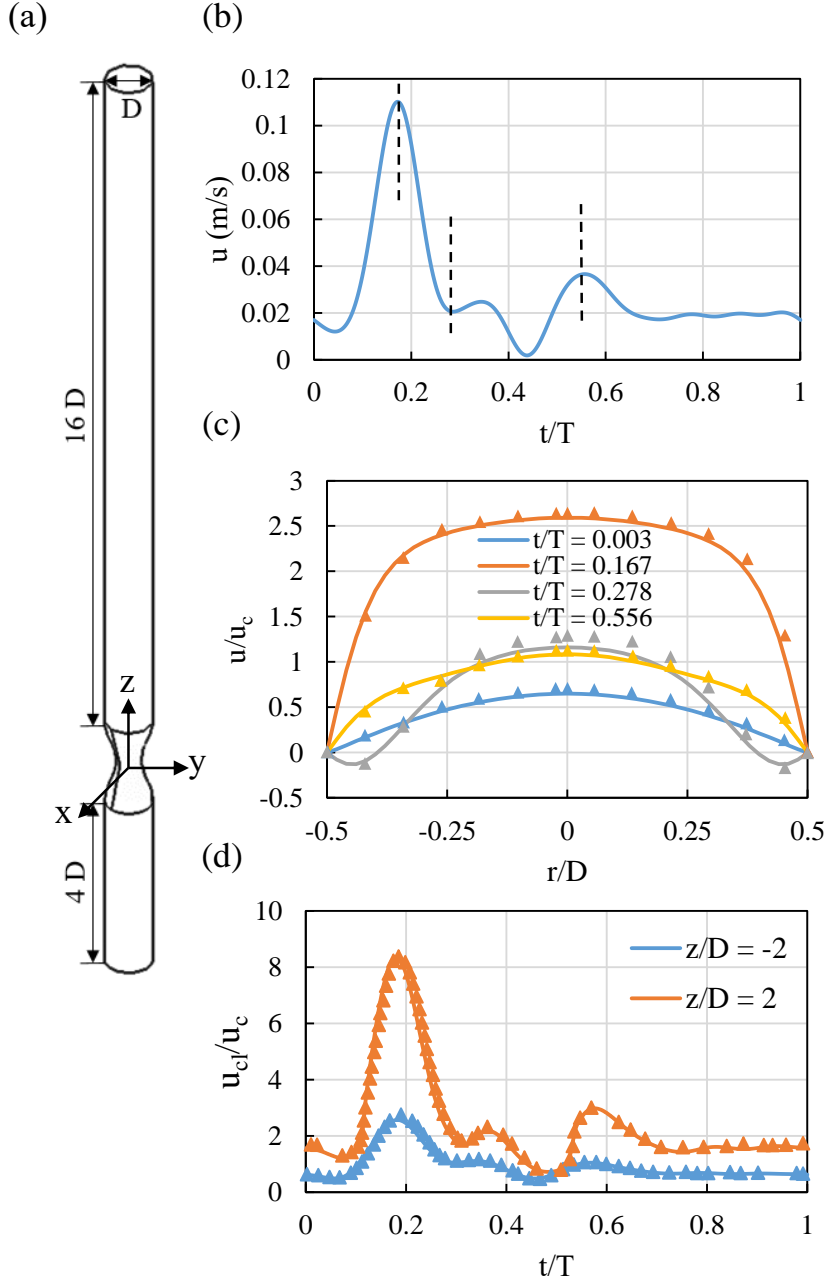


Figure 4.5: (a) Schematic diagram of the artery model ($D=12.6$ mm) with stenosis (Peterson and Plesniak 2008)), (b) Pump input waveform, (c) Fully developed pulsatile pipe flow velocity at various phases, and (d) Centreline velocity waveforms at $2D$ upstream and downstream of the mid-stenosis section (For part (c) and (d): lines are the obtained numerical result of this project and the triangular symbols are experimental data obtained from (Peterson and Plesniak 2008)).

$$S(z) = \frac{D}{2} \left[1 - s_0 \left(1 + \cos \left(\frac{2\pi(z - z_0)}{L} \right) \right) \right], \quad (4.1)$$

$$y = S(z) \cos \theta, \quad (4.2)$$

$$x = S(z) \sin \theta, \quad (4.3)$$

where s_0 is the fraction of un-occluded area and z_0 is the distance from the inception point of the stenosis to the throat. A model with the same geometry and conditions has been developed. Fully developed pulsatile pipe non-dimensionalised flow velocity at various phases including $t/T = 0.003, 0.167, 0.278,$ and 0.556 , which represented different peaks in the inlet waveform, obtained from the current simulation were compared with the experimental data of Peterson and Plesniak (2008) (Fig. 4.5c). Furthermore, another comparison was made between the centreline velocity (u_{cl}) waveforms at $2D$ upstream and downstream of the mid-stenosis section (4.5d). The velocity was non-dimensionalised based on the average value at the centreline of the pipe upstream of the stenosis (u_c). The comparison showed a good agreement between their experimental results and the results of current simulation.

TKE calculation

Although there are different indicators that can be used to quantify the transition to turbulence, the turbulence kinetic energy is selected to quantify the transitional flow behaviour. The reason is the fact that turbulent kinetic energy represents the velocity fluctuations in the three directions in one parameter instead of using different parameters for different velocity directions. Furthermore, the use of turbulent kinetic energy for investigation of transitional flow behaviour of stenosed artery model (Khair et al. 2015) and aortic stenosis model (Zhu et al. 2018) has widely studied in the literature. The calculations were performed over five pulsation cycles. In order to separate small turbulences from the main pulsatile fluctuations, a phase-average technique was utilised to calculate the mean variables as:

$$f_{pa}(x, y, z, t) = \frac{1}{N-1} \sum_{n=1}^{N-1} f(x, y, z, t + nT), \quad (4.4)$$

where f is a flow variable including velocity components in different directions and N is the number of pulsation cycles ($N = 5$). The phase-averaging technique was performed over the last 4 cycles in order to eliminate the errors associated to the model initialisation. The turbulent velocity fluctuations, $f'(x, y, z, t)$, in all directions were then calculated as

$$f'(x, y, z, t) = f(x, y, z, t) - f_{pa}(x, y, z, t), \quad (4.5)$$

The velocity fluctuations were calculated for four pulsation cycles from the second cycle to the fifth cycle using an in-house MATLAB code. The code was developed using the velocity components of each plane for each time step extracted from ANSYS FLUENT. Based on the velocity fluctuations, TKE was calculated by the following:

$$TKE(x, y, z, t) = \left(\frac{1}{2} \right) \left(\overline{(u'(x, y, z, t))^2} + \overline{(v'(x, y, z, t))^2} + \overline{(w'(x, y, z, t))^2} \right), \quad (4.6)$$

working conditions with the heart beat rate of 120 min^{-1} and the mean flow rate of 2.5 ml/s . Different degrees of stenosis are considered in case 4 and 5 representing a mild stenosis 16% (case 4) and a moderate stenosis (case 5) at hyperemic flow conditions. A severe stenosis is considered in all other cases (case 1 to 4). It is important to note that since the susceptibility of heart failure is higher at severe conditions, the highest degree of stenosis is considered for the cases with different heart working conditions while for the hyperemic condition all three degrees of stenosis (i.e. mild, moderate and severe) are studied. At the hyperemic condition, as mentioned earlier, the heart works harder to provide higher pressure to push the blood through the arteries with higher velocity. That is why existence of artery blockage at the hyperemic condition results in more serious problems (which is studied in this project) compared to the heart rest condition. Therefore, different degrees of stenosis were studied at the hyperemic condition.

At different heart working condition, given in table 4.1, the heart beat rate is different and consequently each cardiac cycle time period (T) is different. This results in changing the Womersley number, a dimensionless parameter governing the pulsatile flow, based on its definition which is:

$$Wo = \frac{D}{2} \sqrt{\frac{2\pi \rho}{T \mu}}, \quad (4.8)$$

In this study, Womersley number for the different cases is varied because of the changes in the time period as presented in table 4.1.

Table 4.1: Different cases considered to study the laminar-turbulent blood flow transition of a pulsatile flow.

No.	time period	flow rate (ml/s)	velocity (m/s)	degree of stenosis (%)	Re	Wo
1	1 beat/s ($T = 1$)	1.1	0.155618	67	146	2.10
2	2 beat/s ($T = 0.5$)	2.5	0.353678	67	331	2.97
3	3 beat/s ($T = 0.33$)	3.9	0.551737	67	516	3.64
4	3 beat/s ($T = 0.33$)	3.9	0.551737	16	516	3.64
5	3 beat/s ($T = 0.33$)	3.9	0.551737	39.1	516	3.64

Transitional turbulent behaviour of different phases of a pulsation cycle

The main focus of this section is on the four different phases on the pulsation cycle representing maximum deceleration, minimum velocity, maximum acceleration, and maximum velocity, respectively, because of their importance, as explained in the previous section. Due to the large amount of data, the most physiological severe condition (i.e. hyperemic flow with 67% degree of stenosis) is studied in detail in this section. The area-weighted average of turbulent kinetic energy at different cross-sectional locations along the artery

is displayed in Fig. 4.8 for the four phases for the case with 67% degree of stenosis and hyperemic flow condition. It is worth mentioning that the turbulence generation inside the coronary artery model is not due to the reference Reynolds number, which is calculated based on the mean velocity of the flow and the pipe diameter. Although the mean upstream Reynolds number is relatively low inside the artery (it is about 500 for hyperemic flow condition), the blockage effect due to the stenosis inside the coronary artery creates transitional flow behaviour, which is evidenced by the TKE profile. The mean local Reynolds number at the location of blockage can increase up to about three times for the case with 67% degree of stenosis. Furthermore, the peak velocity during a cardiac cycle, as shown in Fig. 4.4, is about two times higher than the mean velocity that results in the peak Reynolds number about twice as the mean Reynolds number. Hence, the local temporal Reynolds number can increase up to about six times as the mean upstream Reynolds number that results in periodic transition to turbulence during a cardiac cycle. This trend is consistent with the studies in the literature such as Khair et al. (2015) and Zhu et al. (2018), as explained in the introduction section. The TKE profile shows several peaks which are related to the effect of the constriction on the flow. The first noticeable jump occurs immediately after the stenosis for all the phases. This jump in the turbulent kinetic energy is related to the jet effect formed due to the reduction in the flow cross section which causes a considerable increase in the blood velocity. For example, for the case with 67% degree of stenosis, based on the continuity equation, the mean velocity can increase up to three times immediately after the stenosis compared to the upstream mean velocity. This causes a significant shear between the jet flow and the surrounding flow leading to a sudden jump in the TKE profile. Furthermore, this creates intense vortices in the post-stenotic region. The largest jump occurs at the maximum velocity phase at which TKE is significantly higher than the other phases. The minimum velocity phase creates the weakest jet flow effect which is accompanied with the lowest rise in the TKE profile after the stenosis. As the jet flow effects slightly disappear, the turbulent structures grow to reach their maximum intensity at around $5D$ downstream of the stenosis. This causes the second jump in the TKE profile which for all phases happen at about $z/D = 5$. The highest TKE in this phase is related to the maximum velocity phase as the higher jet flow velocity in this phase induces a larger shear layer between the jet flow and the surrounding flow which consequently, increases the velocity fluctuations. However, the lowest TKE at this phase is related to the maximum acceleration phase despite the larger mean velocity compared to the other two cases. In the maximum acceleration phase, the largest acceleration means the largest force on the bulk of the fluid which can result in suppressing the turbulence structures and consequently, reducing TKE. In the deceleration phase, the heart decelerates the blood flow inside the coronary artery which helps the eddies to grow faster. That is why, after the maximum velocity phase, the maximum deceleration phase owns the highest TKE. In the far downstream of the stenosis, all the turbulent structures are vanished and flow re-laminarises. This trend is completely in agreement with the results reported by Khair et al. (2015) where re-laminarisation happens downstream of the stenosis because the turbulence is damped about $10D$ downstream of the stenotic region.

Figure 4.9 displays the instantaneous coherent structures identified by the lambda-2 criterion coloured by the stream-wise velocity at four phases in the fourth pulsation cycle of the case3. Lambda-2 criterion is a detection algorithm that can identify vortices in a 3D fluid velocity field (Jeong and Hussain 2006). The longest vortex structures are

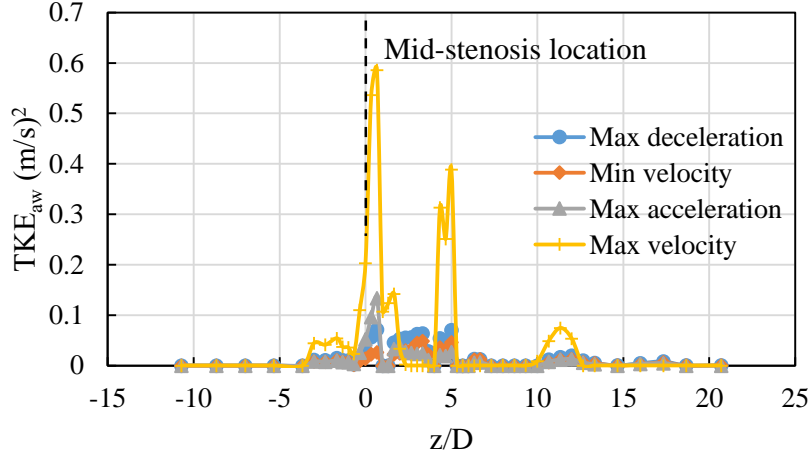


Figure 4.8: Area-weighted average of TKE for 48 different cross-sectional planes in stream-wise direction at four phases of the case 3.

related to the maximum acceleration case (Fig. 4.9c) where the highest forces due to the highest acceleration create these longitudinal structures and prevent the formation of the turbulent structures in this phase after the blockage. This clearly supports the lowest value of the turbulent kinetic energy for the maximum acceleration phase, as presented in Fig. 4.8. There is a general trend of the formation of quite long vortices after the stenotic region in the other phases, which is due to the jet flow effect, as can be observed in Fig. 4.9a, b and d. Further downstream of the stenotic region, the turbulent structures grow creating disturbances in the flow regime in the form of eddies in the flow. Far downstream of the stenosis and near the artery model outlet, the turbulent structures dissipate and the flow becomes relaminarised. The trends are governed for the other phases as well. The turbulent structures have their highest intensity for the maximum velocity phase and after that maximum deceleration phase has more intense turbulences compared to the minimum velocity phase. Therefore, the turbulence structures shown in Fig. 4.9 are in agreement with the variations of TKE given in Fig. 4.8.

Velocity profiles along different lateral lines ($x = 0$ and $-D/2 \leq y \leq D/2$) downstream of the stenotic region up to $10D$ at four phases in the fourth pulsation cycle of the case3 are shown in Fig. 4.10. The general trend in the velocity profile in different cross-sectional planes is that the maximum velocity belongs to the maximum velocity phase and the minimum is for the minimum velocity phase, as expected. However, there are some exceptions. At the beginning stage of the jet flow immediately after the stenosis region, ($z/D = 1$), the maximum velocity is mostly related to the maximum acceleration phase except a small region near the core of the artery model where the maximum velocity phase has the maximum velocity. The jet flow grows past the stenotic region which is more significant in the maximum velocity phase. This increasing trend continues up to $3D$ downstream of the stenosis where the maximum velocity of the jet flow occurs at the centre of the artery model for the maximum velocity phase which is about 3.5 m/s. The largest value of the shear layer between the jet flow and the surrounding blood flow near the wall occurs in this location. After that, the jet flow effect is gradually reduced in the stream-wise direction. The jet flow effect is almost vanished at $8D$ downstream of the stenotic region. After this location, a sudden reduction in the central velocity of the maximum velocity phase is observed ($z/D = 9$) which is related to the positive pressure gradient that is pushing the fluid back. The near wall velocity trend is to some extent

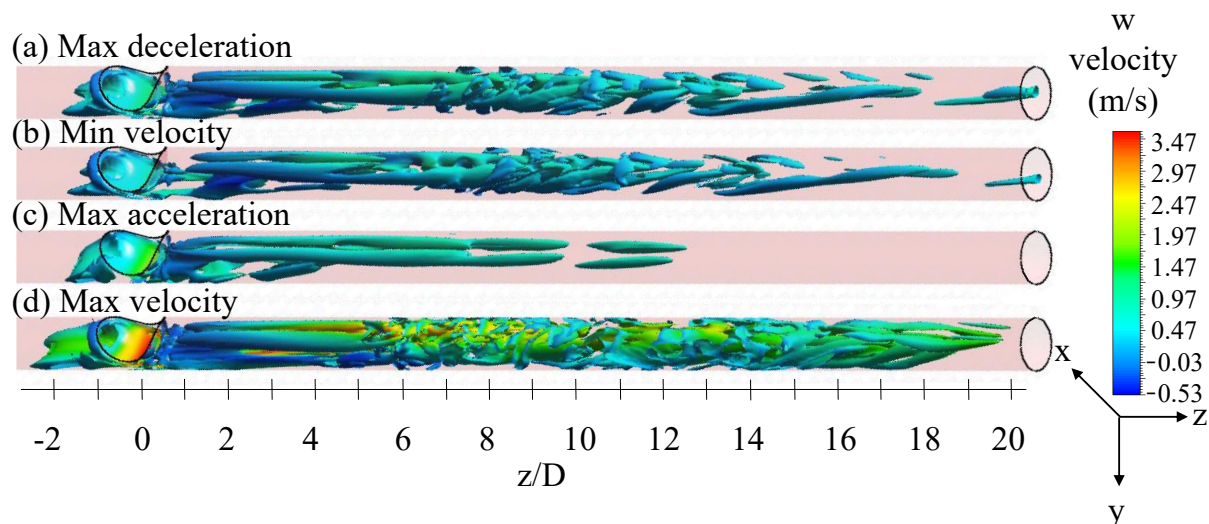


Figure 4.9: Instantaneous coherent structures identified by the lambda-2 criterion ($\lambda_2 = -0.01$) coloured by the stream-wise velocity showing the downstream vortical structures at four phases in the fourth pulsation cycle of the case3 representing the max (a) deceleration and (c) acceleration and (b) min and (d) max velocities.

different from the above-described behaviour. The near wall flow regime is separated from the core jet flow regime by the induced shear layers due to the high central velocity. In the developing jet flow regime, starting from the early post-stenotic region and continuing up to $3D$ downstream of the stenosis, the reverse flow between the artery wall and the shear layers is intensified for all phases. Past the location with maximum jet flow effect, the reverse flow reduces gradually along with the jet velocity reduction. The reverse flow is completely vanished at about $8D$ downstream of the stenosis. It is interesting to note that the higher length of the jet flow, the higher length of the reverse flow for almost all phases. For example, as can be seen in the velocity profile at $z/D = 3$, the highest velocity value of the reverse flow is related to the maximum velocity phase which has the highest core flow velocity. This trend is not valid at the maximum acceleration phase. As explained earlier, in this phase the heart pushes the blood back in the stream-wise direction with its highest acceleration during the cardiac cycle. Therefore, there is no reverse flow during this phase of the cardiac cycle at any stream-wise locations.

Static pressure distribution along the stream-wise direction at four phases in the fourth pulsation cycle of the case3 is displayed in Fig. 4.11. Pressure drop is an important parameter since it represents the power required by the heart to supply the heart muscles with a uniform and constant blood flow rate. Higher pressure drop means higher heart muscle effort to provide the same blood flow rate for the organs to work properly. In order to perform a comparison between the four phases during the cardiac cycle, a zero gauge pressure is considered in the outlet of the artery model (as explained in the boundary condition section, selection of outlet boundary condition has almost insignificant effect on the haemodynamic results (Liu et al. 2015)). The pressure drop across the stenosis is found to vary significantly during the systole and diastole which is in agreement with that reported by Li et al. (2009). The maximum pressure difference between the upstream and downstream of the stenosis is related to the maximum acceleration phase. High acceleration means that large forces are exerted to the flow and consequently, the high pressure differences illustrate the high pressure gradient which is also the reason of the

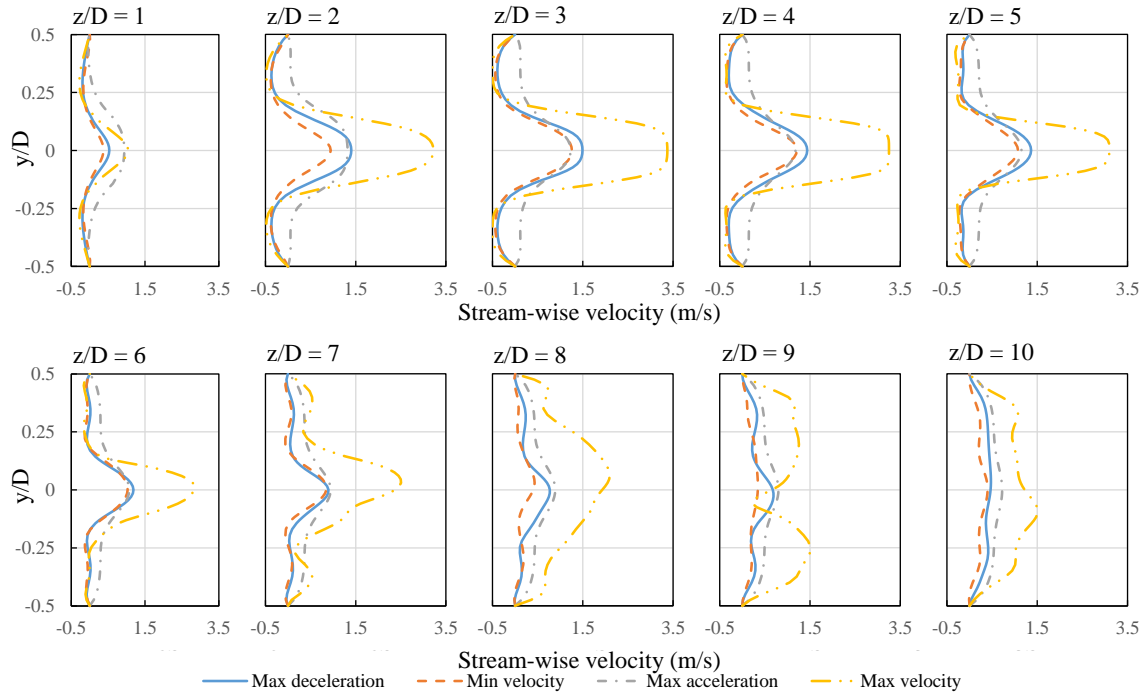


Figure 4.10: Instantaneous velocity profile along different lateral lines in different stream-wise locations at four phases in the fourth pulsation cycle of the case3.

lack of reverse flow in this case. At this phase, as explained before, the blood is pushed through the artery with the highest acceleration during the cardiac cycle and therefore, this creates the highest pressure drop during the cardiac cycle. The minimum pressure difference is related to the minimum velocity phase. For an artery model with a 67%-degree stenosis during the hyperemic flow condition, the maximum pressure difference, which is associated with the maximum acceleration phase, is about 5800 Pa that requires the heart to work harder. Furthermore, the minimum pressure difference, about 280 Pa, happens when the flow velocity is minimum. In the maximum deceleration phase, the heart decelerates the blood flow in the artery consequently creating negative back pressure. The negative back pressure for an artery model with a 67% degree of stenosis during the heart activating mode is about 2700 Pa which occurs far upstream of the stenosis. In all phases during a cardiac cycle, a sudden drop in the pressure distribution profile along the stream-wise direction can be seen which is about a sudden increase in the velocity due to the cross section reduction in the stenosis location. The value of this sudden drop in the pressure is directly related to the value of the jump in the stream-wise velocity where the highest is related to the maximum velocity phase and the lowest is related to the minimum velocity phase. After the stenosis, for both maximum and minimum velocity phases, there is a negative pressure zone spreading from the stenotic region up to $6D$ downstream of the stenosis. Past the stenotic region all the phases of a cardiac cycle retrieve the pressure changes and reach towards the zero gauge pressure at the outlet of the artery model.

Stream-wise distributions of the wall shear stress along the top line (the same side of the stenosis), the side line and the bottom line (the opposite side of the stenosis) at four phases in the fourth pulsation cycle of the case3 are shown in Fig. 4.12. For all line locations (shown in Fig. 4.12a), the maximum wall shear stress happens in the

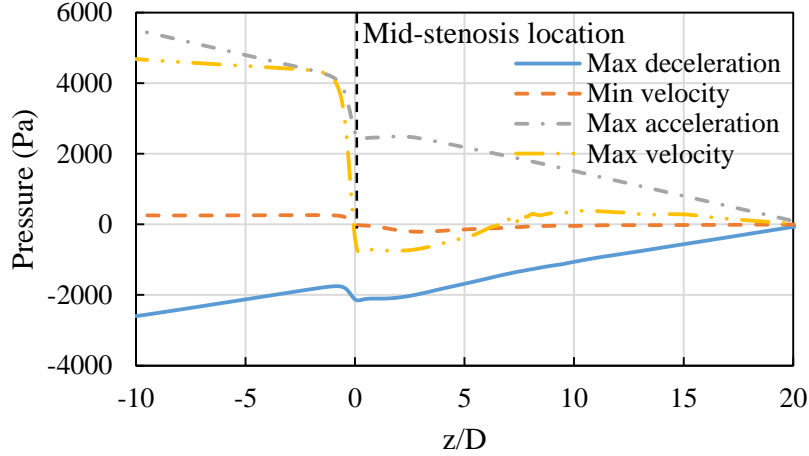


Figure 4.11: Static pressure distribution along the stream-wise line located at $y = -1$ mm at four phases in the fourth pulsation cycle of the case3.

mid-stenosis region. At this location, because of the cross section reduction and the consequent increase of mean velocity, larger shear forces are applied to the walls creating higher wall shear stresses. Far downstream and upstream of the stenotic region near to the inlet and outlet of the model, the value of wall shear stress is considerably small for all phases. The highest wall shear stress is related to the maximum velocity phase which is about 10 Pa while the lowest, about 1 Pa, is related to the minimum velocity phase. Furthermore, the highest wall shear stress in the cardiac cycle is related to the maximum velocity phase and the lowest is for minimum velocity phase. Since the blood force on the stenosis wall is applied to the smaller area, because of the stenosis, compared to the side and bottom regions, it results in larger wall shear stresses in the mid-stenosis part, as can be seen in Fig. 4.12b. Wall shear stress at the sides of the stenosis remains positive in the stream-wise direction except small regions before and after the stenosis. This means that two small separation regions exist before and after the stenosis. After the stenosis, wall shear stress at the same side of the stenosis in the stream-wise direction increases gradually to reach its maximum value around $5D$ downstream of the stenotic region. This trend is valid for all the cardiac cycle phases. However, the corresponding value for the maximum velocity phase is much higher than the other phases. The location of maximum wall shear stress at the downstream of the stenosis is the same as the region with a jump in the TKE profile as explained in Fig. 4.8. The turbulent structures are intensified after the jet-affected region and create considerable wall shear stresses downstream of the stenosis in the same side of the stenosis. The higher shear stress results in the higher possibility of the plaque rupture. Because of the considerable large wall shear stresses downstream of the stenosis at the same side of it, there is almost no possibility for the formation of the second plaque there. Far downstream of the stenosis where the turbulence fades, wall shear stress reduces gradually reaching a constant value which is due to the pressure exerted to the wall from the blood flow. Large recirculation zones can be observed downstream of the stenotic region in the side and bottom of the stenosis which is shown in Fig. 4.10c and d by the zones with negative wall shear stresses. The separation starts after the stenosis in the side part of the stenosis for all cardiac phases (except the maximum acceleration phase) and flow reattaches to the wall far downstream of the stenosis ($z/D = 10$). The flow separation is postponed after the stenosis to about $5D$ downstream of the stenosis in the opposite side of the stenosis and attached to the wall

5D after the separation. Therefore, the region between 5D and 10D after the stenosis, at the side and bottom regions of the first stenosis, is the location with the high possibility of the formation of the second stenosis due to the existence of the recirculation zones. There is no negative wall shear stresses, no flow separation, on the wall for the maximum acceleration phase which is supporting the previous results explained in Figs. 4.10 and 4.11. It is important to note that the coronary stenosis is more likely to form in the locations with disturbed flow conditions which is characterised by low WSS (Zhang et al. 2015). Furthermore, low WSS appears to be the most important hemodynamic parameter promoting atherosclerotic plaque growth that in turn influences the blood flow and WSS distribution (Arzani 2020).

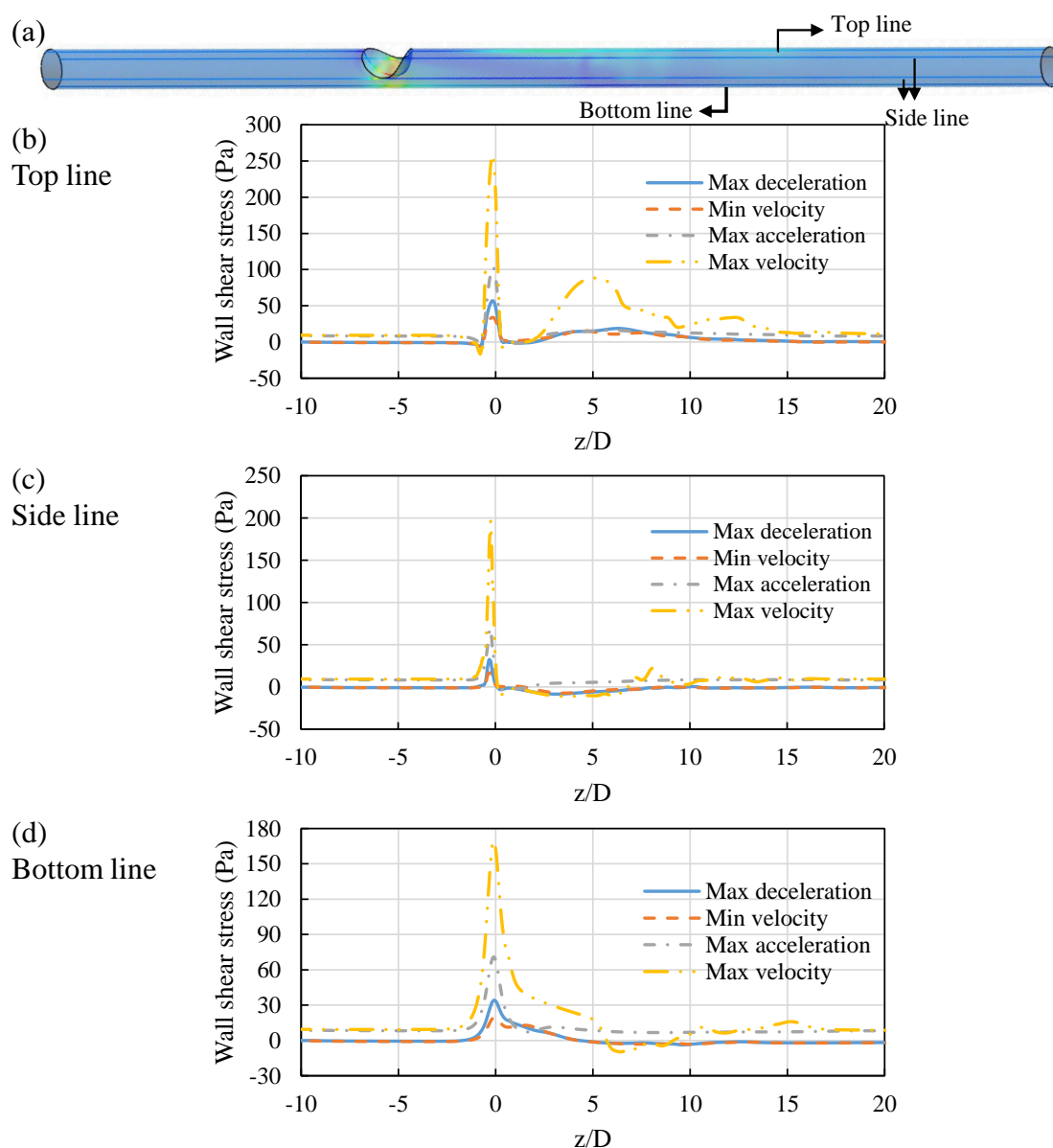


Figure 4.12: (a) Wall shear stress contour and different lines along the stream-wise direction at maximum velocity phase in the fourth pulsation cycle of the case3 and stream-wise distribution of the wall shear stress along the (b) top line, (c) side line and (d) bottom line at four phases in the fourth pulsation cycle of the case3.

As the highest wall shear stress during a cardiac cycle happens during the maximum velocity phase, as explained before, wall shear stress contour of this phase for the fourth pulsation cycle of the case3 from both top and bottom views is displayed in Fig. 4.13. Hence, the maximum velocity phase will be selected for further analysis in the rest of the results. As explained, the maximum wall shear stress occurs at the mid-stenosis location which is highlighted in dark red in the top view and orange in the bottom view. The dark blue region, mainly distributed after the stenosis in the side and bottom parts of the stenosis, represents the separated zones due to their negative values of wall shear stress.

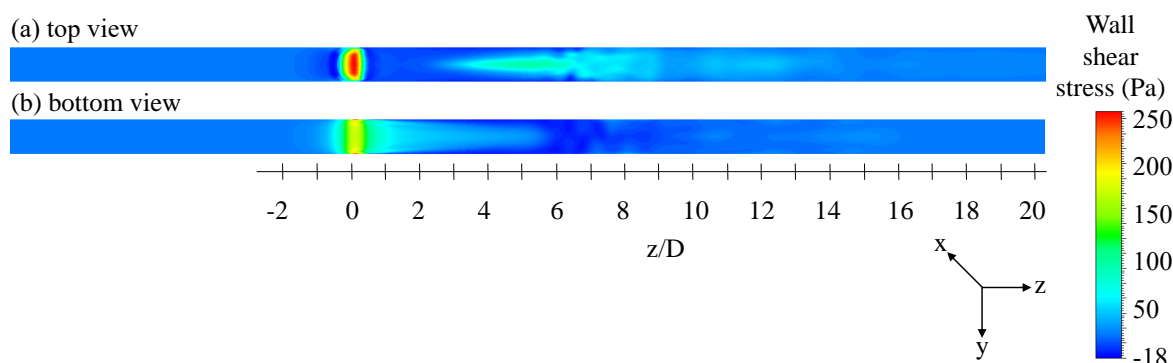


Figure 4.13: Wall shear stress contour of max velocity phase of the fourth pulsation cycle of the case3 from (a) top view and (b) bottom view.

In order to be more accurate in finding the susceptible locations for flow separation based on the wall shear stresses during a cardiac cycle, the stream-wise distributions of the wall shear stress at different lateral and vertical positions of maximum velocity phase is illustrated in Fig. 4.14. The highest shear stress is slightly reduced from the top stenosis region (the same side of the stenosis) to the opposite side. This means that the highest wall shear stress at the mid-stenosis cross section happens in the top side of the stenosis and the lowest happens in the opposite side of it. A small recirculation zone can be seen immediately before and after the stenosis at only the top region of the bump and close to it (line a–b). For these two positions, no more separation occurs in the downstream of the stenosis. Separation starts from the side of the stenosis (line c) and continues up to the opposite side of it (line e). Moving from the side to the opposite region of the stenosis, separation is postponed to the far downstream of the stenosis. For example, at the side of stenosis (line c), separation starts $1D$ after the stenosis which is moved downstream to the $4D$ for line d and finally $6D$ downstream of the stenosis for the opposite region of the stenosis (line e). Based on the results, downstream of the stenosis in the top stenosis region and close to it, there is no possibility for the formation of the second stenosis. However, the possibility of the formation of the second stenosis downstream of the first stenosis increases in the side region of the stenosis up to the opposite region.

More detailed instantaneous velocity contours and vectors at different vertical, lateral and circular cross-sectional planes in stream-wise direction of the maximum velocity phase are shown in Fig. 4.15. The jet flow effect starts at the location of stenosis and therefore, the flow reaches its maximum velocity (about 3.5 m/s) at this location at the vertical direction (Fig. 4.15a). The jet flow effect extends up to about $5D$ downstream of it. The disturbances in the velocity patterns grow after dissipation of the jet effect. It creates turbulent structures in the downstream flow which mainly occur from $5D$ to $10D$

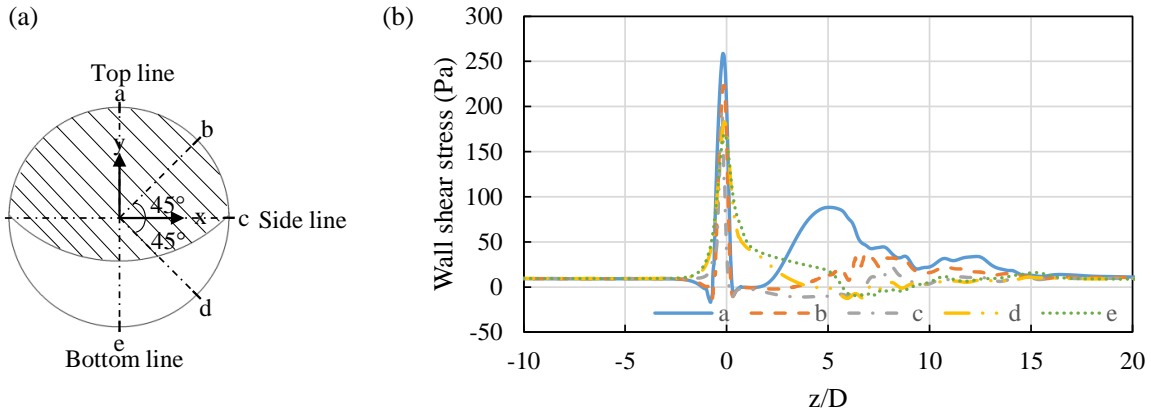


Figure 4.14: Wall shear stress stream-wise distribution for different lateral and vertical positions of max velocity phase of the fourth pulsation cycle of the case3.

downstream of the stenotic region (as displayed in Fig. 4.15a and b). After that the flow starts to re-laminarise which is completed far downstream of the stenosis near the outlet of the artery model ($18D$ downstream). This means that the velocity profiles regain their parabolic shape similar to the upstream of the stenosis (as demonstrated in Fig. 4.15a and b). Two symmetric vortex tubes are formed around the jet flow immediately after the stenosis extending to $5D$ downstream of the stenotic region which is highlighted in dark blue in Fig. 4.15c. This region with the negative velocity value (displayed in dark blue with about -0.53 m/s) is the separated region as a consequence of the adverse pressure gradient. Based on the results of Fig. 4.15, separation is most likely to happen at the side of the stenosis (Fig. 4.15b) and there is almost no possibility for the flow separation at the same side of the stenosis (Fig. 4.15a). Furthermore, a small recirculation zone can be observed far downstream of the stenosis at the bottom side of it, starting from $5D$ and finishing at about $10D$ downstream of the stenotic region (Fig. 4.15a).

Effect of heart working condition and degree of stenosis

In this section, the effects of the degree of stenosis and the heart working conditions for a range of resting to hyperemic conditions are investigated. The area-weighted average of TKE along different cross-sectional planes at the maximum velocity phase of the fourth pulsation cycle for different heart working conditions and degrees of stenosis are shown in Figs. 4.16a and 4.16b, respectively. As shown in Fig. 4.16a, as the heart works harder to provide higher flow rate for different organs, the jump in the TKE profile due to the jet flow effect at the mid-stenosis location is increased significantly, as the corresponding value for the resting condition is 0.05 (m/s)² and for hyperemic condition is 0.6 (m/s)² (more than one order of magnitude larger). It is interesting to note that there is almost no jump in the TKE profile for the resting heart working condition, even for the artery model with 67% degree of stenosis which means that no turbulent structures are formed even after the stenotic region with high degree of stenosis. On the other hand, another jump which is related to the formation of turbulence structures downstream of the stenosis exists for the moderate heart working condition (case 2) and hyperemic one (case 3). For the hyperemic flow condition, the jump in the area-weighted average turbulent kinetic energy profile due to the formation of turbulences occurs at $5D$ downstream of the stenotic

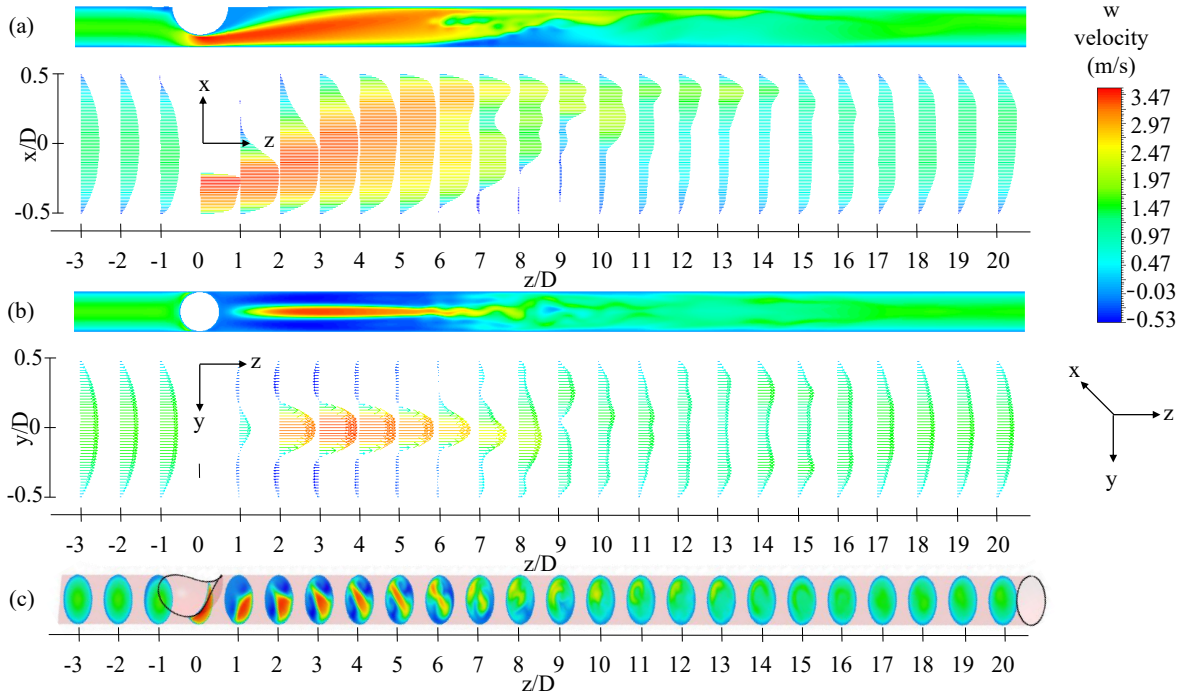


Figure 4.15: Velocity contours and vectors at different planes and lines including (a) vertical direction, (b) lateral direction and (c) different circular cross-sectional planes of max velocity phase of the fourth pulsation cycle of the case3.

region and its value is about 0.4 (m/s)^2 . Whereas, the jump in the TKE profile for the moderate heart working condition (case 2), about 0.13 (m/s)^2 , occurs at around $7D$ downstream of the stenosis. This means that the location where the intensity of the turbulent structures is the highest shifts towards the stenosis for the conditions in which the heart is working harder (hyperemic flow condition) and the turbulence kinetic energy and intensity are much larger in hyperemic flow conditions compare to the others. Since in the hyperemic heart working condition, the heart is required to pump more blood to the arteries and the blood flow rate is larger, the Reynolds number inside the arteries also increases considerably. This finding is in agreement with the results of (Biswas et al. 2016; Khair et al. 2015) reporting that for the higher values of Reynolds number, the transition locations, (the sudden jump in the TKE profile), moved closer to the constricted location.

According to Fig. 4.16b, TKE at the mid stenosis region is larger for the higher the degree of stenosis due to the increased jet flow effect. As for the higher degree of stenosis the cross sectional area of the artery is reduced, and based on the continuity equation, the blood mean velocity increases which consequently leads to increase in the jet flow effect. No turbulence, based on the TKE profile, can be observed in the artery model with the low degree of stenosis (16%). However, by increasing the degree of stenosis, a jump in the TKE profile which is related to the formation of turbulent structures in the downstream of the stenosis is observed. The higher the degree of stenosis, the higher is the value of TKE and the level of the turbulence downstream of the artery. For the 39.1% degree of stenosis, the jump is located at $7D$ downstream of the stenosis with a corresponding TKE value of about 0.1 (m/s)^2 . For the higher degree of stenosis case (67%), the peak location shifts toward the stenosis ($5D$) and its value is increased to 0.6 (m/s)^2 . Therefore, the jump in the TKE profile moves closer to the stenosis for the

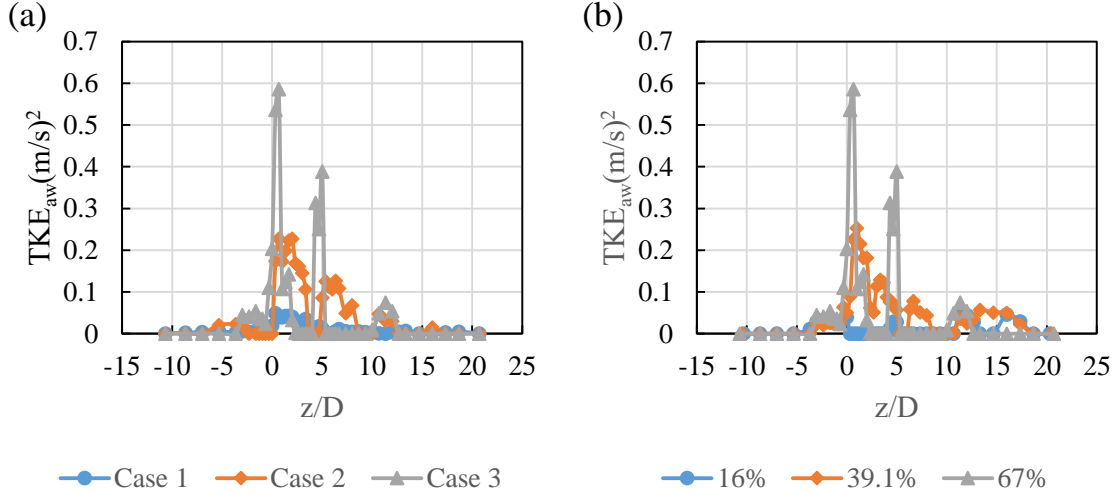


Figure 4.16: Area-weighted average of TKE for 48 different cross-sectional planes in stream-wise direction at max velocity phase of the fourth pulsation cycle for (a) different heart working condition ranging from resting to hyperemic heart working condition and (b) different degrees of stenosis including 16%, 39.1% and 67%.

higher degrees of stenosis. The obtained results about the effect of degree of stenosis on the location of the jump in the TKE profile as well as its corresponding value are strongly supported by the literature (Biswas et al. 2016; Khair et al. 2015). Table 4.2 summarises the maximum values of area-weighted average of TKE for different cases considered in this study based on the results explained in Figs. 4.8 and 4.16. This table shows that the second and fifth cases have almost the same TKE values for different phases. This means that having a moderate stenosis degree in hyperemic heart flow condition will create the same turbulences as having a severe stenosis degree with the heart flow condition in between resting and hyperemic conditions.

The static pressure distribution along the stream-wise line located at $y = -1$ mm at max velocity phase for different heart working conditions ranging from resting to hyperemic and degrees of stenosis are shown in Figs. 4.17(a-b). At the hyperemic heart working condition, in which the arterial system requires more blood flow rate, the value of the pressure drop across the stenosis in the artery model is larger compared to the resting heart working condition which forces the heart to work faster to compensate the pressure drop. The pressure drop in the resting condition is about 700 Pa, in the moderate heart working condition is about 2300 Pa and finally in the hyperemic heart working condition is about 4700 Pa (about twice of the moderate heart working condition and 6 times more than the resting heart working condition). A sudden pressure drop can be observed in all heart working conditions immediately after the stenosis which occurs due to an increase in the velocity which can be explained based on the Bernoulli equation stating that with an increase in the fluid velocity, a decrease in the pressure occurs simultaneously. Furthermore, a region with negative pressure exists for the moderate and hyperemic heart working conditions immediately downstream of the stenosis. At this location, the hyperemic condition leads to a more negative pressure compared to the moderate heart working condition. This implies the existence of recirculation zones with higher pressure gradients after the stenosis in hyperemic heart working condition compared to the other conditions as shown in Figs. 4.15b and 4.15c.

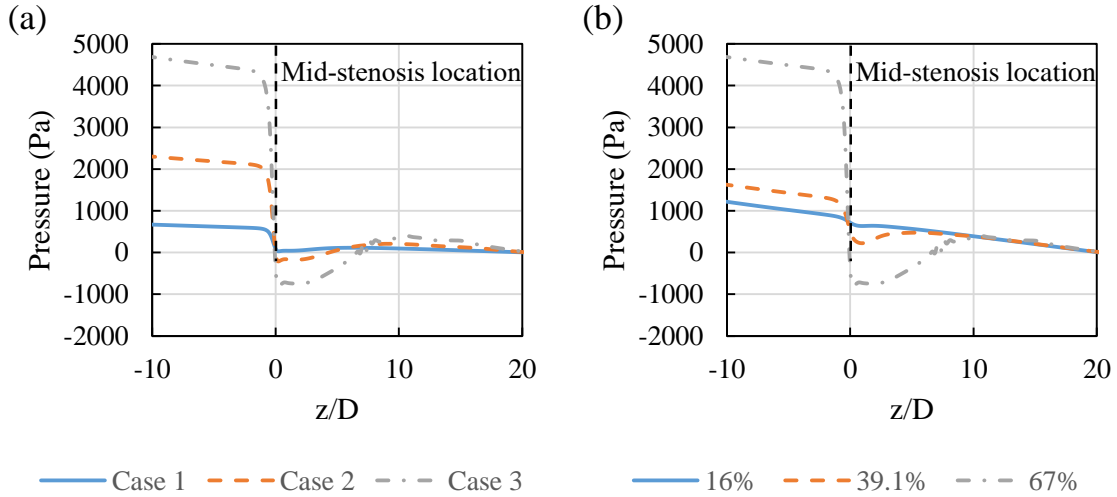


Figure 4.17: Static pressure distribution along the stream-wise line located at $y = -1$ mm at max velocity phase of the fourth pulsation cycle for (a) different heart working condition ranging from resting to hyperemic heart working condition and (b) different degrees of stenosis including 16%, 39.1% and 67%.

The higher degree of stenosis results in a larger pressure drop along the stenotic region in the artery (Fig. 4.17b). The pressure drop is about 1200 Pa and 1600 Pa for the 16% and 39.1% degrees of stenosis, respectively. It increase significantly up to 4700 Pa for the 67% degree of stenosis. The increase of pressure drop with the increase in the degree of stenosis is due to the reduction of the cross sectional area and increase of mean velocity as explained above. The observed trend is in agreement with the results reported by Flanigan et al. (1977) and Young et al. (1975) illustrating a remarkable jump in the pressure drop for the severe degrees of stenosis compared to the early stage stenoses. Furthermore, the same results were reported by Rotman et al. (2017) which found that the pressure drop increases exponentially as the degree of stenosis increases.

Figure 4.18 presents the stream-wise distributions of wall shear stress along the top, side and bottom lines at the maximum velocity phase for different heart working conditions (left column of Fig. 4.18) and different degrees of stenosis (right column of Fig. 4.18). The maximum wall shear stress occurs at the mid-stenosis location for all directions, as explained before, and its maximum value belongs to the hyperemic flow condition. The possibility of the formation of the second plaque for the resting heart working condition is too low except at two small regions immediately before and after the stenosis at the same side of it. Even at these locations, the recirculation zones may change the shape of the first stenosis without any chances for the formation of the second one since they are connected to the first stenosis. According to Fig. 4.18a (left side), a small jump in the value of the wall shear stress downstream of the stenosis at the same side of it (top line) is observed which is more intense for the hyperemic heart working condition (case 3). As explained in the previous section, the separation starts downstream of the stenosis on the lateral areas of the wall (side line) as well as its bottom side (bottom line) for all heart working conditions except the resting condition. The separation and attachment region of the moderate and hyperemic heart working condition at the side line of the stenosis starts $1D$ after the stenosis and ends at about $7D$ downstream of the flow, respectively. The recirculation zones for the opposite side of the stenosis are moved

Table 4.2: The maximum values of area-weighted average of TKE for different cases considered in this study.

	flow condition	flow rate (ml/s)	degree of stenosis (%)	area-weighted average of TKE (m/s) ²			
				maximum deceleration	minimum velocity	maximum acceleration	maximum velocity
case 1	resting	1.1	severe (67%)	0.006	0.004	0.01	0.05
case 2	in-between	2.5	severe (67%)	0.03	0.02	0.05	0.23
case 3	hyperemic	3.9	severe (67%)	0.07	0.05	0.13	0.59
case 4	hyperemic	3.9	early stage (16%)	0.006	0.004	0.01	0.05
case 5	hyperemic	3.9	moderate (39.1%)	0.04	0.03	0.06	0.25

to the downstream of the flow, i.e. the separation starts at about $6D$ and attaches to the wall at around $10D$ downstream of the stenotic region. This means that separation starts from the side of the stenosis and spreads to the bottom side of it further downstream. The magnitude of the wall shear stress is higher in the recirculation zone of the hyperemic heart working condition compared to the moderate and resting conditions.

According to Fig. 4.18 (the right column), the wall shear stress at all sides of the mid-stenosis location is larger for the higher degrees of stenosis, which is due to the large vertical gradient of stream-wise velocity. No flow separation occurs at any sides of the low degree of stenosis (mild stenosis model), except a small region before and after the stenosis at the same side of it. Almost the same trend exists for the moderate stenosis model (39.1%). It can be concluded that there is no separation in the post-stenotic region for the cases with low to moderate stenosis model. However, for the severe stenosis case the trend is different. As explained earlier, the separation occurs by increasing the degree of stenosis to severe stenosis model (67%). The recirculation zone observed in this case has almost the same trend as the one reported by Khair et al. (2015) in terms of the separation and attachment locations.

A case study: blockage inside a patient specific coronary artery model

In this section, to demonstrate the validity of the developed results for an idealised coronary artery model to real cases and since atherosclerosis is highly influenced by the artery geometry (Doutel et al. 2019), a patient specific coronary artery geometry is studied and the flow features, wall shear stress and TKE in a stenosed patient specific coronary artery model are investigated. The results are presented for the hyperemic flow condition case with three beats per second as a cardiac cycle time period and at a flow rate of 3.9 ml/s. A patient specific left anterior descending coronary artery is shown in Fig. 4.19. The inlet geometry of patient specific coronary artery model is in the shape of an ellipse and its cross sectional area is 2.225 mm^2 . The patient specific artery has a degree of stenosis of 57%, as shown in the dashed area in Fig. 4.19. The cross sectional area of the artery after the blockage section expands to a cross-sectional area of 4.69 mm^2 , which is

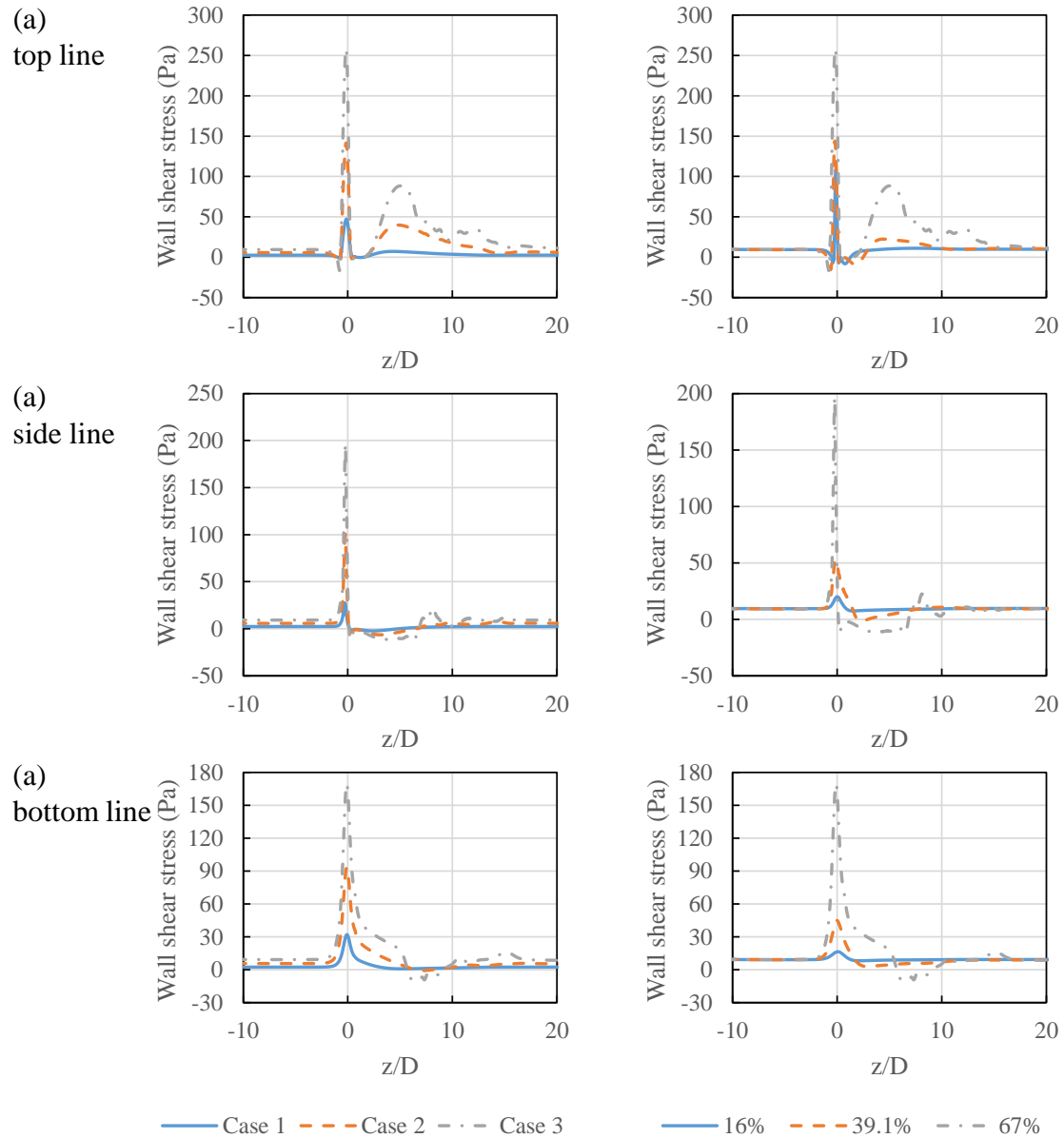


Figure 4.18: Stream-wise distribution of the wall shear stress along the (a) top line, (b) side line and (c) bottom line at max velocity phase of the fourth pulsation cycle for different heart working condition ranging from resting to hyperemic flow condition (left side) and different degrees of stenosis including 16%, 39.1% and 67% (right side).

more than twice the inlet area of the artery. For the patient specific geometry case, since the cross section of the artery is not circular, the application of Womersley velocity profile at the inlet is not valid. The reason is that the application of the parabolic or Womersley velocity profiles is limited to the problems with a circular cross-section, representing the fully developed flow regime at the inlet. Hence, in this case study, a blunt spatial velocity profile with the hyperemic flow rate, and a pulsatile temporal velocity profile were employed as an inlet boundary condition (Fig. 4.4). To eliminate inlet disturbances and high wall shear stresses zone at the inlet, the inlet cross section of the artery was extended for $5D$, as shown in Fig. 4.19. Outlet boundary condition, flow solver, type of working fluid and its physical properties were considered identical to those of the idealised

coronary artery model, as explained in the previous section. A structured mesh grid with 1,383,000 mesh elements was generated using ICEM 18.2. Time-step was set to 5×10^{-6} s that resulted in 66,000 time-steps per cardiac cycle. A total of 35 cross-sectional planes in stream-wise direction were defined with a higher concentration in the vicinity of the stenosis and after it to illustrate the velocity contours and TKE values.

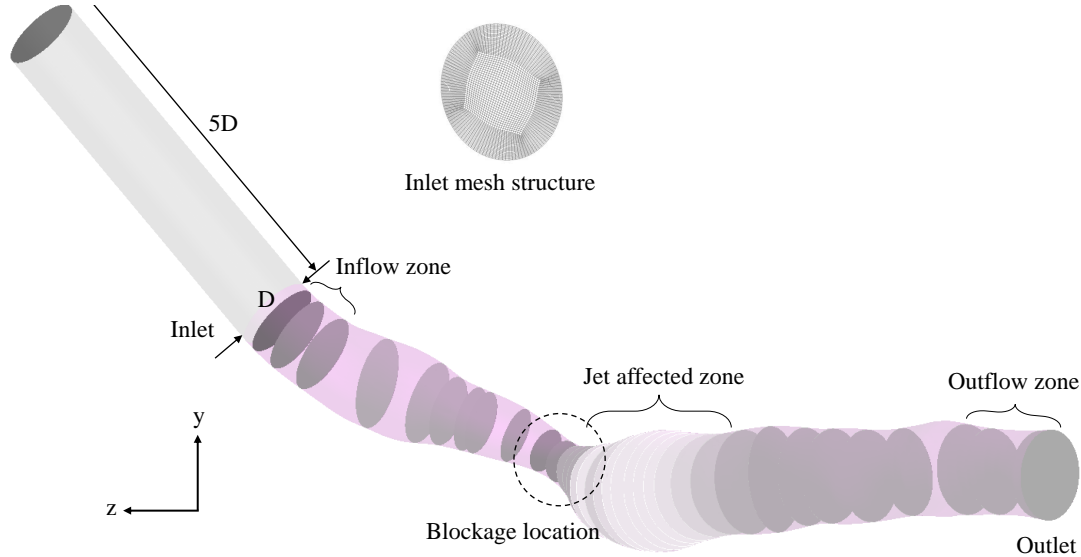


Figure 4.19: Schematic of the patient specific coronary artery model and the defined cross-sectional planes in stream-wise direction.

Figure 4.20 displays the velocity contours at different cross-sectional planes for different phases during the third cardiac cycle. As discussed in Fig. 4.10 and similar to the findings for the idealised geometry, the highest velocity is related to the maximum velocity phase during a cardiac cycle, while the lowest is related to the minimum velocity phase. The velocity contours near the inlet of the artery (inflow zone) for all phases show a uniform structure which demonstrates that the application of the inlet extension eliminates the inlet effects on wall shear stress distribution. The highest velocity for all phases occurs at the location of blockage, as expected, due to the reduction in the cross section of the artery that results in the formation of the jet flow regime after the blockage section (jet affected zone). The jet flow regime continues downstream of the blockage section about 12 planes from the stenosis location (about 0.05 m after the blockage section) and deflects to the bottom side of the artery due to the effect of the curvature in the patient specific artery at the location of blockage. In the far wake and after dissipation of the jet flow energy, the disturbances in the velocity contours appear that result in growth of the turbulent structures. This behaviour is consistent with the turbulence structures reported for the idealised artery geometry. Further downstream, the flow relaminarises near the outlet of the patient specific artery model (outflow zone).

Figure 4.21 shows wall shear stress contours for different phases of the third pulsation cycle for the hyperemic flow conditions. The highest wall shear stress range is related to the phase with a maximum velocity during the cardiac cycle. The highest wall shear stress occurs at the mid-stenosis location for all phases which is related to the induced large shear layer due to the formation of jet regime when the flow passes through the blockage area. As explained in the previous paragraph, the jet is deflected to the outer region of the curvature after the blockage section. This results in a lower wall shear

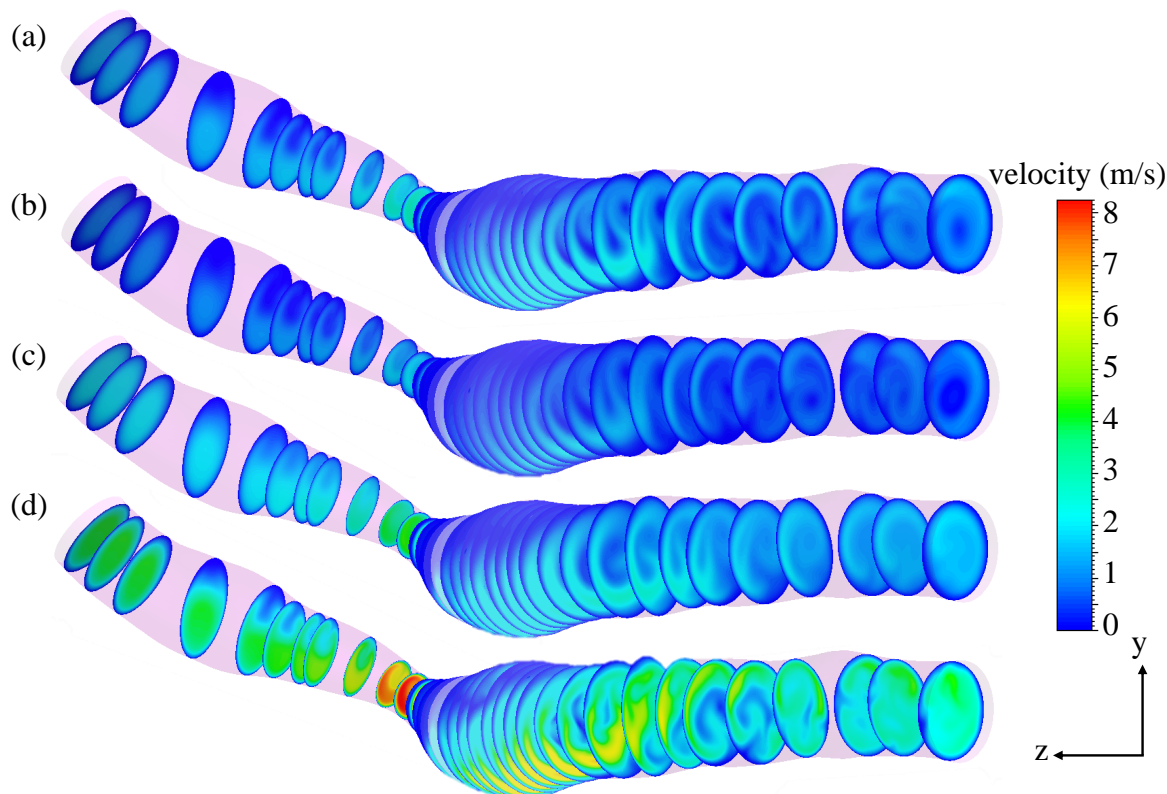


Figure 4.20: Velocity contours at different cross-sectional planes in stream-wise direction for different phases: (a) maximum deceleration, (b) minimum velocity, (c) maximum acceleration, and (d) maximum velocity of the third pulsation cycle for the hyperemic flow conditions.

stress zone at the inner region of the curvature (same side of the stenosis) and a higher wall shear stress zone at the outer region (opposite side of the stenosis). This is slightly different from what was found for the idealised coronary artery model. The reason is the existence of the curvature in the patient specific coronary artery geometry, which did not exist in the idealised model. This curvature changes the direction of the jet flow after the stenosis section.

The area-weighted average of TKE at different cross-sectional planes along the patient specific coronary artery is displayed in Fig. 4.22 for the four phases during a cardiac cycle and for the hyperemic flow conditions. In order to calculate TKE for this case, the simulation was performed for five cardiac cycles, which resulted in 330,000 time-steps. The values of phase-averaged TKE for different cycles were compared and it was shown that the area-weighted average of TKE for all cross-sectional planes are almost the same for the fourth and fifth cardiac cycles (less than 0.5% difference), which is the same as the trend explained in the TKE calculation section for the idealised coronary artery model. The results of the fourth cycle are presented in Fig. 4.22. The distance from the inlet, shown on the primary horizontal axis, was calculated using the distance between the centres of two consecutive planes. On the secondary horizontal axis in Fig. 4.22, the number of cross-sectional planes in stream-wise direction is shown, starting from the inlet of the artery model as shown in Fig. 4.19, where 0 and 36 refer to the inlet and outlet of the patient specific coronary artery model, respectively. The results show that slightly after the location of blockage, TKE reaches to its highest value for all phases,

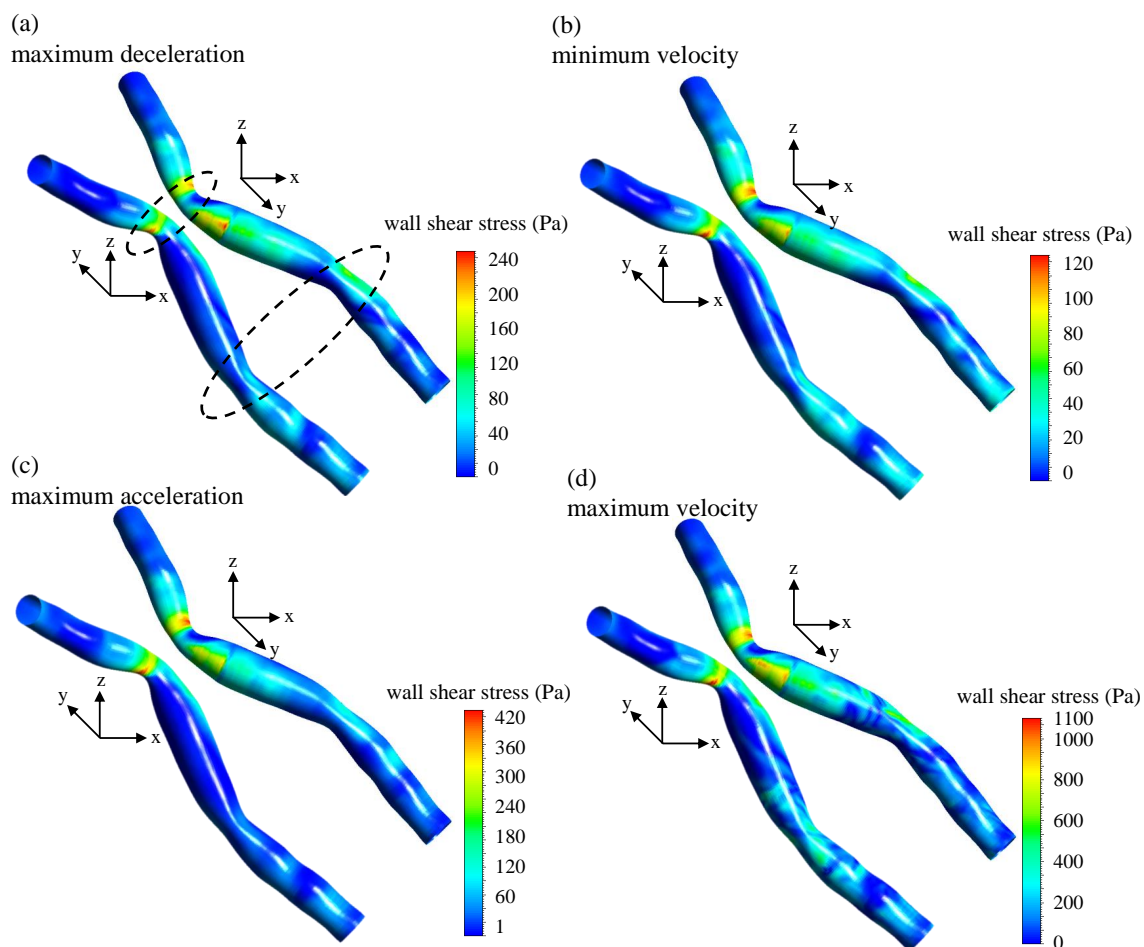


Figure 4.21: Two different views of wall shear stress contours for different phases of the third pulsation cycle for the hyperemic flow conditions.

which is in agreement with the findings for the idealised model, as shown in Fig. 4.8. At this location, the highest TKE is related to the phase with the highest velocity, i.e. maximum velocity phase and the lowest TKE is related to the minimum velocity phase, which can be explained based on the formation of the jet flow regime after the blockage, as discussed for the idealised model. There are two more regions in the patient specific artery model with high values of TKE before the flow re-laminarises. These regions are related to the two curved sections in the geometry model; near the blockage and further downstream, as displayed in Fig. 4.21a. These high TKE regions, due to curvature, are in agreement with the reported high values of TKE at the location of the curvature of aorta reported by Zhu et al. (2018). This phenomenon, is different from what was found earlier for the idealised coronary artery model as the idealised geometry does not include a curved section. It is worth mentioning that there is almost no turbulences at the inflow zone for all phases and the flow relaminarises downstream of the blockage section near the outlet of the geometry model (outflow zone).

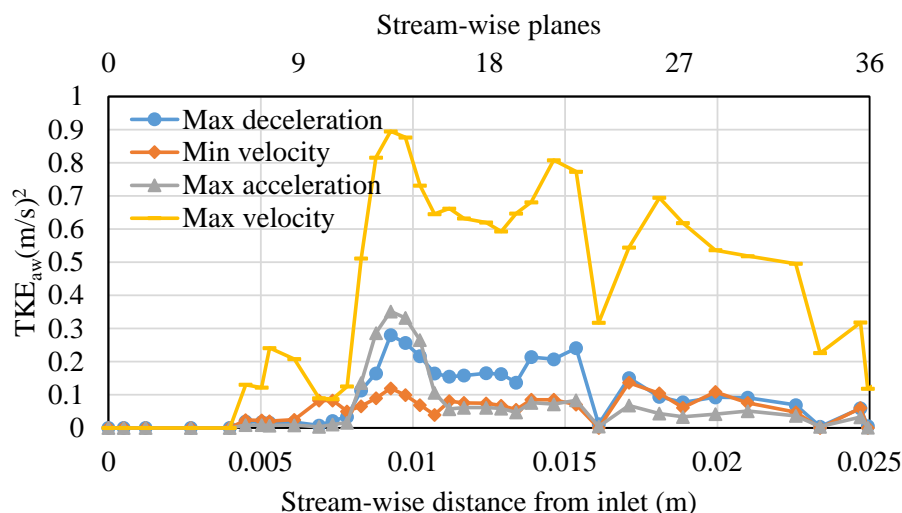


Figure 4.22: Area-weighted average of TKE for 35 different cross-sectional planes in stream-wise direction versus distance of the centre of planes from the inlet and plane numbers for different phases of the fourth pulsation cycle for the hyperemic flow conditions.

4.2.4 Conclusion

In this study, the pulsatile blood flow inside a set of stenosed coronary arteries was modelled and the effect of different asymmetric degrees of stenosis as well as different heart working conditions on the flow patterns and hemodynamic parameters, including pressure drop and wall shear stress, were investigated. Furthermore, area-weighted average TKE along the stream-wise direction was calculated to identify the transition from laminar to turbulent flow after the stenotic region. The computational model was validated against the published results in the literature.

A jump in the TKE profile was observed due to the formation of the turbulence strictures downstream of the stenosis starting from $5D$ downstream, where the jet flow effect due to cross section reduction is faded, to about $10D$, where the blood flow starts re-laminarisation. The location of the jump in TKE was found to be a function of the degree of stenosis and the heart working condition. It moves closer to the stenotic region by increasing the degree of stenosis as well as for the hyperemic flow condition. This region was accompanied with negative wall shear stress which shows the flow separation from the wall and formation of the recirculation zones which are susceptible locations for the formation of the second stenosis downstream of the first one. Furthermore, the results showed that based on the obtained wall shear stress results, the possible location of the second stenosis is not at the same side of the first one. The regions which are most susceptible to second stenosis are located at the opposite side of the first stenosis or at the side part of it both at downstream of it. The results of this study will assist cardiologists for determination of the susceptible locations after the stenotic region for the plaque growth.

For the severe stenosis model with the high degrees of stenosis, the heart needs to work harder to provide the same blood flow inside the arteries. Furthermore, the peak location of TKE due to turbulences moved closer to the stenosis at this condition. The same

trend was also seen for the hyperemic heart working condition. Based on the obtained results, for the more intense situations both in terms of degrees of stenosis and heart working conditions, the closer region after the first stenosis should be considered in terms of the possibility of the formation of the second stenosis. When the degree of stenosis is high, the heart needs to work harder and based on the results, the turbulences and recirculation zones get closer to the stenosis and increase the chance of the growth of the stenosis. However, it is interesting that for the high degree of stenosis case, there was no separation occurred downstream of the stenosis for the resting to moderate heart working condition. This clearly means that one way to have a medically stable condition for a patient suffering from high degrees of atherosclerosis is to prevent them from hyperaemia.

The obtained results of this study were found to be applicable for the patient specific coronary artery geometry. Since the patient specific arteries cannot exactly be classified as straight or curved arteries, there are some differences between the results of idealised straight artery model with the real geometry one. However, the trends, shown in results and discussion section, prove the applicability of the developed results for patient specific geometries, although there are some minor differences. The peak in the wall shear stress distribution and area-weighted average TKE is shown at the location of blockage of the patient specific coronary artery model that is the same as behaviour observed for an idealised geometry.

Acknowledgement

Financial support for the project has been provided by the Australian Government Research Training Program Scholarship. This work was supported with supercomputing resources provided by the Phoenix HPC service at the University of Adelaide.

References

- Arzani A (2020). “Coronary artery plaque growth: A two-way coupled shear stress-driven model”. *International Journal for Numerical Methods in Biomedical Engineering* 36.1, e3293.
- Biswas D, Casey D, Crowder D, Steinman D, Yun Y, and Loth F (2016). “Characterization of transition to turbulence for blood in a straight pipe under steady flow conditions”. *Journal of Biomechanical Engineering* 138.7, pp. 1–12.
- Cheng L, Wei GW, and Leil T (2019). “Review of quantitative systems pharmacological modeling in thrombosis”. *Communications in Information and Systems* 19.3, pp. 219–240.
- Cutnell JD, Johnson KW, Young D, and Stadler S (2015). *Physics, 10th Edition*. Wiley.
- Davies JE, Parker KH, Francis DP, Hughes AD, and Mayet J (2008). “What is the role of the aorta in directing coronary blood flow?” *Heart* 94.12, pp. 1545–1547.
- Doutel E, Viriato N, Carneiro J, Campos JBLM, and Miranda JM (2019). “Geometrical effects in the hemodynamics of stenotic and non-stenotic left coronary arteries—numerical and in vitro approaches”. *International Journal for Numerical Methods in Biomedical Engineering* 35.8, e3207.

- Flanigan DP, Tullis JP, Streeter VL, Whitehouse Jr. WM, Fry WJ, and Stanley JC (1977). “Multiple subcritical arterial stenoses: effect on poststenotic pressure and flow”. *Annals of Surgery* 186.5, pp. 663–668.
- Foucault E, Huberson S, Braud P, and Coisne D (2017). “On the pulsatile flow through a coronary bifurcation with stent”. *European Journal of Mechanics - B/Fluids* 61, pp. 177–186.
- Grist TM, Polzin JA, Bianco JA, Foo TK, Bernstein MA, and Mistretta CM (1997). “Measurement of coronary blood flow and flow reserve using magnetic resonance imaging”. *Cardiology* 88.1, pp. 80–89.
- Haynes RH (1960). “Physical basis of the dependence of blood viscosity on tube radius”. *American Journal of Physiology* 198, pp. 1193–1200.
- Jeong J and Hussain F (2006). “On the identification of a vortex”. *Journal of Fluid Mechanics* 285, pp. 69–94.
- Kefayati S and Poepping TL (2013). “Transitional flow analysis in the carotid artery bifurcation by proper orthogonal decomposition and particle image velocimetry”. *Medical Engineering & Physics* 35.7, pp. 898–909.
- Khair A, Wang BC, and Kuhn DCS (2015). “Study of laminar–turbulent flow transition under pulsatile conditions in a constricted channel”. *International Journal of Computational Fluid Dynamics* 29.9-10, pp. 447–463.
- Kohn JC, Lampi MC, and Reinhart-King CA (2015). “Age-related vascular stiffening: causes and consequences”. *Frontiers in Genetics* 6, p. 112.
- Li S, Chin C, Thondapu V, Poon EKW, Monty JP, Li Y, Ooi ASH, Tu S, and Barlis P (2017). “Numerical and experimental investigations of the flow–pressure relation in multiple sequential stenoses coronary artery”. *The International Journal of Cardiovascular Imaging* 33.7, pp. 1083–1088.
- Li ZY, Taviani V, Tang T, Sadat U, Young V, Patterson A, Graves M, and Gillard JH (2009). “The mechanical triggers of plaque rupture: shear stress vs pressure gradient”. *The British Journal of Radiology* 82 Spec No, S39–45.
- Liu B, Zheng J, Bach R, and Tang D (2015). “Influence of model boundary conditions on blood flow patterns in a patient specific stenotic right coronary artery”. *BioMedical Engineering OnLine* 14.Suppl 1, pp. 6–23.
- Lodahl CR, Sumer BM, and Fredsøe J (1998). “Turbulent combined oscillatory flow and current in a pipe”. *Journal of Fluid Mechanics* 373, pp. 313–348.
- Moreno C and Bhaganagar K (2013). “Modeling of stenotic coronary artery and implications of plaque morphology on blood flow”. *Modelling and Simulation in Engineering* 2013, p. 14.
- Moyle KR, Antiga L, and Steinman DA (2006). “Inlet conditions for image-based CFD models of the carotid bifurcation: is it reasonable to assume fully developed flow?”. *Journal of Biomechanical Engineering* 128.3, pp. 371–379.
- Nichols W, O’Rourke M, and Vlachopoulos C (2011). *McDonald’s blood flow in arteries, Sixth edition: Theoretical, experimental and clinical principles*. CRC Press.
- Ojha M, Cobbald RSC, Johnston KW, and Hummel RL (2006). “Pulsatile flow through constricted tubes: an experimental investigation using photochromic tracer methods”. *Journal of Fluid Mechanics* 203, pp. 173–197.
- Peterson SD and Plesniak MW (2008). “The influence of inlet velocity profile and secondary flow on pulsatile flow in a model artery with stenosis”. *Journal of Fluid Mechanics* 616, pp. 263–301.

- Plesniak MW and Bulusu KV (2016). “Morphology of secondary flows in a curved pipe with pulsatile inflow”. *Journal of Fluids Engineering* 138.10, p. 101203.
- Rotman OM, Zaretsky U, Shitzer A, and Einav S (2017). “Pressure drop and arterial compliance – Two arterial parameters in one measurement”. *Journal of Biomechanics* 50, pp. 130–137.
- Sakariassen KS, Orning L, and Turitto VT (2015). “The impact of blood shear rate on arterial thrombus formation”. *Future Science OA* 1.4, pp. 30–39.
- Jahangiri M, Saghafian M, and Sadeghi MR (2017). “Numerical simulation of non-Newtonian models effect on hemodynamic factors of pulsatile blood flow in elastic stenosed artery”. *Journal of Mechanical Science and Technology* 31.2, pp. 1003–1013.
- Tambasco M and Steinman DA (2003). “Path-dependent hemodynamics of the stenosed carotid bifurcation”. *Annals of Biomedical Engineering* 31.9, pp. 1054–1065.
- Torii R, Wood NB, Hadjiloizou N, Dowsey AW, Wright AR, Hughes AD, Davies J, Francis DP, Mayet J, Yang GZ, Thom SAM, and Xu XY (2009). “Fluid–structure interaction analysis of a patient-specific right coronary artery with physiological velocity and pressure waveforms”. *Communications in Numerical Methods in Engineering* 25.5, pp. 565–580.
- Usmani AY and Muralidhar K (2016). “Pulsatile flow in a compliant stenosed asymmetric model”. *Experiments in Fluids* 57.12, pp. 186–210.
- Valen-Sendstad K and Steinman DA (2014). “Mind the gap: impact of computational fluid dynamics solution strategy on prediction of intracranial aneurysm hemodynamics and rupture status indicators”. *American Journal of Neuroradiology* 35.3, pp. 536–543.
- Varghese SS, Frankel SH, and Fischer PF (2008). “Modeling transition to turbulence in eccentric stenotic flows”. *Journal of Biomechanical Engineering* 130.1, p. 014503.
- Waller BF (1989). “The eccentric coronary atherosclerotic plaque: morphologic observations and clinical relevance”. *Clinical Cardiology* 12.1, pp. 14–20.
- Womersley JR (1955). “Method for the calculation of velocity, rate of flow and viscous drag in arteries when the pressure gradient is known”. *The Journal of Physiology* 127.3, pp. 553–563.
- Young DF, Cholvin NR, and Roth AC (1975). “Pressure drop across artificially induced stenoses in the femoral arteries of dogs”. *Circulation Research* 36.6, pp. 735–743.
- Young DF and Tsai FY (1973). “Flow characteristics in models of arterial stenoses — I. Steady flow”. *Journal of Biomechanics* 6.4, pp. 395–410.
- Zhang JM, Luo T, Tan SY, Lomarda AM, Wong AS, Keng FY, Allen JC, Huo Y, Su B, Zhao X, Wan M, Kassab GS, Tan RS, and Zhong L (2015). “Hemodynamic analysis of patient-specific coronary artery tree”. *International Journal for Numerical Methods in Biomedical Engineering* 31.4, e02708.
- Zhu C, Seo JH, and Mittal R (2018). “Computational modelling and analysis of haemodynamics in a simple model of aortic stenosis”. *Journal of Fluid Mechanics* 851, pp. 23–49.

Chapter 5

Effect of shape of the stenosis on the hemodynamics of blood flow

5.1 Chapter overview

This chapter is built upon the knowledge developed in the previous chapter on the transitional flow behaviour inside a stenosed coronary artery model with an asymmetric shape. This chapter explores the effect of different shapes of the stenosis on the blood flow behaviour with a focus on its cross-sectional variations. As discussed in Section 2.2.2, the degree of stenosis is not the only indicator of the severity of coronary artery diseases, as the shape of the stenosis also plays an important role in the blood flow behaviour. For example, it is reported in the literature that for two models of stenosis with the same degree of stenosis, the one with a high level of eccentricity results in more severe atherosclerosis diseases compared to the case without eccentricity. Hence, investigation of the effect of the shape of the stenosis on the flow behaviour inside a stenosed coronary artery model is of great importance, as it helps to better understand the downstream flow behaviour and the impacted regions.

In this chapter, the effect of the shape of the stenosis on the transitional flow behaviour is investigated. As the cross-sectional shape of the stenosis varies significantly in practice, different shapes of the stenosis are investigated in this chapter including crescent, half-moon, elongated, oval, slit-like, and round. A computational fluid dynamics model is developed to simulate the pulsatile blood flow inside a stenosed coronary artery for different shapes of the stenosis with a similar degree of stenosis. The proper orthogonal decomposition (POD) method is also employed to identify the coherent structures downstream of the stenotic section for different shapes of stenosis. The transitional flow behaviour is also investigated by power spectra density (PSD) analysis.

The findings of this study show that the length of the jet region after the stenotic section depends on the shape of the stenosis. Furthermore, the results of instantaneous velocity and vorticity contours, Q-criterion, turbulent kinetic energy (TKE) contour, and PSD profiles show that eddies are formed after the dissipation of jet flow downstream of the stenosis. The formation of eddies in the downstream flow leads to transition to turbulence, which is accompanied with a jump in TKE profile. Moreover, the result of PSD analysis shows a jump in the level of energy spectra downstream of the stenotic

section, where the jet region dissipates. This jump is related to the frequency of vortex shedding for most of the stenosis shapes. In addition, from the POD analysis, it is shown that the contribution of TKE from the first few modes of POD depends on the shape of the stenosis.

The results of this study show that the shape of the stenosis influences the downstream flow behaviour considerably. For some shapes of the stenosis having a severe degree of stenosis results in less serious hemodynamic complications compared to the other shapes of the stenosis at the same degree of stenosis. This study shows that the clinical diagnosis of severity of a blockage inside the coronary arteries only based on its degree of stenosis without considering its cross-sectional shape will result in miscalculation of hemodynamic parameters.

5.2 Effect of shape of the stenosis

This section consists of the following submitted journal article:

Navid Freidoonimehr, Rey Chin, Anthony Zander, Maziar Arjomandi (2021). “Effect of shape of the stenosis on the hemodynamics of a stenosed coronary artery”. *Physics of Fluids*, under review.

The article is identical to its submitted format with the following exceptions:

- The numbering of figures, tables and equations have been altered to include the chapter number.
- The position of some figures and tables have been changed to improve legibility.

Statement of Authorship

Title of paper	Effect of shape of the stenosis on the transitional flow behaviour inside a stenosed coronary artery model
Publication Status	<input type="checkbox"/> Published <input type="checkbox"/> Accepted for Publication <input checked="" type="checkbox"/> Submitted for Publication <input type="checkbox"/> Unpublished and Unsubmitted work written in manuscript style
Publication Details	Freidoonimehr, N., Chin, R., Zander, A., and Arjomandi, M., "Effect of shape of the stenosis on the transitional flow behaviour inside a stenosed coronary artery model", Physics of Fluids, under review

Principal Author

Name of Principal Author (Candidate)	Navid Freidoonimehr		
Contribution to the Paper	Developed ideas, performed data analysis and interpreted results, wrote manuscript, and acted as corresponding author		
Overall percentage (%)	75%		
Certification:	This paper reports on original research I conducted during the period of my Higher Degree by Research candidature and is not subject to any obligations or contractual agreements with a third party that would constrain its inclusion in this thesis. I am the primary author of this paper.		
Signature		Date	15/02/2021

Co-Author Contributions

By signing the Statement of Authorship, each author certifies that:

- i the candidate's stated contribution to the publications is accurate (as detailed above);
- ii permission is granted for the candidate to include the publication in the thesis; and
- iii the sum of all co-author contributions is equal to 100% less the candidate's stated contribution

Name of Co-Author	Rey Chin		
Contribution to the Paper	Supervised the development of the research, participated in developing ideas and concepts, helped in interpretation of results, provided critical revision of manuscript.		
Signature		Date	15/02/2021

Name of Co-Author	Anthony Zander		
Contribution to the Paper	Supervised the development of the research, participated in developing ideas and concepts, helped in interpretation of results, provided critical revision of manuscript.		
Signature		Date	15/02/2021

Name of Co-Author	Maziar Arjomandi	
Contribution to the Paper	Supervised the development of the research, participated in developing ideas and concepts, helped in interpretation of results, provided critical revision of manuscript.	
Signature	Date	15/02/2021

Effect of shape of the stenosis on the hemodynamics of a stenosed coronary artery

Navid Freidoonimehr, Rey Chin, Anthony Zander, and Maziar Arjomandi

Abstract

The severity of coronary artery disease can be determined by the degree of stenosis and to a lesser extent by its shape. In this study, the effect of the shape of the stenosis on the flow transition in an artery is investigated. Different shapes of the stenosis including round, oval, elongated, half-moon, bean-shape, and crescent with and without eccentricity at a constant degree of stenosis (73%) are studied. A computational model, validated against the in-house Particle Image Velocimetry (PIV) experimental results, is used to investigate the flow behaviour. The results showed that the length of the jet region after the stenotic section varies significantly for different shapes of the stenosis. Based on analysis of Turbulent Kinetic Energy (TKE), Power Spectral Density (PSD), and the spectral entropy of stream-wise velocity fluctuations, it was shown that eddies are formed after the dissipation of jet flow downstream of the stenosis. It was also shown that the intensity of the velocity fluctuations differs for different shapes of the stenosis. Furthermore, using the Proper Orthogonal Decomposition (POD) method, it was shown that the shape of the stenosis has a significant impact on the downstream coherent structures. It was found that regardless of the degree of stenosis, specific shapes of the stenosis, such as round concentric, create less serious hemodynamic complications compared to the other shapes of the stenosis.

Keywords: cross-sectional shape; stenosis; coronary artery; proper orthogonal decomposition; turbulent kinetic energy; power spectral density; transition; pulsatile flow

5.2.1 Introduction

Coronary Artery Diseases (CADs) mainly occur because of the reduction in the cross section of blood vessels due to plaque formation, which may result in difficulties in blood delivery to different human organs. The blockage in a coronary artery, which is called stenosis, creates considerable pressure drop in an artery at the location of the constriction. The formation of stenosis also changes the flow pattern downstream of the stenotic section. Pressure drop is mainly due to the transitional flow downstream of the stenoses because of the changes in the flow patterns. The blood flow before the stenotic region of a coronary artery is mainly laminar due to low flow rate and changes to transitional flow after the stenosis due to the reduction in the artery cross section. This results in the formation of separation zones immediately after the stenosis. Therefore, it is of great importance to investigate the effect of stenosis on the pressure drop, flow patterns, potential separation zones, wall shear stress (WSS), and transitional flow behaviour.

Plaque geometric parameters, such as the shape and the eccentricity of the stenosis are

important parameters influencing flow behaviour and consequently pressure drop inside an artery. These parameters are used to categorise the plaque geometries. It was reported in the literature that not only the severity of a stenosis, but also the eccentricity of the lesion has a significant impact on the severity of CAD (Meier et al. 1983). While the lesions in real arteries are mostly eccentric, it was shown that for patients suffering from a high degree of stenosis in their carotid artery (70% and more), independent of other risk factors, an eccentric plaque can cause more severe cerebrovascular diseases compared to the patients with concentric stenoses (Ohara et al. 2008) .

The effect of stenosis eccentricity on the downstream flow behaviour has been investigated in the literature. A small eccentricity ($e = 5\%$) has been found to trigger post-stenotic transition to turbulence compared to the case without an eccentricity (Varghese et al. 2008). The jet flow, created after the stenosis, is more uneven on a plane with eccentricity compared to the other perpendicular plane. In another study by Javadzadegan et al. (2013), it was shown that increasing stenosis severity and lesion eccentricity can both increase flow recirculation and shear rate in the coronary arteries. The results presented by Guleren (2013) showed that an eccentric stenosis model with a triangular-like cross-section produces a larger pressure drop compared to a concentric model.

Apart from eccentricity, another important parameter for classification of a stenosis is the edge sharpness, which affects the flow characteristics, such as pressure drop (Usmani and Muralidhar 2016). The stenosis shape may have sharp edges. A longer recirculation zone and a higher pressure drop are reported by Young and Tsai (1973) for an asymmetric stenosis with a sharp edge compared to an axisymmetric one without a sharp edge. In a study conducted by Lorenzini and Casalena (2008), it was shown that the length of the consequent flow disturbance downstream of the stenosis is a function of the stenotic shape and height. The effect of stenosis geometry on hemodynamics was investigated by Caruso et al. (2015). They compared three different shapes of stenosis including parabolic, trapezoid and elliptical with the same degree of stenosis inside a right coronary artery and showed that a stenosis with an elliptical shape is characterised by areas with multi-directional velocity and high WSS. In a study of the flow through an asymmetric stenosis by Jabir and Lal (2016), it was shown that the velocity profiles are skewed towards the opposite side of the blocked part immediately after the asymmetric stenosis. In addition, a higher maximum shear rate and a larger recirculation zone were observed by Xie et al. (2018) in the models of the coronary arteries with a sharper stenosis shape. In a recent study by Freidoonimehr et al. (2020b), it was that the cross-sectional shape of a stenosis affects the pressure drop considerably. Furthermore, it was shown that the plaques with eccentricity and sharp edges result in a higher pressure drop compared to a stenosis with the same degree but without any eccentricity and sharp edges.

In summary, apart from the degree of stenosis, the shape of a stenosis also influences the hemodynamics of the flow inside a stenosed artery. The studies in the literature, so far, focusing on the effect of shape of stenosis on the flow behaviour, were mainly limited to a few variations of the shape of a stenosis, such as circular, trapezoid or elliptical. Different shapes of the stenosis are considered in this study with a constant degree of stenosis to isolate the effect of shape of the stenosis on the transitional flow behaviour. The level of flow transition is characterised using TKE, PSD and the spectral entropy analyses. POD analysis is also conducted to identify the most energetic coherent structures for different shapes of the stenosis. The results of this study contribute to a better understanding of the effect of a stenosis inside the coronary arteries and how it influences the downstream

flow behaviour.

5.2.2 Model geometry and computational methodology

Stenosed coronary artery model

A schematic diagram of a coronary artery model with different cross-sectional shapes of stenoses, with an identical degree of stenosis, is shown in Fig. 5.1. The cross-sectional shapes of stenosis considered in this study were round, oval, half-moon, bean-shape, elongated, and crescent, which were selected according to Waller (1989). Both concentric and eccentric shapes were considered for every cross-sectional shape. Eccentricity is defined as the bias from the center of a hosting artery to the center of a stenosis. It is worth mentioning that the half-moon and bean-shape cross-sectional shapes are not inherently concentric. However, due to the definition of the eccentricity and since the centroid of their cross-sectional shape is placed on the centreline of the cross-section of the artery, half-moon and bean-shape can be also considered as a concentric shape. In order to isolate the effect of the shape of the stenosis on the flow behaviour, all cases had a similar degree of stenosis of 73% representing a severe stenosis. In addition, an idealised coronary artery model with a circular cross section and straight length was considered in this study instead of a patient-specific geometry of the coronary artery which varies from one patient to another.

The coronary artery model was considered to be rigid in this study. This is a valid assumption, since the diseases related to the blockage of the coronary arteries mostly occur with ageing when the artery walls become harder and stiffer. It is widely discussed in the literature that arterial stiffness is a key arterial alteration during the ageing process (Benetos 2017; Mitchell et al. 2004; Sun 2015), which is recognised as a primary risk factor of all cardiovascular diseases (Kohn et al. 2015).

As shown in Fig. 5.1, to reduce the measurement errors and account for flow pulsation, the pipe length was extended from both ends with a $5D$ length before and a $20D$ length after the stenotic section, where D is the diameter of the coronary artery set at 3 mm (Freidoonimehr et al. 2020a; Peterson and Plesniak 2008). The extension of the artery length also facilitates the observation of the flow after the stenotic section including jet flow regime, separation and recirculation zones. The length of the stenotic section was $2D$ for all cases based on the clinical data, as it is reported that the plaque length in the coronary arterial system is in the range of $1D$ to $3D$ (Christiansen et al. 2017).

Computational modelling

ANSYS FLUENT 2020 R1 (ANSYS, Inc.) was employed to simulate the pulsatile blood flow inside the stenosed coronary artery model. In order to solve the governing incompressible Navier-Stokes equations, the SIMPLE pressure-velocity coupling method using a laminar solver was employed (Freidoonimehr et al. 2020a; Huang et al. 2009). The pressure and velocity components were spatially discretised using second order and second order upwind, respectively. For the transient formulation, second order implicit method was employed. The residual error convergence threshold was set at 10^{-6} . A time step

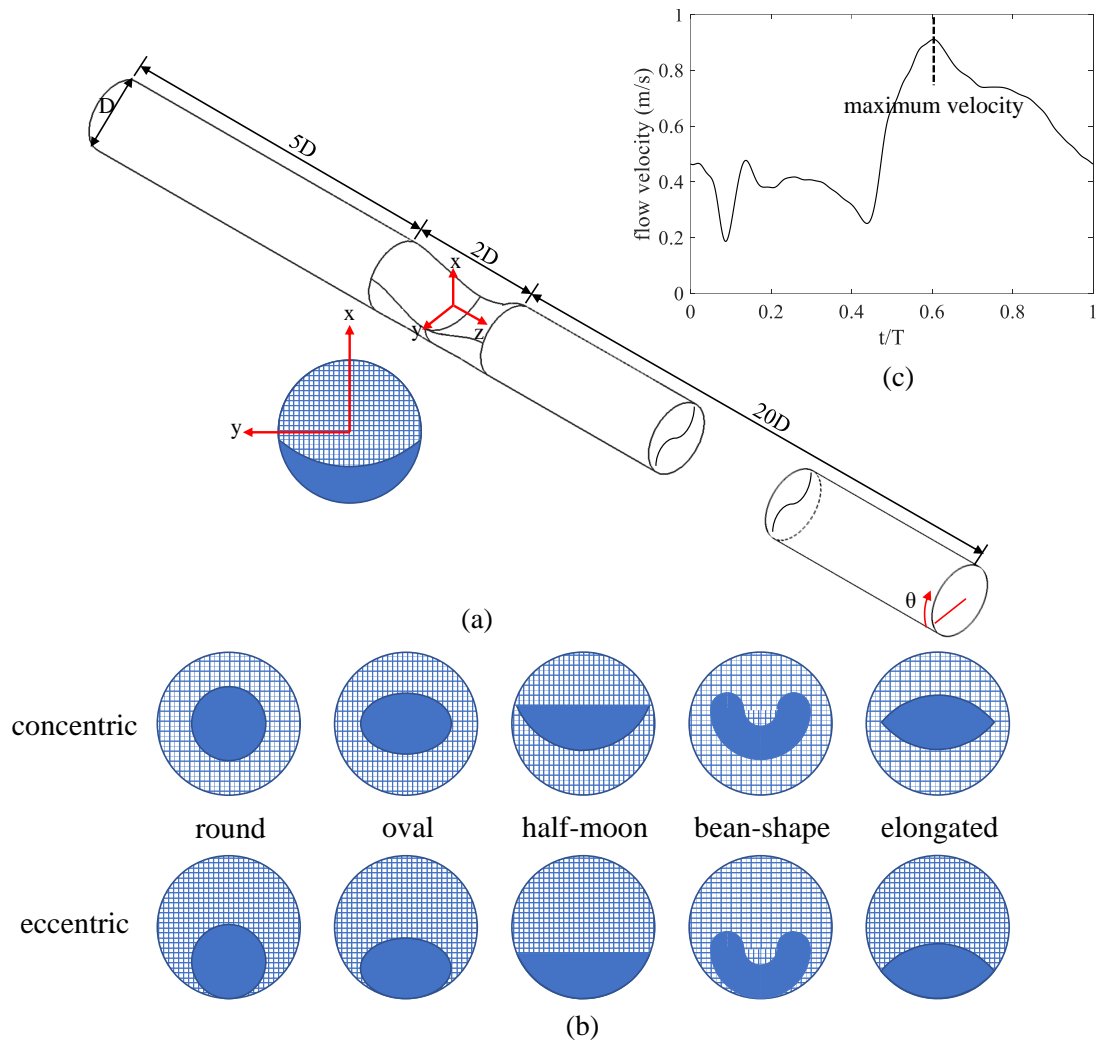


Figure 5.1: (a) A schematic of a stenosed coronary artery model with a crescent shape of the stenosis, (b) the other cross-sectional shapes of the stenosis investigated in the study and (c) the inlet time-dependent physiological left coronary artery flow velocity used for the simulation with the mean flow rate of 3.9 ml/s. All cross-sectional cases had a similar degree of stenosis of 73% representing a severe stenosis. The dashed vertical line in part (c) shows the maximum velocity phase in a cardiac cycle.

size of 10^{-5} s was selected such that the Courant number was much less than unity which means that fluid particles at most move from one cell to another within one time step.

A Womersley velocity profile (Womersley 1955) was employed as the inflow boundary condition to represent a fully developed pulsatile flow (Freidoonimehr et al. 2020a). The choice of the fully developed Womersley velocity profile at the inlet of an artery results in a good estimation of the time-dependent components of velocity in an artery, which are usually unavailable through clinical studies (Moyle et al. 2006). The inlet physiological time-dependent spatial mean velocity of the cross-section of the coronary artery was similar to the one employed in the previously published article by the authors (Freidoonimehr et al. 2020a) with a hyperemic flow condition, as shown in Fig. 5.1(c). At the hyperemic flow condition, the heart beats up to three times per second ($T = 0.33$) s (Joyner and Casey 2015; Kwasiborski et al. 2020) with a mean flow rate of 3.9 ml/s, as reported by Grist et al. (1997). The chosen time step and the cycle duration result in

33,000 time-steps for a cardiac cycle. Furthermore, a pressure outlet with a zero-pressure boundary condition and a no-slip boundary condition at the walls were considered.

In the present study, the blood was modelled as a Newtonian fluid. Despite the non-Newtonian behaviour of blood, it can be considered as a Newtonian fluid in special circumstances (Haynes 1960; Koeppen and Stanton 2018; Nichols et al. 2011; Jahangiri et al. 2017). As reported by Haynes (1960), blood behaves similarly to a Newtonian liquid in tubes with a large internal diameter (compared with the size of the red blood cells). It is shown that the viscosity of blood diminishes progressively as the diameter decreases to less than approximately 0.3 mm (Costa 2016). Hence, blood can be considered as a homogenous liquid with a viscosity that is independent of the velocity gradient in large arteries (Koeppen and Stanton 2018; Nichols et al. 2011). Furthermore, Cho and Kensey (1991) reported that the effect of non-Newtonian behaviour of the blood on the pressure drop across the artery is only significant for flows with a Reynolds number of less than 100. Since the Reynolds number inside the coronary arteries is larger than 100, the assumption of Newtonian fluid is justified. The mean Reynolds number in this study is defined as $Re = \frac{\rho Q D}{\mu A}$, where Q is the mean flow rate, $Q = 3.9$ ml/s, D and A are the diameter and area of the unobstructed cross-section of the artery, respectively. Based on the definition, the mean Reynolds number is 516. Moreover, as suggested by Costa (2016), Johnston et al. (2006), and Jahangiri et al. (2017), blood behaves as a Newtonian fluid at shear rates greater than 100 s^{-1} and considering that the shear rates applied to the coronary arteries are larger than 100 s^{-1} (Sakariassen et al. 2015), blood in the coronary arteries can be considered as a Newtonian fluid. Therefore, in this study, blood was modelled as a single-phase Newtonian fluid. The blood density, ρ , was set as 1060 kg/m^3 (Cutnell et al. 2015) and its kinematic viscosity, μ , to $0.0034 \text{ Pa}\cdot\text{s}$ (Li et al. 2017).

ANSYS ICEM CFD was employed for meshing the model using structured elements as they result in a faster convergence and a higher resolution compared with the unstructured mesh elements with the same number of elements. To prevent the numerical artefacts due to the presence of sharp edges, the defeaturing tolerance in ANSYS ICEM was set smaller than the details of the geometry at the sharp edges. For each case, a total number of 5 million elements was employed. 30 layers of mesh elements were used near the arterial wall with the thickness of closest layer to the wall of 10 microns and the growth rate of 1.2, as shown in Fig. 5.2. The stream-wise distance between two consecutive elements was set at 66 microns and the distance between two consecutive elements in circumferential direction was 100 microns. In order to ensure a smooth transition of the structured mesh elements at the location of the stenosis, the artery model was split into four bodies: upstream and downstream of the stenosis and two bodies at the location of the stenosis. In order to ascertain that the results are independent of the employed mesh structure, a convergence study on the required number of mesh elements was conducted. For example, for the crescent shape of the stenosis, the results show that the by changing the number of mesh elements, including 1.2, 3.8, 5, and 6.1 millions, the peak value of TKE changes to 0.274, 0.317, 0.344, 0.349 $(\text{m/s})^2$, respectively. Hence, the required mesh elements in this study were considered to be about 5 millions, since further increasing the number of mesh elements resulted in less than 1.5% change in the peak value of TKE. The time step size corresponding to each mesh independency case was also selected such that the Courant number was much less than unity which means that fluid particles move from one cell to another within one time step. It was ensured that using the employed mesh structure and time-step size, sufficient spatial and temporal resolutions were achieved

as the major energetic and dissipative frequencies were resolved. For example, for a Nyquist frequency of 50 kHz of the simulation, and the maximum mean velocity of 2.0457 m/s, the smallest length scale that can be resolved by the current mesh structure is approximately $L = \frac{W}{2\pi f} = 6.5 \times 10^{-6}$ m. In the lower velocity regions in the recirculation zones, the minimum spatial resolution becomes smaller with reduction of mean velocity. This minimum resolvable spatial resolution is three orders of magnitude smaller than the artery diameter. The length scale corresponding to the highest frequency of the flow ($f = 8.5$ kHz) is equal to $L = \frac{W}{2\pi f} = 3.8 \times 10^{-5}$ m. Hence, the minimum resolvable length-scale by this mesh structure is one order of magnitude smaller than the smallest length-scale of interest in the flow. Therefore, the choice of laminar flow solver with fine mesh structure and small time-step size helps to resolve the smallest length and time scales of interest and hence, the employed flow solver was capable of resolving the transitional behaviour of the flow.

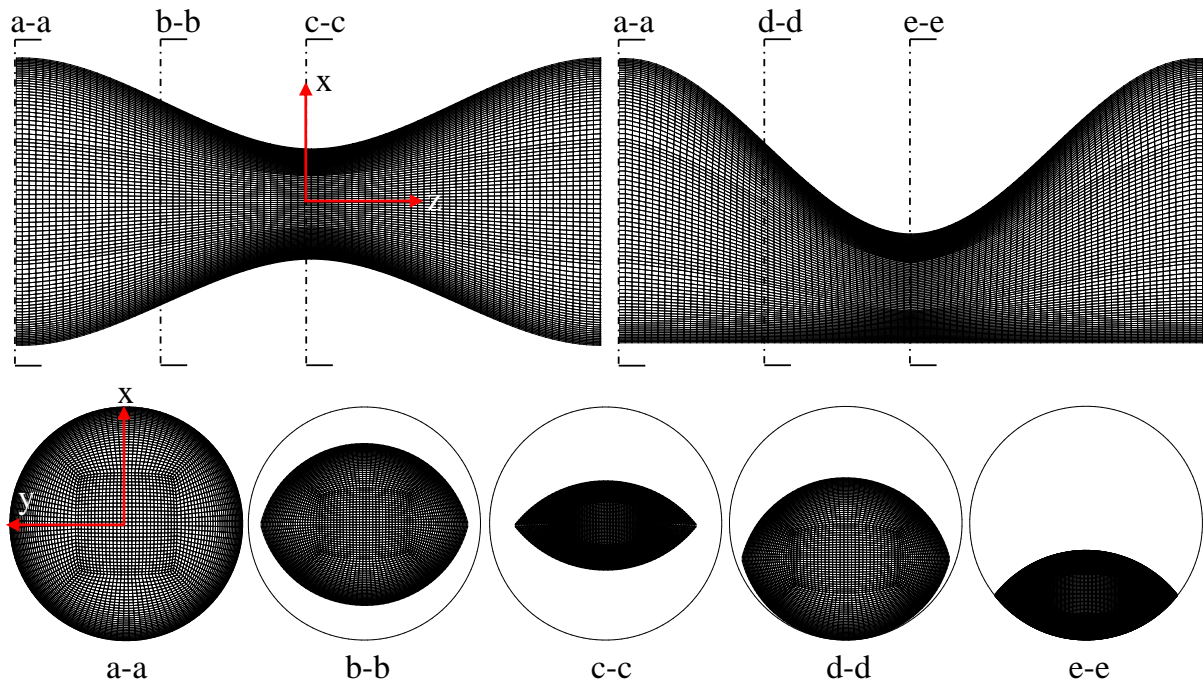


Figure 5.2: Structured mesh elements for stenosed coronary artery models with concentric and eccentric elongated shape of the stenosis in stream-wise and cross-sectional planes created using ICEM.

PIV validation of the model

In order to validate the developed computational model, a PIV experiment was conducted for a case of a stenosed artery model with an asymmetric shape of stenosis and 67% degree of stenosis. The geometry of the CFD model was modified based on the casted stenosed artery model to compare the computational results with the PIV experiments. Figure 5.3 shows a schematic of the coronary arterial test rig. To match the refractive index of the working fluid, Sylgard 184 silicone was used to cast the transparent artery model (Fig. 5.3). The internal diameter of the model was 6.1 mm which is almost twice the diameter of the coronary arteries. To limit the optical distortion, the stenotic section

was constrained by a rectangular silicone box. A mixture of 60 *wt%* distilled water and 40 *wt%* glycerine was used as a working fluid to match the blood viscosity.

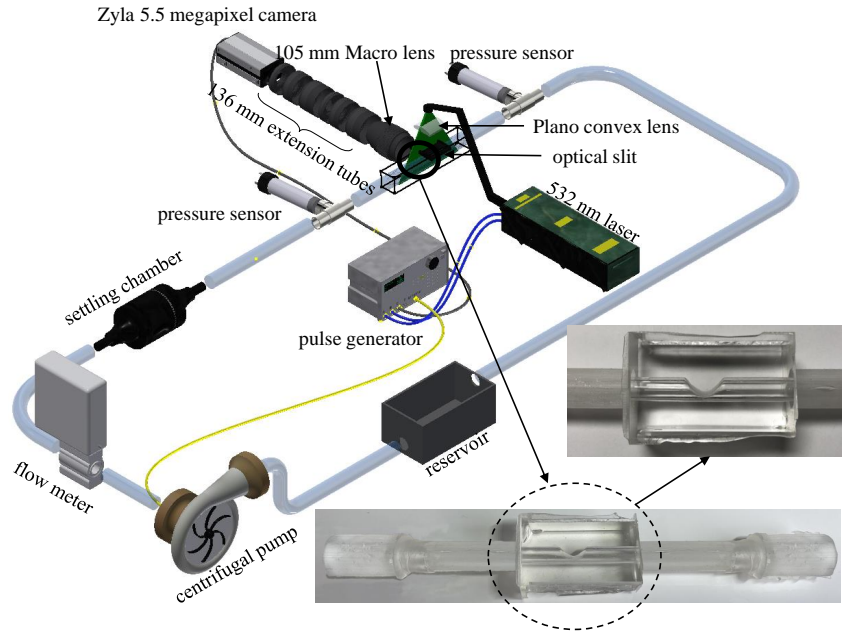


Figure 5.3: A schematic of the coronary arterial test rig showing the PIV setup and the cast stenosed coronary artery model.

A Zyla 5.5 sCMOS camera with a 5.5 mega-pixel resolution and a Sigma macro lens (105mm f2.8) along with 140 mm autofocus macro extension tubes were employed to focus on the region of interest. An EverGreen 532 nm and 200 mJ double-pulse laser at a fixed pulsing frequency of 15 Hz was used to illuminate the field of view. An adjustable optical slit was used to set the laser sheet thickness at 0.5 mm to minimise the out-of-plane loss of particle pairs. Two sets of 3-axis trimming platform linear stages were employed for camera and laser head to allow their precise positioning. Images were captured with an array of 2025×1350 pixels. The field of view for each measurement was set at 9.15×6.1 mm, which resulted in a pixel size of $4.52 \mu\text{m}$. The frame rate of the camera was set such to match the pulsing frequency of the laser.

The flow was seeded with hollow glass sphere (HGS) particles with a nominal mean diameter of 8-12 μm and a density of 1.1 g/cc resulting in a stokes number (Sk_D) of $Sk_D \ll 1$. This means that the particles followed the flow at all length scales which were required to be resolved during the PIV measurements. According to the pulsation frequency of the laser (15 Hz) and the duration of the cardiac cycle (4.4 s), 66 image pairs (16 bit) were recorded for each cardiac cycle. The images were recorded for 16 consecutive pulsation cycles (1056 image pairs). The image-processing was performed using PIVlab software (William Thielicke 2014) with two passes interrogation window sizes of 64×64 and 32×32 pixels with a 50% overlap for both passes, leading to a spatial resolution of 0.14 mm in each direction.

Figure 5.4 shows the comparison between the results from the developed computational model and the PIV results. Different timings between two images in a pair for PIV measurement were used for the jet flow regime (zone 1), recirculation zone (zone 2) and downstream flow (zone 3), which are distinguished by the dashed lines. The results show that the developed CFD model is able to accurately model the flow inside the stenosed

coronary artery model. The comparison of the velocity profiles at different stream-wise locations shows the average and maximum deviations of 2% and 9%, respectively. The small differences in the jet flow region is related to the difference between the stenosed artery model and the model used in CFD due to the fabrication constraints. The 3D-printed model of the stenosed artery was placed in the acetone vapour chamber to improve the quality of the surfaces. This resulted in a small reduction in the cross-section of the final cast artery model during fabrication, compared to the desired diameter. Hence, a small difference between the jet flow diameter was observed between the PIV data and the developed CFD model.

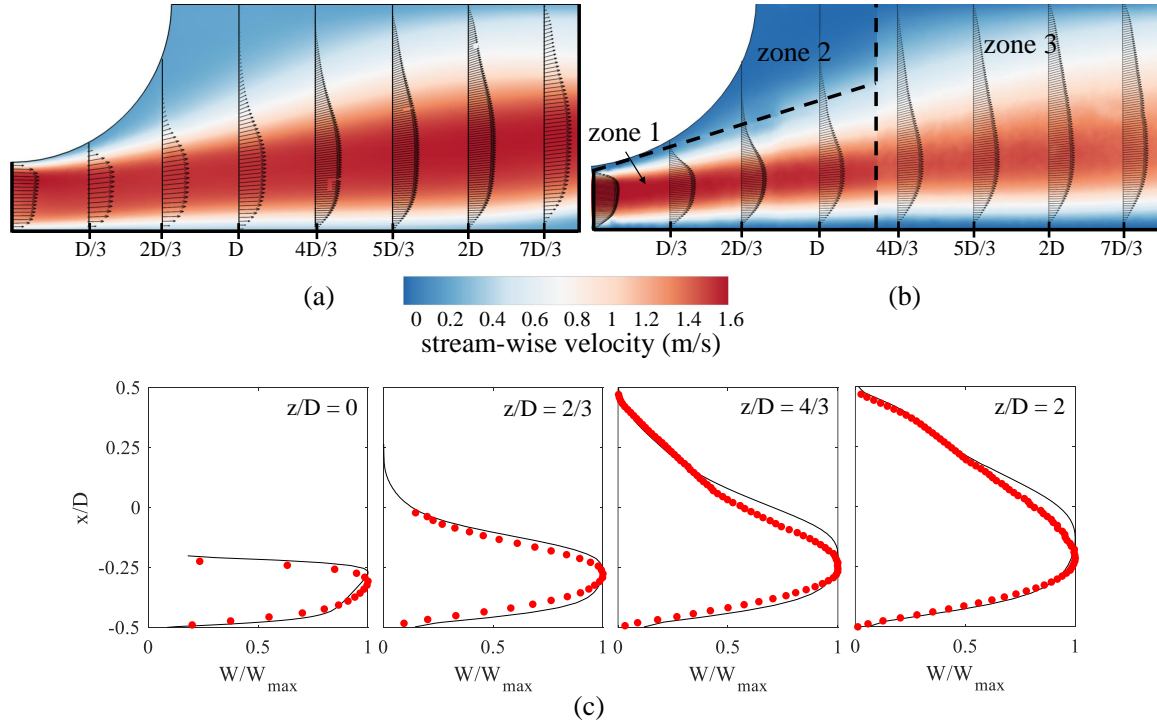


Figure 5.4: Comparison of the velocity contour and vectors obtained from a) developed CFD model and b) PIV experiment for a case with an asymmetric stenosis and 67% degree of stenosis at the mean flow rate of 115 ml/min and the physiological left coronary artery flow profile (Freidoonimehr et al. 2021). The zone 1 is the jet flow regime, zone 2 is the recirculation zone and zone 3 is downstream flow. Comparison of the velocity profiles of mean stream-wise velocity normalised by maximum stream-wise velocity obtained from CFD and PIV at four stream-wise distances is shown in part (c). The black solid lines show the CFD data and the red circular symbols show the PIV results.

TKE calculation

The flow transition inside the arteries can be characterised by a sudden increase in TKE. The benefit of using TKE over the other indicators in the assessments of the transition to turbulence is that TKE, as a scalar parameter, represents the velocity fluctuations in three directions in one parameter instead of using different parameters for different velocity directions. In order to calculate TKE for pulsatile flow problems, first of all, a phase-averaging technique was utilised to separate high frequency fluctuations from the

main low-frequency pulsatile fluctuations. The phase-averaged variables were calculated as:

$$f_{\langle pa \rangle}(x, y, z, t) = \frac{1}{N-1} \sum_{n=1}^{N-1} f(x, y, z, t + nT), \quad (5.1)$$

where f is a flow variable, including velocity components in different directions, $\langle pa \rangle$ subscript refers to the phase-averaged value and N is the number of pulsation cycles ($N = 4$). The simulation in this study was conducted for four cardiac cycles and the phase-averaging was performed over the last three cycles in order to eliminate the errors associated with the model initialisation. The number of cardiac cycles is in the range of most of the studies in the literature (Mahalingam et al. 2016; Molla et al. 2012). The literature shows that the magnitude of velocity fluctuations does not change significantly by increasing the number of cardiac cycles to more than four, although some minor variations can be expected. Furthermore, it was shown in a study by Andersson et al. (2017) that changing the number of cardiac cycles used for the calculation of WSS from 5 cycles to 80 cycles has almost no effect on the time-averaged WSS in an aortic coarctation. In addition, the turbulent WSS, which was calculated based on the rms difference between the instantaneous and phase-averaged WSS components, has a maximum deviation of about 11% for the case calculated using 5 cycles compared to 80 cycles. Moreover, as also acknowledged in the literature the number of cycles in the simulations is limited by the computational resources. Therefore, it is deemed that the number of cycles used in this study to investigate the effect of shape of the stenosis on the transitional flow behaviour is adequate and the obtained results are accurate. The velocity fluctuations were then calculated by subtracting the phase-averaged velocity components from the instantaneous values in a cycle, as:

$$f'(x, y, z, t) = f(x, y, z, t) - f_{\langle pa \rangle}(x, y, z, t), \quad (5.2)$$

The velocity fluctuations were calculated for the last three pulsation cycles using an in-house MATLAB code. Figure 5.5 demonstrates an example of the phase-averaging technique employed in this study. This figure shows the instantaneous, phase-averaged, and fluctuating stream-wise velocity component as a function of stream-wise distance for the case with the bean-shape concentric stenosis. TKE was calculated from the root-mean-square (RMS) of the velocity fluctuations given by $TKE(x,y,z,t) = \frac{1}{2}(\overline{(u')^2} + \overline{(v')^2} + \overline{(w')^2})$ where u' , v' and w' are the velocity fluctuations in different directions in a Cartesian coordinate system, as suggested by Jelly et al. (2020), Khair et al. (2015), Mittal et al. (2003, 2001), and Varghese et al. (2007).

Snapshot Proper Orthogonal Decomposition (POD) and spectral entropy

The snapshot POD, as a quantitative measure of instabilities and flow turbulence, was employed to identify the energetically dominant sets of eigenmodes for the flow inside the stenosed arteries with different shapes of the stenosis. POD was employed to decompose the spatio-temporal instantaneous or fluctuating velocity components to a set of orthogonal basis functions of space $\phi_k(x)$, POD (spatial) modes, and their time coefficients $a_k(t)$.

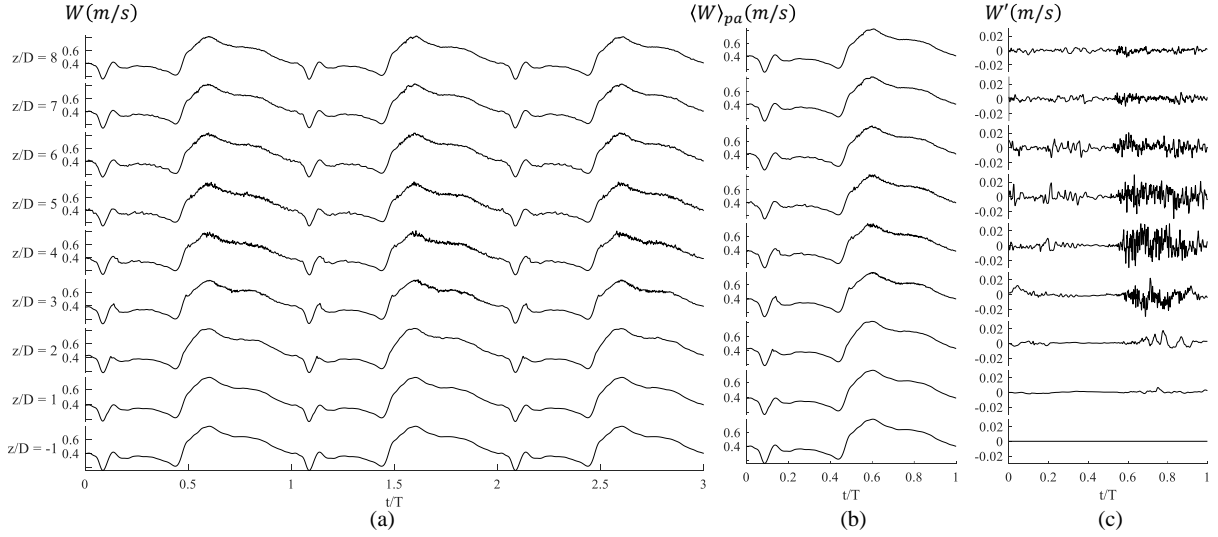


Figure 5.5: (a) Time history of the last 3 cycles of the instantaneous stream-wise velocity components as a function of stream-wise distance for pulsatile flow of the case with the bean-shape concentric stenosis, (b) phase-averaged stream-wise velocity component as a function of stream-wise distance, and (c) the fluctuating stream-wise velocity component as a function of stream-wise distance.

In this study, the stream-wise velocity fluctuating component ($w'(x, t)$) was used for POD analysis to further analyse the transition of the flow inside the stenosed artery models:

$$w'(x, t) = \sum_{k=1}^{\infty} a_k(t) \phi_k(x), \quad (5.3)$$

In the above equation, $\phi_k(x)$ and $a_k(t)$ show the spatial and temporal modes of the flow, respectively. The temporal mode is the series of modal amplitudes corresponding to the change in fluctuating velocity over time (Kefayati and Poepping 2013). The stream-wise fluctuating velocity component ($w'(x, t)$) was calculated using phase-averaging technique, as explained in the TKE calculation section. In this study, the snapshot POD was used, as it is more suitable compared to the conventional POD for analysing large data sets such as CFD or PIV data (Weiss 2019). More details on snapshot POD can be found in Weiss (2019) and Taira et al. (2020).

Spectral entropy is a measure of the flow state and turbulence level, as suggested by Abdelsamie et al. (2017). This parameter, which is obtained from calculating the eigenvalues of the temporal autocorrelation function is employed in this study to directly evaluate the flow transition behaviour after the stenotic sections for different shapes of the stenoses. To calculate spectral entropy, the relative energy of each mode needs to be calculated using the corresponding eigenvalue (λ_k), as (Janiga 2019a; Janiga 2019b; Voss et al. 2018):

$$E_k = \frac{\lambda_k}{\sum_{j=1}^M \lambda_k}, \quad (5.4)$$

where M is the number of modes retained in the analysis. The spectral entropy (S_d) is

hence determined as:

$$S_d = - \sum_{k=1}^M E_k \ln E_k, \quad (5.5)$$

The minimum value of spectral entropy ($S_d = 0$) shows the cases in which the original signal carries only one mode, which means the flow is steady. On the other hand, the maximum value of spectral entropy is achieved for the cases where the energy is equally distributed over all of the retained modes. Hence, in this case, all eigenvalues are equal to each other. In this study, for the calculation of spectral entropy, the eigenvalues were obtained from the snapshot POD for the stream-wise instantaneous velocity component on different stream-wise cross-sectional planes.

Power Spectral Density (PSD)

Energy spectral analysis can provide an additional information about the flow disturbances downstream of the stenosis. The Power Spectral Density (PSD) shows the strength of the velocity fluctuations as a function of frequency. In this study, PSD, S_{ww} , of the stream-wise velocity fluctuation is presented as a function of the Strouhal number. The stream-wise velocity fluctuation is calculated based on the method explained in Eq. 7.2. The Strouhal number is defined as:

$$St = \frac{f D_h}{w_p} \quad (5.6)$$

where f is the frequency of the fluctuations, D_h is the hydraulic diameter of the stenosis throat, and w_p is the cross-sectional averaged velocity at the location with the minimum diameter (jet velocity). D_h is defined as $D_h = 4A(1 - S)/P$, where A is the artery cross-sectional area, S is degree of stenosis, and P is the wetted perimeter of the stenosis cross-section, which varies for different shapes. In addition, w_p was derived from mass conservation as $w_p = W/(1 - S)$, where W is the mean inlet velocity. It is shown that D_h and w_p are appropriate scaling parameters for the spectra because the transition to turbulence in the downstream section is initiated by the stenotic jet velocity (Varghese et al. 2007). The PSD of velocity fluctuations was calculated using the *pwelch* function in MATLAB. The frequency resolution of the spectra, based on the *pwelch* function, was $2\pi/256 = 0.0245$ rad/sample. The signal was split into 20 overlapping data segments with a 50% overlap between the segments. Then, the 20 overlapping data segments were windowed using the Hann window. The velocity signal was obtained at a sampling rate of 100 kHz (every time-step), which was then low-pass filtered at a Nyquist frequency of 50 kHz.

5.2.3 Results and discussion

Mean and instantaneous flow characteristics

Mean stream-wise velocity contours for different shapes of the stenosis are presented in Fig. 5.6. The mean values were calculated as the time-average of the stream-wise velocity component through the entire time domain. It is evident that for all different shapes of stenosis, the jet flow starts at the throat of the stenosis and at this location, the flow reaches its maximum velocity (about 2.5 m/s). The length of the jet flow varies significantly for different shapes of the stenosis. The longest jet is formed for the round concentric shape of the stenosis. For this shape, the jet region is surrounded by a symmetric vortex tube at a lower velocity. The locations where the jet flow dissipates and the eddies are formed are shown with a plus sign in Fig. 5.7. The recirculation zones with reverse flow (negative flow velocity in stream-wise direction) were observed in all cases around the jet region with separation initiating at the edges of the stenosis. The stronger the jet, the stronger the reverse flow. This means that further downstream of the stenotic section, where the jet flow starts to diminish, the recirculation zones are weakened. The second longest jet flow is for the crescent shape of the stenosis. For the crescent shape, the jet flow starts at the throat of the stenosis and continues further downstream to the opposite side of the stenosis. The results show that the shortest jet flow is related to the bean-shape concentric stenosis in which the jet flow diminishes at about $4D$ downstream of the stenosis, and the second shortest jet flow length is for the half-moon concentric shape.

Figure 5.7 shows the instantaneous stream-wise velocity contours at the maximum velocity phase in the fourth pulsation cycle for different shapes of stenosis. The instantaneous velocity for the maximum velocity phase at the location of stenosis is about 1.8 times higher than the mean velocity at the same location. The instantaneous velocity distributions follow similar patterns to the mean velocity in all cases. However, the difference between the mean and instantaneous velocity contours appears at the locations where the jet flow weakens. The disturbances in the stream-wise velocity component grow after the dissipation of the jet flow. Eddies are formed after the dissipation of jet flow downstream of the stenosis, where the eddies start to grow and the intensity of eddies differs for different shapes of the stenosis. For example, the closest distance from the centre of stenosis where the eddies start to grow is about $z/D = 5$ which is related to the cases of half-moon concentric and bean-shape concentric. The farther distance is related to the oval concentric and crescent shapes of the stenosis in which the eddies start at about $z/D = 10$. After the formation of the eddies, they move farther downstream and after that, flow starts to relaminarise. This means that the velocity profiles regain their parabolic shape similar to the upstream of the stenosis. The relaminarisation distance can take up to the outlet of the model which also varies for different shapes of the stenosis.

In order to visualise the cross-sectional shape of the jet flow and eddies for different shapes of the stenosis, Fig. 5.8 presents the instantaneous cross-sectional velocity contours at different stream-wise distances. The velocity contours at immediate downstream of the stenotic section, $z/D = 1$, are dominated by the jet flow which has a similar shape to the stenosis shape. At $z/D = 3$, the cross-sectional velocity is still dominated by the jet flow with lower velocity values for all shapes of the stenosis. The cross-section of the artery model at this stream-wise distance also has regions with negative velocity values

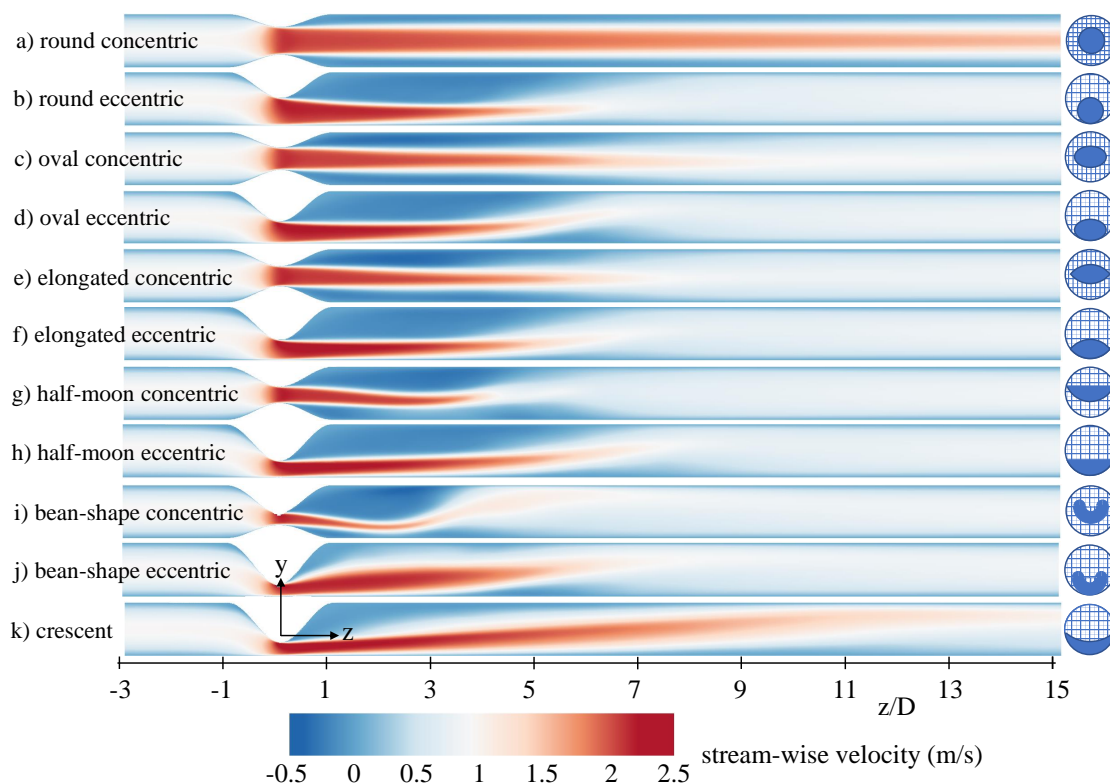


Figure 5.6: Mean stream-wise velocity contours in $y - z$ plane with $x = 0$ for different shapes of stenosis including a) round concentric, b) round eccentric, c) oval concentric, d) oval eccentric, e) elongated concentric, f) elongated eccentric, g) half-moon concentric, h) half-moon eccentric, i) bean-shape concentric, j) bean-shape eccentric, and k) crescent.

which are due to the reverse flow created after the stenotic sections. Farther away from the stenotic section, $z/D = 5$, the jet flow is dissipated for most of the shapes of the stenosis and the cross-sections of the artery models are covered with the eddies formed after the jet regions are disappeared. The dissipation of the jet region and formation of the eddies are also shown in Fig. 5.7. It is worth mentioning that for the oval concentric and crescent shapes of the stenosis, the jet region is still present at this stream-wise distance.

Contours of instantaneous stream-wise vorticity magnitude for the concentric and eccentric half-moon shape of the stenosis are presented in Fig. 5.9. As the vorticity distributions of most of the shapes are similar, the vorticity contour is only presented for the half-moon shape. The results show two regions with strong shear layers, identified by a higher vorticity, initiating from the edges of the stenosis in concentric shapes, and edge of the stenosis and the opposite wall in eccentric shapes. The vorticity magnitudes of the eccentric shapes are stronger compared to the similar concentric shapes. Furthermore, the regions with a higher vorticity are placed at the locations surrounded by the jet regions. Farther downstream of the stenotic section, where the jet region is vanished, the shear layers dissipate and hence, the level of vorticity of the flow drops.

The pressure drop inside the stenosed artery models with different shapes of the stenosis and a constant degree of stenosis is presented in Fig. 5.10. The presented values correspond to the maximum velocity phase in the fourth pulsation cycle. The pressure drop of the concentric shapes of the stenosis is lower compared to the similar eccentric

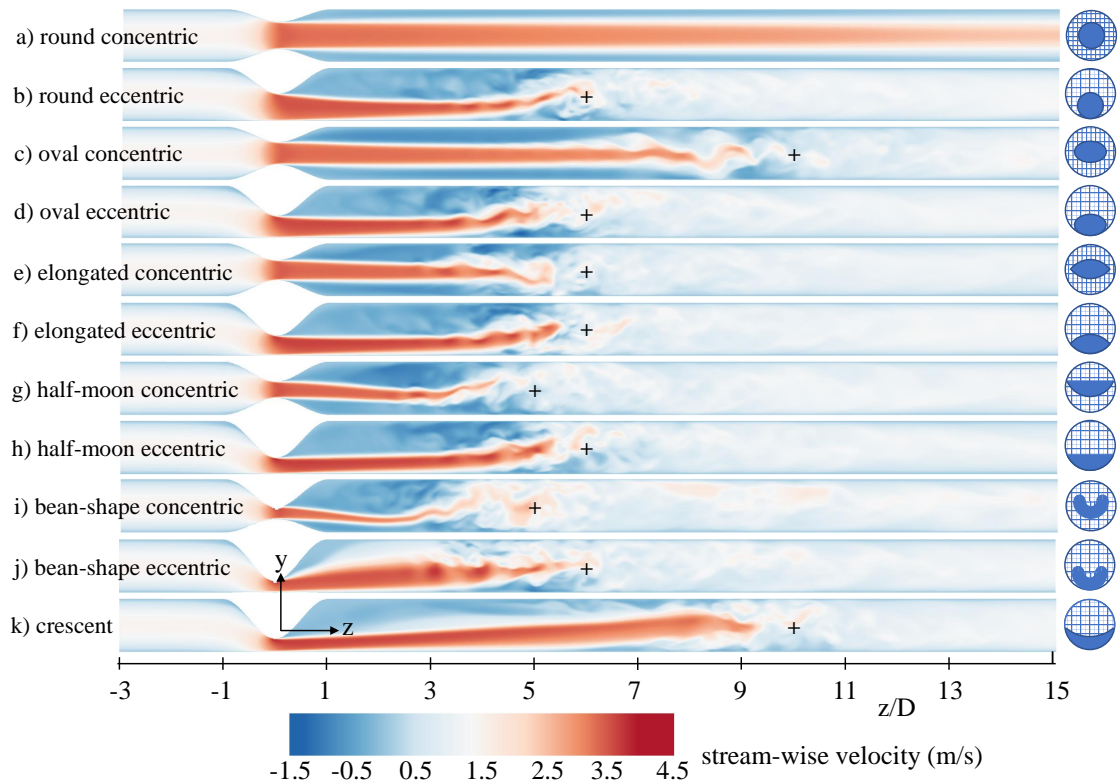


Figure 5.7: Instantaneous stream-wise velocity contours at the maximum velocity phase in the fourth pulsation cycle in $y - z$ plane with $x = 0$ for different shapes of stenosis including a) round concentric, b) round eccentric, c) oval concentric, d) oval eccentric, e) elongated concentric, f) elongated eccentric, g) half-moon concentric, h) half-moon eccentric, i) bean-shape concentric, j) bean-shape eccentric, and k) crescent.

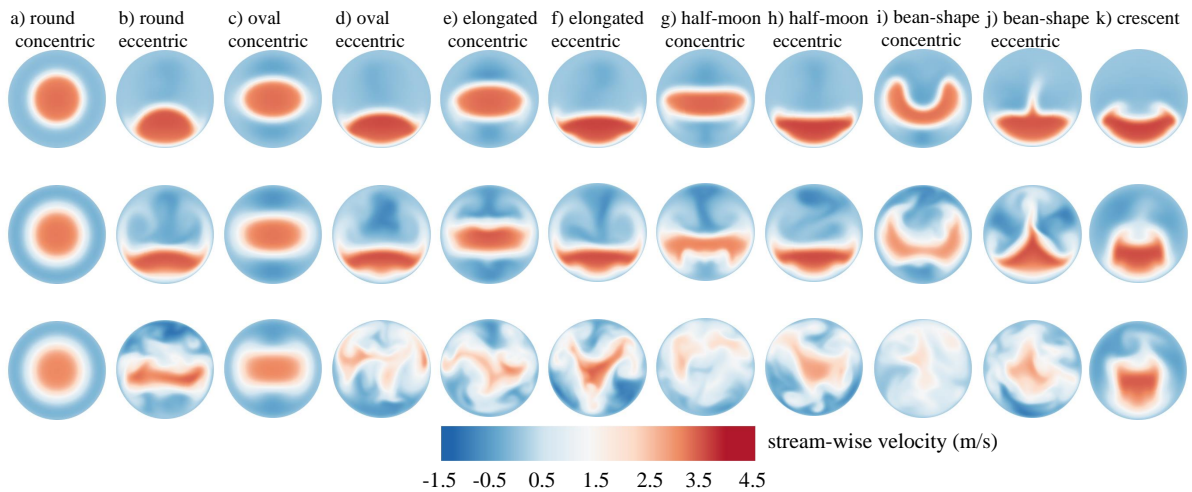


Figure 5.8: Instantaneous cross-sectional velocity contours in $x - y$ plane at different stream-wise distances, $z/D = 1$ (first row), $z/D = 3$ (second row), and $z/D = 5$ (last row), at the maximum velocity phase in the fourth pulsation cycle for different shapes of stenosis including a) round concentric, b) round eccentric, c) oval concentric, d) oval eccentric, e) elongated concentric, f) elongated eccentric, g) half-moon concentric, h) half-moon eccentric, i) bean-shape concentric, j) bean-shape eccentric, and k) crescent.

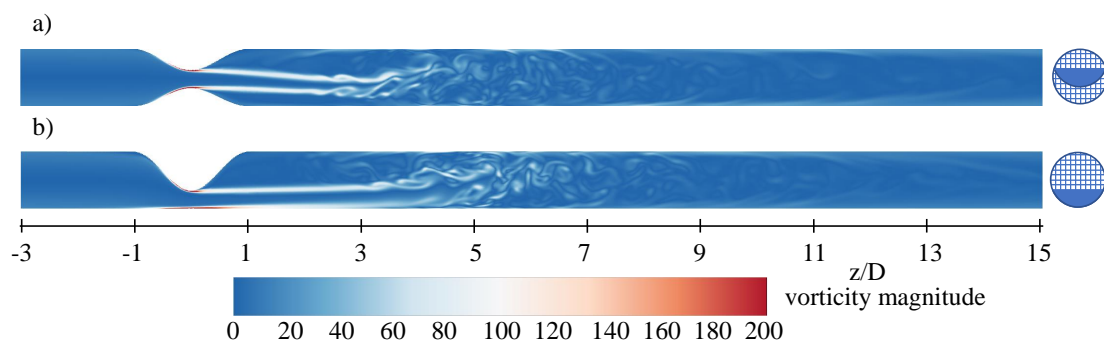


Figure 5.9: Instantaneous stream-wise vorticity magnitude contours normalised by W_i/D at the maximum velocity phase in the fourth pulsation cycle for a) concentric and b) eccentric half-moon shape of stenosis. W_i is the mean inlet velocity.

shapes. This means that the eccentricity of the stenosis for all shapes results in a higher pressure drop. Furthermore, the lowest pressure drop is observed for the shape of the stenosis without sharp edges (round shape). The highest values of pressure drop is related to the cases with sharp edges, with the highest pressure drop for the half-moon shape and the second highest for the crescent shape. The observed effects of the shape of the stenosis on pressure drop are in agreement with the experimental measurements by Freidoonimehr et al. (2020b).

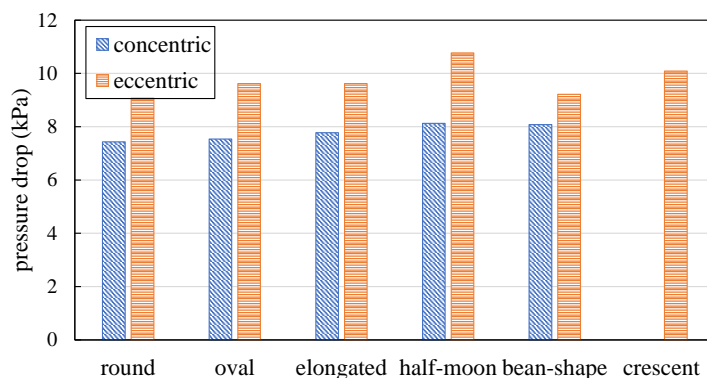


Figure 5.10: Pressure drop along the length of the artery model at the maximum velocity phase in the fourth pulsation cycle for different shapes of stenosis.

Turbulence statistics

In order to better characterise the flow structures and transition in the post-stenotic flow field for different shapes of the stenosis, Figs. 5.11 and 5.12 show the TKE distributions inside the stenosed artery models with different shapes of stenosis. TKE can be employed to determine the level of flow transition. In the context of the flow inside the stenosed coronary artery models, the flow is initially laminar upstream of the stenosis with a TKE equal to zero. As the flow passes through the stenotic section, the flow becomes unstable and the eddies start to form leading to an increase in the TKE. Therefore, the transitional flow behaviour appears with a jump in the TKE. Further downstream of the stenotic section, where the eddies break up, the flow is relaminarised, and consequently, TKE decays. The production and dissipation of TKE or the conversion between these

two determine the mechanical energy loss or pressure drop. The resultant pressure drop which is affected by flow transition across the stenosis is used in hospitals to diagnose the stenosis (Choi et al. 2018). Figure 5.11 presents the TKE contours in a stream-wise plane with $x = 0$. The results show that the non-zero TKE regions are located downstream of the stenotic section, where the jet flow initiated at the centre of stenosis is dissipated. The TKE distribution for the round concentric shape of the stenosis remains almost equal to zero throughout the artery. As also displayed in Figs. 5.6, 5.7, and 5.8, the flow remains laminar for this case throughout the artery and hence no transition occurs downstream of the stenotic section.

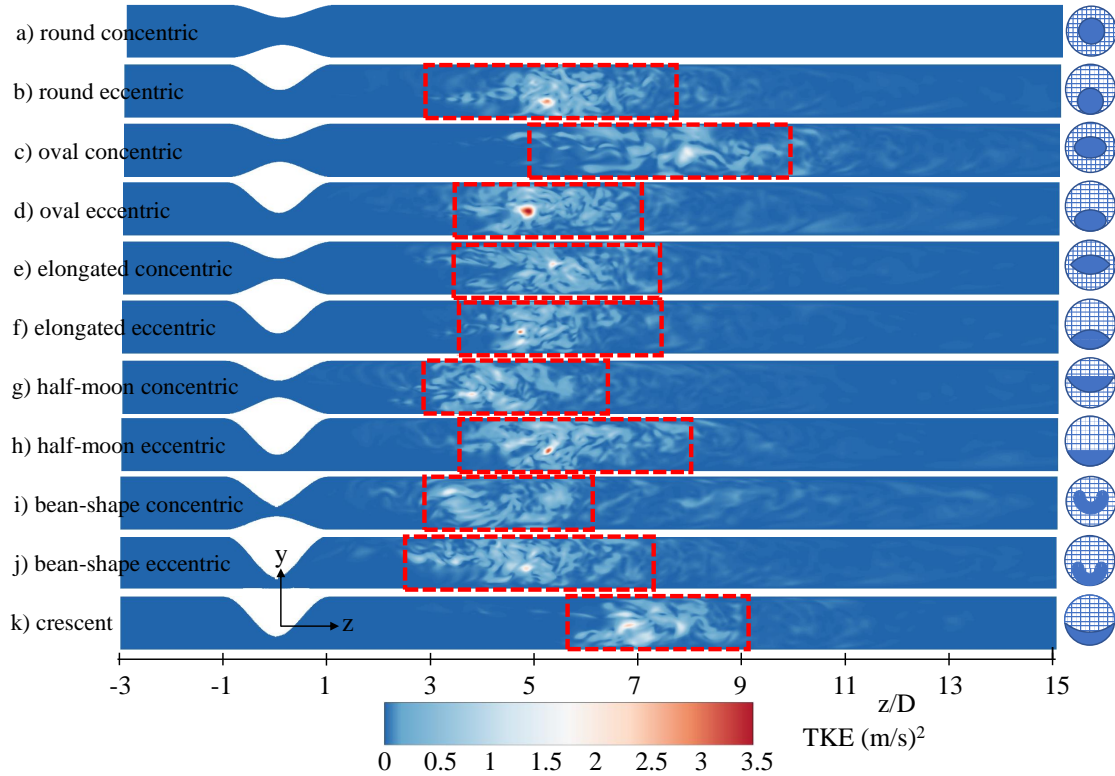


Figure 5.11: TKE contours in $y - z$ plane with $x = 0$ for different shapes of stenosis including a) round concentric, b) round eccentric, c) oval concentric, d) oval eccentric, e) elongated concentric, f) elongated eccentric, g) half-moon concentric, h) half-moon eccentric, i) bean-shape concentric, j) bean-shape eccentric, and k) crescent. The red dashed boxes show the regions of maximum TKE.

Figure 5.12 presents the area-averaged TKE values including the mean value (Fig. 5.12(a)) and maximum value (Fig. 5.12(b)) the for a cardiac cycle for different cross-sectional planes at different stream-wise distances. It is shown that TKE has the highest value at the stream-wise distance where the jet flow is dissipated and the eddies are formed. After that, the magnitude of TKE is reduced which is accompanied by the flow relaminarisation. The stream-wise location of the peak values of TKE is at the location where the jet flow is dissipated. The highest value of maximum TKE is related to the crescent and half-moon eccentric shapes. The level of TKE for the round concentric shape of the stenosis agrees with the findings of the previous figures in which no flow transition was observed. The results of maximum TKE value show a similar trend as the results of mean TKE value. However, the magnitude TKE of the maximum value is about one order of magnitude larger than its mean value.

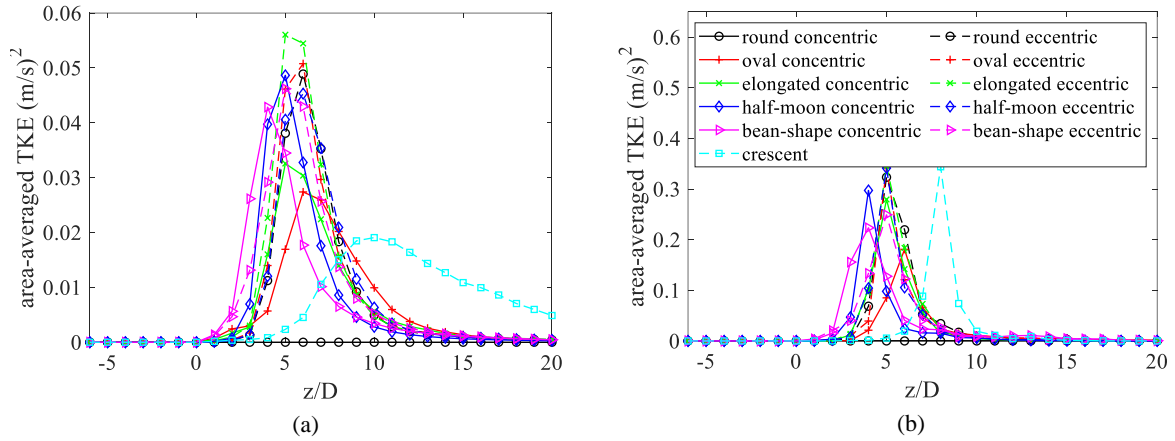


Figure 5.12: Area-averaged TKE for different cross-sectional planes in stream-wise direction with a consecutive distance of D for a) mean value and b) maximum TKE values in a cardiac cycle for different shapes of stenosis. $z/D = 0$ is the location of stenosis centre.

POD analysis

POD analyses of the transitional flow inside the stenosed artery models with different shapes of the stenosis are presented in Figs. 5.13 and 5.14. Note that the round concentric shape of the stenosis is not shown as no transitional flow was observed for this case based on the results of the previous sections (Fig. 5.11). Figure 5.13 shows the first two spatial POD modes of stream-wise fluctuating velocity component for different shapes of the stenosis. The modes are ranked based on their contribution to the total kinetic energy of the flow. Only the first two modes which have a larger contribution to the TKE are shown. For example, the first mode of the transitional flow inside the artery with the crescent stenosis shape contributes 24% to the total TKE of the flow, while the second spatial mode of the flow contributes 7.3%. The first two POD modes for all cases show the presence of structures resembling vortices in the flow. There are patches with opposite signs in the flow (shown in orange and blue colours) after the stenosis for all cases which demonstrate that the fluctuating stream-wise velocity components in these areas are anti-correlated. When the fluctuating velocity moves up in the orange zone, it tends to move down in the blue zone and vice versa. These patches in the flow are located where the jet region ends and the flow transition occurs. It is observed that the coherent structures for oval and elongated concentric cases are stretched longitudinally, while for the other cases, these correlated and anti-correlated structures are mainly skewed towards the artery wall and located after the jet dissipation.

Figure 5.14 shows the contribution to the TKE of the first ten spatial POD modes for different shapes of the stenosis. The larger contribution to TKE from the first POD modes indicates a less complex transitional flow. For example, it can be seen that for the half-moon concentric shape of the stenosis, the contribution of the first mode to TKE is 35.2%. The second mode contributes 9.3% and the contribution from the higher modes diminishes slowly. This indicates that a large portion of the total stream-wise fluctuations of the flow is well represented by the first mode, whereas the remaining fluctuations of the flow are spread among the higher modes. Hence, considering the first few modes in the less complex flow is usually sufficient to identify the dominant coherent motions. However, there are some cases which need a larger number of modes for

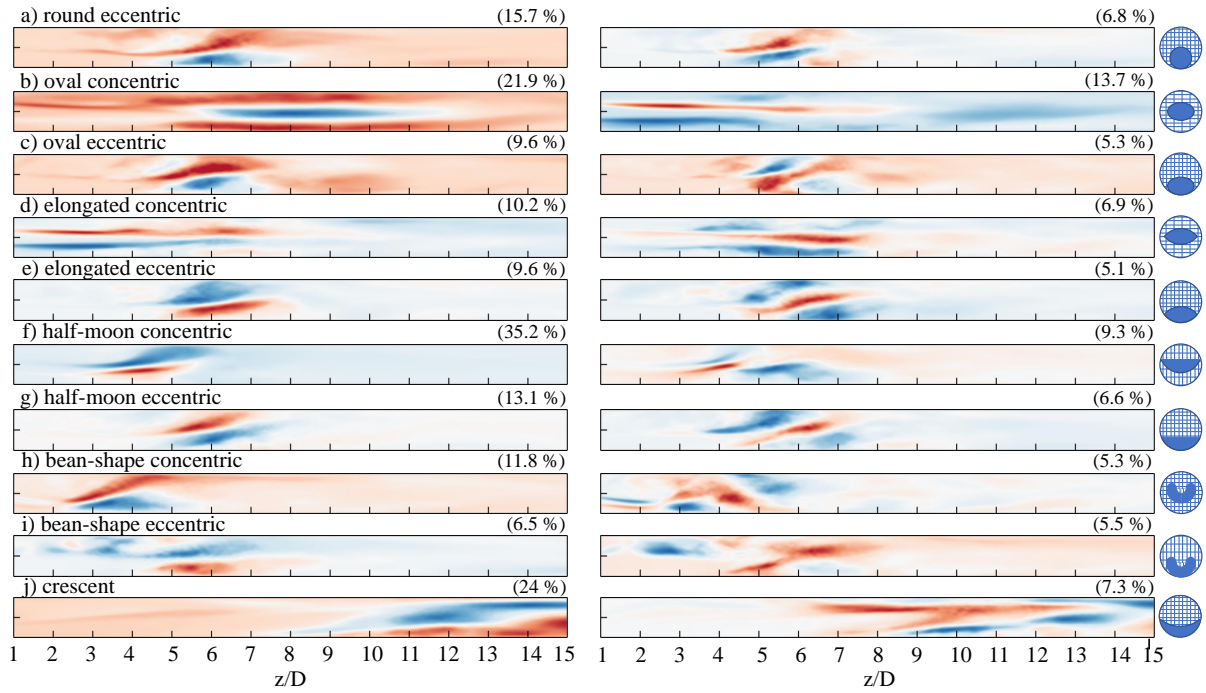


Figure 5.13: First two POD modes of stream-wise velocity fluctuating component in $y - z$ plane with $x = 0$ starting at $z/D = 1$ for different shapes of stenosis including a) round eccentric, b) oval concentric, c) oval eccentric, d) elongated concentric, e) elongated eccentric, f) half-moon concentric, g) half-moon eccentric, h) bean-shape concentric, i) bean-shape eccentric, and j) crescent. The vertical axis is the artery diameter in $y - z$ plane. First mode is shown on the left and the second mode is shown on the right. The percentage in the parenthesis on top of each contour shows the contribution to the TKE of each mode. In the contour plots of modes 1 and 2, regions with orange (positive) and blue (negative) colours are with opposite sign.

identification of the dominant coherent structures and flow reconstruction. For example, for the case with a bean-shape eccentric stenosis, the first POD mode contributes 6.5% and the second mode contributes 5.5% to the total TKE. This means that a higher numbers of POD modes are required to identify the coherent structures. For this case, the first two modes contribute about 12% to the total TKE, while for the case with half-moon concentric shape, the first two modes contributes 44.5% to the total TKE. As the spatial mode number increases, the strength and size of the vortices decrease, which reflects the characteristic property of higher POD modes being associated with smaller flow structures (Kefayati and Poepping 2013). Therefore, the differences between the first POD modes of different cases in Fig. 5.13 shows the impact of the shape of the stenosis on the downstream flow structures.

Figure 5.15 presents the spectral entropy of instantaneous stream-wise velocity component at different cross-sectional planes in stream-wise direction. It was discussed by Abdelsamie et al. (2017) that $0 \leq S_d \leq 0.7$ represents that the flow remains quasi-laminar. Transition occurs in the intermediate range of spectral entropy with the corresponding values of $0.7 \leq S_d \leq 1.1$. Moreover, it was shown that $S_d > 1.1$ corresponds to turbulent conditions. The results show that the transition occurs downstream of the stenotic sections for almost all shapes of the stenosis, except the round concentric one. For most of the cases, transition starts from about $z/D = 3$ and the transitional flow remains up

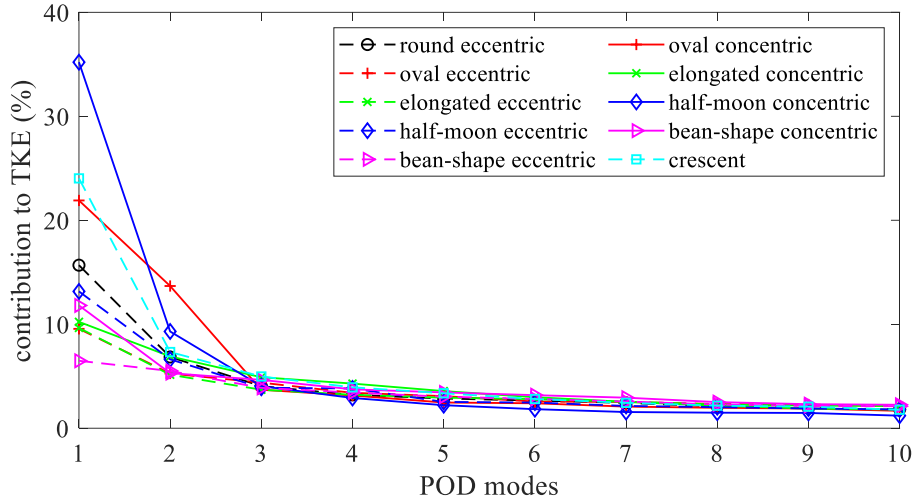


Figure 5.14: The contribution to TKE of the first ten modes of POD for different shapes of the stenosis.

to about $z/D = 8$ before the flow relaminarisation occurs. However, the transitional behaviour for crescent shape of the stenosis and to a lesser degree the oval concentric shape is different. For example, transition starts at about $z/D = 7$ for the crescent case and flow relaminarisation starts from about $z/D = 13$. Furthermore, it is shown that the spectral entropy values increase to more than the limit for flow transition for the round, oval, elongated, half-moon, and bean-shape eccentric shapes of the stenosis. However, the turbulent flow fades quickly and the spectral entropy returns to the level of flow transition. It is worth mentioning that the flow transitions, presented in this figure based on the spectral entropy concept, shows a similar flow trend compared to those shown by the TKE metric, as discussed in Fig. 5.12.

Spectral analysis

Figure 5.16 shows the energy spectra of the centre-point fluctuating stream-wise velocity component for different shapes of the stenosis. Note that the PSD of the round concentric shape is not presented in this section, as the flow after the stenosis remains laminar without any transitional behaviour which was also discussed in the results of velocity contours, WSS, and TKE. The stream-wise distances where the PSDs are plotted varies based on the shape of the stenosis. The stream-wise location for each case is selected where the jet flow is dissipated, which is shown by a ‘plus’ sign in Fig. 5.7. The peak energy values in the PSDs show the frequency of the vortex shedding. The frequencies related to this peak energy correspond to the Strouhal numbers between 0.47 and 0.75 for all cases with different stenosis shapes. The reason that in some cases the peak energy is not clearly visible is the fact that the stream-wise centre-points where the time-dependent data were collected are $1D$ apart from each other. Hence, the peak spectrum of vortex shedding may happen in another stream-wise distance in which the data are not collected. As the area under the PSD profile shows the stream-wise turbulent intensity, the results show that the energy of the velocity fluctuations has the highest value for the oval concentric case both in low and high frequency ranges. The second highest is related to the bean-shape eccentric stenosis shape.

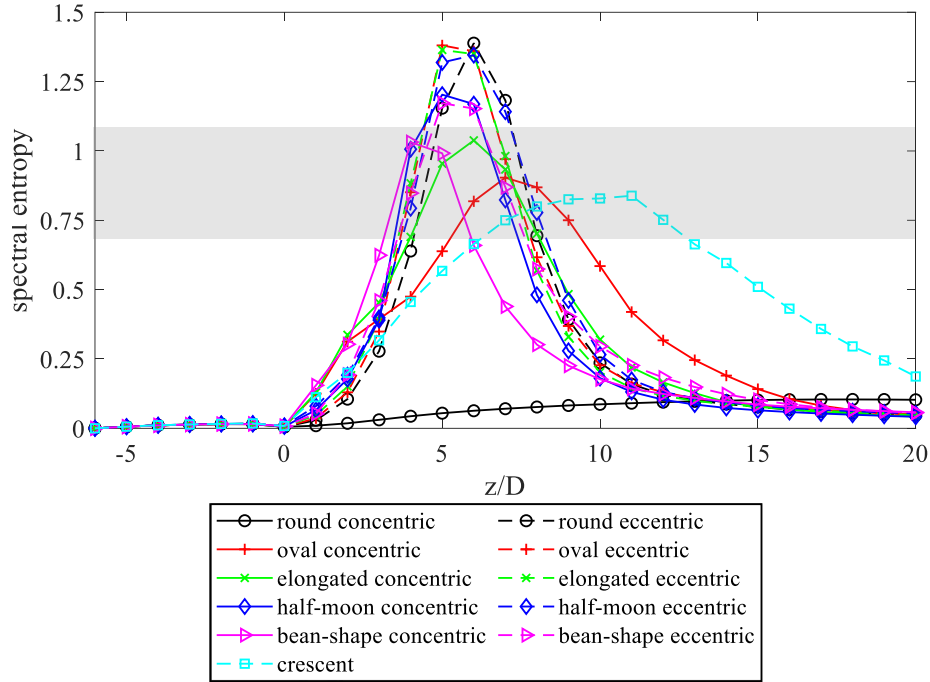


Figure 5.15: Spectral entropy of stream-wise instantaneous velocity component for different cross-sectional planes in stream-wise direction with a consecutive distance of D for different shapes of stenosis. $z/D = 0$ is the location of stenosis centre. The grey shaded zone represents the transitional region starting from $S_d = 0.7$ to $S_d = 1.1$.

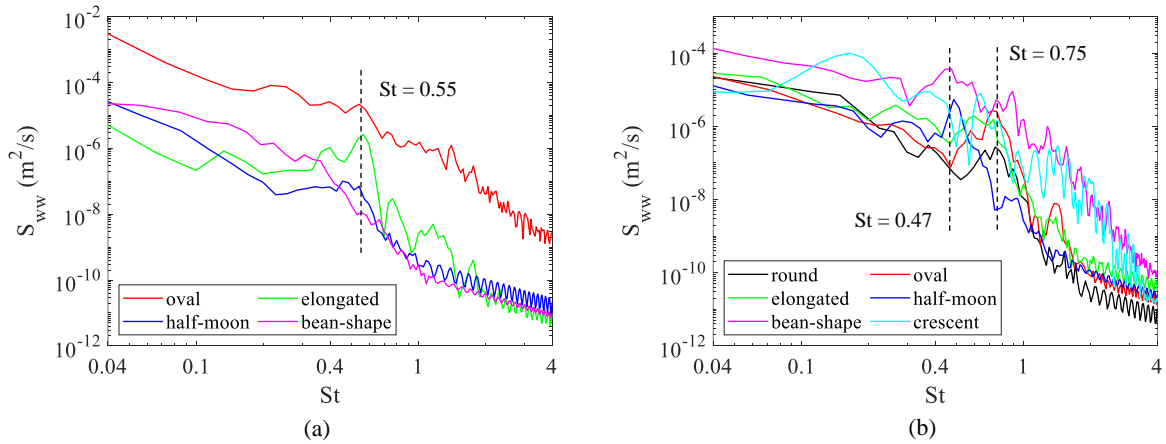


Figure 5.16: Energy spectral of centre-point stream-wise velocity fluctuations for different a) concentric and b) eccentric shapes of the stenosis. The stream-wise distances where the PSDs are plotted vary based on the shape of the stenosis, which are shown with a ‘plus’ sign in Fig. 5.7.

Figure 5.17 shows the energy spectra of stream-wise velocity fluctuations at different stream-wise distances along the centreline for two shapes of stenosis. The stream-wise regions shown in this figure are based on the location where the jet flow dissipates and the transitional behaviour occurs. Furthermore, the PSD plots of upstream and further downstream of this region are also presented in order to compare the level of flow transition. The results of half-moon eccentric case shows that for the stream-wise location

upstream of the location where the jet region is disappeared, $z/D = 5$, no transition is observed in the flow. The intensity of the spectral peak rises with increasing stream-wise distance, indicating more energy transfer into the starting vortex structure from $z/D = 6$ onwards, and the spectrum starts to take on a more broadband nature as turbulent breakdown starts. The dominant vortex shedding frequency can be observed from the PSD profiles at $St = 0.49$ at downstream distances of $z/D = 6$ and $z/D = 7$. As the vortices are convected downstream, they break down into smaller vortex structures, resulting in the peaks being dispersed over a broader range of frequencies. Further downstream, at $z/D = 8$ and beyond, the peaks characterising the vortex shedding are no longer present, and broadband spectrum, which is a characteristic of energy transfer between randomly distributed eddies in turbulent flows, is observed. The region between $z/D = 8$ and $z/D = 10$ has the highest energy at both low and high frequency ranges corresponding to the large and small scale eddies, respectively, with intensities dropping after $z/D = 10$. The lines with $-5/3$ and $-10/3$ slopes are also plotted in this figure. It was shown in the literature that the $-5/3$ slope is associated with the range of frequencies in which the energy cascading is dominated by the inertial transfer, known as the inertial sub-range. A similar trend is also observed in this study. For the post-stenotic distances, where the transitional behaviour occurs, the velocity spectra show a $-5/3$ slope followed by a $-10/3$ slope at higher frequencies. The existence of the inertial sub-range was also reported by Varghese et al. (2007), Mittal et al. (2001), Mittal et al. (2003), and Khair et al. (2015) for the transitional flow downstream of the stenotic section of an artery. Furthermore, the $-10/3$ slope variation was identified by Kim and Corcoran (1974) and Lu et al. (1980), as they found the evidence of such a range in the velocity spectra of the flow downstream of the stenotic section. It was observed by Lu et al. (1980) that the velocity spectra of post-stenotic flows fell from a $-5/3$ slope to $-10/3$ slope at a frequency associated with arterial murmurs.

The PSD profiles for the crescent shape of the stenosis are similar to the half-moon eccentric shape. The main difference is related to the stream-wise location where the transition occurs. This is also due to the stream-wise length of the jet region which is longer for the crescent shape compared to the half-moon eccentric shape. Based on Fig. 5.7, the stream-wise location where the jet flow is dissipated for half-moon eccentric and crescent are $z/D = 6$ and $z/D = 10$, respectively. The results of PSD analysis demonstrate the flow transition downstream of the stenotic section and show that the different shapes of the stenosis result in different transitional flow behaviour.

Wall shear stress

The WSS contours for different shapes of stenosis distal to the stenotic sections are displayed in Fig. 5.18. In order to better visualise the WSS, the contours are unwrapped along the θ and z/D direction, where θ is defined as $\arctan \frac{x}{y}$ and starts from 0° to 360° , as shown in Fig. 5.1. The reason that the WSS contours are plotted for the downstream of the stenotic section is the fact that the target of this study is mainly to investigate the effect of shape of the stenosis on the downstream flow behaviour. Due to the wide range of variations in the WSS values for different shapes of the stenosis, a separate colour-bar is plotted for each case.

The results show that in most cases, there is an area with high WSS values at the

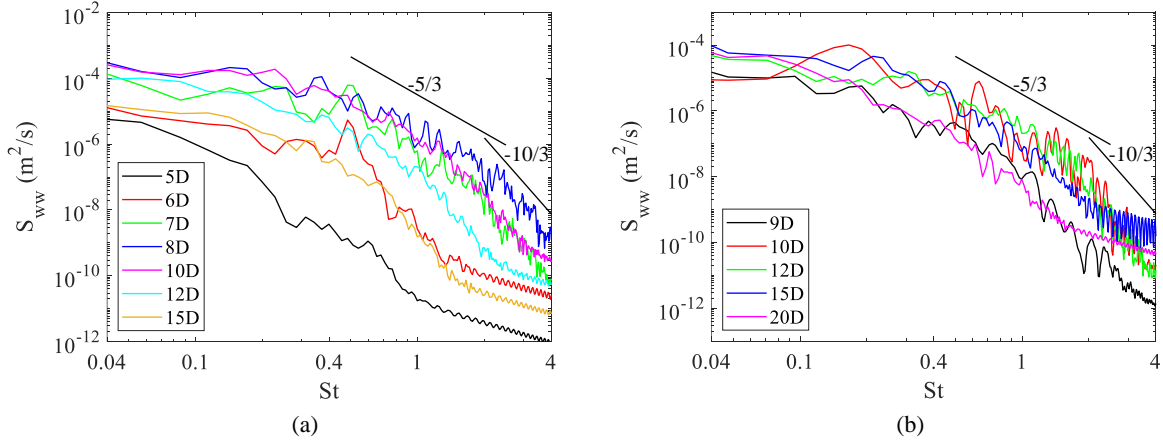


Figure 5.17: Energy spectral of centre-points stream-wise velocity fluctuations at different stream-wise distances for a) half-moon eccentric and b) crescent cases.

edges of the jet region, which is surrounded by the negative WSS regions due to the flow recirculation. The high WSS regions weaken gradually by dissipation of the jet regions farther downstream of the stenosis. After dissipation of the jet flow, where the flow transition increases due to the formation of the eddies, scattered distributions of the regions with high and low WSS are observed. The stream-wise distance of these regions from the stenotic sections varies for different shapes of the stenosis. For example, it is located between $z/D = 3$ to $z/D = 7$ for round and oval eccentric, elongated concentric and eccentric, half-moon concentric and eccentric, and bean-shape concentric. This region is further shifted to downstream between $z/D = 7$ to $z/D = 10$ for crescent shape and $z/D = 13$ to $z/D = 16$ for oval concentric shape. After dissipation of fluctuations in the flow and the relaminarisation initiated, the WSS values become positive which means that the flow starts regaining its parabolic shape. As there is no flow transition for the round concentric shape, as discussed in Figs. 5.7-5.8, no disturbances in the WSS distribution can be observed in this case. In this case, the region of negative WSS values covers the artery wall after the stenosis which is due to the flow recirculation. After a certain distance (around $z/D = 13$), the flow recirculation region ends and hence, the WSS becomes positive.

The highest changes in the magnitude of the downstream WSS distribution are related to the oval eccentric and half-moon eccentric, while the lowest is related to the round concentric shape. It is also observed that the eccentric stenoses produce a larger WSS compared to the concentric stenoses, since the near-wall velocity gradient is larger for eccentric stenoses. Note that this comparison is performed based on the downstream of the stenotic sections. Different results may be obtained if considering the WSS distribution at the location of stenosis and adjacent to it. The coronary stenosis is more likely to form at the locations with disturbed flow conditions characterised by low WSS (Zhang et al. 2015). Low WSS appears to be the most important hemodynamic parameter promoting atherosclerotic plaque growth that in turn influences the blood flow and WSS distribution (Arzani 2020). On the other side, it is reported that the high WSS triggers the outward vascular remodelling (Dolan et al. 2012). Therefore, the extreme of WSS distribution results in inward or outward vascular remodelling.

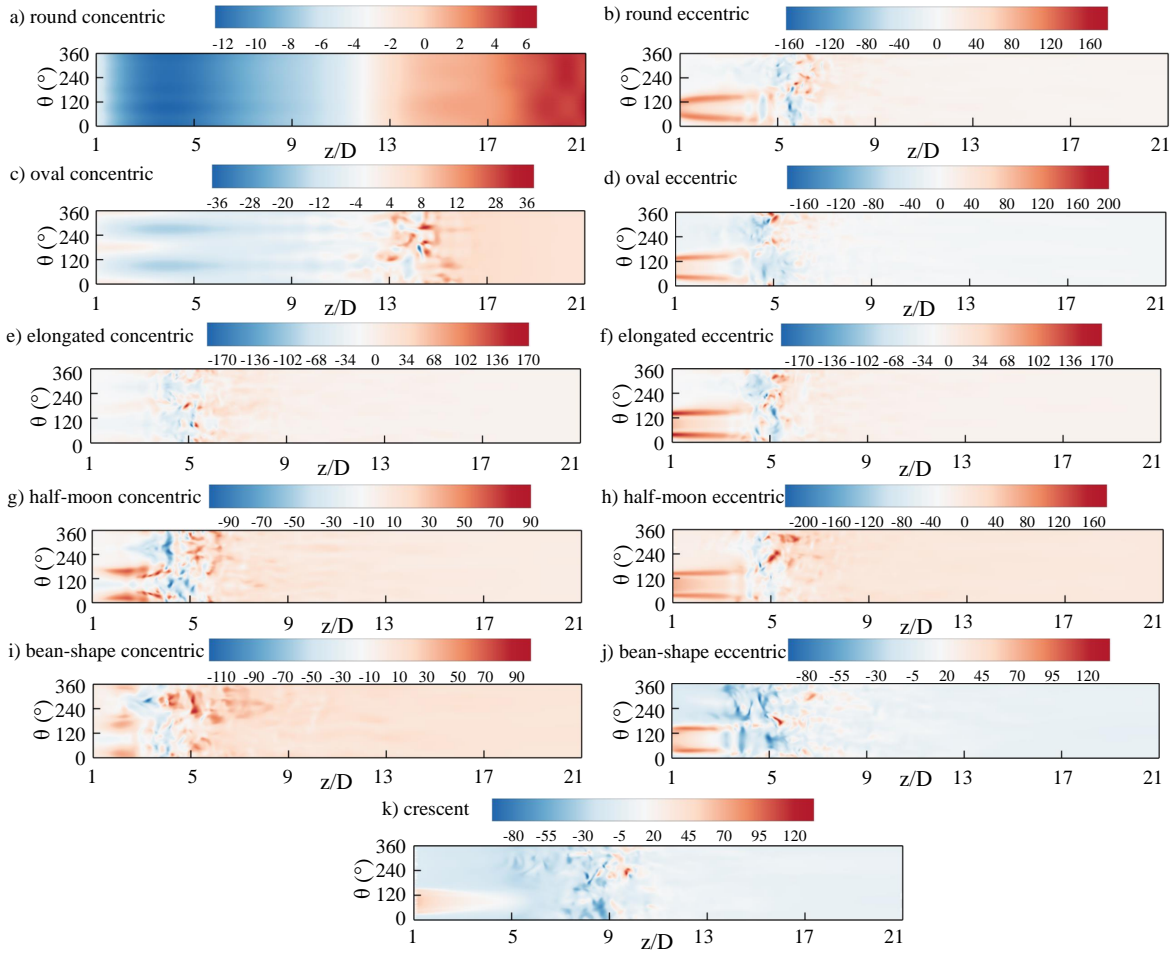


Figure 5.18: Unwrapped WSS distributions downstream of the stenosis starting at $z/D = 1$ at the maximum velocity phase in the fourth pulsation cycle for different shapes of stenosis including a) round concentric, b) round eccentric, c) oval concentric, d) oval eccentric, e) elongated concentric, f) elongated eccentric, g) half-moon concentric, h) half-moon eccentric, i) bean-shape concentric, j) bean-shape eccentric, and k) crescent.

5.2.4 Conclusions

In this study, the effect of cross-sectional shape of the stenosis on the transitional flow behaviour inside the stenosed coronary artery model was investigated. A computational model, validated against the PIV experimental results, was developed to solve the Navier-Stokes equations. The mean and instantaneous velocity contours, pressure drop, WSS distribution, and TKE contour and profile were calculated. The transitional flow behaviour was also investigated by PSD analysis. The Snapshot POD was employed to identify the coherent structures downstream of the stenotic sections.

The results showed that the length of the jet region after the stenotic section depends on the shape of the stenosis. The longest jet is related to the round concentric, oval concentric and crescent, while the shortest is related to the half-moon concentric and bean-shape concentric. The results of instantaneous velocity and vorticity contours, TKE contour, and PSD profiles showed that the eddies are formed after the dissipation of jet flow downstream of the stenosis. The formation of eddies in the downstream flow leads to flow transition, which is accompanied with a jump in TKE profile. The flow transition

is maintained for a certain stream-wise distance before relaminarisation occurs. Furthermore, the location where the eddies start to grow, and the intensity of the eddies differs for different shapes of the stenosis. The PSD analysis shows a jump in the level of energy spectral downstream of the stenotic section, where the jet region is dissipated, related to the frequency of vortex shedding for most of the shapes of the stenosis. Furthermore, the PSD profile further downstream shows the turbulent behaviour with the $-5/3$ slope which is associated with the range of inertial sub-range frequencies for most cases. It was also discussed that the larger contribution to the TKE from the first POD modes indicates a less complex transitional flow which means that the flow can be reconstructed using a fewer number of POD modes. For example, the first two POD modes for the half-moon concentric shape contribute 44.5% to the total TKE, while this percentage for bean-shape eccentric drops down to about 12%. Therefore, the differences between the first POD modes of different cases show the impact of the shape of the stenosis on the downstream flow structure.

From this study, it can be concluded that the shape of the stenosis influences the downstream flow behaviour considerably. For some shapes of the stenosis such as round concentric, having even a severe degree of stenosis results in less serious hemodynamic complications compared to the other shapes of the stenosis at the same degree of stenosis. Comparing different shapes of the stenosis, half-moon eccentric and crescent shapes of the stenosis result in higher levels of flow transitional behaviour which, in turn, result in higher pressure drop at the same degree of stenosis. This study shows that the clinical diagnosis of severity of a blockage inside the coronary arteries only based on its degree of stenosis without considering its cross-sectional shape results in miscalculation of hemodynamic parameters. Future investigations are suggested to study the effects of shape of the stenosis on the flow behaviour in the tapered and bend arteries.

5.2.5 Acknowledgement

Financial support for the project has been provided by the Australian Government Research Training Program Scholarship. The authors would like to thank the workshops of the School of Mechanical Engineering at The University of Adelaide. This work was supported with supercomputing resources provided by the Phoenix HPC service at the University of Adelaide.

5.2.6 Conflict of interest

The authors declare that they have no conflict of interest.

5.2.7 Data availability statement

The data that support the findings of this study are available from the corresponding author upon reasonable request.

References

- Abdelsamie A, Janiga G, and Thévenin D (2017). “Spectral entropy as a flow state indicator”. *International Journal of Heat and Fluid Flow* 68, pp. 102–113.
- Andersson M, Lantz J, Ebbers T, and Karlsson M (2017). “Multidirectional WSS disturbances in stenotic turbulent flows: A pre- and post-intervention study in an aortic coarctation”. *Journal of Biomechanics* 51, pp. 8–16.
- Arzani A (2020). “Coronary artery plaque growth: A two-way coupled shear stress-driven model”. *International Journal for Numerical Methods in Biomedical Engineering* 36.1, e3293.
- Benetos A (2017). “Assessment of arterial stiffness in an older population: the interest of the cardio-ankle vascular index (CAVI)”. *European Heart Journal Supplements* 19.suppl_B, B11–B16.
- Caruso MV, Rosa SD, Indolfi C, and Fragomeni G (2015). “Computational analysis of stenosis geometry effects on right coronary hemodynamics”. *37th Annual International Conference of the IEEE Engineering in Medicine and Biology Society (EMBC)*. IEEE.
- Cho YI and Kensey KR (1991). “Effects of the non-Newtonian viscosity of blood on flows in a diseased arterial vessel. Part 1: Steady flows”. *Biorheology* 28.3-4, pp. 241–262.
- Choi W, Park JH, Byeon H, and Lee SJ (2018). “Flow characteristics around a deformable stenosis under pulsatile flow condition”. *Physics of Fluids* 30.1, p. 011902.
- Christiansen MK, Jensen JM, Nørgaard BL, Dey D, Bøtker HE, and Jensen HK (2017). “Coronary plaque burden and adverse plaque characteristics are increased in healthy relatives of patients with early onset coronary artery disease”. *JACC: Cardiovascular Imaging* 10.10, Part A, pp. 1128–1135.
- Costa ED (2016). “Hemodynamics in the left coronary artery - numerical and in vitro approaches”. PhD thesis. Department of Chemical Engineering, University of Porto.
- Cutnell JD, Johnson KW, Young D, and Stadler S (2015). *Physics, 10th Edition*. Wiley.
- Dolan JM, Kolega J, and Meng H (2012). “High wall shear stress and spatial gradients in vascular pathology: A review”. *Annals of Biomedical Engineering* 41.7, pp. 1411–1427.
- Freidoonimehr N, Arjomandi M, Sedaghatizadeh N, Chin R, and Zander A (2020a). “Transitional turbulent flow in a stenosed coronary artery with a physiological pulsatile flow”. *International Journal for Numerical Methods in Biomedical Engineering* 36.7, e3347.
- Freidoonimehr N, Arjomandi M, Zander A, and Chin R (2021). “Effect of artery curvature on the coronary fractional flow reserve”. *Physics of Fluids* 33.3, p. 031906.
- Freidoonimehr N, Chin R, Zander A, and Arjomandi M (2020b). “An experimental model for pressure drop evaluation in a stenosed coronary artery”. *Physics of Fluids* 32.2, p. 21901.
- Grist TM, Polzin JA, Bianco JA, Foo TK, Bernstein MA, and Mistretta CM (1997). “Measurement of coronary blood flow and flow reserve using magnetic resonance imaging”. *Cardiology* 88.1, pp. 80–89.
- Guleren KM (2013). “Numerical flow analysis of coronary arteries through concentric and eccentric stenosed geometries”. *Journal of Biomechanics* 46.6, pp. 1043–1052.
- Haynes RH (1960). “Physical basis of the dependence of blood viscosity on tube radius”. *American Journal of Physiology* 198, pp. 1193–1200.

- Huang J, Lyczkowski RW, and Gidaspow D (2009). “Pulsatile flow in a coronary artery using multiphase kinetic theory”. *Journal of Biomechanics* 42.6, pp. 743–754.
- Jabir E and Lal SA (2016). “Numerical analysis of blood flow through an elliptic stenosis using large eddy simulation”. *Proceedings of the Institution of Mechanical Engineers, Part H: Journal of Engineering in Medicine* 230.8, pp. 709–726.
- Janiga G (2019a). “Quantitative assessment of 4D hemodynamics in cerebral aneurysms using proper orthogonal decomposition”. *Journal of Biomechanics* 82, pp. 80–86.
- Janiga G (2019b). “Novel feature-based visualization of the unsteady blood flow in intracranial aneurysms with the help of proper orthogonal decomposition (POD)”. *Computerized Medical Imaging and Graphics* 73, pp. 30–38.
- Javadzadegan A, Yong ASC, Chang M, Ng ACC, Yiannikas J, Ng MKC, Behnia M, and Kritharides L (2013). “Flow recirculation zone length and shear rate are differentially affected by stenosis severity in human coronary arteries”. *American Journal of Physiology-Heart and Circulatory Physiology* 304.4, H559–H566.
- Jelly TO, Chin RC, Illingworth SJ, Monty JP, Marusic I, and Ooi A (2020). “A direct comparison of pulsatile and non-pulsatile rough-wall turbulent pipe flow”. *Journal of Fluid Mechanics* 895.
- Johnston BM, Johnston PR, Corney S, and Kilpatrick D (2006). “Non-Newtonian blood flow in human right coronary arteries: Transient simulations”. *Journal of Biomechanics* 39.6, pp. 1116–1128.
- Joyner MJ and Casey DP (2015). “Regulation of increased blood flow (Hyperemia) to muscles during exercise: A hierarchy of competing physiological needs”. *Physiological Reviews* 95.2, pp. 549–601.
- Kefayati S and Poepping TL (2013). “Transitional flow analysis in the carotid artery bifurcation by proper orthogonal decomposition and particle image velocimetry”. *Medical Engineering & Physics* 35.7, pp. 898–909.
- Khair A, Wang BC, and Kuhn DCS (2015). “Study of laminar–turbulent flow transition under pulsatile conditions in a constricted channel”. *International Journal of Computational Fluid Dynamics* 29.9-10, pp. 447–463.
- Kim BM and Corcoran WH (1974). “Experimental measurements of turbulence spectra distal to stenoses”. *Journal of Biomechanics* 7.4, pp. 335–342.
- Koeppen B and Stanton B (2018). *Berne & Levy physiology*. Philadelphia, PA: Elsevier - HealthSciences Division.
- Kohn JC, Lampi MC, and Reinhart-King CA (2015). “Age-related vascular stiffening: causes and consequences”. *Frontiers in Genetics* 6, p. 112.
- Kwasiborski PJ, Czerwinski W, Kowalczyk P, Buksinska-Lisik M, Horszczaruk G, Aboodi MS, Derbisz K, Hochul M, Janas A, Cwetsch A, Wasek W, Buszman PP, Bartunek J, Buszman PE, Serruys PW, and Milewski K (2020). “Influence of heart rate on FFR measurements: An experimental and clinical validation study”. *International Journal of Cardiology* 317, pp. 13–17.
- Li S, Chin C, Thondapu V, Poon EKW, Monty JP, Li Y, Ooi ASH, Tu S, and Barlis P (2017). “Numerical and experimental investigations of the flow–pressure relation in multiple sequential stenoses coronary artery”. *The International Journal of Cardiovascular Imaging* 33.7, pp. 1083–1088.
- Lorenzini G and Casalena E (2008). “CFD analysis of pulsatile blood flow in an atherosclerotic human artery with eccentric plaques”. *Journal of Biomechanics* 41.9, pp. 1862–1870.

- Lu P, Gross D, and Hwang N (1980). “Intravascular pressure and velocity fluctuations in pulmonic arterial stenosis”. *Journal of Biomechanics* 13.3, pp. 291–300.
- Mahalingam A, Gawandalkar UU, Kini G, Buradi A, Araki T, Ikeda N, Nicolaidis A, Laird JR, Saba L, and Suri JS (2016). “Numerical analysis of the effect of turbulence transition on the hemodynamic parameters in human coronary arteries”. *Cardiovascular Diagnosis and Therapy* 6.3, pp. 208–220.
- Meier B, Gruentzig AR, Hollman J, Ischinger T, and Bradford JM (1983). “Does length or eccentricity of coronary stenoses influence the outcome of transluminal dilatation?” *Circulation* 67.3, pp. 497–499.
- Mitchell GF, Parise H, Benjamin EJ, Larson MG, Keyes MJ, Vita JA, Vasani RS, and Levy D (2004). “Changes in arterial stiffness and wave reflection with advancing age in healthy men and women”. *Hypertension* 43.6, pp. 1239–1245.
- Mittal R, Simmons SP, and Najjar F (2003). “Numerical study of pulsatile flow in a constricted channel”. *Journal of Fluid Mechanics* 485, pp. 337–378.
- Mittal R, Simmons SP, and Udaykumar HS (2001). “Application of large-eddy simulation to the study of pulsatile flow in a modeled arterial stenosis”. *Journal of Biomechanical Engineering* 123.4, pp. 325–332.
- Molla MM, Wang BC, and Kuhn DCS (2012). “Numerical study of pulsatile channel flows undergoing transition triggered by a modelled stenosis”. *Physics of Fluids* 24.12, p. 121901.
- Moyle KR, Antiga L, and Steinman DA (2006). “Inlet conditions for image-based CFD models of the carotid bifurcation: is it reasonable to assume fully developed flow?” *Journal of Biomechanical Engineering* 128.3, pp. 371–379.
- Nichols W, O’Rourke M, and Vlachopoulos C (2011). *McDonald’s blood flow in arteries, Sixth edition: Theoretical, experimental and clinical principles*. CRC Press.
- Ohara T, Toyoda K, Otsubo R, Nagatsuka K, Kubota Y, Yasaka M, Naritomi H, and Minematsu K (2008). “Eccentric stenosis of the carotid artery associated with ipsilateral cerebrovascular events”. *American Journal of Neuroradiology* 29.6, pp. 1200–1203.
- Peterson SD and Plesniak MW (2008). “The influence of inlet velocity profile and secondary flow on pulsatile flow in a model artery with stenosis”. *Journal of Fluid Mechanics* 616, pp. 263–301.
- Sakariassen KS, Orning L, and Turitto VT (2015). “The impact of blood shear rate on arterial thrombus formation”. *Future Science OA* 1.4, pp. 30–39.
- Sun Z (2015). “Aging, arterial stiffness, and hypertension”. *Hypertension* 65.2, pp. 252–256.
- Jahangiri M, Saghafian M, and Sadeghi MR (2017). “Numerical simulation of non-Newtonian models effect on hemodynamic factors of pulsatile blood flow in elastic stenosed artery”. *Journal of Mechanical Science and Technology* 31.2, pp. 1003–1013.
- Taira K, Hemati MS, Brunton SL, Sun Y, Duraisamy K, Bagheri S, Dawson STM, and Yeh CA (2020). “Modal analysis of fluid flows: Applications and outlook”. *AIAA Journal* 58.3, pp. 998–1022.
- Usmani AY and Muralidhar K (2016). “Pulsatile flow in a compliant stenosed asymmetric model”. *Experiments in Fluids* 57.12, pp. 186–210.
- Varghese SS, Frankel SH, and Fischer PF (2008). “Modeling transition to turbulence in eccentric stenotic flows”. *Journal of Biomechanical Engineering* 130.1, p. 014503.
- Varghese SS, Frankel SH, and Fischer PF (2007). “Direct numerical simulation of stenotic flows. Part 2. Pulsatile flow”. *Journal of Fluid Mechanics* 582, pp. 281–318.

- Voss S, Arens C, and Janiga G (2018). “Assessing transitional air flow during human exhalation from large eddy simulations based on spectral entropy”. *Flow, Turbulence and Combustion* 102.1, pp. 117–128.
- Waller BF (1989). “The eccentric coronary atherosclerotic plaque: morphologic observations and clinical relevance”. *Clinical Cardiology* 12.1, pp. 14–20.
- Weiss J (2019). “A tutorial on the proper orthogonal decomposition”. *AIAA Aviation 2019 Forum*. American Institute of Aeronautics and Astronautics.
- William Thielicke EJS (2014). “PIVlab – towards user-friendly, affordable and accurate digital particle image velocimetry in MATLAB”. *Journal of Open Research Software* 2.1, e30.
- Womersley JR (1955). “Method for the calculation of velocity, rate of flow and viscous drag in arteries when the pressure gradient is known”. *The Journal of Physiology* 127.3, pp. 553–563.
- Xie X, Li Y, and Xie S (2018). “Computation of hemodynamics in eccentric coronary stenosis: A morphological parametric study”. *Technology and Health Care* 26, pp. 229–238.
- Young DF and Tsai FY (1973). “Flow characteristics in models of arterial stenoses — I. Steady flow”. *Journal of Biomechanics* 6.4, pp. 395–410.
- Zhang JM, Luo T, Tan SY, Lomarda AM, Wong AS, Keng FY, Allen JC, Huo Y, Su B, Zhao X, Wan M, Kassab GS, Tan RS, and Zhong L (2015). “Hemodynamic analysis of patient-specific coronary artery tree”. *International Journal for Numerical Methods in Biomedical Engineering* 31.4, e02708.

Chapter 6

Pressure drop in stenosed coronary arteries

6.1 Chapter overview

Following the investigation of the effects of different shapes and the degrees of stenosis and the heart working conditions on the transitional flow behaviour inside a stenosed coronary artery model, this chapter focuses on the investigation of the pressure drop and fractional flow reserve (FFR) inside the stenosed coronary artery models. As discussed in Section 2.3.3, a mathematical model of the pressure drop inside the stenosed coronary artery models can be used as a gatekeeper to reduce the risks associated with an unnecessary invasive measurement of the pressure drop using FFR and provide more patient comfort. Considering more realistic flow conditions and geometries of the artery and stenosis results in a more accurate non-invasive estimation of the pressure drop. Hence, developing a mathematical model based on in-vitro experimental coefficients which is able to account for different shapes of the stenosis and arterial curvature results in an improvement to the models currently available in the literature by taking into account more realistic geometrical and physiological conditions.

This chapter starts with a non-invasive evaluation of pressure drop inside a straight stenosed coronary artery model in Section 6.2. In Section 6.3, results from experimental measurements of the pressure drop and FFR inside a curved model of the coronary artery are presented, since there are curvatures in coronary arterial trees. An in-vitro coronary arterial test rig is developed and extensive pressure measurements are conducted to investigate the effects of the shape of the stenosis, blood flow profile, arterial curvature angle and radius on the pressure drop and FFR.

The results in Section 6.2 show that the pressure drop is a function of the degree of stenosis, the shape of the stenosis, the blood flow profile, and the blood physical properties, such as blood viscosity and density, and the arterial length and cross section. A mathematical equation is developed based on the results of the experiments to evaluate pressure drop inside a straight coronary artery model. This equation relies on two experimental coefficients including the blockage factor, which is a function of the degree and shape of the stenosis, and pulsatility factor, which is only a function of the degree of stenosis and is independent of the blood profile. These factors are calculated for a wide

range of shapes and degrees of stenosis as well as different unsteady flow profiles. Furthermore, in order to illustrate the validity of the developed equation, the pressure drop in stenosed coronary artery models with physiological flow profiles of the actual left and right coronary arteries is predicted and compared with experimental measurements. The comparison shows that the mean and peak pressure drop estimated using the developed equation deviate from the experimental data by less than 0.5% and approximately 6%, respectively.

Section 6.3 investigates the effect of arterial curvature on the pressure drop and FFR. 3D-printed curved artery models of various arterial curvature angles and radii are employed in the experiments. The equation developed in Section 6.2 is extended with an additional term to account for the effect of arterial curvature on the pressure drop. It is found that the effect of the degree of stenosis on the FFR and pressure drop is more significant compared to the effect of the curvature angle for the range of curvature angles considered in this study (from 30° to 90°) indicating that pressure drop inside a diseased artery is highly dependent on the degree of stenosis. The results also show that neglecting the effect of curvature on pressure drop leads to its underestimation by 25%–35% compared to a straight artery.

The equation developed in this chapter is able to accurately determine the pressure drop inside a curved or straight stenosed coronary artery using measurements of the flow profile inside the artery as well as the images of the stenosed coronary artery obtained from the non-invasive methods. The developed equation can provide cardiologists with a non-invasive tool to replace the more invasive methods such as FFR to calculate the pressure drop inside stenosed arteries and quantify the severity of stenosis.

6.2 Pressure drop in straight stenosed coronary arteries

This section consists of the following published journal article:

Navid Freidoonimehr, Rey Chin, Anthony Zander, Maziar Arjomandi (2020). “An experimental model for pressure drop evaluation in a stenosed coronary artery”. *Physics of Fluids*, 32 pp. 021901.

The article is identical to its published format with the following exceptions:

- The numbering of figures, tables and equations have been altered to include the chapter number.
- The position of some figures and tables have been changed to improve legibility.

The article in its published format is available at:

<https://doi.org/10.1063/1.5139701>

Statement of Authorship

Title of paper	An experimental model for pressure drop evaluation in a stenosed coronary artery
Publication Status	<input checked="" type="checkbox"/> Published <input type="checkbox"/> Accepted for Publication <input type="checkbox"/> Submitted for Publication <input type="checkbox"/> Unpublished and Unsubmitted work written in manuscript style
Publication Details	Freidoonimehr, N., Chin, R., Zander, A., and Arjomandi, M., 2020, "An experimental model for pressure drop evaluation in a stenosed coronary artery", Physics of Fluids, 32(2), p. 021901

Principal Author

Name of Principal Author (Candidate)	Navid Freidoonimehr		
Contribution to the Paper	Developed ideas, conducted experiments, performed data analysis and interpreted results, wrote manuscript, and acted as corresponding author		
Overall percentage (%)	75%		
Certification:	This paper reports on original research I conducted during the period of my Higher Degree by Research candidature and is not subject to any obligations or contractual agreements with a third party that would constrain its inclusion in this thesis. I am the primary author of this paper.		
Signature		Date	15/02/2021

Co-Author Contributions

By signing the Statement of Authorship, each author certifies that:

- i the candidate's stated contribution to the publications is accurate (as detailed above);
- ii permission is granted for the candidate to include the publication in the thesis; and
- iii the sum of all co-author contributions is equal to 100% less the candidate's stated contribution

Name of Co-Author	Rey Chin		
Contribution to the Paper	Supervised the development of the research, participated in developing ideas and concepts, helped in interpretation of results, provided critical revision of manuscript.		
Signature		Date	15/02/2021

Name of Co-Author	Anthony Zander		
Contribution to the Paper	Supervised the development of the research, participated in developing ideas and concepts, helped in interpretation of results, provided critical revision of manuscript.		
Signature		Date	15/02/2021

Name of Co-Author	Maziar Arjomandi	
Contribution to the Paper	Supervised the development of the research, participated in developing ideas and concepts, helped in interpretation of results, provided critical revision of manuscript.	
Signature		Date 15/02/2021

✓ ✓

An experimental model for pressure drop evaluation in a stenosed coronary artery

Navid Freidoonimehr, Rey Chin, Anthony Zander, and Maziar Arjomandi

Abstract

Non-invasive measurement of pressure drop has great clinical significance for the treatment of coronary artery diseases. The objective of this study is to develop a relationship that can estimate pressure drop in a stenosed coronary artery model as a function of different parameters such as blood viscosity, artery length and diameter, flow rate and flow profile, and shape and degrees of stenosis. Experimental pressure measurements from a wide range of degrees of stenosis and critical simplified geometries of stenosis along with different unsteady flow profiles are employed to evaluate the pressure drop equation. To calculate the blockage term of the pressure drop, several experimental cases are investigated and the results show that the blockage factor is strongly dependent on the shape and degree of stenosis. Furthermore, different unsteady flow profiles are applied to calculate the pulsatile pressure drop term, and it is found that the pulsatility parameter is not a function of the flow profile or the shape of the stenosis. However, it is only a function of the degree of stenosis. To test the validity of the developed equation, pressure drops through stenosed coronary artery models with the real physiological flow profile of the left and right coronary arteries were predicted and compared with the experimental measurements. The proposed equation is able to determine the pressure drop inside a stenosed coronary artery non-invasively using the measurement of the flow profile inside the artery as well as the images of the stenosed coronary artery obtained based on the non-invasive methods.

6.2.1 Introduction

Pressure drop is an important parameter in the coronary arterial system since it is directly proportional to the amount of the power required by the heart to supply the organs with a uniform and constant blood flow rate. Plaque formation in the arteries creates a considerable pressure drop inside the artery. A higher pressure drop means a higher heart muscle effort is required to provide the same blood flow rate to different organs. Hence, an accurate measurement of the pressure drop inside the arteries is of great importance. One of the most common methods to evaluate the amount of the pressure drop is Fractional Flow Reserve (FFR), which is a technique used in coronary catheterization to measure the pressure drop across a stenotic coronary artery. In FFR measurement, a micro-catheter connected with a miniaturised pressure sensor is inserted into the coronary artery to measure the pressure drop before and after the stenotic section (Achenbach et al. 2017). This method, which is widely used as the gold standard for detecting early stage and middle stage coronary artery diseases, improves the clinical outcome, and hence reduces the mortality rate of the people suffering from coronary artery diseases. However, its invasive nature along with its cost limit its clinical applications (Fearon et al. 2007; Li et

al. 2017; Morris et al. 2015). Therefore, it is important to develop a non-invasive method to measure the pressure drop accurately and prevent all operational and economical disadvantages of the invasive methods.

The pressure drop inside a stenosed artery model is associated with three major components including the viscous friction effect, the blockage effect and the pulsatility effect (Young et al. 1975). The viscous friction effect occurs due to the frictional forces acting on the blood flow as it goes through the artery. The blockage effect is due to the presence of the stenosis which blocks the artery and changes the flow pattern near and after the constricted section, and consequently leads to flow separation immediately after the stenotic section and, hence creates a pressure drop. Finally, the pulsatility effect is due to the blood flow acceleration and deceleration due to unsteadiness of the inflow regime. Hence, different flow features including blood viscosity, flow rate and flow profile as well as the blockage morphology influence the total pressure drop in a constricted artery. Understanding the effect of these parameters is therefore of great importance for an accurate evaluation of the pressure drop inside the coronary arterial system.

Plaque morphology, namely the shape and degree of blockage inside the artery, are important parameters that affect the flow behaviour and consequently the pressure drop. The degree of stenosis (S) is defined as the percentage of the arterial cross section, which is blocked due to the formation of the plaque. The plaque may occupy almost the entire cross section of the artery (severe constriction case) or just a small part of it (mild constriction case). Stenosis come in different geometrical shapes and can be characterised based on two main parameters, eccentricity and edge sharpness.

Eccentricity represents the bias from the centre of the hosting artery to the centre of stenosis. This parameter varies from the case with no eccentricity, i.e., equal to zero, to the highest eccentricity, i.e., equal to unity. As discussed by Ohara et al. (2008), for patients suffering from a high degree of stenosis in their carotid artery (70% and more), independent of other risk factors and features of plaque morphology, an eccentric plaque can cause more severe cerebrovascular diseases compared to the patients with concentric stenoses. According to Ohara et al. (2008), lesions in real arteries are mostly eccentric in geometry. Eccentricity causes considerable changes in the flow behaviour such as velocity distributions, wall shear stress and turbulence structures. In a study of the flow through an asymmetric stenosis, Jabir and Lal (2016), found that the velocity profiles are skewed towards the opposite side of the blocked part immediately after the stenosis. The distribution of wall shear stress over the pipe wall is uneven due to the turbulent breakdown of jet (the jet flow effect changes the turbulent structures and shifts the eddies far downstream) along with the presence of geometric eccentricity of stenosis. Moreover, a small eccentricity index (only 5%) can trigger post-stenotic transition to turbulence and promote turbulent flow compared to the case without eccentricity (Varghese et al. 2008). In a study by Varghese et al. (2007) on steady flow through a 75% degree of stenosis for concentric and eccentric models at $3D$, where D shows the internal diameter of the artery model, downstream of the stenosis, a significant divergence between the stream-wise velocity distributions was observed. It was found that the laminar flow changed to a turbulent flow for up to about $12D$ downstream in the eccentric case. After $12D$, the level of fluctuations reduced and reached an asymptotic value, which is lower than the corresponding value of an axisymmetric case. Therefore, it is important to study and consider eccentricity as one of the physiological parameters of the stenosis morphology that affects the flow behaviour considerably.

Apart from eccentricity, the other important parameter in classification of the shape of the stenoses that needs to be studied in detail is the edge sharpness on which the flow characteristics such as pressure loss are strongly dependent (Usmani and Muralidhar 2016). The stenosis inside the arteries can be formed either with or without any sharp edges. A longer recirculation zone and a higher pressure drop are reported by Young and Tsai (1973b) for an asymmetric stenosis with the sharp edge compared to an axisymmetric one without the sharp edge. Furthermore, asymmetric geometries are also susceptible to plaque growth (Tambasco and Steinman 2003). Therefore, as the second important physiological parameter, the effect of sharpness of the plaque edge needs to be taken into account in the calculation of the pressure drop inside the stenosed arteries.

There are some studies in the literature, which estimated the pressure drop across the arterial stenosis by algebraic equations considered the three pressure drop components including viscous friction pressure drop, pressure drop due to the blockage effect of the stenosis and also the pressure drop due to unsteadiness of the flow, as mentioned earlier. To the best of authors' knowledge, Young et al were the first who presented an algebraic equation to estimate pressure drop both for steady flow (Young and Tsai 1973b) and unsteady flow (Young and Tsai 1973a). Their model was based on only two stenosis models including an axisymmetric model and a non-symmetric shape with half round-edge and half sharp-edge. Hence, the applicability of their model for other shapes was not investigated. Clark (1976) used different stenosed valves to simulate the aortic stenosis and developed an equation to estimate the pressure drop. Their study was performed using the steady flow measurement of the pressure drop. Furthermore, Seeley and Young (1976) studied the effect of length and the degree of stenosis with the well-defined configuration of a blunt plug on the pressure drop across an arterial stenosis by using in-vitro steady flow tests. Their developed model was based on steady flow measurement and the effect of the unsteadiness of the flow inside the arteries was not considered. More recently, Huo et al. (2012) developed an analytical model to determine FFR based on the general Bernoulli equation. Their model was only based on steady flow and considered length and degree of stenosis as the only parameters affecting the blockage pressure drop. More recently, Mirramezani et al. (2018) presented different algebraic models based on their CFD simulations to compute pressure drop in the coronary arterial stenosis. Their models ranged from one-dimensional to three-dimensional time-dependent simulations. None of the developed models in the literature considered the effect of the shape of the stenosis including its level of eccentricity and curvature. Furthermore, the models in the literature have been developed for specific flow profiles and their applicability to any general form of flow profiles has not been thoroughly investigated. Therefore, there are limitations in the equations in the literature which can be used to predict pressure drop for various shape and degree of stenosis and flow profile.

The aim of this study, for the first time, is to develop a relationship between the pressure drop and the geometric features of a stenosis such as its degree, eccentricity and edge sharpness. Such relationship can be employed to predict pressure drop inside a stenosed coronary artery. Furthermore, to be able to apply the developed equation for real pulsatile flow profiles, the effect of the unsteadiness of the inflow on the pressure drop fluctuations will be investigated. The developed equation is then evaluated for estimation of pressure drop inside a stenosed coronary artery with a physiological pulsatile flow profile of a coronary artery. The results of this study will provide a non-invasive tool to evaluate the pressure drop inside a stenosed artery based on the flow features and geometrical

parameters of the plaque.

6.2.2 Methodology

From the dimensional analysis, the pressure drop across a constricted simplified straight coronary artery model can be expressed in the form of,

$$\Delta P = f\left(Re, \frac{L}{D}, \frac{A_1}{A_0}, \frac{l}{D}, e, \frac{dV}{dt}\right), \quad (6.1)$$

where ΔP is the pressure drop along the pipe with the length of L and the internal diameter of D , Re is the Reynolds number ($\rho V_{avg} D / \mu$), ρ is the fluid density, V_{avg} is the time-averaged mean velocity in the unobstructed section of the pipe, μ is the fluid viscosity, A_0 and A_1 represent the cross-sectional area of the unobstructed artery and the minimum constricted cross sectional area, respectively, l is the plaque length, e is the plaque eccentricity, and V is the instantaneous velocity of the unobstructed artery (average over the entire cross section (A_0)).

In general, the shape of the coronary arteries can be categorised as straight, curved or bifurcated arteries. In order to develop a general pressure drop equation, a simplified model of the artery in form of a straight circular artery model, was considered in this study instead of a patient-specific geometry of the artery since the latter varies from a patient to another. It is also noteworthy to mention that the wall of a healthy coronary artery is flexible and its flexibility has an effect on the pressure drop. A higher pressure drop occurs inside a rigid artery model compared to the pressure drop when the wall of the artery is considered flexible (Jahangiri et al. 2015). The diseases related to the blockage of the coronary artery mostly occur with ageing (as a primary risk factor of all cardiovascular diseases (Kohn et al. 2015)). The artery wall becomes harder and stiffer with ageing as a common disorder and loses its flexibility. Hence, rigid wall assumption is valid when focusing on the stenosed coronary artery. Many studies in the literature also model the artery wall rigid, such as Zhu et al. (2018), Li et al. (2017), Foucault et al. (2017), and Plesniak and Bulusu (2016).

The other simplification used in the study was considering blood as a Newtonian fluid. There are different techniques in the literature used to simulate the non-Newtonian nature of the blood. One of the techniques is to simulate blood as a two-phase model of the mixture of red blood cells inside the plasma region (Alonso et al. 1993). The other technique is to use continuous viscosity functions. This technique is widely accepted and used in the literature due to the low computational costs and smooth velocity profiles obtained from these methods. There are different functions in the literature that are used to represent the shear thinning behaviour of the blood. Casson model (Blair 1959), as a yield stress blood model, is one of these functions. The Casson fluid behaves as rigid until the yield parameter is reached and after that behaves as a shear thinning fluid. The other yield stress model for blood is Bingham model (Prager 1961) that behaves as a rigid body at low stresses, while it flows as a viscous fluid at high stress. Quemada model (Quemada 1978), as one of the other functions, defines viscosity of the blood as a function of shear rate and level of hematocrit. The above-mentioned techniques are some of the non-Newtonian models used to simulate blood behaviour. However, as widely used in the

literature blood can be considered as a Newtonian fluid in special circumstances ((Haynes 1960; Nichols et al. 2011; Jahangiri et al. 2017)). As reported by Haynes (1960), blood behaves as a Newtonian liquid in tubes in which the internal diameter is large compared with the size of the red blood cells. Moreover, blood can be considered as a homogenous liquid with a viscosity that is independent of the velocity gradient in large arteries (e.g. larger than 1 mm in diameter) (Nichols et al. 2011). Cho and Kensey (1991) reported that the effect of non-Newtonian behaviour of the blood on the pressure drop across the artery is significant for the flow with the Reynolds number of less than 100. Since the Reynolds number inside the coronary arteries is larger than 100, the blood can be assumed as Newtonian. Also as suggested by Jahangiri et al. (2017), the blood behaves as a Newtonian fluid at shear rates greater than 100 s^{-1} and considering that the shear rates applied to the coronary arteries are larger than 100 s^{-1} (Sakariassen et al. 2015), blood behaviour in the coronary arteries can be considered as Newtonian fluid.

Pressure drop along a stenotic simplified coronary artery model with pulsatile flow, is the function of three major effects, as mentioned in the introduction section. First is the viscous friction effect ($\Delta P_{viscous}$) which is a function of fluid velocity inside the pipe, fluid viscosity, pipe length and its internal diameter. The second major effect is related to the blockage effect ($\Delta P_{blockage}$) which is dependent on the geometry of the stenosis, namely its degree, shape, eccentricity, and plaque length. The third effect is related to the pulsatile flow behaviour ($\Delta P_{pulsatile}$) which is a function of the time derivation of the instantaneous fluid velocity. The mathematical modelling of each of the three effects is described in the following sections.

Pressure drop due to viscous effect

Darcy-Weisbach equation is an empirical equation that can be employed to calculate the pressure drop due to the viscous friction along a given length of the coronary artery model using the average velocity of the blood flow. This equation is derived based on the force balance between the pressure and shear forces of the fluid disk element. Darcy-Weisbach equation, as a pressure drop equation due to viscous friction effect which is used in this study, gives:

$$\Delta P_{viscous} = \frac{128 \mu q(t)}{\pi D_h^4} L, \quad (6.2)$$

where $\Delta P_{viscous}$ is the viscous pressure drop along the pipe length of L , $q(t)$ is the instantaneous flow rate, D_h is the hydraulic diameter of the pipe, and μ is the blood viscosity. In the calculation of above Darcy-Weisbach equation, laminar flow assumption is employed, since it is a valid and applicable assumption in the majority of the healthy coronary arterial system (Zhu et al. 2018). In this study, for the section of the artery model with the constriction inside, the hydraulic diameter is calculated using the local wetted area and the local perimeter of the cross section of the constriction. For the upstream and downstream of the obstruction, the hydraulic diameter is the same as the diameter of the unobstructed artery model. Both laminar and turbulent flow assumptions are considered in this work. For the calculation of viscous friction term, a laminar model assumption is used. To consider the effect of blockage of the artery on the pressure drop, a turbulent pressure drop model due to the blockage is employed which will be explained in the next

section.

Pressure drop due to blockage effect

Bernoulli equation in the stream-wise direction of the artery model is employed to calculate the pressure drop due to the blockage effect:

$$\Delta P_{blockage} = \frac{kt}{2} \left(\left(\frac{A_0}{A_1} \right)^2 - 1 \right) \rho V |V|, \quad (6.3)$$

where kt is a constant which needs to be determined experimentally. To do so, pressure drop for models with different plaque morphologies and for constant flow rates is measured. kt is then determined from Eq. 6.3 using the experimental pressure drop data. The flow rate range is between 200 to 530 ml/min, approximately which is displayed by the shaded area in Fig. 6.5. This range accounts for both resting coronary blood flow and hyperemic blood flow ranges. It was shown by Ramanathan and Skinner (2005) that the resting coronary blood flow is about 250 ml/min. Furthermore, the coronary blood flow during the hyperemic condition can increase up to twice of the resting condition. This was shown by Uren et al. (1994) in the form of an increase in the value of the myocardial blood flow which is an indicator of the volume of blood per unit of time per unit of cardiac mass.

In order to study the effect of plaque morphology, different shapes, degrees, eccentricity and lengths of plaques are considered. As explained in the introduction section, different shapes of the stenosis can be formed inside the coronary arteries, as shown in Fig. 6.1 (Beach et al. 2011). Most stenoses can be categorised in three main shapes. The first category is the circular shape of stenosis. Stenoses with a circular cross section are presented in Fig. 6.1(a-e) with different degrees of stenosis. The second category is the stenosis with elliptic cross section (Fig. 6.1(f-j)). Sharp-edge stenosis is another shape of the cross section of the stenosis, as displayed in Fig. 6.1(k-o). The stenosis in each of the three categories can be of different levels of eccentricity. For example, Fig. 6.1(a) and Fig. 6.1(l) show concentric round and sharp-edge stenosis while Fig. 6.1(d) shows an eccentric round stenosis.

In this study, four main categories of the stenosis shapes are selected for the experiments including axisymmetric, eccentric, sharp-edge concentric, and asymmetric (Fig. 6.2). They account for extremum cases with the lowest (axisymmetric and eccentric) and the highest (sharp-edge concentric and asymmetric) sharp-edges. The selected shapes of the stenosis with different degrees of stenosis between 25% to 94% are 3D-printed using ABS material. Figure 6.2 shows the longitudinal cross sections of the 3D printed models for all four shapes of the stenosis with the degree of stenosis of 84%.

Eccentricity index (e) of a plaque, as explained earlier, refers to the distance between the centre of stenosis and the centre of the hosting artery (Fig. 6.3, $e = ((E1 - E2))/E1$, where $E1$ and $E2$ are the maximum and minimum thicknesses of the plaque, respectively). In this study, both the curved and sharp-edges of the stenosis shapes are studied with the lowest (axisymmetric and sharp-edge concentric cases) and the highest eccentricity (eccentric and asymmetric) as the critical representatives of the different stenosis shapes. Furthermore, different levels of eccentricity are studied for the curved edge case starting

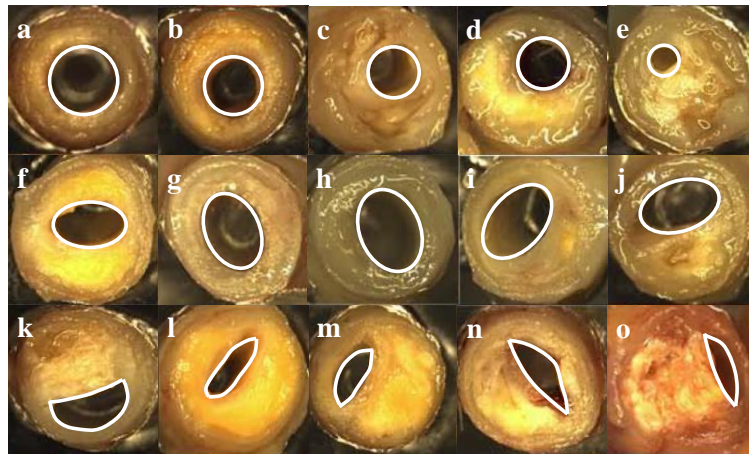


Figure 6.1: Cross sections of different shapes of the stenosed coronary arteries categorised in three main sections including circular stenosis shapes (a–e), elliptic stenosis shapes (f–j) and sharp-edge shapes (k–o). All can be categorised in different degrees of stenosis and levels of eccentricity (different concentric and eccentric cases are displayed.) [Thomas G Beach, Chera L Maarouf, Reed G Brooks, Scophil Shirohi, Ian D Dausg, Lucia I Sue, Marwan N Sabbagh, Douglas G Walker, LihFen Lue, and Alex E Roher, BMC Geriatrics, Vol.11, 3, 2011; licensed under a Creative Commons Attribution (CC BY) license.].

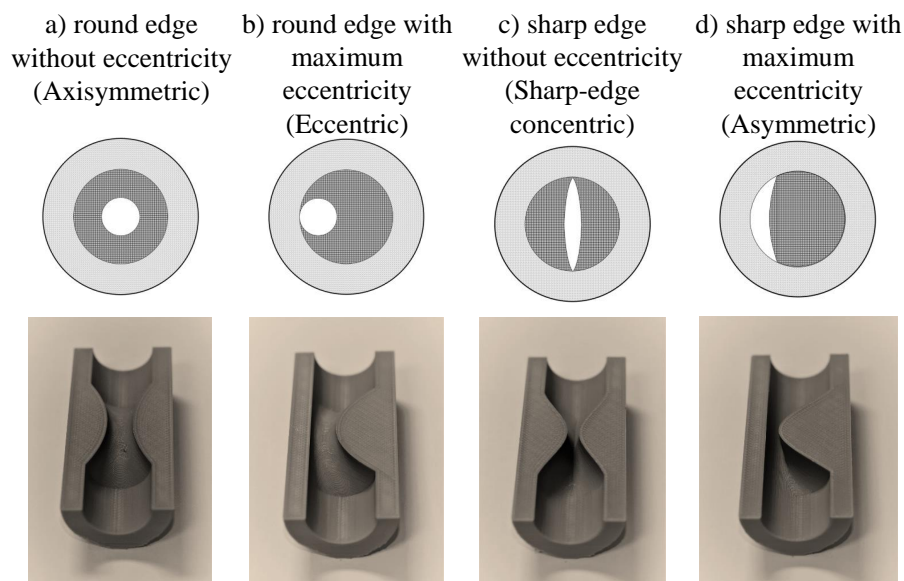


Figure 6.2: Vertical (top row) and longitudinal (bottom row) cross sections of different stenoses considered in this study including a) axisymmetric, b) eccentric, c) sharp-edge concentric, and d) asymmetric (In all cases, $S = 0.84$). The outer light shaded area is the artery wall and the inner dark shaded area introduces the stenosis.

from the axisymmetric case with zero eccentricity to eccentric case with unity eccentricity, as shown in Fig. 6.3.

Another important parameter in the study of the plaque morphology is the plaque length, which represents the length of the artery covered by the stenosis. The changes in the plaque length affect the stenosis morphology and consequently influence the flow behavior and haemodynamic parameters downstream of the stenosis. It is found that, the

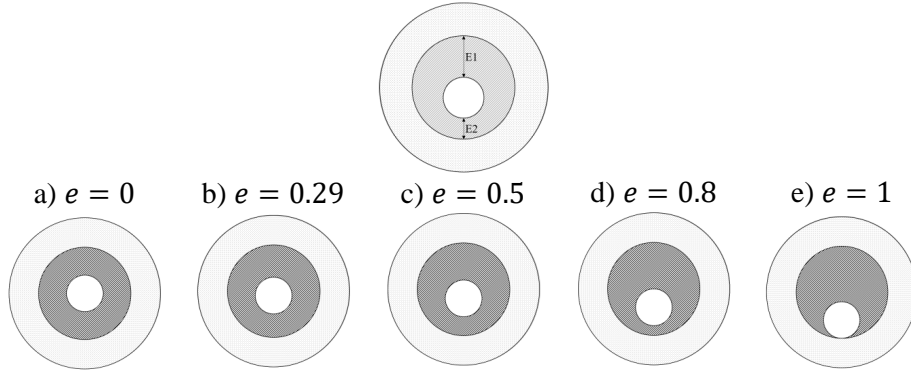


Figure 6.3: Schematic of the cross section of an artery with eccentric stenosis (top). Bottom shows different levels of eccentricity considered in this study including a) $e = 0$, b) $e = 0.29$, c) $e = 0.5$, d) $e = 0.8$, and e) $e = 1$ (In all cases, $S = 0.84$). The shaded area introduces the stenosis.

length of recirculation zone is a direct function of the plaque length (Stroud et al. 2000). Based on the clinical data, the plaque length in the coronary arterial system changes in the range of $1D$ to $3D$ (Christiansen et al. 2017). Hence, to study the effect of this parameter three different plaque lengths are considered in this study including $1D$, $2D$ and $3D$ (Fig. 6.4).

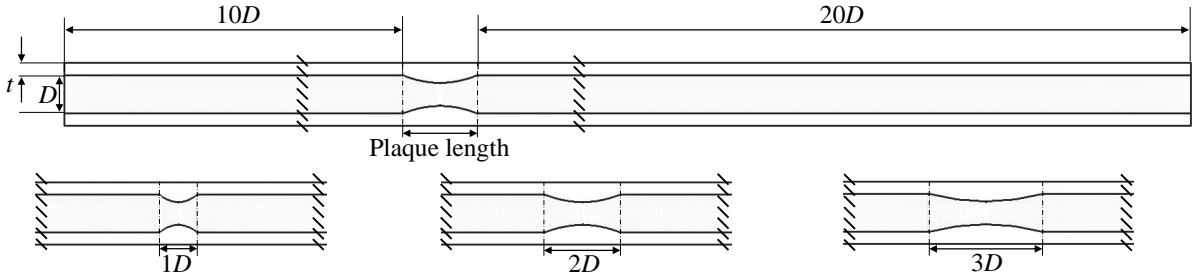


Figure 6.4: Cross section of a semi-blocked artery with $10D$ upstream and $20D$ downstream of the blockage and different plaque lengths considered in this study.

Pressure drop due to pulsatile effect

The pressure drop due to the acceleration and deceleration caused by the pulsatile flow effect can be found by applying the stream-wise momentum equation (Young and Tsai 1973a),

$$\Delta P_{pulsatile} = ku\rho L \frac{dV}{dt}, \quad (6.4)$$

where ku is a constant which needs to be calculated for different cases with different flow profiles.

Since the physiological flow profiles inside different arteries can be expressed based on the combination of different Fourier series modes, different simple sinusoidal flow profiles (Fig. 6.5a) and the combination of them (Fig. 6.5b), given in Eqs. 6.5 and

6.6, respectively, with different periods (T) and amplitudes (A) are employed in the experiments in order to calculate ku for different stenosis morphologies explained in the previous section.

$$q(t) = q_{mean} + 131 \cos\left(\left(\frac{2\pi}{T}\right)t\right), \quad (6.5)$$

$$q(t) = q_{mean} + 131A \left(\cos\left(\left(\frac{2\pi}{T}\right)t\right) + \sin\left(\left(\frac{2\pi}{T}\right)t\right) + \cos\left(2 \times \left(\frac{2\pi}{T}\right)t\right) + \sin\left(2 \times \left(\frac{2\pi}{T}\right)t\right) \right), \quad (6.6)$$

where q_{mean} is the mean flow rate of the flow profile in ml/min.

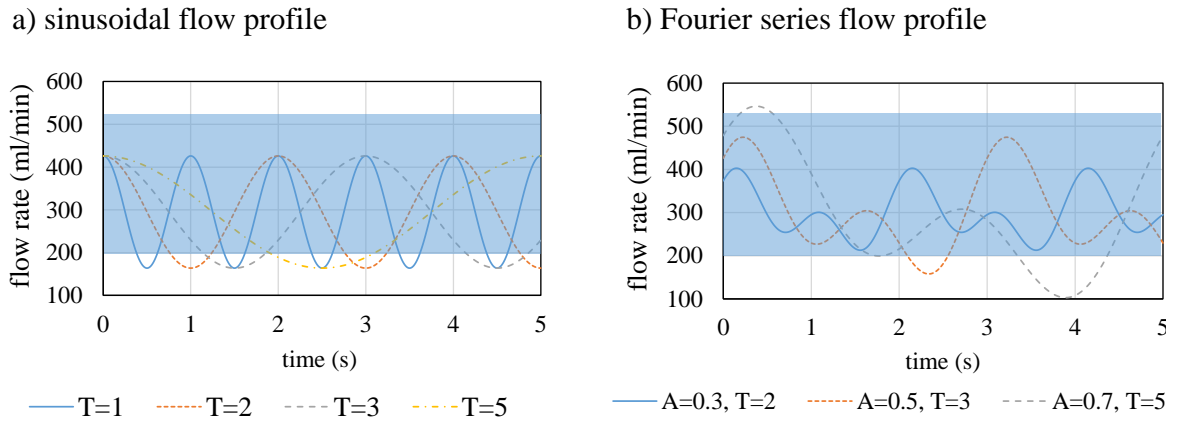


Figure 6.5: Different flow profiles employed in this study a) sinusoidal flow profile (Eq. 6.5) and b) Fourier series flow profile (Eq. 6.6) to train the pulsatile part of the developed pressure drop equation with $q_{mean} = 295$ ml/min. The constant flow rate in the shaded area is used to calculate blockage parameter.

Total pressure drop

Finally, the total pressure drop can be expressed by the linear sum of the corresponding pressure drop terms due to viscous friction, blockage and pulsatile effects as:

$$\Delta P(t) = \underbrace{\frac{128}{\pi} \frac{\mu q(t)}{D_h^4} L}_{\text{viscous friction part}} + \underbrace{\frac{kt}{2} \left(\left(\frac{A_0}{A_1} \right)^2 - 1 \right) \rho V |V|}_{\text{blockage part}} + \underbrace{ku \rho L \frac{dV}{dt}}_{\text{pulsation part}}, \quad (6.7)$$

It is to note that L is the length of the artery model that includes the downstream and upstream lengths of the artery as well as the plaque length $L = \underbrace{10D}_{\text{downstream}} + \underbrace{20D}_{\text{upstream}} + l$. As explained earlier, this equation relies on two parameters of kt and ku , which are required to be determined from the experiments. According to Eq. 6.7 and since the pulsatile part is only responsible for the pressure drop fluctuations and does not affect the mean values

of the pressure drop, blockage factor is calculated by subtracting the viscous friction pressure drop (calculated from Eq. 6.2) from the mean total pressure drop measured in the experiments. Therefore, the pulsatile part and consequently pulsatility factor is calculated by subtracting the time-averaged pressure drop from the total time dependent pressure drop.

Experimental setup

Figure 6.6 shows the experimental rig consisting of: (1) a programmable centrifugal pump (RS pro direct coupling centrifugal pump) and its controller (RS pro process pump controller for brushless micro-pump), (2) an electromagnetic flowmeter (Krohne, Batchflux 5500C), (3) a 3D-printed settling chamber, (4) a pressure sensor (UNIK 5000 silicon pressure sensor), (5) a 3D printed stenosed artery model (Zortrax M300), (6) a valve, (7) a water reservoir, and (8) a computer, power supply and DAQ card (NI USB-6211). A long acrylic pipe (about 2 m) is installed before the test section and after the settling chamber to allow the pulsatile flow inside the system to become fully developed. The input voltage of the pump is controlled using a data acquisition card to simulate the physiological pulsatile velocity waveform. The internal diameter of the model, D , is 6.1 mm corresponding to double the diameter of coronary arteries. The reason that the model is designed at a larger diameter than the coronary artery is to reduce the measurement errors compared to when a smaller diameter was used. However, by matching the Reynolds number and Womersley number, as two dimensionless parameters governing the blood flow regime, flow similarity is achieved, and the results are independent of the artery diameter. As an example of dimensionless parameters which used to match the results, for a heart beating value of 1 beat/s and the flow rate of 1.1 ml/s which represent the resting condition, the value of Reynolds and Womersley numbers are selected as 146 and 2.1, respectively. A $10D$ and $20D$ lengths are considered before and after the stenotic part, respectively. A mixture of water and glycerine which has almost the same viscosity as blood is usually employed to mimic the blood rheological characteristics. The viscosity of the water-glycerine mixture is a function of temperature and varies significantly when the ambient temperature changes. Due to the large number of measurements for this study, more than 200 cases, and to make the results independent of the room temperature, distilled water was used as the working fluid for the experiments. The viscosity of distilled water is not a function of the temperature and therefore it was deemed suitable for the experiments. It must be noted that the effect of viscosity is taken into account by matching the Reynolds number. Furthermore, changing the fluid viscosity will not affect the calculated factors in the developed pressure drop equation. Viscosity appears in the pressure drop term due to viscous friction (Eq. 6.2), and by calculating the viscous term using the corresponding fluid viscosity (in this case, distilled water), its effect on the other two terms is removed. Hence, the blockage (Eq. 6.3) and the pulsatility pressure drop terms remain unchanged. This means that regardless of the type of the working fluid, the developed pressure drop equation and the constant parameters remain unchanged. Furthermore, in order to present the physical and rheologic characteristics of arterial blood, in the case study section, a mixture of water and glycerine is used as a blood mimicking fluid which matches the viscosity of the blood. The mixture consists of 60% water and 40% glycerine by mass fraction based on literature (Charonko et al. 2009; Deplano et al. 2007; Tanné et al. 2010). Two pressure sensors are used to measure the

pressure differences before and after the test section.

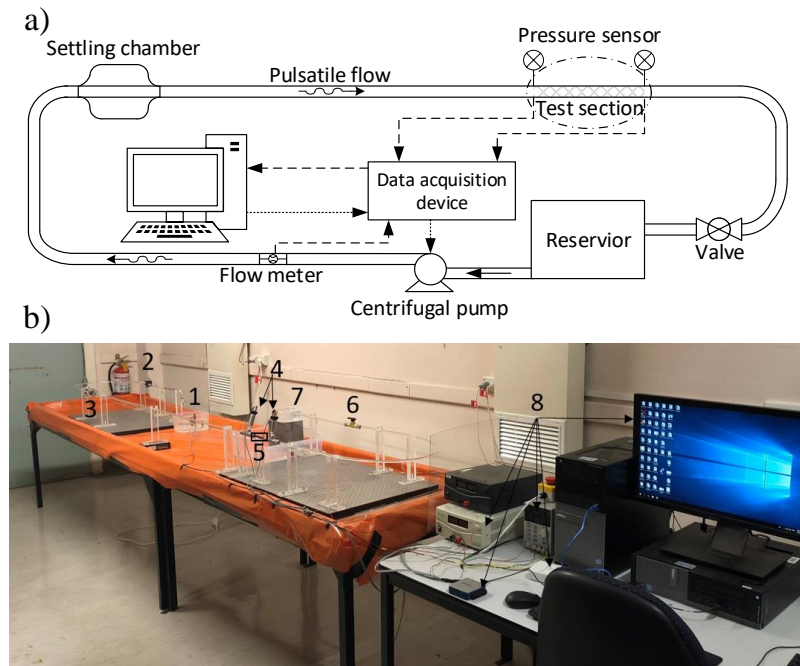


Figure 6.6: a) Schematic of the test setup and b) Experimental test setup: (1) centrifugal pump; (2) flow sensor; (3) settling chamber; (4) pressure sensor; (5) 3D-printed test section; (6) valve; (7) water reservoir; (8) computer, power supply and DAQ card.

3D-printed stenosed artery model

An acrylonitrile butadiene styrene (ABS), common thermoplastic polymer, was used to 3D-print the stenosed coronary artery models with a sub-layer height of 0.09 mm using Zortrax M-200. After 3D printing the models, the models were polished using fine sandpapers and placed in acetone vapour chamber for about 20 minutes to improve the quality of the surface of the 3D-printed models. To evaluate the relative surface height of the models, a surface roughness measuring tester machine was employed. Four samples from different 3D-printed models were selected and for each sample, a 3-mm length in longitudinal direction was chosen. Figure 6.7 displays the relative surface height for one of the samples which shows that the variation of the surface height for this model is in the range of $-0.1 \mu\text{m}$ to $0.1 \mu\text{m}$ representing the high surface smoothness of the models.

The relative pipe roughness, which is defined as the ratio of the relative surface height over the model diameter, for four printed samples was calculated and the average was 6.25×10^{-6} . Based on the Moody diagram and since the flow is laminar, the 3D-printed models can be considered as a smooth pipe.

Uncertainty analysis

Two main sources of the uncertainty in this study are the uncertainty related to the measurement devices and the one associated with the measured values. As discussed in the previous section, the uncertainties related to the measurement devices were provided

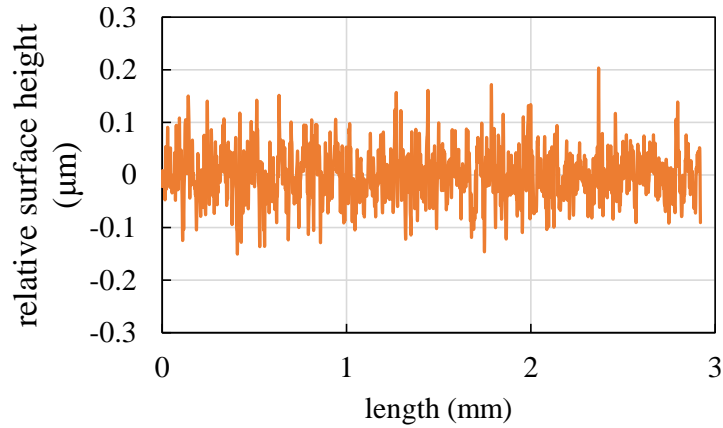


Figure 6.7: Relative surface height of the 3D-printed model with ABS material using Surface Roughness Measuring Tester Mitutoyo SJ-410.

by the manufacturers. The pressure transducers have a full-scale accuracy of 0.04% and the flowmeter has a measurement accuracy of 0.4% of measured value. The uncertainty of the measured values includes the uncertainty of the pipe diameter and roughness. After 3D printing of the models, the internal pipe diameter were measured carefully at two ends with a micro-meter with a maximum error of ± 0.1 mm, while the uncertainty of the relative internal surface roughness of the models was ± 1 . In order to account for bias and precision errors arising due to calibration of the pressure sensors and the flow meter and also the sensitivity of the measurement devices, each experiment was repeated for five times under identical conditions. According to method recommended in (American Society of Mechanical 2006), all the results in next section are reported as the average of the five measurements and the experimental measurement error, determined as the standard deviation of five measurements, is found to be 0.5%. The uncertainties are shown by error bars in the graphs of the results section.

6.2.3 Results

Total pressure drop measurement

The effect of different degrees of stenosis ($S = 0.28 - 0.94$) on the pressure drop for a wide range of flow rates for a case with an axisymmetric shape of stenosis is displayed in Fig. 6.8. All data in this section are presented for the plaque length of the 2D unless otherwise is stated. The higher the flow rate, the higher the pressure drop. This occurs due to an increase in the fluid velocity that leads to an increase in the viscous friction and blockage pressure drops (first and second terms of Eq. 6.7). Furthermore, increasing the degree of stenosis increases the pressure drop because of an increase in the blockage term of Eq. 6.7. Due to the sudden change in the flow pattern because of the stenosis as well as an increase in the fluid velocity passing over the stenosis, the turbulence structures start to grow after the constriction. The turbulence due to the constriction inside the pipe is intensified with an increase in the cross sectional area covered by the fat plaques in the artery. It is reported in the literature that by increasing the degree of stenosis, a jump in the turbulent kinetic energy (TKE) profile, as an indicator of transition to turbulence that is related to the formation of turbulent structures in the downstream of

the stenosis, was observed (Biswas et al. 2016; Khair et al. 2015). The local Reynolds number immediately after the stenosis increases considerably, due to a sudden jump in the velocity, which leads to the formation of turbulent structures. The turbulence causes an increased pressure drop across the constrictions with higher degrees of stenosis.

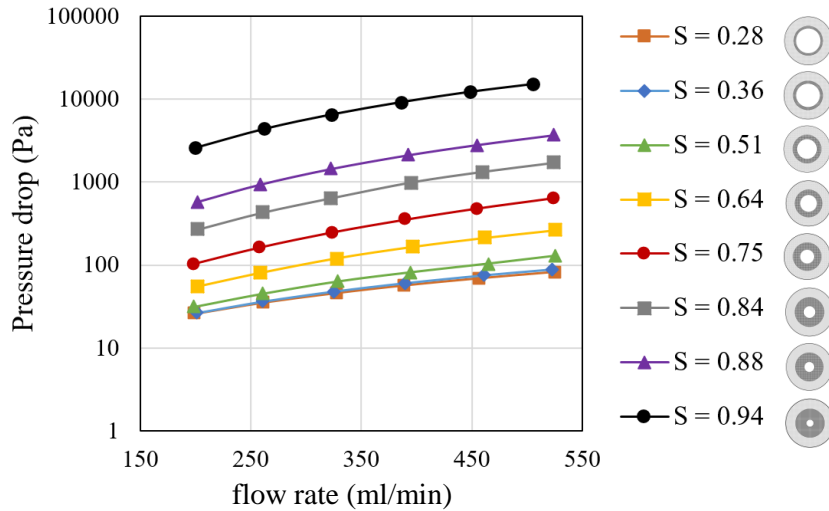


Figure 6.8: Pressure drop for different degrees of stenosis inside a coronary artery model with an axisymmetric stenosis for a wide range of flow rate.

Figure 6.9 displays the effect of stenosis shape including axisymmetric, eccentric, sharp-edge concentric, and asymmetric on the pressure drop for a specific degree of stenosis ($S = 0.84$). The highest pressure-drop is related to the asymmetric case with the maximum eccentricity and sharp-edge, while the lowest is related to the axisymmetric case with no eccentricity and no sharp-edge. Furthermore, pressure drop for the other two stenosis shapes (Eccentric and sharp-edge concentric) lies between the two extremum shapes with the highest and lowest sharp-edge and eccentricity (axisymmetric and asymmetric). The results show that the pressure drop due to both eccentric and sharp-edge concentric shapes of the stenosis are almost the same. However, the eccentric shape of the stenosis leads to a slightly larger pressure drop compared to the sharp-edge concentric case. This illustrates that eccentricity plays a more significant role in the pressure drop compared to the effect of the sharp-edge cross section.

The effect of the shape of the stenosis on the pressure drop can be explained through the changes in the flow behaviour. A recirculating flow develops immediately downstream of the stenosis. This recirculation flow regime changes for different shapes of the stenosis and consequently changes the amount of the pressure drop. In other words, the sudden changes in the fluid velocity because of the stenosis inside the artery generates turbulence in which energy is dissipated and consequently pressure is decreased. If the shape of the stenosis is well-rounded (axisymmetric and eccentric cases), the fluid is able to follow the stenosis boundary without separation at low flow rates. Since the location of the separation is delayed for higher flow rates, the pressure drop is increased. In the presence of the eccentricity in the shape of the stenosis, velocity distributions are shifted to the opposite side of the eccentricity part after the constriction. This results in an asymmetric wall shear stress distribution over the pipe wall after the stenotic section (Jabir and Lal 2016). This also results in higher pressure-drop, as it is displayed in Fig. 6.9, for the cases with eccentricity (eccentric and asymmetric).

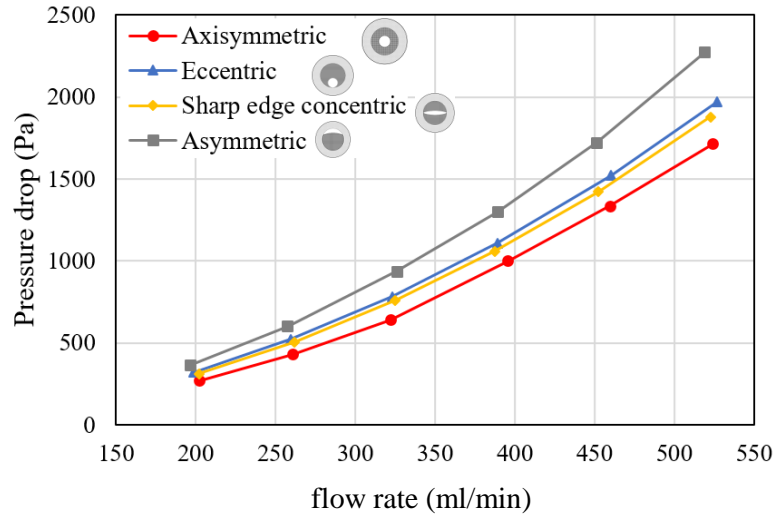


Figure 6.9: Pressure drop versus a wide range of flow rate for different shapes of stenosis including axisymmetric, eccentric, sharp-edge concentric, and asymmetric inside a coronary artery model with $S = 0.84$ for a wide range of flow rate.

Evaluation of the blockage factor

Blockage factor versus different degrees of stenosis for different shapes of the stenosis is displayed in Fig. 6.10. Blockage factor was calculated by subtracting the time-averaged viscous pressure drop from the total time-averaged pressure drop. Since the time-averaged value of the unsteady pressure drop term is zero, the time-averaged total pressure drop is equal to the sum of the time-averaged viscous and time-averaged blockage terms. The time-dependent blockage term was then determined using the calculated blockage factor and the phase-averaged flow velocity from Eq. 6.3. The blockage factor is found to be a function of both shape and degree of stenosis. The blockage factor increases with increasing the degree of stenosis for all four shapes of the stenosis. Constriction inside the artery with a high degree of stenosis blocks the artery more, hence increases the pressure drop, and consequently increases the blockage factor. Following the same trend as Fig. 6.9, axisymmetric shape of the stenosis has the lowest blockage factor, while the asymmetric one has the highest blockage factor. According to Fig. 6.10, the blockage factor versus degrees of stenosis for all different shapes of the stenosis follows the second-order exponential fit profiles, as shown in Fig. 6.10 with solid lines for two extremum cases with and without eccentricity and sharp edges. Table 6.1 presents the curve fitting parameters of the two-extremum cases as well as the r-square values. The shaded area represents the range of the blockage factor for different shapes of the stenosis. The lower limit of the shaded area refers to the shape of the stenosis without eccentricity and sharp edge, i.e. axisymmetric, while the upper limit stands for the shape of the stenosis with the maximum eccentricity and sharp edge, i.e. asymmetric. The blockage factor for the other two shapes of the stenosis, i.e. sharp edge concentric and eccentric, is found to be within the shaded area, as shown in Fig. 6.10.

The error bars in Fig. 6.10 represent the standard deviation of the calculated blockage factor for six different flow rates at each shape and degree of stenosis. The error bars are larger at lower degrees of stenosis where the viscous friction and blockage pressure drops are almost of the same order and hence the blockage factor is more dependent on

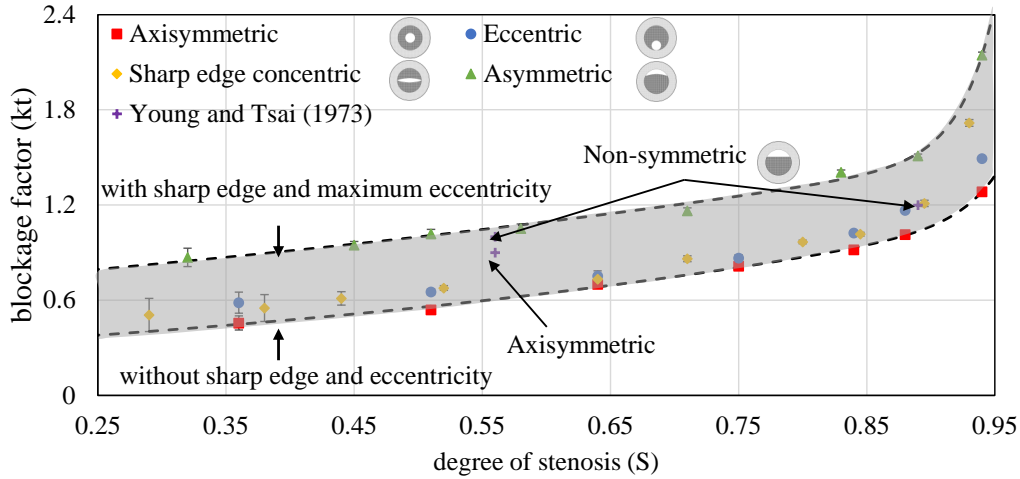


Figure 6.10: Blockage factor versus different degrees of stenosis for different shapes of stenosis including axisymmetric, eccentric, sharp-edge concentric and asymmetric for the case with the plaque length of $2D$.

Table 6.1: Curve fit parameters of the blockage factor (kt) versus degree of stenosis (S) for two extremum cases of the stenosis shape with and without sharp edge and eccentricity as $kt = a \times \exp(b \times S) + c \times \exp(d \times S)$.

curve fit parameter	$a(\times 10^{-16})$	b	c	d	R-square
axisymmetric shape of the stenosis (without sharp edge and eccentricity)	27.3	34	0.26	1.51	0.9977
asymmetric shape of the stenosis (with sharp edge and eccentricity)	2.6	37.72	0.63	0.92	0.9945

the flow rate. The blockage factor from the literature (Young and Tsai 1973b) for two shapes and degrees of stenosis are also illustrated in Fig. 6.10. Their results demonstrated that the asymmetry leads to a higher blockage factor, which agrees with the results of this study. Furthermore, the ranges of the blockage factor for the cases studied by Young and Tsai (1973a) agree reasonably well with the obtained results of the present study. However, the difference is related to the different shapes of stenosis and the plaque growth pattern. The reason that the blockage factor of the non-symmetric shape of the stenosis in their study placed in between the blockage factor curves of the sharp edge and round edge obtained in the current study is the fact that the non-symmetric shape of the stenosis, in their study, has half round-edge and half sharp-edge.

The blockage factor which is shown in Fig. 6.10 is calculated by subtracting the viscous friction term from the time-averaged pressure drop, as explained in the methodology section. To calculate the viscous friction term, the wetted area of the stenotic section of the artery model in addition to the rest of the wetted area of the pipe needs to be calculated in the form of the hydraulic diameter as explained by the Darcy-Weisbach equation (Eq. 6.2). The wetted area of the stenosis is a function of the shape of the stenosis, degree of stenosis and the growth profile of the stenosis along the plaque length. Hence, precise knowledge of these parameters is required for calculation of the wetted area. As this is not feasible in application, to develop a general pressure drop equation that can be applied to different shapes and degrees of stenosis and different physiological

flow profiles, the viscous friction pressure drop is proposed to be calculated based on the healthy coronary artery model without considering the effect of the stenosis on the viscous friction term. This means that the viscous friction pressure drop, calculated from the Darcy-Weisbach equation, can be calculated from the upstream flow velocity and the diameter of the coronary artery model without the stenosis. The effect of this assumption on the blockage pressure drop and blockage factor for all shapes of the stenosis is calculated. Figure 6.11 compares the blockage pressure drop and factor versus different degrees of stenosis for the cases with the estimated and actual wetted areas for the case of the stenosis shape of the sharp-edge concentric as an example. The higher the degree of stenosis, the larger the wetted area. Furthermore, the larger the wetted area, the higher the interaction between the fluid and the artery wall and hence the higher the viscous friction pressure drop. According to Fig. 6.11, not considering the actual wetted area of the constricted artery brings maximum 9% overestimation of the blockage factor. However, since the time-averaged pressure drop is the sum of the viscous friction and blockage terms, the overestimation of the blockage term which is followed by the underestimation of the viscous friction term does not change the time-averaged pressure drop. Since calculating the actual wetted area is almost impossible in real shapes of stenosis and as the objective of this study is the development of a generalised pressure drop equation for the stenosed coronary artery model, the results in this section are presented using this assumption.

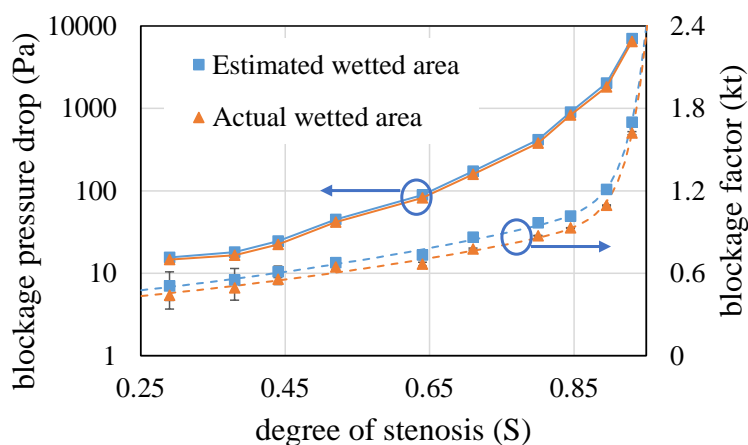


Figure 6.11: Blockage pressure drop and factor versus different degrees of stenosis for the cases with the estimated (square symbol) and actual (triangular symbol) wetted areas and the stenosis shape of the sharp-edge concentric. Blockage pressure drops (solid lines) are displayed at the flow rate of 325 ml/min.

Figure 6.12 displays the effect of the degree of eccentricity, starting from axisymmetric case with no eccentricity to the maximum degree of eccentricity corresponding to the eccentric case, on the blockage factor. As it was shown in Fig. 6.10, a higher degree of eccentricity leads to a higher blockage factor, regardless of the degree of stenosis.

The effect of changing the plaque length from $1D$ to $3D$ on the pressure drop for all different shapes of stenosis is investigated. The maximum difference in the pressure drop for two cases with the highest and the lowest plaque length for a constant degree of stenosis and for all shapes of the stenosis is found to be about 10%. For example, Figure 6.13 presents the effect of plaque length on the experimental pressure drop as well as the viscous friction and blockage pressure drop terms for the case with axisymmetric shape of

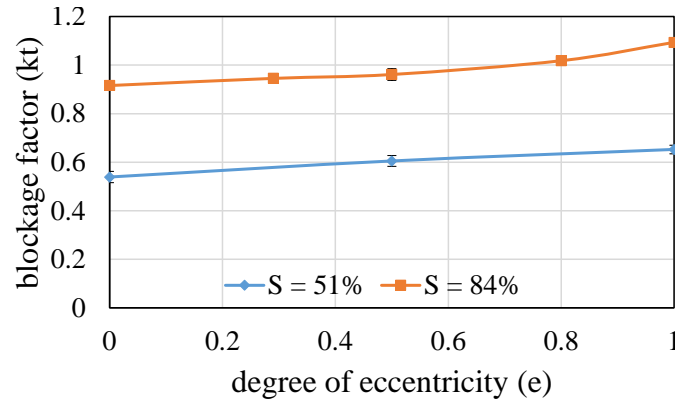


Figure 6.12: Blockage factor versus different degrees of eccentricity starting from zero degree of eccentricity corresponding the axisymmetric case to maximum degree of eccentricity (equals to one) corresponding to the eccentric case for two different degrees of stenosis ($S = 0.51$ and 0.84) with the plaque length of $2D$.

stenosis. The higher the plaque length, the higher the pressure drop. The increase in the pressure drop due to an increase in the plaque length is because of two effects; first, the increase in the viscous friction pressure drop. Increasing the plaque length increases the wetted area and consequently increases the viscous friction pressure drop. The second effect is due to the changes in the blockage pressure drop. In the stenosis with longer plaque length, flow is able to follow the stenosis pattern longer compared to the case with shorter plaque length before the separation happens due to the reduction in the sharpness of the stenosis. Hence, the recirculation zones are continued far downstream of the stenosis in the case with longer plaque length compared to the shorter plaque length. Therefore, the blockage pressure drop is higher in the cases with the longer plaque length.

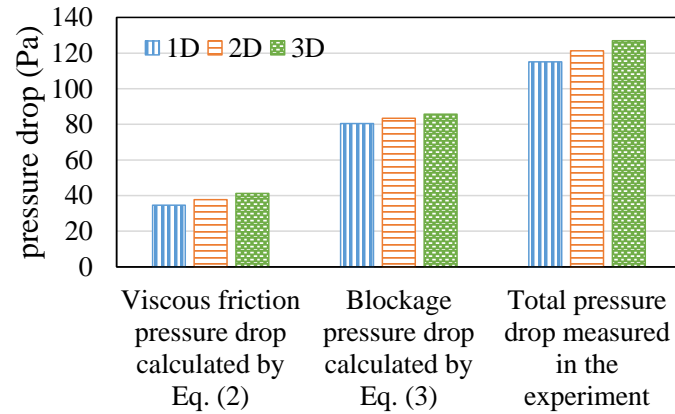


Figure 6.13: Experimental pressure drop as well as its viscous friction and blockage pressure drops for different plaque lengths and the axisymmetric shape of the stenosis for the case with $S = 0.64$ and the flow rate of 325 ml/min.

Evaluation of the pulsatility factor

The pulsatility factor is calculated for each profile, explained in the methodology section (Fig. 6.5), and different stenosis geometries from the unsteady pressure drop. Since sum

of the time-derivation of the fluid velocity over one cycle is equal to zero, the third term in the developed pressure drop equation (Eq. 6.7) is only responsible for the pressure fluctuations. This means that the time-averaged pressure drop over a coronary artery model with the stenosis inside is only because of the viscous friction and blockage effects and hence the first two terms in the developed equation are responsible for the evaluation of the mean pressure drop. Hence, unsteady pressure drop is calculated by subtracting the time-dependent viscous and blockage pressure drops from the total time-dependent pressure drop (or in other words by subtracting the time-averaged pressure drop from the total time-dependent pressure drop). Using Eq. 6.4 and by substituting the calculated unsteady pressure drop and the phase-averaged measured flow velocity from the flow meter, the pulsation factor was calculated. Figure 6.14 displays the pulsatility factor versus different degrees of stenosis for different shapes of stenosis calculated from the pressure drop measurements for different flow profiles. The results show that this factor is not a function of the profiles of the unsteady flow. Furthermore, unlike the blockage factor, which is a function of the shape of the stenosis, pulsatility factor is not a function of the stenosis shape. As shown in Fig. 6.14, ku can be expressed as a second-order power function of the degree of the stenosis. The higher the degree of the stenosis, the higher the pulsatility factor. As shown in the shaded area of Fig. 6.14, pulsatility factor is almost constant ($ku = 1.77$) for the degrees of the stenosis less than $S = 0.6$, and for higher degrees of stenosis, it can be described as $ku = 1.77 + 4.23S^{8.23}$. The error bars in Fig. 6.14 show the standard deviation of the pulsatility factor calculated for seven different sinusoidal flow profiles.

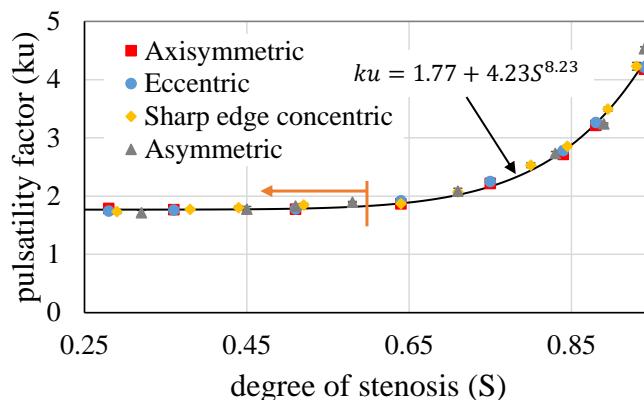


Figure 6.14: Pulsatility factor versus different degrees of stenosis for different shapes of stenosis including axisymmetric, eccentric, sharp-edge concentric, and asymmetric as well as the corresponding second-order power fit profile for the case with the plaque length of $2D$.

Evaluation of the total pressure drop

Figure 6.15 presents the evaluated pressure drop based on the developed equation for a few cases with different shapes and degrees of stenosis. The corresponding values of the blockage and pulsatility factors for calculation of the total pressure drop are selected using Figs. 6.10 and 6.14. The evaluated pressure drop from the developed equation match the experimental results as shown in Fig. 6.15. Table 6.2 shows the mean and peak deviation of the evaluated pressure drop for different cases. The maximum mean

and peak deviations are about 0.7% and 1%, respectively. This means that the developed pressure drop equation is able to accurately estimate the total unsteady pressure drop for different unsteady flow profiles with different shapes and degrees of stenosis with less than 1% deviation for the mean values of the pressure drop. A summary of the procedure to use the developed pressure drop equation for different conditions including the type of the flow profile (steady or unsteady), healthy or stenosed artery models, shapes and degrees of stenosis is given in the flowchart in Fig. 6.16.

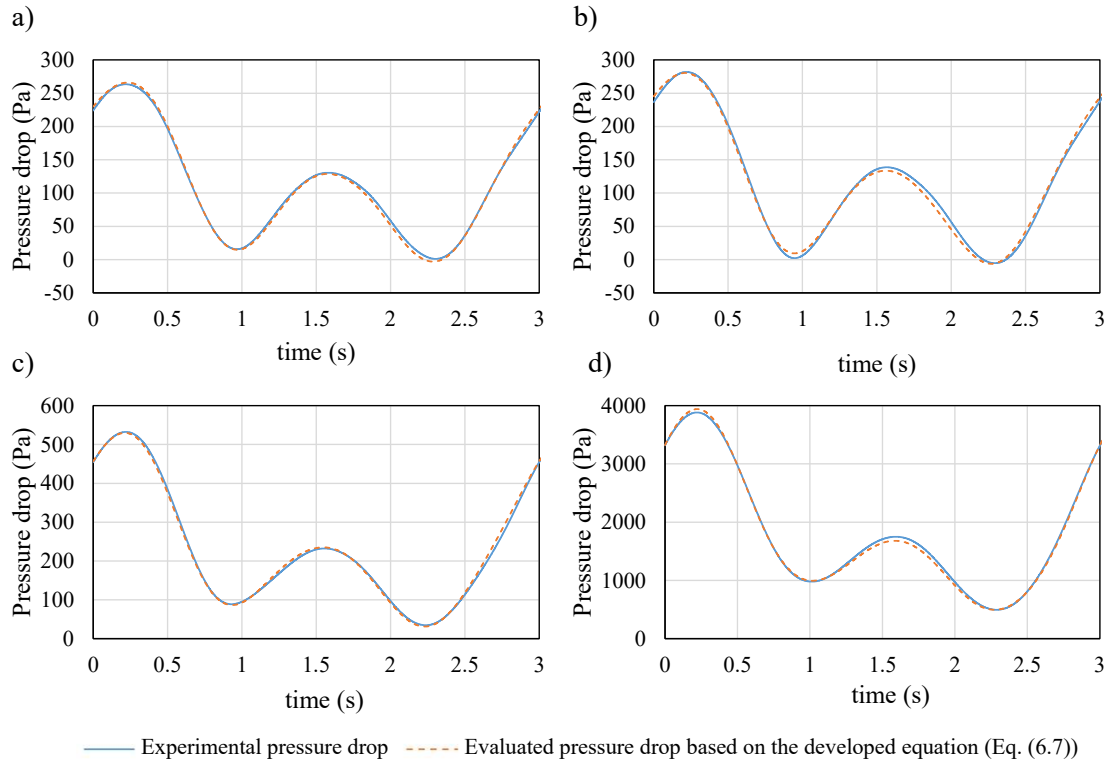


Figure 6.15: Evaluated pressure drop (dashed line) based on the developed equation (Eq. 6.7) and the experimental pressure drop (solid line) for the second order Fourier series with $A = 0.5$ and $T = 3$ and different shapes and degrees of stenosis including a) asymmetric with $S = 0.58$, b) eccentric with $S = 0.64$, c) axisymmetric with $S = 0.75$, and d) sharp edge concentric with $S = 0.895$. The maximum mean and peak deviations are about 0.7% and 1%, respectively.

Table 6.2: Mean and peak errors of the evaluated pressure drop for different cases with different shapes and degrees of stenosis.

	Mean errors (%)	Peak error (%)
asymmetric with $S = 0.58$	0.7	1
eccentric with $S = 0.64$	0.6	0.5
axisymmetric with $S = 0.75$	0.2	0.4
sharp edge concentric with $S = 0.895$	0.1	1

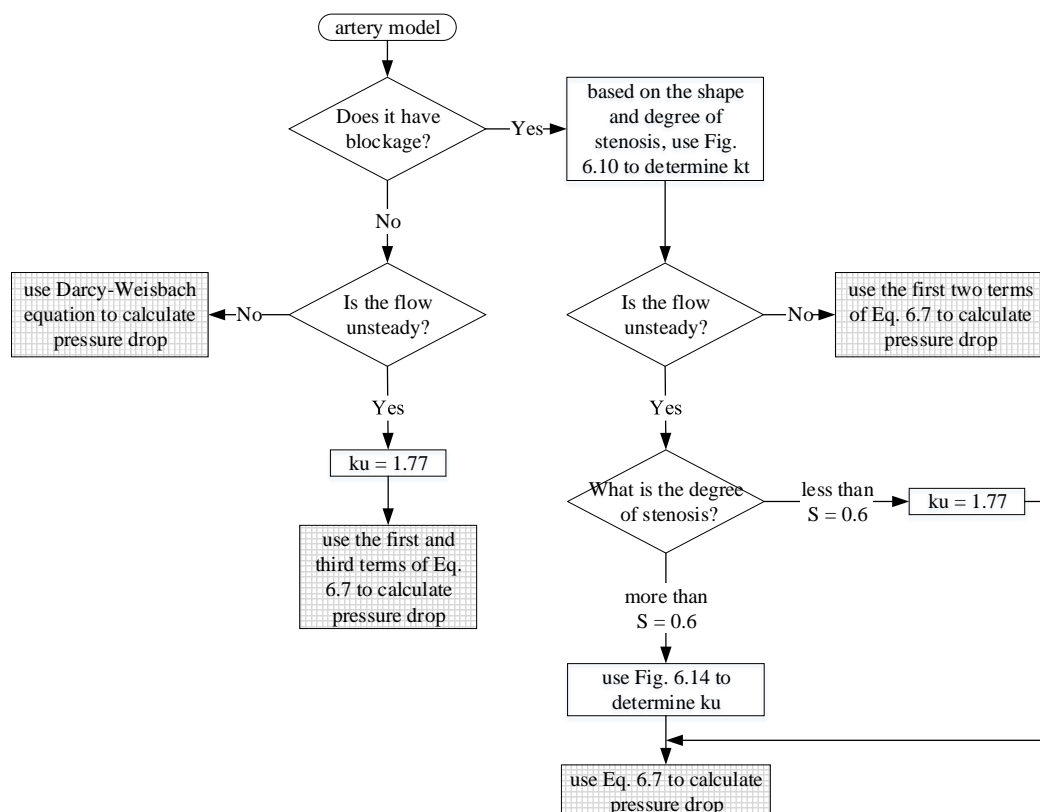


Figure 6.16: Flowchart of using the developed pressure drop equation for different conditions.

6.2.4 A pulsatile model with the physiological flow profile of the coronary artery: case studies

In order to test the validity of the developed pressure drop equation, two physiological flow profiles are used, as displayed in Fig. 6.17. These flow profiles represent the blood flow profile inside the left (Davies et al. 2008) and right (Kim et al. 2010) coronary arteries. These waveforms, as the inlet flow profiles for the experiments, are modelled using the first 16 and 32 Fourier harmonics of Fast Fourier Transform (FFT), respectively, that accurately represents the original waveform. Systolic squeezing of the heart muscles collapses the coronary arteries, and it is not until diastole when the heart relaxes that coronary resistance decreases and blood flow increases (Bartoli et al. 2012). That is why the majority of the blood flow occurs during the diastole, as shown in Fig. 6.17. It is worth mentioning that the contraction and expansion of the right coronary artery during a cardiac cycle is completely different as the left coronary artery that results in different flow profile for the right coronary artery as shown in Fig. 6.17.

To mimic the blood rheological characteristics, a mixture of water and glycerine is used as the working fluid in this section. Furthermore, as explained in the methodology section, Reynolds and Womersley numbers are matched with the corresponding values obtained from the coronary arteries for the case studies. By matching the Reynolds number, the corresponding flow rate is obtained and also by matching the Womersley number, the period of the cardiac cycle for both left and right coronary artery flow profiles is determined. The flow rate of the right coronary artery in the experiment is

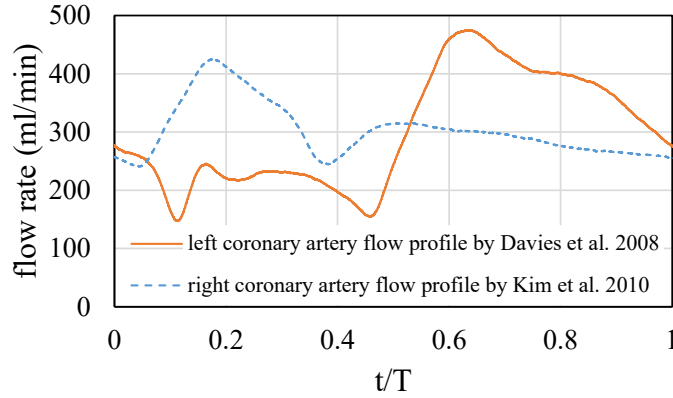


Figure 6.17: Physiological pulsatile left and right coronary artery blood flow profiles.

higher than the corresponding value achieved from the flow similarity matching due to the limitation of the pump, which cannot provide flow rates less than about 100 ml/min. However, the modelled flow profile of the right coronary artery matches the physiological profile obtained from (Kim et al. 2010), despite the higher mean flow rate.

Figures 6.18 and 6.19 display the evaluated pressure drop based on the developed equation and the experimental pressure drop as well as different terms of pressure drop including viscous friction, blockage and pulsation parts for left coronary artery flow profile and for sharp edge concentric shape of the stenosis with $S = 0.52$ and axisymmetric shape of the stenosis with $S = 0.64$. To estimate the total pressure drop from the developed equation, the procedure shown in the flow chart in Fig. 6.16 is employed. The blockage factor is determined from Figure 10 for the specific shape and degree of stenosis, Furthermore, the pulsatility factor is determined based on the corresponding degree of stenosis from Fig. 6.14. The flow velocity measured by the flow meter is also employed as an input to the algebraic model to estimate the pressure drop. Then, the calculated pressure drop using the equation was compared with the data measured by the pressure sensors. The results of Figs. 6.18a and 6.19a display a good correlation between the evaluated results obtained from the equation with the experimental pressure drop results. The mean deviations of the estimated pressure drop from the experimental data are less than 0.1% for both cases. The peak errors are 11% and 8% for two cases of Figs. 6.18a and 6.19a, respectively.

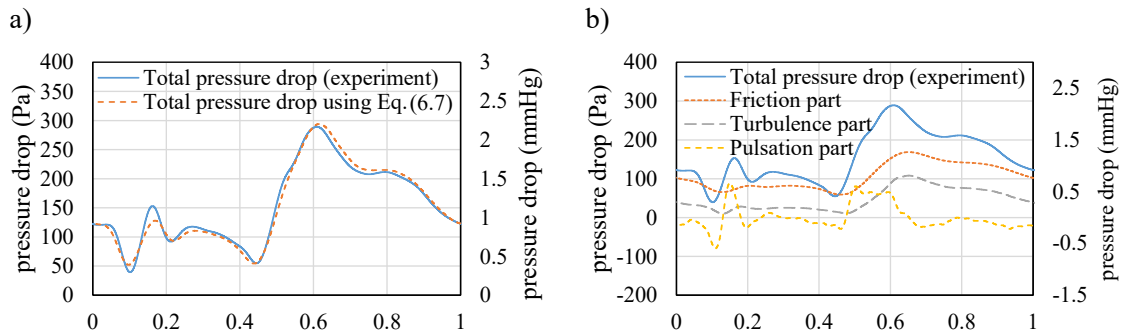


Figure 6.18: a) Evaluated pressure drop based on the developed equation and the experimental pressure drop and b) different components of it including viscous friction, blockage and pulsation parts for the left coronary artery flow profile with the stenosis shape of the sharp edge concentric and $S = 0.52$.

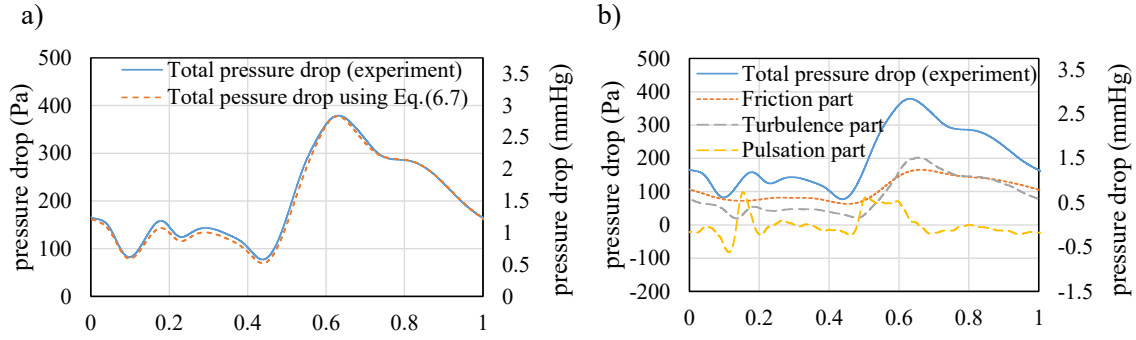


Figure 6.19: a) Evaluated pressure drop based on the developed equation and the experimental pressure drop and b) different components of it including viscous friction, blockage and pulsation parts for the left coronary artery flow profile with the stenosis shape of the axisymmetric and $S = 0.64$.

As explained earlier, the pulsation term is responsible for the pressure drop fluctuations (peak accelerations and decelerations) and the mean value of the pressure drop is determined from the viscous and blockage terms of the pressure drop. For low degree of stenosis, the viscous friction term is higher than the blockage pressure drop term, as shown in Fig. 6.18b. However, for moderate degree of stenosis, the viscous friction and blockage pressure drop terms are at the same order of magnitude and both determine the amounts of the time-averaged pressure drop, as shown in Fig. 6.19b.

Figures 6.20 and 6.21 display the evaluated pressure drop based on the developed equation and the experimental pressure drop as well as different terms of pressure drop including viscous friction, blockage and pulsation parts for right coronary artery flow profile and for asymmetric shape of the stenosis with $S = 0.71$ and eccentric shape of the stenosis with $S = 0.88$. The mean deviations of the estimated pressure drop from the experimental data are less than 0.5% and 0.1% for asymmetric and eccentric cases, respectively. The peak errors are approximately 6% for both cases.

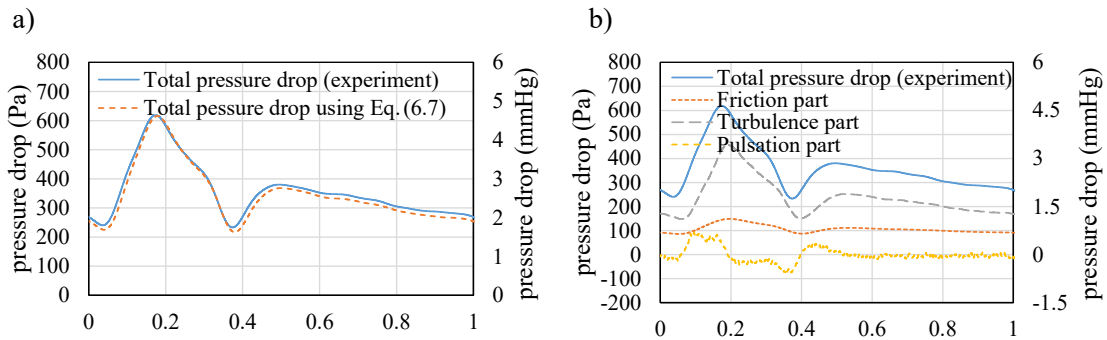


Figure 6.20: a) Evaluated pressure drop based on the developed equation and the experimental pressure drop and b) different components of it including viscous friction, blockage and pulsation parts for the right coronary artery flow profile with the stenosis shape of the asymmetric and $S = 0.71$.

For moderate to high degrees of stenosis cases, the blockage pressure drop term gradually becomes dominant in the total pressure drop value compared to the viscous friction term, as shown in Fig. 6.20b. On the other hand, for the higher degree of stenosis (Fig. 6.21b), the blockage term becomes more dominant with a value about one order of mag-

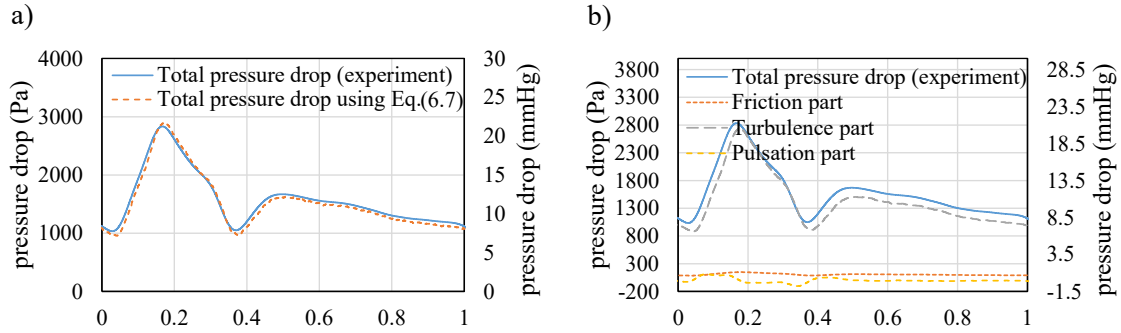


Figure 6.21: a) Evaluated pressure drop based on the developed equation and the experimental pressure drop and b) different components of it including viscous friction, blockage and pulsation parts for the right coronary artery flow profile with the stenosis shape of the eccentric and $S = 0.88$.

nitude larger compared to the viscous friction pressure drop term. Hence, it constitutes the major part of the mean pressure drop, and the viscous friction pressure drop term is almost negligible compared to the blockage term at a high degree of stenosis.

6.2.5 Conclusions

In this study, for the first time, a pressure drop equation was developed to evaluate the pressure drop across a stenosed coronary artery model with pulsatile inflow. Different shapes of the stenosis accounting for the critical physiological stenosis cases were studied. These cases included the stenosis shapes with and without sharp edges and eccentricity. Furthermore, a wide range of low to high degrees of stenosis with the flow rate varied from about 200 ml/min to 530 ml/min were considered. The proposed equation was developed based on the three major effects including the viscous friction effect, blockage effect and unsteady effect. The blockage factor and the pulsatility factor were determined based on experimental pressure measurements for different flow rates, shapes and degrees of stenosis as well as flow profiles.

Based on the results, both the blockage and pulsatility factors are not a function of flow rate. The blockage factor is strongly dependent on the shape and the degree of stenosis. The higher the degree of stenosis, the higher the blockage factor, regardless of the shape of the stenosis. The lowest blockage factor is related to the shape of stenosis with no sharp edge and no eccentricity, axisymmetric, while the highest one is related to the case with maximum sharp edge and eccentricity, asymmetric. Furthermore, the results showed that the pulsatility factor is not a function of shape of the stenosis and is only dependent on the degree of stenosis. The pulsatility factor is found to be constant ($kt = 1.77$) for the degrees of stenosis up to $S = 0.6$. Moreover, it was found that pulsatility factor is not a function of the type of the unsteady flow profile, which implies that the obtained results of pulsatility factor can be applied to any kind of pulsatile flow profile that can be presented in any form of the sinusoidal terms.

Although there are some simplifications in developing this equation such as assuming that the arteries are straight and their walls are rigid, the developed equation can be used as a tool to evaluate the pressure drop based on the flow rate and profile as well as the stenosis geometry. The impact of this equation is to help cardiologist to avoid using

any invasive methods such as FFR to calculate the pressure drop inside the stenosed arteries to evaluate the degree of stenosis. This equation can be employed to calculate the pressure drop non-invasively by using the flow data including instantaneous blood flow velocity and the stenosis geometry. The former can be determined using several non-invasive methods such as Doppler Ultrasonography and the latter can be determined using Computed Tomography (CT) images. Furthermore, the effect of the shape of the arteries such as curvature, which will increase the pressure drop compared to the straight artery models depending on the curvature angle and radius, can be studied in the future to expand the application of developed algebraic model.

Acknowledgement

Financial support for the project has been provided by the Australian Government Research Training Program Scholarship. The authors would also like to thank the workshops of the school of mechanical engineering at The University of Adelaide.

The authors declare that they have no conflict of interest.

References

- Achenbach S, Rudolph T, Rieber J, Eggebrecht H, Richardt G, Schmitz T, Werner N, Boenner F, and Mollmann H (2017). “Performing and interpreting fractional flow reserve measurements in clinical practice: An expert consensus document”. *Interventional Cardiology* 12.2, pp. 97–109.
- Alonso C, Pries AR, and Gaehtgens P (1993). “Time-dependent rheological behavior of blood at low shear in narrow vertical tubes”. *American Journal of Physiology* 265.2 Pt 2, H553–61.
- American Society of Mechanical E (2006). *Test uncertainty*. New York, N.Y.: American Society of Mechanical Engineers.
- Bartoli CR, Wead WB, Giridharan GA, Prabhu SD, Koenig SC, and Dowling RD (2012). “Mechanism of myocardial ischemia with an anomalous left coronary artery from the right sinus of Valsalva”. *The Journal of Thoracic and Cardiovascular Surgery* 144.2, pp. 402–408.
- Beach TG, Maarouf CL, Brooks RG, Shirohi S, Dausgs ID, Sue LI, Sabbagh MN, Walker DG, Lue L, and Roher AE (2011). “Reduced clinical and postmortem measures of cardiac pathology in subjects with advanced Alzheimer’s Disease”. *BMC Geriatrics* 11, p. 3.
- Biswas D, Casey D, Crowder D, Steinman D, Yun Y, and Loth F (2016). “Characterization of transition to turbulence for blood in a straight pipe under steady flow conditions”. *Journal of Biomechanical Engineering* 138.7, pp. 1–12.
- Blair GWS (1959). “An equation for the flow of blood, plasma and serum through glass capillaries”. *Nature* 183.4661, pp. 613–614.
- Charonko J, Karri S, Schmiegl J, Prabhu S, and Vlachos P (2009). “In vitro, time-resolved PIV comparison of the effect of stent design on wall shear stress”. *Annals of Biomedical Engineering* 37.7, pp. 1310–1321.

- Cho YI and Kensey KR (1991). “Effects of the non-Newtonian viscosity of blood on flows in a diseased arterial vessel. Part 1: Steady flows”. *Biorheology* 28.3-4, pp. 241–262.
- Christiansen MK, Jensen JM, Nørgaard BL, Dey D, Bøtker HE, and Jensen HK (2017). “Coronary plaque burden and adverse plaque characteristics are increased in healthy relatives of patients with early onset coronary artery disease”. *JACC: Cardiovascular Imaging* 10.10, Part A, pp. 1128–1135.
- Clark C (1976). “The fluid mechanics of aortic stenosis—I. Theory and steady flow experiments”. *Journal of Biomechanics* 9.8, pp. 521–528.
- Davies JE, Parker KH, Francis DP, Hughes AD, and Mayet J (2008). “What is the role of the aorta in directing coronary blood flow?” *Heart* 94.12, pp. 1545–1547.
- Deplano V, Knapp Y, Bertrand E, and Gaillard E (2007). “Flow behaviour in an asymmetric compliant experimental model for abdominal aortic aneurysm”. *Journal of Biomechanics* 40.11, pp. 2406–2413.
- Fearon WF, Tonino PA, De Bruyne B, Siebert U, and Pijls NH (2007). “Rationale and design of the Fractional Flow Reserve versus Angiography for Multivessel Evaluation (FAME) study”. *American Heart Journal* 154.4, pp. 632–636.
- Foucault E, Huberson S, Braud P, and Coisne D (2017). “On the pulsatile flow through a coronary bifurcation with stent”. *European Journal of Mechanics - B/Fluids* 61, pp. 177–186.
- Haynes RH (1960). “Physical basis of the dependence of blood viscosity on tube radius”. *American Journal of Physiology* 198, pp. 1193–1200.
- Huo Y, Svendsen M, Choy JS, Zhang ZD, and Kassab GS (2012). “A validated predictive model of coronary fractional flow reserve”. *Journal of the Royal Society Interface* 9.71, pp. 1325–1338.
- Jabir E and Lal SA (2016). “Numerical analysis of blood flow through an elliptic stenosis using large eddy simulation”. *Proceedings of the Institution of Mechanical Engineers, Part H: Journal of Engineering in Medicine* 230.8, pp. 709–726.
- Jahangiri M, Saghafian M, and Sadeghi MR (2015). “Numerical simulation of hemodynamic parameters of turbulent and pulsatile blood flow in flexible artery with single and double stenoses”. *Journal of Mechanical Science and Technology* 29.8, pp. 3549–3560.
- Khair A, Wang BC, and Kuhn DCS (2015). “Study of laminar–turbulent flow transition under pulsatile conditions in a constricted channel”. *International Journal of Computational Fluid Dynamics* 29.9-10, pp. 447–463.
- Kim HJ, Vignon-Clementel IE, Coogan JS, Figueroa CA, Jansen KE, and Taylor CA (2010). “Patient-specific modeling of blood flow and pressure in human coronary arteries”. *Annals of Biomedical Engineering* 38.10, pp. 3195–3209.
- Kohn JC, Lampi MC, and Reinhart-King CA (2015). “Age-related vascular stiffening: causes and consequences”. *Frontiers in Genetics* 6, p. 112.
- Li S, Chin C, Thondapu V, Poon EKW, Monty JP, Li Y, Ooi ASH, Tu S, and Barlis P (2017). “Numerical and experimental investigations of the flow–pressure relation in multiple sequential stenoses coronary artery”. *The International Journal of Cardiovascular Imaging* 33.7, pp. 1083–1088.
- Mirramezani M, Diamond S, Litt H, and Shadden SC (2018). “Reduced order models for transstenotic pressure drop in the coronary arteries”. *Journal of Biomechanical Engineering*, p. 31005.

- Morris PD, Vosse FN van de, Lawford PV, Hose DR, and Gunn JP (2015). ““Virtual” (computed) fractional flow reserve: current challenges and limitations”. *JACC: Cardiovascular Interventions* 8.8, pp. 1009–1017.
- Nichols W, O’Rourke M, and Vlachopoulos C (2011). *McDonald’s blood flow in arteries, Sixth edition: Theoretical, experimental and clinical principles*. CRC Press.
- Ohara T, Toyoda K, Otsubo R, Nagatsuka K, Kubota Y, Yasaka M, Naritomi H, and Minematsu K (2008). “Eccentric stenosis of the carotid artery associated with ipsilateral cerebrovascular events”. *American Journal of Neuroradiology* 29.6, pp. 1200–1203.
- Plesniak MW and Bulusu KV (2016). “Morphology of secondary flows in a curved pipe with pulsatile inflow”. *Journal of Fluids Engineering* 138.10, p. 101203.
- Prager W (1961). *Introduction to Mechanics of Continua*. Ginn.
- Quemada D (1978). “Rheology of concentrated disperse systems III. General features of the proposed non-newtonian model. Comparison with experimental data”. *Rheologica Acta* 17.6, pp. 643–653.
- Ramanathan T and Skinner H (2005). “Coronary blood flow”. *BJA Education* 5.2, pp. 61–64.
- Sakariassen KS, Orning L, and Turitto VT (2015). “The impact of blood shear rate on arterial thrombus formation”. *Future Science OA* 1.4, pp. 30–39.
- Seeley BD and Young DF (1976). “Effect of geometry on pressure losses across models of arterial stenoses”. *Journal of Biomechanics* 9.7, pp. 439–448.
- Stroud JS, Berger SA, and Saloner D (2000). “Influence of stenosis morphology on flow through severely stenotic vessels: implications for plaque rupture”. *Journal of Biomechanics* 33.4, pp. 443–455.
- Jahangiri M, Saghafian M, and Sadeghi MR (2017). “Numerical simulation of non-Newtonian models effect on hemodynamic factors of pulsatile blood flow in elastic stenosed artery”. *Journal of Mechanical Science and Technology* 31.2, pp. 1003–1013.
- Tambasco M and Steinman DA (2003). “Path-dependent hemodynamics of the stenosed carotid bifurcation”. *Annals of Biomedical Engineering* 31.9, pp. 1054–1065.
- Tanné D, Bertrand E, Kadem L, Pibarot P, and Rieu R (2010). “Assessment of left heart and pulmonary circulation flow dynamics by a new pulsed mock circulatory system”. *Experiments in Fluids* 48.5, pp. 837–850.
- Uren NG, Melin JA, Bruyne BD, Wijns W, Baudhuin T, and Camici PG (1994). “Relation between myocardial blood flow and the severity of coronary-artery stenosis”. *New England Journal of Medicine* 330.25, pp. 1782–1788.
- Usmani AY and Muralidhar K (2016). “Pulsatile flow in a compliant stenosed asymmetric model”. *Experiments in Fluids* 57.12, pp. 186–210.
- Varghese SS, Frankel SH, and Fischer PF (2008). “Modeling transition to turbulence in eccentric stenotic flows”. *Journal of Biomechanical Engineering* 130.1, p. 014503.
- Varghese SS, Frankel SH, and Fischer PF (2007). “Direct numerical simulation of stenotic flows. Part 1. Steady flow”. *Journal of Fluid Mechanics* 582, pp. 253–280.
- Young DF, Cholvin NR, and Roth AC (1975). “Pressure drop across artificially induced stenoses in the femoral arteries of dogs”. *Circulation Research* 36.6, pp. 735–743.
- Young DF and Tsai FY (1973a). “Flow characteristics in models of arterial stenoses. II. Unsteady flow”. *Journal of Biomechanics* 6.5, pp. 547–559.
- Young DF and Tsai FY (1973b). “Flow characteristics in models of arterial stenoses — I. Steady flow”. *Journal of Biomechanics* 6.4, pp. 395–410.

Zhu C, Seo JH, and Mittal R (2018). “Computational modelling and analysis of haemodynamics in a simple model of aortic stenosis”. *Journal of Fluid Mechanics* 851, pp. 23–49.

6.3 Pressure drop in curved stenosed coronary arteries

This section consists of the following submitted journal article:

Navid Freidoonimehr, Maziar Arjomandi, Anthony Zander, Rey Chin (2021). “Effect of artery curvature on the coronary fractional flow reserve”. *Physics of Fluids*, 33 pp. 031906.

The article is identical to its submitted format with the following exceptions:

- The numbering of figures, tables and equations have been altered to include the chapter number.
- The position of some figures and tables have been changed to improve legibility.

The article in its published format is available at:

<https://doi.org/10.1063/5.0042601>

Statement of Authorship

Title of paper	Effect of artery curvature on the coronary fractional flow reserve
Publication Status	<input type="checkbox"/> Published <input checked="" type="checkbox"/> Accepted for Publication <input type="checkbox"/> Submitted for Publication <input type="checkbox"/> Unpublished and Unsubmitted work written in manuscript style
Publication Details	Freidoonimehr, N., Arjomandi, M., Zander, A., and Chin, R., 2021, "Effect of artery curvature on the coronary fractional flow reserve", Physics of Fluids, accepted for publication

Principal Author

Name of Principal Author (Candidate)	Navid Freidoonimehr		
Contribution to the Paper	Developed ideas, conducted experiments, performed data analysis and interpreted results, wrote manuscript, and acted as corresponding author		
Overall percentage (%)	75%		
Certification:	This paper reports on original research I conducted during the period of my Higher Degree by Research candidature and is not subject to any obligations or contractual agreements with a third party that would constrain its inclusion in this thesis. I am the primary author of this paper.		
Signature		Date	15/02/2021

Co-Author Contributions

By signing the Statement of Authorship, each author certifies that:

- i the candidate's stated contribution to the publications is accurate (as detailed above);
- ii permission is granted for the candidate to include the publication in the thesis; and
- iii the sum of all co-author contributions is equal to 100% less the candidate's stated contribution

Name of Co-Author	Maziar Arjomandi		
Contribution to the Paper	Supervised the development of the research, participated in developing ideas and concepts, helped in interpretation of results, provided critical revision of manuscript.		
Signature		Date	15/02/2021

Name of Co-Author	Anthony Zander		
Contribution to the Paper	Supervised the development of the research, participated in developing ideas and concepts, helped in interpretation of results, provided critical revision of manuscript.		
Signature		Date	15/02/2021

Name of Co-Author	Rey Chin		
Contribution to the Paper	Supervised the development of the research, participated in developing ideas and concepts, helped in interpretation of results, provided critical revision of manuscript.		
Signature		Date	15/02/2021

Effect of artery curvature on the coronary fractional flow reserve

Navid Freidoonimehr, Maziar Arjomandi, Anthony Zander, and Rey Chin

Abstract

Understanding the effect of artery curvature on the pressure drop inside the arteries is of great importance due to the existence of several curved portions inside the coronary arterial system. In this paper, an experimental model is developed to account for the effect of the curvature of the coronary arteries on the pressure drop and Fractional Flow Reserve (FFR). FFR is an index for the evaluation of the functional significance of coronary stenosis and is defined as the ratio of the coronary pressure downstream of the stenosis to its upstream value. To measure pressure drop and FFR across curved artery models, three-dimensional-printed curved artery models are fabricated and installed in the test section of the experimental rig. For ratios of curvature radius over the artery diameter ranging from 2 to 7, there is a minimum value for pressure drop and hence a corresponding maximum value for FFR at a ratio of approximately 3. For the curved arteries with larger curvature radii, pressure drop increases, and consequently FFR decreases with an increase in the radius. The results showed that an accurate evaluation of pressure drop and FFR inside a curved coronary artery can only be achieved by accounting for the effect of curvature parameters including curvature angle and radius, such that neglecting the effect of artery curvature results in an underestimation of pressure drop by about 25-35%. The developed equation is able to determine the pressure drop inside a curved coronary artery model non-invasively.

Keywords: Artery curvature; Pressure drop; FFR; Artery blockage

6.3.1 Introduction

One of the most common clinical methods for evaluation of pressure drop across a stenotic coronary artery is Fractional Flow Reserve (FFR), which is defined as the ratio of the distal coronary pressure to the proximal (aortic) pressure, where distal and proximal represent the immediate downstream and upstream of the stenosis, respectively. In a normal healthy coronary artery, FFR is expected to be close to unity, regardless of the patient or the specific vessel studied (Pijls et al. 1995). An FFR value of 0.75 or less identifies ischemia-causing coronary stenoses with an accuracy of more than 90% which mostly require revascularisation (Tonino et al. 2009). Furthermore, for the FFR values of greater than 0.8, medical therapy is suggested as it represents the non-ischemia-producing stenosis. However, the FFR values between 0.75 to 0.8 are located in the grey zone, in which, either of revascularisation or medical therapy may be suggested as a treatment (Pijls et al. 2007). For measuring FFR, a micro-catheter connected to a miniature pressure sensor is inserted into the coronary artery to measure pressure before and after the stenotic section (Achenbach et al. 2017). The use of an intracoronary pressure wire has been validated ex vivo and in vivo and has been shown in clinical studies to lead to improved

outcomes for patients, largely through the avoidance of unnecessary stenting of non-significant lesions. However, this method is complex, invasive and carries high procedural risk ($>1/1000$ risk of heart attack, stroke, and death) and is also expensive (Morris et al. 2015; Patel et al. 2010). It is reported in the literature that about half of the patients who undergo invasive tests such as FFR, to measure the pressure difference before and after the blockage, have no significant blockage (Douglas et al. 2016) and hence, are unnecessarily subjected to its risks and costs. It is also reported that 61% of patients would prefer to avoid an invasive angiogram if there was a non-invasive option for them (Douglas et al. 2015).

There are some clinical non-invasive methods to estimate FFR which attempt to be a gatekeeper for this invasive procedure, such as cardiac stress test, stress perfusion MRI and myocardial perfusion imaging. All these methods fail to correlate with the results of invasive FFR in most cases by underestimating or overestimating the calculated FFR values. For example, it was found that about 35% of patients despite their positive cardiac stress test results needed to undergo revascularization (Vavalle et al. 2016). Furthermore, the drawback of myocardial perfusion imaging is the high radiation exposure for the patients undertaking it, more than 50% higher radiation exposure compared to those undertaking CT scan, (Stocker et al. 2018) and also poor concordance with FFR and tending to underestimate or overestimate the functional importance of coronary stenosis compared to the FFR (Melikian et al. 2010). There are also some other image-based approaches to measure FFR non-invasively such as CT-FFR (Tu et al. 2019). These methods were mainly developed using the images of the coronary arterial system. However, they are simplistic by not accounting for the patient-specific blood viscosity and coronary arterial blood flow profile. All these methods are prone to errors in the estimation of FFR through poor specificity and sensitivity. Thus, there is still a need for a non-invasive method that is able to produce an estimation of FFR that more tightly correlates with invasive FFR.

There are some mathematical models developed in biomechanical research for calculating pressure drop across the coronary arterial stenosis. Young et al. presented an algebraic equation for estimation of pressure drop for steady (Young and Tsai 1973b) and unsteady flows (Young and Tsai 1973a) inside the straight artery models. Clark (1976) used different stenosed valves to simulate the aortic stenosis and developed an equation to estimate the pressure drop. Seeley and Young (1976) studied the effect of length and the degree of stenosis on the pressure drop across an arterial stenosis by using in-vitro steady flow tests. Furthermore, Huo et al. (2012) developed an analytical model to determine FFR based on the general Bernoulli equation. Their models were based on steady flow and considered the artery to be straight. Mirramezani et al. (2018) presented and compared different algebraic models based on the CFD simulations to evaluate pressure drop in a coronary arterial stenosis. More recently, Freidoonimehr et al. (2020b) developed an experimental model to estimate pressure drop in a straight stenosed coronary artery model as a function of different parameters including blood viscosity, artery length and diameter, flow rate and flow profile, and shape and degrees of stenosis. The mentioned studies in the literature focus on the pressure drop measurement inside straight arteries. However, since most of the arteries in the arterial system are curved, straight pipe simulation for curved arteries can lead to inaccuracies in calculations such as substantial quantitative differences in the wall shear stress distribution and pressure drop (Siggers and Waters 2005; Verkaik et al. 2009). There are only a few studies addressing the effect

of curved arteries on the flow behaviour in the literature. In a study by Yao (2000) on blood flow in curved arteries with a stenosis, the pressure drop is found to increase across the stenotic section due to the curvature. It was found that a mild stenosis in a curved artery results in more intense secondary flow structures and higher wall shear stresses in comparison with a higher degree of stenosis in a straight artery (Yao et al. 2000). Their study was limited to computational investigation of wall shear stress distribution in a curved stenotic artery using numerical modelling.

Apart from the previous studies which are focused on the mathematical modelling of pressure drop inside the diseased coronary arteries, other studies in the literature investigate the effects of different physiological and geometrical parameters of the stenosed arteries on the pressure drop through experimental and numerical simulations. These parameters include the stenosis shape and its degree. In a study by Wu et al. (2015), it was shown that the formation of a stenosis in an artery can significantly influence the hemodynamic parameters, wall shear stresses and pressure drop. A higher pressure drop was observed for a higher degree of stenosis due to the flow acceleration as the result of a higher blockage by the stenosis, thus leading to a larger pressure drop (Khair et al. 2015). In another study, Li et al. (2017) investigated the pressure variation in an idealised multiple sequential stenoses coronary artery model. Their results showed that pressure drop is linearly correlated with flow rate irrespective of the number of stenoses. In addition to the stenosis, arterial curvature has been found to be an important parameter affecting the hemodynamics. Wong et al. (2020) studied the effects of arterial geometry such as arterial curvature on the hemodynamic parameters. Their results showed that increasing the narrowing and curvature of a coronary artery results in an increase in the pressure difference between the proximal and distal segments. Furthermore, Hong et al. (2017) characterised pulsatile flows in curved stenosed channels both experimentally and numerically. Their results showed that as the bend angle increases, a higher centrifugal force is generated which leads to more skewed vortex. Moreover, the pulsatility of the flow was found to impact pressure drop in a 180° bend artery such that increasing pulsatile frequency and Womersley number results in decreasing pressure drop (Wyk et al. 2015). Hence, the studies in the literature show that the existence of a stenosis, arterial curvature, and pulsatility of the flow affect the hemodynamic parameters of the flow inside the arteries, specifically the pressure drop.

Based on clinical studies, arterial diseases primarily occur in curved areas or bifurcations of blood vessels rather than throughout the straight section of blood vessels (Malek et al. 1999). Najjari and Plesniak (2016) studied the steady flow and physiological pulsatile flow in a rigid 180° curved tube. Their results of steady flow showed that the primary flow tended to separate from the inner wall at high Reynolds number, but no separation was observed at low Reynolds number. Furthermore, for the pulsatile flow, at the end of systolic deceleration, a recirculation zone was observed in the initial section of the curve between about 10° and 35° . In another study by the authors, secondary flow structures in a 180° curved pipe model of an artery with nonplanar curvature and vessel dilatation were studied (Najjari and Plesniak 2018). Their results showed that the secondary flow structures in rigid and elastic models were similar, and hence the local compliance of the vessel did not affect the morphology of secondary flow structures. Zhu et al. (2018) investigated the hemodynamics of the steady flow in a simple model of an aorta with an aortic stenosis. The stenotic aorta was modelled as a curved pipe with a 180° turn, and three different stenoses with area reductions of 50%, 62.5% and 75%. It

was shown that the post-stenotic flow was dominated by the jet that originated from the stenosis as well as the secondary flow induced by the curvature, and both contributed significantly to the flow turbulence. Moreover, spectral analysis showed that for all three stenoses, the Strouhal number of the vortex shedding of the jet shear layer was higher than the shedding frequency of a corresponding free jet or a jet confined in a straight pipe. Three-dimensional vortical structures and wall shear stress in a curved artery model were investigated by Cox et al. (2019). Peak streamwise velocities were found to shift toward the outer wall, setting up a pressure gradient within the cross section with high pressures on the outer walls and lower pressures on the inner walls of the curved artery. They also showed that a combination of intense secondary flow and flow reversal near the inner wall led to local increases in wall shear stress. Therefore, the effect of arterial curvature on the flow behaviour including the formation of secondary flow and separation zone is important for an accurate prediction of wall shear stresses and pressure drop.

This study aims to build upon the previous developed models for calculation of FFR inside the straight arteries by investigating the effect of artery curvature on the pressure drop and FFR values. The effect of different parameters including curvature angle and radius and degree of stenosis on pressure drop and FFR are studied. The results of this study will provide a better understanding of how FFR of stenotic curved arteries differ from stenotic straight arteries.

6.3.2 Experimental setup

The experimental rig for the measurement of pressure drop in the coronary artery models and different configurations of the investigated curved coronary arteries are shown in figures 6.22a and 6.22b. The details of the setup and the equipment can be found in the authors' previously published study (Freidoonimehr et al. 2020b). A mixture of water and glycerine, with same viscosity of blood, was employed to mimic the blood rheological characteristics. The mixture consists of 60% water and 40% glycerine by mass fraction based on literature (Charonko et al. 2009; Deplano et al. 2007; Tanné et al. 2010). The experiments were performed at a room temperature of 25°C where the viscosity (μ) and density (ρ) of the blood mimicking mixture were 0.00312 Pa.s and 1096 kg/m³, respectively.

Curved artery models with different curvature angles (θ), curvature radii (r), downstream lengths, and degrees of stenosis (S) were considered in this study, as shown in figure 6.22b. Figure 6.23 shows different artery models with different degrees of stenosis including without stenosis (healthy artery), 46% (mild), 63% (moderate) and 78% (severe) and curvature angles of 30°, 60° and 90°. All stenosis shapes were asymmetric. The arteries are scaled up by a factor of two such that the inside diameter (D) is equal to 6.1 mm in order to reduce the measurement errors associated with smaller model dimensions. Despite the change in diameter, the results are representative of a real artery by matching the dimensionless governing parameters, namely Reynolds number, Dean number, and Womersley number (Freidoonimehr et al. 2020a,b). Reynolds number is defined based on the blood mean flow rate (Q) as $Re = 4\rho Q / \pi\mu D$. In order to match the Reynolds number and since the arteries are scaled up by a factor of two, the blood flow rate is doubled compared to the values in the coronary arteries. Dean number, as a dimensionless parameter employed in the studies of flow in curved pipes, is defined as

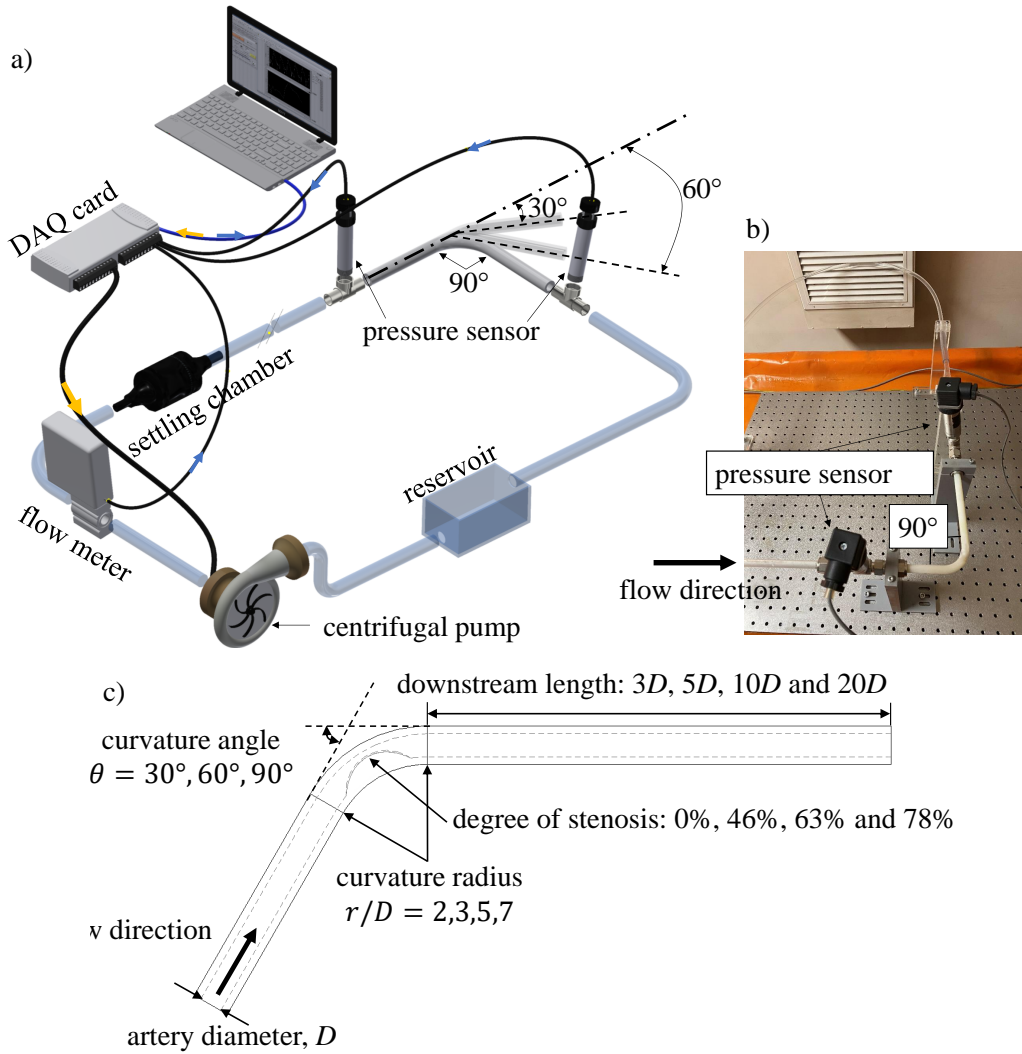


Figure 6.22: a) Schematic of the test setup to measure FFR in curved coronary artery models, b) a view of the experimental test rig displaying a curved model of artery with $\theta = 90^\circ$, and c) Schematic of curved coronary artery model showing different related parameters including curvature angle and radius, degree of stenosis and downstream length.

$De = Re\sqrt{(D/2r)}$. By matching the Reynolds number and using a similar range for the r/D as of coronary arteries, the Dean number is matched in the experiments with that of human coronary arteries. Furthermore, Womersley number, a dimensionless parameter governing the pulsatile flow, is defined as $Wo = (D/2)\sqrt{(2\pi/T)(\rho/\mu)}$. In order to match the Womersley number and since the arteries are scaled up by a factor of two, the cycle time period (T) is four times higher than that of in human arteries.

For printing the models of the curved coronary arteries, an acrylonitrile butadiene styrene (ABS) was used. The employed 3D-printer, Zortrax M-200 is a high-accuracy printer with a sub-layer height of 0.09 mm. To improve the quality of the surfaces of the models, the printed models were placed in an acetone vapour chamber for about 20 minutes. To evaluate the relative surface height of the models several random samples were cut in a 3-mm length in longitudinal direction and placed in a surface roughness measuring machine (Freidoonimehr et al. 2020b). Based on the calculated relative pipe

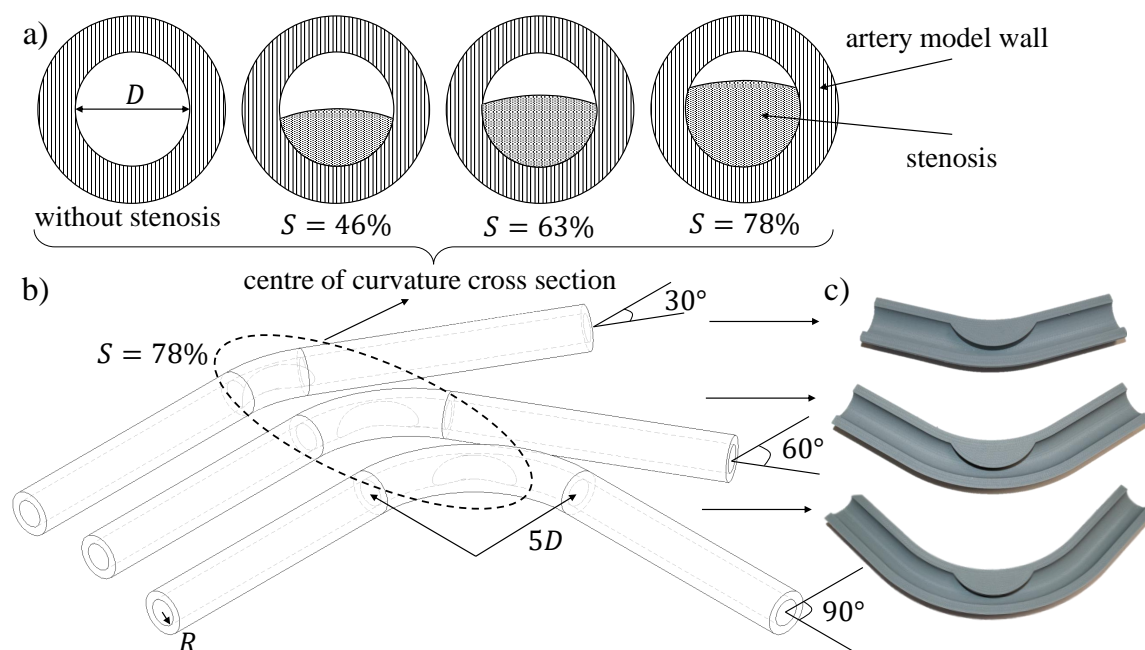


Figure 6.23: Schematics of a) centre of curvature cross section with different degrees of stenosis, b) curved artery models with different curvature angles and c) cross sectional view of three-dimensional-printed artery models. The degree of stenosis and curvature radius in parts b and c are $S = 78\%$ and $r/D = 5$, respectively.

roughness and since the flow was laminar, the 3D-printed models were considered as a smooth pipe. This means that the flow behaviour inside the artery models was independent from the surface roughness of the models.

The artery wall was considered to be rigid in this study, although there are some studies in the literature modelling the arteries to be elastic (Anssari-Benam and Korakianitis 2013; M et al. 2019; Pielhop et al. 2012). As the artery walls become harder and stiffer with ageing and lose their flexibility, considering arteries to be rigid results in reliable estimation of the hemodynamic parameters. It is widely covered in the literature that arterial stiffness is a key arterial alteration during the ageing process (Benetos 2017; Mitchell et al. 2004; Sun 2015), which is recognised as a primary risk factor of all cardiovascular disease (Kohn et al. 2015). Furthermore, arterial stiffness has a relation with the atherosclerotic lesions. The patients with cardiovascular disease often develop central artery stiffness (Benetos et al. 2002). It is reported that assuming healthy arteries to be rigid and hence disregarding its elasticity changes the pressure drop and the computed FFR values insignificantly with less than 2% and about 0.26% obtained from the results of (Mirramezani et al. 2018) and (Siogkas et al. 2015), respectively.

In this study, the uncertainties related to the measurement devices were provided by the manufacturers. The pressure transducers have a full-scale accuracy of 0.04% and the flowmeter has a measurement accuracy of 0.4% of measured value. In order to account for bias and precision errors arising due to calibration of the pressure sensors and the flow meter and the sensitivity of the measurement devices, all the experiments were performed over a five-minute period and the experiments were repeated five times under identical conditions. To account for the total errors in measurements, the standard deviations of the five measurements were determined according to method recommended in American

Society of Mechanical (2006), which are displayed by error bars in the graphs of the results section.

6.3.3 Results

Effect of downstream length

Figure 6.24 displays the effect of downstream length on FFR and pressure drop for different flow rates. Four different downstream lengths are considered in this study including $3D$, $5D$, $10D$ and $20D$, as shown in figure 6.24a. It is worth mentioning that the curvature radius equals $5D$. As FFR is calculated based on the ratio of the downstream pressure after the blockage to the upstream pressure, this figure explains how the changes in the downstream length affect FFR and pressure drop values. The results display a slight reduction in the pressure drop value along with an increase in the FFR value with the increase of the downstream length from $3D$ to $5D$. The results in figure 6.24b show that a change in the downstream length of up to $20D$ does not significantly change the values of pressure drop and FFR. For example, for the case with the flow rate of 300 ml/min , pressure drop and FFR change only about 0.9% and 1.7% , respectively, for the changes in the downstream length from $3D$ to $20D$. Hence, although in actual FFR measurement, the cardiologists measure FFR right after the location of stenosis, in order to reduce the errors associated with the end effects, the rest of the results is presented for the case with $20D$ downstream length.

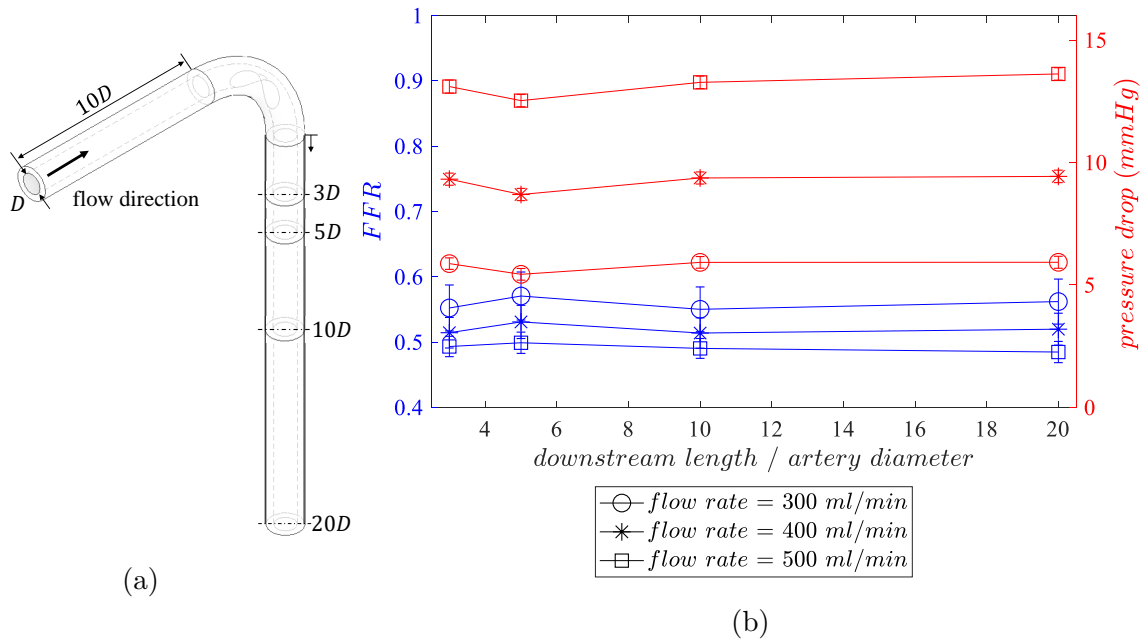


Figure 6.24: (a) Schematics of a 90° curved coronary artery model with the degree of stenosis of 78% and different downstream length including $3D$, $5D$, $10D$, and $20D$ and (b) FFR and pressure drop values versus different downstream lengths for different flow rates.

Effects of degree of stenosis and curvature angle

FFR and pressure drop versus flow rate for different degrees of stenosis and different curvature angles are shown in figure 6.25. The results show that a higher degree of stenosis leads to a higher pressure drop and consequently lower values of FFR for all curvature angles. FFR values lower than 0.8 are critical treatment cases since they are associated with myocardial ischemia and need coronary revascularization procedures. The results in figure 6.25 illustrate that FFR values are not critical and are in the normal range for the cases without and with stenoses inside the curved arteries for the degree of stenosis up to 46% and for all curvature angles. Furthermore, the FFR values for the case with a degree of stenosis of 63% are about 0.75 to 0.8 for all curvature angles. This range is referred to as a grey zone, which requires the cardiologists' judgments to decide the course of management (Mehra and Mohan 2015). For the case with a degree of stenosis of 78%, the values of FFR are less than 0.7 for all flow rates and curvature angles. Furthermore, FFR values reduce for the hyperemic flow condition with high flow rate values up to about 0.5 for all curvature angles. This means that without considering the arteries' curvature angle and hence similar to the straight arteries, coronary revascularization procedures such as stenting are needed to reduce the risk of death for the patients with a degree of stenosis of 78% and higher, and indicates the significant effect of stenosis degree on FFR.

Figure 6.26 shows the effect of curvature angle on FFR and pressure drop for one specific degree of stenosis of 78%. It was found that a larger curvature angle of the artery, results in a slightly higher pressure drop and consequently a slightly lower FFR. Comparing the results of figures 6.25 and 6.26 show that the degree of stenosis has a more significant effect on FFR and pressure drop compared to the curvature angle. For example, as shown in figure 6.25c, for $\theta = 90^\circ$ and the flow rate of about 310 ml/min, FFR reduces from 0.86 to 0.54 for the case without stenosis and $S = 0.78\%$, respectively, resulting in about 37% changes in FFR. On the other hand, FFR drops from about 0.56 to 0.54 for the change in the curvature angle from 30 to 90 for the flow rate of 310 ml/min, resulting in about 3% changes in FFR.

Effect of curvature radius

The effect of curvature radius of the curved arteries on pressure drop and FFR values for different flow rates is presented in figure 6.27b for a range of curvature radii between $2D$ and $7D$ shown schematically in figure 6.27a. According to figure 6.27b, for all flow rates, FFR reaches a maximum at $r/D = 3$, and decreases slightly afterwards. For example, for the flow rate of 200 ml/min, FFR increases from 0.58 at $r/D = 2$ and reaches to its maximum value, 0.61, at $r/D = 3$ and decreases slightly up to 0.56 at $r/D = 7$. This means that having a sharp curvature in the coronary arteries with a curvature ratio of less than 3 results in a higher pressure drop and FFR compared to the curved coronary arteries with a medium curvature ratio of more than 3 and less than 5.

The observed trend is due to simultaneous effects of flow separation and viscous friction. One of the dominant effects in a curved artery is flow separation on the curved walls, which leads to the formation of a swirling secondary flow arising from the centripetal acceleration (Cox et al. 2019). Consequently, pressure drop is larger compared to a straight artery. However, flow separation and secondary flow formation decrease with an

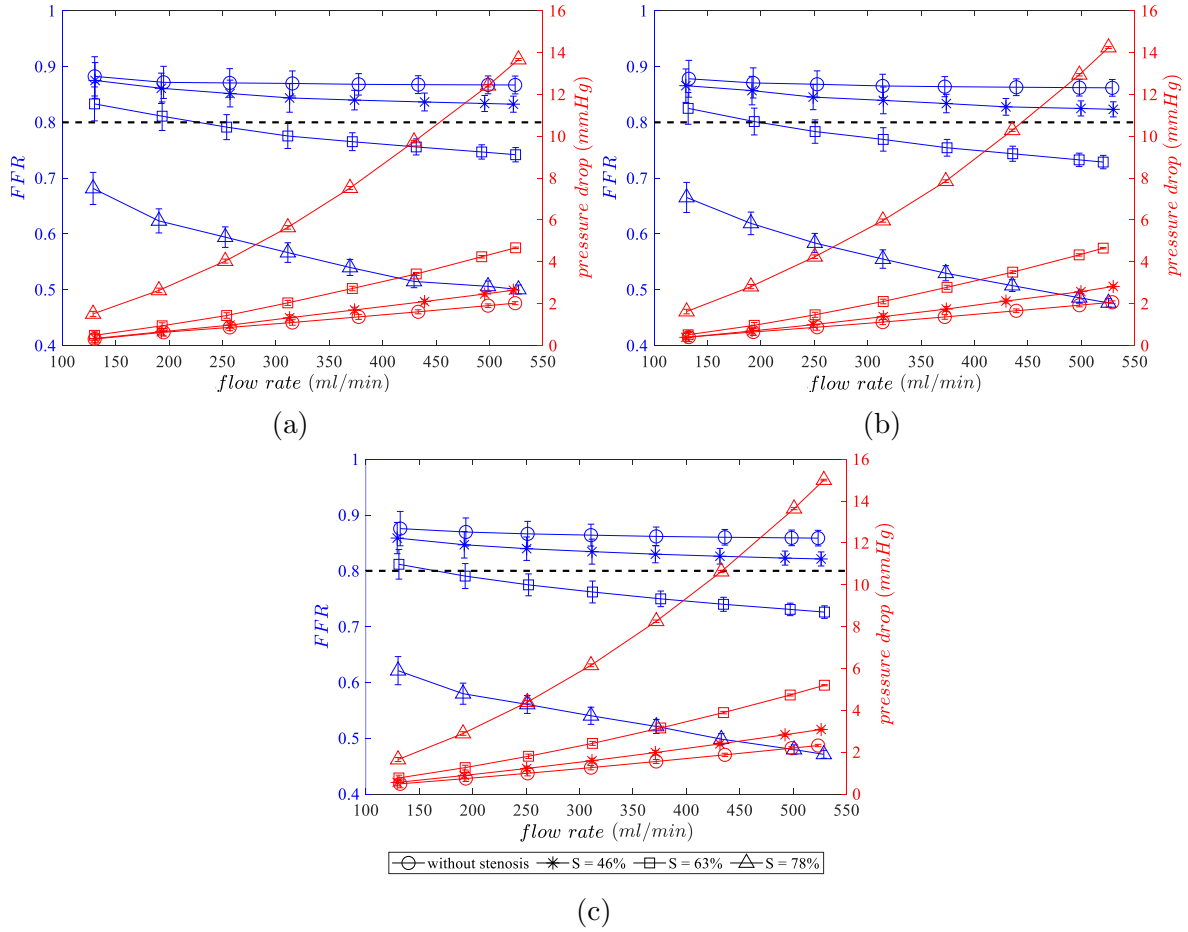


Figure 6.25: FFR and pressure drop values versus flow rate for different degree of stenosis and different curvature angles including (a) $\theta = 30^\circ$, (b) $\theta = 60^\circ$ and (c) $\theta = 90^\circ$. For all the cases, curvature radius is equal to $5D$. Horizontal black dashed line refers to the critical value of FFR (FFR = 0.8).

increase in r/D . Hence, the pressure drop due to flow separation reduces with increasing r/D . On the other hand, at a higher curvature radius, the viscous friction pressure drop is larger due to an increase in the total length of the artery model. These two simultaneous opposing effects lead to a minimum value in the pressure drop profile (White 2016), which in this study occurs at $r/D = 3$. As the curvature radius increases to larger values, an increase in pressure drop and a decrease in FFR is found due to the dominance of the viscous friction effect over the flow separation and the secondary flow formation for larger curvature radii.

6.3.4 Discussion

Based on the previously developed model by the authors (Freidoonimehr et al. 2020b) for prediction of pressure drop inside straight arteries, there are several parameters affecting the pressure drop inside the straight coronary arteries including: Reynolds number, artery length, degree of stenosis, length of the stenosis, shape of the stenosis, eccentricity, and blood flow acceleration and deceleration during a cardiac cycle. A minor loss is added to the pressure drop due to the presence of the bend. As the results of this study shows,

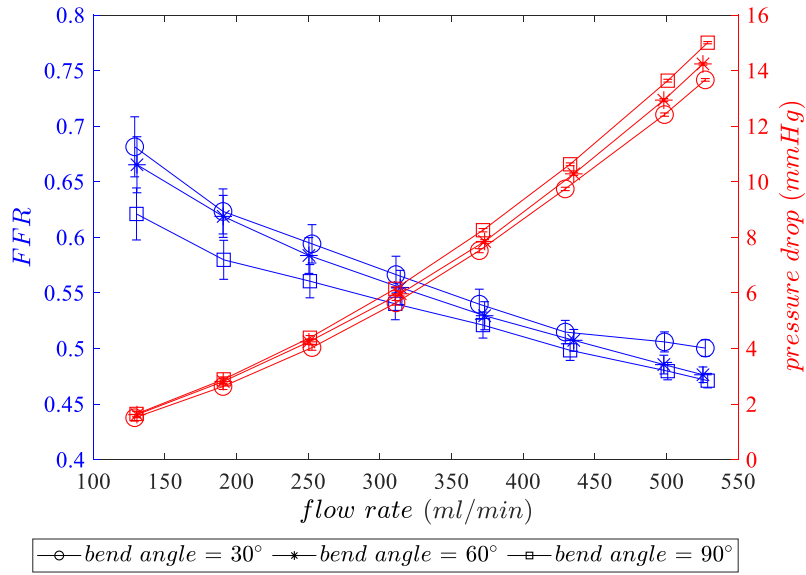


Figure 6.26: FFR and pressure drop values versus flow rate for different curvature angles with $S = 78\%$ and a curvature radius of $5D$.

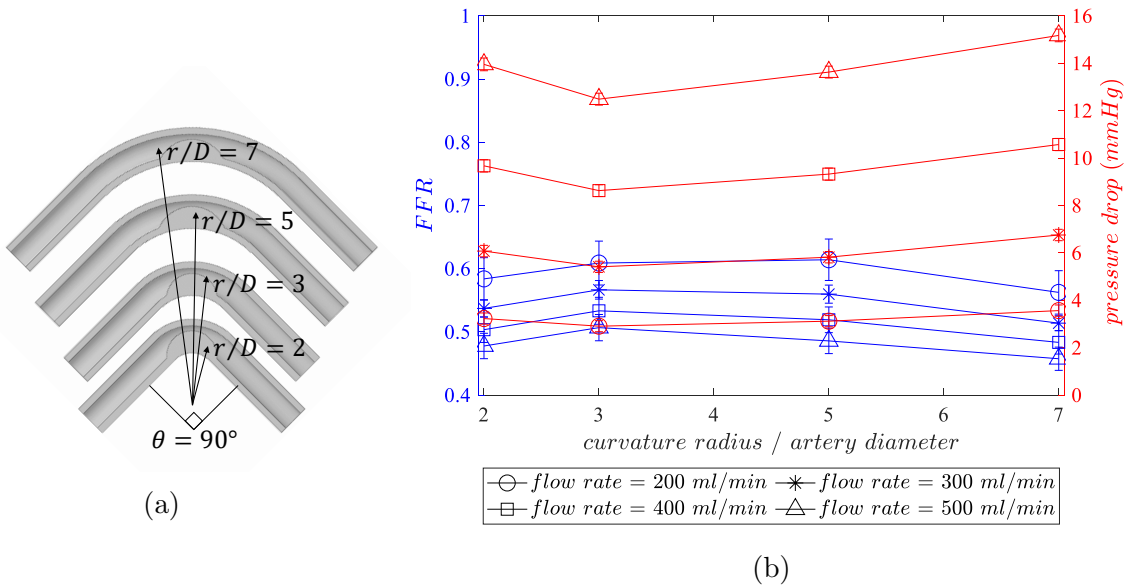


Figure 6.27: (a) Schematics of curved arteries with different curvature radius and $S = 78\%$ and $\theta = 90^\circ$ and (b) FFR and pressure drop values versus different curvature radii for different flow rates and $S = 78\%$ and curvature angle of 90° .

this minor loss is a function of the curvature angle and curvature radius which need to be considered as the additional important parameters for the measurement of the pressure drop and FFR for a curved artery along with the previously-mentioned parameters for the pressure drop inside a straight artery. Therefore, pressure drop (ΔP) inside an idealised curved coronary artery models can be expressed as:

$$\Delta P = f\left(Re, \frac{L}{D}, \frac{A_1}{A_0}, \frac{l}{D}, e, \frac{dV}{dt}, \frac{r}{D}, \theta\right), \quad (6.8)$$

where L is the artery length with the internal diameter of D , Re is the Reynolds number defined based on the inlet average flow velocity, A_0 and A_1 represent the cross-sectional

area of the unobstructed artery and the minimum constricted cross sectional area, respectively, l is the plaque length, e is the plaque eccentricity, V is the time-dependent velocity of the unobstructed artery (averaged over the entire cross section (A_0)), r is the curvature radius, and θ is the curvature angle.

Based on the equation developed by Freidoonimehr et al. (2020b) and a minor loss equation due to the presence of bend (White 2016), the total pressure drop inside a curved coronary artery model can be expressed as:

$$\Delta P(t) = \underbrace{\frac{128 \mu q(t)}{\pi D^4} L}_{\text{viscous friction part}} + \underbrace{\frac{kt}{2} \left(\left(\frac{A_0}{A_1} \right)^2 - 1 \right) \rho V(t) |V(t)|}_{\text{blockage part}} + \underbrace{ku \rho L \frac{dV(t)}{dt}}_{\text{pulsation part}} + \underbrace{\frac{kb}{2} \rho V(t)^2}_{\text{bend head loss}}, \quad (6.9)$$

where μ is the fluid viscosity, ρ is the fluid density, $q(t)$ is the instantaneous flow rate, kt and ku are the blockage and pulsatility constants, respectively, that were defined experimentally by Freidoonimehr et al. (2020b), and kb is the bend loss coefficient. The Eq.6.9 shows that pressure drop inside a curved coronary artery model is a function of four different effects including viscous friction, turbulence due to blockage inside the artery, pulsation, and turbulence due to artery curvature. The results of this study showed that the turbulence effect due to artery curvature and hence kb are a function of curvature radius over the artery diameter (r/D) and the curvature angle (θ), as shown in figures 6.26 and 6.27.

In order to further explore the effect of the curvature-induced pressure drop, pressure drop for the curved artery models with different degrees of stenosis was measured for a pulsatile inlet velocity profile corresponding to the left coronary artery (Davies et al. 2008). To simulate the physiological pulsatile velocity waveform, the input voltage of the pump was controlled by a data acquisition card, as shown in Fig. 6.28. This waveform, as an inlet velocity, was modelled using the first 32 Fourier modes of the Fast Fourier Transform (FFT) of the original waveform (with less than one percent difference between the maximum flow velocities during a cardiac cycle). The created flow rate profile was then determined by the measurement of flow rate using a flow meter. The created profile and the pump input profile were compared to ensure that the created profile agrees with the input physiological profile, as shown in Fig. 6.28. Based on the employed flow profile and the cycle duration (4.4 s), the mean value of Reynolds number is 292 and the Womersley number is 2.12. The mean values of the experimental pressure drop over a cardiac cycle given by the inlet profile in figure 6.28 are presented in table 6.3. The calculated values of the pressure drop for a straight artery using the first three terms of Eq.6.9 are also given in table 6.3. The last column of table 6.3 shows the deviations between the experimental pressure drop for a curved artery and a straight artery of the same length and stenosis. Comparison of the measured values for the curved arteries with a straight artery of a similar length and stenosis clearly shows an increased pressure drop for the curved arteries such that the pressure drop for the curved arteries are between 25% and 35% larger than similar straight arteries. This confirms that not accounting for the effect of curvature on the pressure drop results in a considerable underestimation. Hence, in order to accurately evaluate pressure drop and FFR inside the curved coronary artery models, the effect of curvature parameters, such as curvature angles and radii should be

taken into account.

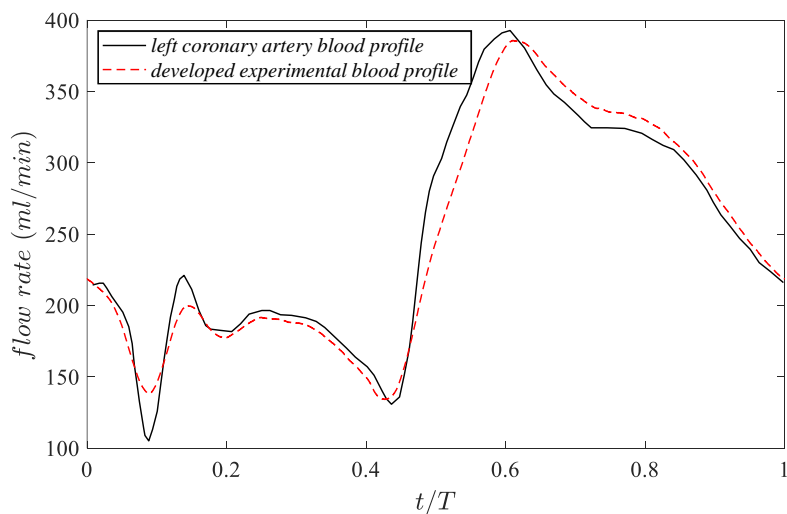


Figure 6.28: The physiological pulsatile left coronary artery blood flow profile (Davies et al. 2008) and the developed experimental blood flow profile. The black solid line is the physiological left coronary artery blood flow profile, as the input of the pump, and the dashed red line is the developed experimental blood profile measured by the flowmeter.

Table 6.3: Comparison between the mean values of the experimental pressure drop over a cardiac cycle and the calculated values based on the straight artery model (Eq.6.9), for different curvature angles and degree of stenoses. 0% degree of stenosis denotes the model without stenosis.

Curvature angle	Degree of stenosis (%)	Experimental pressure drop (mmHg)	Calculated pressure drop based on Eq.6.9 for straight artery (mmHg)	Deviation (%)
30°	0	0.85	0.57	32.94
	46	1.05	0.79	24.76
	63	1.65	1.22	26.06
	78	4.14	2.85	31.16
60°	0	0.87	0.62	27.74
	46	1.13	0.84	25.66
	63	1.73	1.27	26.59
	78	4.36	2.92	32.03
90°	0	0.99	0.67	32.32
	46	1.23	0.89	27.64
	63	1.82	1.31	28.02
	78	4.6	3	34.78

Figure 6.29 compares the mean pressure drop for different degrees of stenosis for curved and straight arteries given in table 6.3. It is demonstrated in figure 6.29 that the increase in pressure drop with increasing the degree of stenosis in curved arteries follows the same trend as that for a straight artery, showing a significantly large pressure drop for the degree of stenosis of 78%. Furthermore, the results show that the degree of stenosis has a stronger impact on the total mean pressure drop compared to the curvature angle.

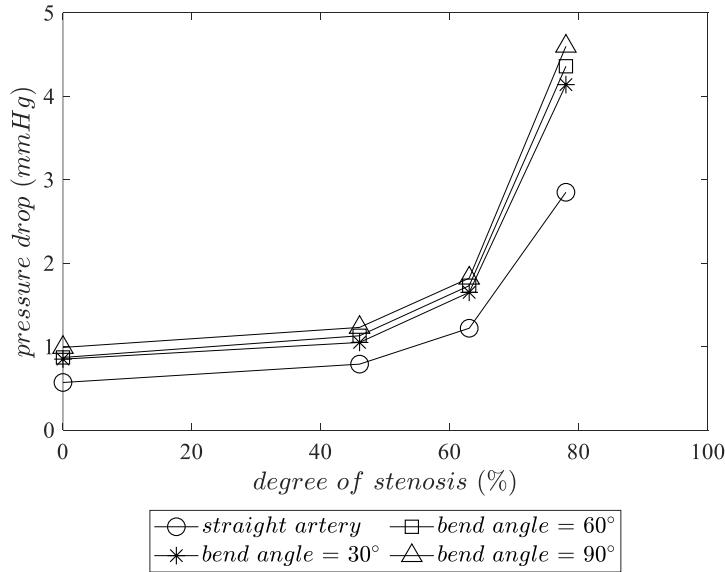


Figure 6.29: Mean values of pressure drop over a cardiac cycle versus different degree of stenosis for different curved artery models including straight (without curvature), 30°, 60°, and 90° with $r/D = 5$. Pressure drop for straight artery is calculated based on the corresponding artery length with the bend angle of 30°.

The results of this study mainly focus on measurement of FFR and mean pressure drop. However, unsteady variations of pressure drop during a cardiac cycle are of great importance due to the presence of flow acceleration and deceleration during a cardiac cycle. Hence, the effect of curvature on the unsteady pressure drop is shown in figure 6.30. The unsteady pressure drop during a cardiac cycle with the inflow profile of figure 6.28 measured for two curvature angles of 30° and 90° at a degree of stenosis of 78%, which as shown in figure 6.29 has the largest mean pressure drop, is presented in figure 6.30. The experimental values for the curved arteries are compared with the calculated unsteady pressure drop for a straight artery using Eq.6.9. Figure 6.30 shows a distinct increase in the unsteady pressure drop in the curved arteries compared to the straight artery. The difference as discussed above is due to the effect of turbulence induced by the curvature (Cox et al. 2019), which leads to an increased pressure drop.

As discussed at the beginning of this section, pressure drop due to curvature of the artery can be evaluated based on the minor head loss effect, as discussed by White (2016). This head loss effect is dependent on a bend coefficient which is a function of arterial curvature radius and angle. There are some attempts in the literature to mathematically model the pressure drop inside the curved pipe models. However, most of these studies were focused on the turbulent flow conditions (Berger et al. 1983; Stultz and Kitto 2005), while the blood flow inside the coronary arteries is mainly laminar with low Reynolds number (Kirpalani et al. 1999; Perktold et al. 1991; Qiu and Tarbell 2000; Wells et al. 1977). A model for the evaluation of the pressure drop inside a curved pipe model with the laminar flow regime was developed by White (1929), as $C^{-1} = 1 - \left(1 - \left(\frac{11.6}{De}\right)^{0.45}\right)^{\frac{1}{0.45}}$, where C is the ratio of the friction factor of curved pipe over the straight pipe. This equation is valid for the laminar flow regime with $11.6 < De < 2000$.

Figure 6.31 shows the evaluated pressure drop based on Eq.6.9 and that obtained

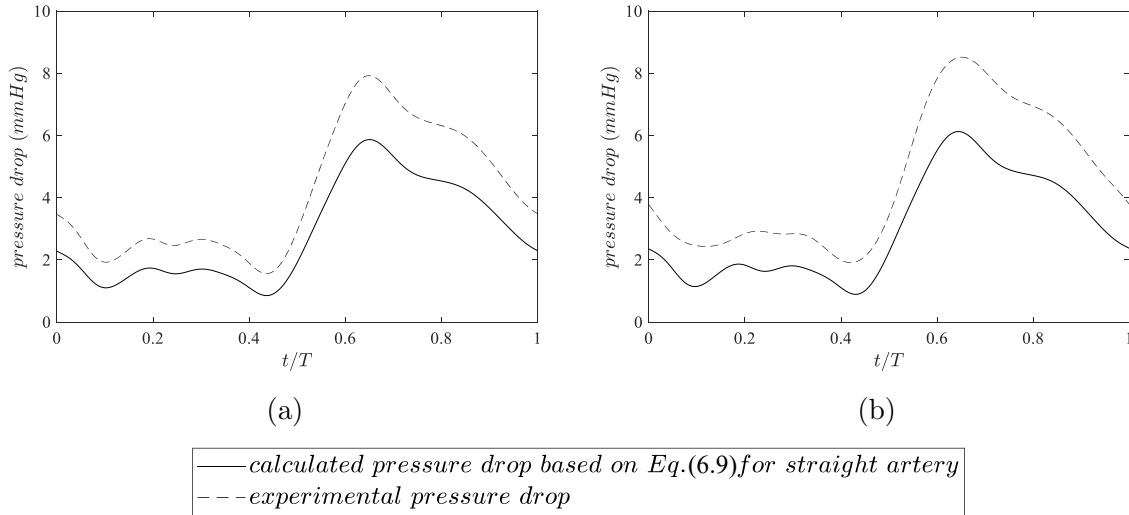


Figure 6.30: Phase-averaged experimental pressure drop and the calculated values based on the first three terms of Eq.6.9 for straight artery versus dimensionless cycle period for $S=78\%$ and two curvature angles including (a) $\theta = 30^\circ$ and (b) $\theta = 90^\circ$ with $r/D = 5$. Solid line refers to the calculated pressure drop based on Eq.6.9 for straight artery and dashed line refers to the experimental pressure drop.

from the coefficient developed by White (1929) and the experimental pressure drop. The evaluated pressure drop from Eq.6.9 is obtained with $kb = 1.455$ and $kb = 1.9$ for the cases with $r/D = 5$ and $r/D = 7$, respectively. The bend head loss pressure drop term is determined by subtracting the first three terms of Eq.6.9 from the experimental pressure drop and kb is obtained by dividing the bend head loss pressure drop term by the $(1/2)\rho V^2$. Furthermore, this figure presents the results of pressure drop obtained from the coefficient developed by White (1929). The bend-induced pressure drop calculated using this coefficient, C , is added to the first three terms of Eq.6.9 to evaluate the pressure drop inside the curved arteries. The bend-induced pressure drop is obtained by multiplying C by the viscous pressure drop. The results show that the mean values of pressure drop evaluated based on Eq.6.9 and the coefficient developed by White (1929) are in excellent agreement with the experimental pressure drop with less than 1% and about 3% deviations, respectively. The peak values have an average deviation of about 7% and 15%, respectively. Therefore, it is proposed that Eq.6.9 can provide an evaluation of pressure drop inside the curved artery models. However, extensive sets of experiments for a wide range of arterial curvature radii and angles need to be conducted to determine the bend head loss coefficient as a function of these parameters.

Further studies in future can focus on establishing the effect of the curvature on the pressure drop in order to expand the previously developed equation for curved stenosed arteries. The cases discussed in figure 6.31 are all for the healthy arteries without any stenoses. However, it is worth mentioning that the location of the stenoses inside the curved arteries, whether it is located upstream or downstream of the curvature or at the centre of curvature, is another important parameter affecting the pressure drop. Moreover, the position of the stenosis on the inner or outer walls of the arteries also affects the pressure drop. Hence, in order to accurately evaluate pressure drop inside the stenosed curved coronary arteries, another term should be added to the pressure drop equation to account for the effect of position of the stenosis with respect to the location

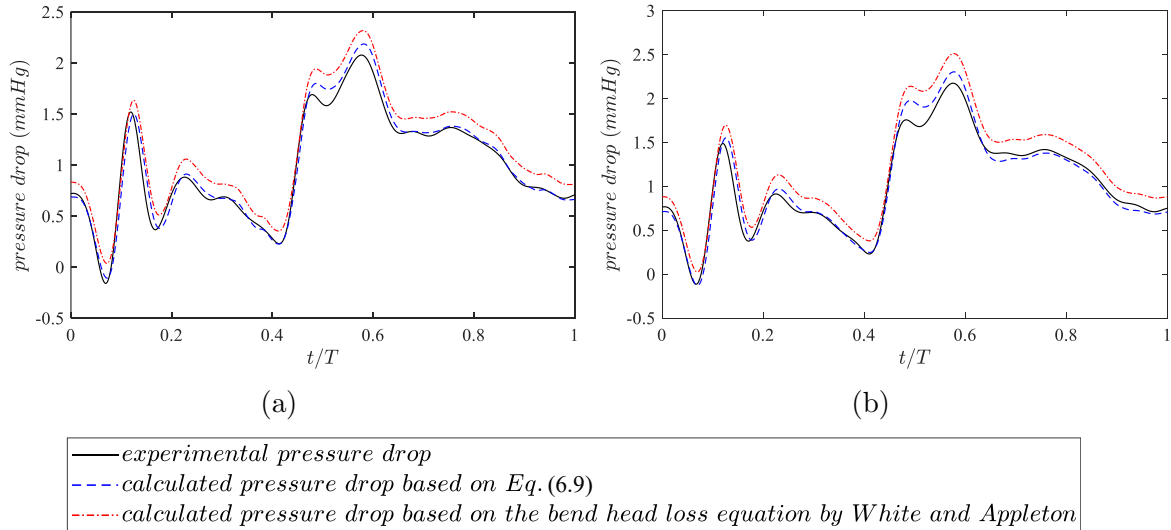


Figure 6.31: Phase-averaged experimental pressure drop and the calculated values based on the Eq.6.9 for curved artery model and that of obtained based on the bend head loss equation by White (1929) for a healthy artery with $\theta = 90^\circ$ without stenosis and two curvature radii including a) $r/D = 5$ and b) $r/D = 7$. Solid line refers to the experimental pressure drop, dashed line refers to the calculated pressure drop based on Eq.6.9, and dashed-dotted line refers to the calculated pressure drop based on the bend head loss equation by White (1929).

of the arterial curvature in a future study.

6.3.5 Conclusions

In this study, for the first time, the effect of artery curvature on the pressure drop and FFR was studied experimentally. The effect of different governing parameters including curvature angles and radii, degree of stenosis, and downstream length for a wide range of flow rates were investigated. The results illustrated that the curvature radius over the artery diameter and the curvature angle are two parameters affecting pressure drop inside the curved arteries. It was demonstrated that neglecting the effect of curvature on pressure drop leads to its underestimation by 25%–35%. Hence, an accurate evaluation of pressure drop and FFR inside a curved coronary artery can only be achieved by accounting for the effect of curvature parameters including curvature angle and radius. Furthermore, it was found that the effect of the degree of stenosis on FFR and pressure drop is more significant compared to the effect of the curvature angle for the range of curvature angles studied in this study from 30° and 90° indicating that pressure drop inside a diseased artery is highly dependent on the degree of stenosis. Although there are some simplifications in developing this equation such as assuming that the arteries' walls are rigid, the developed equation can be used as a tool to evaluate the pressure drop inside the curved coronary arteries non-invasively based on the flow rate and profile as well as the curvature geometry. The former can be determined using several non-invasive methods such as Doppler Ultrasonography and the latter can be determined using Computed Tomography (CT) images. The results of this study provide a better understanding of pressure drop in curved arteries and can assist cardiologists in the estimation of FFR.

Furthermore, the findings of this study provide a basis for development of non-invasive methods for estimation of pressure drop inside the stenosed curved coronary arteries.

Acknowledgement

Financial support for the project has been provided by the Australian Government Research Training Program Scholarship. The authors would also like to thank the workshops of the school of mechanical engineering at The University of Adelaide.

Conflict of interest

The authors declare that they have no conflict of interest.

Data availability statement

The data that support the findings of this study are available from the corresponding author upon reasonable request.

References

- Achenbach S, Rudolph T, Rieber J, Eggebrecht H, Richardt G, Schmitz T, Werner N, Boenner F, and Mollmann H (2017). “Performing and interpreting fractional flow reserve measurements in clinical practice: An expert consensus document”. *Interventional Cardiology* 12.2, pp. 97–109.
- American Society of Mechanical E (2006). *Test uncertainty*. New York, N.Y.: American Society of Mechanical Engineers.
- Anssari-Benam A and Korakianitis T (2013). “An experimental model to simulate arterial pulsatile flow: In vitro pressure and pressure gradient wave study”. *Experimental Mechanics* 53.4, pp. 649–660.
- Benetos A (2017). “Assessment of arterial stiffness in an older population: the interest of the cardio-ankle vascular index (CAVI)”. *European Heart Journal Supplements* 19.suppl_B, B11–B16.
- Benetos A, Waeber B, Izzo J, Mitchell G, Resnick L, Asmar R, and Safar M (2002). “Influence of age, risk factors, and cardiovascular and renal disease on arterial stiffness: clinical applications”. *American Journal of Hypertension* 15.12, pp. 1101–1108.
- Berger SA, Talbot L, and Yao LS (1983). “Flow in Curved Pipes”. *Annual Review of Fluid Mechanics* 15.1, pp. 461–512.
- Charonko J, Karri S, Schmiegl J, Prabhu S, and Vlachos P (2009). “In vitro, time-resolved PIV comparison of the effect of stent design on wall shear stress”. *Annals of Biomedical Engineering* 37.7, pp. 1310–1321.
- Clark C (1976). “The fluid mechanics of aortic stenosis—I. Theory and steady flow experiments”. *Journal of Biomechanics* 9.8, pp. 521–528.
- Cox C, Najjari MR, and Plesniak MW (2019). “Three-dimensional vortical structures and wall shear stress in a curved artery model”. *Physics of Fluids* 31.12, p. 121903.

- Davies JE, Parker KH, Francis DP, Hughes AD, and Mayet J (2008). “What is the role of the aorta in directing coronary blood flow?” *Heart* 94.12, pp. 1545–1547.
- Deplano V, Knapp Y, Bertrand E, and Gaillard E (2007). “Flow behaviour in an asymmetric compliant experimental model for abdominal aortic aneurysm”. *Journal of Biomechanics* 40.11, pp. 2406–2413.
- Douglas PS, De Bruyne B, Pontone G, Patel MR, Norgaard BL, Byrne RA, Curzen N, Purcell I, Gutberlet M, Rioufol G, Hink U, Schuchlenz HW, Feuchtner G, Gilard M, Andreini D, Jensen JM, Hadamitzky M, Chiswell K, Cyr D, Wilk A, Wang F, Rogers C, and Hlatky MA (2016). “1-year outcomes of FFRCT-guided care in patients with suspected coronary disease: The platform study”. *Journal of the American College of Cardiology* 68.5, pp. 435–445.
- Douglas PS, Pontone G, Hlatky MA, Patel MR, Norgaard BL, Byrne RA, Curzen N, Purcell I, Gutberlet M, Rioufol G, Hink U, Schuchlenz HW, Feuchtner G, Gilard M, Andreini D, Jensen JM, Hadamitzky M, Chiswell K, Cyr D, Wilk A, Wang F, Rogers C, and De Bruyne B (2015). “Clinical outcomes of fractional flow reserve by computed tomographic angiography-guided diagnostic strategies vs. usual care in patients with suspected coronary artery disease: the prospective longitudinal trial of FFR(CT): outcome and resource impacts st”. *European Heart Journal* 36.47, pp. 3359–3367.
- Freidoonimehr N, Arjomandi M, Sedaghatzadeh N, Chin R, and Zander A (2020a). “Transitional turbulent flow in a stenosed coronary artery with a physiological pulsatile flow”. *International Journal for Numerical Methods in Biomedical Engineering* 36.7, e3347.
- Freidoonimehr N, Chin R, Zander A, and Arjomandi M (2020b). “An experimental model for pressure drop evaluation in a stenosed coronary artery”. *Physics of Fluids* 32.2, p. 21901.
- Hong H, Yeom E, Ji HS, Kim HD, and Kim KC (2017). “Characteristics of pulsatile flows in curved stenosed channels”. *PLoS One* 12.10, e0186300.
- Huo Y, Svendsen M, Choy JS, Zhang ZD, and Kassab GS (2012). “A validated predictive model of coronary fractional flow reserve”. *Journal of the Royal Society Interface* 9.71, pp. 1325–1338.
- Khair A, Wang BC, and Kuhn DCS (2015). “Study of laminar–turbulent flow transition under pulsatile conditions in a constricted channel”. *International Journal of Computational Fluid Dynamics* 29.9-10, pp. 447–463.
- Kirpalani A, Park H, Butany J, Johnston KW, and Ojha M (1999). “Velocity and wall shear stress patterns in the human right coronary artery”. *Journal of Biomechanical Engineering* 121.4, pp. 370–375.
- Kohn JC, Lampi MC, and Reinhart-King CA (2015). “Age-related vascular stiffening: causes and consequences”. *Frontiers in Genetics* 6, p. 112.
- Li S, Chin C, Thondapu V, Poon EKW, Monty JP, Li Y, Ooi ASH, Tu S, and Barlis P (2017). “Numerical and experimental investigations of the flow–pressure relation in multiple sequential stenoses coronary artery”. *The International Journal of Cardiovascular Imaging* 33.7, pp. 1083–1088.
- M KR, DasGupta S, and Chakraborty S (2019). “Biomimetic pulsatile flows through flexible microfluidic conduits”. *Biomicrofluidics* 13.1, p. 014103.
- Malek AM, Alper SL, and Izumo S (1999). “Hemodynamic shear stress and its role in atherosclerosis”. *JAMA* 282.21, pp. 2035–2042.
- Mehra A and Mohan B (2015). “Value of FFR in clinical practice”. *Indian heart journal* 67.1, pp. 77–80.

- Melikian N, De Bondt P, Tonino P, De Winter O, Wyffels E, Bartunek J, Heyndrickx GR, Fearon WF, Pijls NH, Wijns W, and De Bruyne B (2010). “Fractional flow reserve and myocardial perfusion imaging in patients with angiographic multivessel coronary artery disease”. *JACC: Cardiovascular Interventions* 3.3, pp. 307–314.
- Mirramezani M, Diamond S, Litt H, and Shadden SC (2018). “Reduced order models for transstenotic pressure drop in the coronary arteries”. *Journal of Biomechanical Engineering*, p. 31005.
- Mitchell GF, Parise H, Benjamin EJ, Larson MG, Keyes MJ, Vita JA, Vasani RS, and Levy D (2004). “Changes in arterial stiffness and wave reflection with advancing age in healthy men and women”. *Hypertension* 43.6, pp. 1239–1245.
- Morris PD, Vosse FN van de, Lawford PV, Hose DR, and Gunn JP (2015). ““Virtual” (computed) fractional flow reserve: current challenges and limitations”. *JACC: Cardiovascular Interventions* 8.8, pp. 1009–1017.
- Najjari MR and Plesniak MW (2016). “Evolution of vortical structures in a curved artery model with non-Newtonian blood-analog fluid under pulsatile inflow conditions”. *Experiments in Fluids* 57.6.
- Najjari MR and Plesniak MW (2018). “Secondary flow vortical structures in a 180 elastic curved vessel with torsion under steady and pulsatile inflow conditions”. *Physical Review Fluids* 3.1, p. 13101.
- Patel MR, Peterson ED, Dai D, Brennan JM, Redberg RF, Anderson HV, Brindis RG, and Douglas PS (2010). “Low diagnostic yield of elective coronary angiography”. *The New England Journal of Medicine* 362.10, pp. 886–895.
- Perktold K, Nerem RM, and Peter RO (1991). “A numerical calculation of flow in a curved tube model of the left main coronary artery”. *Journal of Biomechanics* 24.3-4, pp. 175–189.
- Pielhop K, Klaas M, and Schröder W (2012). “Analysis of the unsteady flow in an elastic stenotic vessel”. *European Journal of Mechanics - B/Fluids* 35, pp. 102–110.
- Pijls NH, Gelder BV, Voort PV der, Peels K, Bracke FA, Bonnier HJ, and Gamal MIE (1995). “Fractional flow reserve”. *Circulation* 92.11, pp. 3183–3193.
- Pijls NH, Schaardenburgh P van, Manoharan G, Boersma E, Bech JW, Veer M van’t, Bär F, Hoorntje J, Koolen J, Wijns W, and Bruyne B de (2007). “Percutaneous coronary intervention of functionally nonsignificant stenosis”. *Journal of the American College of Cardiology* 49.21, pp. 2105–2111.
- Qiu Y and Tarbell JM (2000). “Numerical simulation of oxygen mass transfer in a compliant curved tube model of a coronary artery”. *Annals of Biomedical Engineering* 28.1, pp. 26–38.
- Seeley BD and Young DF (1976). “Effect of geometry on pressure losses across models of arterial stenoses”. *Journal of Biomechanics* 9.7, pp. 439–448.
- Siggers JH and Waters SL (2005). “Steady flows in pipes with finite curvature”. *Physics of Fluids* 17.7, p. 77102.
- Siogkas PK, Papafaklis MI, Sakellarios AI, Stefanou KA, Bourantas CV, Athanasiou LS, Exarchos TP, Naka KK, Michalis LK, Parodi O, and Fotiadis DI (2015). “Patient-specific simulation of coronary artery pressure measurements: an in vivo three-dimensional validation study in humans”. *BioMed Research International* 2015. Ed. by K Bendjelid, p. 628416.
- Stocker TJ, Deseive S, Leipsic J, Hadamitzky M, Chen MY, Rubinshtein R, Heckner M, Bax JJ, Fang XM, Grove EL, Lesser J, Maurovich-Horvat P, Otton J, Shin S, Pontone G, Marques H, Chow B, Nomura CH, Tabbalat R, Schermund A, Kang JW,

- Naoum C, Atkins M, Martuscelli E, Massberg S, and Hausleiter J (2018). “Reduction in radiation exposure in cardiovascular computed tomography imaging: results from the prospective multicenter registry on radiation dose estimates of cardiac CT angiography in daily practice in 2017 (PROTECTION VI)”. *European Heart Journal* 39.41, pp. 3715–3723.
- Stultz SC and Kitto JB (2005). *Steam: Its generation and use*. 41st ed. The Babcock & Wilcox Company. Chap. 3-14.
- Sun Z (2015). “Aging, arterial stiffness, and hypertension”. *Hypertension* 65.2, pp. 252–256.
- Tanné D, Bertrand E, Kadem L, Pibarot P, and Rieu R (2010). “Assessment of left heart and pulmonary circulation flow dynamics by a new pulsed mock circulatory system”. *Experiments in Fluids* 48.5, pp. 837–850.
- Tonino PA, Bruyne BD, Pijls NH, Siebert U, Ikeno F, `t Veer M van, Klauss V, Manoharan G, Engstrøm T, Oldroyd KG, Lee PNV, MacCarthy PA, and Fearon WF (2009). “Fractional flow reserve versus angiography for guiding percutaneous coronary intervention”. *New England Journal of Medicine* 360.3, pp. 213–224.
- Tu S, Westra J, Adjedj J, Ding D, Liang F, Xu B, Holm NR, Reiber JHC, and Wijns W (Sept. 2019). “Fractional flow reserve in clinical practice: from wire-based invasive measurement to image-based computation”. *European Heart Journal* 41.34, 3271–3279.
- Vavalle JP, Shen L, Broderick S, Shaw LK, and Douglas PS (2016). “Effect of the presence and type of angina on cardiovascular events in patients without known coronary artery disease referred for elective coronary angiography”. *JAMA Cardiology* 1.2, pp. 232–234.
- Verkaik AC, Beulen BWAMM, Bogaerds ACB, Rutten MCM, and Vosse FNVD (2009). “Estimation of volume flow in curved tubes based on analytical and computational analysis of axial velocity profiles”. *Physics of Fluids* 21.2, p. 23602.
- Wells MK, Winter DC, Nelson AW, and McCarthy TC (1977). “Blood velocity patterns in coronary arteries”. *Journal of Biomechanical Engineering* 99.1, pp. 26–32.
- White CM (1929). “Streamline flow through curved pipes”. *Proceedings of the Royal Society of London. Series A, Containing Papers of a Mathematical and Physical Character* 123.792, pp. 645–663.
- White FM (2016). *Fluid Mechanics*. McGraw Hill. Chap. 384.
- Wong KKL, Wu J, Liu G, Huang W, and Ghista DN (2020). “Coronary arteries hemodynamics: effect of arterial geometry on hemodynamic parameters causing atherosclerosis”. *Medical & Biological Engineering & Computing* 58.8, pp. 1831–1843.
- Wu J, Liu G, Huang W, Ghista DN, and Wong KKL (2015). “Transient blood flow in elastic coronary arteries with varying degrees of stenosis and dilatations: CFD modelling and parametric study”. *Computer Methods in Biomechanics and Biomedical Engineering* 18.16, pp. 1835–1845.
- Wyk S van, Wittberg LP, Bulusu KV, Fuchs L, and Plesniak MW (2015). “Non-Newtonian perspectives on pulsatile blood-analog flows in a 180° curved artery model”. *Physics of Fluids* 27.7, p. 071901.
- Yao H, Ang KC, Yeo JH, and Sim EK (2000). “Computational modelling of blood flow through curved stenosed arteries”. *Journal of Medical Engineering & Technology* 24.4, pp. 163–168.
- Young DF and Tsai FY (1973a). “Flow characteristics in models of arterial stenoses. II. Unsteady flow”. *Journal of Biomechanics* 6.5, pp. 547–559.

- Young DF and Tsai FY (1973b). “Flow characteristics in models of arterial stenoses — I. Steady flow”. *Journal of Biomechanics* 6.4, pp. 395–410.
- Zhu C, Seo JH, and Mittal R (2018). “Computational modelling and analysis of haemodynamics in a simple model of aortic stenosis”. *Journal of Fluid Mechanics* 851, pp. 23–49.

Chapter 7

Hemodynamics of stented arteries

7.1 Chapter overview

As discussed in Section 2.4, one of the most common treatments for coronary artery diseases is coronary stent implantation. The literature suggests that there are several parameters related to the stent design affecting the success rate of coronary stent implantation procedure by lowering the likelihood of thrombosis and in-stent restenosis (ISR). One of these parameters is the stent pattern. The effect of the stent design on the hemodynamics of the stented arteries has been the subject of several studies in the literature both experimentally and numerically. As discussed in Section 2.4.2, all the flow visualisation experiments of stented arteries to date have been limited due to the presence of the metallic or non-transparent stent struts in the field of view. As a proper experimental validation is an important part of all computational fluid dynamics (CFD) simulations, development of a technique to overcome this limitation of the previous flow visualisation experimental studies of stented arteries is of great importance.

This chapter consists of two sections: Section 7.2 introduces a novel technique to overcome the limitation of previous flow visualisation experimental studies on the stented arteries, followed by the hemodynamic investigation of four artery stent models with different stent patterns. Section 7.3 describes the CFD results for the hemodynamics of the investigated stented arteries. Utilising the developed novel technique, the time-averaged and -dependent wall shear stress (WSS) distributions of the four different stent patterns are calculated and compared. Furthermore, the results obtained from the developed CFD model presented in Section 7.3 are validated against the experimental results obtained using particle image velocimetry (PIV) in Section 7.2. The application of CFD modelling of the stented arteries is of great importance, since it enables the calculation of the micro-recirculation zones adjacent to the struts and the WSS distributions. Experimental measurement of these parameters is very challenging.

The novel technique presented in Section 7.2 is based on the construction of a transparent stented artery using silicone cast in a single piece, instead of inserting a metal or non-metallic stent inside a cast artery model, which are translucent and distort the field of view. Slender rods with different stent patterns engraved on them are 3D-printed using PolyJet technology. They are used as a negative mould part of the silicone casting to make the cast stented artery models. Furthermore, PIV is employed to investigate

the bulk flow behaviour and near wall WSS distribution of the stented arteries. The results show that with the help of the developed technique, bulk flow velocity and WSS can be calculated without any blockages of the field of view due to the presence of the non-transparent struts providing a more complete picture of the effect of the stents on the flow behaviour.

Section 7.3 investigates the effect of the stent pattern on the WSS of the stented coronary artery models using CFD. The computational model in this study is validated against the PIV data. The results of this section show that WSS is strongly dependent on the pattern of the stent, has higher values in the vicinity of the struts and lower values immediately upstream and downstream of the struts. Furthermore, comparison of the WSS distribution for different stents shows that WSS is highest in the vicinity of the struts and overall lowest adjacent to the struts for the stent pattern with a wavy connector relative to the other patterns studied.

The results of this chapter show that connectors, as a part that hold hoops together and maintain the longitudinal stability of the stent, have an important effect on the hemodynamic performances of the stents. The developed technique will help to improve the future generation stent designs. Furthermore, identification of the stent patterns which create smaller regions of low WSS adjacent to the struts will finally result in better patient outcomes.

7.2 Flow visualisation of the stented arteries

This section consists of the following submitted journal article:

Navid Freidoonimehr, Maziar Arjomandi, Anthony Zander, Rey Chin (2021). “A novel technique towards investigating wall shear stress within the stent struts using Particle Image Velocimetry”. *Experiments in Fluids*, 62 pp. 133.

The article is identical to its submitted format with the following exceptions:

- The numbering of figures, tables and equations have been altered to include the chapter number.
- The position of some figures and tables have been changed to improve legibility.

The article in its published format is available at:

<https://doi.org/10.1007/s00348-021-03230-7>

Statement of Authorship

Title of paper	A novel technique towards investigating wall shear stress within the stent struts using Particle Image Velocimetry
Publication Status	<input type="checkbox"/> Published <input type="checkbox"/> Accepted for Publication <input checked="" type="checkbox"/> Submitted for Publication <input type="checkbox"/> Unpublished and Unsubmitted work written in manuscript style
Publication Details	Freidoonimehr, N., Arjomandi, M., Zander, A., and Chin, R., 2021, "A novel technique towards investigating wall shear stress within the stent struts using Particle Image Velocimetry", Experiments in Fluids, under review

Principal Author

Name of Principal Author (Candidate)	Navid Freidoonimehr		
Contribution to the Paper	Developed ideas, conducted experiments, performed data analysis and interpreted results, wrote manuscript, and acted as corresponding author		
Overall percentage (%)	75%		
Certification:	This paper reports on original research I conducted during the period of my Higher Degree by Research candidature and is not subject to any obligations or contractual agreements with a third party that would constrain its inclusion in this thesis. I am the primary author of this paper.		
Signature		Date	15/02/2021

Co-Author Contributions

By signing the Statement of Authorship, each author certifies that:

- i the candidate's stated contribution to the publications is accurate (as detailed above);
- ii permission is granted for the candidate to include the publication in the thesis; and
- iii the sum of all co-author contributions is equal to 100% less the candidate's stated contribution

Name of Co-Author	Maziar Arjomandi		
Contribution to the Paper	Supervised the development of the research, participated in developing ideas and concepts, helped in interpretation of results, provided critical revision of manuscript.		
Signature		Date	15/02/2021

Name of Co-Author	Anthony Zander		
Contribution to the Paper	Supervised the development of the research, participated in developing ideas and concepts, helped in interpretation of results, provided critical revision of manuscript.		
Signature		Date	15/02/2021

Name of Co-Author	Rey Chin		
Contribution to the Paper	Supervised the development of the research, participated in developing ideas and concepts, helped in interpretation of results, provided critical revision of manuscript.		
Signature		Date	15/02/2021

A novel technique towards investigating wall shear stress within the stent struts using Particle Image Velocimetry

Navid Freidoonimehr, Maziar Arjomandi, Anthony Zander, and Rey Chin

Abstract

Understanding the effects of a stent design on the flow behaviour especially near the artery wall can lead to choosing or designing more haemodynamically compatible stents that can reduce the chances of restenosis inside the stented arteries. In this study, a novel technique is presented for the visualisation of the entire flow and the investigation of wall shear stress (WSS) within the stent struts without covering the field of view (FOV) inside a stented coronary artery model using particle image velocimetry. This novel technique is based on the construction of a transparent stented artery using silicone casted in one piece, instead of inserting a metal or non-metallic stent inside a casted artery model, which are translucent and distort the FOV. The effect of the stent pattern on the WSS and oscillatory shear index of a coronary artery is investigated for the models of four stents to identify the locations with the high chances of restenosis. The developed technique will help to improve the stent designs to achieve better patient outcome.

7.2.1 Introduction

Coronary stent implantation, as a minimally invasive alternative for Coronary Artery Bypass Grafting (CABG) surgery, is one of the most common treatments for Coronary Artery Disease (CAD). Although there are several benefits of stenting over the CABG such as lower risks of complications and much shorter recovery period, it can result in thrombosis and in-stent restenosis (ISR) which are the major drawbacks of coronary stent placement in patients with CAD (Kastrati et al. 2001a). It is shown that there is a direct link between low WSS locations and ISR and thrombosis and consequently patient outcome (Chatzizisis et al. 2008; Chatzizisis et al. 2007; Gijssen et al. 2019). The locations with a lower WSS especially adjacent to the stent struts are the possible locations for the formation of ISR and thrombosis (Koskinas et al. 2012; Morlacchi et al. 2011). Furthermore, the use of stents with thinner struts is associated with a significantly lower chance of ISR after coronary artery stenting (Kastrati et al. 2001b). However, there are some drawbacks for the thinner struts such as less successful drug delivery for drug-eluting stents and reduced angiographic visibility (Pache et al. 2003). Furthermore, it is shown that for the strut with tear drop profile, up to 96% of the area between the struts is exposed to the WSS levels above the critical value required for the onset of restenosis while for the square profile, the corresponding value is 19.4% (Mejia et al. 2009). Although the shape of the stent geometry is usually limited by the manufacturing processes, it can play an important role in the improvement of hemodynamic performance (Mejia et al. 2009). It is also shown that different commercial stents result in different levels of WSS especially adjacent to the struts (Charonko et al. 2009). Therefore, the possibilities of

ISR and thrombosis should be better understood by investigating WSS distribution for different typical commercial stent designs with different geometrical features (Beier et al. 2016).

In-vitro experimental and numerical studies of stented arteries have been conducted in the literature to better understand the WSS of the stented arteries with the aim to identify the causes of ISR and thrombosis (Foin et al. 2017; Ng et al. 2017). The main hemodynamic effect of a stent in the coronary artery is an overall reduction of the WSS in the entire treated region in the immediate post-implantation period (Chiastra et al. 2020). Numerical analysis of the flow behaviour near the wall, specifically for identification of micro-recirculation zones near the stent struts and evaluation of WSS distribution, is a useful complement to experiments in advancing knowledge. A CFD model which is validated against experiments can help to improve the understandings of the flow features and hemodynamics of the stented arteries. That is why the in-vitro experimental studies are in high demand. However, the results of experimental studies especially those focusing on the flow visualisation of the stented arteries in the literature, so far, were limited due to the use of metallic or non-metallic stents, which partially obscured the FOV. Berry et al. (2000) studied the local flow separation created by a metallic stent in a coronary artery model using dye injection flow visualisation experiments. Their results showed that the largest Recirculation Zones (RZs) were observed distal to the stent. The limitations of their study were, first, related to the use of dye injection method, which resulted in the qualitative comparison of the results. A reported limitation was the lack of experimentally visualisation of the stented regions. In another study, Natarajan and Mokhtarzadeh-Dehghan (2000) investigated the effect of the presence of a stent on the blood flow behaviour. Their results showed that the predicted time-averaged WSS around the top of the struts was 2-3 times greater than that found in the equivalent normal artery. Their study, however, was limited in the experimental part and was mainly based on the numerical simulation. They only used experimental results to validate the numerical simulation results based on a simplified non-physiological flow profile. Charonko et al. (2009) took the next step and improved the PIV studies of the stented arteries by investigating the flow behaviour within the stented region near the wall using time-resolved digital PIV. They deployed drug-eluting commercial stents inside the casted arteries out of silicone. They reported that the stent struts along the artery wall disturb the nearby flow, making it more receptive to changes in direction and decrease the peak WSS. In another study by the same authors (Charonko et al. 2010), they studied the distributions of WSS and Oscillatory Shear Index (OSI) for different configurations including baseline (the normal stenting procedure), over-expanded (inflated to 125%), increased artery diameter, two overlapped stents, and increased stent length experimentally using time-resolved digital PIV. They reported an overall correlation between decreased WSS values and elevated OSI for all configurations. Their studies, however, were still limited because of the obscuration of the FOV by the other stent struts, which made their measurements unreliable at those locations. Other studies investigated the effect of stent on the coronary bifurcated arteries experimentally and numerically (Brindise et al. 2017; García Carrascal et al. 2018; García García et al. 2017; Raben et al. 2015). In all the mentioned bifurcation studies, PIV is used to validate the developed CFD models. To sum up, all the studies in the literature focusing on the in-vitro flow visualisation investigation of the flow behaviour inside the stented arteries were limited due to obscuration of the view of the region of interest by the stent struts. This obscuration effect caused by the stent

struts has resulted in dark regions in the PIV images, hence velocity measurements are not available at these locations (Raben et al. 2015). Therefore, velocity calculated in FOV was affected by these narrow shadows and resulted in reduced accuracy.

The aim of this study is, for the first time, to introduce a novel experimental technique to perform flow visualisation inside a stented artery using transparent casting of stented arteries to eliminate the problem of blockage of the region of interest due to the presence of the metallic stent struts. The second objective of the present study is to characterise WSS for the models of four different stents and provide a comparison. This technique will provide a better understanding of the flow physics in experimental ex-vivo studies, which can assist design of new stents and evaluate their performances ex-vivo before inserting the real stents inside the patient arteries.

7.2.2 Materials and methods

Design and casting of the transparent stented coronary artery model

Four typical stents are modelled using the geometrical data presented in Charonko et al. (2009). Figure 7.1 illustrates the procedure for constructing a transparent silicone model of a stented coronary artery. The casting components consist of two main parts, a stent rod (Figure 7.1a) and a casing mould (Figure 7.1b). The stent patterns on the casting rods are 3D printed out of VeroClear material using Stratasys J750 PolyJet Printer with a horizontal build layer of about 14 microns. The casing, Figure 7.1b, is 3D printed using ABS material. As shown in the schematic in Figure 7.1b, to limit optical distortion, the mid-section including the stent was constrained by a rectangular box surrounded by four pieces of glass plates. The stent rods were placed in the middle of the casing at the designated location and then the glass plates were placed. After ensuring that all the gaps were sealed, silicone was injected through the injection hole at the bottom of the mould. To match the refractive index of the working fluid, a Sylgard 184 silicone was used for casting. The final product, as shown in Figure 7.1c, was obtained after removing the casing and the stent rods. For separating the two sides of the casing from the model, they were detached carefully and then the glass rectangular plates were removed. To remove the stent rod from the interior of the model, it was required to slowly twist the stent rod to allow air to penetrate the area between the stent rod and the interior of the model. Once air had filled the entire area between the stent rod and model interior, the stent rod was slowly pulled out from the model interior to avoid any damages to the interior of the model. The inside diameter of the model, D , is 6.4 mm corresponding to almost double the diameter of coronary arteries (Dodge et al. 1992). The reason that the model was designed at a larger diameter than a real coronary artery was to reduce the errors associated with the PIV measurements compared to when a smaller diameter is used. Note that by matching the Reynolds and the Womersley numbers, as two non-dimensional parameters governing the blood flow regime, flow similarity is achieved, and hence the results are independent of the artery diameter. With the cardiac cycle period of 4.4 s and the mean flow rate of 210 mL/min, the corresponding mean flow Reynolds and the Womersley numbers are 210 and 2.1, respectively, which is in a range of the values reported for the coronary arteries (Freidoonimehr et al. 2020a; Ku 1997). Figure 7.1e shows the geometrical specifications of a single pattern of each stent. In this study,

the cross section of the stent models was considered to be the same in the square shape with 200-micron strut thickness and depth, as shown in Figure 7.1e. The length of the stented section, L , for each stent is $6D < L < 7D$. The slight variation in the length of the stents is to prevent an incomplete repetition of a single stent pattern.

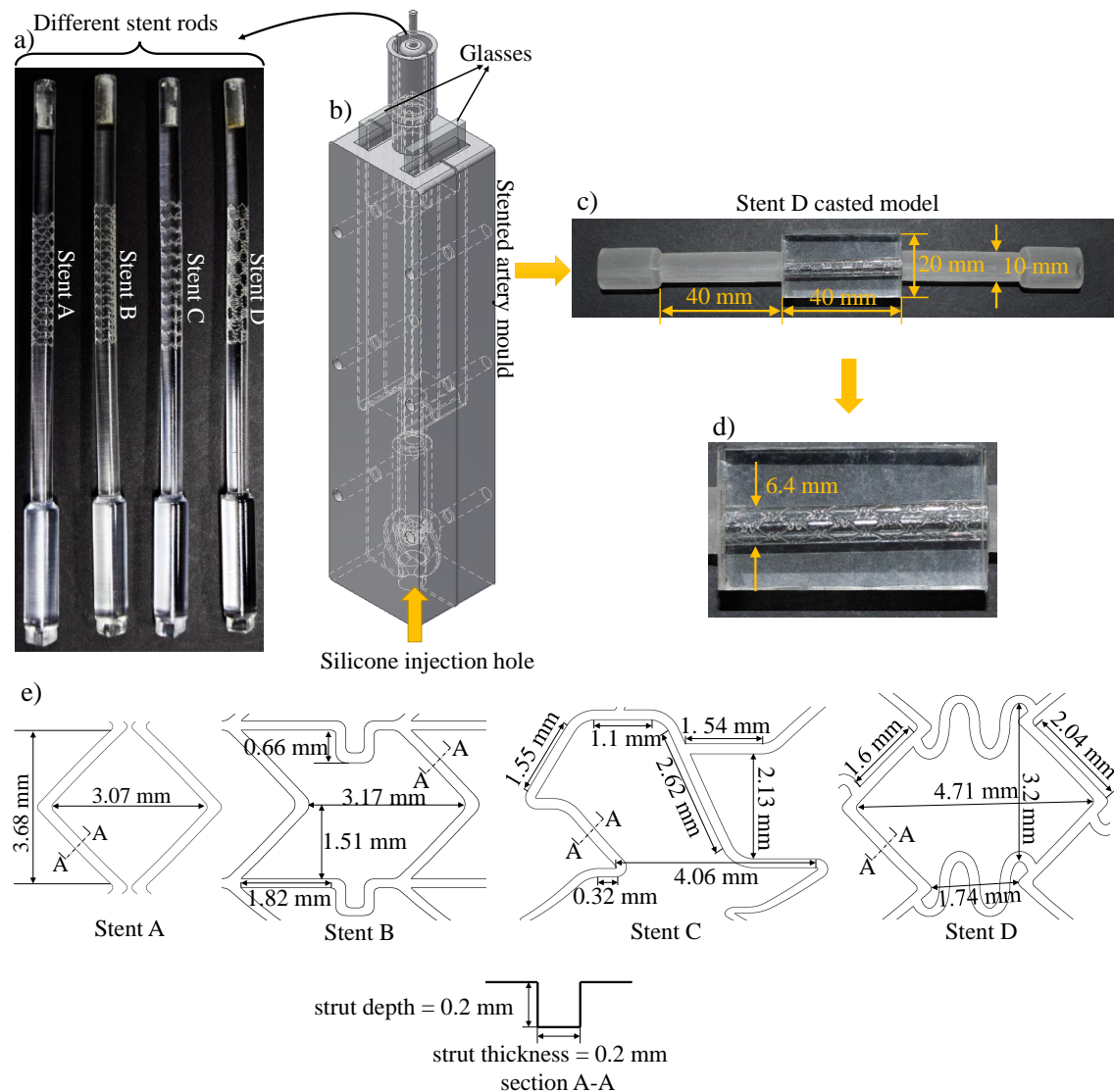


Figure 7.1: Steps for generating a transparent silicone model of stented coronary artery showing a) casting rods of different stents, b) schematics of the stented artery mould, c) the final stent D casted model, d) detail view of the stent region of the casted artery, and e) geometrical specifications of a single pattern of each stent.

It is important to note that since the struts' depth is about 200 microns, the resolution of the employed 3D printer to print the stent rods is of great importance for achieving a perfect cast of the stented arteries. Direction of printing is also an important factor in the quality of the product. Ideally, the stent rods should be printed vertically on the bed of the printer to achieve its best quality. However, because the stent rods are a slender body, printing in vertical direction causes stability issues, which eventually degrade the quality of the printed product as it becomes taller. Hence, the stent rods should be printed horizontally to avoid stability issues. However, printing horizontally results in a larger attachment area of the supports to the stent rods especially at the

location of stent struts. Therefore, post processing to remove supports from the stent rods should be performed carefully to avoid damage to the stent struts that are connected to the supports. Therefore, the choice of 3D printing process and 3D printers are of great importance in the quality of the printed stent rods and hence the casted stented arteries. On the other side, 3D printing technology is improving rapidly and hence the mentioned limitation of the 3D printing will not pose any issues in the near future.

In order to show the quality of the 3D printed stent rod models, Figure 7.2 shows the surface roughness analysis of stent B. The 3D laser confocal scanning microscope, named Olympus LEXT OLS5000 profilometer, is employed to show the surface details of the stent models. The results are presented for the selected area in Figure 7.2a, as an example. The area was captured using the 20x objective and was a montage of a 9×7 frame stitch (63 images). Figures 7.2b and 7.2c show the 2D raw intensity image and the 3D surface contour of the selected area, respectively. The patterns of the stent as well as the location of the struts can be identified in the surface counter of the models. Figure 7.2d shows the surface roughness contour of the area shown in orange dashed line box in Figure 7.2b. A total least square filter is applied to the surface contour to eliminate the effect of the curvature of the stent models on the surface roughness, prior to the calculation of the roughness contour. The height histogram of the roughness of the selected surface is displayed in Figure 7.2e. Roughness parameters for the selected area are listed in Table 7.1. The roughness parameters are Sq , Sp , Sv , Sz , and Sa , defined as one standard deviation of the height distribution, difference in height between the mean plane and the highest point, difference in height between the mean plane and the lowest point, total height difference from max to min value, and mean difference in height from the mean plane, respectively. A typical measure of the roughness on a surface is Sa which is around 800 nm. Therefore, the relative roughness parameter which is defined as a ratio of the mean height of the roughness of the pipe to the pipe diameter, is about 1.56×10^{-4} . Furthermore, the reported surface roughness is in the same order of magnitude of those reported in the literature for the bioactive polymeric drug eluting stents (McKittrick et al. 2020). Finally, the roughness profile across the line shown in part b is displayed in Figure 7.2f. This line shows the location of the struts as well as their depths and thicknesses. To conclude, the 3D printed stent models are produced to a high degree of accuracy.

Table 7.1: Roughness parameters for the evaluation of surface unevenness of the selected area in Figure 7.2d.

$Sq(\mu\text{m})$	$Sp(\mu\text{m})$	$Sv(\mu\text{m})$	$Sz(\mu\text{m})$	$Sa(\mu\text{m})$
1.251	4.711	12.069	16.780	0.826

Figure 7.3 shows a comparison between the quality of the surface of the stent rod and the silicone model. The silicone models of the stents, as shown in Figure 7.1c, were cut into two halves along their centrelines and a laser confocal scanning microscope was used to measure the quality of their surface. To increase the laser reflection from the surface of silicone models and improve the quality of the scan, surfaces of the models were coated by platinum with a maximum thickness of 10 nm. Comparing the profiles of the silicone model and the stent rod shows that the silicone casting process could replicate the stent patterns on the stent rod with a high degree of accuracy. The small difference that can be observed between the surface quality of the stent rod and the silicone model is due to the fact that the laser confocal scanning data for the same region of interest in stent

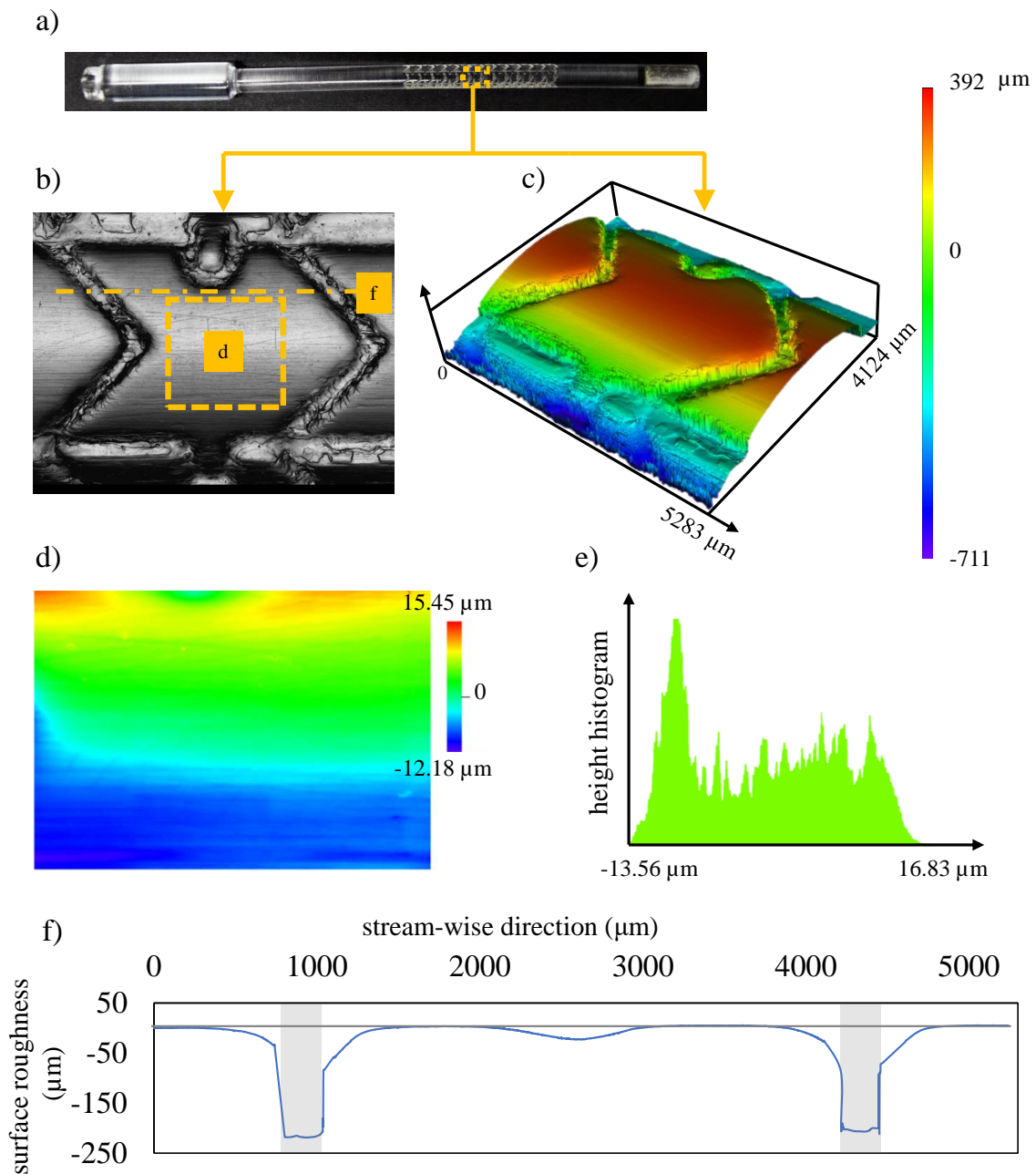


Figure 7.2: Casting rod of stent B, b) 2D view of the raw intensity image of the selected area shown in part a, c) 3D surface contour of the selected area showing the curvature of the stent model and the depth of the struts, d) surface roughness contour of the area shown by orange dashed line box in part b after removing the effect of model curvature, e) height histogram of the area highlighted in part b, and f) roughness profile across the line shown in part b. The locations of struts as well as their depths and thicknesses are shown in the grey shaded area.

rod and silicone model was not available. Furthermore, the choice of SYLGARD 184 for the silicone stent model results in a negligible polymerisation shrinkage error and hence the effect of polymerisation shrinkage on the measurement uncertainty can be neglected, as widely explained by Johnston et al. (2014) and Müller et al. (2019). As discussed by Lee and Lee (2007), the effect of polymerisation shrinkage is heavily dependent on the curing temperature and increases linearly with increasing the curing temperature.

Hence, since the curing process in this study was performed at the room temperature, the shrinkage effect is deemed negligible. Figure 7.3e and 7.3f also show the angles of the edges of the struts. As shown in Figure 1e, the struts were designed to be vertical to the wall. However, due to the limitation of manufacturing method and material used, the edges are not completely vertical, and their slopes deviate from vertical by about $\pm 25^\circ$. This deviation of the slope of the edges is expected to have a minor effect on the results of this study. In a study by Jiménez and Davies (2009) on the effect of cross-sectional shape of the struts on the WSS, it was shown that the spatial average WSS values on top of the struts for square shape and circular arc shape with the same aspect ratio were almost similar. However, the spatial WSS distribution on the struts was different with a higher WSS value at the corners of the square shape struts compared to the circular arc shape struts. Therefore, it can be concluded that the spatial averaged WSS values on top of the struts are not significantly affected by the sharp or rounded angles and the results remain consistent in this study with those with the sharp edge struts. However, it is expected that due to the slight deviation of the strut slopes from vertical (less than 25°), the magnitude of the peak WSS value at the strut corners can be lower compared to a similar case with square shape struts. It is also important to note that the difference observed in the results of Jiménez and Davies (2009) between the square and round shapes of the struts on the WSS is higher than those expected between the current sloped edge struts with the corresponding square shapes. The reason is due to the fact that the sloped edges in this study were closer to the vertical edge compared to the cases studied by Jiménez and Davies (2009) which presented an extreme case with square shape and circular arc shape.

Experimental test setup

The experimental test setup was similar to Freidoonimehr et al. (2020b), as shown in Figure 7.4. The flowmeter had a measurement accuracy of 0.4% of the measured value. The input voltage of the pump was governing by a data acquisition card to simulate the physiological pulsatile velocity waveform, as shown in Figure 7.4e (Davies et al. 2008). A mixture of distilled water and glycerine (with the weight mixture percentage of 60% and 40%, respectively) was used as a working fluid to match the blood viscosity with the viscosity of 3.67 mPa.s and to match the refractive index of the silicone artery models. Although the blood is inherently a non-Newtonian fluid, it can be assumed to be Newtonian in some conditions, as reported in the literature (Freidoonimehr et al. 2020a; Pinto et al. 2020). It is reported that blood can be assumed as a Newtonian fluid in arteries with a diameter above 0.5 mm due to the high Reynolds number (Nichols et al. 2011). Hence, in coronary arteries with the mean average diameter of 3 mm, assuming blood to be Newtonian provides accurate results.

In the PIV experiment, two setups were used to achieve a high-resolution result over the whole artery cross section and the regions near the artery wall. A Zyla 5.5 sCMOS camera with a 5.5-megapixel resolution and a Sigma macro lens (105 mm f2.8) along with a 140 mm autofocus macro extension tubes was employed to focus on the mid-cross-sectional plane of the artery in stream-wise direction. Moreover, the Zyla sCMOS camera along with a zoom lens with a 6X magnification was employed to focus closely to the near wall region, which is further explained in the next section. An EverGreen 532 nm laser with 200 mJ at a fixed pulsing frequency of 15 Hz was used to illuminate the FOV. A

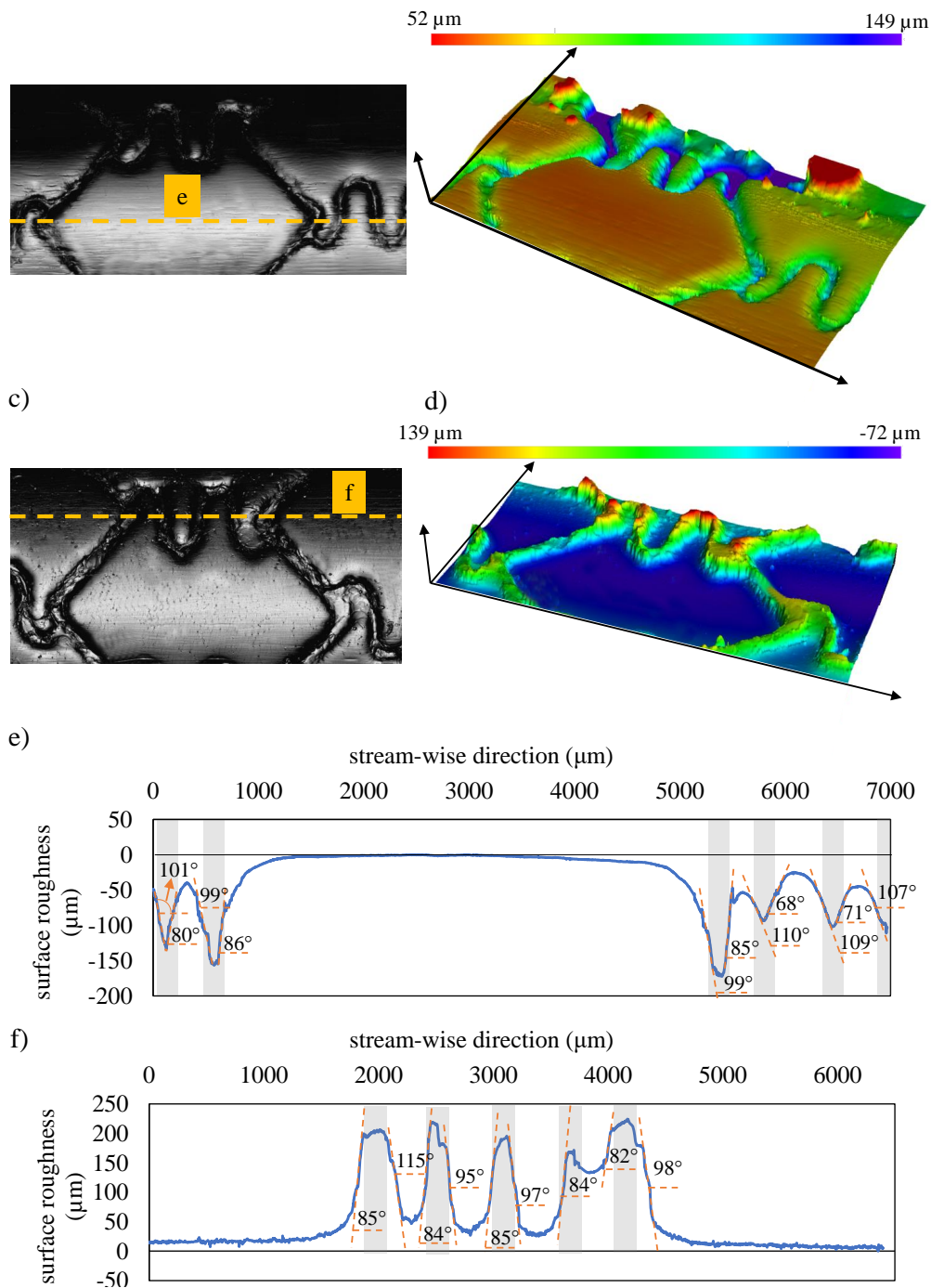


Figure 7.3: Comparison of the surface quality of the stent rod and the cast stent silicone model. a) and b) shows the 2D raw intensity image and 3D surface contour of the stent rod, and c) and d) shows the 2D raw intensity image and 3D surface contour of the cast stent silicone model, e) roughness profile across the line shown in Fig 7.3a, and f) roughness profile across the line shown in Fig 7.3c of the cast stent silicone model. The locations of struts as well as their depths and thicknesses are shown in the grey shaded area. In parts b and d, the curvature of the stent rod and cast stent silicone model is removed to better visualise the depth of the struts. The angles of the edges are also displayed in Figs. 7.3e and 7.3f.

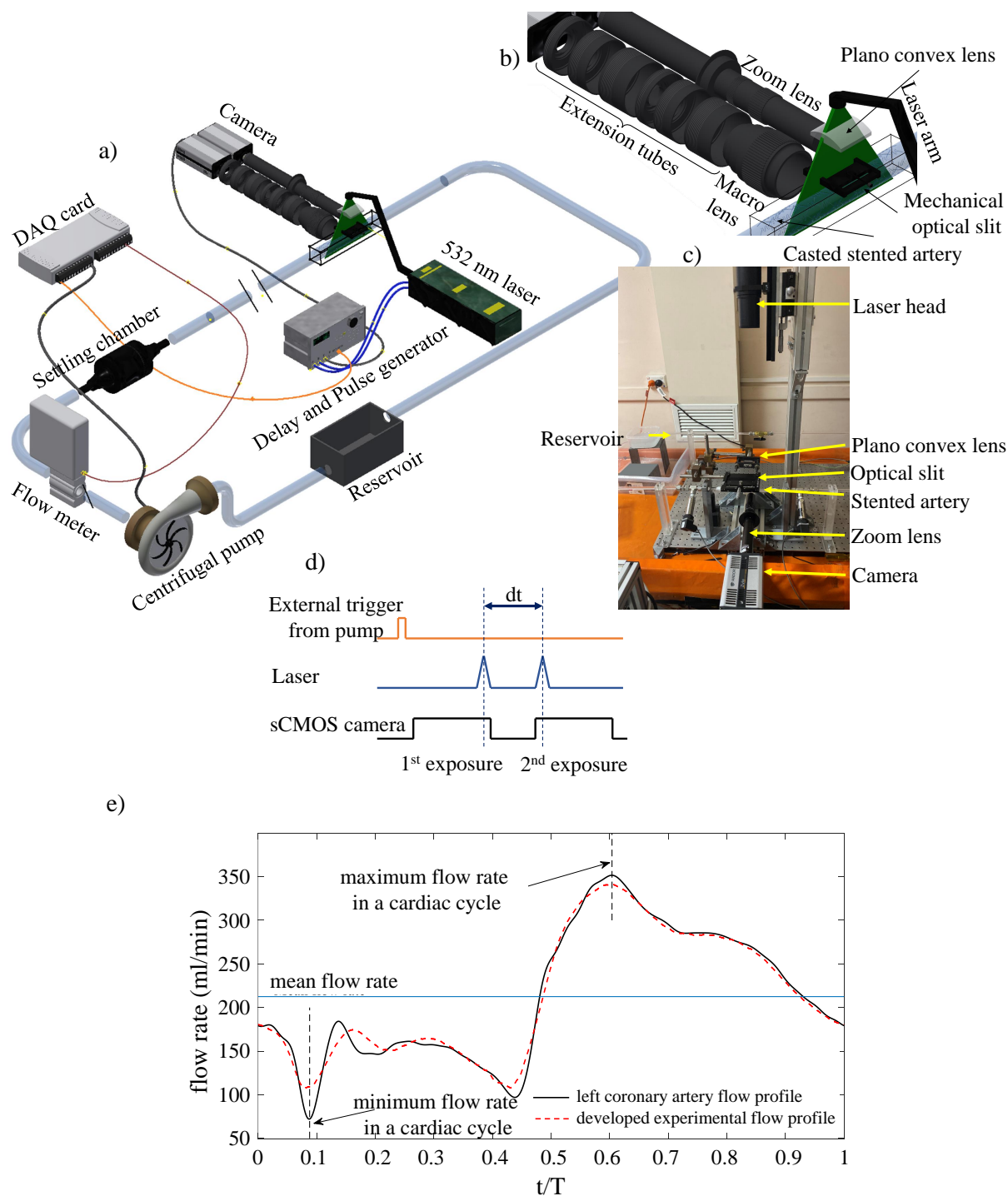


Figure 7.4: a) Schematics of the coronary artery test rig, b) schematics of PIV setup, c) photograph of the PIV setup, d) timing diagram for the synchronisation of the laser and camera with the external trigger from the centrifugal pump. e) The physiological pulsatile left coronary artery blood flow profile (Davies et al. 2008) and the developed experimental blood flow profile. This waveform, as an inlet velocity, was modelled using the first 32 Fourier modes of Fast Fourier Transform (FFT) that accurately represents the original waveform (with less than one percent difference between the maximum flow velocities during a cardiac cycle).

plano-convex lens and an adjustable optical slit were located between the laser head and the artery model, respectively, to set the laser sheet thickness at 0.5 mm to minimise the out-of-plane loss of particle pairs. Two sets of 3-axis trimming platform linear stages were employed for both camera and laser head to adjust their positions allowing displacements with the precision of 0.03 mm.

PIV settings

Two types of seeding particles, Hollow Glass Sphere (HGS) and Poly (methyl methacrylate) (PMMA), were employed to visualise both stream-wise flow inside the whole artery cross section and to focus on the near wall region to calculate WSS within the stented artery models, respectively. The HGS has the mean diameter of 10 μm , the density of 1.1 gr/cm^3 and the refractive index of 1.52. Moreover, PMMA particle has the mean diameter of 6 μm , the density of 1.19 gr/cm^3 and the refractive index of 1.49. To visualise the stream-wise plane, images were captured with an array of 2220×1480 pixels. The FOV for each measurement was set to $9.6 \text{ mm} \times 6.4 \text{ mm}$, which resulted in a pixel size of 4.32 μm . The image-processing was performed using PIVlab software (William Thielicke 2014) with two passes interrogation window sizes of 64×64 and 32×32 pixels with 50% overlap for both passes, leading to a spatial resolution of 0.07 mm in each direction. FFT window deformation PIV algorithm was employed in this study due to its higher accuracy compared to the window shifting methods. Furthermore, to measure the velocity distribution near the wall, images were captured with an array of 2200×400 pixels. The FOV near the wall was set to $5.5 \text{ mm} \times 1 \text{ mm}$, resulting in a pixel size of 2.5 μm . The interrogation window was set with two passes of 32×32 pixels and 24×24 pixels with a 75% overlap, resulting in a spatial resolution of 0.015 mm in each direction. The Stokes numbers (SkD) for both regimes with different particles were $\text{SkD} \ll 1$ which means that particles were able to follow the flow at the length scales that can be resolved with the PIV measurement.

Due to the limited pulsation frequency of the laser (15 Hz) and the duration of the cardiac cycle (4.4 s), 66 image pairs (16 bit) were recorded for each cardiac cycle. The time was off-set between two images in a pair (dt) by 70 microseconds. The images were recorded for 100 consecutive pulsation cycles (6600 image pairs). To synchronise the pulsation of the pump, laser pulses and camera, a LabVIEW code was used. This code sends a signal to the pulse generator as soon as the pump starts working from a specified instance during a cardiac cycle. The signal is used as an external trigger to start the laser pulses and camera shots. This process is schematically shown in Figure 7.4d.

In this experiment, the uncertainties were reported at ± 1 standard deviation. The first uncertainty is in viscosity due to temperature differences between the experiment runs. The viscosity of the mixture of water and glycerine is highly temperature dependent. The PIV measurements were performed at a room temperature of $24 \pm 1^{\text{circ}}\text{C}$. Therefore, the uncertainty in viscosity is estimated to be less than 3%. The Primary Peak Ratio (PPR) method developed by Charonko and Vlachos (2013) was employed to estimate the level of uncertainty of the velocities. The full 3-term expression of peak ratio was used to evaluate the uncertainty in the displacement magnitude as presented in Charonko and Vlachos (2013). As the coefficients of the expression were not specifically calibrated for PIVlab, the accuracy of the uncertainty estimate may be slightly affected. This uncertainty

estimation is a conservative estimate since the outlier removal method was employed in PIVlab and hence, it includes the error due to removed outliers. Based on the peak ratio results, the average uncertainty of velocities was calculated to be 9%. Furthermore, based on the propagation of errors formula and considering the uncertainties of velocities and fluid viscosity and spatial resolution of near wall measurements, the uncertainties related to the WSS were calculated to be 21%. Moreover, the uncertainty related to the spatial-averaged WSS was reported based on the number of spatial WSS vectors, as 1.3%. Similarly, the phased-averaged WSS uncertainty was reported as 2.1% and the phase and spatial averaged WSS uncertainty was reported as 0.25%. This shows an acceptable level of the accuracy of the presented results in this study.

Hemodynamic indices calculations

As mentioned in the PIV setting section, the measurements were conducted for 100 consecutive pulsation cycles. A phase-average technique was utilised as:

$$f_{pa}(x, y, t) = \frac{1}{N-1} \sum_{n=1}^{N-1} f(x, y, t + nT), \quad (7.1)$$

where f is a flow variable including velocity components, u and v , in different directions, x and y , respectively, N is the number of pulsation cycles ($N = 95$), t is the time, and T is the cardiac cycle duration. The phase-averaging technique was performed over the last 95 cycles in order to eliminate the errors associated to the model initialisation by removing the first 5 cardiac cycles. Each time-dependent cardiac cycle shows less than 1% deviation from the time-dependent phase-averaged flow profile demonstrating the repeatability of the flow loop.

From the resulting images and after conducting phase-averaging technique, velocity components were identified as a function of time in a cardiac cycle and position of the region of interest. WSS is defined based on the velocity gradient of the closest interrogation windows near the wall by multiplying the dynamic viscosity (μ) and the component of the fluid strain rate tensor oriented tangential to the wall. This tangential component of the strain rate tensor in a wall-oriented coordinate system, as shown in Figure 7.5, is obtained by computing the strain rate tensor from the planar components of velocity, u and v , in a Cartesian coordinate system, x and y ,

$$\tau_w = WSS = \mu \left(\frac{\partial u}{\partial y} + \frac{\partial v}{\partial x} \right), \quad (7.2)$$

The gradients were calculated using a window of 4 by 4 points of interest near the wall resulting in 3 by 3 gradient vectors. In order to ascertain that all points were located inside the viscous sublayer ($y^+ < 5$) where $U^+ = y^+$, an estimation of y^+ was conducted using the empirical formulae for the calculation of C_f for internal flows. After ensuring that all points were located inside the viscous sub-layer, an average of three gradient vectors was evaluated for the calculation of WSS. To check the validity of the estimation of the length of the viscous sub-layer, the calculated WSS was used to verify the estimation of the y^+ . The results show that the considered points of interest, a window of 4 by 4 points, are

located inside the viscous sub-layer. For example, the length of viscous sub-layer based on the maximum spatial and temporal velocity inside the flow was calculated at about 400 microns, while the window considered for the calculation of the gradients was located within 100 microns from the wall. A moving average filter was employed in this study via the smooth function in MATLAB to smoothen the measured WSS data. OSI, as a dimensionless hemodynamic metric, which quantifies the deviations in the direction of the wall shear stress vector throughout the cardiac cycle, is defined as:

$$OSI = \frac{1}{2} \left(1 - \frac{\frac{1}{T} \left| \int_0^T \tau_w dt \right|}{\frac{1}{T} \int_0^T |\tau_w| dt} \right), \quad (7.3)$$

OSI is calculated based on the time and position dependent results of phase-averaged WSS during a cardiac cycle.

7.2.3 Results

A sample of PIV images of the stent A with the PMMA particles and the wall (highlighted in yellow) is shown in Figure 7.5. To detect the wall, an algorithm in which the wall is located at the position with a sharp change in the pixel intensity of the PIV images was implemented. Figure 7.5 also shows the position of stent struts on the wall.

Contour of mean stream-wise velocity during a cardiac cycle for stent A, as an example, is shown in Figure 7.6b. The contour is presented for half of the mid-cross-sectional plane illuminated by the laser sheet as shown in Figure 7.6a. The results clearly show that using the proposed method, the flow can be visualised without any blockage of the FOV. The highest velocity is about 0.22 m/s located at the centre of the artery. The velocity profile and its magnitude are almost the same for all stents, which meant that far away from the wall, the flow behaviour for all stents is similar. Therefore, the key parameter in distinguishing different stent behaviours is WSS which is related to the velocity gradients near the wall. Furthermore, Figure 7.6b shows the formed RZ near one of the stent struts.

Figure 7.6c shows the time dependent value of spatially-averaged WSS profile for the stent A, which follows the same shape as the inlet flow profile. The same trend is reported by Charonko et al. (2009). A similar pattern is also observed for the other three stents.

To calculate WSS for the different stents, an area of 5.5 mm × 1 mm in the region of interest was illuminated. The illuminated area was located as close as possible to the plane of symmetry of the stent. Figure 7.7 displays the distribution of the time-averaged WSS values over the streamwise direction for all stents. The values of WSS at the maximum and minimum velocity phases during a cardiac cycle (shown in Figure 7.4) are also shown in Figure 7.7. The results show that for all stents WSS is the highest at the phase with a maximum velocity, and the lowest at the phase with a minimum velocity during a cardiac cycle. The results in Figure 7.7 show that for each stent, the highest WSS occurs at the location of stent struts. WSS values on top of the struts, for all stents, are almost two or three times higher than the WSS values on the stent walls, as the first instance of the experiments reporting the WSS on top of the struts. For all stents, WSS values are very low at adjacent to the stent struts upstream and downstream

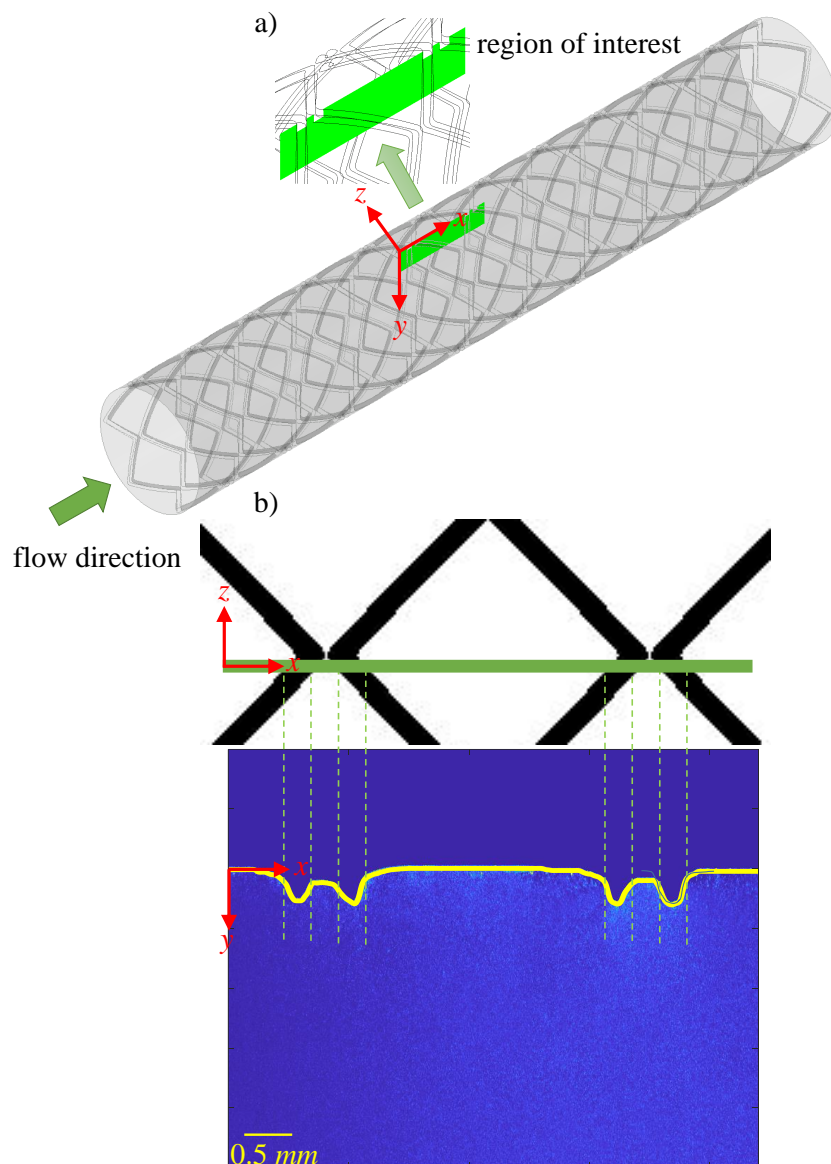


Figure 7.5: a) 3D view of the region of interest to calculate the WSS with the considered coordinate system and b) PIV light intensity image of the stent A with yellow solid line representing the wall boundary.

of them. The reason for a lower WSS upstream and downstream the stent struts is the formation of micro-recirculation zones at these locations, as discussed by Gijsen et al. (2019). The low WSS regions at immediate upstream and downstream of the struts, due to the formation of recirculation zones, are the regions with higher tendency for the atherosclerotic formation.

A comparison of phase- and spatially averaged WSS between different stents is displayed in Figure 7.8a. The maximum WSS per length is related to the stent D, while the lowest is related to the stent B for the selected regions of interest and for all two phases in a cardiac cycle. Furthermore, the spatially averaged WSSs over the locations on the struts and near the struts are displayed in Figure 7.8a. The results are presented as the spatial average of WSS over each segment (on the struts or between them) divided by their corresponding length. The highest value of WSS on the struts per their length is

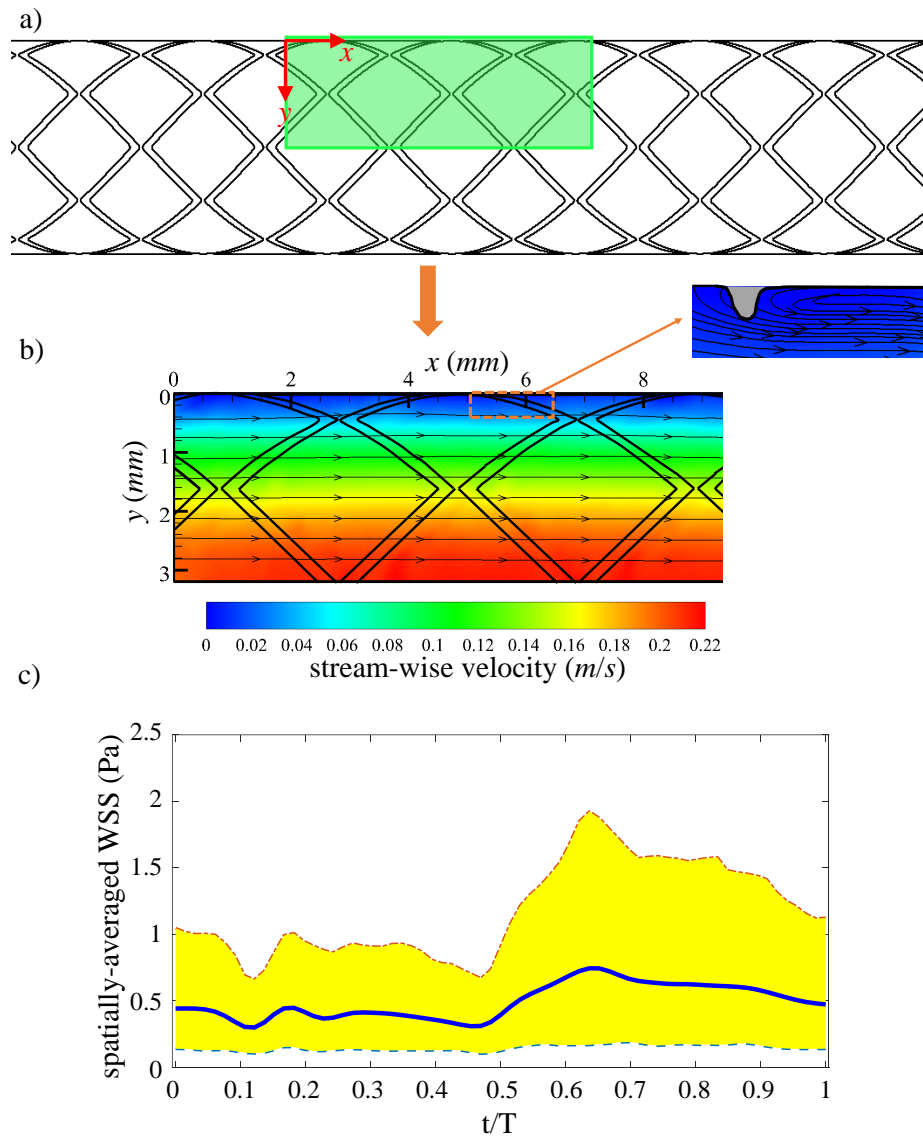


Figure 7.6: a) Area illuminated by the laser, b) contour of mean stream-wise velocity during a cardiac cycle for the stent A and c) time dependent value of spatially-averaged WSS for the stent A. The solid blue line shows the spatially-averaged WSS and the yellow area represents the variation of the spatially-averaged WSS with green and red dash lines referring to locally minimum and maximum values.

related to stent D, while stent B has the lowest WSS per length. A similar pattern is also observed for the value of WSS near the struts per length of the arterial wall. The highest value of WSS near the struts per their length is related stent D. Figure 7.8b presents the results of OSI for different stents. The highest OSI is for stent B, while the lowest is for stent C. The results show that there is an inverse correlation between the average WSS and OSI.

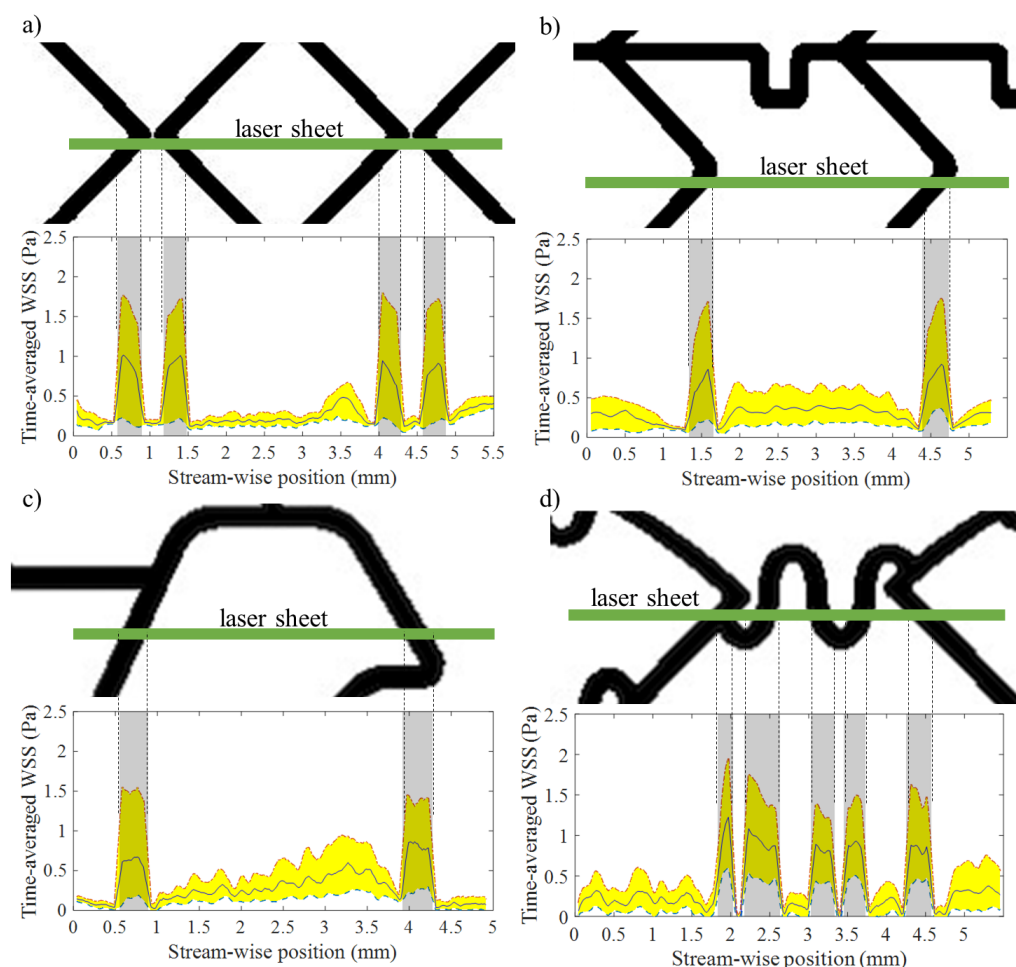


Figure 7.7: Spatial profile of the phase-averaged WSS values for different stents for the ROI shown by the laser sheet. The grey shaded areas are the location of stent struts. The green and red dash lines refer to minimum and maximum velocity phases during a cardiac cycle, respectively. The solid blue line shows the mean value of the time-averaged WSS and the yellow area covers the variation of the time-averaged WSS during a cardiac cycle.

7.2.4 Discussion

The stent models can be characterised based on their cross sections, strut thicknesses and depths, and the distance between two consecutive struts. The definition of strut thickness and depth is shown in Figure 1e. The ratio of the distance of two consecutive struts over the strut depth is an important parameter for the formation of RZs between the struts (Berry et al. 2000). The distance between two consecutive struts in the stents B and C is much larger than the strut depth. In stent A, there is a weak intrusion of the flow inside the gap between two neighbouring struts, as the ratio of the distance between two struts over the strut depth is small. The area between struts D can be categorised in two types. The first is where the distances between two struts is much larger than the strut depth. This is where the RZs formed at immediate after the first struts and faded before reaching the second strut. In another word, the flow reattaches after the first strut before reaching to the next strut. This is also happening for the stents B and C as well as the locations of stent A where there is a large distance between two consecutive struts.

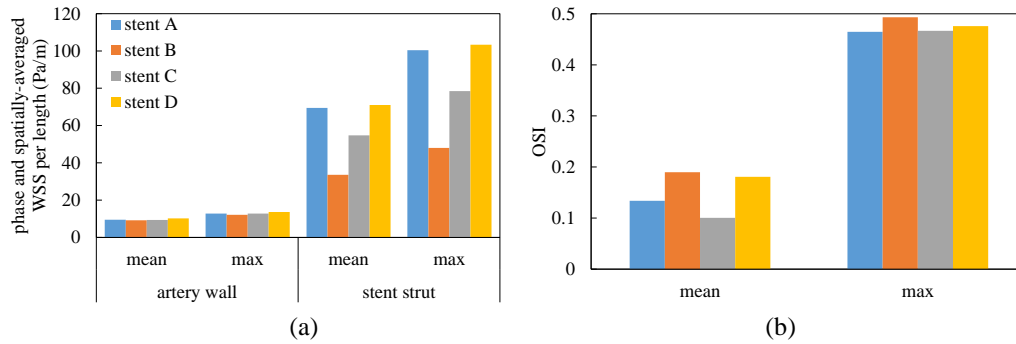


Figure 7.8: a) Effect of different types of stent on phase and spatially averaged WSS in two phases in a cardiac cycle. The WSS results for artery wall and stent struts are presented per length of the arterial wall and stent struts located in the region of interest. b) Effect of different types of stent on OSI for spatially mean and maximum values near the struts.

The second type of struts for stent D is near the wavy connectors of two stent patterns, where the distance between two consecutive struts is comparable with the strut depth. In these locations, the RZs cover the gap between two struts (Berry et al. 2000). The mean flow separates at the trailing edge of the first strut and reattaches at the leading edge of the downstream strut. In these locations, it is reported that a higher WSS at the crest of struts is observed compared to the previous type (Leonardi et al. 2007). Furthermore, increasing the number of consecutive struts results in decreasing viscous stress below the crest of roughness and enhanced viscous stress above the crest (MacDonald et al. 2016). As explained earlier, stent D has the highest portion of WSS on the struts per their length and also has the highest WSS on the artery wall near the struts per their corresponding length, for the selected regions of interest for different stents.

The results of this study are compared with those available in the literature, as shown in Table 7.2. The ranges of changes in the non-dimensional time-averaged WSS for the locations of the struts and between them are shown in Figure 7.9a. The comparison is conducted for the non-dimensional time-averaged WSS values due to the fact that even by maintaining the similarity using the Reynolds number and Womersley, WSS value can be different for different artery cases with different arterial diameters. In order to maintain similarity of the Reynolds number, increasing the artery diameter is compensated by decreasing fluid velocity. However, since the scale of WSS is a function of U/D , changing arterial diameter can change the calculated WSS values. Hence, the non-dimensional time-averaged WSS is calculated by dividing time-averaged WSS over $(\frac{1}{2})\rho U^2$, where U is mean bulk flow velocity. Furthermore, as a model scale of 2 : 1 was used in this study, the non-dimensional WSS values presented in this section can provide an evaluation of WSS values in full scale coronary arteries.

The obtained non-dimensional time-averaged WSS results in this study are in the same range of those available in the literature. A comparison between validation case 2 in Figure 7.9a and the results for stent B shows a good agreement with small discrepancies between the values of WSS between the struts. These differences can be attributed to, first, the difference in the inflow conditions and the Reynolds number, which resulted in slightly different values for the hemodynamic parameters such as WSS. Secondly, they used metal stents inserted inside the transparent artery resulting in the blockage of some

areas of the region of interest shadowed by the struts. This blockage did not allow them to determine WSS over some locations. They acknowledged the limitation and inaccuracy of the results when FOV is obstructed by the stents. Furthermore, the results of validation cases 4 and 5 showed higher values of non-dimensional time-averaged WSS compared to other studies. The reason is due to considerably lower Reynolds values in their study (Beier et al. 2016) compared to other studies. This can be explained as there is an inverse relationship between the Reynolds number and skin friction coefficient in laminar pipe flows. Therefore, the lower Reynolds number in the study of Beier et al. (2016) resulted in a higher skin friction coefficient or non-dimensional WSS.

Table 7.2: Different cases used for validation of the results. These cases are chosen from literature that have the closest matching parameters to the current experiment.

	artery diameter (mm)	mean Reynolds number	Womersley number	stent model	method	Ref
stent model 1	6.4	210	2.1	stent A	PIV	this study
stent model 2	6.4	210	2.1	stent B	PIV	this study
stent model 3	6.4	210	2.1	stent C	PIV	this study
stent model 4	6.4	210	2.1	stent D	PIV	this study
validation case 1	2.7	210	1.95	Absorb	FSI	Chiastra et al. (2014)
validation case 2	3	160	2.09	XIENCE	PIV	Charonko et al. (2009)
validation case 3	3	139	2.16	Absorb	CFD	Tarrahi et al. (2020)
validation case 4	4	80	3.1	Omega	CFD	Beier et al. (2016)
validation case 5	4	80	3.1	Biomatrix	CFD	Beier et al. (2016)

Figure 7.9b presents a comparison of the spatial distribution of non-dimensional time-averaged WSS adjacent to one stent strut between the current experiments with the results of the numerical simulation of a stent in the literature (Beier et al. 2016; Chiastra et al. 2014). The patterns of non-dimensional time-averaged WSS on the struts and between them found in this study and in the literature are similar. The differences in the non-dimensional time-averaged WSS are due to the differences in the stent specifications such as stent pattern, its thickness and the inflow conditions. However, the overall trend of calculated WSS in this study agrees with the available results. As discussed in the results section, the top of the stent struts experiences the higher values of WSS, while at the locations at immediate upstream and downstream of the struts, the lowest values of WSS are present, which is in agreement with the reported values in the literature.

7.2.5 Conclusions

This study, for the first time, introduced a novel technique to investigate WSS on the wall of the stented arteries experimentally using PIV without any obstructions from the stents. This study overcame the limitations of previous studies by providing reliable results at the location of stent struts. The developed technique can be applied for future studies related to experimental investigation of flow behaviour inside the stented arteries using flow visualisation techniques. The experimental limitation of the current measurement includes the low frequency of the laser and also the camera. This limits the number of image pairs in each cardiac cycle that can be collected. However, this limitation can be overcome by using a time-resolved PIV system. Another limitation of this study is

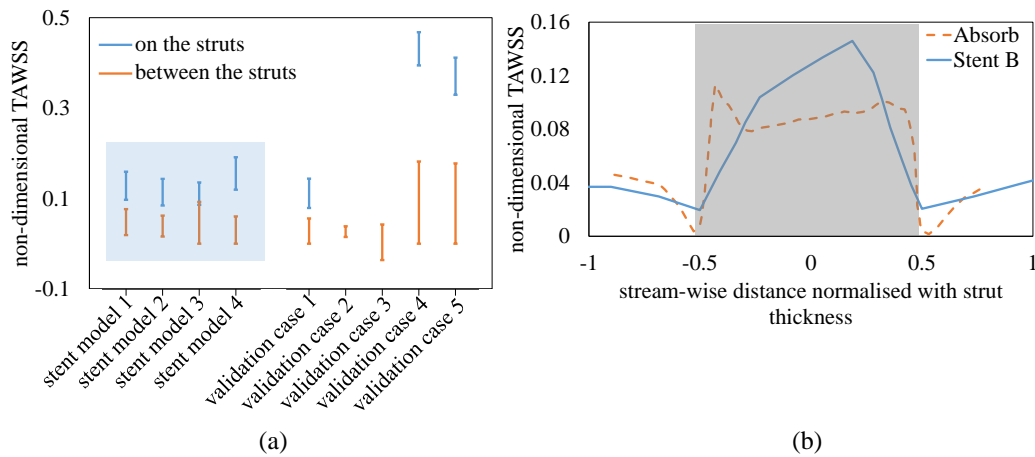


Figure 7.9: a) Variation of non-dimensional time-averaged WSS of different stent models studied in this study and the ones reported in the literature for the locations both on the struts and between the struts. The time-averaged WSS is non-dimensionalised using $(\frac{1}{2})\rho U^2$. Each bar represents the minimum and maximum ranges of the variations in non-dimensional time-averaged WSS on the strut and in the distance between them. Light blue shaded area shows the stents in this study. b) Comparison of non-dimensional time-averaged WSS in the zone adjacent to one stent strut of two stents including Absorb (Chiastra et al. 2014) and stent B from the current study. The grey shaded area is the location of stent struts. The horizontal axis shows the stream-wise distance normalised by the corresponding stent thickness to allow a comparison between the stents of different thickness.

related to the resolution limitation of the 3D printer used to print the stent rods. Since the struts' depth is about 200 microns, the resolution of the employed printer to print stent rods is of great importance for a perfect casting of the stented arteries. The above-discussed limitations were related to our currently available equipment. Accessing to extremely high-resolution 3D printers will help to improve the accuracy of the results; however, the proposed technique remains the same. Another limitation of this study is related to lack of interaction between the fluid mechanics and the solid mechanics of the vessel wall and stent strut which is a reasonable trade-off in many studies specifically those focusing on the visualising the flow behaviour inside the stented arteries. In future, in order to further advance the developed technique, these limitations can be overcome by using higher frequency laser and camera to conduct a time-resolved PIV measurement of the near wall flow of the stented arteries. Furthermore, the continuing improvement of 3D-printing technology will help to further increase the resolution of the cast models.

References

Beier S, Ormiston J, Webster M, Cater J, Norris S, Medrano-Gracia P, Young A, and Cowan B (2016). "Hemodynamics in idealized stented coronary arteries: important stent design considerations". *Annals of Biomedical Engineering* 44.2, pp. 315–329.

- Berry JL, Santamarina A, Moore JE, Roychowdhury S, and Routh WD (2000). “Experimental and computational flow evaluation of coronary stents”. *Annals of Biomedical Engineering* 28.4, pp. 386–398.
- Brindise MC, Chiastra C, Burzotta F, Migliavacca F, and Vlachos PP (2017). “Hemodynamics of stent implantation procedures in coronary bifurcations: An in vitro study”. *Annals of Biomedical Engineering* 45.3, pp. 542–553.
- Charonko J, Karri S, Schmieg J, Prabhu S, and Vlachos P (2009). “In vitro, time-resolved PIV comparison of the effect of stent design on wall shear stress”. *Annals of Biomedical Engineering* 37.7, pp. 1310–1321.
- Charonko JJ and Vlachos PP (2013). “Estimation of uncertainty bounds for individual particle image velocimetry measurements from cross-correlation peak ratio”. *Measurement Science and Technology* 24.6, p. 65301.
- Charonko J, Karri S, Schmieg J, Prabhu S, and Vlachos P (2010). “In vitro comparison of the effect of stent configuration on wall shear stress using time-resolved particle image velocimetry”. *Annals of Biomedical Engineering* 38.3, pp. 889–902.
- Chatzizisis YS, Jonas M, Coskun AU, Beigel R, Stone BV, Maynard C, Gerrity RG, Daley W, Rogers C, Edelman ER, Feldman CL, and Stone PH (2008). “Prediction of the localization of high-risk coronary atherosclerotic plaques on the basis of low endothelial shear stress: an intravascular ultrasound and histopathology natural history study”. *Circulation* 117.8, pp. 993–1002.
- Chatzizisis YS, Coskun AU, Jonas M, Edelman ER, Feldman CL, and Stone PH (2007). “Role of endothelial shear stress in the natural history of coronary atherosclerosis and vascular remodeling: molecular, cellular, and vascular behavior”. *Journal of the American College of Cardiology* 49.25, pp. 2379–2393.
- Chiastra C, Dubini G, and Migliavacca F (2020). “Chapter 11 - Hemodynamic perturbations due to the presence of stents”. *Biomechanics of Coronary Atherosclerotic Plaque*. Ed. by J Ohayon, G Finet, and RI Pettigrew. Vol. 4. Academic Press, pp. 257–278.
- Chiastra C, Migliavacca F, Martínez MÁ, and Malvè M (2014). “On the necessity of modelling fluid–structure interaction for stented coronary arteries”. *Journal of the Mechanical Behavior of Biomedical Materials* 34, pp. 217–230.
- Davies JE, Parker KH, Francis DP, Hughes AD, and Mayet J (2008). “What is the role of the aorta in directing coronary blood flow?” *Heart* 94.12, pp. 1545–1547.
- Dodge JT, Brown BG, Bolson EL, and Dodge HT (1992). “Lumen diameter of normal human coronary arteries. Influence of age, sex, anatomic variation, and left ventricular hypertrophy or dilation”. *Circulation* 86.1, pp. 232–246.
- Foin N, Lu S, Ng J, Bulluck H, Hausenloy DJ, Wong PE, Virmani R, and Joner M (2017). “Stent malapposition and the risk of stent thrombosis: mechanistic insights from an in vitro model”. *EuroIntervention* 13.9, e1096–e1098.
- Freidoonimehr N, Arjomandi M, Sedaghatizadeh N, Chin R, and Zander A (2020a). “Transitional turbulent flow in a stenosed coronary artery with a physiological pulsatile flow”. *International Journal for Numerical Methods in Biomedical Engineering* 36.7, e3347.
- Freidoonimehr N, Chin R, Zander A, and Arjomandi M (2020b). “An experimental model for pressure drop evaluation in a stenosed coronary artery”. *Physics of Fluids* 32.2, p. 21901.
- García Carrascal P, García García J, Sierra Pallares J, Castro Ruiz F, and Manuel Martín FJ (2018). “Benchmark for numerical models of stented coronary bifurcation flow”. *Journal of Biomechanical Engineering* 140.9.

- García García J, García Carrascal P, Castro Ruiz F, Manuel Martín F, and Fernández JA (2017). “Effects of bifurcation-specific and conventional stents on coronary bifurcation flow. An experimental and numerical study”. *Journal of Biomechanics* 54, pp. 64–72.
- Gijzen F, Katagiri Y, Barlis P, Bourantas C, Collet C, Coskun U, Daemen J, Dijkstra J, Edelman E, Evans P, Heiden K van der, Hose R, Koo BK, Krams R, Marsden A, Migliavacca F, Onuma Y, Ooi A, Poon E, Samady H, Stone P, Takahashi K, Tang D, Thondapu V, Tenekecioglu E, Timmins L, Torii R, Wentzel J, and Serruys P (2019). “Expert recommendations on the assessment of wall shear stress in human coronary arteries: existing methodologies, technical considerations, and clinical applications”. *European Heart Journal* 40.41, pp. 3421–3433.
- Jiménez JM and Davies PF (2009). “Hemodynamically driven stent strut design”. *Annals of Biomedical Engineering* 37.8, pp. 1483–1494.
- Johnston ID, McCluskey DK, Tan CKL, and Tracey MC (2014). “Mechanical characterization of bulk Sylgard 184 for microfluidics and microengineering”. *Journal of Micromechanics and Microengineering* 24.3, p. 035017.
- Kastrati A, Mehilli J, Dirschinger J, Pache J, Ulm K, Schühlen H, Seyfarth M, Schmitt C, Blasini R, Neumann FJ, and Schömig A (2001a). “Restenosis after coronary placement of various stent types”. *The American Journal of Cardiology* 87.1, pp. 34–39.
- Kastrati A, Mehilli J, Dirschinger J, Dotzer F, Schühlen H, Neumann FJ, Fleckenstein M, Pfafferoth C, Seyfarth M, and Schömig A (2001b). “Intracoronary stenting and angiographic results”. *Circulation* 103.23, pp. 2816–2821.
- Koskinas KC, Chatzizisis YS, Antoniadis AP, and Giannoglou GD (2012). “Role of endothelial shear stress in stent restenosis and thrombosis”. *Pathophysiologic Mechanisms and Implications for Clinical Translation* 59.15, pp. 1337–1349.
- Ku DN (1997). “Blood Flow in Arteries”. 29.1, pp. 399–434.
- Lee SW and Lee SS (2007). “Shrinkage ratio of PDMS and its alignment method for the wafer level process”. *Microsystem Technologies* 14.2, pp. 205–208.
- Leonardi S, Orlandi P, and Antonia RA (2007). “Properties of d- and k-type roughness in a turbulent channel flow”. *Physics of Fluids* 19.12, p. 125101.
- MacDonald M, Chan L, Chung D, Hutchins N, and Ooi A (2016). “Turbulent flow over transitionally rough surfaces with varying roughness densities”. *Journal of Fluid Mechanics* 804, pp. 130–161.
- McKittrick CM, Cardona MJ, Black RA, and McCormick C (2020). “Development of a Bioactive Polymeric Drug Eluting Coronary Stent Coating Using Electrospraying”. *Annals of Biomedical Engineering* 48.1, pp. 271–281.
- Mejia J, Ruzzeh B, Mongrain R, Leask R, and Bertrand OF (2009). “Evaluation of the effect of stent strut profile on shear stress distribution using statistical moments”. *BioMedical Engineering OnLine* 8.1, p. 8.
- Müller A, Wapler MC, and Wallrabe U (2019). “A quick and accurate method to determine the Poisson's ratio and the coefficient of thermal expansion of PDMS”. *Soft Matter* 15.4, pp. 779–784.
- Morlacchi S, Keller B, Arcangeli P, Balzan M, Migliavacca F, Dubini G, Gunn J, Arnold N, Narracott A, Evans D, and Lawford P (2011). “Hemodynamics and in-stent restenosis: micro-CT images, histology, and computer simulations”. *Annals of Biomedical Engineering* 39.10, p. 2615.
- Natarajan S and Mokhtarzadeh-Dehghan MR (2000). “A numerical and experimental study of periodic flow in a model of a corrugated vessel with application to stented arteries”. *Medical Engineering & Physics* 22.8, pp. 555–566.

- Ng J, Bourantas CV, Torii R, Ang HY, Tenekecioglu E, Serruys PW, and Foin N (2017). “Local hemodynamic forces after stenting: implications on restenosis and thrombosis”. *Arteriosclerosis, Thrombosis, and Vascular Biology* 37.12, pp. 2231–2242.
- Nichols W, O’Rourke M, and Vlachopoulos C (2011). *McDonald’s blood flow in arteries, Sixth edition: Theoretical, experimental and clinical principles*. CRC Press.
- Pache J, Kastrati A, Mehilli J, Schühlen H, Dotzer F, Hausleiter J, Fleckenstein M, Neumann FJ, Sattelberger U, Schmitt C, Müller M, Dirschinger J, and Schömig A (2003). “Intracoronary stenting and angiographic results: strut thickness effect on restenosis outcome (ISAR-STEREO-2) trial”. *Journal of the American College of Cardiology* 41.8, pp. 1283–1288.
- Pinto SIS, Romano E, António CC, Sousa LC, and Castro CF (2020). “The impact of non-linear viscoelastic property of blood in right coronary arteries hemodynamics — A numerical implementation”. *International Journal of Non-Linear Mechanics* 123, p. 103477.
- Raben JS, Morlacchi S, Burzotta F, Migliavacca F, and Vlachos PP (2015). “Local blood flow patterns in stented coronary bifurcations: an experimental and numerical study”. *Journal of Applied Biomaterials & Functional Materials* 13.2, pp. 116–126.
- Tarrahi I, Colombo M, Hartman EMJ, Forero MNT, Torii R, Chiastra C, Daemen J, and Gijzen FJH (2020). “Impact of bioresorbable scaffold design characteristics on local hemodynamic forces - an ex vivo assessment with computational fluid dynamics simulations”. *EuroIntervention* 16.11, e930–e937.
- William Thielicke EJS (2014). “PIVlab – towards user-friendly, affordable and accurate digital particle image velocimetry in MATLAB”. *Journal of Open Research Software* 2.1, e30.

7.3 Computational modelling of the stented arteries

This section consists of the following conference paper:

Navid Freidoonimehr, Maziar Arjomandi, Anthony Zander, Rey Chin (2020). “Hemodynamics of stented coronary arteries: Experimental and numerical investigations”. *22nd Australasian Fluid Mechanics Conference*, Brisbane, Australia.

The article is identical to its published format with the following exceptions:

- The numbering of figures, tables and equations have been altered to include the chapter number.
- The position of some figures and tables have been changed to improve legibility.

The article in its published format is available at the proceedings of the 22nd Australasian Fluid Mechanics Conference at:

<https://doi.org/10.14264/b68207f>

Statement of Authorship

Title of paper	Hemodynamics of stented coronary arteries: Experimental and numerical investigations
Publication Status	<input checked="" type="checkbox"/> Published <input type="checkbox"/> Accepted for Publication <input type="checkbox"/> Submitted for Publication <input type="checkbox"/> Unpublished and Unsubmitted work written in manuscript style
Publication Details	Freidoonimehr, N., Arjomandi, M., Zander, A., and Chin, R., 2020, "Hemodynamics of stented coronary arteries: Experimental and numerical investigations", 22nd Australasian Fluid Mechanics Conference AFMC2020, Brisbane, Australia

Principal Author

Name of Principal Author (Candidate)	Navid Freidoonimehr		
Contribution to the Paper	Developed ideas, conducted experiments, performed data analysis and interpreted results, wrote manuscript, and acted as corresponding author		
Overall percentage (%)	75%		
Certification:	This paper reports on original research I conducted during the period of my Higher Degree by Research candidature and is not subject to any obligations or contractual agreements with a third party that would constrain its inclusion in this thesis. I am the primary author of this paper.		
Signature		Date	15/02/2021

Co-Author Contributions

By signing the Statement of Authorship, each author certifies that:

- i the candidate's stated contribution to the publications is accurate (as detailed above);
- ii permission is granted for the candidate to include the publication in the thesis; and
- iii the sum of all co-author contributions is equal to 100% less the candidate's stated contribution

Name of Co-Author	Maziar Arjomandi		
Contribution to the Paper	Supervised the development of the research, participated in developing ideas and concepts, helped in interpretation of results, provided critical revision of manuscript.		
Signature		Date	15/02/2021

~

Name of Co-Author	Anthony Zander		
Contribution to the Paper	Supervised the development of the research, participated in developing ideas and concepts, helped in interpretation of results, provided critical revision of manuscript.		
Signature		Date	15/02/2021

Name of Co-Author	Rey Chin		
Contribution to the Paper	Supervised the development of the research, participated in developing ideas and concepts, helped in interpretation of results, provided critical revision of manuscript.		
Signature		Date	15/02/2021

Hemodynamics of stented coronary arteries: Experimental and numerical investigations

Navid Freidoonimehr, Maziar Arjomandi, Anthony Zander, and Rey Chin

Abstract

Low wall shear stress inside the stented arteries results in endothelial cell changes and increases the chance of restenosis. Understanding the effects of a stent design on the flow behaviour especially near the artery wall can lead to choosing or designing more hemodynamically compatible stents that can reduce the chances of in-stent restenosis inside the stented arteries. In this study, the effect of the stent pattern on the wall shear stress of a coronary artery is investigated for four models of stents to identify the locations of low wall shear stress. A computational fluid dynamics model, validated against the particle image velocimetry experiments, is developed to calculate flow field and wall shear stress distribution inside the stented arteries. The developed computational model is able to capture micro-recirculation zones adjacent to the stent struts. The results showed that wall shear stress is strongly dependent on the design of the stent.

Keywords: coronary artery; stent; hemodynamics; wall shear stress; computational fluid dynamics; particle image velocimetry

7.3.1 Introduction

Coronary stent implantation, as a minimally invasive alternative for Coronary Artery Bypass Grafting (CABG) surgery, is one of the most common treatments for Coronary Artery Disease (CAD). Although there are several benefits of stenting over the CABG surgery such as lower risks of complications and much shorter recovery period, stenting can result in in-stent restenosis (ISR), as the major drawback of coronary stent placement in patients with CAD (Kastrati et al. 2001). It has been shown that there is a direct link between the stent type, patient outcome, ISR, thrombosis, and WSS (Charonko et al. 2009). The locations with a lower wall shear stress (WSS) especially adjacent to the stent struts are possible locations for the formation of ISR (Beier et al. 2016). Therefore, the possibilities of ISR could be better understood by investigating WSS distribution for different commercial stent designs available in the market. Understanding the flow behaviour inside the stented arteries can lead to the identification of low WSS locations around the struts, which can help to reduce the possibilities of ISR by improving the design of stents that will finally lead to better patient outcome.

In-vitro experimental and numerical studies of stented arteries have been conducted in the literature to better understand the WSS of the stented arteries with the aim to identify the causes of ISR. In an experimental study by Natarajan and Mokhtarzadeh-Dehghan (2000), the effect of the presence of a stent on the blood flow behaviour was investigated. Their results showed that the time-averaged WSS predicted around the top of the struts was 2-3 times greater than that found in the equivalent normal artery.

Furthermore, Benard et al. (2003) showed that the strong recirculation zones after the struts were associated with a high risk of restenosis. In another study, Charonko et al. (2009) reported that the stent struts along the artery wall disturb the nearby flow, making it more receptive to changes in direction and suppressing the peak WSS experienced. The results of experimental studies especially those focusing on the flow visualisation of the stented arteries in the literature, so far, were limited due to the use of metallic or non-metallic stents, which partially obscured the field of view (FOV) (Charonko et al. 2009; Charonko et al. 2010).

The aim of this study is to investigate the hemodynamics and WSS of four models of stents. The developed computational model is validated against the particle image velocimetry (PIV) results obtained for the models of different stented arteries. A novel experimental technique, recently developed by the authors (Freidoonimehr et al. 2021), is employed to perform flow visualisation inside a stented artery using transparent casting of stented arteries to eliminate the problem of blockage of the region of interest (ROI) due to presence of the metallic stent struts. The WSS distribution of four models is also compared for locations on the stent struts and adjacent to them.

7.3.2 Methodology

Experimental test setup

The experimental test setup was similar to Freidoonimehr et al. (2020b), as shown in Fig. 7.10, and consisted of a programmable centrifugal pump and a pump controller, an electromagnetic flowmeter, a 3D-printed settling chamber, a water reservoir, a DAQ card, and the PIV experimental facility. The pulsatile waveform, representing the blood flow inside a coronary artery, is shown in Fig. 7.11 (Davies et al. 2008), created by the centrifugal pump. The input voltage of the pump was governing by a data acquisition card to simulate the physiological pulsatile velocity waveform. A mixture of distilled water and glycerine (with the weight mixture percentage of 60% and 40%, respectively) was used as a working fluid to match the blood viscosity with the viscosity of 3.67 mPa.s and to match the refractive index of the silicone artery models.

In the PIV experiment, Zyla sCMOS camera along with a zoom lens with a 6X magnification was employed to focus closely to the near wall region. An EverGreen 532 nm laser with 200 mJ at a fixed pulsing frequency of 15 Hz was used to illuminate the FOV. A plano-convex lens and an adjustable optical slit were located between the laser head and the artery model, respectively, to set the laser sheet thickness at 0.5 mm to minimise the out-of-plane loss of particle pairs. Poly (methyl methacrylate) (PMMA) seeding particles were employed in this study to focus on the near wall region to calculate WSS within the stented artery models. The particles have the mean diameter of $6 \mu\text{m}$, density of 1.19 gr/cm^3 and the refractive index of 1.49. Images were captured with an array of 2200×400 pixels. The FOV near the wall was set to $5.5 \text{ mm} \times 1 \text{ mm}$, resulting in a pixel size of $2.5 \mu\text{m}$. The interrogation window size was set to 32×32 pixels with 75% overlap, resulting in a spatial resolution of 0.02 mm in each direction. Due to the limited pulsation frequency of the laser (15 Hz) and the duration of the cardiac cycle (4.4 s), 66 image pairs (16 bit) were recorded for each cardiac cycle. The time was off-set between two images in a pair (dt) by 70 microseconds. The images were recorded for

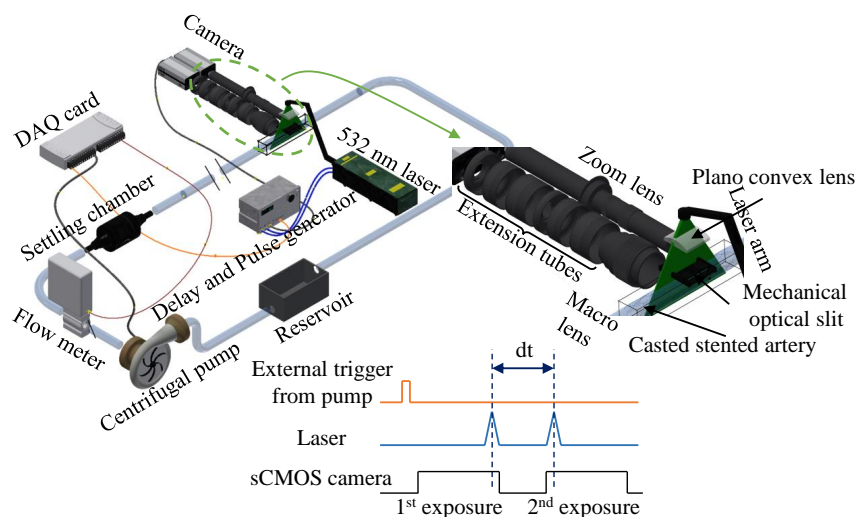


Figure 7.10: Schematics of the coronary artery test rig.

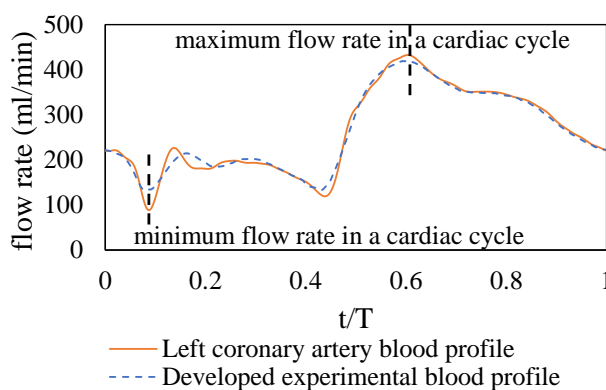


Figure 7.11: The physiological pulsatile left coronary artery blood flow profile (Davies et al. 2008) and the developed experimental blood flow profile.

100 consecutive pulsation cycles (6600 image pairs). From the resulting images and after conducting phase-averaging technique, velocity components were identified as a function of time in a cardiac cycle and position of the region of interest. WSS was defined based on the velocity gradient of the closest interrogation windows near the wall by multiplying the dynamic viscosity (μ) and the component of the fluid strain rate tensor oriented tangential to the wall. The estimation showed that the $y^+ = 1$ value for different flow velocities in a cardiac cycle changes from 50 microns to 200 microns from the wall. The estimation was made based on the empirical equation for the calculation of skin friction coefficient as a function of Reynolds number for internal flow. The estimated skin friction coefficient was used to calculate frictional velocity and hence, using the friction velocity the first cell height value corresponding to the $y^+ = 1$ was calculated. The first velocity vector obtained from PIV was located 40 microns from the wall with an increment of 20 microns for consecutive velocity vectors. Since the bulk Reynolds number in the viscous sub-layer ($y^+ < 5$) is low, u^+ changes linearly with y^+ . In this region, we captured at least 11 velocity vectors for the highest velocity in a cardiac cycle. For the calculation of WSS, however, the first two velocity vectors normal to the wall were considered. The frame rate of the camera was set at the required frequency of the laser. To synchronise the pulsation of the pump, laser pulses and camera, a LabVIEW code was used. This

code sends a signal to the pulse generator as soon as the pump starts working from a specified instance during a cardiac cycle. The signal is used as an external trigger to start the laser pulses and camera shots. This process is schematically shown in Fig. 7.10.

Computational modelling

Four models of stents, shown in Fig. 7.12, are designed using the geometrical data presented in Charonko et al. (2009). The inside diameter of the model, D , is 6.4 mm corresponding to almost double the diameter of coronary arteries. The reason that the model was designed at a larger diameter than a real coronary artery was to allow for comparison of the results with the PIV measurements which helped reduce the measurement errors compared to when a smaller diameter was used. Figure 7.13 shows the schematics of stented artery covered with stent C with the stream-wise, z , and angular, θ , coordinate system. To eliminate the artificial effects of the inlet and the outlet on the ROI, the artery length was extended from both sides (a 3- D length before and a 1- D after the stented region). The computational modelling procedures were similar to Freidoonimehr et al. (2020a). A time step size of 5×10^{-5} s was selected such that the Courant number is less than unity. The chosen time scale results in 88,000 time steps per cardiac cycle. The simulations were carried out for two cardiac cycles and the results were presented for the second cardiac cycle. Fine mesh elements specially near the struts, as shown in Fig. 7.14, were employed to make sure that the micro-recirculations adjacent to the struts are captured. For different stents, 9 to 10 million mesh elements were used.

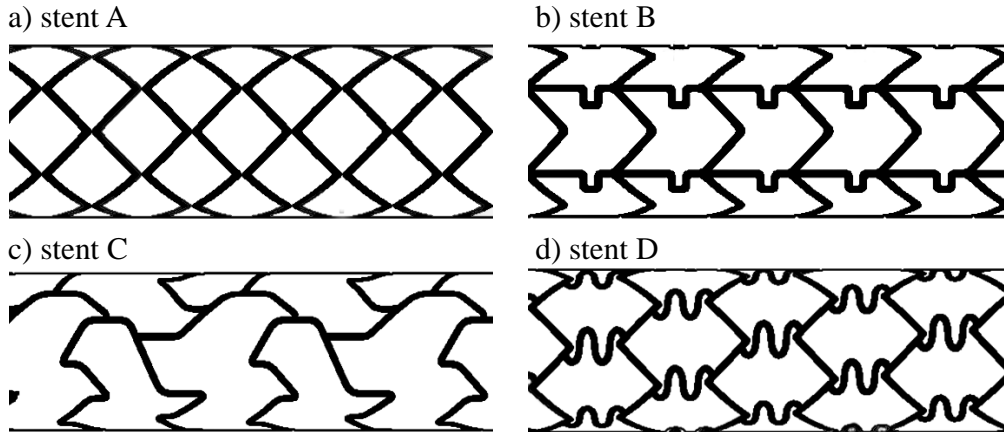


Figure 7.12: Four models of the stents employed in this study.

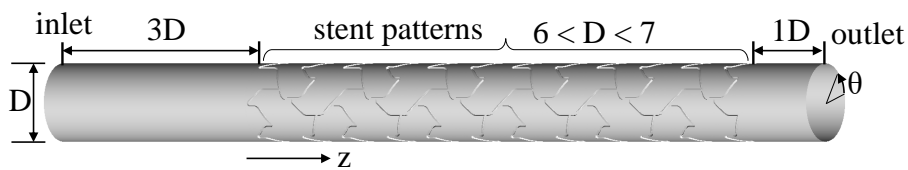


Figure 7.13: Schematic of the stented artery covered with stent C showing the dimensions and the coordinate system.

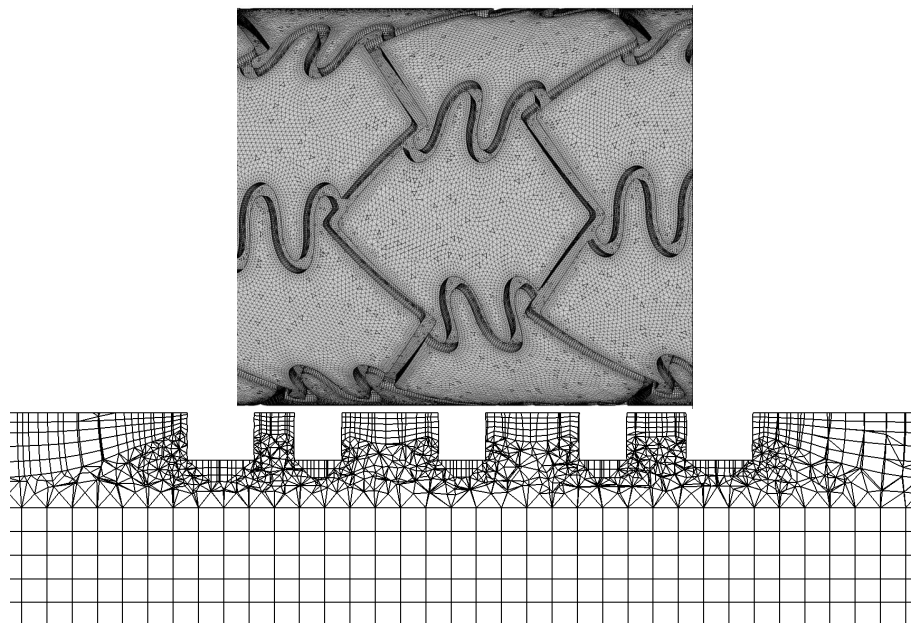


Figure 7.14: A close-up view of the mesh structures for the stent D with a zoom view of the mesh near the stent struts.

7.3.3 Results

The results of the developed computational model were validated with those from PIV. Figure 7.15 shows the time-averaged WSS along the stream-wise direction for the ROI located near the mid-section of the stented artery in stream-wise direction for the stent B for the phase with maximum velocity in a cardiac cycle. The results of CFD and PIV demonstrate that the developed CFD model is well correlated with the PIV results. It is also shown that the values of WSS on the stent struts are higher compared to the adjacent values on the artery wall which agrees with the findings of Natarajan and Mokhtarzadeh-Dehghan (2000) who reported that the values of WSS on top of the struts are about 2-3 times higher than the adjacent values. Furthermore, there are locations with low values of WSS immediately proximal and distal to the struts which are related to the formation of micro-recirculation zones (as also shown in Fig. 7.16) which was also reported by Gijssen et al. (2019). Blood flow around the stent struts creates small vortices which are of different strengths depending on depth and thickness of the struts. The vortices are stronger downstream the stent struts compared to their immediate upstream, which results in formation of stronger micro-recirculation zones downstream. WSS is created by the viscous friction effect due to the frictional forces acting on the flow as it goes through the artery. WSS at the location of the stent struts is considerably higher than the other regions of the artery wall. The reason is because the flow on the struts is characterised by an accelerated flow region that is leading to a high WSS on the abluminal strut surface.

Figure 7.16 shows the stream-wise velocity contour and streamlines on the mid-cross-sectional plane for the stent C as well as the zoomed views of the streamlines near the stent struts for different stents. In the chosen ROI for stents B and C, the only strut in the ROI blocks the flow and hence creates micro-recirculation zones before and after the strut. It is shown that the recirculation zone distal the strut is larger than the one proximal to it. This was also found by Gijssen et al. (2019). As mentioned previously,

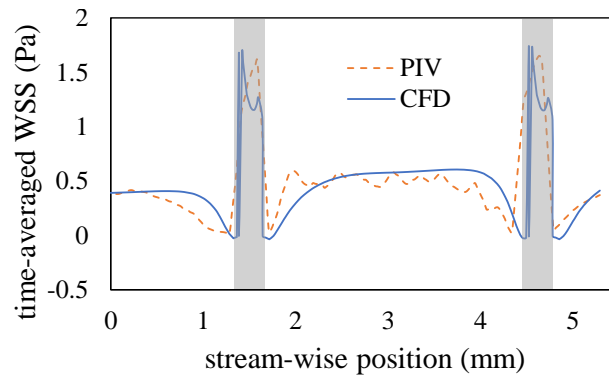


Figure 7.15: A comparison between the CFD and PIV results of the spatial profile of the phase-averaged WSS for the stent B for the phase with maximum velocity in a cardiac cycle. The grey shaded area shows the location of stent struts.

these micro-recirculation zones are susceptible locations for the formation of the ISR. Moreover, in stent A, there is a weak intrusion of the flow inside the gap between two neighbouring struts and hence there is not enough space to form the micro-recirculation zones. However, the micro-recirculation zones are observed before and after the neighbouring struts. Moreover, it is shown that the stent D has the highest number of struts in the ROI. This results in trapping flow between the neighbouring struts and hence the formation of recirculation zones there. The struts can be interpreted as roughness elements based on their depths and thicknesses. In the context of stented arteries, roughness elements are stent struts and hence the height of the elements is the depth of the struts. All the recirculation zones for different stents, shown in Fig. 7.16, can be further discussed based on the ratio of the distance between two consecutive roughness elements and their height (MacDonald et al. 2016). Therefore, the stent pattern, interpreted as the roughness elements, is an important parameter in the WSS comparison of different stents.

Figure 7.17 shows the contour plot of WSS on the artery wall for the phases with minimum and maximum velocity (refer to Fig. 7.11) during a cardiac cycle for stent C and maximum velocity phase for the other stents. The results show that the WSS is higher for the maximum velocity phase compared to the minimum one. The highest value of WSS for all the four stent types exists on the struts. The WSS near the struts has the lowest value which is due to the formation of micro recirculation zones. The WSS values recover in the area between to struts.

A comparison of the spatially-averaged WSS for different stent models in the phase with maximum flow rate in a cardiac cycle is presented in Fig. 7.18. The comparison is made for a random stream-wise line for all the stents. The results show that the maximum total WSS is related to the stent D, while the lowest is related to the stent B. On the other hand, the highest value of WSS on the struts is related to the stent D, while stents B and C have the lowest values. In contrast, the highest value of WSS adjacent to the struts were related to the stents B and C. Hence, the stent, in which smaller regions of low WSS adjacent to the struts are created, will result in lower chances of ISR. These comparisons guide the engineers to improve the stent design.

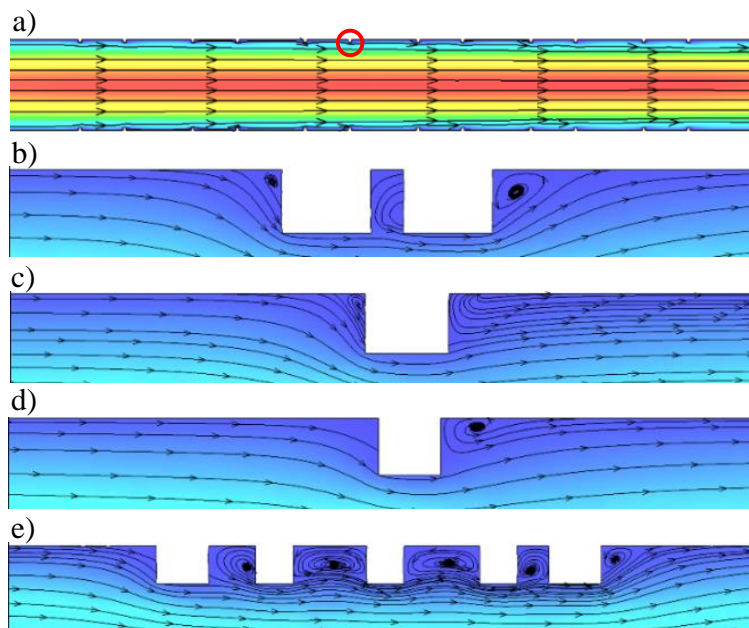


Figure 7.16: a) The stream-wise velocity contour and streamline of mid-cross-sectional plane for the stent C and near the stent struts micro-recirculation structures of b) stent A, c) stent B, d) stent C, and e) stent D for the phase with maximum velocity during a cardiac cycle.

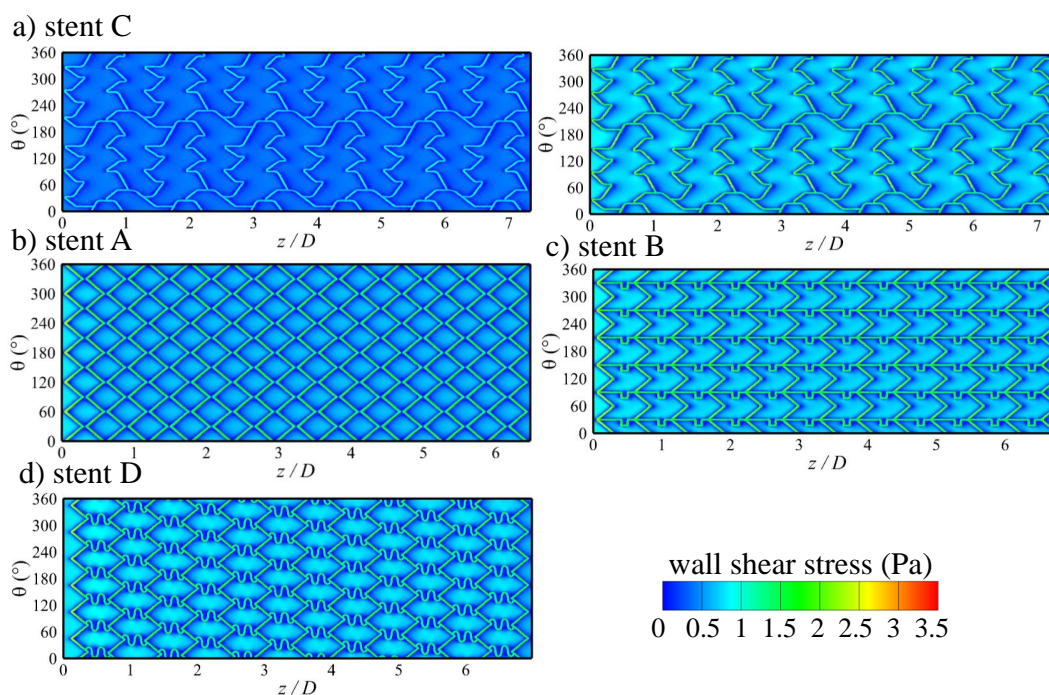


Figure 7.17: Unwrapped contour plots of WSS for a) two phases of minimum (top) and maximum (bottom) velocities during a cardiac cycle for stent B, and b-d) a phase with maximum velocity in a cardiac cycle for the other stents. The horizontal axis shows the stream-wise direction, normalised by the artery diameter. The vertical axis shows the angular direction.

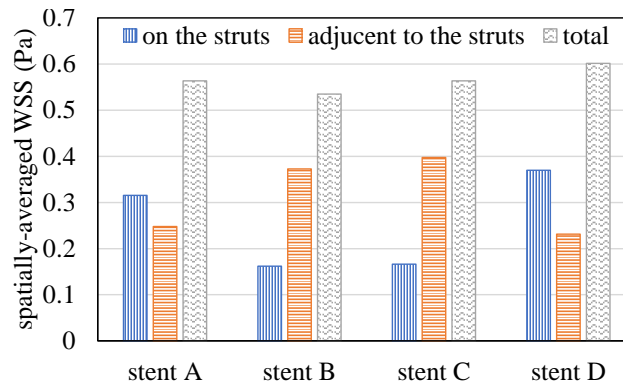


Figure 7.18: A comparison of the spatially-averaged WSS for different stent models in the phase with maximum flow rate in a cardiac cycle. The comparison includes the values of spatially-averaged WSS on the location of stent struts, adjacent to them as well as the total values.

7.3.4 Conclusion

This study investigated the flow and WSS distributions inside the four models of the stents computationally. The computational model was validated against PIV. The results showed that the highest WSS was related to the stent D, while the lowest one was for the stent B. Furthermore, the highest spatially averaged WSS for locations on the stent struts was related to the stent D with the second highest to stent A struts. Moreover, the spatially averaged value of WSS over the locations near the struts had the highest values for both stents B and C. Stent D pattern owned the highest WSS portion on the struts and simultaneously owned the lowest WSS on the artery walls near the struts, for the studied ROI for different stents. For all the stents, micro-recirculation zones were formed in the immediate upstream and downstream of the struts with stronger values downstream of the struts. The present study has shown that the type of stent patterns is of significance especially in the investigation of WSS distribution. Identification of the stent patterns which create smaller regions of low WSS adjacent to the struts will finally result in better patient outcome.

Acknowledgement

Financial support for the project has been provided by the Australian Government Research Training Program Scholarship. The authors would like to thank the workshops of the School of Mechanical Engineering at The University of Adelaide. This work was supported with supercomputing resources provided by the Phoenix HPC service at the University of Adelaide.

References

- Beier S, Ormiston J, Webster M, Cater J, Norris S, Medrano-Gracia P, Young A, and Cowan B (2016). "Hemodynamics in idealized stented coronary arteries: important stent design considerations". *Annals of Biomedical Engineering* 44.2, pp. 315–329.

- Benard N, Coisne D, Donal E, and Perrault R (2003). “Experimental study of laminar blood flow through an artery treated by a stent implantation: characterisation of intra-stent wall shear stress”. *Journal of Biomechanics* 36.7, pp. 991–998.
- Charonko J, Karri S, Schmieg J, Prabhu S, and Vlachos P (2009). “In vitro, time-resolved PIV comparison of the effect of stent design on wall shear stress”. *Annals of Biomedical Engineering* 37.7, pp. 1310–1321.
- Charonko J, Karri S, Schmieg J, Prabhu S, and Vlachos P (2010). “In vitro comparison of the effect of stent configuration on wall shear stress using time-resolved particle image velocimetry”. *Annals of Biomedical Engineering* 38.3, pp. 889–902.
- Davies JE, Parker KH, Francis DP, Hughes AD, and Mayet J (2008). “What is the role of the aorta in directing coronary blood flow?” *Heart* 94.12, pp. 1545–1547.
- Freidoonimehr N, Arjomandi M, Sedaghatizadeh N, Chin R, and Zander A (2020a). “Transitional turbulent flow in a stenosed coronary artery with a physiological pulsatile flow”. *International Journal for Numerical Methods in Biomedical Engineering* 36.7, e3347.
- Freidoonimehr N, Arjomandi M, Zander A, and Chin R (2021). “A novel technique towards investigating wall shear stress within the stent struts using particle image velocimetry”. *Experiments in Fluids* 62.6, p. 133.
- Freidoonimehr N, Chin R, Zander A, and Arjomandi M (2020b). “An experimental model for pressure drop evaluation in a stenosed coronary artery”. *Physics of Fluids* 32.2, p. 21901.
- Gijsen F, Katagiri Y, Barlis P, Bourantas C, Collet C, Coskun U, Daemen J, Dijkstra J, Edelman E, Evans P, Heiden K van der, Hose R, Koo BK, Krams R, Marsden A, Migliavacca F, Onuma Y, Ooi A, Poon E, Samady H, Stone P, Takahashi K, Tang D, Thondapu V, Tenekecioglu E, Timmins L, Torii R, Wentzel J, and Serruys P (2019). “Expert recommendations on the assessment of wall shear stress in human coronary arteries: existing methodologies, technical considerations, and clinical applications”. *European Heart Journal* 40.41, pp. 3421–3433.
- Kastrati A, Mehilli J, Dirschinger J, Pache J, Ulm K, Schühlen H, Seyfarth M, Schmitt C, Blasini R, Neumann FJ, and Schömig A (2001). “Restenosis after coronary placement of various stent types”. *The American Journal of Cardiology* 87.1, pp. 34–39.
- MacDonald M, Chan L, Chung D, Hutchins N, and Ooi A (2016). “Turbulent flow over transitionally rough surfaces with varying roughness densities”. *Journal of Fluid Mechanics* 804, pp. 130–161.
- Natarajan S and Mokhtarzadeh-Dehghan MR (2000). “A numerical and experimental study of periodic flow in a model of a corrugated vessel with application to stented arteries”. *Medical Engineering & Physics* 22.8, pp. 555–566.

Chapter 8

Conclusions and future work

The flow behaviour inside the stenosed and stented coronary arteries was investigated in this thesis. This study commenced with investigation of the necessity of modelling the temporal variations of coronary arteries for study of the hemodynamics through an extensive literature review. A computational model validated against the experimental data was developed to investigate the transitional flow behaviour inside stenosed coronary arteries with different shapes, degrees of stenosis, and heart working conditions. Comprehensive experimental investigations were conducted for a wide range of degrees and shapes of stenosis to develop a mathematical model based on the experimental coefficients for evaluation of the pressure drop inside straight and/or curved coronary artery models. Furthermore, a novel technique was developed to visualise the flow inside stented coronary arteries using particle image velocimetry (PIV) without blocking the field of view. The PIV results along with the validated computational fluid dynamics (CFD) model of the stented artery provide important findings on the effect of the stent design on the wall shear stress (WSS) distribution. In the following sections, the main outcomes and achievements of the research with respect to the defined objectives presented in Chapter 1 are outlined. The chapter concludes with a discussion of recommendations for future work.

8.1 Investigation of the post-stenotic transition to turbulence inside stenosed coronary arteries

Investigation of the transition to turbulence inside stenosed coronary arteries is of great importance, as the production, or dissipation of turbulence or the interaction between them after the stenotic sections determines the mechanical energy loss or pressure drop. The resultant pressure drop which is affected by the turbulence across the stenosis is used as a clinical measure to diagnose the severity of stenosis. The effect of degree of stenosis and heart working conditions on the transitional flow behaviour was investigated in Chapter 4.

A computational model, validated against experimental data published in the literature, was developed to simulate the pulsatile blood flow inside a stenosed coronary artery with an asymmetric shape and different degrees of stenosis (mild, moderate, and severe

cases) and heart working condition (rest to hyperemic conditions). The transitional flow behaviour was qualitatively demonstrated by plotting instantaneous coherent structures identified by the λ_2 criterion and was quantified by investigation of the changes in the turbulence kinetic energy (TKE). The transitional flow behaviour is indicated by a jump in the level of TKE. Further downstream of the stenotic section, where the eddies break up, the flow relaminarises, and consequently, the energy of the eddies decays. The reported jump in the TKE starts from $5D$ downstream of the stenotic section (where D is the artery diameter), where the jet flow starts to break down and becomes less distinct, and continues to about $10D$, where the flow inside the arteries starts to relaminarise. It was also found that the location of the TKE jump is a function of the degree of stenosis and the heart working condition. The TKE peak location moves closer to the stenotic section for higher degrees of stenosis and for the hyperemic heart working condition. Furthermore, it was shown that there are some regions with low WSS downstream of the stenotic section which can result in the formation of a secondary stenosis. These regions with low WSS mainly occur due to the flow recirculation after the stenotic section resulting in a change in the direction of the WSS and hence exposing the artery wall to a region of low WSS. The regions which are most susceptible to the formation of a second stenosis are located downstream at the opposite side to the first stenosis. Moreover, it was shown that for severe stenosis (with a degree of stenosis of 67%), there was no separation downstream of the stenosis for resting to moderate heart working conditions. Hence, it is suggested that one way to have a medically stable condition for a patient suffering from a high level of atherosclerosis is to prevent them from hyperaemia. Finally, a patient-specific stenosed coronary artery model was employed to illustrate the applicability of the obtained results for realistic geometry models. Peaks in the WSS distribution and the area-weighted average TKE were observed at the location of stenosis and distal to it, respectively, in the patient specific coronary artery model, which was similar to the behaviour observed for an idealised geometry.

8.2 Establishment of a link between variations in the shape of stenosis and the downstream blood flow behaviour

Building upon the knowledge developed in Chapter 4, in Chapter 5 the effect of the shape of the stenosis on the transitional flow behaviour was investigated for a stenosed coronary artery model with a constant degree of stenosis. As discussed in Section 2.2.2, the degree of stenosis is not the only indicator of the severity of coronary artery diseases associated with the blockage. It was shown that the shape of the stenosis is also an important parameter that needs to be taken into account for investigation of the flow behaviour inside stenosed coronary artery models.

A flow visualisation technique, PIV, was employed to validate the computational model developed and to investigate the flow behaviour inside the stenosed coronary artery models with different shapes of the stenosis. Different shapes of stenosis with and without eccentricity including round, oval, elongated, half-moon, bean-shape, and crescent were considered in this study for a constant degree of stenosis of 73%. The hyperemic heart working condition was employed for the simulation, as it was discussed in Chapter 4

that the hyperemic condition resulted at higher pressure drop and more hemodynamically unstable conditions compared to the rest heart working condition. The mean and instantaneous velocity contours, pressure drop, WSS, and TKE were calculated to characterise the effect of the stenosis shape on the flow behaviour. Furthermore, the proper orthogonal decomposition (POD) method was employed to identify the coherent structures downstream of the stenotic sections for different shapes of stenosis. The transitional flow behaviour was also investigated by power spectral density (PSD) analysis.

It was shown that the shape of the stenosis affects the flow behaviour and pressure drop considerably. Eccentricity of the stenosis and the presence of sharp edges on the stenosis increase the pressure drop. The length of the jet region after the stenotic section varies significantly for different shapes of stenosis, with the longest jets corresponding to the round concentric, oval concentric and crescent and the shortest corresponding to the half-moon concentric and bean-shape concentric. It was shown that for most of the stenosis shapes, vortical structures form downstream of the stenotic section where the jet flow region starts to break down and becomes less distinct. The analysis of the TKE distributions for different shapes of stenosis showed that the eddies form after the dissipation of the jet flow downstream of the stenosis. At this location the eddies start to grow and the intensity of the eddies differs for different shapes of stenosis. No turbulence structures were observed for the round concentric shape of stenosis and the flow after the stenotic section stayed laminar throughout the artery with a long recirculation zone which extends to about $13D$ downstream of the stenotic section. For other cases, a peak in the TKE profile is observed beyond the dissipation of the jet flow. After this stream-wise location, the eddies break up and the flow starts relaminarisation. The highest peak values of TKE are observed for the half-moon eccentric and crescent shapes of stenosis which have the highest eccentricity and sharp edges. It can be concluded that for some shapes of stenosis such as the round concentric, having even a severe degree of stenosis results in less serious hemodynamic complications compared to the other shapes of stenosis at the same degree of stenosis. The frequency of vortex shedding was calculated as a jump in the PSD profiles downstream of the stenotic regions where the jet flow dissipated. Furthermore, further downstream of the jet dissipated regions, it was observed that most of the stenosis shapes experienced a turbulent behaviour with the $-5/3$ slope which was associated with the range of inertial sub-range frequencies. The POD analysis shows that the coherent structures for oval and elongated concentric cases are stretched longitudinally, while for the other cases, these correlated and anti-correlated structures are predominantly skewed towards the artery wall and located following the jet dissipation. The larger contribution to the TKE from the first POD modes indicates a less complex transitional flow. The first two POD modes for the half-moon concentric shape contribute 44.5% to the total TKE, while for the bean-shape eccentric this drops to about 12%. Therefore, the differences between the first POD modes of different cases show the impact of the shape of the stenosis on the downstream flow structures.

8.3 Development of a non-invasive approach to evaluate pressure drop inside coronary arteries

Pressure drop is an important physical parameter as it relates to the power required by the heart to supply the organs with sufficient oxygenated blood. Higher pressure drop means a higher heart muscle effort to provide the same blood flow rate to different organs for proper function of the organs. After developing in-depth knowledge on the effects of stenosis degree and shape, and heart working conditions on the downstream flow behaviour in Chapter 4 and Chapter 5, a non-invasive approach to evaluate pressure drop inside the coronary arteries was developed in Chapter 6.

Extensive pressure measurement experiments were conducted to investigate the effects of the different governing parameters on the pressure drop inside straight (Section 6.2) and curved (Section 6.3) coronary artery models. Different geometrical and physiological parameters including the degree of stenosis, the shape of the stenosis, the blood flow profile, the blood viscosity and density, and the arterial length and cross section were considered in Section 6.2 for the development of a mathematical model to evaluate pressure drop based on experimentally derived constants. The developed equation relies on two experimental coefficients, namely, the blockage factor, which was found to be a function of the degree and shape of the stenosis, and pulsatility factor, which was shown to be only a function of the degree of stenosis and was independent of the blood profile. Different shapes of stenosis including with and without eccentricity and sharp edges as the extreme cases were employed for the development of the model. It was shown that the developed model is able to accurately evaluate pressure drop inside stenosed coronary arteries for the physiological left and right coronary artery flow profiles. The comparison showed that the mean and peak deviations of the estimated pressure drop using the equation developed from the experimental data are less than 0.5% and approximately 6%, respectively.

Section 6.3 was built upon the model developed for straight arteries in Section 6.2 and presented the experimental measurements of the pressure drop and fractional flow reserve (FFR) inside a curved model of the coronary artery. Various models of curved arteries with different curvature angles and radii were considered in this study to investigate the effect of arterial curvature on the pressure drop. The developed equation presented in Section 6.2 was further extended to account for the effect of arterial curvature. The added term was a function of the curvature angle and the curvature radius over the artery diameter. It was shown that although the effect of the degree of stenosis on the pressure drop was higher than the effect of arterial curvature, neglecting the effect of arterial curvature can result in underestimation of the pressure drop by 25%-35%. The proposed model presented in Chapter 6 is able to accurately determine the pressure drop inside either a curved or straight stenosed coronary artery using the coronary artery shape and flow profile inside the artery. In order to implement the developed model for patient-specific coronary artery geometries, modification on the model is required to account for the effects of local changes in the curvature, torsion, and cross-sectional area throughout the coronary arteries. Development of such a model can ultimately help cardiologists to have a tool as a gatekeeper for invasive methods such as FFR to calculate the pressure drop inside the stenosed arteries non-invasively.

8.4 Investigation of the hemodynamics of stented arteries

One of the most common treatments for cardiovascular diseases (CVDs) is Percutaneous Coronary Intervention (PCI) treatment (coronary angioplasty). It was discussed in Section 2.4 that stent design is one of the many parameters affecting the success rate of PCI treatment by lowering the chances of thrombosis and in-stent restenosis (ISR). Therefore, the effect of stent design on the WSS distribution was investigated both experimentally (Section 7.2) and computationally (Section 7.3).

All the previous flow visualisation experiments of stented arteries to date have been limited due to the presence of metallic or non-transparent stent struts which block the field of view (FOV), as discussed in Section 2.4.2. A novel technique was developed to visualise the flow inside stented arteries using PIV in Section 7.2. The developed novel technique is based on the construction of a transparent stented artery using silicone cast in a single piece, instead of inserting a metal or non-metallic stent inside a cast artery model, which are translucent and distort the FOV. With the help of the developed novel technique, the time-averaged and -dependent WSS distributions of four different stent patterns were calculated and compared. In Section 7.3, a computational model with a high mesh resolution, especially near the arterial wall, was developed which is able to capture the small micro-recirculation zones adjacent to the stent struts. The developed computational model was validated against the results of PIV measurement. It was shown that the WSS distribution is strongly dependent on the stent design, such that the higher and lower values occur at the location of the struts and immediately upstream or downstream, respectively. It was also shown that the stent connectors, which maintain the longitudinal stability of the stent and hold the hoops together, have an important effect on the hemodynamic performances of the stents. It was found that the distance between two consecutive struts divided by the strut depth was an important parameter for the formation of recirculation zones between the struts and therefore had an impact on the WSS distribution. With the development of the novel experimental technique in this study, the computational modelling results were validated and furthermore, a comprehensive understanding of the fluid mechanics of the stented arteries was achieved. Moreover, the research conducted on stented arteries can help to identify the stent patterns which create smaller regions of low WSS adjacent to the struts and finally result in better patient outcomes.

8.5 Recommendations for future work

The findings of the research presented in this thesis have contributed to the development of an in-depth understanding of the flow inside stenosed and stented coronary arteries. However, the complexity of the flow inside stenosed or stented coronary arteries warrants further investigation in the future. While this study mainly focused on the development of greater in-depth knowledge of the effects of different parameters on the flow behaviour inside the simplified models of coronary arteries, further complementary work is required to implement this knowledge for patient-specific coronary artery geometries with an ultimate goal of improving patient outcomes. Some recommendations for future

investigations are discussed in the following.

i Development of a model to non-invasively evaluate pressure drop inside patient-specific coronary arteries:

A mathematical model based on the in-vitro experimental coefficients for the evaluation of the pressure drop inside straight and curved coronary artery models was developed in Chapter 6. While the model developed in this study is for simplified shapes of coronary arteries, future research is required to extend the developed model to account for local geometrical changes in the coronary arteries. Development of such a model can help to evaluate the pressure drop inside the patient-specific coronary arteries non-invasively. The impact of this model is to help cardiologists via a tool that can be used as a gatekeeper for the invasive methods such as FFR to calculate the pressure drop inside stenosed arteries non-invasively and hence, measure the severity of the stenosis.

ii Investigation of the transitional flow behaviour inside patient-specific coronary artery models:

The knowledge developed on the transitional flow behaviour inside the stenosed coronary artery models was mainly based on coronary arteries of simplified shape. Although a patient-specific geometry for the coronary artery was employed in Chapter 4 to demonstrate the validity of the developed results for an idealised coronary artery model, future research can focus on the effect of the shape of the artery on the transitional flow behaviour. Various patient-specific stenosed coronary artery geometries with different curvature and tortuosity can be considered to further investigate the transition to turbulence inside them. A better understanding of the transition to turbulence inside the patient-specific geometries would result in more accurate prediction of the pressure drop inside them and hence improve patient outcomes, as the resultant pressure drop is affected by turbulence across the stenosis, and is used as a clinical measure to diagnose the stenosis.

iii Investigation of the flow inside the coronary artery models with multiple sequential stenoses

In this study, the flow behaviour inside a stenosed coronary artery model with a single stenosis was thoroughly investigated. However, multiple stenoses are common with diffuse atherosclerosis (Flanigan et al. 1977). It is expected that if multiple stenoses are located far from each other, the induced pressure drop can be calculated by adding the pressure drop due to the presence of each of them individually. However, there are gaps in the literature regarding the flow inside the artery with multiple stenoses: How does the distance between two stenoses influence the transitional flow behaviour? Do multiple stenoses trigger or mitigate the transition to turbulence? What is the effect of the presence of multiple stenoses on each other? Does the presence of multiple stenoses result in the progression or regression of the degree of stenosis of each of the stenoses over time? How does the PCI treatment of one of the stenoses affect the other ones? Therefore, further studies on the flow behaviour inside stenosed coronary arteries with multiple stenoses are suggested to address these research questions.

iv Development of fundamental knowledge on the flow structures in stented arteries:

From a fluid mechanics point of view, stents can be interpreted as a roughness element based on their typical depth and thickness. In the context of stented arteries, struts can be considered to be roughness elements with height of the elements is the depth of the struts. In Chapter 7, it was shown that the distance between two consecutive struts divided by the strut height is an important parameter impacting on the WSS distribution. Further analysis is recommended on the flow structures in a stented artery, interpreted as a rough pipe model. A computational model which is able to fully resolve the smallest spatial and temporal scales of the flow accompanied with a PIV flow visualisation technique would help to further analyse the flow structures and the role of the stent design on the WSS distribution.

v Optimisation of the stent design with the aim to reduce the likelihood of in-stent restenosis:

As covered in Section 2.4, there is a direct link between the stent design and the WSS distributions and hence the chances of ISR and thrombosis. In this study, a novel experimental technique and a computational model were developed to investigate the flow inside stented arteries for different stent designs. However, further studies are needed to optimise the stent design based on their geometric parameters such as the strut thickness, the strut depth, the strut cross-section, the shape of the strut connector, the longitudinal distance between two consecutive struts, shape of the hosting artery, and the patient-specific physiological flow profile. To do so, a machine learning algorithm needs to be employed to optimise the performance of the stent by finding a more hemodynamically compatible stent pattern. The input layers are the artery and stent geometrical parameters as well as the flow profile, with their corresponding wall shear stress (WSS), pressure drop, and oscillatory shear index (OSI). The target of the optimisation is to find a novel stent pattern with fewer regions exposed to low WSS (< 0.5 Pa) and lower values of pressure drop.

vi Investigation of the effects of dynamic vessel motion and wall compliance on the hemodynamics of the flow:

As the arterial stiffness is a key arterial alteration during the ageing process, which is recognised as a primary risk factor for all cardiovascular diseases, the artery wall in this study was assumed to be rigid. However, young people may also develop stenosis, although in lower rates compared to the elderly. Hence, a comprehensive simulation is suggested to accurately investigate the effects of temporal variations on the hemodynamic parameters. It is proposed that the simulation should cover the entire coronary arterial system in order to account for the interaction of different branches of the coronary arteries with each other. The methodology suggested for this simulation is a combination of fully-coupled fluid structure interaction (FSI) with the arbitrary Lagrangian–Eulerian (ALE) formulation and with a realistic choice of wall arterial material with a heterogeneous and anisotropic structure. However, such a simulation is highly computationally expensive and difficult to conduct. For the experimental modelling of the wall compliance, a compliance chamber is recommended to mimic the arterial ability to expand and contract with cardiac pulsation and relaxation. This investigation will help to provide a better

understanding of the effects of dynamic vessel motion and wall compliance of the coronary arteries for the investigation of their hemodynamics.

These suggested future studies could extend the current knowledge on the coronary arterial system and be beneficial for clinical practices, both for diagnosis and personalised treatments.

References

Flanigan DP, Tullis JP, Streeter VL, Whitehouse WM, Jr, Fry WJ, and Stanley JC (1977). “Multiple subcritical arterial stenoses: effect on poststenotic pressure and flow.” *Annals of Surgery* 186.5, p. 663.

Appendices

Appendix A:

Effect of degree of stenosis on the pulsatile flow pressure drop

In this study, the pressure drop of a pulsatile flow is calculated experimentally in stenosed coronary artery models with different degrees of stenosis and for blood with different levels of blood viscosity. It is shown that the pressure drop is higher at the severe degree of stenosis (more than 60%) compared to the mild and moderate cases. Furthermore, the effect of changes in the level of blood viscosity on the pressure drop is more significant for the early stages of atherosclerosis (mild degree of stenosis). The results of this study provide an improved prediction of pressure drop and blood flow rate which can be applied to investigate heart muscle work rate and the required heart power.

This section consists of the following published conference paper:

Navid Freidoonimehr, Rey Chin, Maziar Arjomandi, Anthony Zander (2018). “Effect of degree of stenosis on the pulsatile flow pressure drop in a coronary artery”. *21st Australasian Fluid Mechanics Conference*, Adelaide, Australia.

The article is identical to its published format with the following exceptions:

- The numbering of figures, tables and equations have been altered to include the chapter number.
- The position of some figures and tables have been changed to improve legibility.

The article in its published format is available at:

https://people.eng.unimelb.edu.au/imarusic/proceedings/21/Contribution_662_final.pdf

Statement of Authorship

Title of paper	Effect of degree of stenosis on the pulsatile flow pressure drop in a coronary artery
Publication Status	<input checked="" type="checkbox"/> Published <input type="checkbox"/> Accepted for Publication <input type="checkbox"/> Submitted for Publication <input type="checkbox"/> Unpublished and Unsubmitted work written in manuscript style
Publication Details	Freidoonimehr, N., Chin, R., Arjomandi, M., and Zander, A., 2018, "Effect of degree of stenosis on the pulsatile flow pressure drop in a coronary artery", 21st Australasian Fluid Mechanics Conference AFMC2018, Adelaide, Australia

Principal Author

Name of Principal Author (Candidate)	Navid Freidoonimehr		
Contribution to the Paper	Developed ideas, conducted experiments, performed data analysis and interpreted results, wrote manuscript, and acted as corresponding author		
Overall percentage (%)	75%		
Certification:	This paper reports on original research I conducted during the period of my Higher Degree by Research candidature and is not subject to any obligations or contractual agreements with a third party that would constrain its inclusion in this thesis. I am the primary author of this paper.		
Signature		Date	15/02/2021

Co-Author Contributions

By signing the Statement of Authorship, each author certifies that:

- i the candidate's stated contribution to the publications is accurate (as detailed above);
- ii permission is granted for the candidate to include the publication in the thesis; and
- iii the sum of all co-author contributions is equal to 100% less the candidate's stated contribution

Name of Co-Author	Rey Chin		
Contribution to the Paper	Supervised the development of the research, participated in developing ideas and concepts, helped in interpretation of results, provided critical revision of manuscript.		
Signature		Date	15/02/2021

Name of Co-Author	Maziar Arjomandi		
Contribution to the Paper	Supervised the development of the research, participated in developing ideas and concepts, helped in interpretation of results, provided critical revision of manuscript.		
Signature		Date	15/02/2021

Name of Co-Author	Anthony Zander		
Contribution to the Paper	Supervised the development of the research, participated in developing ideas and concepts, helped in interpretation of results, provided critical revision of manuscript.		
Signature		Date	15/02/2021

Effect of degree of stenosis on the pulsatile flow pressure drop

Navid Freidoonimehr, Rey Chin, Maziar Arjomandi, Anthony Zander

Abstract

Artery blockage due to plaque formation affects the performance of the heart considerably. These plaques are formed inside an artery and forced the heart to work harder to feed the vessels and organs with oxygenated blood. In this study, the pressure drop of a pulsatile flow is calculated in diseased coronary arteries with different degrees of stenosis and for blood with different levels of blood viscosity. Pressure drop is much more significant at the severe degrees of stenosis (more than 60%) compared to the mild and moderate cases. The effect of changes in the level of blood viscosity on the pressure drop is more significant at early stages of atherosclerosis (mild degrees of stenosis). The comparison of the pressures measured before and after stenoses with the ones for healthy arteries is recommended to be used to estimate the severity of vessel constriction, which can be helpful in early detection of atherosclerosis via a non-invasive diagnostic procedure.

Introduction

Cardiovascular diseases are considered as one of the main causes of death worldwide. Among these diseases, atherosclerosis caused by plaque deposition on the arterial wall, known as stenosis, leads to the obstruction of the blood flow. These plaques, comprised of lipid, calcium, bad cholesterol (LDL), and also a specific type of white blood cells (macrophage cell), can occupy almost the entire cross section of the artery and cause difficulty for the heart to provide oxygenated blood to the various organs. The power which is required by the heart to supply the organs with a uniform blood flow rate can be determined by the pressure drop throughout the artery. The degree of stenosis, representing the area reduction percentage of a normal artery because of the plaque deposition, directly influences the amount of pressure drop. Higher pressure drop means higher heart muscle work rate to provide the same blood flow to the various organs.

Pressure drop is increased in the presence of flow separation and transitional flow after the stenosis. The pressure drop can also be changed due to the presence of the pulsatile flow introducing flow acceleration and deceleration during a cardiac cycle which is neglected in the steady flow assumption. Hence, it is necessary to study the pulsatile blood flow inside the blood vessels to observe the pressure drop and flow patterns before and after the constriction (Li et al. 2017). Although blood flow in the human arterial system is predominantly laminar, transition to turbulence can also be observed because of the fluctuations happening at different arterial locations. The transitional flow causes a higher velocity gradient and consequently higher values of wall shear stress. Higher shear stress leads to a higher pressure drop inside the artery due to the stenosis. One of the susceptible locations for laminar transitional flow is near the stenotic regions. Flow at and after the stenosis will become transitional even at lower flow velocities compared to

a healthy artery. Furthermore, stenosis in the artery results in changes in the blood flow patterns. The flow patterns in models of a normal internal carotid artery (ICA) as well as two diseased ICAs with 50% and 70% degrees of stenosis were studied by Kefayati and Poepping (2013). Blood flow was uniform in both internal and external carotid arteries (both left and right sides of bifurcation) for the healthy artery. Reversed flow patterns were also observed along the inner wall of both diseased ICA models.

To observe the laminar flow transition in a channel, Khair et al. (2015) performed direct numerical simulation (DNS) modelling to investigate the pulsatile flow in a constricted rectangular channel. The peak value of turbulent kinetic energy (TKE), representing the transition to turbulence point, is located after the constricted section for all cases. For higher values of Reynolds number and higher degrees of stenosis, the transition location moved closer to the constricted location. After reaching the transitional point, the TKE value gradually reduces which indicates that the flow is re-laminarised.

Blood in large arteries (diameter > 0.5 mm) is considered as a Newtonian fluid where the Reynolds number is high (Nichols et al. 2011). Furthermore, since the blood behaves as a Newtonian fluid at shear rates greater than 100 s^{-1} (Jahangiri et al. 2017) and considering that the shear rates applied to the coronary arteries are larger than 100 s^{-1} (Sakariassen et al. 2015), blood behaviour in the coronary arteries is considered as Newtonian fluid. The blood viscosity can be interpreted as the resistance of blood to flow through the arteries. The higher the viscosity, the more difficult it is for the blood to pass through and consequently the heart needs to work harder to provide the same flow rate compared to the normal viscosity blood case. Blood consists of different components including red (about 45 volume percentage) and white (about 0.7 volume percentage) blood cells and platelets (about 54.3 volume percentage). Whole blood viscosity is mostly dependent on the red blood cells since the white blood cells and platelets do not have a great influence on the blood viscosity (Pop et al. 2002). Hematocrit is a volume percentage of red blood cells in the blood. The change in the level of hematocrit causes the change in the blood viscosity. It has been hypothesised that increasing the levels of blood viscosity may lead to an increase in the cardiovascular diseases such as atherosclerosis and thrombogenesis related diseases (Lowe et al. 1997). Furthermore, low levels of hematocrit, i.e. anemia, may cause some serious symptoms such as fatigue, shortness of breath and fast heartbeat. Thus, it is of great importance to study the effect of blood viscosity on the pressure drop through a diseased coronary artery.

In this study, the blood flow-pressure drop relation across a diseased coronary artery with different degrees of stenosis and different levels of blood hematocrit are investigated. An experimental setup was designed and built to measure the flow rate and pressure drop before and after the diseased part of the coronary artery. Furthermore, a realistic physiological pulsatile flow profile is applied to mimic the blood flow inside the coronary arteries.

Experimental methodology

The schematic diagram of a diseased coronary artery is presented in figure A-1. The diseased coronary artery is modelled as a rigid asymmetric spherical constriction inside a rigid pipe. Different degrees of stenosis including 11.2%, 39.1%, 56.5%, 65.4%, and 74.2% cross section area reduction are considered to address different amounts of plaque

deposition at susceptible locations of coronary arteries. The inside diameter of the model, D , is 6.1 mm corresponding to almost double the diameter of coronary arteries. Since the flow inside the artery is pulsatile, a $10 - D$ length is considered both before and after stenosis part to account for the beginning and end effects.

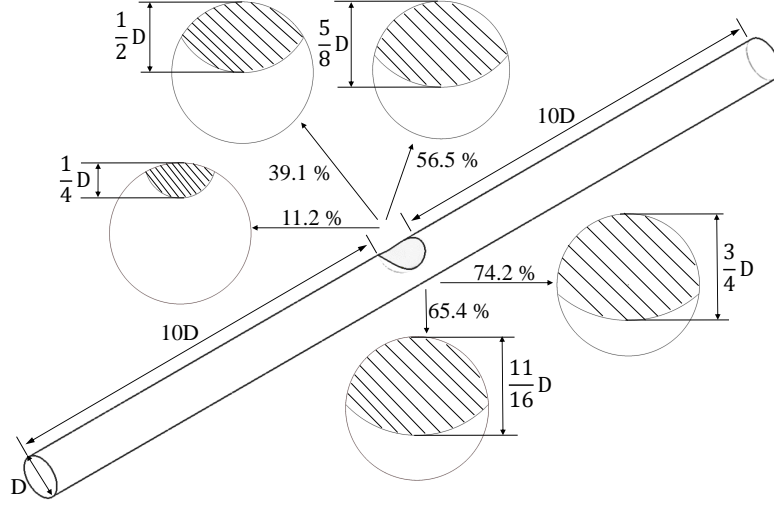


Figure A-1: Schematic diagram of 3D asymmetric diseased coronary artery with different degrees of stenosis shown with the percentage of degrees of stenosis.

Figure A-2 displays the experimental rig and its components: (1) programmable centrifugal pump (RS pro direct coupling centrifugal pump) and its controller (RS pro process pump controller for brushless micro-pump pump), (2) flow sensor (Omega, FLR1000), (3) 3D-printed settling chamber, (4) pressure sensor (UNIK 5000 silicon pressure sensor), (5) 3D printed diseased artery model (Zortrax M300), (6) valve, (7) water reservoir, and (8) computer, power supply and DAQ card (NI USB-6211). It is worth mentioning that a long acrylic pipe (about 2 m) is inserted before the test section and after the settling chamber to allow the pulsatile flow inside the system to become fully developed.

Three different working fluids were chosen for this experiment; one of them matching the typical blood viscosity (3.2 mPa.s), the second representing the low hematocrit related diseases (with viscosity about half of the typical blood viscosity, 1.8 mPa.s) and another one to account for high levels of hematocrit (with viscosity about double of the typical blood viscosity, 6.4 mPa.s). In order to obtain fluids with the above-mentioned viscosities, a mixture of distilled water and glycerine was employed based on the classic Grunberg and Nissan (1949) liquid mixture equation

$$\ln \mu_{mix} = \sum_{i=1}^N x_i \ln \mu_i, \quad (1)$$

where μ_{mix} is the viscosity of the liquid mixture, μ_i is the viscosity of the pure fluid component and x_i is the mole fraction of component i in the liquid mixture. The three working fluids were made from distilled water and glycerine portions according to equation 1. The viscosity of the final mixture was then determined by testing the samples in an AntonPaar MCR 301 Rheometer. Accuracy of the measured viscosities of the mixture was $\pm 1.5\%$. All experiments and viscosity calculations were performed at room temperature ($23^\circ C$). The blood viscosity in the body temperature ($37^\circ C$) is modelled with the glycerol-water mixture at the room temperature.

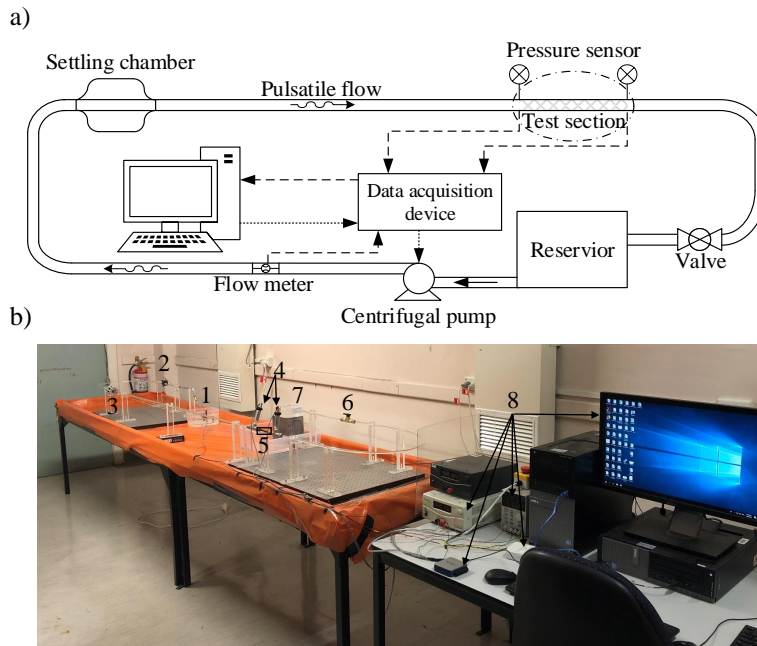


Figure A-2: a) Schematic of the test setup and b) Experimental test setup: (1) centrifugal pump; (2) flow sensor; (3) settling chamber; (4) pressure sensor; (5) 3D-printed test section; (6) valve; (7) water reservoir; (8) computer, power supply and DAQ card.

The pulsatile waveform, representing the blood flow inside the coronary artery, is shown in figure A-3 (Huo and Kassab 2006). This waveform, as an inlet velocity boundary condition, is modelled using the first 4 Fourier modes of Fast Fourier Transform (FFT) which accurately represents the original waveform. The input voltage of the pump is controlled using a data acquisition card to simulate the physiological velocity waveform of the coronary artery as represented in figure A-3. A slight difference can be observed between the required inlet profile signal and the one the pump creates. The maximum deviation between the achieved signal and the original inlet profile signal is 1.6% for the low hematocrit blood model, 1.8% for the blood mimicking fluid and 2.3% for the high level of hematocrit fluid model.

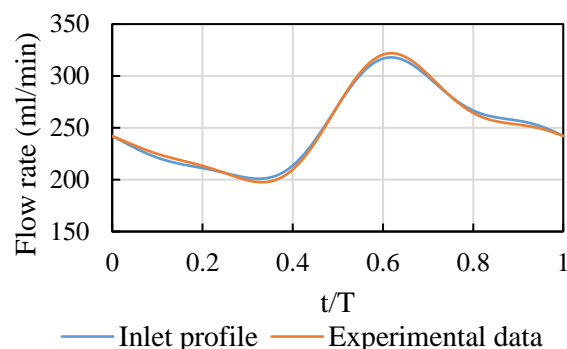


Figure A-3: The physiological pulsatile inlet velocity boundary condition (Huo and Kassab 2006).

Two pressure sensors are used to measure the pressure differences before and after the test section. The pressure transducers have a full scale accuracy of 0.04% and the flow meter has a measurement accuracy of 1%.

The mean flow rate changes from the resting blood flow rate (1.1 ml/s) to hyperemic flow rate (3.9 ml/s) (Grist et al. 1997). Because of the limitation of the centrifugal pump, the resting blood flow condition was slightly higher in this experiment (slightly above 100 ml/min).

The Womersley number, a dimensionless parameter governing the pulsatile flow, is defined as:

$$Wo = \frac{D}{2} \sqrt{\frac{2\pi \rho}{T \mu}}, \quad (2)$$

where T is the a cycle time period and ρ is the fluid density. The blood density is considered to be 1060 kg/m³ (Cutnell et al. 2015). The Womersley number was set to be 1.9, representing the value for coronary artery (Li et al. 2017), for all experiments. In order to keep the Womersley number constant and since viscosity changes for different fluid models, the time period is changed accordingly. For the blood mimicking fluid, the time period is 5.54 s, for the fluid with a lower viscosity ($\mu = 1.8$ mPa.s) the time period is 9.85 s and finally for the higher viscosity fluid model ($\mu = 6.4$ mPa.s) the time period becomes 2.77 s.

Results and discussion

The pressure difference before and after the stenosis of a diseased coronary artery model with different degrees of stenosis ranging from 11.2% to 74.2% degrees of stenosis for working fluids with different viscosities is displayed in figure A-4. The mean flow rate varies from about 110 ml/min to 280 ml/min for all cases. A linear relation between the flow rate and pressure drop is observed for all cases which can be explained based on Darcy-Weisbach equation that is valid for laminar pipe flow without any constrictions:

$$\frac{\Delta P}{L} = \frac{128 \mu \dot{Q}}{\pi D^4}, \quad (3)$$

where ΔP is the pressure drop, L is the pipe length and \dot{Q} is the volumetric flow rate. Based on the Darcy-Weisbach equation, the pressure drop is related to viscous effects which means that the higher the flow rate, the higher the pressure drop (As displayed by black dash line in figure A-4). To account for the effect of the pulsatile flow regime and constrictions inside the pipe, the following equation was proposed by Young et al. (1975):

$$\Delta P = \frac{K_v \mu}{D} V + \frac{K_t}{2} \left(\frac{A_0}{A_1} - 1 \right)^2 \rho |V| V + K_u \rho L \frac{dV}{dt}, \quad (4)$$

where K_v , K_t and K_u are experimentally determined coefficients, A_0 is the area of the pipe with the diameter of D , A_1 is the cross sectional area of the stenosis, and V is the plane average flow velocity of the unobstructed pipe. The first term is almost the same as the Darcy-Weisbach equation which represents the friction loss effect. The second term denotes the pressure drop due to the non-linear changes in the cross section of the pipe because of the stenosis and the last term represents the differential pressure required to accelerate or decelerate the fluid inside the pipe. The difference between steady and

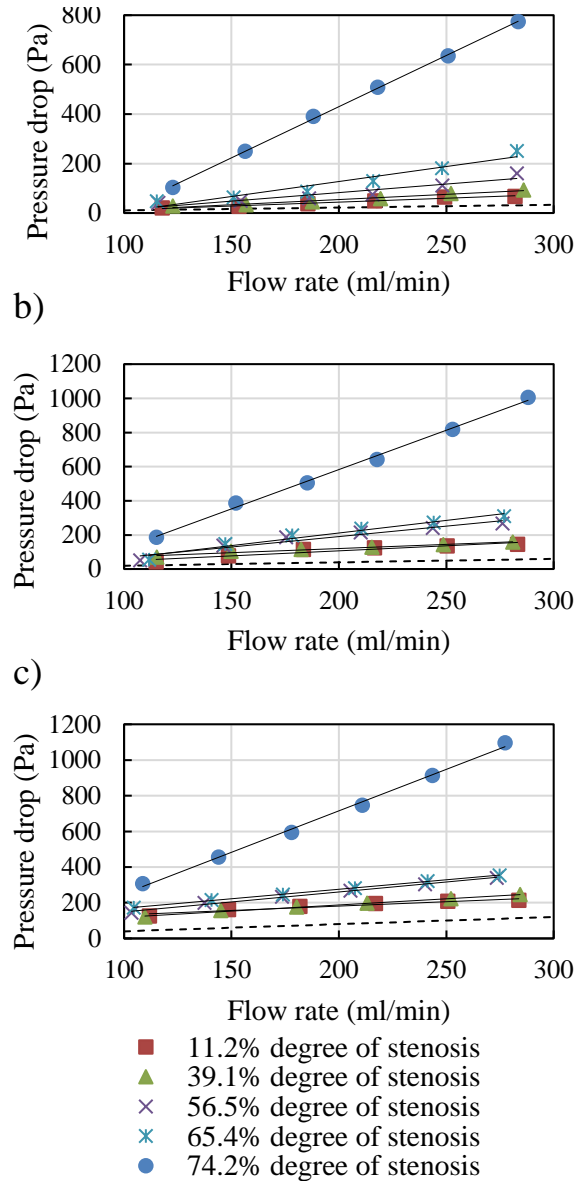


Figure A-4: The pressure drop calculated from Darcy-Weisbach equation and measured across different degrees of stenosis in the pipe with flow rate change for different viscosities of a) 1.8 mPa.s ($200 < Re < 600$), b) 3.2 mPa.s ($115 < Re < 350$) and c) 6.4 mPa.s ($60 < Re < 180$).

pulsatile flow regimes in terms of pressure drop is represented using the last term of Eq. 4 which is related to the time-dependent nature of pulsatile flow.

Due to the sudden change in the flow pattern because of the stenosis as well as an increase in the fluid velocity passing the stenosis, the turbulence structures start to grow after the constriction. The velocity fluctuations due to the constriction inside the pipe are intensified with an increase in the cross sectional area covered by the fat plaques in the artery. These turbulent structure cause a more significant pressure drop across the constrictions with higher degrees of stenosis (figure A-4). The Reynolds number range based on the diameter of the artery model and upstream velocity for different fluid viscosity is displayed in figure A-4. The Reynolds number immediately after the stenosis due to a sudden jump in the velocity increases considerably leading to the formation

of turbulent structures. A remarkable jump in pressure drop is seen for the case with 74.2% degree of stenosis compared to the others, which was also observed by Young et al. (1975) and Flanigan et al. (1977). The results show that an increase in the degree of stenosis to 75% increases the pressure drop dramatically, independent of the blood viscosity. The same trend exists for figures A-4(b) and A-4(c) associated with different viscosities. Moreover, the pressure drop calculated from Darcy-Weisbach equation for the straight pipe without any constrictions is considerably lower than the other cases with different degrees of stenosis representing the effect of constriction in the flow path on the pressure drop.

The pressure drop for different degrees of stenosis and viscosities for both resting flow rate (120 ml/min, part a) and hyperemic flow rate (250 ml/min, part b) are displayed in figure A-5. According to figure A-5, the pressure drop increases with an increase in the degree of stenosis. The effect of the degree of stenosis on the pressure drop is more significant as the stenosis degree increases above approximately 60%. According to figure A-5(a), an increase in the degree of stenosis from 56.5% to 74.2% increases the pressure drop from 170 Pa to 342 Pa for $\mu = 6.4$ mPa.s. Furthermore, for the hyperemic flow rate, the pressure drop increases from 315 Pa to 947 Pa with increasing the degree of stenosis from 56.5% to 74.2% (figure A-5(b)). The observed trend is in agreement with the results reported by Rotman et al. (2017) which found that the pressure drop increases exponentially as the degree of stenosis increases in the presence of arterial compliance effect.

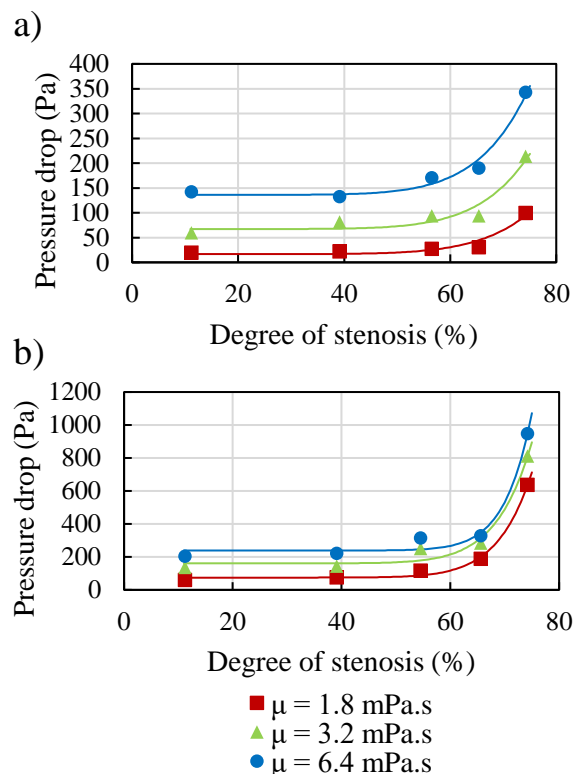


Figure A-5: Pressure drop for different degrees of stenosis and viscosities for a) flow rate = 120 ml/min and b) 250 ml/min.

Furthermore, for a flow rate of 250 ml/min, the increase of viscosity from 1.8 to 6.4 mPa.s (more than 2 times higher), increases the pressure drop by 50% for a 74.2% degree

of stenosis while the increase of viscosity from 1.8 to 6.4 mPa.s increases pressure drop by more than 3 times for a 11.2% degree of stenosis. The same trend can be seen for the flow rate of 120 ml/min. Hence, apart from the flow rate, the effect of viscosity on pressure drop is more significant at lower degrees of stenosis.

Figure A-6 presents the pressure drop at different flow rates for different levels of hematocrit in the blood for a 74.2% degree of stenosis. An increase in the levels of hematocrit which is equal to the increase in viscosity, increases the pressure drop. This means that the heart needs to work harder to push the blood through the semi-blocked artery for patients suffering from hyper-viscosity syndromes. For example, for the hyperemic flow rate (about 250 ml/min), an increase in viscosity from 1.8 to 6.4 mPa.s increases the pressure drop from about 600 Pa to 950 Pa.

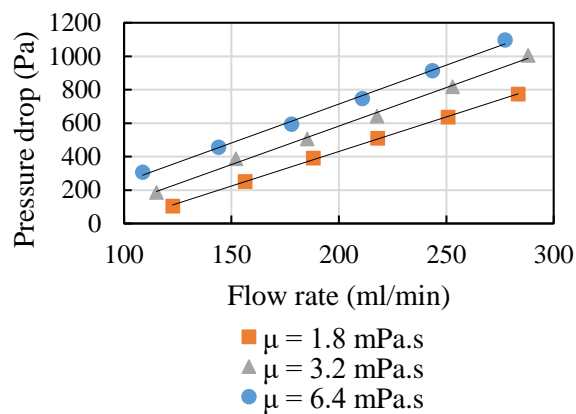


Figure A-6: The pressure drop measured across the stenotic pipe with flow rate change for a 74.2% degree of stenosis.

Conclusion

The pressure drop has been measured inside a pipe model representing a coronary artery suffering from atherosclerosis with the change in the level of blood hematocrit. The effect of changes in the level of hematocrit on the pressure drop is more significant at early stages of atherosclerosis. On the other hand, at the more progressive levels of atherosclerosis, the pressure drop changes are more significant compared to the changes that occur due to the hematocrit level in the blood. The results of this study provide a better prediction of pressure drop and blood flow rate which can be applied to investigate heart muscle work rate and the required heart power.

Acknowledgement

Financial support for the project has been provided by the Australian Government Research Training Program and the University of Adelaide Scholarship. The authors would like to acknowledge the School of Mechanical Engineering and the Mechanical Workshop at the University of Adelaide. The authors acknowledge the financial support of the Australian Research Council.

References

- Cutnell JD, Johnson KW, Young D, and Stadler S (2015). *Physics, 10th Edition*. Wiley.
- Flanigan DP, Tullis JP, Streeter VL, Whitehouse Jr. WM, Fry WJ, and Stanley JC (1977). “Multiple subcritical arterial stenoses: effect on poststenotic pressure and flow”. *Annals of Surgery* 186.5, pp. 663–668.
- Grist TM, Polzin JA, Bianco JA, Foo TK, Bernstein MA, and Mistretta CM (1997). “Measurement of coronary blood flow and flow reserve using magnetic resonance imaging”. *Cardiology* 88.1, pp. 80–89.
- Grunberg L and Nissan AH (1949). “Mixture Law for Viscosity”. *Nature* 164, p. 799.
- Huo Y and Kassab GS (2006). “Pulsatile blood flow in the entire coronary arterial tree: theory and experiment”. *American Journal of Physiology-Heart and Circulatory Physiology* 291.3, H1074–H1087.
- Kefayati S and Poepping TL (2013). “Transitional flow analysis in the carotid artery bifurcation by proper orthogonal decomposition and particle image velocimetry”. *Medical Engineering & Physics* 35.7, pp. 898–909.
- Khair A, Wang BC, and Kuhn DCS (2015). “Study of laminar–turbulent flow transition under pulsatile conditions in a constricted channel”. *International Journal of Computational Fluid Dynamics* 29.9-10, pp. 447–463.
- Li S, Chin C, Thondapu V, Poon EKW, Monty JP, Li Y, Ooi ASH, Tu S, and Barlis P (2017). “Numerical and experimental investigations of the flow–pressure relation in multiple sequential stenoses coronary artery”. *The International Journal of Cardiovascular Imaging* 33.7, pp. 1083–1088.
- Lowe GD, Lee AJ, Rumley A, Price JF, and Fowkes FG (1997). “Blood viscosity and risk of cardiovascular events: the Edinburgh Artery Study”. *British Journal of Haematology* 96.1, pp. 168–173.
- Nichols W, O’Rourke M, and Vlachopoulos C (2011). *McDonald’s blood flow in arteries, Sixth edition: Theoretical, experimental and clinical principles*. CRC Press.
- Pop GAM, Duncker DJ, Gardien M, Vranckx P, Versluis S, Hasan D, and Slager CJ (2002). “The clinical significance of whole blood viscosity in (cardio)vascular medicine”. *Netherlands Heart Journal* 10.12, pp. 512–516.
- Rotman OM, Zaretsky U, Shitzer A, and Einav S (2017). “Pressure drop and arterial compliance – Two arterial parameters in one measurement”. *Journal of Biomechanics* 50, pp. 130–137.
- Sakariassen KS, Orning L, and Turitto VT (2015). “The impact of blood shear rate on arterial thrombus formation”. *Future Science OA* 1.4, pp. 30–39.
- Jahangiri M, Saghafian M, and Sadeghi MR (2017). “Numerical simulation of non-Newtonian models effect on hemodynamic factors of pulsatile blood flow in elastic stenosed artery”. *Journal of Mechanical Science and Technology* 31.2, pp. 1003–1013.
- Young DF, Cholvin NR, and Roth AC (1975). “Pressure drop across artificially induced stenoses in the femoral arteries of dogs”. *Circulation Research* 36.6, pp. 735–743.

Appendix B:

Hemodynamic of a coronary artery: a PIV measurement

In this study, the mean and instantaneous flow fields downstream of a stenosed coronary artery model are investigated experimentally using particle image velocimetry (PIV). The results show that the largest turbulent kinetic energy is related to the case with the maximum velocity during a cardiac cycle and the lowest is related to the phase with a minimum flow velocity. Understanding the flow features downstream of the stenotic section is critical for identifying the possible mechanisms contributing to progression of coronary artery disease.

This section consists of the following published conference paper:

Navid Freidoonimehr, Rey Chin, Anthony Zander, Maziar Arjomandi (2019).
“Hemodynamic of a coronary artery: a PIV measurement”. *IX Australian Conference on Laser Diagnostics*, Adelaide, Australia.

The article is identical to its published format with the following exceptions:

- The numbering of figures, tables and equations have been altered to include the chapter number.
- The position of some figures and tables have been changed to improve legibility.

The article in its published format is available at the proceedings of the IX Australian Conference on Laser Diagnostics at:

https://www.aclld.org.au/wp-content/uploads/2019/11/Zeyad-Alwahabi-Hemodynamic_Freidoonimehr.pdf

Statement of Authorship

Title of paper	Hemodynamic of a coronary artery: a PIV measurement
Publication Status	<input checked="" type="checkbox"/> Published <input type="checkbox"/> Accepted for Publication <input type="checkbox"/> Submitted for Publication <input type="checkbox"/> Unpublished and Unsubmitted work written in manuscript style
Publication Details	Freidoonimehr, N., Chin, R., Zander, A., and Arjomandi, M., 2019, "Hemodynamic of a coronary artery: a PIV measurement", IX Australian Conference on Laser Diagnostics, Adelaide, Australia

Principal Author

Name of Principal Author (Candidate)	Navid Freidoonimehr		
Contribution to the Paper	Developed ideas, conducted experiments, performed data analysis and interpreted results, wrote manuscript, and acted as corresponding author		
Overall percentage (%)	75%		
Certification:	This paper reports on original research I conducted during the period of my Higher Degree by Research candidature and is not subject to any obligations or contractual agreements with a third party that would constrain its inclusion in this thesis. I am the primary author of this paper.		
Signature		Date	15/02/2021

Co-Author Contributions

By signing the Statement of Authorship, each author certifies that:

- i the candidate's stated contribution to the publications is accurate (as detailed above);
- ii permission is granted for the candidate to include the publication in the thesis; and
- iii the sum of all co-author contributions is equal to 100% less the candidate's stated contribution

Name of Co-Author	Rey Chin		
Contribution to the Paper	Supervised the development of the research, participated in developing ideas and concepts, helped in interpretation of results, provided critical revision of manuscript.		
Signature		Date	15/02/2021

Name of Co-Author	Anthony Zander		
Contribution to the Paper	Supervised the development of the research, participated in developing ideas and concepts, helped in interpretation of results, provided critical revision of manuscript.		
Signature		Date	15/02/2021

Name of Co-Author	Maziar Arjomandi	
Contribution to the Paper	Supervised the development of the research, participated in developing ideas and concepts, helped in interpretation of results, provided critical revision of manuscript.	
Signature		Date 15/02/2021

✓ ✓

Hemodynamic of a coronary artery: a PIV measurement

Navid Freidoonimehr, Rey Chin, Anthony Zander, Maziar Arjomandi

Abstract

Understanding the flow features near the stenosis location inside a coronary artery is critical for identifying the possible mechanisms contributing to the disease progression. In this study, a Planar Particle Image Velocimetry (PIV) was employed to study the mean and instantaneous flow fields downstream of a semi-blocked artery model. Application of PIV for these types of problems is associated with some challenges such as the small region of interest, which is usually less than 1 cm and the pulsatile nature of the blood flow inside the arteries. The latter needs different timings between the images of a pair of PIV images with respect to the corresponding velocity during different phases of a cardiac cycle. By addressing all the challenges, PIV can be used as a powerful method to visualise the flow features inside the different arteries with the pulsatile in-flow regime.

Introduction

The flow in most part of a coronary artery is laminar due to its low Reynolds number and if there is no obstacle inside the artery. When a blockage is formed inside an artery, the flow downstream of the stenosis becomes transitional due to the instabilities created by the obstruction. The constriction inside the artery results in the formation of a jet flow, which creates an increased flow velocity and forms the recirculation zones around the jet section. Therefore, a laminar flow transition is most likely to occur after the constricted sections. Flow transition to turbulence in an artery leads to a higher wall shear stress (WSS) level and results in a higher pressure drop inside the artery. Turbulence can also affect the important haemodynamic indexes such as wall shear stress as well as the location and persistence in time of recirculation regions. One of the parameters, which triggers turbulence, is the heart pulsations. Many of the studies in the literature which investigated turbulence in a stenosed artery model assume a steady inlet velocity profile (Biswas et al. 2016). However, turbulence inside the constricted coronary artery with the pulsatile flow is different from a model with the steady flow due to the unsteadiness behaviour of the pulsatile flow compared to the steady flow. Furthermore, the effect of the flow acceleration and deceleration on the dynamics of the flow is not considered by the steady flow assumption since the physiological flow is pulsatile with a complex time varying profile (Zhu et al. 2018). Therefore, flow behaviour inside the coronary artery models needs to be investigated under the pulsatile flow regime.

On the other side, the flow characteristics such as the length of the recirculation zones and pressure losses are strongly dependent on the general shape of the stenosis (Usmani and Muralidhar 2016). For example, a longer recirculation zone and a higher pressure drop were reported by Young and Tsai (1973) for an asymmetric stenosis compared to an axisymmetric one. Axisymmetric stenosis leads to the formation of an axisymmetric jet

flow after the constricted section. While, for an asymmetric stenosis, the jet flow occurring after the stenosis slightly shifts to the same side of the stenosis. Hence, the other side of the stenosis is a susceptible location for the plaque growth (Tambasco and Steinman 2003). While most of the studies in the literature are focused on the axisymmetric-shaped stenosis (Peterson and Plesniak 2008), an asymmetric stenosis inside an artery model has only been investigated in a few studies. Based on the considerable differences in downstream flow behaviour between the axisymmetric and asymmetric constrictions (as mentioned above) and due to the high possibility of formation of asymmetric stenosis inside the coronary arteries (Waller 1989), in this study the effect of the asymmetric stenosis on the flow behaviour inside the coronary artery models is investigated.

The PIV measurement of the flow inside the coronary artery models with the pulsatile in-flow condition faces some challenges, which is likely to be the reason for its limited application for the study of flow in such problems. The first challenge is associated with the small region of interest (usually less than 1 cm by 1 cm) which makes the measurements more complicated. The choice of the material for building the artery model is also another important parameter in PIV measurement. The artery model should be transparent to let the laser sheet to go through the model and the camera to capture the illuminated area. Furthermore, it should have almost the same refractive index as the working fluid to avoid any light distortion. As explained by Yazdi et al. (2018), different materials were used in the literature to make models of different arteries such as Estane 5714 (polyurethane) and silicone (mainly Sylgard 184). The choice of the blood mimicking fluid depends on the fluid mixture viscosity that should be the same as the blood viscosity. Furthermore, the refractive index of the working fluid should match the refractive index of the casted artery model to avoid any optical distortions. Different mixture percentages of water and glycerine were used as a blood mimicking fluid in the literature. A 60% water and 40% glycerine of mass fraction is the most common mixture in the literature (Charonko et al. 2009) with the mixture viscosity of 3.67 mPa.s at room temperature. Another challenge is the formation of the blockage inside the artery model that creates a jet flow regime after the stenotic section. This requires different PIV timings between two images in a pair (dt) for both jet flow regime and recirculation zone. The jet flow regime requires a shorter dt , while the recirculation zone requires a longer dt due to their different velocities. This challenge is also applied to any kind of problems where a significant velocity gradient occurs. The last important challenge is about the unsteady nature of the flow inside the coronary arteries. Since the blood flow inside the arteries is time-dependent pulsatile flow, a phase average of a cardiac cycle needs to be calculated to address the time dependent nature of the flow. This needs a longer period measurement over a large number of the cardiac cycles.

This study aims to investigate the flow behaviour downstream of a plaque in a diseased coronary artery with a physiological pulsatile inlet velocity experimentally using PIV. Turbulent kinetic energy (TKE), as an indicator of transition to turbulence and a method for predicting the turbulence energy loss of the blood flow through the diseased coronary artery, is evaluated for different cases.

Experimental methodology

To match the refractive index of the working fluid, a Sylgard 184 silicone was used to cast a transparent artery model (Fig. B-1). The inside diameter of the model, D , is 6.1 mm corresponding to almost double the diameter of coronary arteries. The degree of blockage (stenosis) of the model is set to 67%, which is defined based on the ratio of the cross sectional area covered by the stenosis to the whole cross sectional area of the artery. As displayed in Fig. B-1, to limit optical distortion, the section including the blockage was constrained by a rectangular silicone box. A mixture of distilled water and glycerine (with the weight mixture percentage of 60% and 40%, respectively) is used as a working fluid to match the blood viscosity with the viscosity of 3.67 mPa.s.

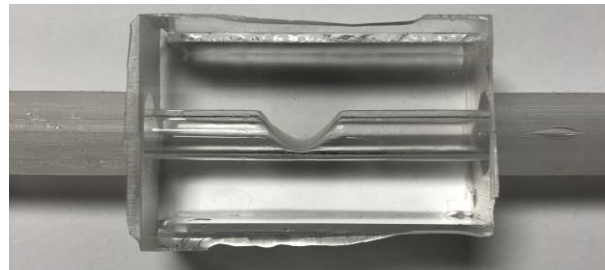


Figure B-1: A transparent artery model with blockage made out of Sylgard 184 silicone.

Figure B-2 displays the experimental rig with different components. The input voltage of the pump was controlled using a data acquisition card to simulate the physiological pulsatile velocity waveform. The flowmeter, used in this experiment, has a measurement accuracy of 0.4% of measured value. The pulsatile waveform, representing the blood flow inside the coronary artery, is shown in Fig. B-3 (Davies et al. 2008). This waveform, as an inlet velocity boundary condition, was modelled using the first 32 Fourier modes of Fast Fourier Transform (FFT) that accurately represents the original waveform (with less than one percent difference between the maximum flow velocities during a cardiac cycle).

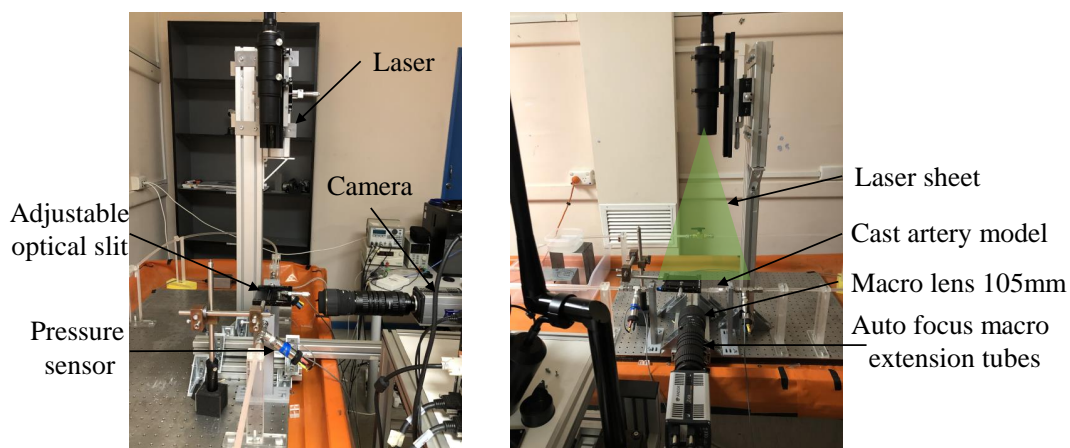


Figure B-2: Two different views of the test rig displaying different components.

In the PIV experiment, as shown in Figs. B-2b and B-2c, a Zyla 5.5 sCMOS camera with 5.5 megapixel resolution and a Sigma macro lens (105mm f2.8) along with 140 mm autofocus macro extension tubes was employed to focus on the small region of interest.

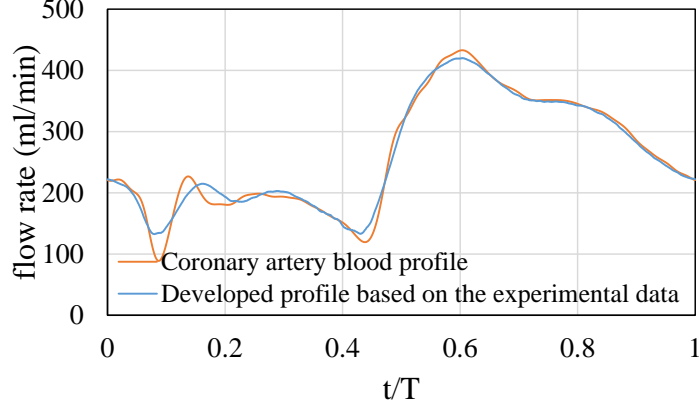


Figure B-3: The physiological pulsatile inlet velocity boundary condition (Davies et al. 2008).

Furthermore, an EverGreen 532 nm laser with 200 mJ at a fixed pulsing frequency of 15 Hz was used to illuminate the field of view. An adjustable optical slit was used to set the laser sheet thickness at 0.5 mm to minimise the out-of-plane loss of particle pairs. Two sets of 3-axis trimming platform linear stages were employed for both camera and laser head to be able to move them precisely. Images were captured with an array of 2025×1350 pixels. The field of view for each measurement was set to 9.15×6.1 mm, which resulted in the pixel size of $4.52 \mu\text{m}$. The frame rate of the camera was set to match the pulsing frequency of the laser.

The flow was seeded with hollow glass sphere particles with a nominal mean diameter of 8-12 μm and density of 1.1 g/cc resulting in a stokes number (Sk_D) of $Sk_D \ll 1$ which means the particles are able to follow the flow down to the length scales that can be resolved with the PIV measurement (Long et al. 2017). Due to the limited pulsation frequency of the laser (15 Hz) and the duration of the cardiac cycle (4.4 s), 66 image pairs (16 bit) were recorded for each cardiac cycle. The images were recorded for 16 consecutive pulsation cycles (1056 image pairs). In order to separate small turbulences from the main pulsatile fluctuations, a phase-average technique was utilised to calculate the mean variables as:

$$f_{pa}(x, y, z, t) = \frac{1}{N-1} \sum_{n=1}^{N-1} f(x, y, z, t + nT), \quad (5)$$

where f is a flow velocity components in different directions and N is the number of pulsation cycles ($N = 16$). The turbulent velocity fluctuations, $f'(x, y, z, t)$, in all directions were then calculated as:

$$f'(x, y, z, t) = f(x, y, z, t) - f_{pa}(x, y, z, t), \quad (6)$$

Based on the velocity fluctuations, TKE was calculated by the following equation:

$$TKE(x, y, z, t) = \left(\frac{1}{2} \right) \left(\overline{(u'(x, y, z, t))^2} + \overline{(v'(x, y, z, t))^2} \right), \quad (7)$$

where u' and v' are the velocity fluctuations in stream-wise and radial directions, respectively. Averaged TKE values were obtained using phase-average technique over all the 16 pulsation cycles. The image-processing was performed using PIVlab software (William Thielicke 2014) with two passes interrogation window sizes of 64×64 and 32×32 pixels with 50% overlap for both passes, leading to a spatial resolution of 0.14 mm in each direction.

The overall uncertainty associated with the PIV measurements comprises both systematic and measurement errors. The systematic errors arise both from geometric uncertainty, derived from casting tolerances, and from measurement uncertainties. As explained earlier, the measurement uncertainties from the flowmeter was measured to be 0.4% of the measured value. Based on the evaluation of systematic and measurement errors (American Society of Mechanical 2006), the overall uncertainty of the measured mean velocities for this study is estimated to be less than $\pm 2\%$.

Figure B-4 displays three phases of interest in this study including two phases with the maximum and minimum flow velocities during a cardiac cycle as well as a case with a steady flow velocity with the corresponding mean flow velocity of a cardiac cycle. As explained before for the PIV measurement of the pulsatile flow, different values of dt need to be used to make sure that the particle movements can be monitored in a set of image pairs. The shaded areas in Fig. B-4 display different dt values corresponding to different flow velocity changes in a pulsation cycle. A shorter dt is used for the grey shaded area compared to the light green shaded area that needs a longer dt . For example, for the jet flow regime, $dt = 50 \mu\text{m}$ is used for the phase with the maximum flow rate during a cardiac cycle, while $dt = 100 \mu\text{m}$ is used for the phase with the minimum flow rate during a cardiac cycle.

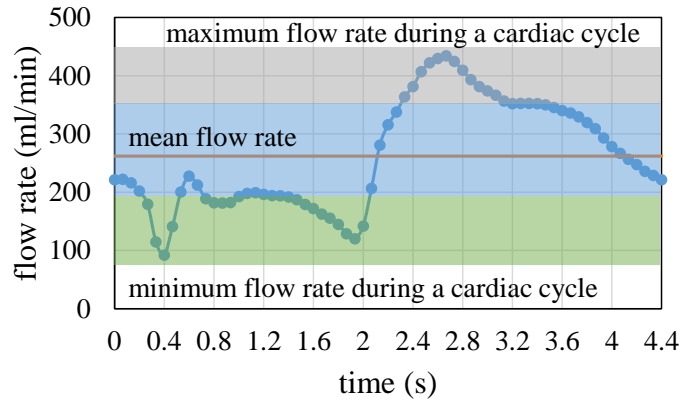


Figure B-4: Three phases of interest in a cardiac cycle for PIV measurement. Three shaded areas represent three different dt considered for PIV measurement corresponding to different flow rates.

As discussed before, different values of dt are required for the jet flow regime, starting from the centre of the blockage section with the minimum cross section, recirculation zone induced after the blockage between the wall and jet regime, and also downstream of the blockage, since the flow velocity changes noticeably in these regions. In this study, three different zones were selected as regions of interest, as shown in Fig. B-5. For all these time phases and stream-wise locations, dt was changed between $50 \mu\text{m}$ to $500 \mu\text{m}$. For example, for the recirculation zone, dt is set to $300 \mu\text{m}$ for the phase of the cardiac

cycle of the maximum velocity, while dt is set to $500 \mu\text{m}$ for the phase of the cardiac cycle of the minimum velocity.

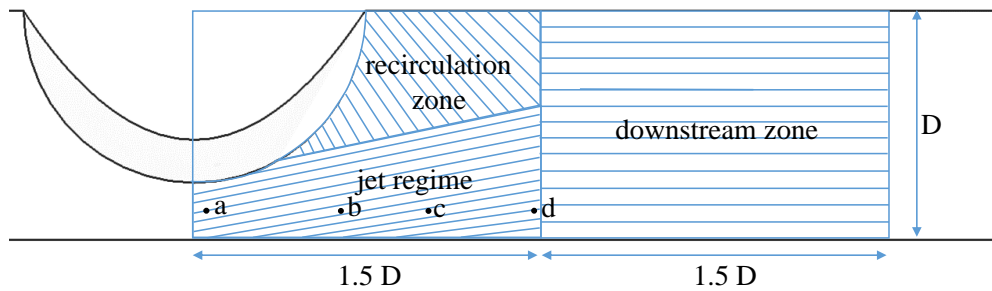


Figure B-5: Three regions of interest including recirculation zone, jet flow regime and downstream zone.

Results and discussion

Figure B-6 displays the velocity profile versus time during a cardiac cycle for different stream-wise locations (as shown in Fig. B-5) in the jet flow regime (radially started from the centre of artery at the location of the blockage) of a stenotic artery model with a 67% degree of stenosis. The results show that the velocity has the maximum value for the node closest to the centre of the jet regime (node a). The velocity drops as moving to the downstream of the blockage that mean that the effect of jet flow regime decreases gradually. The highest velocity is related to the closest node to the jet regime (node a) and the lowest velocity is related to the node which is located far downstream of the blockage (node d).

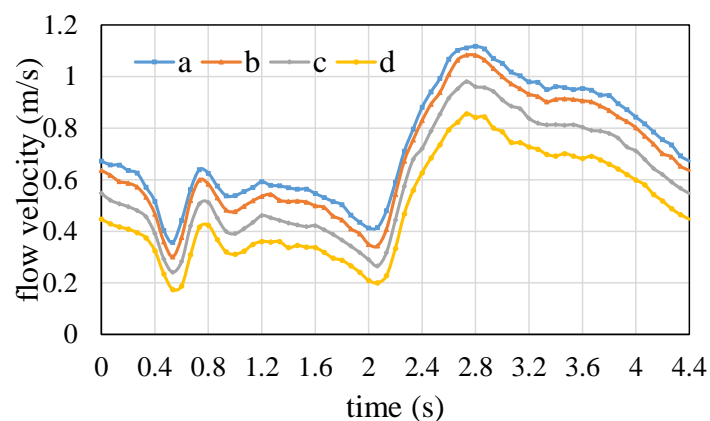


Figure B-6: Velocity profile versus time during a cardiac cycle for different stream-wise nodes in the jet flow regime (radially located on the centre of the jet regime).

Figure B-7 shows the stream-wise velocity contours, streamlines and velocity vectors for three different cases including minimum and maximum velocity during a cardiac cycle and the steady velocity corresponding to the mean velocity of a cardiac cycle for a stenotic artery model with a 67% degree of stenosis from the centre of stenosis to 3D downstream of the blockage. As mentioned in the methodology section, different values of dt were used for different flow regimes including jet regime, recirculation zone and downstream

of the flow each three phases during a cardiac cycle. The results show that the jet flow regime is stronger for the maximum velocity phase (Fig. B-7b) during a cardiac cycle compared to the minimum velocity phase (Fig. B-7a) and the mean velocity case (Fig. B-7c). Furthermore, the velocity vectors become almost uniform about the centre of the artery model downstream of the blockage area (about 3D), which is along with the gradually fading of the jet flow regime.

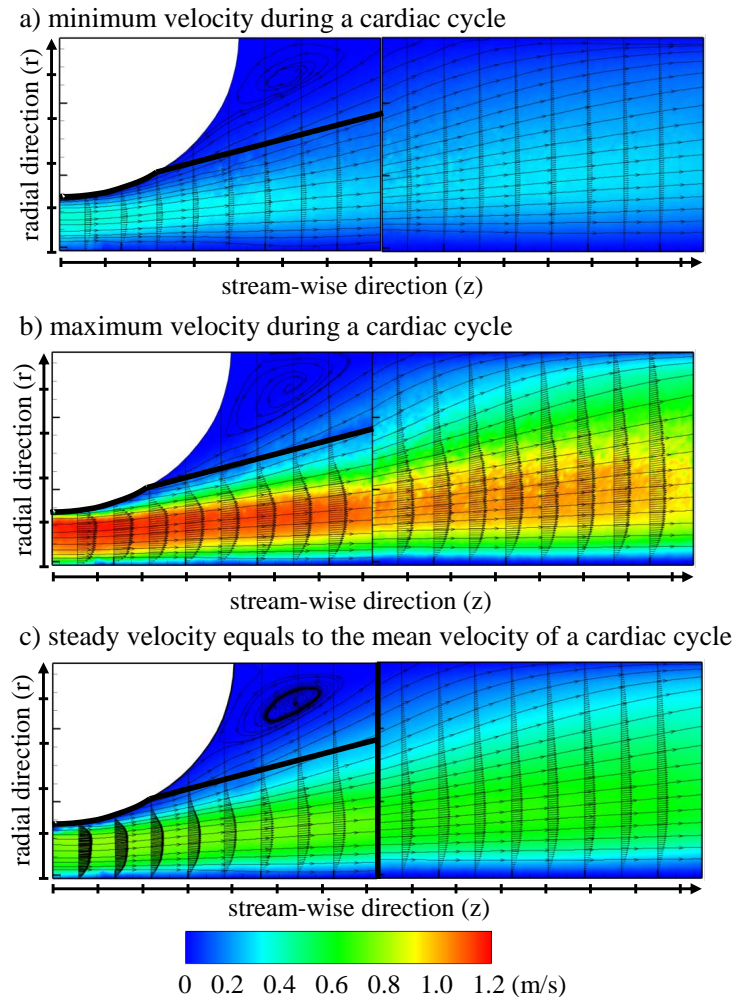


Figure B-7: Stream-wise velocity contours, streamlines and velocity vectors for three different cases including minimum and maximum velocity during a cardiac cycle and the steady velocity corresponding to the mean velocity of a cardiac cycle.

Figure B-8 displays the TKE profile for four different radially located lines distributed in stream-wise direction for three different phases of a cardiac cycle. The maximum TKE for all lines is related to the phase with maximum velocity during a cardiac cycle. While, the minimum TKE is related to the minimum velocity phase of a cardiac cycle. Furthermore, the TKE of the steady velocity case corresponding to the mean velocity of a cardiac cycle is between the minimum and maximum phases. TKE increases significantly near the jet flow regime for all cases. Furthermore, it is observed that the core of the jet flow region moves gradually to the other side of the stenotic artery by getting away from the centre of the blockage. The TKE profile for the line that is the closest to the centre of the blockage (line a) has its maximum value near the edges of the jet flow where the shear layer rate is the highest. A sudden increase in the value of the TKE for line a

compared to the other lines is related to the effect of strong shear layer near the centre of the blockage. In contrast, for line b and afterwards, the maximum TKE value occurs in the centre of the jet regime because the shear layer effect is reduced by getting away from the blockage centre. Hence, turbulence grows which results in increasing the TKE value from line b to line d.

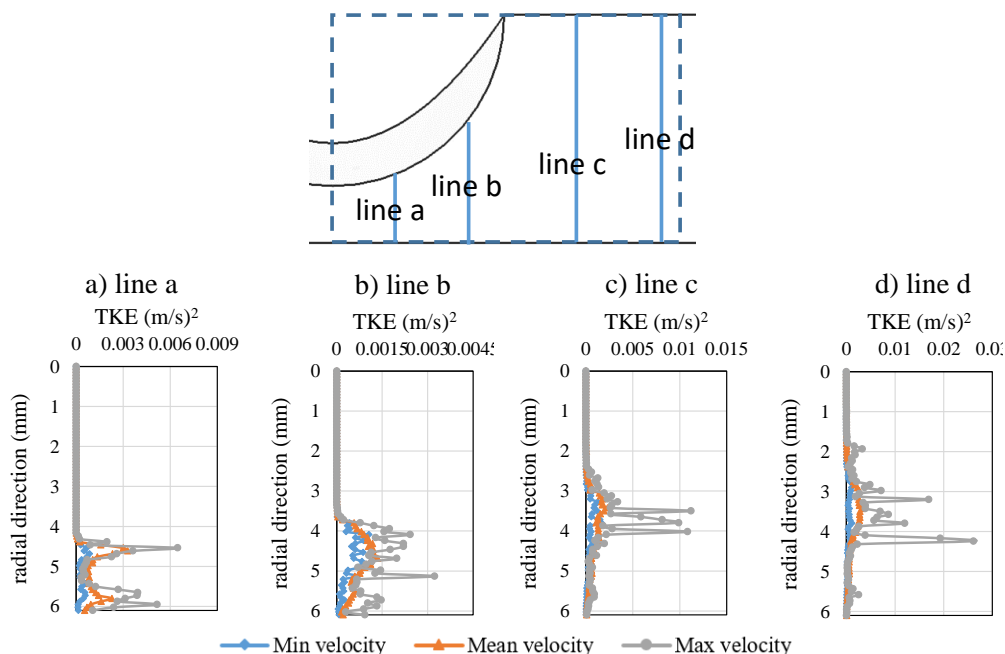


Figure B-8: TKE for four different radially located lines distributed in stream-wise direction from close to the centre of the blockage (line a) to downstream of it (line d).

Conclusion

In this study, PIV experiment was used to investigate the flow features near the blockage section of a stenosed coronary artery model with the pulsatile flow. Jet flow regime-induced by the blockage inside the artery, recirculation zone between the jet regime and the artery wall as well as the further downstream of the blockage section were studied for three different time phases including the minimum and maximum flow rates during a cardiac cycle and also a steady flow case with the corresponding mean flow velocity of a cardiac cycle inside a coronary artery. The most challenging parts of PIV measurement for these kinds of problem included:

- Selecting proper material for the casted artery model. A Sylgard 184 silicone was used which is both transparent and has the same refractive index of the blood mimicking fluid.
- Proper choice of the blood mimicking fluid. A mixture of distilled water and Glycerine was used that matches the blood viscosity and has the same refractive index as the casted artery model.
- Small region of interest. A set of macro lens as well as three sets of extension tubes were used to focus on the field of view.

- Formation of the jet flow effect after the blockage section. Different timings for PIV measurement were used for the jet flow regime, recirculation zone and its further downstream.
- Pulsatile nature of the blood flow inside the arteries. Different timings for PIV measurement were used with respect to the corresponding velocity during different phases of a cardiac cycle.

By adopting the above-mentioned techniques, it was shown that PIV could be used to study the flow features in this problem. The results showed that the highest velocity and TKE are related to the case with the maximum velocity during a cardiac cycle and the lowest is related to the phase with a minimum flow velocity during a cardiac cycle.

References

- American Society of Mechanical E (2006). *Test uncertainty*. New York, N.Y.: American Society of Mechanical Engineers.
- Biswas D, Casey D, Crowder D, Steinman D, Yun Y, and Loth F (2016). “Characterization of transition to turbulence for blood in a straight pipe under steady flow conditions”. *Journal of Biomechanical Engineering* 138.7, pp. 1–12.
- Charonko J, Karri S, Schmieg J, Prabhu S, and Vlachos P (2009). “In vitro, time-resolved PIV comparison of the effect of stent design on wall shear stress”. *Annals of Biomedical Engineering* 37.7, pp. 1310–1321.
- Davies JE, Parker KH, Francis DP, Hughes AD, and Mayet J (2008). “What is the role of the aorta in directing coronary blood flow?” *Heart* 94.12, pp. 1545–1547.
- Long S, Lau TCW, Chinnici A, Tian ZF, Dally BB, and Nathan GJ (2017). “Experimental and numerical investigation of the iso-thermal flow characteristics within a cylindrical chamber with multiple planar-symmetric impinging jets”. *Physics of Fluids* 29.10, p. 105111.
- Peterson SD and Plesniak MW (2008). “The influence of inlet velocity profile and secondary flow on pulsatile flow in a model artery with stenosis”. *Journal of Fluid Mechanics* 616, pp. 263–301.
- Tambasco M and Steinman DA (2003). “Path-dependent hemodynamics of the stenosed carotid bifurcation”. *Annals of Biomedical Engineering* 31.9, pp. 1054–1065.
- Usmani AY and Muralidhar K (2016). “Pulsatile flow in a compliant stenosed asymmetric model”. *Experiments in Fluids* 57.12, pp. 186–210.
- Waller BF (1989). “The eccentric coronary atherosclerotic plaque: morphologic observations and clinical relevance”. *Clinical Cardiology* 12.1, pp. 14–20.
- William Thielicke EJS (2014). “PIVlab – towards user-friendly, affordable and accurate digital particle image velocimetry in MATLAB”. *Journal of Open Research Software* 2.1, e30.
- Yazdi SG, Geoghegan PH, Docherty PD, Jermy M, and Khanafer A (2018). “A review of arterial phantom fabrication methods for flow measurement using PIV techniques”. *Annals of Biomedical Engineering* 46.11, pp. 1697–1721.
- Young DF and Tsai FY (1973). “Flow characteristics in models of arterial stenoses — I. Steady flow”. *Journal of Biomechanics* 6.4, pp. 395–410.

Zhu C, Seo JH, and Mittal R (2018). “Computational modelling and analysis of haemodynamics in a simple model of aortic stenosis”. *Journal of Fluid Mechanics* 851, pp. 23–49.